JCTC Journal of Chemical Theory and Computation

Extracting Markov Models of Peptide Conformational Dynamics from Simulation Data

Verena Schultheis, Thomas Hirschberger, Heiko Carstens, and Paul Tavan*

Lehrstuhl für Biomolekulare Optik, Ludwig-Maximilians-Universität, Oettingenstrasse 67, 80538 München, Germany

Received February 3, 2005

Abstract: A high-dimensional time series obtained by simulating a complex and stochastic dynamical system (like a peptide in solution) may code an underlying multiple-state Markov process. We present a computational approach to most plausibly identify and reconstruct this process from the simulated trajectory. Using a mixture of normal distributions we first construct a maximum likelihood estimate of the point density associated with this time series and thus obtain a density-oriented partition of the data space. This discretization allows us to estimate the transfer operator as a matrix of moderate dimension at sufficient statistics. A nonlinear dynamics involving that matrix and, alternatively, a deterministic coarse-graining procedure are employed to construct respective hierarchies of Markov models, from which the model most plausibly mapping the generating stochastic process is selected by consideration of certain observables. Within both procedures the data are classified in terms of prototypical points, the conformations, marking the various Markov states. As a typical example, the approach is applied to analyze the conformational dynamics of a tripeptide in solution. The corresponding high-dimensional time series has been obtained from an extended molecular dynamics simulation.

1. Introduction

The analysis of time series[1] is important in many areas of science. Depending on the data considered, different methods are applied.[1−4] For instance, in speech recognition[5] and other fields[6] hidden Markov models[7] found important applications. They describe a dynamical system by two parametric time-discrete processes: an underlying nonobservable Markov process[8] and an observation process, defined by a sequence of conditionally independent random variables depending at each time step only on the state of the Markov chain. In many of these applications, relatively low-dimensional data are analyzed. Frequently the treatment of higher dimensional data can be simplified by first reducing the dimension, for instance using a principal component analysis.[9] Generally, the analysis of high-dimensional data mapping complex dynamical systems requires special care and the application of methods, which by construction can cope with the peculiarities of the metrics in high-dimensional data spaces.

Here, we consider a class of extremely high-dimensional and complex dynamical systems, which exhibit a largely stochastic behavior and show Markovian transitions between coarse-grained states. A typical example for such systems is the thermal motion of proteins or peptides[10] in solution. Associated time series are generated by molecular dynamics (MD) simulations[11,12] of that motion.

MD simulations treat biological macromolecules and their solvent environments as classical many-body systems composed of atoms and account for the quantum mechanical forces acting on the nuclei and caused by the electrons through a parametrized molecular mechanics force field. In MD the coupled Newtonian equations of atomic motion are integrated numerically using time steps Δt of typically 1 fs. The result of such a simulation is a trajectory $\mathbf{x}_t = \mathbf{x}(t\cdot\Delta t)$, $t = 1, 2, \ldots T$, in a high-dimensional space $\mathbf{R}^D$ (e.g. the space $\mathbf{R}^{3N}$ of the Cartesian coordinates of all $N = 100-10\,000$ atoms of a protein) describing the time sequence of configurations $\mathbf{x}_t$ sampled by the macromolecule in solution upon thermal motion. Typical simulation times are nowadays in the range of a few tens of nanoseconds ($T \approx 10^7$).

* Corresponding author phone: +49-89-2180-9220; e-mail: tavan@physik.uni-muenchen.de.

10.1021/ct050020x CCC: $30.25
Published on Web 06/08/2005

Proteins are prototypes of complex dynamical systems in soft condensed matter. In addition to high-frequency thermal fluctuations of the atoms around their equilibrium positions that are also found in solids, they show large-scale low-frequency transitions between several metastable states, the so-called conformations.[13] This slow conformational dynamics is essential for protein function in biology. Various methods[14−21] have been suggested for the extraction of protein conformations from MD trajectories. Some make use of the fact that the conformations are marked by minima of the energy landscape,[15,19,22] some apply clustering procedures based on structural similarities,[16,21] and others[14] analyze the potential energy time series by the means of recurrence plot analysis.[23]

Grubmüller and Tavan[13] have demonstrated for a simplified protein model that its conformational dynamics can be described by a simple Markov model composed of only a few conformational states. Following this principle and considering only a few so-called essential degrees of freedom Dellnitz, Schütte, and others[18,20] chose a regular lattice for discretization of the thus reduced configuration space and determined the transfer matrix of the system by counting transitions between lattice cells. They identified the conformational states defining a coarse-grained Markov model by a rather complicated analysis of the eigenvectors and -values of the transfer matrix.

Following these general concepts we here propose an alternative approach toward the analysis of high-dimensional time series, which exhibit the characteristics of a Markov chain switching among a few states. In particular, the use of a density-oriented discretization of the data space[24−26] allows us to avoid the *curse of dimensionality* inherent to grid partitions. That curse expresses the common problem, that the number of parameters, which have to be statistically estimated from the data for the construction of a simplified model, grows exponentially with the dimension of the data space.

By modifying and expanding a self-organizing and biologically plausible neural network model originally suggested for the clustering of data sets[27] but without explicitly employing the language of neural networks, we construct from the time series a transfer matrix, whose dimension is kept relatively small due to the use of the density-oriented discretization.[25] As opposed to the Kohonen algorithm[28,29] used in ref 27 for discretization, our approach does not introduce distortions into the metrics of the data space.[24,30] The analysis of the transfer matrix is either performed by a nonlinear dynamics related to the neural network used previously for clustering[27] or by a deterministic coarse-graining procedure. Both methods generate hierarchies of Markov models at varying coarseness and provide the means to identify the particular hierarchy level which most plausibly maps the generating Markov process. We start with the explanation of the methods, and, to provide a relevant example, we subsequently analyze the MD trajectory of a small peptide in water.

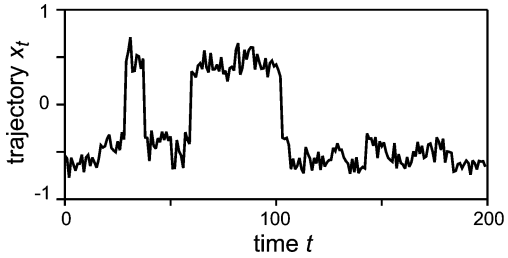

Figure 1. The first 200 steps of a time series of one-dimensional data created by a four-state Markov process. At the first glance, one can distinguish two ranges of frequent x_t values.

2. Method

For a simple graphical illustration of the employed concepts and methods, we first introduce a one-dimensional model time series, which, despite its simplicity and low-dimensionality, covers key ingredients of the problem. Figure 1 shows the first 200 steps of this time series $\mathcal{X} = \{x_t | t = 1, 2, ..., T\}$, which covers $T = 10^6$ data points. The series has been generated from the Markov matrix

$$\mathbf{C}^{ex} = \begin{pmatrix} 0.8 & 0.17 & 0 & 0 \\ 0.2 & 0.8 & 0.03 & 0 \\ 0 & 0.03 & 0.8 & 0.2 \\ 0 & 0 & 0.17 & 0.8 \end{pmatrix} \tag{1}$$

by mapping the associated four-state Markov chain onto a one-dimensional dynamical system. The Markov chain generates *slow* transitions *among* the states i, $i = 1, ..., 4$. These transitions are differentiated by certain degrees of slowness: Very slow are the $2 \leftrightarrow 3$ transitions, much faster but still slow are the transitions $1 \leftrightarrow 2$ and $3 \leftrightarrow 4$. A subsequent random process completes the mapping by creating *fast* one-dimensional jumps *within* the four coarse-grained states (jumps drawn from normal distributions $g(x|x_i,\sigma)$ of standard deviation $\sigma = 0.07$ and centered at $x_i \in \{\pm 0.4, \pm 0.6\}$, see Figure 2). The resulting one-dimensional time series shares the characteristics of fast fluctuations within and differently slow transitions among coarse-grained states with peptide and protein conformational dynamics.

Note that the Markov matrix (1) generating our model time series obeys the property of detailed balance,[8,31] which requires that there are nonzero numbers f_r with

$$C^{ex}_{r'r} f_r = C^{ex}_{rr'} f_{r'}$$

Up to a constant factor these numbers f_r are the components $p_{r,stat}$ of the stationary distribution $\mathbf{p}_{stat} = (0.17, 0.2, 0.2, 0.17)^T/0.74$, which is the right eigenvector of $\mathbf{C}^{ex}$ to the eigenvalue $\lambda_1 = 1$. In general, R-dimensional Markov matrices $\mathbf{C}$ generating a time discrete stochastic process

$$\mathbf{p}(t + \Delta t) = \mathbf{C}\mathbf{p}(t)$$

and obeying detailed balance have a set of nice mathematical properties:[31] (i) although they are usually nonsymmetric, their eigenvalues λ_r, $r = 1, ..., R$, are all real with $1 \geq \lambda_r > 0$ ($\lambda_r \geq \lambda_{r'}$ for $r < r'$), (ii) for simply connected state spaces there is exactly one largest eigenvalue $\lambda_1 = 1$ marking the

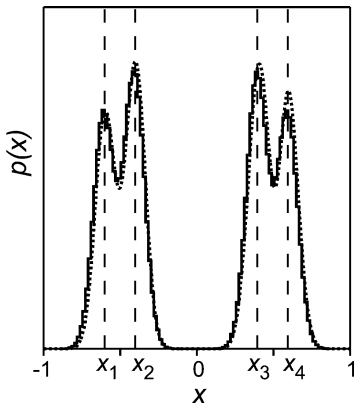

Figure 2. Histogram (solid line) and normal mixture density estimate (dotted line) of all $T = 10^6$ data points $x_t \in \mathcal{X}$ (both estimates comprise the same number $R = 100$ of local components). The four density maxima marking the Markov states are clearly distinguished. Within the two pairs (1,2) and (3,4) of the generating Gaussians considerable overlaps and between the pairs a strict separation are observed.

stationary distribution $\mathbf{p}_{stat}$, and (iii) for every initial distribution $\mathbf{p}(0)$ the iteration of the process converges to $\mathbf{p}_{stat}$.

For physical systems in thermal equilibrium the property of detailed balance frequently applies and then derives from the principle of microscopic reversibility. By applying the arguments in chapter 5.3.6b of ref 8, the following sufficient condition may be formulated for the equilibrium conformational fluctuations of a peptide sampled by an MD simulation: If the resulting trajectory $\mathcal{X}$ provides a statistically sufficient sampling of the accessible configuration space and if the observed transitions among arbitrarily defined coarse-grained states are statistically independent of the previous history of the process, i.e., are Markovian, then the associated conformational dynamics obeys detailed balance (like our simple model process does by construction).

For this simple example the particular task of time series analysis treated in this paper can now be stated as follows: Identify and reconstruct the generating Markov model (1) from the observed time series $\mathcal{X}$ as well as possible!

2.1. Partitioning the Data Space. For an ergodic system the distribution of the configurations $\mathbf{x}_t$ sampled by the trajectory $\mathcal{X}$ in the limit $t \to \infty$ defines the so-called invariant density $p_{inv}(\mathbf{x})$.[32] A parametric model for $p_{\mathrm{inv}}(\mathbf{x})$ can be estimated from a sufficiently extended sample trajectory $\mathcal{X}$ by using a mixture

$$\hat{p}(\mathbf{x}|\mathcal{W},\sigma) = \frac{1}{R}\sum_{r=1}^{R} g(\mathbf{x}|\mathbf{w}_r,\sigma) \tag{2}$$

of R univariate normal distributions $g(\mathbf{x}|\mathbf{w}_r, \sigma)$ of identical widths σ and statistical weights $1/R$ centered at points $\mathbf{w}_r \in \mathbf{R}^D$. With the exception of the number R, the model parameters, i.e., the *codebook* $\mathcal{W} \equiv \{\mathbf{w}_r | r = 1,...., R\}$ and the common width σ, are adapted to the data set $\mathcal{X}$ according to the *maximum likelihood* criterion[33] by a safely converging deterministic annealing algorithm.[24−26,34] The extraordinary robustness of this quite simple algorithm critically depends on the choice of identical widths σ for the normal distributions, although an extension toward more complicated multivariate mixture models is available.[25,26] The algorithm guarantees that the univariate normal distributions associated with the resulting optimal parameters $\mathcal{W}^{ML}$ and σ^{ML} represent roughly the same number of data points each. This property of the optimal density estimate (2) is called *load balance*[24−26] and induces a first guideline for the choice of the remaining model parameter R through the following considerations.

The components of the mixture model (2) are R class-conditional probability densities and indicate how the data belonging to class r are distributed. By Bayes' theorem every point $\mathbf{x} \in \mathbf{R}^D$ is assigned to the class r with the probability[25]

$$\hat{P}(r|\mathbf{x},\mathcal{W},\sigma) = \frac{(1/R)\, g(\mathbf{x}|\mathbf{w}_r,\sigma)}{\hat{p}(\mathbf{x}|\mathcal{W},\sigma)} \tag{3}$$

Due to the normalization

$$\sum_{r=1}^{R} \hat{P}(r|\mathbf{x},\mathcal{W},\sigma) = 1 \tag{4}$$

the probabilities (3) define a fuzzy partition of the data space when considered as functions of $\mathbf{x}$. In the limit $\sigma \to 0$ this partition becomes a crisp Voronoi tessellation[35] of the data space. Because of the load balance, each of the partition volumes covers approximately the same number T/R of data points, independently of the dimension D of the data. For a given data set of size T, the choice of the codebook size R determines T/R and thus defines the statistical quality, at which each $\mathbf{w}_r \in \mathcal{W}$ is estimated from the data $\mathbf{x}_t \in \mathcal{X}$.[26] Therefore, this type of density-oriented data space discretization can avoid the curse of dimensionality mentioned in the Introduction. For our one-dimensional example, Figure 2 compares a grid discretization (histogram) with the mixture model (2) and demonstrates the quality of the mixture estimate. Note that, because of load balance, the distribution $\tilde{p}(w)$ of codebook vectors closely models the distribution $p_{inv}(x)$ of the data ($\tilde{p} \approx p_{inv}$).[24]

2.2. Transfer Operator. The transfer operator describing the observed dynamical system is estimated using the partition described above. To simplify the notation, we extract from the trajectory $\mathcal{X}$ the set Y of all $T - 1$ pairs $y_t \equiv (\mathbf{x}_t, \mathbf{x}_{t+1})$ and define the correlation product

$$\langle f(\mathbf{x}_{t+1}) g(\mathbf{x}_t)\rangle_Y \equiv \frac{1}{T-1}\sum_{y_t \in Y} f(\mathbf{x}_{t+1}) g(\mathbf{x}_t) \tag{5}$$

where f and g are functions of $\mathbf{x}_t$. The transfer matrix $\mathbf{C}$ defined by the partition (3) then is[36]

$$C_{rr'} = \frac{\langle \hat{P}(r|\mathbf{x}_{t+1},\mathcal{W},\sigma)\hat{P}(r'|\mathbf{x}_t,\mathcal{W},\sigma)\rangle_Y}{\langle \hat{P}(r'|\mathbf{x}_t,\mathcal{W},\sigma)\rangle_Y} \tag{6}$$

Clearly, $\mathbf{C}$ depends on the parameters $\{\mathcal{W}, \sigma\}$ as well as on the choice of the codebook size R. There are R^2 matrix-elements $C_{rr'}$, which have to be statistically estimated from the $T - 1$ data points $y_t \in Y$ by evaluation of the correlation products in eq 6. To ensure sufficient statistics one should therefore demand that $R^2/T \ll 1$: This requirement thus represents a second guideline for the choice of R. Note that large values of σ, though helping to improve the statistics,

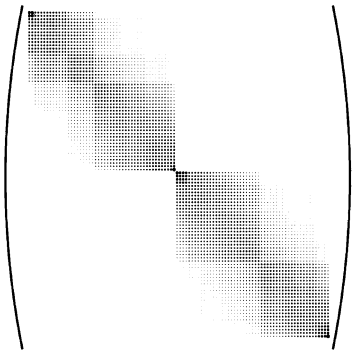

Figure 3. Transfer matrix (6) for the sample trajectory $\mathcal{X}$. The radii of the circles code the sizes of the matrix elements. On a coarse level, two diagonal blocks with non-zero elements are seen. The elements outside these blocks are substantially smaller and, therefore, are invisible here. Each of the coarse diagonal blocks decomposes into two diagonal sub-blocks, partly linked by off-diagonal blocks.

decrease the information content of **C** by smoothening. This aspect of the dependence of **C** on the fuzziness parameter σ is further discussed in section 2.7.

Because the partition functions $\hat{P}(r|\mathbf{x}, \mathscr{W}, \sigma)$ are centered around the points $\mathbf{w}_r \in \mathbf{R}^D$ and assume values close to 1 for points $\mathbf{x}$ near $\mathbf{w}_r$, the matrix (6) codes the spatial correlations between consecutive points. The elements of **C** are non-negative, and its columns are normalized to 1 ($\forall r'$: $\sum_{r=1}^{R} C_{rr'} = 1$). Therefore, **C** is an R-state Markov matrix. As it is generated from a trajectory, the associated state space is simply connected. Correspondingly, **C** has only one right eigenvector $\mathbf{p}_{stat}$ to the eigenvalue 1 marking the stationary state. As one can easily show from the definition (6) of the transfer matrix **C** and using the normalization (4) of the partition functions the stationary distribution is given by the loads of the partition volumes, i.e., $p_{r,stat} \approx \langle \hat{P}(r|\mathbf{x}_t, \mathscr{W}, \sigma)\rangle_Y$ up to corrections smaller than $1/T$. The property of load balance characteristic for our partition then implies that $\mathbf{p}_{stat}$ approximately represents a uniform distribution, that is $p_{r,stat} \approx 1/R$.

Figure 3 shows the transfer operator (6) for the time series of Figure 1. This matrix, like all other Markov matrices discussed further below, obeys detailed balance to a very good approximation: the statistical errors $|C_{rr'}p_{r',stat} - C_{r'r}p_{r,stat}|/\max\{C_{r'r}p_{r,stat}\}$ are all smaller than 1%. Because $\mathbf{p}_{stat}$ is nearly uniform, it is nearly symmetric. Apart from the eigenvalue 1, the matrix has three sizable eigenvalues (0.969, 0.442, 0.421), whereas all the remaining 96 eigenvalues are smaller than 0.002. According to refs 20 and 18 such a distribution of eigenvalues indicates the existence of two long-lived or four somewhat shorter lived metastable states. This dynamical structure of the sample trajectory is also visible in the hierarchical block structure of the depicted matrix, which clearly reveals the underlying Markov process (1). The visibility of that Markov process results from ordering the codebook elements w_r according to size ($w_r < w_{r'} \Rightarrow r < r'$), which is only feasible in one dimension.

2.3. Analysis of the Transfer Operator. Since there is no natural ordering of the codebook vectors $\mathbf{w}_r$ in higher-dimensional cases, the analysis of transfer matrices requires other means than simple visual inspection. For this purpose

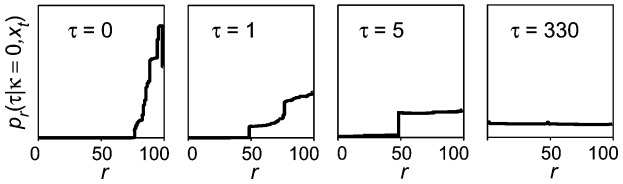

Figure 4. Linear ($\kappa = 0$) dynamics eq 8 elicited by the randomly chosen point $x_t = 0.66$ for **C** from Figure 3. Left to right: The initial distribution ($\tau = 0$) associated with x_t spreads rapidly filling predominantly the right quarter of the state space ($\tau = 1$); within the next five time steps a second metastable state appears covering predominantly the right half of the state space; at $\tau = 330$ the nearly uniform stationary distribution is reached.

we define the time-dependent probability vector[37]

$$\mathbf{p}(\tau|\mathbf{x}_t) \equiv \begin{pmatrix} \hat{P}(1,\tau|\mathbf{x}_t, \mathscr{W}, \sigma) \\ \vdots \\ \hat{P}(R,\tau|\mathbf{x}_t, \mathscr{W}, \sigma) \end{pmatrix} \tag{7}$$

whose initial components $\hat{P}(r, 0|\mathbf{x}_t, \mathscr{W}, \sigma) = \hat{P}(r|\mathbf{x}_t, \mathscr{W}, \sigma)$ are given by the posterior probabilities (3) of a given point $\mathbf{x}_t$. Furthermore we consider the evolution of the components $p_r(\tau)$ of $\mathbf{p}(\tau|\mathbf{x}_t)$ described by the following family of nonlinear differential equations

$$\frac{d}{d\tau} p_r = (\mathbf{L}\mathbf{p})_r + \kappa p_r(p_r - \mathbf{p}^2) \tag{8}$$

where the family parameter $\kappa \geq 0$ scales the nonlinear term. The matrix **L** derives from the transfer operator **C** and from the associated sampling time step $\Delta\tilde{t}$ according to

$$\mathbf{L} = \frac{1}{\Delta\tilde{t}} \ln \mathbf{C} \tag{9}$$

Note that the nonlinear dynamics (8) conserves the normalization $\sum_{r=1}^{R} p_r(\tau|\mathbf{x}_t) = 1$ of the probabilities. Since the time evolution of $\mathbf{p}(\tau|\mathbf{x}_t)$ depends on κ, we extend the notation to $\mathbf{p}(\tau|\kappa, \mathbf{x}_t)$. To calculate that evolution numerically, a discretization of (8) is used as described in Appendix A.

For an understanding of the dynamics (8), we look at the linear and the nonlinear terms of eq 8 separately. The purely linear dynamics (i.e. $\kappa = 0$) describes a Markov process of probability redistribution. Independent of the initial condition $\mathbf{x}_t$, the distribution $\mathbf{p}(\tau|\kappa = 0, \mathbf{x}_t)$ is temporarily caught in some metastable intermediate states but eventually converges toward the single stationary right eigenvector $\mathbf{p}_{stat}$ of **C**. This process is illustrated in Figure 4, which also demonstrates that $\mathbf{p}_{stat}$ is nearly uniform as claimed above.

As we explain in Appendix B, the purely nonlinear dynamics has $2^R - 1$ stationary points, each given by distributions $\mathbf{p}^{\mathscr{M}}$, which are uniform on a nonempty subset $\mathscr{M} \subset \{1,...., R\}$ and vanish elsewhere. However, only R of these distributions, the δ-distributions $p_r = \delta_{rs}$, are stable attractors of the nonlinear dynamics. The attractor δ_{rs} selected by the dynamics is defined by the largest component $p_s(0|\kappa,\mathbf{x}_t)$ of the initial distribution. Thus, the nonlinearity generates a winner-takes-all dynamics of *Darwinian selection*[27] and may be considered as the inverse of the diffusion operator.

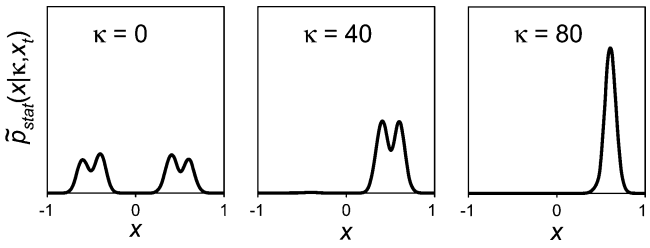

Figure 5. Stationary virtual densities associated with the starting point $x_t = 0.66$ at various strengths κ of the nonlinearity. At $\kappa = 0$ the attractor is the mixture model (2) of the invariant density depicted in Figure 2, because the generating Markov model (1) obeys detailed balance. At increasing κ the virtual density first ($\kappa = 40$) becomes confined to the two overlapping Gaussian components $i = 3$, 4 and eventually ($\kappa = 80$) to component $i = 4$ of the generating model shown in Figure 2.

By combining these mutually counteracting processes as given by eq 8 one obtains a dynamics capable of stabilizing and focusing metastable intermediates of the linear ($\kappa = 0$) relaxation process. It exhibits N_κ attractors $\mathbf{p}^n_{stat}(\kappa)$, $n = 1,...., N_\kappa$, where N_κ increases with κ ($1 \le N_\kappa \le R$). The specific attractor $\mathbf{p}^n_{stat}(\kappa)$ selected by the dynamics depends on the initial condition $\mathbf{x}_t$ and, therefore, classifies these initial conditions by $n \equiv n(\mathbf{x}_t|\kappa)$. Figure 1 in the Supporting Information illustrates how larger strengths κ of the nonlinearity stabilize increasingly short-lived metastable intermediates, prevent their diffusive spreading, and correspondingly identify metastable states at a decreasing level of coarse-graining.

2.4. Virtual Density. The distributions $\mathbf{p}(\tau|\kappa, \mathbf{x}_t) \in \mathbf{R}^R$ can be mapped onto *virtual*[38] probability densities

$$\tilde{p}(\mathbf{x}|\tau,\kappa,\mathbf{x}_t) \equiv \sum_{r=1}^{R} p_r(\tau|\kappa,\mathbf{x}_t) g(\mathbf{x}|\mathbf{w}_r,\sigma) \tag{10}$$

in the data space. For a given parameter set $\mathcal{Z} = \{\mathcal{W}, \sigma, \mathbf{C}\}$ the virtual density $\tilde{p}(\mathbf{x}|\tau,\kappa,\mathbf{x}_t)$ depends on the time τ, the nonlinearity parameter κ, and the initial condition $\mathbf{x}_t$. By eq 10, the dynamics (8) of the distributions $p_r(\tau|\kappa,\mathbf{x}_t)$ is mapped onto an equivalent temporal evolution of the virtual densities. At convergence one obtains the stationary virtual density $\tilde{p}^n_{stat}(\mathbf{x}|\kappa)$, which is associated with the initial data point $\mathbf{x}_t$ by the dynamics [$n \equiv n(\mathbf{x}_t|\kappa)$]. Particularly in the linear case ($\kappa = 0$) and for a transfer matrix (6) obeying detailed balance,[31] the virtual density $\tilde{p}(\mathbf{x}|\tau,\kappa,\mathbf{x}_t)$ converges for each $\mathbf{x}_t$ toward the mixture model (2) of the invariant density (cf. Figure 2 in the Supporting Information).

For increasing values of the nonlinearity κ, Figure 5 depicts the mapping (10) of the stationary distributions $\mathbf{p}^n_{stat}(\kappa)$ (see Figure 1 of the Supporting Information) onto the corresponding stationary virtual densities $\tilde{p}^n_{stat}(x|\kappa)$. At growing nonlinearity κ these densities $\tilde{p}^n_{stat}(x|\kappa)$ are confined to increasingly narrow and short-lived substructures of our model (2) for the invariant density. Depending on the strength κ of the nonlinearity, differently coarse-grained classes $\tilde{p}^n_{stat}(x|\kappa)$ are associated with the initial condition x_t. Thus, the stationary virtual densities turn out to represent density models for the metastable states.

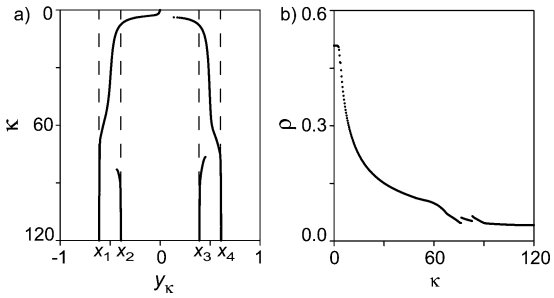

Figure 6. (a) Prototypes y_κ for $\kappa \in [0,120]$ and all data $x_t \in \mathcal{X}$. For comparison also the centers x_i for the four Gaussians associated with the states of the original Markov chain (1) are indicated by dashed lines. (b) Dependency of the average spread ρ of the stationary virtual densities on κ. The initial value $\rho \approx 0.5$ decreases almost monotonously with growing κ. At values of k near bifurcations in (a) $\rho(\kappa)$ is steeper. The small discontinuities of $\rho(\kappa)$ in the vicinity of bifurcations are due to numerics.

2.5. Moments of the Virtual Density. The first moments

$$\mathbf{y}^n_\kappa = \int \mathbf{x}\ \tilde{p}^n_{stat}(\mathbf{x}|\kappa) dx \tag{11}$$

of the stationary virtual densities (10) are obtained by integrating over the local normal distributions as[39]

$$\mathbf{y}^n_\kappa = \sum_{r=1}^{R} \mathbf{w}_r p^n_{r,stat}(\kappa) \tag{12}$$

Because at each κ the label n classifies the $\mathbf{x}_t$, the stationary solutions of (8) thus associate to each data point $\mathbf{x}_t \in \mathbf{R}^D$ a prototypical point $\mathbf{y}^n_\kappa \in \mathbf{R}^D$.

For our sample trajectory $\mathcal{X}$, Figure 6a depicts all prototypes y^n_κ associated with the $x_t \in \mathcal{X}$ as a function of the nonlinearity parameter $\kappa \in [0, 120]$. The figure shows that they remain invariant over wide ranges of κ while exhibiting bifurcations at certain critical values κ_i. The prototypes y^n_κ mark metastable states, characterized by fast transitions within, and slow transitions among the states of the original two-stage Markovian dynamics x_t. According to Figure 6, the boundary between *slow* and *fast* shifts toward shorter time scales with increasing κ because more and more short-lived metastable states are identified. At large κ the nonlinear dynamics eventually identifies the four prototypical points x_i characterizing the states of the original Markov model (1). Thus, the depicted bifurcation pattern reflects the hierarchical block structure of the transfer matrix (cf. Figure 3) analyzed by the nonlinear dynamics (8) at varying κ.

Higher moments of the stationary virtual densities can be calculated analogously. For a given initial condition $\mathbf{x}_t$ the variance is given by

$$\mathcal{V}[\mathbf{x}_t] = \sum_{r=1}^{R} p^{n(\mathbf{x}_t)}_{r,stat}(\kappa) [\mathbf{y}^{n(\mathbf{x}_t)}_\kappa - \mathbf{w}_r]^2 + \sigma^2 \tag{13}$$

and is—apart from the constant variance σ^2 of the Gaussians g in (10)—the sum of the squared distances between the prototypes $\mathbf{y}_\kappa$ and the codebook vectors $\mathbf{w}_r$ weighted by the probabilities (7). The value of $\rho(\mathbf{x}_t) \equiv \sqrt{\mathcal{V}[\mathbf{x}_t] - \sigma^2}$ mea-

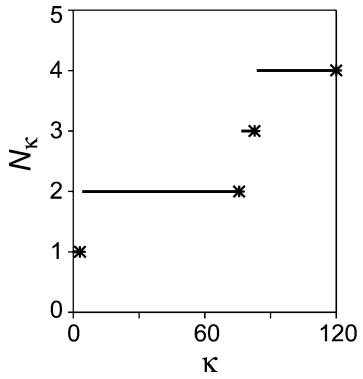

Figure 7. Number N_κ of prototypes of the trajectory from Figure 1. The asterisks mark the values of κ_ℓ, at which bifurcations occur in Figure 6a, and the value $\kappa_{max} = 120$.

sures the spread of the virtual density in data space. The dependency of the data average spread $\rho \equiv \langle \rho(\mathbf{x}_t) \rangle_Y$ on κ is plotted in Figure 6b and clearly indicates the contraction of the $\tilde{p}_{stat}$ with increasing κ.

2.6. Hierarchical Classification. For higher-dimensional dynamics one cannot visualize bifurcation patterns. Therefore other means are required to obtain insight into the hierarchy of classes identified by the nonlinear dynamics at increasing κ. A generally applicable procedure is to determine all prototypes (12) for all vectors $\mathbf{x}_t \in \mathcal{X}$, which results for each value of κ in a prototype set $\mathcal{P}_\kappa = \{\mathbf{y}_\kappa^n | n = 1,...,N_\kappa\}$ (cf. Figure 6a). The number N_κ of different stationary solutions can then be plotted as a function of κ and gives a first insight into the coarse-grained structure of the dynamics.

Figure 7 shows such a plot for our sample dynamics. The number N_κ grows monotonically with κ and remains constant within certain intervals $[\kappa_\ell, \kappa_{\ell+1}]$ ($\ell = 1, 2,...$ and $\kappa_1 < \kappa_2 < ...$). These intervals differ strongly in widths. Two large intervals belong to the values $N_\kappa = 2$ and $N_\kappa = 4$. They indicate that the system has two and four differently coarse-grained states with strongly different lifetimes. Thus, the corresponding two or four classes may be good choices for the intended construction of coarse-grained models, and we know in this case, of course, that they are. There is also a very small interval marking a three-state model, which finds no correspondence in the generating process given by eq 1. This three-state model is due to statistical fluctuations affecting the elements of the 100-dimensional transfer matrix and, therefore, the classification of the data points by the nonlinear dynamics. However, the small range of κ-values, within which the three-state model is predicted, indicates that it is not an intrinsic feature of the monitored time series. Similar structures are expected to be found in such plots whenever a reasonably clear-cut separation of time scales happens to exist in the dynamics represented by the transfer matrix (6). Also here large intervals with constant N_κ will point to plausible models.

It now remains to be seen at which values of κ these models should be determined. For this purpose we use the observation (cf. Figure 6a) that the prototypes $\mathbf{y}_\kappa^n$ do not vary much as κ approaches a critical bifurcation value κ_ℓ from below. Therefore, we reduce the continuous family $\{\mathcal{P}_\kappa | \kappa \in \mathbf{R}_0^+\}$ of prototype sets $\mathcal{P}_\kappa$ to a minimal discrete family

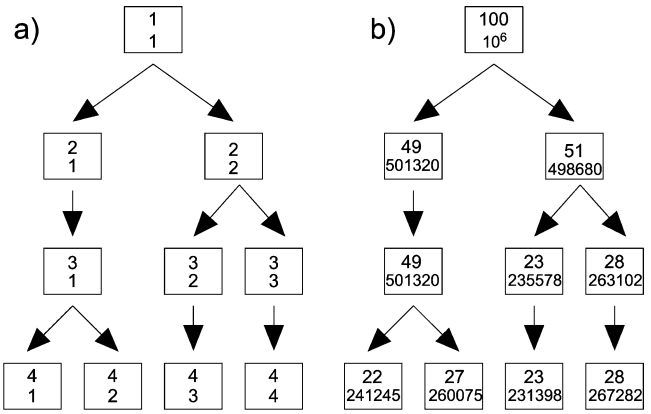

Figure 8. (a) The hierarchy of prototypes as a tree. The nodes (boxes) characterize the prototypes $\mathbf{y}_\ell^n$ by the upper index ℓ and lower index n. The edges (opposite to the arrow) denote the association of a prototype $\mathbf{y}_{\ell+1}^n$ to a prototype $\mathbf{y}_\ell^{n'}$. (b) The classification of the data set $\mathcal{X}$. Here, the upper index denotes the number of codebook vectors, $\mathbf{w}_r$ associated with the respective prototype, and the lower index the corresponding number of data $\mathbf{x}_t$.

$\{\mathcal{P}_\ell | \ell = 1,..., \ell_{max}\}$ of ℓ_{max} prototype sets $\mathcal{P}_\ell$ by selecting the prototype sets $\mathcal{P}_\ell \equiv \mathcal{P}_{\kappa_\ell}$, which are located just before the jumps of N_κ to higher values. In our simple example these values κ_ℓ are marked by asterisks in Figure 7.

In the next step we arrange the thus determined discrete family of prototype sets into a hierarchy by associating with a higher-level prototype $\mathbf{y}_\ell^{n'}$ each lower-level prototype $\mathbf{y}_{\ell+1}^n$, whose probability vector $\mathbf{p}(\tau|\kappa, \mathbf{y}_{\ell+1}^n)$ converges at $\kappa = \kappa_\ell$ under the dynamics (8) to $\mathbf{p}^{stat}(\kappa_\ell, \mathbf{y}_\ell^{n'})$. For our standard example the resulting hierarchy is drawn as a directed tree in Figure 8a.

Analogously we can classify the codebook $\mathcal{W}$ and the data set $\mathcal{X}$ on the hierarchy level ℓ by calculating for each of their elements the first moment (12) of the stationary virtual density at $\kappa = \kappa_\ell$. The result of this classification for the sample data set is shown in Figure 8b. As a result of the load balance of the mixture model (2) mentioned in 2.1, the percentage of codebook vectors $\mathbf{w}_r$ associated with a prototype $\mathbf{y}_\ell^n$ reproduces approximately the respective percentage of data points $\mathbf{x}_t$.

2.7. Extracting a Markov Model at a Hierarchy Level. Having set up a hierarchy of classifiers, which, at each hierarchy level ℓ, associate the codebook vectors $\mathbf{w}_r$ and data points $\mathbf{x}_t$ to one of N_ℓ prototypes $\mathbf{y}_\ell^n$, $n = 1,..., N_\ell$, it remains to be clarified as to how one should calculate correspondingly coarse-grained N_ℓ-state Markov matrices $\mathbf{C}^\ell = \{C_{nn'}^\ell\}$. As discussed above, such matrices can represent plausible coarse-grained descriptions of the observed dynamics, if the associated number N_ℓ of prototypes has been found to be stable over a wide range of the nonlinearity parameter κ.

There are two different choices for the computation of the $\mathbf{C}^\ell$. One can (i) reduce the original R-state Markov matrix (6) by using the classification of the codebook vectors $\mathbf{w}_r$ or (ii) directly set up the coarse-grained matrices by employing the classification of all data $\mathbf{x}_t$. To make notation simpler

we consider a single selected hierarchy level ℓ and discuss choice (i) first.

Let $I_n = \{r|\mathbf{y}_\ell(\mathbf{w}_r) = \mathbf{y}_\ell^n\}$ be the set of all indices r of codebook vectors $\mathbf{w}_r$, which are classified to a given prototype $\mathbf{y}_\ell^n$. Summing the associated partition volumes $\hat{P}(r|\mathbf{x}_t, \mathscr{W}, \sigma)$ according to

$$\tilde{P}_n(\mathbf{x}_t) \equiv \sum_{r\in I_n} \hat{P}(r|\mathbf{x}_t, \mathscr{W}, \sigma) \tag{14}$$

we obtain the partition function of the prototype $\mathbf{y}_\ell^n$, which measures the *posterior* probability that the point $\mathbf{x}_t$ belongs to $\mathbf{y}_\ell^n$. Like the original R-state Markov model defined by eq 6 also the correspondingly reduced Markov matrix $C_{nn'}^\ell$ should fulfill the analogous relation

$$C_{nn'}^\ell = \frac{\langle \tilde{P}_n(\mathbf{x}_{t+1})\, \tilde{P}_{n'}(\mathbf{x}_t)\rangle_Y}{\langle \tilde{P}_{n'}(\mathbf{x}_t)\rangle_Y} \tag{15}$$

with $n, n' \in \{1,..., N_\ell\}$. Inserting the *posterior* probabilities (14) into (15) and taking into account the definition (6) as well as the fact that the index sets I_n and $I_{n'}$ are disjoint for all classes $n \neq n'$, we obtain a reduced Markov matrix $C_{nn'}^\ell$ from the original matrix $C_{rr'}$ by

$$C_{nn'}^\ell = \frac{\sum_{r'\in I_{n'}} [\langle \hat{P}(r'|\mathbf{x}_t, \mathrm{W}, \sigma)\rangle_Y \sum_{r\in I_n} C_{rr'}]}{\sum_{r'\in I_{n'}} \langle \hat{P}(r'|\mathbf{x}_t, \mathscr{W}, \sigma)\rangle_Y} \tag{16}$$

Note that this coarse graining procedure of Markov matrices preserves detailed balance, i.e., if detailed balance holds for $C_{rr'}$, it also holds for $C_{nn'}^\ell$ as can be seen by a few lines of algebra. The stationary distribution at level ℓ follows by $p_{n,stat}^\ell = \sum_{r\in I_n} p_{r,stat}$ from $\mathbf{p}_{stat}$ associated with $\mathbf{C}$. For our synthetic sample time series, in particular, one can additionally show that in the limit of infinite sampling the detailed balance of the generating Markov matrix (1) induces detailed balance also into the discretized transfer operator $\mathbf{C}$ given by eq 6. In this case one therefore expects that detailed balance holds at all levels of coarse graining up to statistical errors.

Following choice (ii) we can alternatively count all initial data pairs $(\mathbf{x}_{t+1}, \mathbf{x}_t)$ which the nonlinear dynamics maps to the prototype pairs $(\mathbf{y}_\ell^n, \mathbf{y}_\ell^{n'})$ and all initial data points $\mathbf{x}_t$ mapped to $\mathbf{y}_\ell^{n'}$. Calling the respective numbers $T_{nn'}$ and $T_{n'}$, with $\sum_n T_{nn'} = T_{n'}$, the reduced transfer matrix is

$$\tilde{C}_{nn'}^\ell = \frac{T_{nn'}}{T_{n'}} \tag{17}$$

For overlapping coarse-grained classes both choices will overestimate the transition probabilities due to unavoidable Bayesian decision errors. For explanation consider our standard example, in which the classes associated with the Gaussians $i = 1, 2$ and $i = 3, 4$ of the generating dynamics exhibit considerable overlaps (cf. Figure 2). Even an optimal Bayesian classifier[26] will, e.g., erroneously associate data $x_t > -0.5$ that have been drawn from the normal distribution 1 to class 2. As a result, fast transitions within class 1 are erroneously counted as $1 \rightarrow 2$ transitions, and the corresponding off-diagonal element $\tilde{C}_{21}^4$ of a four-state Markov model is overestimated at the expense of the diagonal element $\tilde{C}_{11}^4$. The size of this Bayesian decision error can be estimated by comparing the four-state Markov matrix

$$\tilde{\mathbf{C}}^4 = \begin{pmatrix} 0.72 & 0.24 & 0.00 & 0.00 \\ 0.28 & 0.73 & 0.03 & 0.00 \\ 0.00 & 0.03 & 0.72 & 0.28 \\ 0.00 & 0.00 & 0.25 & 0.72 \end{pmatrix} \tag{18}$$

which has been calculated by eq 17 at the highly plausible level $\ell = 4$ of the hierarchy in Figure 8, with the generating Markov model (1). In fact, a Bayesian classification of the data $x_t \in \mathscr{X}$ (using the knowledge on the four class-conditional distributions from which the data have been drawn) numerically reproduces the four-state Markov matrix (18). As a result of the Bayesian decision error the estimated lifetimes

$$\tau_n = \frac{\Delta\tilde{t}}{1 - \tilde{C}_{nn}^\ell} \tag{19}$$

of the various coarse-grained states n are lower bounds to the true lifetimes of the generating dynamics.

For a related reason, small additional errors of this type will be introduced, if a Markov model on a given hierarchy level is estimated by the efficient reduction algorithm (16) instead by the computationally more demanding counting algorithm (17). The additional errors arising in the description of transitions among overlapping states are now due to the fuzziness σ of the partition (3) used both for the original discretization (6) of the transfer operator and for the coarse-grained partition functions (14). Correspondingly, they can be reduced by decreasing σ beyond the value σ^{ML} determined by the maximum likelihood estimate (cf. section 2.1). For our standard example and $\sigma = \sigma^{ML}$, they can be estimated by comparing the four-state matrix

$$\mathbf{C}^4 = \begin{pmatrix} 0.69 & 0.26 & 0.00 & 0.00 \\ 0.31 & 0.71 & 0.03 & 0.00 \\ 0.00 & 0.03 & 0.71 & 0.32 \\ 0.00 & 0.00 & 0.26 & 0.68 \end{pmatrix} \tag{20}$$

extracted by eq 16 with the optimal estimate (18) and the underlying Markov model (1). For instance, due to the Bayesian decision error the lifetime of state 1 is underestimated in (18) by about 30%, to which the fuzziness affecting (20) adds another 5%.

Fortunately, overlapping coarse-grained states are unlikely in high-dimensional data spaces, particularly in the ones one may use for the characterization of peptide conformational dynamics. Therefore, the unavoidable Bayesian decision errors are expected to be small. For the same reason the use of a fuzzy partitioning should not introduce large errors here, because overlapping partition volumes will mainly occur in the mapping of statistically predominant states and will then be combined by eq 14 into the associated coarse partition volumes. Because they then belong to the same state, they cannot affect the critical statistics of interstate transitions.

As a result, both algorithms should be equally applicable here and Bayesian decision errors will hardly deteriorate the results.

2.8. Alternative Construction of a Hierarchy. To check our results, we now will explain an alternative, deterministic, and very fast algorithm for constructing a hierarchy of coarse-grained Markov models from the original R-dimensional transfer matrix (6) and for identifying most plausible levels within that hierarchy. Here, the basic idea is to consecutively unite those Markov states that are mutually connected by the fastest transitions.

The alternative procedure is solely applicable to dynamical processes obeying *detailed balance* (see the introductory remarks to section 2), because this principle allows us to uniquely assign a *time scale* to the mutual transitions at the various levels of the hierarchy. The R-state Markov model (6) obeys detailed balance, if

$$C_{rr'}\langle \hat{P}(r'|\mathbf{x}_t, \mathscr{W}, \sigma)\rangle_Y = C_{r'r}\langle \hat{P}(r|\mathbf{x}_t, \mathscr{W}, \sigma)\rangle_Y \qquad (21)$$

meaning that the probability flow between any two states r and r' is equal in the stationary distribution. Dividing eq 21 by the components of the stationary distribution we immediately see that the matrix

$$D_{rr'} \equiv \frac{C_{rr'}}{\langle \hat{P}(r|\mathbf{x}_t, \mathscr{W}, \sigma)\rangle_Y} \qquad (22)$$

is symmetric. Therefore, its off-diagonal elements measure flow rates of the mutual transitions $r \leftrightarrow r'$, and we denote the maximal rate by D_{max}.

If we collect the index pair $\{r, r'\}$ belonging to D_{max} into an index set I_{R-1} and define one-member index sets I_n, $n = 1,..., R-2$, to contain the indices r'' of the remaining states, we obtain the $R-1$ index sets I_n, required for a first coarse-graining of partition volumes (14) and Markov matrices (16). The resulting $(R-1)$-state Markov matrix $\hat{\mathbf{C}}^{R-1}$ can be considered as the level $\ell = R-1$ of a model hierarchy, whose basis is formed by $\mathbf{C} \equiv \hat{\mathbf{C}}^R$. At this level, the coarse-grained partition volumes (14) provide a Bayesian classifier for the data $\mathscr{X}$ in terms of $R-1$ Markov states.

The above process of combining the fastest mixing states into new and coarser states can be iterated until the level $\ell = 2$ just below the top of the hierarchy is reached. In this recursive coarse-graining scheme, the set $\hat{\mathscr{P}}^{\ell-1}$ of prototypes $\mathbf{y}_n^{\ell-1}$ is obtained for $n = 1,..., \ell-2$ by

$$\hat{\mathbf{y}}_n^{\ell-1} = \mathbf{y}_{r''}^{\ell}, \quad \text{if } I_n = \{r''\} \qquad (23)$$

and for $n = \ell - 1$ by

$$\hat{\mathbf{y}}_n^{\ell-1} = \frac{A_r^{\ell}\hat{\mathbf{y}}_r^{\ell} + A_{r'}^{\ell}\hat{\mathbf{y}}_{r'}^{\ell}}{A_r^{\ell} + A_{r'}^{\ell}}, \quad \text{if } I_n = \{r, r'\} \qquad (24)$$

from $\hat{\mathscr{P}}^{\ell}$, where the coefficient A_r^{ℓ} denotes the number of codebook vectors $\mathbf{w}_r$ previously united into the prototype $\mathbf{y}_r^{\ell}$. Note here the initial conditions $\hat{\mathscr{P}}^R = \mathscr{W}$ and $\hat{\mathbf{y}}_r^R = \mathbf{w}_r$.

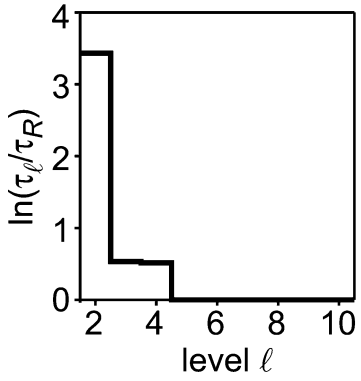

Figure 9. Time scales τ_ℓ for the last nine steps of the recursive coarse-graining procedure applied to our standard example. As time unit we have chosen the fastest time scale τ_R, which is given by the smallest eigenvalue λ_{min}^R of **C**. For explanation see the text.

At each level ℓ the fastest relaxation time scale can be characterized by considering the quantity

$$\tau_\ell \equiv \frac{1}{1-\lambda_{min}^{\ell}} \qquad (25)$$

where λ_{min}^{ℓ} is the smallest eigenvalue of $\hat{\mathbf{C}}^{\ell}$. Due to the consecutive removal of the most rapidly mixing states during our recursive coarse-graining, τ_ℓ is expected to increase in the sequence $\ell = R,..., 2$. Therefore the question, whether a given level of the resulting hierarchy furnishes a plausible coarse-grained model for the observed dynamics, can be decided by considering the ℓ-dependence of the fastest relaxation time scale τ_ℓ remaining at level ℓ. If $\tau_\ell \gg \tau_{\ell+1}$, then the model at level ℓ is considered to be plausible, because a large jump toward slower time scales indicates the presence of slowly mixing, i.e., metastable states at ℓ and of rapidly mixing states at the preceding level $\ell + 1$.

Figure 9 shows such a plot for our standard example using a logarithmic time scale. Large jumps of $\ln(\tau_\ell/\tau_R)$ occur when ℓ approaches the levels four and two from above. Thus the plot clearly reveals the hierarchical four- and two-scale structure of our example. Although the model hierarchy obtained by recursive coarse-graining generally differs from that generated by the nonlinear dynamics, the two procedures predict essentially identical models at the relevant levels $\ell = 2, 4$. Here, particularly the matrices $\hat{\mathbf{C}}^{\ell}$ calculated by the recursion are identical to the $\mathbf{C}^{\ell}$ obtained by version (i) of the dynamics-based procedure. Thus, the aim of validating the latter procedure has been reached.

2.9. Merits and Deficiencies of the Various Schemes. Up to this point we have introduced three algorithmic schemes by which one can derive a hierarchy of coarse-grained Markov models $\mathbf{C}^{\ell}$ from the transfer operator **C** defined by eq 6.

Scheme 1, which represents version (ii) of the dynamics-based procedure, relies at each hierarchy level ℓ on a crisp partitioning of the data $\mathbf{x}_t \in \mathscr{X}$ into N_ℓ coarse-grained classes n by the nonlinear dynamics (8) and a subsequent counting (17) of transitions among classes. Remarkably, in this scheme the fuzziness of the partition employed for the evaluation of the transfer operator **C** does not introduce errors into the

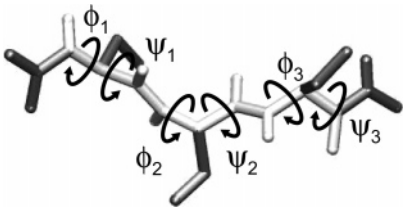

Figure 10. Tripeptide consisting of the backbone (light gray) and the serine side chains (dark gray) and definition of the dihedral angles (ϕ_i,ψ_i), $i = 1, 2, 3$. Most of the hydrogen atoms and all surrounding water molecules are omitted for clarity of representation.

computation of the coarse grained models $\mathbf{C}^{\ell}$. Experience has even shown that the nonlinear dynamics for classification of the data becomes more stable, if one increases the fuzziness of the partition in the computation of $\mathbf{C}$. In scheme 1, solely the limited statistics and Bayesian decision errors, which are unavoidable in the case of overlapping coarse-grained states, are sources of errors. The scheme is computationally expensive, because all T data points have to be classified by iteration of eq 8 at the $\ell = 1,..., \ell_{max}$ stages of the hierarchy.

Scheme 2, which represents version (i) of the dynamics-based procedure, classifies solely the R codebook vectors $\mathbf{w}_r$ by the nonlinear dynamics (8) and builds the hierarchy of ℓ_{max} Markov models $\mathbf{C}^{\ell}$ by a corresponding coarse-graining (16) of $\mathbf{C}$. Because the original partition used for the computation of $\mathbf{C}$ is preserved, small errors may be induced by its fuzziness. Therefore, one should reduce the fuzziness of the partition for the computation of $\mathbf{C}$ in this case below the value σ^{ML} obtained from codebook optimization. The computational effort is smaller by a factor R/T than in scheme 1.

Scheme 3 directly constructs the $\mathbf{C}^{\ell}$ from $\mathbf{C}$ by a deterministic and iterative unification of partition volumes and, thus, avoids costly iterations of the nonlinear dynamics (8). It is the computationally fastest procedure, shares the fuzziness errors with scheme 2, but is applicable solely to transfer operators exhibiting detailed balance to a good approximation. Because detailed balance requires extended trajectories this requirement limits the applicability of scheme 3.

In contrast, the other two schemes can also cope with a less extensive sampling and will render reasonable Markov models for a trajectory simulating equilibrium fluctuations (or for a set of trajectories starting from a given nonequilibrium state) as long as the data exhibit Markovian transitions among the various coarse-grained states. Therefore, they are also capable of modeling nonequilibrium relaxation processes. All three schemes provide the means to distinguish relevant levels of the hierarchy from spurious ones, and in all cases the computational effort is very small as compared to the cost of generating an extended MD-trajectory for a peptide in solution.

3. Sample Application

In the above explanation of algorithms we have considered a simple one-dimensional time series for purposes of illustration. To give an impression of more realistic applications, we will now consider a six-dimensional time series obtained from a 50 ns MD simulation of a serine tripeptide in water at room temperature and ambient pressure. Details of the simulation are given in Appendix C.

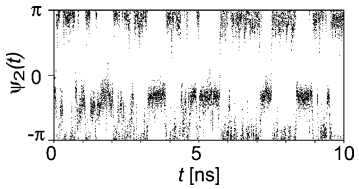

Figure 11. Time evolution of the angle ψ_2 (cf. Figure 10) during the first 10 ns of the MD simulation. Note that ψ_2 is a circular variable.

Figure 10 shows a configuration of the tripeptide molecule. At physiological temperatures its backbone (light gray) exhibits only six large-scale torsional degrees of freedom around chemical bonds, which are described by the dihedral angles ϕ_i and ψ_i. Thus, the temporal fluctuations of these six angles can be employed to determine the conformational dynamics of the backbone sampled by the MD trajectory.

Correspondingly we have generated a time series $\mathcal{X}$ from the MD trajectory, which consists of $T = 50\,001$ six-dimensional vectors $\mathbf{x}_t = [\phi_1(t),\psi_1(t),...,\psi_3(t),\psi_3(t)] \in (-\pi,\pi]^6$ and represents the backbone configurations at sampling intervals $\Delta\tilde{t} = 1$ps. Note that the torsion angles are circular variables and have to be treated accordingly.[21,40]

While the ϕ-angles fluctuate around $\approx -\pi/2$ (data not shown), the ψ-angles show a more interesting behavior. As an example Figure 11 shows the angle $\psi_2(t)$ during the first 10 ns of the simulation. Two ranges of values for $\psi_2(t)$ can be distinguished. One is given by the interval $I_\alpha = [-5\pi/6, \pi/6]$ and the other by its complement I_β. The angles ψ_1 and ψ_3 exhibit a similar bimodal behavior (data not shown) as is typical for polypeptides or proteins. Following the usual nomenclature[41] we classify local backbone configurations as α-helical, if $\psi_i \in I_\alpha$, and otherwise as extended or β-strandlike. Because each ψ-angle is either in the α- or in the β-range, we a priori expect the tripeptide to populate $2^3 = 8$ different conformations.

For time series analysis we first modeled the data distribution by a 25-component mixture density $\hat{p}(\mathbf{x}_t|\mathcal{W}^{ML},\sigma^{ML})$ as described in section 2.1. Here, the value $R = 25$ was chosen, because the quotient $R^2/T \approx 1.25\%$ appeared to be small enough as to enable a reasonably accurate statistics in the estimation of the transfer operator $\mathbf{C}$ by (6). $\mathbf{C}$ turned out to have eight large eigenvalues in the range [1.0,0.78]. The remaining eigenvalues were all smaller than 0.48. As discussed in section 2.2 such a structure of the eigenvalue spectrum points toward an eight-state model in agreement with our above expectation.

The plausibility of an eight-state Markov model was subsequently confirmed by classifying the data $\mathbf{x}_t$ through the nonlinear dynamics (8) at varying κ, because $N_\kappa = 8$ prototypes $\mathbf{y}_\kappa^n$ were found to be stable attractors of that dynamics over a wide range of κ-values. A classification of the three ψ_i values of these prototypes in terms of the α- and β-ranges introduced above then revealed that the $\mathbf{y}_\kappa^n$ are

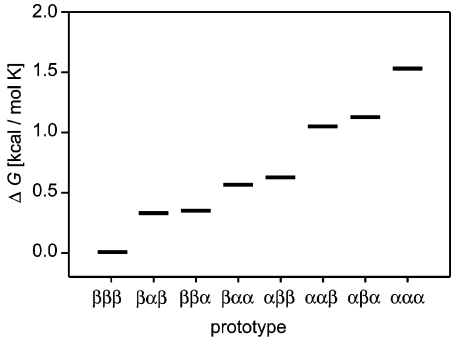

Figure 12. Free energy differences $\Delta G_n = G_n - G_1$ for an eight-state model with states n ordered according to increasing free energy $G_n = -k_B T \ln(P_n)$ and labeled by the simple (α/β)-classification of the three ψ-angles occurring in the prototypes $\mathbf{y}_\kappa^n$.

characterized by the eight possible triples $\alpha\alpha\alpha$, $\beta\alpha\alpha$, ..., which can be formed from the symbols α and β. Also the recursive coarse-graining of $\mathbf{C}$ explained in section 2.8 and a time scale analysis analogous to that in Figure 9 (see Figure 3 of the Supporting Information) indicated an eight-state model. Furthermore, the two thus determined eight-state Markov matrices turned out to be identical, i.e., $\mathbf{C}^8 = \hat{\mathbf{C}}^8$ (data not shown).

The nonlinear dynamics classification of the data $\mathbf{x}_t \in \mathcal{X}$ at the eight-state level of the model hierarchy yielded the statistical weights P_n of the states $n = 1, ..., 8$. According to the arguments in ref 13 they determine the free energies $G_n = -k_B T \ln(P_n)$ of these states, where k_B is the Boltzmann constant and T is the temperature. The resulting relative energies of the eight conformational states are depicted in Figure 12. Interestingly the fully extended conformation $\beta\beta\beta$ is seen to be energetically most favorable and, therefore, is most frequently encountered in the trajectory. Furthermore, a $\beta \rightarrow \alpha$ transition is seen to be energetically most favorable at ψ_2 and least favorable at ψ_1.

However, the dynamical connectivity of the eight states, which is visualized in Figure 13 by a plot of the Markov matrix $\mathbf{C}^8$, does not simply reflect the energetic state ordering. For instance, transitions $\beta\beta\beta \rightarrow \beta\beta\alpha$ are seen to be more likely than $\beta\beta\beta \rightarrow \beta\alpha\beta$ although the latter target state has a slightly lower free energy than the former. Furthermore, the various conformations are mainly connected by single $\beta \rightarrow \alpha$ transitions at individual angles ψ_i, whereas correlated transitions at pairs of these angles are quite rare.

By looking at further details of the connectivity displayed in Figure 13 and of the energetics shown in Figure 12, by analyzing the structures of the prototypes $\mathbf{y}_\kappa^n$ through molecular graphics, etc. one could now derive a lively picture and physical understanding concerning the conformational dynamics of serine tripeptide in water. However, these issues are beyond the scope of this paper. In the present context the given example solely serves to illustrate the kind of insights into complex dynamical systems, which now can be gained by applying the methods of time series analysis outlined above.

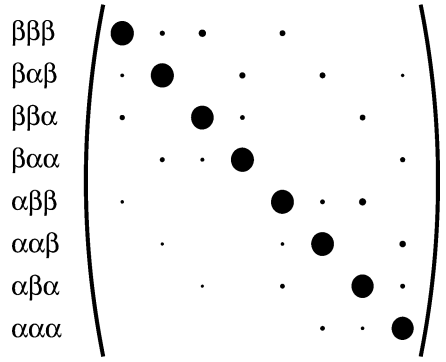

Figure 13. Graphical representation of the Markov matrix $\mathbf{C}^8$ extracted from the trajectory. The diameters of the dots code the sizes of the matrix elements $C^8_{nn'}$. (Matrix elements $C^8_{nn'} < 0.01$ not drawn.)

4. Summary and Conclusion

For the analysis of high-dimensional time series in terms of coarse-grained Markov models we first have applied a density-oriented discretization of the data space. The properties of this partition ensure a balanced statistics for the estimation of all elements of the correspondingly discretized transfer operator $\mathbf{C}$. The nonlinear dynamics eq 8 involving $\mathbf{C}$ was shown to classify the elements $\mathbf{x}_t$ of the time series in terms of prototypical points $\mathbf{y}_\prime^n$ marking the states $n = 1,..., N_\prime$ of coarse-grained Markov models $\mathbf{C}^\prime$. By varying the strength κ of the nonlinearity a hierarchy of such models is obtained, in which the number of states monotonically increases with κ in the range $N_\prime = 1,..., R$. Here, the case $N_\prime = 1$ is the trivial stationary model, and $N_\prime = R$ recovers the original discretization. Two different algorithms have been introduced to construct coarse-grained transfer operators $\mathbf{C}^\prime$ at the intermediate levels $\prime$ of the hierarchy. Here, the more time-consuming but accurate approach applies a classification of the data $\mathcal{X}$, whereas the other variant rests on a classification of prototypical points. The correctness of the latter procedure has been demonstrated by comparison with a deterministic and stepwise coarse-graining of the original R-state transfer operator $\mathbf{C} \equiv \mathbf{C}^R$.

For all these approaches observables were introduced, which allow for identifying the most plausible level within the thus constructed hierarchies of models. Their validity has been checked using a synthetic one-dimensional time series, which, apart from its low-dimensionality, exhibits all the characteristics of the relevant model class.

As an example for a more realistic application we have analyzed a six-dimensional time series obtained from a MD simulation of a tripeptide in aqueous solution. In this case the most plausible Markov model could be a priori guessed by physical knowledge on the conformational dynamics of such systems, and our approach actually recovered this guess by analysis of the simulation data. Although in practical applications questions concerning e.g. the number of partition volumes, by which the data space is discretized, the size of the time step, at which a dynamics is sampled, or the validity of the Markovian assumption for the coarse-grained time series have to be additionally addressed, the presented results demonstrate that our approach toward the identification of the most plausible coarse-grained Markov model compatible

with the observations is actually viable. We would like to stress that the approach is applicable also to extremely high-dimensional data sets, which could result, e.g., from simulations of protein folding.

Appendix A: Discrete Dynamics

To solve the differential eq 8 numerically for given $\mathbf{x}_t$ and κ, we use the following algorithm, where $\tau = 1, 2, ...$ denotes discrete time steps of widths $\Delta\tilde{t}$.

- Calculate the probability vector (7).
- While $|\mathbf{p}(\tau + 1) - \mathbf{p}(\tau)| > \epsilon$, $0 \leq \epsilon \ll 1$:

$$\mathbf{p}^{(1)} = \mathbf{C}\mathbf{p}(\tau) \tag{26}$$

$$p_r^{(2)} = p_r^{(1)} + \tilde{\kappa} p_r^{(1)}[p_r^{(1)} - (\mathbf{p}^{(1)})^2] \tag{27}$$

$$p_r^{(3)} = \begin{cases} 0, & \text{if } p_r^{(2)} < 0 \\ 1, & \text{if } p_r^{(2)} > 1 \\ p_r^{(2)}, & \text{otherwise} \end{cases} \tag{28}$$

$$\mathbf{p}(\tau + 1) = \frac{\mathbf{p}^{(3)}}{\sum_{r'} p_{r'}^{(3)}} \tag{29}$$

Equations 26 and 27 discretize the differential eq 8 under the approximation

$$\ln[(\mathbf{C} - 1) + 1] = \sum_{n=1}^{\infty} \frac{(-1)^{n+1}(\mathbf{C}\text{-}1)^n}{n} \approx (\mathbf{C} - 1) \tag{30}$$

and with $\tilde{\kappa} = \Delta\tilde{t}\kappa$. The cutoff (28) and the renormalization (29) serve to stabilize the algorithm numerically.

Appendix B: Attractors of the Nonlinear Dynamics

Here, we consider the nonlinear part

$$\frac{d}{d\tau} p_r = p_r(p_r - \mathbf{p}^2) \tag{31}$$

of (8) for the probability distribution (7). The uniform distribution

$$p_r = \begin{cases} \dfrac{1}{|\mathscr{M}|}, & r \in \mathscr{M} \\ 0, & \text{otherwise} \end{cases} \tag{32}$$

over a nonempty subset $\mathscr{M} \subset \{1,..., R\}$ of indices $r \in \mathscr{M}$ is stationary under (31), as can be seen by inserting (32) into (31). For each $M \equiv |\mathscr{M}|$ there are

$$\binom{R}{M}$$

possibilities to choose an index set $\mathscr{M}$. Therefore, there are a total of

$$\sum_{M=1}^{R} \binom{R}{M} = 2^R - 1$$

stationary solutions of (31). By applying a small deviation to one component p_s, $s \in \mathscr{M}$, one can easily show that only the R δ-distributions ($M = 1$) are stable attractors of (31).

Appendix C: Simulation Method

As a simulation system we have chosen a periodic rhombic dodecahedron (inner radius $R_I = 17$ Å) filled with 930 water molecules and one serine tripeptide molecule with acetylated N- and amidated C-termini. A Berendsen thermostat and barostat[42] were used to control the temperature at 300 K and the pressure at 1 atm. The molecular mechanics of the system was described by means of the all-atom force field CHARMM22.[43] Toroidal boundary conditions were applied to the computation of the electrostatics. As described in detail in refs 44 and 45 they comprise a moving-boundary reaction field description for electrostatic interactions beyond a distance of about R_I and fast hierarchical multipole expansions combined with a multiple time step integrator[46] at smaller distances. The basic integration time step was $\Delta t = 1$ fs. By periodically saving the peptide configuration the sampling time step was set to $\Delta\tilde{t} = 1$ ps.

Acknowledgment. This work was supported by the Deutsche Forschungsgemeinschaft (SFB 533/C1).

Supporting Information Available: Stationary distributions $\mathbf{p}_{\text{stat}}$ (Figure 1), temporal evolution of the virtual density (Figure 2), and relaxation time scales (Figure 3). This material is available free of charge via the Internet at http://pubs.acs.org.

References

(1) Hamilton, J. D. *Time series analysis;* Princeton University Press: Princeton, 1994.

(2) Bloomfield, P. *Fourier analysis of time series;* Wiley: New York, 2000.

(3) Percival, D. B.; Walden, A. T. *Wavelet methods for time series analysis;* Cambridge University Press: Cambridge, 2000.

(4) Bradley, E. Analysis of time series. In *Intelligent data analysis*; Berthold, M., Hand, D. J., Eds.; Springer: Berlin, 2003, 199−227.

(5) Rabiner, L. R. *Proc. IEEE* **1989**, *77*, 257−286.

(6) Coast, D. A.; Stern, R. M.; Cano, G. G.; Briller, S. A. *IEEE Trans. Biomed. Eng.* **1990**, *37*, 826−836.

(7) Ephraim, Y.; Merhav, N. *IEEE Trans. Inform. Theory* **2002**, *48*, 1518−1569.

(8) Gardiner, C. W. *Handbook of stochastic methods;* Springer: Berlin, 1990.

(9) Taylor, P. Statistical methods. In *Intelligent data analysis*; Berthold, M., Hand, D. J., Eds.; Springer: Berlin, 2003; pp 69−129.

(10) Branden, C.; Tooze, J. *Introduction to protein structure*; Garland: New York, 1999.

(11) Allen, M. P.; Tildesley, D. J. *Computer simulation of liquids;* Clarendon Press: Oxford, 1987.

(12) van Gunsteren, W. F.; Berendsen, H. J. C. *Angew. Chem., Int. Ed. Engl.* **1990**, *29*, 992−1023.

(13) Grubmüller, H.; Tavan, P. *J. Chem. Phys.* **1994**, *101*, 5047−5057.

(14) Giuliani, A.; Manetti, C. *Phys. Rev. E* **1996**, *53*, 6336−6340.

(15) Becker, O. M.; Karplus, M. *J. Chem. Phys.* **1997**, *106*, 1495−1517.

(16) Daura, X.; Gademann, K.; Jaun, B.; Seebach, D.; van Gunsteren, W. F.; Mark, A. E. *Angew. Chem., Int. Ed.* **1999**, *38*, 236−240.

(17) Huisinga, W.; Best, C.; Roitzsch, R.; Schütte, C.; Cordes, F. *J. Comput. Chem.* **1999**, *20*, 1760−1774.

(18) Deuflhard, P.; Huisinga, W.; Fischer, A.; Schütte, C. *Linear Algebra Appl.* **2000**, *315*, 39−59.

(19) Hamprecht, F. A.; Peter, C.; Daura, X.; Thiel, W.; van Gunsteren, W. F. *J. Chem. Phys.* **2001**, *114*, 2079−2089.

(20) Schütte, C.; Huisinga, W.; Deuflhard, P. Transfer operator approach to conformational dynamics in biomolecular systems. In *Ergodic theory, analysis, and efficient simulation of dynamical systems*; Fiedler, B., Ed.; Springer: Berlin, 2001; pp 191−224.

(21) Carstens, H.; Renner, C.; Milbradt, A.; Moroder, L.; Tavan, P. *Biochemistry* **2005**, *44*, 4829−4840.

(22) Frauenfelder, H.; Sligar, S. G.; Wolynes, P. G. *Science* **1991**, *254*, 1598−1603.

(23) Eckmann, J. P.; Kamphorst, S. O.; Ruelle, D. *Europhys. Lett.* **1987**, *4*, 973−977.

(24) Dersch, D. R.; Tavan, P. Load balanced vector quantization. In *Proc. ICANN'94, Sorrento*; Moreno, M., Morasso, P. G., Eds.; Springer: London, 1994.

(25) Kloppenburg, M.; Tavan, P. *Phys. Rev. E* **1997**, *55*, 2089−2092.

(26) Albrecht, S.; Busch, J.; Kloppenburg, M.; Metze, F.; Tavan, P. *Neural Networks* **2000**, *13*, 1075−1093.

(27) Hillermeier, C.; Kunstmann, N.; Rabus, B.; Tavan, P. *Biol. Cybern.* **1994**, *72*, 103−117.

(28) Kohonen, T. *Biol. Cybern.* **1982**, *43*, 59−69.

(29) Kohonen, T. *Biol. Cybern.* **1982**, *44*, 135−140.

(30) Dersch, D. R.; Tavan, P. *IEEE Trans. Neural Networks* **1995**, *6*, 230−236.

(31) Haken, H. *Synergetics;* Springer: Berlin, 1983.

(32) Dellnitz, M.; Hohmann, A.; Junge, O.; Rumpf, M. *CHAOS: Interdiscip. J. Nonlinear Sci.* **1997**, *7*, 221−228.

(33) Duda, R. O.; Hart, P. E. *Pattern classification and scene analysis;* Wiley: New York, 1973.

(34) The optimization of $\tilde{p}(\mathbf{x}|\mathscr{W},\sigma)$ can be interpreted as a self-organizing learning process of forward connections within a two-layer generalized radial basis functions (GRBF) network.[26,47]

(35) Voronoi, G. F. *J. Reine Angew. Math.* **1908**, *134*, 198−287.

(36) The matrix **C** can be interpreted as a self-organizing matrix of lateral connections in the central layer of a recurrent three-layer GRBF network (cf. ref 27).

(37) In the following the parameter τ denotes the time of a probability dynamics. It should not be confused with the time steps t of the analyzed time series.

(38) In the theory of neural networks the centers $\mathbf{w}_r$ of the Gaussians in (2) are also called the *virtual positions* of the associated mapping neurons.[48]

(39) The $\mathbf{y}_\kappa^n$ can be interpreted as the output of the neural network addressed in ref 36.

(40) Jammalamadaka, S. R.; Gupta, A. S. *Topics in circular statistics;* World Scientific: Singapore, 2001.

(41) Hu, H.; Elstner, M.; Hermans, J. *Proteins: Struct., Funct., Genet.* **2003**, *50*, 451−463.

(42) Berendsen, H. J. C.; Postma, J. P. M.; van Gunsteren, W. F.; DiNola, A.; Haak, J. R. *J. Chem. Phys.* **1984**, *81*, 3684−3690.

(43) MacKerell, A. D. et al. *J. Phys. Chem. B* **1998**, *102*, 3586−3616.

(44) Mathias, G.; Tavan, P. *J. Chem. Phys.* **2004**, *120*, 4393−4403.

(45) Mathias, G.; Egwolf, B.; Nonella, M.; Tavan, P. *J. Chem. Phys.* **2003**, *118*, 10847−10860.

(46) Eichinger, M.; Grubmüller, H.; Heller, H.; Tavan, P. *J. Comput. Chem.* **1997**, *18*, 1729−1749.

(47) Bishop, C. *Neural networks for pattern recognition*; Clarendon Press: Oxford, 1997.

(48) Tavan, P.; Grubmüller, H.; Kühnel, H. *Biol. Cybern.* **1990**, *64*, 95−105.

CT050020X

JCTC Journal of Chemical Theory and Computation

Non-Born-Oppenheimer Liouville-von Neumann Dynamics. Evolution of a Subsystem Controlled by Linear and Population-Driven Decay of Mixing with Decoherent and Coherent Switching

Chaoyuan Zhu, Ahren W. Jasper, and Donald G. Truhlar*

Department of Chemistry and Supercomputing Institute, 207 Pleasant Street S.E., University of Minnesota, Minneapolis, Minnesota 55455-0431

Received February 3, 2005

Abstract: Electronic energy flow in an isolated molecular system involves coupling between the electronic and nuclear subsystems, and the coupled system evolves to a statistical mixture of pure states. In semiclassical theories, nuclear motion is treated using classical mechanics, and electronic motion is treated as an open quantal system coupled to a "bath" of nuclear coordinates. We have previously shown how this can be simulated by a time-dependent Schrödinger equation with coherent switching and decay of mixing, where the decay of mixing terms model the dissipative effect of the environment on the electronic subdynamics (i.e., on the reduced dynamics of the electronic subsystem). In the present paper we reformulate the problem as a Liouville-von Neumann equation of motion (i.e., we propagate the reduced density matrix of the electronic subsystem), and we introduce the assumption of first-order linear decay. We specifically examine the cases of equal relaxation times for both longitudinal (i.e., population) decay and transverse decay (i.e., dephasing) and of longitudinal relaxation only, yielding the linear decay of mixing (LDM) and the population-driven decay of mixing (PDDM) schemes, respectively. Because we do not generally know the basis in which coherence decays, that is, the pointer basis, we judge the semiclassical methods in part by their ability to give good results in both the adiabatic and diabatic bases. The accuracy in the prediction of physical observables is shown to be robust not only with respect to basis but also with respect to the way in which demixing is incorporated into the master equation for the density matrix. The success of the PDDM scheme is particularly interesting because it incorporates the least amount of decoherence (i.e., the PDDM scheme is the most similar of the methods discussed to the fully coherent semiclassical Ehrenfest method). For both the new and previous decay of mixing schemes, four kinds of decoherent state switching algorithms are analyzed and compared to one another: natural switching (NS), self-consistent switching (SCS), coherent switching (CS), and globally coherent switching (GCS). The CS formulations are examples of a non-Markovian method, in which the system retains some memory of its history, whereas the GCS, SCS, and NS schemes are Markovian (time local). These methods are tested against accurate quantum mechanical results using 17 multidimensional atom−diatom test cases. The test cases include avoided crossings, conical interactions, and systems with noncrossing diabatic potential energy surfaces. The CS switching algorithm, in which the state populations are controlled by a coherent stochastic algorithm for each complete passage through a strong interaction region, but successive strong-interaction regions are not mutually coherent, is shown to be the most accurate of the switching algorithms tested for the LDM and PDDM methods as well as for the previous decay of mixing methods, which are reformulated here as Liouville-von Neumann equations with nonlinear decay of mixing (NLDM). We also demonstrate that one variant of the PDDM method with CS performs almost equally well in the adiabatic and diabatic representations, which is a difficult objective for semiclassical methods. Thus decay of mixing methods provides powerful mixed quantum-classical methods for modeling non-Born-Oppenheimer polyatomic dynamics including photochemistry, charge-transfer, and other electronically nonadiabatic processes.

I. Introduction

The Born-Oppenheimer approximation assumes that the relatively slow motion of nuclei can be separated from the faster electronic motion, and thus the nuclei effectively move on a single electronically adiabatic potential energy surface. Due to the prohibitive computational expense of using quantum mechanics to treat the nuclear motion of large systems (say, for systems larger than four atoms), molecular

* Corresponding author e-mail: truhlar@umn.edu.

10.1021/ct050021p CCC: $30.25
Published on Web 06/14/2005

dynamics (MD) simulations often treat the nuclear motion using classical mechanics. The combination of quantal electronic motion and classical nuclear motion for such a Born-Oppenheimer process leads to the classical trajectory[1] or quasiclassical trajectory[2] (QCT) method when applied to gas-phase systems or the molecular dynamics (MD) method[3] when applied to condensed-phase systems. However, when the system has low-lying excited electronic states, the Born-Oppenheimer approximation may break down, and nonadiabatic transitions may couple nuclear motion in the various low-lying electronic states. To extend the QCT and MD methods to treat nonadiabatic transitions caused by breakdown of the Born-Oppenheimer approximation, two new issues arise, namely that nuclear motion is governed by two or more potential energy surfaces and that these surfaces are coupled, leading to non-Born-Oppenheimer trajectories. Various mixed quantum-classical methods have been proposed to incorporate electronically nonadiabatic dynamics,[4] and in this article we call these semiclassical methods because some degrees of freedom (the electronic ones) are quantal, and others (the nuclear ones) are classical.

A general problem faced by all mixed quantum-classical approaches is the problem of how to couple classical nuclear motion to quantal electronic motion to best simulate the true overall dynamics, which is of course fully quantal. If the goal is to calculate detailed quantum state-to-state transitions, then one must include all phase and interference effects, which is difficult in an approximate calculation; however, most experimentally interesting observables in practical problems involving photochemistry are highly averaged quantities in which much of the phase and interference information is washed out. In most applications the goal is to develop general methods to calculate these averaged quantities, such as total quenching cross sections or rate constants for photoinduced reactions. For this reason it is sufficient to consider predicting the diagonal elements of the density matrix[5] because they control the final state populations. There is, however, a second reason to formulate the problem in terms of the density matrix, namely that the electronic degrees of freedom constitute a subsystem, and the Liouville-von Neumann equation of motion[6−16] (also called the quantum Liouville equation) provides a theoretical framework for propagating the density matrix of a subsystem. In particular it provides a widely accepted language for characterizing relaxation and decoherence (also described as dissipation and dephasing). Relaxation and decoherence of the electronic degrees of freedom in a "bath" of nuclear degrees of freedom can be and have been described in wave function language,[15,17,18] but in the present article, following earlier work,[8−16] we use density matrix language.

In formulating the semiclassical aspect of the problem, we limit our attention to methods that involve independent trajectories since coupling trajectories together, although it may better simulate a wave packet,[19] raises unsolved questions of computational efficiency and how best to treat the coupling. Independent-trajectory methods may be classified into two main categories: (1) trajectory surface hopping (TSH) methods[20−33] in which the classical motion at any given time is governed by one or another potential energy surface (each associated with a given electronic state in a given representation), and this motion is interrupted by hops (jumps, switches) between surfaces and/or bifurcations into two or more independent daughter trajectories (on different surfaces), each of which can further hop or bifurcate; and (2) self-consistent potential (SCP) methods[15−18,34−48] in which trajectories are governed by a weighted averaged of the coupled potential energy surfaces, where the weight changes continuously as a function of time. The most consistent of the TSH methods are based on Tully's fewest-switches (TFS) criterion,[24] which attempts to make the electronic probability distribution averaged over an ensemble of trajectories equal to the probability distribution computed from the electronic density matrix. The most straightforward of the SCP methods is the semiclassical Ehrenfest (SE) method.[40]

Some TSH methods are reasonably accurate for treating classical allowed transitions, where energy conservation is achieved during hops or in daughter trajectories by adjusting a component of the nuclear momentum (the direction of this component is called the hopping vector). In many cases, though, the algorithm may call for a hop that is not allowed by conservation of energy or momentum. Such a hop is called a frustrated hop, and in general frustrated hops cause the number of trajectories propagating on each surface to become inconsistent with the electronic density matrix. Although the fewest switches with time uncertainty (FSTU) method[31] and the later FSTU∇V method[33] have been reasonably successful at producing accurate results despite these difficulties, they occasionally show a strong dependence on the representation used (adiabatic or diabatic), and even when the empirically best representation is used they have been found to be less accurate than the best of the SCP methods described below.

The SE method involves mean-field trajectories, and it can sometimes produce accurate electronic transition probabilities. However, the SE method (even if or when it gives accurate average results) cannot, in general, give accurate final energy distributions because the electronic and translational energies of each trajectory correspond to average energies, whereas the correct physical observables, due to decoherence, correspond to a statistical mixture of the discrete, allowed final values. In a semiclassical method where quantum mechanics is used for the electronic motion and classical mechanics is used for the nuclear motion, the electronic density matrix decoheres due to the "bath" of nuclear coordinates (even for small, isolated, gas-phase systems). The realization that this effect must be introduced explicitly into the SE equation is the motivation for the development of the decay of mixing (DM) methods. To include this decoherence into the mean field approaches, the first DM method, called the natural decay of mixing (NDM) method,[18] replaced the mean-field state with a decohering one by adding decay into the coupled-states electronic Schrödinger equation. A DM trajectory behaves like the mean-field trajectory when the system is in a region of strongly interacting electronic states, but it gradually decoheres into a single-state trajectory when the system leaves the strong interaction region.[15,16,18] As decoherence is built into the quantum electronic motion, it naturally induces an extra force acting back on the classical nuclear motion. This

force is called the decoherent force, and its magnitude is determined by the requirement of energy conservation. The DM formalism has been shown to provide a more accurate description of non-Born-Oppenheimer dynamics than either the SE or the surface-hopping formalism.[15,16,18]

The state to which the decohering state is locally decaying is called the decoherent state. This could be an adiabatic or diabatic state; the basis in which physical decoherence occurs is called the pointer basis[49] or the environmentally induced superselection basis.[50] Instead of describing nonadiabatic transitions as trajectories hopping discontinuously and stochastically from one potential energy surface to another, as in trajectory surface hopping methods, DM trajectories evolve continuously on a weighted average of the potential energy surfaces, with continuously evolving weights that tend to unity on one surface (in the adiabatic or diabatic basis) and zero on all the others. The decoherent state, rather than the propagation surface, is switched.[15,16,18] The result is similar to allowing nonvertical hops. The NDM method[18] was the first implementation of the DM formalism, and in the NDM method the switching occurs stochastically according to the TFS algorithm using the decohering electronic density. This was shown to be more accurate than the TFS surface hopping method. The NDM approach has nevertheless been further improved as described below.

In the original formulation of the NDM method, the switching probability artificially favors decoherence to the local decoherent state. This means that the system either decoheres too fast or the switching probability balances coherence with decoherence inappropriately. With this problem in mind, we developed the self-consistent decay of mixing (SCDM) method[15] in which we do not consider the contribution to population transfer due to decay when we compute the switching probabilities. This improves accuracy of the DM method.

Subsequent analysis led to an even more accurate DM method in which the switching probability is governed by the coherent part of the coupled-states electronic Schrödinger equation over each pass through a strong interaction region. Globally coherent switching (i.e., coherent switching over the entire trajectory) is, however, not the best algorithm for simulating full quantum dynamics. The importance of decoherence between successive passages through strong interaction regions was demonstrated most clearly by Thachuk et al.[42] in a low-dimensionality problem, namely the evolution of a two-state diatomic molecule in a strong electromagnetic field; their discussion makes it clear that the combination of coherent evolution through a strong interaction region and decoherence between such passages is a more realistic model of quantum dynamics than is completely coherent dynamics and that maintaining coherence over an entire trajectory may lead to significant errors. One semiclassical method that was developed with this kind of consideration as a motivation is the surface hopping method of Parlant and Gislason,[22,23] in which each strong interaction region is treated coherently, and then electronic wave functions are reinitialized before encountering the next strong interaction region. This method, like all TSH methods, models one aspect of decoherence by the hopping events themselves. However, our tests of the Parlant−Gislason TSH method showed[16] that it is less accurate than the fewest-switches TSH method. We used a similar but different strategy to incorporate decoherence between strong-interaction regions and coherence within strong-interaction regions in the DM method. In particular, we modified the DM method to calculate switching probabilities using fully coherent electronic wave functions, and we reset the coherent wave functions to the decohering ones between strong-interaction regions (rather than reinitializing them). We call this method the coherent switching decay of the mixing (CSDM) method, and we found that it is more accurate than SCDM and NDM.[16]

The three methods (NDM, SCDM, and CSDM) differ only in how the decoherent state evolves during the trajectory. Trajectories evolve continuously in all DM methods, and there is no frustrated switching. When a DM trajectory attempts to decohere to an energetically forbidden state, the decoherence slows down, and the trajectory then evolves coherently in a mixed state until the forbidden state becomes allowed or until the dynamics changes in some other way, i.e., though the trajectory cannot fully occupy an energetically forbidden state, it may evolve on an average potential that contains some character of the forbidden state. This differs from TSH methods, where forbidden hops cause the distribution of TSH trajectories to no longer match the distribution called for by the electronic density matrix.

All of the DM methods mentioned so far involve nonlinear decay of mixing of the density matrix because of the way that we originally introduced the decay terms in terms of the wave function; in particular, the off-diagonal terms contain one density matrix element divided by another. From now on, we call these DM methods nonlinear decay of mixing method (NLDM) methods. The key goal of the present paper is to test the sensitivity to recasting the decay of mixing in a linear form, as postulated by most methods cast originally in density matrix language.

Quantum simulation can have two different meanings. It can mean the use of quantum mechanics to simulate physical systems, or it can mean the use of semiclassical algorithms or macroscopic models to simulate quantum systems. We are interested in the latter.

A quantum system interacts with its environment, which destroys the coherence in a robust basis,[51,52] called the pointer basis or the einselected (environmentally induced superselected) basis.[52,53] The system decoheres to a statistical classical mixture. We simulate this as stochastic demixing to an ensemble of classical states. The essence of decoherence is finding the robust basis in which the density matrix becomes diagonal; the density matrix is always diagonal in some basis (since it is a Hermitan operator, it has eigenvectors), but only in the pointer basis does it remain diagonal.[53]

Decoherence is an essential part of any quantum subsystem in contact with an environment, i.e., of any system smaller than the entire universe, and its implications have a profound effect on emergence of applicability of classical modes of thought to quantum systems, that is of classical mechanics as a good approximation to quantum mechanics under certain circumstances.[50] However, much less attention has been paid

to its relevance for quantum simulation, that is, practical classical-like approximations to quantum systems under conditions where classical mechanics is not applicable and quantum effects are large.[54]

Although more general formulations are available,[55] considerable attention has been paid to the evolution of a quantum system interacting linearly and perturbatively with a high-temperature thermal environment.[50,56] However, these assumptions are not always applicable; decoherence is more general, and in some cases we want to concentrate on the more general features of decoherence and the properties it has even when the system-environment interaction is nonlinear, strong, and nonthermal, and when the environmental relaxation time is not fast compared to the primary system dynamical time scale. As an example of a more general property of decoherence, Zurek has pointed out that in general the decoherence rate cannot be faster than the inverse of the spectral cutoff of the environment or the rate at which coherence is created.[50] An example of a general feature that might be relevant for our work here is that if the environment is more classical than the system, decoherence should be rapid compared to relaxation. For example, if vibronic relaxation occurs on the picosecond time scale, decoherence might be much faster, for example, faster than a tenth of a picosecond.

The approach to the quantum simulation embodied in the decay of mixing methods is to replace the Liouville-von Neumann (LvN) equation, which is equivalent to the Schrödinger equation and describes the "apparent ensemble"[57] corresponding to a pure superposition state, by a fictitious, stochastic ensemble evolving according to a modified LvN equation containing relaxation terms. To emphasize the distinction, the original LvN equation may be called the unitary LvN equation, and the modified one may be called a quantum master equation. The use of stochastic ensembles has a long history in the quantum theory of open systems,[58] and the decay of mixing methods involves using the concept to create new semiclassical algorithms. We will see that some old questions appear in new guises. For example, "What is the pointer basis?" becomes "Is the adiabatic or diabatic representation a closer approximation to the true pointer basis in the interaction region?" or even "Since the true pointer basis in the interaction region is unknown, can we devise an algorithm whose accuracy does not depend strongly on the choice of representation?". Similarly, the question "What is the physical decoherence rate?" becomes "What algorithmic decoherence rate allows the observables calculated from an ensemble of semiclassical trajectories to best simulate the observables calculated from a quantum wave packet?".

Note that we have used the term "quantum master equation" rather than "dissipative LvN equation"—either can be used in this context. It is important though to keep in mind that "dissipation" often refers to essentially irreversible transfer of energy into a subsystem with many degrees of freedom, where it is lost; and the decoherence that has been most heavily discussed involves transfer of information into a many-degrees-of-freedom subsystem where it is lost. Even "relaxation" sometimes has the connotation of interaction with a heat bath. In contrast, consistent with recent appreciations of the broader context in which decoherence must be studied,[59] here we consider a small environment, the nuclear degrees of freedom of a gas-phase molecule. Furthermore, whereas the goal of much master equation work is to eliminate the need to treat the environmental system explicitly, in the present work we treat the environment explicitly, but because we make a classical approximation for the environment, we need to introduce decoherence explicitly into the quantum primary system. A question we have asked in previous work is as follows: Can we formulate stochastic demixing of the primary system (the electronic degrees of freedom) to an ensemble of noninterfering states by adding relaxation terms (a time-asymmetric mechanism) to a Schrödinger equation and transforming to the density matrix language (as has been done in the decay of mixing methods)? In the present article we follow this with the following: How does this compare to adding relaxation terms directly to the LvN equation, as is usually done? Is there an essential reason to prefer one or another of these methods for formulating a statistical, irreversible, local equation of motion that describes a subsystem (the electronic degrees of freedom) strongly coupled to an environment (the nuclear degrees of freedom)?

Master equations (equations, usually approximate, for the evolution of a density matrix or the diagonal elements of a density matrix) may be classified as Markovian (time local, generated by a positive semigroup of irreversible time evolution[60]) or non-Markovian.[54,55,61,62] We have used both approaches: the natural switching and self-consistent switching methods are Markovian, whereas our more recent coherent switching method is non-Markovian, and the time nonlocality (memory) is controlled by an auxiliary density matrix and a strong-interaction criterion that controls the time interval over which the auxiliary density matrix is propagated coherently. One of the attractive features of the coherent switching decay of the mixing method is that although it describes non-Markovian evolution, it does so entirely in terms of differential equations, without the requirement for integrodifferential equations, a feature that has also occurred in some earlier work.[61] We will see that the various elements may, in principle, be combined in more than one way, and one of the goals of the present paper is to test the robustness of the resulting semiclassical methods to changing these elements.

Although the NLDM schemes were originally developed by adding decay terms to the time-evolution of the electronic wave function, i.e., to the time-dependent Schrödinger equation,[18] the Schrödinger equation of motion including these decay terms may be transformed into a Liouville-von Neumann equation.[15,16] Although these equations of motion are theoretically equivalent, it is easier to reformulate the DM methods in a linear way if one works directly with the density matrix, and this is accomplished in section II. Section III presents various switching algorithms for decoherent states in this context. Section IV reviews the decay time and the decoherent direction. Section V presents several computational details. Section VI tests several semiclassical methods, involving both linear and nonlinear decay of mixing with decoherent and coherent switching, for 17 test cases involv-

ing 8 three-dimensional atom−diatom systems. Section VII presents concluding remarks.

II. Decay of Mixing Methods

In this section, we present the theory entirely in terms of the density matrix without referring to the equations of motion for the wave function. In the decay of mixing methods, the time derivative of the density matrix has two components: one arising as the solution to the fully coherent Liouville-von Neumann equation and one that incorporates electronic decoherence. In general, we write[16]

$$\dot{\rho}_{kk'} = \dot{\rho}^C_{kk'} + \dot{\rho}^D_{kk'} \tag{1}$$

where the coherent part is given in a general representation (diabatic or adiabatic) by

$$i\hbar\dot{\rho}^C_{kk'} = \sum_l ([U_{kl} - i\hbar\dot{\mathbf{R}}\cdot\mathbf{d}_{kl}]\rho_{lk'} - \rho_{kl}[U_{lk'} - i\hbar\dot{\mathbf{R}}\cdot\mathbf{d}_{lk'}]) \tag{2}$$

where k, k', and l label electronic states (k, k', $l = 1, 2, ..., m$, where m is the number of electronic states), $\mathbf{R}$ is an N-dimensional vector of nuclear coordinates, an overdot denotes a time derivative, and $U_{kk'}$ is the symmetric potential energy matrix defined by

$$U_{kk'} = \langle k|H_{\mathrm{el}}|k'\rangle \tag{3}$$

where H_{el} is the electronic Hamiltonian plus nuclear repulsion. The nonadiabatic coupling vector $\mathbf{d}_{kk'}$ is an $m \times m$ anti-Hermitian matrix in electronic state space, and each element is a vector in $\mathbf{R}$

$$\mathbf{d}_{kk'} = \langle k|\nabla_{\mathbf{R}}|k'\rangle \tag{4}$$

where $\nabla_{\mathbf{R}}$ is the N-dimensional nuclear gradient. In the adiabatic representation, $\mathbf{U}$ is a diagonal matrix called $\mathbf{V}$; and one can define a "diabatic" representation where $\mathbf{d}_{kk'}$ is zero and $\mathbf{U}$ is not diagonal (although true diabatic representations do not exist,[63] approximate diabatic representations[63−66] are very useful and are widely used in approximations). The second term of eq 1 is an algorithmic control term added to simulate decoherence.

By conservation of density

$$\sum_{k=1}^{m} \dot{\rho}_{kk} = 0 \tag{5}$$

and eq 2 leads to conservation for the coherent terms

$$\sum_{k=1}^{m} \dot{\rho}^C_{kk} = 0 \tag{6}$$

thus we obtain a restriction on the decay terms:

$$\sum_{k=1}^{m} \dot{\rho}^D_{kk} = 0 \tag{7}$$

Clearly $\dot{\rho}_{kk}$, $\dot{\rho}^C_{kk}$, and $\dot{\rho}^D_{kk}$ can be either negative or positive. Whereas $\dot{\rho}^C_{kk}$ is determined by the time-dependent Schrödinger equation, $\dot{\rho}^D_{kk}$ results from algorithmic choice. We formulate the DM methods such that there is some electronic state K (the "decoherent state") toward which the system is decohering, and this requires that $\dot{\rho}^D_{kk} < 0$ for $k \neq K$ and $\dot{\rho}^D_{KK} > 0$. This guarantees that the trajectory corresponds asymptotically to a particular electronic state in the pointer basis. Assuming that the diagonal elements decay by a linear, first-order process yields

$$\dot{\rho}^D_{kk} = -\frac{1}{\tau_{kK}}\rho_{kk}, \quad k \neq K \tag{8}$$

and

$$\dot{\rho}^D_{KK} = \sum_{k\neq K} \frac{1}{\tau_{kK}}\rho_{kk} \tag{9}$$

where τ_{kK} is a first-order decay time to be specified. The time derivatives $\dot{\rho}^D_{kk'}$ of the off-diagonal matrix elements are not yet specified, and they are discussed later.

The introduction of the decay term of eq 8 is the key element of the decay-of-mixing methods. In a real physical situation, a system interacting with an environment ends in a mixed state, rather than a pure state, which would result if the density matrix, originally assumed pure, were evolved by the time-dependent Schrödinger equation. We want to simulate the final ensemble corresponding to the mixed state of the electronic subsystem by an ensemble of pure states. Thus, whereas the destruction of interference in the real system leads to a mixture that corresponds to a probability distribution of final observables, the simulation system tends to a probabilistic distribution of pure states, each corresponding to different observables.

Next, we consider the nuclear motion. We use an isoinertial, mass-scaled nuclear coordinate system $\mathbf{R}$ in which all nuclear masses are scaled to the same reduced mass μ, and the momentum conjugate to $\mathbf{R}$ is called $\mathbf{P}$. The nuclear motion is represented by an ensemble of classical trajectories, and the nuclear position and momentum of each trajectory evolve according to classical equations of motion

$$\dot{\mathbf{R}} = \mathbf{P}/\mu \tag{10}$$

and

$$\dot{\mathbf{P}} = \dot{\mathbf{P}}^C + \dot{\mathbf{P}}^D \tag{11}$$

where the coherent part is[15,16]

$$\dot{\mathbf{P}}^C(t) = -\sum_k \rho_{kk}\nabla_{\mathbf{R}}U_{kk} - \sum_k \sum_{k'<k} (2\mathrm{Re}\rho_{kk'})\nabla_{\mathbf{R}}U_{kk'} + \sum_j \sum_k \sum_{k'} (2\mathrm{Re}\rho_{kj})U_{kk'}\mathbf{d}_{k'j} \tag{12}$$

and the decoherent part is[15,16,18]

$$\dot{\mathbf{P}}^D = -\frac{\mu\dot{V}^D}{\mathbf{P}\cdot\hat{\mathbf{s}}}\hat{\mathbf{s}} \tag{13}$$

where[15,16]

$$\dot{V}^D = \sum_k \dot{\rho}^D_{kk}U_{kk} + \sum_k \sum_{k'<k} 2\mathrm{Re}(\dot{\rho}^D_{kk'})U_{kk'} \tag{14}$$

and $\hat{\mathbf{s}}$ is a unit vector (specified below) that represents the decoherence direction into which energy is deposited and

out of which energy is consumed. The right-hand side of eq 13 is the negative of the decoherent force, and it drives the trajectory to a pure electronic state. The decay of mixing methods differ in the off-diagonal matrix elements $\dot{\rho}^D_{kk'}$, as discussed next.

A. Nonlinear Decay of Mixing (NLDM). Previously, we added first-order decay to the electronic wave function.[15,16,18] By making the reasonable assumption[18] that the real and imaginary parts of the component of the electronic wave function corresponding to a given electronic state decay at the same rate (in a particular representation, i.e., in the pointer basis), we obtained equations which are equivalent to the following decay law for the decoherence in the pointer representation[15,16]

$$\dot{\rho}^D_{ij} = \begin{cases} -\frac{1}{2}\left(\frac{1}{\tau_{iK}} + \frac{1}{\tau_{jK}}\right)\rho_{ij} & i \neq K \;\; j \neq K \qquad (15a) \\ \frac{1}{2}\left(\frac{1}{\rho_{KK}}\left(\sum_{k \neq K}\frac{\rho_{kk}}{\tau_{Kk}}\right) - \frac{1}{\tau_{jK}}\right)\rho_{ij} & i = K \;\; j \neq K \qquad (15b) \\ \frac{1}{2}\left(\frac{1}{\rho_{KK}}\left(\sum_{k \neq K}\frac{\rho_{kk}}{\tau_{Kk}}\right) - \frac{1}{\tau_{iK}}\right)\rho_{ij} & i \neq K \;\; j = K \qquad (15c) \end{cases}$$

where the decay terms for the diagonal elements push ρ_{KK} in the denominator to unity and ρ_{kk} in the summation to zero. The nonlinear terms in eq 15 therefore vanish asymptotically.

B. Linear Decay of Mixing (LDM). We linearize the decay of mixing by ignoring nonlinear terms in eq 15. Then we have

$$\dot{\rho}^D_{kk'} = -\frac{1}{2\tau_{kk'}}\rho_{kk'}, \; k \neq k' \qquad (16)$$

where the factor of 2 in eq 16 is not necessary, and we could put any nonzero constant there; however, here we define the decay time to be consistent with notation used above. The decay times in eq 16 need not be the same as those that appear in the diagonal matrix elements in eqs 8 and 9, but in the present article we take them to be the same for simplicity.

Equations 15a and 16 lead to the widely assumed situation where coherence decays exponentially. This form for the decay can be derived under reasonable sets of assumptions for other problems,[67] but for the present problem of the decoherence of the electronic degrees of freedom by the nuclear ones, it has the status of a possible fundamental assumption.

C. Population-Driven Decay of Mixing (PDDM). In the population-driven decay of mixing (PDDM) method, we assume that there is no decoherent decay of the off-diagonal matrix, i.e.

$$\dot{\rho}^D_{kk'} = 0, \; k \neq k' \qquad (17)$$

Note that this method, like LDM, is linear. If we use the usual convention that the relaxation time for the diagonal elements is called T_1 and that for the off-diagonal elements is called T_2, this corresponds to $T_2 = \infty$ and T_1 finite, whereas usually $T_2 \leq T_1$. However, we should keep in mind that the decoherent decay in the DM methods is algorithmic decay, not physical decay. We are adding decay terms to the equations for an ensemble of independent semiclassical trajectories so that the ensemble average best simulates the behavior of a quantum wave packet. In this case, it is interesting to test the effect of making a minimal perturbation to the equations of motion consistent with forcing the system to continuously switch to a single potential energy surface asymptotically. In the PDDM scheme, we make only this minimal perturbation.

Note that $\rho_{kk'}$ for $k \neq k'$ does not tend to zero in this method, just as it also stays finite in trajectory surface hopping. However, as compared to trajectory surface hopping, the system has no discontinuous changes in momenta, and it uses Ehrenfest-like dynamics in regions where the potential energy surfaces are strongly coupled. Thus the PDDM method provides an algorithmic density matrix that may be useful for calculations, but it does not necessarily satisfy the constraint[8]

$$\rho_{nn}\rho_{mm} \geq |\rho_{nm}|^2$$

which holds for true density matrices.

III. Decoherent and Coherent Switching

Next we discuss how the decoherent state is switched along the DM trajectory. In the TSH method, at a hop, the trajectory discontinuously switches from one pure electronic state to another pure electronic state. In DM methods we instead switch the decoherent state.

A. Natural Switching (NS). The natural switching (NS) scheme is a direct application of Tully's fewest-switches scheme. For example, in the two-state case, the probability of switching from a decoherent state K to some other decoherent state K' between time t and time $t + dt$ is given by

$$P_{K\rightarrow K'} = \max\left(-\frac{\dot{\rho}_{KK}dt}{\rho_{KK}},0\right) = \max\left(-\frac{(\dot{\rho}^C_{KK} + \dot{\rho}^D_{KK})dt}{\rho_{KK}},0\right) \qquad (18)$$

The multistate generalization of eq 18 is given in Appendix A of ref 16.

B. Self-Consistent Switching (SCS). In eq 18 above, the change in the density matrix elements, including the change due to decoherence, is used to calculate the switching probability. In the self-consistent switching (SCS) scheme, the switching probability is calculated using only the coherent part of the change in elements of the density matrix. In the two-state case this yields

$$P_{K\rightarrow K'} = \max\left(-\frac{\dot{\rho}^C_{KK}dt}{\rho_{KK}},0\right) \qquad (19)$$

This may be interpreted as "semicoherent switching" because the instantaneous change in the density matrix due to decoherence is not included, although the decoherence due to the trajectory's history is included in the denominator of

eq 19, since ρ_{KK} is the decohered density. The multistate generalization of eq 19 is given in Appendix A of ref 16.

C. Globally Coherent Switching (GCS). The globally coherent switching (GCS) method preserves coherence in the populations used to control switching over the entire trajectory. To accomplish this, we define a set of coherent state populations $\tilde{\rho}_{KK'}$ which satisfy the fully coherent evolution given in eq 2. Initially $\tilde{\rho}_{kk'} = \rho_{kk'}$, but these two density matrices are propagated separately. In the two-state case the switching probability is given by

$$P_{K\to K'} = \max\left(-\frac{\tilde{\rho}_{KK}dt}{\tilde{\rho}_{KK}},0\right) \tag{20}$$

D. Coherent Switching (CS). The above schemes are all time-local (or Markovian), but the actual time derivatives of the density matrix are not only solely determined by information about the current state of the system but also by its time history, i.e., the evolution is nonlocal in time or non-Markovian. In this section we discuss a key feature that accounts for such time nonlocality, and we show how to include a critical aspect of memory into the propagation by incorporating the concept of a localized (but not instantaneous) interaction between the quantum states.

Parlant and Gislason[3] introduced a method in the framework of trajectory surface hopping (TSH) that we called exact coherent passage TSH (ECP-TSH). In this method (for a two-state case) the following coupling function is monitored:

$$\Omega(t) = |\dot{\mathbf{R}}\cdot\mathbf{d}_{12}(t)| \tag{21}$$

At each local minimum of Ω, the density matrix is reinitialized to correspond to a pure state, i.e., $\rho_{KK} = 1$ and all other elements equal zero. The ECP-TSH method integrates the electronic equations of motion in a coherent way throughout each complete transversal of a strong coupling region, but it handles decoherence differently from the DM methods in several respects. First, there is no decay of mixing term. Second, each trajectory propagates locally on a single potential surface rather than an Ehrenfest-weighted surface. Third, the ECP-TSH method involves hops with discontinuities in the nuclear momentum, and when a hop occurs it requires that the semiclassical trajectory be repropagated from a point of maximal coupling. Fourth, whether a hop occurs, at each local minimum of $\Omega(t)$, the electronic coefficients are reinitialized to unity or zero. This means that decoherence is instantaneous in the ECP-TSH method, and it appears from the results[16] that this does not describe decoherence as well as possible. Nevertheless, this idea provided stimulation for a (locally) coherent switching scheme that we abbreviate CS.

In the CS scheme, the switching probability is defined as in eq 20 for the GCS method. In the CS scheme however, $\tilde{\rho}_{KK'}$ is set equal to $\rho_{KK'}$ at all local minima of some coupling function. *Note that we sync the switch-controlling density matrix to the decohered one (that controls the effective potential) rather than reinitialize it.* By setting $\tilde{\rho}_{KK'} = \rho_{KK'}$, the amount of decoherence is determined by the difference between the two sets of electronic density matrices: the one that is propagated with decay-of-mixing terms and the one that is propagated coherently. Thus, in particular, the amount of decoherence introduced at a local minimum of the coupling function depends on the size of the coupling region and other dynamical factors. We emphasize that the equations of motion governing the $\tilde{\rho}_{ij}$ elements and hence governing the switching probability in the CS method are treated in a coherent and uninterrupted way throughout each complete passage through a strong coupling region (although one does allow switches in the decoherent state), but decoherence is introduced into $\tilde{\rho}_{ij}$ between different strong coupling regions by setting $\tilde{\rho}_{ij} = \rho_{ij}$ at minima of the coupling function.

We have not used the same coupling function as Parlant and Gislason. We previously defined the following functions for both adiabatic and diabatic representations[16]

$$D_K(t) = \sum_j |\mathbf{d}_{Kj}|^2 \tag{22}$$

and

$$C_K(t) = \sum_j |\mathbf{d}_{Kj}\cdot\dot{\mathbf{R}}_{\mathrm{vib}}|^2 \tag{23}$$

Calculations employing eq 22 are called CS, and those employing eq 23 are called CS-C. These coupling functions arise from the adiabatic representation where the coupling is determined by the nonadiabatic coupling vector, but it is clear (at least for the two-state case) that they also provide a measure of coupling in the diabatic representation. Nevertheless, it is interesting to ask if a quantity computed directly in the diabatic representation works as well. Thus we define

$$S_K(t) = \sum_{j\neq K} |U_{Kj}|^2 \tag{24}$$

and

$$L_K(t) = \sum_j |U_{KK} - U_{jj}|^2 \tag{25}$$

The first quantity, eq 24, is a direct expression in terms of the scalar-coupling (S) matrix elements, and the second, eq 25, is a measure of deviation from the crossing point where a local minimum (which might be zero) occurs in the diabatic level-spacing (L). We also consider using the reciprocal of eq 25. Equations 22, 24, and 25 and the reciprocal of 25 will be considered as alternative demarcation schemes for strong-coupling regions in CS calculations. Note that these four equations give qualitatively different definitions of a strong-coupling region for many problems.

When it is desired to associate a unique abbreviation with each choice, calculations carried out using eq 22 may be labeled CS(D), that is, coherent switching based on the magnitude of the derivative coupling; those with eq 23 may be labeled CS-C, that is, coherent switching with strong interaction boundaries based on a component; those carried out with eq 24 may be labeled CS(S), that is, coherent switching with strong-interaction boundaries based on scalar diabatic coupling; those carried out with eq 25 may be labeled CS(L), that is, coherent switching in the diabatic representation with strong-interaction boundaries based on diabatic level-spacing; and those carried out with the

reciprocal of (25) will be labeled CS(1/L). A possible advantage of choosing the S, L, or 1/L expressions in the diabatic representation is that one can avoid the diabatic−adiabatic transformation. This may be useful for some systems, although in general, given a diabatic representation, this transformation is not computationally demanding. Thus the motivation for choosing a particular demarcation scheme will be the consistency of the semiclassical formulation, as judged by the accuracy of the results for a diverse set of problems.

E. Combinations. We have defined five switching schemes (natural switching, self-consistent switching, globally coherent switching, coherent switching basis on a component, and coherent switching) in the adiabatic representation. Any of these schemes may be used in combination with the three decay of mixing algorithms (NLDM, LDM, and PDDM) discussed in section II for a total of 15 semiclassical methods in the adiabatic representation. In the diabatic representation we will consider the D, S, L, and 1/L criteria for strong-interaction regions in the CS scheme, for a total of eight schemes and 24 combinations. However some of these are only of academic interest at this point since we know from previous work[15,16] that the NS, SCS, and CS-C schemes are less accurate than CS. But the GCS, CS(S), CS(L), and CS-(1/L) schemes have never been tested. Some of the combinations are equivalent to previous methods: NLDM with NS is NDM; NLDM with SCS is SCDM; NLDM with CS-C is CSDM-C; and NLDM with CS is CSDM. The other 20 are new. To emphasize the essential characteristics, LDM with CS is abbreviated CSDM/L, and PDDM with CS is abbreviated CSDM/PD. Furthermore, NLDM, LDM, and PPDM with GCS may be abbreviated GCSDM, GCSDM/L, and GCSDM/PP, respectively.

IV. Decay Time and Decoherence Direction

Next we review how the decay time and decoherent direction are determined. The same prescriptions[16] are used for all of the combinations, and they are summarized briefly here to make this paper more self-contained.

The unit vector in eq 13 represents the direction into which nuclear kinetic energy is deposited or out of which energy is consumed, and in the two-state case it is given by[16]

$$\hat{\mathbf{s}} = (d_{Kk}a_0(\mathbf{P}\cdot\hat{\mathbf{d}}_{Kk})\mathbf{d}_{\hat{K}k} + P_{\text{vib}}\hat{\mathbf{P}}_{\text{vib}})/||d_{Kk}a_0(\mathbf{P}\cdot\hat{\mathbf{d}}_{Kk})\mathbf{d}_{\hat{K}k} + P_{\text{vib}}\hat{\mathbf{P}}_{\text{vib}}|| \quad (26)$$

where a_0 is a bohr length, $\hat{\mathbf{P}}_{\text{vib}}$ and $\hat{\mathbf{d}}_{Kk}$ are unitless unit vectors in the direction of $\mathbf{P}_{\text{vib}}$ (the local vibrational momentum[26]) and $\mathbf{d}_{Kk}$, respectively, and d_{Kk} is the magnitude of $\mathbf{d}_{Kk}$. The generalization of eq 26 to multiple states has been given previously.[15,16]

The decay time we use is[16]

$$\tau_{kK} = \frac{\hbar}{|V_{kk} - V_{KK}|}\left(1 + \frac{E_0}{(\mathbf{P}\cdot\hat{\mathbf{s}})^2/2\mu}\right) \quad (27)$$

where E_0 is a constant. In the present work we use $E_0 = 0.1$ E_h (where 1 $E_h \equiv 1$ hartree $= 27.2116$ eV), which is the same value as used in ref 16.

Equation 27 exhibits two very interesting qualitative features. First, individual off-diagonal density matrix elements do not all decohere at the same rate, and coherences between levels that are widely separated decay faster than those between levels that are close to each other. This behavior has been observed in semiclassical studies of an oscillator coupled to a bath.[68,69] Second, the decoherence time tends to ∞ as the momentum tends to zero. This feature, which follows in our work from the self-consistent treatment of the system-environment interaction, is consistent with a study[70] based on a general master equation that showed that coherence decay becomes slower than any exponential as the environmental temperature tends to zero.

V. Three-Dimensional, Two-State Test Cases

The model systems we consider here are two-state atom−diatom nonadiabatic collisions and have the form

$$\text{A}^* + \text{BC}(v,j) \rightarrow \begin{cases} \text{B} + \text{AC}(E'_{\text{int}}) & (28a) \\ \text{A} + \text{BC}(E''_{\text{int}}) & (28b) \end{cases}$$

where A, B, and C label atoms, the asterisk indicates electronic excitation, and v and j are the initial vibrational and rotational quantum numbers. Equation 28a describes the nonadiabatic reaction, where E'_{int} is the final internal (i.e., rovibrational) energy of the AC diatom, and eq 28b describes quenching, where E''_{int} is the final internal energy of the BC diatom. We label the initial conditions by the total energy E and the initial vibrational and rotational quantum numbers v and j of the diatomic molecule. For all of the cases considered here, the total angular momentum of the system is zero. Electronic angular momentum is neglected consistently in both the quantal and semiclassical calculations.

For the collision energies used in this paper, there are only three possible collision outcomes (combinations of the final arrangement and electronic state): adiabatic collision in the electronically excited state, reactive de-excitation, and quenching (nonreactive de-excitation).

The semiclassical trajectory calculations and the accurate quantum mechanical results are compared for the following six quantities ($i = 1, 2, ..., 6$): P_{R}, the probability of reaction, which is the outcome in eq 28a; P_{Q}, the probability of quenching, which is the outcome in eq 28b; P_{N}, the total probability of a nonadiabatic event, which is the sum of P_{R} and P_{Q}; F_{R}, the reactive branching fraction, which is defined as $P_{\text{R}}/P_{\text{N}}$; $\langle E'_{\text{int}}\rangle$, the average internal (vibrational−rotational) energy of the diatomic fragment in eq 28a; and $\langle E''_{\text{int}}\rangle$, the average internal (vibrational−rotational) energy of the diatomic fragment in eq 28b. For the three probabilities the error $\epsilon_{i\alpha}$ for quantity i and test case α (nine cases for MXH, five cases for MCH, and three case for YRH) is calculated as the logarithmically averaged percentage error computed as described elsewhere,[71] and for the remaining three quantities, F_{R}, $\langle E'_{\text{int}}\rangle$, and $\langle E''_{\text{int}}\rangle$, the error $\epsilon_{i\alpha}$ is defined as the unsigned relative percentage error computed as described elsewhere.[16] The average of the logarithmically averaged percentage errors in P_{R}, P_{Q}, and P_{N} is called the average unsigned percentage error in probabilities (column heading "Prob"), and the average of the unsigned relative

percentage errors in F_R, $\langle E'_{int}\rangle$, and $\langle E''_{int}\rangle$ is called the average unsigned percentage error in fractional distributions (column heading "Fract"); the latter name is appropriate because the relative error in internal energy is identical to the relative error in the fraction of total energy that is deposited in internal energy. Finally, we average the two averages to obtain an average unsigned percentage error for all six observables (column heading "All").

The model systems feature three types of nonadiabatic transitions and are labeled as MXH, MCH, or YRH.

The MXH systems feature avoided crossings of the Landau−Zener type[72−74] in which the two diabatic potential energy surfaces cross with nonzero diabatic coupling. Nine MXH cases are included: the SB, SL, and WL parametrizations, with total energy $E = 1.1$ eV, $v = 0$, and $j = 0$, 1, 2. Details of the MXH parametrizations and the accurate quantum mechanical calculations have been given previously.[47] For the MXH systems, the quantum transition probabilities show oscillations, but the semiclassical methods do not. Therefore, for MXH systems, semiclassical results for P_R, P_Q, P_N, and F_R at 1.1 eV are compared to quantal results averaged over an energy interval. When a quantity, say α, is quantum mechanically averaged at E_0, it means

$$\bar{\alpha}(E_0) = \frac{1}{2N+1}\sum_{j=-N}^{N} \alpha(E_0 - j\delta E) \qquad (29)$$

where δE is small increment around E_0. In applying eq 29 to the MXH systems in the present paper, N is 2 and $\delta E = 0.0055$ eV. The values of $\langle E'_{int}\rangle$ and $\langle E''_{int}\rangle$ are not averaged.

The MCH systems feature conical intersections[75−77] in which the two diabatic potential energy surfaces cross at some geometries where the diabatic coupling is zero. Five MCH cases are included: the SB, SL, TL, WB, and WL parametrizations, with $E = 1.1$ eV and $v = j = 0$. Details of the MCH parametrizations and the accurate quantum mechanical calculations have been given previously.[78] For MCH and YRH systems, the quantal results used for comparison in this article are not averaged.

The YRH systems feature interactions of the Rosen-Zener-Demkov type,[79−81] by which we mean cases where the two diabatic potential energy surfaces do not cross and are weakly coupled. Three YRH cases are included: the YRH(0.1) parametrization with $E = 1.1$ eV and $v = j = 0$ and the YRH(0.2) parametrization with $E = 1.02$ eV and $v = j = 0$ and $E = 1.1$ eV, $v = 0$, and $j = 6$. The number in parentheses denotes the strength of the coupling; this and other details of the YRH parametrizations and the accurate quantum mechanical calculations have been given previously.[82]

For the decay of mixing trajectories, the coordinates and momenta of the nuclei and the electronic state populations are integrated using an adaptive integration algorithm that was designed for use with semiclassical trajectory calculations.[28] The algorithm uses a Bulirsch-Stoer integrator with polynomial extrapolation[83] modified such that the integrator is prohibited from stepping over local peaks and minima in the electronic probabilities. For the present calculations, the integration parameters were given the following values:[47] $\epsilon_{BS} = 10^{-12}$ E_h and $h_{min} = 10^{-4}$ aut (1 aut = 1 atomic unit of time = 2.4189×10^{-2} fs), which gives converged results for the MXH, MCH, and YRH systems. The trajectories begin the simulation with the lone atom (Y in the case of YRH and M in the case of MXH and MCH) separated from the center-of-mass of the diatom by 35 a_0 (1 a_0 = 0.52918 Å) for the MXH, MCH cases and by 20 a_0 for the YRH cases, and the simulation was ended when the product fragments were separated by at least 30 a_0 for all three systems. We have verified that the results of the semiclassical simulations do not change when these distances are increased.

For the decay of mixing trajectories, the final state internal energies, E'_{int} or E''_{int}, are determined without quantization. In particular, the relative translational energy becomes constant after the collision, and the internal energy is computed as total energy minus the final relative translational energy minus the minimum electronic energy of the diatomic fragment.

Calculations are performed in the adiabatic (a) and diabatic (d) representations. Calaveras County (CC) calculations with three combinations of adiabatic and diabatic representations are also performed. The Calaveras County representation[48] is defined as the representation with the fewest hopping attempts in a trajectory surface hopping calculation, and previous work has shown[48,77] that this representation is, on average, the most accurate representation for non-Born-Oppenheimer semiclassical trajectory calculations.

All new calculations in this paper were run with the NAT computer code—version 9.0, whereas results in previous papers (some of which are reanalyzed below for the final table) are calculated with the NAT-version 8.1.[84]

VI. Results and Discussion

The Supporting Information provides full sets of calculated observables and average errors for all 15 combinations (see section III.E) in the adiabatic representation and for 18 of the possible combinations in the diabatic representation. In the printed article, that is, in this section, we tabulate and discuss only the most interesting new results.

Table 1 presents the mean percentage errors for the NLDM, LDM, and PDDM methods employing CS switching. The table is based on 17 cases for 10 different systems of three different types, and so it provides a broad assessment of the accuracy and robustness of the methods. The table shows that the YRH systems present the most critical test of which algorithm is the best. All NLDM, LDM, and PDDM methods with CS switching work almost equally well in the adiabatic and Calaveras County representations, but the NLDM and PDDM methods are slightly better than the LDM method in the diabatic representation. The S and L criteria for strong interaction regions appear to work well for diabatic LDM and PDDM calculations. In comparing the results in Table 1 it is not necessary to consider costs since the costs for all methods in the table are within about a factor of 2 or even closer.

The overall results in the last column of Table 1 are obtained by averaging over the three types of system, with each type weighted one-third. The NLDM method with CS switching, which is the CSDM method presented previ-

Table 1. Average Unsigned Percentage Errors Computed for the Coherent Switching Method

		MXH (avoided crossing)			MCH (conical interaction)			YRH (noncrossing)			
method	rep	prob	fract	all[a]	prob	fract	all[a]	prob	fract	all[a]	all overall[b]
NLDM	a	28	20	24	44	24	34	16	17	17	25
	d(D)	21	16	19	34	21	28	43	22	32	26
	d(S)	22	16	19	34	21	27	36	23	29	25
	d(L)	21	16	19	34	21	28	49	26	38	28
	d(1/L)	21	17	19	33	21	27	64	29	47	31
	CC(D)	29	20	24	34	23	29	16	17	17	24
	CC(D,S)	29	20	25	34	23	29	16	17	17	24
	CC(D,L)	29	20	25	34	23	28	16	17	17	23
LDM	a	24	18	21	43	23	33	18	17	18	24
	d(D)	27	20	24	36	21	29	106	15	61	38
	d(S)	27	20	23	34	20	27	53	14	33	28
	d(L)	26	20	23	37	22	29	44	16	30	27
	d(1/L)	27	20	23	34	21	28	51	17	34	28
	CC(D)	28	18	23	35	22	29	18	17	18	23
	CC(D,S)	27	18	23	34	22	28	18	17	18	23
	CC(D,L)	27	18	22	36	23	29	18	17	18	23
PDDM	a	27	20	23	42	22	32	20	16	18	24
	d(D)	26	16	21	37	19	28	78	15	47	32
	d(S)	26	16	21	37	19	28	33	14	24	24
	d(L)	25	16	20	38	20	29	27	16	22	24
	d(1/L)	25	16	20	37	19	28	32	18	25	24
	CC(D)	20	19	25	38	20	29	20	16	18	24
	CC(D,S)	30	19	25	38	20	29	20	16	18	24
	CC(D,L)	29	19	24	38	21	30	20	16	18	24

[a] All six observables (average of two previous columns). [b] This column is the average of the three previous "all" columns.

ously,[16] has a mean error of 25% in the adiabatic representation, 26% in the diabatic representation with the original D criterion for strong interaction regions, and 25% in the diabatic representation with the new S criterion. The Calaveras County representation with the D criterion for both representations has 24% error, and using D in the adiabatic representation and S in the diabatic representation gives 23% error. All of these average errors, in the range of 23−26%, are comparable to the kind of error one can get from trajectory calculations for Born-Oppenheimer systems,[85] so it seems unlikely that further reductions are possible by changing the treatment of nonadiabaticity. Indeed the linearized method, LDM, is slightly worse. Furthermore, decreasing the decoherent algorithmic control to the minimum necessary to guarantee physical final electronic states, as in the PDDM method, gives almost the same overall mean errors, ∼24%, as the CSDM, provided one uses either the S or L criterion in the diabatic representation. We conclude that the decay-of-mixing methods are very robust with respect to details of the implementation and that the linearized methods perform equally as well as our wave function version in the adiabatic representation, which gives nonlinear decay of the density matrix. The fact that the PDDM method with the D criterion in the adiabatic approximation and the S criterion in the diabatic approximation are sometimes slightly more accurate than the CSDM method is interesting, but it is outweighed by the more physical character of the CSDM in driving the off-diagonal elements of the density matrix toward zero and by the fact that the overall errors of the CSDM and the PDDM are almost identical.

Although we have emphasized the physicality of the DM methods in driving the coherences (the off-diagonal elements of the density matrix are called coherences in the density matrix literature) to zero, the nonlinear and linearized versions of the method differ in the way that they accomplish this. This is best illustrated by considering the two-state case. For two states, with $k = 1$, $K = 2$, and $\tau_{21} = \tau_{12}$, eq 15 of the CSDM method yields

$$\dot{\rho}_{12}^{D} = -\left(\frac{\rho_{11}}{\rho_{22}} - 1\right)\frac{\rho_{12}}{2\tau_{12}} \tag{30}$$

whereas eq 16 of the LDM yields

$$\dot{\rho}_{12}^{D} = -\frac{\rho_{12}}{2\tau_{12}} \tag{31}$$

Equation 31 has the behavior that the decoherent control terms always decrease $|\rho_{12}|$, as assumed by phenomenological theories of decoherence, whereas eq 30 does not have this behavior. However, since we are working with algorithmic demixing rather than physical demixing, and since eq 30 follows from adding a decay mechanism to the wave function equation of motion, one can argue that the requirement that $\dot{\rho}_{12}^{D}/\rho_{12}$ is negative need not be enforced and might even be inappropriate. In fact, Elran and Brumer,[69] in a study of an anharmonic oscillator coupled to a bath, found that coherence both increased and decreased, and they called into question the utility of Markovian master equations that predict only decay. Since Table 1 shows that the LDM method gives significantly less robust results in the diabatic representation,

Table 2. Average Unsigned Percentage Errors in All Six Observables for GCS and CS Switching Schemes and the D Criterion for Strong Interaction Regions[a]

			MXH	MCH	YRH	overall
NLDM	a	GCS	21	33	66	40
		CS[a]	24	34	17	25
	d	GCS	17	29	389	145
		CS[a]	19	28	32	26
LDM	a	GCS	21	34	67	41
		CS	21	33	18	24
	d	GCS	22	30	661	238
		CS	24	29	61	38
PDDM	a	GCS	21	33	61	38
		CS	23	32	18	24
	d	GCS	18	29	453	167
		CS	21	28	47	32

[a] This is equivalent to original CSDM.

we are hesitant to recommend it for electronically nonadiabatic processes, although it should be noted that if one uses the L criterion in the diabatic representation, the LDM results are good.

Table 2 also shows some results for global coherent switching (GCS). This scheme is interesting because it is the scheme that has always been used in TFS and FSTU∇V surface hopping calculations. It works well for the MXH and MCH systems, and GCS switching in both adiabatic and diabatic representations is about as accurate as CS switching for these cases. However, GCS switching is inaccurate for the YRH system.

The full results in Supporting Information confirm that the CS prescription is the best switching algorithm as concluded[16] previously. The self-consistent switching (SCS) algorithm works almost as well as the CS algorithm for the MXH and MCH systems and it shows very good results for the YRH system when simulations are done in the adiabatic representation, but SCS shows poorer results when YRH simulations are carried out in the diabatic representation. The natural switching (NS) algorithm shows the same tendencies as the SCS algorithm, except that NS shows more representation dependence than SCS for the YRH systems. The full tables in Supporting Information also show that all three decay-of-mixing methods (NLDM, LDM, and PDDM) have similar behavior when used with the same switching algorithm. The results are more dependent on the choice of switching algorithm than on the choice of the decay-of-mixing method.

Next, we consider how fast or slow the system decoheres. The region where the trajectory has negligible nonadiabatic and/or diabatic coupling is not interesting. Therefore, we average the decay time only over the portions of the trajectories where $0.02 \le \rho_{kk} \le 0.98$. Recall that $\tau_{kk'}$ is, except for a factor of 2, the reciprocal of a first-order rate constant, and we therefore average the rates, $1/\tau_{12}$, not the decay times. The result is re-expressed in time units by taking a reciprocal, i.e.

$$\bar{\tau} \equiv \frac{1}{\langle 1/\tau_{12} \rangle} \tag{32}$$

Table 3. Mean Decay of Mixings Times (fs) for the CS Switching Algorithm with the NLDM, LDM, and PDDM Decay of Mixing Schemes[a]

rep	MXH (SB) $j = 0$	MXH (WL) $j = 0$	MCH (SB) $j = 0$	MCH (WL) $j = 0$	YRH(0.2) $E = 1.02$ eV
			Nonlinear Decay of Mixing (NLDM)		
a	7.8(57)	8.5(52)	8.0(37)	26.7(53)	34.8(76)
d(D)	9.5(57)	7.4(52)	9.4(37)	10.9(53)	35.2(84)
d(S)	9.5(67)	7.4(51)	9.4(44)	10.9(54)	35.3(84)
d(L)	9.4(103)	7.4(74)	9.4(79)	10.8(79)	35.4(61)
			Linear Decay of Mixing (LDM)		
a	7.7(56)	8.3(53)	7.9(38)	25.9(54)	34.4(77)
d(D)	9.6(66)	7.3(5)	9.2(38)	10.8(53)	34.4(85)
d(S)	9.6(70)	7.4(51)	9.2(44)	10.8(54)	34.4(85)
d(L)	9.4(109)	7.4(74)	9.0(77)	10.7(80)	34.5(63)
			Population-Driven Decay of Mixing (PDDM)		
a	7.8(50)	8.6(52)	7.8(37)	26(54)	34.4(76)
d(D)	9.4(57)	7.3(52)	9.1(37)	10.2(53)	35.0(83)
d(S)	9.4(65)	7.3(52)	9.1(44)	10.2(55)	35.0(83)
d(L)	9.2(101)	7.3(75)	9.0(78)	10.3(80)	35.0(61)

[a] Numbers in parentheses are the average number of minima of D, S, or L per trajectory.

The results for the CS switching algorithm with NLDM, LDM, and PDDM decay of mixing methods are shown for five of the 17 cases in Table 3. Notice that the average decay-of-mixing time is slightly shorter in the adiabatic representation than in the diabatic representation for MXH (SB) with $j = 0$ and MCH (SB) with $j = 0$, but the average decay-of-mixing time is much longer in the adiabatic representation than in the diabatic representation for MXH (WL) with $j = 0$ and MCH (WL) with $j = 0$. For YRH (0.2) with $j = 0$ the average decay-of-mixing is about the same. NLDM, LDM, and PDDM decay of mixing methods give similar average decay-of-mixing times. For the MXH (SB) and MCH (SB) cases with $j = 0$, the Calaveras County representation is the adiabatic representation, while for the MXH (WL) and MCH (WL) cases with $j = 0$, the Calaveras County representation is the diabatic representation. The examples in Table 3 show that the representation with the shorter average decay-of-mixing time corresponds to the Calaveras County representation for the crossing and conical intersection cases of nonadiabatic transitions. For the noncrossing cases, the average decay-of-mixing times are about the same.

Since the method of comparing semiclassical calculations to quantum ones is improved in this paper (as compared to our previous ones), we also compared other semiclassical results to the quantum ones by precisely the same procedure. Table 4 compares the overall errors for the present methods to trajectory surface hopping and the semiclassical Ehrenfest method. The improvement is significant. Again, it is not necessary to include computation costs since the cost for all methods in the table are similar.

VII. Concluding Remarks

The decay of mixing (DM) formalism[18] was developed by adding decoherence to the semiclassical Ehrenfest method and has been shown to be more accurate than surface hopping methods for non-Born-Oppenheimer collisions. In this article,

Table 4. Comparison of Average Unsigned Percentage Errors of Present Methods to Those for Trajectory Surface Hopping and Ehrenfest Methods

method	rep	MXH	MCH	YRH	overall
ECP[a]	a	97	49	201	116
	d	117	55	495	222
TFS+[b]	a	64	48	29	47
	d	51	40	361	151
FSTU∇V[c]	a	52	52	24	43
	d	28	36	125	63
SE[d]	a	65	55		
	d	65	55		
CSDM	a	24	34	17	25
	d(D)	19	28	32	26
CSDM/L	a	21	33	18	24
	d(L)	23	29	30	27
CSDM/PD	a	23	32	18	24
	d(L)	20	29	22	24

[a] Exact complete passage trajectory surface hopping method of Parlant and Gislason. [b] Tully's fewest-switches trajectory surface hopping method. Note that we denote this as TFS+ because frustrated hops are ignored in the original method, and in a notation established in earlier articles,[16,33] this is denoted by a + sign. Originally (refs 82 and 31), we denoted this as ++. [c] Fewest switches with time uncertainty and grad *V* criterion for frustrated hops (trajectory surface hopping). [d] Semiclassical Ehrenfest. Mean errors cannot be computed for YRH because SE incorrectly predicts no reactive or quenching trajectories for two of the three YRH cases.

we have tested the sensitivity of the DM method to details of how decoherence is introduced into the off-diagonal elements of the density matrix and how the switching probability is computed. The comparison of our previous coherent switches with decay of mixing (CSDM) method to the new methods shows that CSDM is very robust with respect to details of the implementation. In particular, numerical tests based on ensembles of trajectories show that allowing for new forms of decoherence and changes in the switching algorithm do not lead to significant overall improvement, although we can achieve an average improvement of a couple of percentage points.

Although the present article only involves two-state applications, all methods are applicable to general multistate cases. The new methods presented here complement the older methods in that we now have a series of methods with various levels of coherence and decoherence. (The PDDM method is more coherent than the LDM method, and the LDM method has similar coherence to the NLDM method. Among the four switching algorithms, GCS is the most coherent, CS is less, SCS is even less, and NS is the least coherent.) This may help us to better understand the physical nature of decoherence.

Acknowledgment. The authors are grateful to Shikha Nangia for many helpful contributions and to David Micha for helpful suggestions. This work was supported in part by the National Science Foundation under grant no. CHE03-49122.

Supporting Information Available: A list of acronyms and abbreviations, mean unsigned errors not reported in the text, mean decay of mixing times, quantum mechanical results, and semiclassical trajectory results. This material is available free of charge via the Internet at http://pubs.acs.org.

References

(1) Bunker, D. L. *Methods Comput. Phys*. **1971**, *10*, 287.

(2) Truhlar, D. G.; Muckerman, J. T. In *Atom-Molecule Collision Theory: A Guide for the Experimentalist;* Bernstein, R. B., Ed.; Plenum: New York, 1979; p 505.

(3) (a) Allen, M. P.; Tildesley, D. J. *Computer Simulation of Liquids*; Clarendon Press: Oxford, 1987. (b) Brooks, C. L., III; Karplus, M.; Pettit, B. M. *Adv. Chem. Phys*. **1988**, *71*, 1. (c) Benjamin, I. In *Modern Methods for Multidimensional Dynamics Computations in Chemistry*; Thompson, D. L., Ed.; World Scientific: Singapore, 1998; p 101. (d) Stanton, R. V.; Miller, J. L.; Kollman, P. A. In *Modern Methods for Multidimensional Dynamics Computations in Chemistry*; Thompson, D. L., Ed.; World Scientific: Singapore, 1998; p 255. (e) Rice, B. M. In *Modern Methods for Multidimensional Dynamics Computations in Chemistry*; Thompson, D. L., Ed.; World Scientific: Singapore, 1998; p 472.

(4) For recent review papers, see: (a) Tully, J. C. In *Modern Methods for Multidimensional Dynamics* Computations in Chemistry, Thompson, D. L., Ed.; World Scientific: Singapore, 1998; p 34. (b) Ben-Nun, M.; Martinez, T. J. *Adv. Chem. Phys*. **2002**, *121*, 439. (c) Jasper, A. W.; Kendrick, B. K.; Mead, C. A.; Truhlar, D. G. In *Modern Trends in Chemical Reaction Dynamics, Part I*; Yang, X., Liu, K., Eds.; World Scientific: Singapore, 2004; pp 329−392. (d) Worth, G. A.; Robb, M. A. *Adv. Chem. Phys*. **2002**, *124*, 355. (e) Zhu, C.; Mil'nikov, G. V.; Nakamura, H. In *Modern Trends in Chemical Reaction Dynamics, Part I*; Yang, X., Liu, K., Eds.; World Scientific: Singapore, 2004; pp 393−473. (f) Jasper, A. W.; Zhu, C.; Nangia, S.; Truhlar, D. G. *Faraday Discuss.* **2004**, *127*, 1. (g) Stock, G.; Thoss, M. In *Electronic Structure, Dynamics and Spectroscopy*; Domcke, W., Yarkony, D. R., Köppel, H., Eds.; World Scientific: Singapore, 2004; p 619.

(5) (a) Sakurai, J. J. *Modern Quantum Mechanics*; Addison-Wesley: Redwood City, CA, 1985. (b) Bohm, A. *Quantum Mechanics: Foundations and Applications*, 3rd ed.; Springer-Verlag: New York, 1993; p 64. (b) Gottfried. K.; Yan, T.-M. *Quantum Mechanics: Fundamentals*, 2nd ed.; Springer: New York, 2003; p 46.

(6) (a) Fano, U. *Rev. Mod. Phys*. **1957**, *29*, 74. (b) Blum, K. *Density Matrix Theory and Applications*; Plenum: New York, 1981. (c) Schatz, G. C.; Ratner, M. A. *Quantum Mechanics in Chemistry*; Prentice Hall: Englewood Cliffs, 1993; p 277. (d) May, V.; Kühn, O. *Charge and Energy Transfer Dynamics in Molecular Systems*; Wiley-VCH: Berlin, 2000; p 73.

(7) (a) Johnson, C. S., Jr.; Tully, J. C. *J. Chem. Phys*. **1964**, *40*, 1764. (b) Coalson, R. D.; Karplus, M. *J. Chem. Phys.* **1983**, *79*, 6150. (c) Bittner, E. R.; Light, J. C. *J. Chem. Phys*. **1994**, *101*, 2446. (d) Berman, M.; Kosloff, R.; Tal-Ezer, H. *J. Phys. A* **1992**, *25*, 1283. (e) Pesce, L.; Saalfrank, P. *J. Chem. Phys.* **1998**, *108*, 3045. (f) Guo, H.; Chen, R. *J. Chem. Phys*. **1999**, *110*, 6626. (g) Costella, F. *J. Stat. Phys*. **2001**, *104*, 387. (h) Kristensen, J. H.; Hoatson, G. L.; Vold, R. L. *J. Comput. Phys.* **2001**, *170*, 415. (i) Horenko, I.; Weiser, M.; Schmidt, B.; Schütte, C. *J. Chem. Phys.* **2004**, *120*, 8913. (j) Shi, Q.; Geva, E. *J. Chem. Phys*. **2004**, *121*, 3393.

(8) Mukamel, S. *Principles of Nonlinear Optical Spectroscopy*; Oxford University Press: New York, 1995.

(9) Beksic, D.; Micha, D. A. *J. Chem. Phys*. **1995**, *103*, 3795.

(10) Bittner, E. R.; Rossky, P. J. *J. Chem. Phys*. **1995**, *103*, 8130.

(11) Ashkenaz, G.; Kosloff, R.; Ratner, M. A. *J. Am. Chem. Soc*. **1999**, *121*, 3386.

(12) Prezhdo, O. V. *Phys. Rev. Lett*. **2000**, *85*, 4413.

(13) Santer, M.; Manthe, U.; Stock, G. *J. Chem. Phys*. **2001**, *114*, 2001.

(14) Prezhdo, O. V.; Rossky, P. J. *J. Chem. Phys*. **1997**, *107*, 5863.

(15) Zhu, C.; Jasper, A. W.; Truhlar, D. G. *J. Chem. Phys*. **2004**, *120*, 5543.

(16) Zhu, C.; Nangia, S.; Jasper, A. W.; Truhlar, D. G. *J. Chem. Phys*. **2004**, *121*, 7658.

(17) Wong, K. F.; Rossky, P. J. *J. Chem. Phys*. **2002**, *116*, 8418, 8429.

(18) Hack, M. D.; Truhlar, D. G. *J. Chem. Phys*. **2001**, *114*, 9305.

(19) (a) Burant, J. C.; Tully, J. C. *J. Chem. Phys*. **2000**, *112*, 6097. (b) Wan, C. C.; Schofield, J. *J. Chem. Phys*. **2002**, *116*, 494. (c) Ben-Num, M.; Martinez, T. J. *Adv. Chem. Phys*. **2002**, *121*, 439. (d) Donoso, A.; Zheng, Y.; Martens, C. C. *J. Chem. Phys*. **2003**, *119*, 5010. (e) Roman, E.; Martens, C. C. *J. Chem. Phys*. **2004**, *121*, 11572.

(20) Tully, J. C.; Preston, R. K. *J. Chem. Phys*. **1971**, *55*, 562.

(21) Blais, N. C.; Truhlar, D. G. *J. Chem. Phys*. **1983**, *79*, 1334.

(22) Parlant, G.; Gislason, E. A. *J. Chem. Phys*. **1989**, *91*, 4416.

(23) Parlant, G.; Alexander, M. H. *J. Chem. Phys*. **1990**, *92*, 2287.

(24) Tully, J. C. *J. Chem. Phys*. **1990**, *93*, 1061.

(25) Coker, D. F.; Xiao, L. *J. Chem. Phys*. **1995**, *102*, 496.

(26) Topaler, M. S.; Hack, M. D.; Allison, T. C.; Liu, Y.-P.; Mielke, S. L.; Schwenke, D. W.; Truhlar, D. G. *J. Chem. Phys*. **1997**, *106*, 8699.

(27) Sizun, M.; Song, J.-B.; Gislason, E. A. *J. Chem. Phys*. **1998**, *109*, 4815.

(28) Hack, M. D.; Jasper, A. W.; Volobuev, Y. L.; Schwenke, D. W.; Truhlar, D. G. *J. Phys. Chem. A* **1999**, *103*, 6309.

(29) Babikov, D.; Gislason, E. A.; Sizun, M.; Aguillon, F.; Sidis, V. *J. Chem. Phys*. **2000**, *112*, 7032.

(30) Hack, M. D.; Jasper, A. W.; Volobuev, Y. L.; Schwenke, D. W.; Truhlar, D. G. *J. Phys. Chem. A* **2000**, *104*, 217.

(31) Jasper, A. W.; Stechmann, S. N.; Truhlar, D. G. *J. Chem. Phys*. **2002**, *116*, 5424; **2002**, *117*, 10247(E).

(32) Zhu, C.; Kamisaka, H.; Nakamura, H. *J. Chem. Phys*. **2002**, *116*, 3234.

(33) Jasper, A. W.; Truhlar, D. G. *Chem. Phys. Lett*. **2003**, *369*, 60.

(34) Meyer, H.-D.; Miller, W. H. *J. Chem. Phys*. **1979**, *70*, 3214.

(35) Kuntz, P. J.; Kendrick, J.; Whitton, W. N. *Chem. Phys*. **1979**, *38*, 147.

(36) Meyer, H.-D.; Miller, W. H. *J. Chem. Phys*. **1980**, *72*, 2272.

(37) Micha, D. A. *J. Chem. Phys*. **1983**, *78*, 7138.

(38) Amarouche, M.; Gadea, F. X.; Durup, J. *Chem. Phys.* **1989**, *130*, 145.

(39) Garcia-Vela, A.; Gerber R. B.; Imre, D. G. *J. Chem. Phys*. **1992**, *97*, 7242.

(40) Billing, G. D. *Int. Rev. Phys. Chem*. **1994**, *13*, 309.

(41) Kohen, D.; Stillinger, F. H.; Tully, J. C. *J. Chem. Phys*. **1998**, *109*, 4713.

(42) Thachuk, M.; Ivanov, M. Y.; Wardlaw, D. M. *J. Chem. Phys.* **1998**, *109*, 5747.

(43) Micha, D. A. *Adv. Quantum Chem*. **1999**, *35*, 317.

(44) Yolobuev, Y. L.; Hack, M. D.; Truhlar, D. G. *J. Phys. Chem. A* **1999**, *103*, 6225.

(45) Mavri, J. *Mol. Simul*. **2000**, *23*, 389.

(46) Hack, M. D.; Jasper, A. W.; Volobuev, Y. L.; Schwenke, D. W.; Truhlar, D. G. *J. Phys. Chem. A* **2000**, *104*, 217.

(47) Volobuev, Y. L.; Hack, M. D.; Topaler, M. S.; Truhlar, D. G. *J. Chem. Phys*. **2000**, *112*, 9716.

(48) Hack, M. D.; Truhlar, D. G. *J. Phys. Chem. A* **2000**, *104*, 7917.

(49) Zurek, W. H. *Phys. Rev. D* **1981**, *24*, 1516.

(50) Zurek, W. H. *Rev. Mod. Phys*. **2003**, *75*, 715.

(51) Zurek, W. H. *Phys. Rev. D* **1982**, *26*, 1862.

(52) Zeh, H. D. In *New Developments on Fundamental Problems in Quantum Physics*; Ferrero, M., van der Merwe, A., Eds.; Kluwer: Dordrecht, 1997.

(53) Zurek, W. H. *Philos. Trans. R. Soc. London, Ser. A* **1998**, *356*, 1793.

(54) Stock, G. *Phys. Rev. E* **1995**, *51*, 2004.

(55) (a) Nakajima, S. *Prog. Theor. Phys.* **1958**, *20*, 948. (b) Zwanzig, R. *Physica* **1964**, *30*, 1109.

(56) (a) Feynman, R. P.; Vernon, F. L., Jr. *Ann. Phys. (N.Y.)* **1963**, *24*, 118. (b) Caldeira, A. O.; Leggett, A. *J. Physica A* **1983**, *121*, 587.

(57) Zeh, H. D. *Lect. Notes Phys.* **2000**, *538*, 19.

(58) (a) Gisin, N.; Percival, I. C. *J. Phys. A* **1992**, *25*, 5677. (b) Diosi, L.; Gisin, N.; Strunz, W. T. *Phys.* Rev. A **1998**, *58*, 1699.

(59) Anglin, J. R.; Paz, J. P.; Zurek, W. H. *Phys. Rev. A* **1997**, *55*, 4041.

(60) (a) Bloch, F. *Phys. Rev.* **1946**, *70*, 460. (b) Redfield, A. G. *Adv. Magn. Reson.* **1965**, *1*, 1. (c) Lindblad, G. *Commun. Math. Phys.* **1976**, *48*, 119. (d) Gorini, V.; Kossalowski, A.; Sudarshan, E. C. G. *J. Math. Phys.* **1976**, *17*, 821. (e) Haake, F.; Risken, H.; Savage, C.; Walls, D. *Phys. Rev. A* **1986**, *34*, 3969. (f) Laird, B. B.; Budimir, J.; Skinner, J. L. *J. Chem. Phys.* **1991**, *94*, 4391. (g) Suarez, A.; Silbey, R.; Oppenheim, I. *J. Chem. Phys.* **1992**, *97*, 5101. (h) Diosi, L.; Kiefer, C. *Phys. Rev. Lett.* **2000**, *85*, 3552. (i) Zhao, Y.; Chen, G. H. *J. Chem. Phys.* **2001**, *114*, 10623.

(61) (a) Hu, B. L.; Paz, J. P.; Zhang, Y. *Phys. Rev. D* **1992**, *45*, 2843. (b) Hu, B. L.; Paz, J. P.; Zhang, Y. *Phys. Rev. D* **1993**, *47*, 1576.

(62) (a) Lindblad, G. *J. Phys. A* **1996**, *29*, 4197. (b) Makri, N. *J. Phys. Chem. A* **1998**, *102*, 4414. (d) Meier, C.; Tannor, D. J. *J. Chem. Phys.* **1999**, *111*, 3365. (d) Burghardt, I. *J. Chem. Phys.* **2001**, *114*, 89. (e) Wilkie, J. *J. Chem. Phys.* **2001**, *114*, 7736. (f) Shi, Q.; Geva, E. *J. Chem. Phys.* **2003**, *119*, 12063. (g) Rau, A. R. P.; Zhao, W. *Phys. Rev. A* **2003**, *68*, 52102. (h) Kleinekathoefer, *J. Chem. Phys.* **2004**, *121*, 2505. (i) Shi, G.; Geva, E. *J. Chem. Phys.* **2004**, *121*, 3393. (j) Lee, J.; Kim, I.; Ahn, D.; McAneney, H.; Kim, M. S. *Phys. Rev. A* **2004**, *70*, 24301.

(63) Mead, C. A.; Truhlar, D. G. *J. Chem. Phys*. **1982**, *77*, 6090.

(64) Nakamura, H.; Truhlar, D. G. *J. Chem. Phys*. **2001**, *115*, 10353.

(65) Kuppermann, A.; Abrol, R. *Adv. Chem. Phys*. **2002**, *124*, 283.

(66) Köppel, H. In *Conical Intersections: Electronic Structure, Dynamics and Spectroscopy*; Domcke, W., Yarkony, D. R., Köppel, H., Eds.; World Scientific: Singapore, 2004; p 175.

(67) Kleckner, M.; Ron, A. *Phys. Rev. A* **2001**, *63*, 22110.

(68) Kohen, D.; Tannor, D. J. *J. Chem. Phys*. **1997**, *107*, 5141.

(69) Elran, Y.; Brumer, P. *J. Chem. Phys*. **2004**, *121*, 2673.

(70) Sinha, S. *Phys. Lett. A* **1997**, *228*, 1.

(71) Allison, T. C.; Truhlar, D. G. In *Modern Methods for Multidimensional Dynamics Computations in Chemistry*; Thompson, D. L., Ed.; World Scientific: Singapore, 1998; p 618.

(72) Landau, L. D. *Phys. Z. Sowjet*. **1932**, *2*, 46.

(73) Zener, C. *Proc. R. Soc. London Ser. A* **1932**, *137*, 696.

(74) Stückelberg, E. C. G. *Helv. Phys. Acta* **1932** *5*, 369.

(75) Teller, E. *J. Phys. Chem*. **1937**, *41*, 109.

(76) Longuet-Higgins, H. C. *Adv. Spectrosc*. **1961**, *2*, 429.

(77) Herzberg, G. *Electronic Spectra and Electronic Structure of Polyatomic Molecules*; van Nostrand Reinhard: New York 1966; p 442.

(78) Jasper, A. W.; Truhlar, D. G. *J. Chem. Phys*. **2005**, *22*, 044101.

(79) Rosen, N.; Zener, C. *Phys. Rev*. **1932**, *18*, 502.

(80) Demkov, Y. N. *Zh. Eksp. Teor. Fiz*. **1963**, *45*, 195 [English transl.: *Sov. Phys. JETP* **1964**, *18*, 138].

(81) Osherov, V. L.; Voronin, A. L. *Phys. Rev. A* **1994**, *49*, 265.

(82) Jasper, A. W.; Hack, M. D.; Truhlar, D. G. *J. Chem. Phys*. **2001**, *115*, 1804.

(83) Press, W. H.; Teukolsky, S. A.; Vetterling, W. T.; Flannery, B. P. *Numerical Recipes in fortran*, 2nd ed; Cambridge University Press: Cambridge, U.K., 1994; p 716.

(84) Zhu, C.; Nangia, S.; Jasper, A. W.; Volobuev, Y.; Topaler, M. S.; Allison, T. C.; Hack, M. D.; Liu, Y.-P.; Anderson, A. G.; Stechmann, S. N.; Miller, T. F., III; Blais, N. C.; Truhlar, D. G. NAT-version 8.1, University of Minnesota, 2004.

(85) Topaler, M. S.; Allison, T. C.; Schwenke, D. W.; Truhlar, D. G. *J. Chem. Phys*. **1998**, *109*, 3321; **1999**, *110*, 687(E).

CT050021P

JCTC Journal of Chemical Theory and Computation

Assessment of Density Functionals for Predicting One-Bond Carbon−Hydrogen NMR Spin−Spin Coupling Constants

Sergey N. Maximoff, Juan E. Peralta, Verónica Barone, and Gustavo E. Scuseria*

Department of Chemistry, Rice University, Houston, Texas 77005-1892

Received March 31, 2005

Abstract: We benchmark the performance of 20 approximate density functionals for the calculation of one-bond carbon−hydrogen NMR spin−spin coupling constants (SSCCs). These functionals range from the simplest local-spin density approximation to novel meta-generalized gradient approximation and hybrid density functionals. Our testing set consists of 72 diverse molecules that represent multiple types of hybridization of the carbon atom corresponding to 96 experimentally measured one-bond carbon−hydrogen SSCCs. Our results indicate that generalized gradient approximations perform best for this type of coupling.

1. Introduction

Nuclear magnetic resonance (NMR) spectroscopy has become an indispensable instrument of structural analysis for many experimental chemists, largely because of the high sensitivity of chemical shifts and indirect spin−spin coupling constants (SSCCs) to the chemical environment.

Back in 1970, John Pople and co-workers[1] recognized in a seminal paper the importance of NMR spectroscopy as a powerful tool for structural chemistry and computed the leading contribution to one-bond carbon-proton $^1J_{CH}$ SSCCs (the Fermi contact term) for a series of molecules using the self-consistent perturbation theory based on the INDO approximation, one of the most advanced techniques at the time. Since that paper was published, applied computational quantum chemistry has advanced enormously. The niche previously filled with semiempirical methods has been taken over by rapidly developing approximate approaches based on density functional theory (DFT).[2,3] This remarkable method has received widespread recognition among chemists due to its relatively high accuracy and attractively modest computational cost compared to computationally demanding wave function-based techniques (see ref 4 and references therein). Despite this success, little is known about the accuracy of approximate functionals in predicting SSCCs except for the works of Helgaker, Handy, Cremer, and co-workers,[5−7] who found that the hybrid B3LYP functional delivers satisfactory accuracy for SSCCs over a small set of molecules. The performance of three functionals for other types of coupling was also reported in ref 8.

Here, we follow Pople's endeavor and present a *comprehensive* benchmark study of various DFT functionals in predicting one-bond C−H SSCCs. We attempt to answer the important practical question of how well approximate functionals predict experimental SSCCs.

2. Spin−Spin Coupling Constants

The basic theory of nonrelativistic SSCCs was outlined by Ramsey back in 1953.[9] He identified four distinct contributions to an isotropic SSCC: the Fermi contact (FC), spin-dipolar (SD), the paramagnetic spin−orbit (PSO), and diamagnetic spin−orbit (DSO) terms. The FC and SD triplet perturbations originate from the interaction between the electronic spin and the nuclear momenta, while the PSO and DSO singlet perturbations arise from the interaction between the electron orbital and the nuclear magnetic momenta. The DSO contribution appears in first-order and is evaluated as an expectation value over the ground state. The remaining FC, SD, and PSO terms appear in second-order and involve the first-order response of the molecular orbital coefficients available from solving the first-order coupled-perturbed equations for 10 external perturbations per coupled atom pair. In many cases, the isotropic FC contribution dominates the total value of SSCC, thus only one external perturbation per

* Corresponding author phone: (713)348-5336; fax: (713)348-2727; e-mail: guscus@rice.edu.

10.1021/ct050083f CCC: $30.25
Published on Web 06/04/2005

Table 1: Properties of Approximate Functionals Employed in This Work

functional	class	CPU[a]	refs
LSDA[b]	local approximation	1.0	2,31
PW91	GGA	1.3	32,33
PBE	GGA	1.3	28
BLYP	GGA	1.3	34
OLYP	GGA	1.4	35
BP86	GGA	1.3	36,37
KT2	GGA	1.4	29
HCTH407	GGA	1.4	38
PKZB	meta-GGA	1.8	39
VSXC	meta-GGA	1.9	40
TPSS	meta-GGA	1.8	41
B3LYP[c]	GGA hybrid	6.6	42
B3P86	GGA hybrid	6.5	17
O3LYP	GGA hybrid	6.3	35
PBE0	GGA hybrid	6.7	22,43
B971	GGA hybrid	6.6	44
B972	GGA hybrid	6.6	45
B98	GGA hybrid	6.9	46
B1B95	meta-GGA hybrid	7.3	47
TPSSh	meta-GGA hybrid	6.6	20

[a] We estimate the approximate computational cost (two 900 MHz Intel Itanium2 CPUs) required for the evaluation of all SSCCs in $C_6H_5NO_2$ with 514 basis functions. The quoted computational cost is measured relative to LSDA (162 s). [b] The sum of the Dirac exchange and Vosko-Wilk-Nusair (VWN5) parametrization (formula V of ref 31) of the correlation energy of the homogeneous electron gas. [c] The local component is VWN3 functional (formula I of ref 31) as implemented in Gaussian.[17]

coupled atom pair needs to be considered, dramatically reducing the computational cost. We refer the interested reader to the reviews on the theory of SSCCs by Fukui,[10] Contreras,[11,12] and Helgaker.[13,14]

To calculate SSCCs, we evaluate the four Ramsey's contributions using the algorithms[5,6,15,16] implemented in the Gaussian03 suite of programs.[17] The FC term, characterized by the value of the electron density at the nuclei, imposes stringent requirements on the quality of the basis set in the core region. Therefore, we employ the aug-cc-pVTZ-J basis set designed for the calculation of SSCCs.[18] Peralta et al. have found that this basis set yields SSCCs in satisfactory close agreement to the complete basis set limit for DFT (B3LYP) calculations.[19] In fact, the difference between the basis set limit and the aug-cc-pVTZ-J values is less than 0.3 Hz for $^1J_{CH}$ SSCCs in CH_4, FCH_3, and C_2H_4.[19]

3. Approximate Density Functionals

Among numerous approximations to the exchange-correlation energy available in the literature, we select 20 exchange-correlation functionals for this study. A brief description of these approximations is assembled in Table 1.

The computational cost of an approximate functional is in practice controlled by the nature of the variables included and the complexity of its expression. The simplest functional, the local spin-density approximation (LSDA), depends solely on the electron spin-density. Addition of the density first derivatives leads to Generalized Gradient Approximations (GGAs). Many prominent functionals belong to the meta-GGA class, a family of functionals that additionally depend on the noninteracting kinetic energy density along with the GGA ingredients. Hybrid functionals introduce a mixture of exact (Hartree−Fock type) exchange, yielding very successful functionals for thermochemistry.[20]

4. Calculation Details

To ensure the validity of our assessment, we benchmark the 20 chosen functionals over an extensive set of 72 chemically diverse molecules that correspond to 96 experimentally measured one-bond C−H couplings involving 22 aromatic, 28 sp^3, 34 sp^2, and 12 sp C atoms (see Supporting Information). All calculated NMR couplings as well as their individual contributions are available as Supporting Information. This set encompasses the original Pople set[1] and also includes additional couplings taken from ref 21. Since accurate experimental geometries are only available for a few molecules in this set, we optimized the geometries of the sample molecules at the hybrid PBE0/6-31+G(2df,p) level of theory,[22] which is deemed sufficiently accurate for the present purpose.

Although rovibrational effects notably impact SSCCs,[23,24] their evaluation is computationally demanding.[25] Lutnaes, Ruden, and Helgaker note, however, that the zero-point vibrational contribution (ZPVCs) prevails in the rovibrational effects.[26] Ruden et al.[25] have shown that the value of the ZPVC for one-bond carbon−hydrogen SSCCs appear to be very close to 5 Hz (within tenths of Hz). Hence, an ad hoc correction of 5 Hz was added to all calculated one-bond C−H SSCCs, to effectively account for the ZPVC.

The experimental SSCCs are measured at temperatures that imply free rotation in flexible species rendering indistinguishable otherwise chemically different atoms. We account for this effect by averaging over equivalent pairs of atoms considering only one conformer, however.

Experimental SSCCs are often measured in solution, while our calculations correspond to an isolated molecule, i.e., solvent effects are neglected.[21,27] We rank the performance of the approximate functionals according to the values of the mean error (ME), the mean absolute error (MAE), the standard deviation (STDEV), and the minimum and maximum deviations with respect to the experimental data. Whenever the sign is important, we assume that the experimental values are subtracted from the theoretical ones. We use accuracy and computational cost as a guide in selecting the most prominent functional. In this comparison, we consider equivalent all errors bellow the margin of ±2 Hz set by the solvent, geometry, rovibrational, and finite basis set size effects.

5. Results and Discussion

In Table 2 we present the statistics for the complete benchmark set. All GGA functionals improve over the simpler LSDA functional. Accuracy of the nonempirical GGAs PW91 and PBE is similar. This does not come as a surprise since PBE is conceived as a computationally equivalent simplification of the PW91 functional.[28] The PBE0 ab initio hybrid (based on the PBE functional) worsens the overestimation of PBE. PKZB, the meta-GGA extension of

Table 2: Statistical Results for 96 One-Bond $^1J_{CH}$ Coupling Constants in a Set of 72 Molecules Using Several Functionals (in Hz)[a]

functional	MAE	ME	STDEV	max.(+)	min.(−)
LSDA	23.07	−23.07	4.47		−43.27
PW91	3.54	1.38	5.17	18.80	−11.21
PBE	3.49	−0.26	4.91	15.39	−14.51
BLYP	16.41	16.41	7.47	42.13	
OLYP	4.78	3.91	5.95	24.52	−8.31
BP86	3.90	−1.77	4.79	13.89	−15.60
KT2	20.48	20.48	10.40	58.70	
HCTH407	9.01	−8.56	5.05	5.70	−23.41
PKZB	4.72	−3.45	4.78	10.77	−21.55
VSXC	9.00	−8.72	4.88	6.44	−25.98
TPSS	24.98	24.98	7.56	52.64	
B3LYP	15.89	15.89	6.73	38.26	
B3P86	3.56	2.32	4.75	17.57	−10.01
O3LYP	5.40	4.95	5.68	23.95	−6.94
PBE0	5.51	5.20	4.97	21.35	−7.22
B971	11.94	11.89	4.94	26.94	−2.44
B972	3.51	1.78	4.60	14.79	−12.89
B98	12.42	12.40	5.12	27.65	−1.29
B1B95	7.98	7.83	4.87	23.25	−4.27
TPSSh	26.43	26.43	7.62	53.68	

[a] Individual values can be obtained from the Supporting Information.

Table 3: Statistical Results for 12 One-Bond $^1J_{CH}$ sp-Type Couplings in a Set of 12 Molecules Using Several Functionals (in Hz)[a]

functional	MAE	ME	STDEV	max.(+)	min.(−)
LSDA	23.83	−23.83	4.28		−34.69
PW91	12.08	11.65	5.30	18.80	−2.57
PBE	9.50	8.46	5.40	15.39	−6.25
BLYP	33.87	33.87	4.86	42.13	
OLYP	16.30	16.27	5.97	24.52	−0.19
BP86	8.19	6.93	5.36	13.89	−7.59
KT2	44.73	44.73	8.04	58.70	
HCTH407	3.56	−0.01	5.74	5.70	−16.34
PKZB	5.40	2.89	6.31	10.77	−15.01
VSXC	3.45	−1.21	6.01	6.44	−18.19
TPSS	42.30	42.30	6.12	52.64	
B3LYP	31.50	31.50	4.06	38.26	
B3P86	11.67	11.67	4.50	17.57	
O3LYP	16.82	16.82	5.20	23.95	
PBE0	15.33	15.33	4.52	21.35	
B971	21.47	21.47	3.95	26.94	
B972	10.14	9.66	4.68	14.79	−2.87
B98	22.24	22.24	3.83	27.65	
B1B95	16.82	16.82	4.39	23.25	
TPSSh	44.05	44.05	5.62	53.68	

[a] Individual values can be obtained from the Supporting Information.

the PBE functional, features performance resembling that of PBE. TPSS, a recent attempt to further improve over PKZB, severely overestimates one-bond C−H SSCCs. The semiempirical hybrid fit TPSSh to atomization energies based on TPSS worsens the TPSS performance, too. The combination OLYP of semiempirical exchange functional OPTX of Handy and Cohen and the Lee−Yang−Parr correlation functional outperforms the older and better known combination BLYP. The corresponding hybrid functionals, O3LYP and B3LYP, display a performance pattern similar to that of the parent GGAs OLYP and BLYP. The recently developed KT2 functional, a GGA which is fitted to accurate exchange-correlation potential data and known for its excellent description of NMR shielding tensors,[29] delivers high errors for one-bond C−H SSCCs. Two highly parametrized semiempirical functionals, VSXC and HCTH407, produce very similar results. Becke's hybrid fit B98 and its later revision B971 feature similar performance. The later parametrization B972 that relies on accurate exchange-correlation potential data significantly improves over B98 and B971. Overall, only the GGAs PW91, PBE, and BP86 and the hybrid B3P86 and B972 functionals achieve a MAE smaller than 4 Hz.

Our results for BLYP, B3LYP, and KT2 functionals are in line with the findings of Keal et al. in a set of 11 molecules.[30] Although the number of $^1J_{CH}$ calculated by these authors is too small to draw statistically significant conclusions, they found that calculated one-bond C−H SSCCs are systematically overestimated by these three functionals. These authors[30] report that the error for the KT2 functional ranges from +8 Hz to +38 Hz, while we report a KT2 ME of +20 Hz. Lutnæs et al. have investigated the performance of B3LYP for a set of 10 rigid molecules[26] and concluded that this functional overestimates experimental values by ∼10%, in agreement with our conclusions. Most of the SSCCs in the present study are overestimated. Taking into account that $^1J_{CH}$ couplings are dominated by the FC contribution, it seems this term is responsible for such an overestimation (see Supporting Information).

In Table 3 we present the results for one-bond SSCCs between H and sp-type carbon atoms. Most of the functionals strongly overestimate this type of couplings except for VSXC and HCTH407, which agree fairly well with experiment. The standard deviations from experiment vary for different functionals from 3.8 Hz (B98) to 8.0 Hz (KT2).

In Table 4 we present the statistical results for sp^2-type SSCCs. The performance of PW91, PBE, and BP86 functionals is the best. For this set of 34 $^1J_{CH}$ SSCCs, standard deviations range from 3.0 Hz (B3LYP) to 5.0 Hz (LSDA).

For the sp^3-type SSCCs, five functionals give MAEs of about 2 Hz: PW91, OLYP, and the hybrids B3P86, B972, and O3LYP (see Table 5). Standard deviations for this type of SSCCs range from 2.1 Hz (B3LYP) to 4.8 Hz (LSDA).

For $^1J_{CH}$ SSCCs involving a C atom belonging to an aromatic ring (see Table 6), PW91, PBE, and the hybrid B972 yield MAE below 2 Hz. For this type of SSCCs, all functionals give a standard deviation between 2.3 Hz (OLYP) and 2.9 Hz (TPSS and TPSSh), i.e., the errors for the aromatic SSCCs are confined within a narrow band around their mean value.

Interestingly, the width of the error distribution increases along the series aromatic → sp^3 → sp^2 → sp type of SSCCs.

6. Conclusions

We have computed one-bond C−H SSCCs with 20 distinct approximate density functionals over a comprehensive set of experimental data. All GGA functionals overall outperform LSDA. Meta-GGA and hybrid functionals, however,

Table 4: Statistical Results for 34 One-Bond $^1J_{CH}$ sp^2-type Coupling Constants in a Set of 21 Molecules Using Several Functionals (in Hz)[a]

functional	MAE	ME	STDEV	max.(+)	min.(−)
LSDA	23.62	−23.62	5.04		−43.27
PW91	2.78	0.36	3.54	6.92	−11.21
PBE	2.64	−1.55	3.75	5.23	−14.51
BLYP	15.46	15.46	3.22	21.84	
OLYP	4.22	3.21	3.56	10.37	−8.31
BP86	3.09	−2.82	3.78	3.98	−15.60
KT2	19.41	19.41	3.55	25.34	
HCTH407	8.76	−8.76	4.16		−23.41
PKZB	4.97	−4.56	4.95	4.11	−21.55
VSXC	9.38	−9.38	4.41		−25.98
TPSS	23.60	23.60	3.52	30.30	
B3LYP	15.29	15.29	2.97	21.75	
B3P86	3.14	1.65	3.36	8.35	−10.01
O3LYP	5.04	4.44	3.42	11.60	−6.94
PBE0	5.12	4.62	3.30	11.41	−7.22
B971	11.50	11.35	3.92	18.74	−2.44
B972	3.40	1.51	3.95	9.25	−12.89
B98	12.12	12.04	3.85	19.22	
B1B95	7.29	7.02	3.34	13.47	−4.27
TPSSh	25.31	25.31	3.38	31.96	

[a] Individual values can be obtained from the Supporting Information.

Table 5: Statistical Results for 29 One-Bond $^1J_{CH}$ sp^3-type Coupling Constants Using Several Functionals (in Hz)[a]

functional	MAE	ME	STDEV	max.(+)	min.(−)
LSDA	23.25	−23.25	4.79		−35.25
PW91	2.23	−1.37	2.54	3.05	−8.79
PBE	3.30	−2.03	3.46	4.55	−10.45
BLYP	11.65	11.65	2.37	16.25	
OLYP	1.73	0.10	2.44	5.33	−6.96
BP86	3.99	−3.90	2.68	0.61	−11.52
KT2	13.27	13.27	3.23	27.79	
HCTH407	11.61	−11.61	2.84		−19.51
PKZB	5.10	−5.07	2.76	0.38	−12.48
VSXC	11.18	−11.18	2.95		−19.04
TPSS	21.54	21.54	3.01	34.11	
B3LYP	11.37	11.37	2.07	15.47	
B3P86	1.69	−0.38	2.34	4.15	−7.25
O3LYP	1.95	1.17	2.33	6.29	−5.68
PBE0	2.60	2.15	2.18	6.74	−4.29
B971	9.17	9.17	2.58	13.94	
B972	2.02	−0.80	2.66	3.82	−8.10
B98	9.72	9.72	2.55	14.57	
B1B95	5.31	5.14	3.56	18.95	−2.45
TPSSh	22.60	22.60	2.96	34.90	

[a] Individual values can be obtained from the Supporting Information.

do not necessarily improve over GGA functionals for this particular type of coupling. Our findings indicate that for one-bond C−H couplings, the most accurate functionals are PW91 and PBE and the semiempirical hybrids B3P86 and B972. In contrast to B3P86 and B972, PW91 and PBE do not require computing an expensive exact exchange component and thus are preferred computationally. The PBE functional gives accurate $^1J_{CH}$ SSCCs involving sp^2, sp^3, and aromatic carbon atoms. The semiempirical HCTH407 and VSXC, however, rival PBE performance for the $^1J_{CH}$ SSCCs involving a sp carbon atom.

Table 6: Statistical Results for 21 One-Bond $^1J_{CH}$ Coupling Constants in a Set of 11 Aromatic Molecules Using Several Functionals (in Hz)[a]

functional	MAE	ME	STDEV	max.(+)	min.(−)
LSDA	21.52	−21.52	2.75		−28.38
PW91	1.73	0.94	2.34	8.71	−3.07
PBE	1.68	−0.74	2.33	6.96	−4.70
BLYP	14.52	14.52	2.46	22.42	
OLYP	3.32	3.25	2.30	10.83	−0.78
BP86	2.65	−2.11	2.33	5.62	−5.96
KT2	18.33	18.33	2.77	25.85	
HCTH407	8.93	−8.93	2.32		−12.74
PKZB	3.41	−3.03	2.30	4.00	−7.04
VSXC	8.57	−8.57	2.33		−11.96
TPSS	22.06	22.06	2.88	30.27	
B3LYP	14.18	14.18	2.42	22.13	
B3P86	2.17	1.80	2.35	9.63	−2.17
O3LYP	4.21	4.21	2.31	11.87	
PBE0	4.56	4.56	2.36	12.37	
B971	11.04	11.04	2.38	18.90	
B972	1.95	1.29	2.34	8.96	−2.56
B98	11.49	11.49	2.37	19.36	
B1B95	7.71	7.71	2.37	15.56	
TPSSh	23.44	23.44	2.89	31.68	

[a] Individual values can be obtained from the Supporting Information.

Our findings do not support the common belief that hybrid functionals (particularly B3LYP) surpass GGAs for one bond C−H NMR SSCCs.

Acknowledgment. This work was supported by NSF CHE-9982156 and the Nanoscale Science and Engineering Initiative of the National Science Foundation under NSF Award Number EEC-0118007. Computational time provided by the Rice Terascale Cluster funded by NSF under Grant EIA-0216467, Intel, and HP was employed in this work. V.B. and J.E.P. thank Professor R. H. Contreras for useful comments on this manuscript.

Supporting Information Available: All calculated NMR couplings and their individual contributions. This material is available free of charge via the Internet at http://pubs.acs.org.

References

(1) Maciel, G. E.; J. W. McIver, J.; Ostlund, N. S.; Pople, J. A. *J. Am. Chem. Soc.* **1970**, *92*, 1.

(2) Parr, R. G.; Yang, W. *Density-Functional Theory of Atoms and Molecules;* Oxford University Press: Oxford, 1989.

(3) Dreizler, R. M.; Gross, E. K. U. *Density Functional Theory;* Springer-Verlag: Berlin, 1990.

(4) Kaupp, M.; Bühl, M.; Malkin, V. *Calculation of NMR and EPR parameters;* Wiley-VCH Verlag GmbH & Co KGaA: 2004.

(5) Sychrovský, V.; Gräfenstein, J.; Cremer, D. *J. Chem. Phys.* **2000**, *113*, 3530.

(6) Helgaker, T.; Watson, M.; Handy, N. C. *J. Chem. Phys.* **2000**, *113*, 9402.

(7) Lantto, P.; Vaara, J.; Helgaker, T. *J. Chem. Phys.* **2003**, *117*, 5998.

(8) Lantto, P.; Vaara, J.; Helgaker, T. *J. Chem. Phys.* **2002**, *117*, 1.

(9) Ramsey, N. F. *Phys. Rev.* **303**, *91*, 1953.

(10) Fukui, H. *Prog. NMR Spectrosc.* **1999**, *35*, 267.

(11) Contreras, R. H.; Peralta, J. E.; Giribet, C. G.; de Azúa, M. C.; Facelli, J. C. *Annu. Rep. NMR Spectrosc.* **2000**, *41*, 55.

(12) Contreras, R. H.; Barone, V.; Facelli, J. C.; Peralta, J. E. *Annu. Rep. NMR Spectrosc.* **2003**, *51*, 167.

(13) Helgaker, T.; Jaszuñski, M.; Ruud, K. *Chem. Rev.* **1999**, *99*, 293.

(14) Helgaker, T.; Pecul, M. In *Calculation of NMR and EPR parameters*; Kaupp, M., Bühl, M., Malkin, V. G., Eds.; Wiley-VCH: Weinheim, 2004; Chapter 7, pp 101−121.

(15) Barone, V.; Peralta, J. E.; Contreras, R. H.; Snyder, J. P. *J. Phys. Chem. A* **2002**, *106*, 5607.

(16) Peralta, J. E.; Barone, V.; Contreras, R. H.; Zaccari, D. G.; Snyder, J. P. *J. Am. Chem. Soc.* **2001**, *123*, 9162.

(17) Frisch, M. J. et al. Gaussian 03, Revision C.02, Gaussian, Inc., Wallingford, CT, 2004.

(18) Provasi, P. F.; Aucar, G. A.; Sauer, S. P. A. *J. Chem. Phys.* **2001**, *115*, 1324.

(19) Peralta, J. E.; Scuseria, G. E.; Cheeseman, J. R.; Frisch, M. J. *Chem. Phys. Lett.* **2003**, *375*, 452.

(20) Staroverov, V. N.; Scuseria, G. E.; Tao, J.; Perdew, J. P. *J. Chem. Phys.* **2003**, *119*, 12129.

(21) Hansen, P. E. *Prog. NMR Spectrosc.* **1981**, *14*, 175.

(22) Ernzerhof, M.; Scuseria, G. E. *J. Chem. Phys.* **1999**, *110*, 5029.

(23) Geertsen, J.; Oddershede, J.; Scuseria, G. E. *J. Phys. Chem.* **1987**, *87*, 2138.

(24) Oddershede, J.; Geertsen, J.; Scuseria, G. E. *J. Phys. Chem.* **1988**, *92*, 3056.

(25) Ruden, T. A.; Lutnæs, O. B.; Helgaker, T.; Ruud, K. *J. Chem. Phys.* **2003**, *118*, 9572.

(26) Lutnæs, O. B.; Ruden, T. A.; Helgaker, T. *Magn. Reson. Chem.* **2004**, *42*, S117.

(27) Ruud, K.; Frediani, L.; Cammi, R.; Menucci, B. *Int. J. Mol. Sci.* **2003**, *4*, 119.

(28) Perdew, J. P.; Burke, K.; Ernzerhof, M. *Phys. Rev. Lett.* **1996**, *77*, 3865.

(29) Keal, T. W.; Tozer, D. J. *J. Chem. Phys.* **2003**, *119*, 3015.

(30) Keal, T. W.; Tozer, D. J.; Helgaker, T. *Chem. Phys. Lett.* **2004**, *391*, 374.

(31) Vosko, S. H.; Wilk, L.; Nusair, M. *Can. J. Phys* **1980**, *58*, 1200.

(32) Perdew, J. P. Unified theory of exchange and correlation beyond the local density approximation. In *Electronic Structure of Solids '91*; Ziesche, P., Eschrig, H., Eds.; Akademie Verlag: Berlin, 1991.

(33) Perdew, J. P.; Chevary, J. A.; Vosko, S. H.; Jackson, K. A.; Pederson, M. R.; Singh, D. J.; Fiolhais, C. *Phys. Rev. B* **1992**, *46*, 6671, **1993**, *48*, 4978(E).

(34) Becke, A. D. *Phys. Rev. A* **1988**, *38*, 3098. Lee, C.; Yang, W.; Parr, R. G. *Phys. Rev. B* **1988**, *37*, 785. Miehlich, B.; Savin, A.; Stoll, H.; Preuss, H. *Chem. Phys. Lett.* **1989**, *157*, 200.

(35) Handy, N. C.; Cohen, A. J. *Mol. Phys.* **2001**, *99*, 403.

(36) Becke, A. D. *Phys. Rev. A* **1988**, *38*, 3098.

(37) Perdew, J. P. *Phys. Rev. B* **1986**, *33*, 8822.

(38) Boese, A. D.; Handy, N. C. *J. Chem. Phys.* **2001**, *114*, 5497.

(39) Perdew, J. P.; Kurth, S.; Zupan, A.; Blaha, P. *Phys. Rev. Lett.* **1999**, *82*, 2544.

(40) van Voorhis, T.; Scuseria, G. E. *J. Chem. Phys.* **1998**, *109*, 400.

(41) Tao, J.; Perdew, J. P.; Staroverov, V. N.; Scuseria, G. E. *Phys. Rev. Lett.* **2003**, *91*, 146401.

(42) Stephens, P. J.; Devlin, F. J.; Chabalowski, C. F.; Frisch, M. J. *J. Chem. Phys.* **1994**, *98*, 11623. See, also: Hertwig, R. H.; Koch, W. *Chem. Phys. Lett.* **1997**, *268*, 345.

(43) Perdew, J. P.; Ernzerhof, M.; Burke, K. *J. Chem. Phys.* **1997**, *105*, 9982.

(44) Cohen, A. J.; Handy, N. C. *Chem. Phys. Lett.* **2000**, *316*, 160.

(45) Wilson, P. J.; Bradley, T. J.; Tozer, D. J. *J. Chem. Phys.* **2001**, *115*, 9233.

(46) Schmider, H. L.; Becke, A. D. *J. Chem. Phys.* **1998**, *109*, 6264.

(47) Becke, A. D. *J. Chem. Phys.* **1996**, *104*, 1040.

CT050083F

JCTC Journal of Chemical Theory and Computation

Accurate Atomic and Molecular Calculations without Gradient Corrections: Scaled SVWNV Density Functional

Kevin E. Riley, Edward N. Brothers, Kenneth B. Ayers, and Kenneth M. Merz*

Department of Chemistry, The Pennsylvania State University, 104 Chemistry Building, University Park, Pennsylvania 16802

Received January 12, 2005

Abstract: The local spin density approximation (LSDA) approximation was one of the first density functional theory (DFT) methods employed to calculate atomic and molecular properties. As newer, more sophisticated methods, such as BLYP and B3LYP, were developed, the LSDA approximation has grown less popular for molecular systems. In this paper we revisit the LSDA method and investigate a simple way to improve the results that can be obtained using this approximation. By scaling the contribution of the local correlation to the SVWNV functional, improved results can be obtained for heats of formation, ionization potentials, electron affinities, bond angles, bond distances, vibrational frequencies, conformational energies, interaction energies, and barrier heights. The results of our studies show that scaling the SVWNV functional yields heats of formations with average unsigned errors up to about nine times smaller than those of the standard SVWNV functional. The decreases in the errors of other properties studied in this work were not as dramatic as those of the heat of formation but were, in most cases, significant. There is a notable time saving in this density only functional. For a 9-alanine system SVWNV is 55% faster than B3LYP and 40% faster than BLYP at a 3-21G* basis set. Based on our observations we propose an improved SVWNV density functional that is suitable for the study of molecular systems at a fraction of the cost of more sophisticated DFT methods, which also produces reasonable accuracy at small basis sets. One type of application for which the improved SVWNV functional would be extremely well suited is QM/QM methods where a fairly inexpensive method is needed for the larger part of a system that is treated at a lower level of theory.

Introduction

As the speed of modern computers increases while their cost decreases it becomes possible to consider the use of ab initio methods to calculate properties of very large molecules, such as biomolecules. These types of calculations promise to greatly increase our understanding of the structure and function of large molecular systems.[1] Although a few efforts have already been made to make such large scale calculations,[2−6] it is not yet a common practice due to the great computational expense.[1] The first step one would take when making ab initio calculation on very large systems would be to use a relatively inexpensive density functional theory (DFT) method,[7,8] such as LSDA, along with a small split valence basis set with a low degree of contraction, such as 3-21G*.[9−11] The problem with such an approach is that the LSDA method is known to give inaccurate results when used to calculate such properties as the heat of formation.[12,13] In this study we use an empirical technique to scale the correlation (VWNV)[14] part of the SVWNV functional in order to improve the overall accuracy of several atomic and molecular properties as calculated using the LSDA method. This approach was initially described by Brothers and Merz, and we have expanded on the initial observation herein.[13]

* Corresponding author phone: (814)865-3623; e-mail: merz@psu.edu.

10.1021/ct050007c CCC: $30.25
Published on Web 06/02/2005

DFT has become an extremely popular method for studying the physical properties of molecules within the past decade, and there have been many advances made in the quality of the functionals available. Most modern functionals include terms that are dependent on the gradient of the density (these are known as generalized gradient approximation, or GGA functionals),[13] adding an extra calculation over a local only functional. The SVWNV functional is composed of a Slater exchange functional[7,8,15] combined with a VWNV correlation functional and has no functional dependence on the density gradient; this functional is given as

$$\epsilon_{\mathrm{SVWN5}} = \epsilon_{\mathrm{Slater}} + \epsilon_{\mathrm{VWN5}} \tag{1}$$

where

$$\epsilon_{\mathrm{Slater}} = -\left(\frac{3}{4}\right)\left(\frac{6}{\pi}\right)^{1/3}\left(\rho_{\alpha}{}^{4/3} + \rho_{\beta}{}^{4/3}\right) \tag{2}$$

and

$$\epsilon_{\mathrm{VWN5}} = \rho\epsilon_{\mathrm{c}}(x,\xi)$$

$$\rho = \rho_{\alpha} + \rho_{\beta}, \quad x = \left(\frac{3}{4\pi\rho}\right)^{1/6}, \quad \xi = \frac{\rho_{\alpha} + \rho_{\beta}}{\rho} \tag{3}$$

the correlation potential is given by

$$\epsilon_{\mathrm{c}}(x,\xi) = \epsilon_{\mathrm{c}}{}^{\mathrm{P}}(x) + \epsilon_{\mathrm{c}}{}^{\mathrm{A}}(x)g(\xi)\left\{1 + \left[\frac{4}{9(2^{1/3}-1)}\frac{\epsilon_{\mathrm{c}}{}^{\mathrm{F}}(x) - \epsilon_{\mathrm{c}}{}^{\mathrm{P}}(x)}{\epsilon_{\mathrm{c}}{}^{\mathrm{A}}(x)} - 1\right]\xi^4\right\} \tag{4}$$

where

$$g(\xi) = \frac{9}{8}\left[(1+\xi)^{4/3} + (1-\xi)^{4/3} - 2\right] \tag{5}$$

the various ϵ_c are given as

$$\epsilon_{\mathrm{c}}(x) = A\left\{\ln\left(\frac{x^2}{X(x)}\right) + \frac{2b}{Q}\tan^{-1}\left(\frac{Q}{2x+b}\right) - \frac{bx_0}{X(x_0)}\left[\ln\left(\frac{(x-x_0)^2}{X(x)}\right) + \frac{2(2x_0+b)}{Q}\tan^{-1}\left(\frac{Q}{2x+b}\right)\right]\right\} \tag{6}$$

with

$$X(x) = x^2 + bx + c, \quad Q = (4c - b^2)^{1/2} \tag{7}$$

with parameters

$$A^{\mathrm{P}} = 0.0310907,\ b^{\mathrm{P}} = 3.72744,\ c^{\mathrm{P}} = 12.9352,\ x_{\mathrm{o}}{}^{\mathrm{P}} = -0.10498$$

$$A^{\mathrm{F}} = 0.0155454,\ b^{\mathrm{F}} = 7.06042,\ c^{\mathrm{F}} = 18.0578,\ x_{\mathrm{o}}{}^{\mathrm{F}} = -0.32500$$

$$A^{\mathrm{A}} = -0.016887,\ b^{\mathrm{A}} = 1.13107,\ c^{\mathrm{A}} = 13.0045,\ x_{\mathrm{o}}{}^{\mathrm{A}} = -0.004758$$

The parameters within this functional were determined by fitting the functional's calculated correlation energy density to that of the homogeneous electron gas as calculated by Ceperly and Alder using quantum Monte Carlo methods.[14,16]

In this study we restructure the SVWNV functional to include a parameter that can be varied in order to minimize the errors with respect to experimental values for the various properties we are investigating

$$\epsilon_{\mathrm{c-SVWN5}} = \epsilon_{\mathrm{Slater}} + c\epsilon_{\mathrm{VWNV}} \tag{8}$$

To avoid ambiguity, this form of the functional is referred to as the c-SVWNV functional. Several other studies have been done where parameters within a functional are modified in order to reduce the errors in the values of some physical property compared to experimental data.[13,17−21]

The atomic and molecular properties studied in this work are heat of formation, ionization potential, electron affinity, ground-state geometry, ground-state vibration frequencies, conformational energies, hydrogen bonding interaction energies, and transition state barrier heights. For the heat of formation, ionization potential, and electron affinity calculations the Gaussian G3 test set is used;[22,23] this set includes 223 heats of formation, 88 atomic and molecular ionization potentials, and 58 atomic and molecular electron affinities. The molecules used for investigating geometric and frequency predictive accuracy were taken from the work of Johnson, Gill, and Pople.[24] This set includes 32 molecules for ground-state geometries and ground-state vibration frequencies. Conformational energies were calculated for ammonia (planar vs pyramidal), ethane (staggered vs eclipsed), and ethylene (orthogonal vs planar). Hydrogen bonding interaction energies for the water dimer and the transition state barrier height for the [1,5] sigmatropic shift of 1,3-pentadiene were also calculated.[25]

The primary objective of this investigation is to study the behavior of the modified SVWNV functional used with small basis sets, and to this end we have carried out studies using the small 3-21G* and 3-21+G* [26] split valence basis sets. We have also carried out calculations using the much larger 6-311G** [27] and 6-311+G** [28] basis sets in order to have a set of higher quality data to which we can compare the small basis set results. To compare the results obtained using the modified c-SVWNV functionals to more widely used DFT methods, calculations were carried out using the BLYP and B3LYP functionals.[29−32]

Due to our interest in using the c-SVWNV functional for calculating heats of formation of biological molecules, we have calculated average signed and unsigned errors for the heats of formation of the systems in the set that contain only the carbon, hydrogen, oxygen, nitrogen, and sulfur atoms. We refer to this subset as the CHONS set. These are the atoms most commonly contained in proteins.

One of the goals of this study is to establish a single c-SVWNV scaling parameter that obtains reasonably accurate results for a wide variety of atomic and molecular properties. Among the scaling curves for all of the properties studied above, the one for heat of formation is by far the steepest and displays the most dramatic improvement. Because this is the case, we have determined that the average optimum heat of formation scaling parameter of 0.30 is the most appropriate universal parameter.

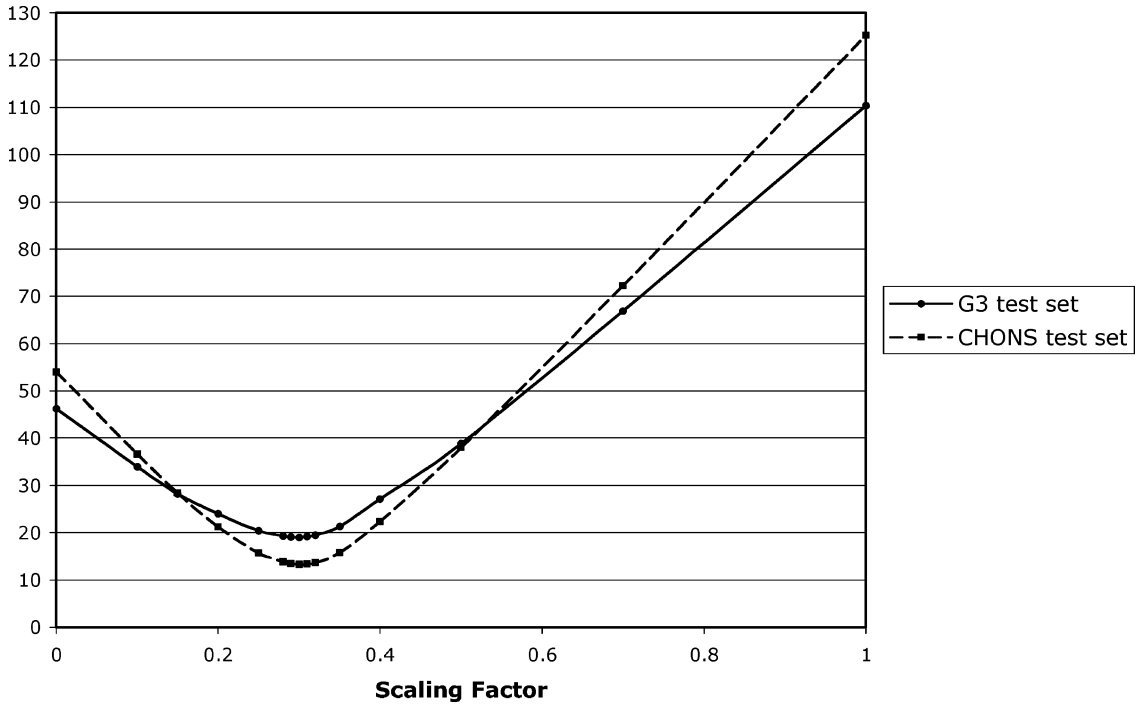

Figure 1. Average unsigned deviations of c-SVWNV with 3-21G* when VWNV part is scaled (errors in kcal/mol).

Methods

All of the calculations carried out in this study were performed using Gaussian 98.[33] Heats of formation were calculated using the method specified in "Thermochemistry in Gaussian" white paper available at http://www.Gaussian-.com/g_whitepap/thermo.htm.[34] Experimental heats of formation, ionization potentials, and electron affinities were obtained from the G2/97 and G3 test set papers.[22,23] Experimental bond lengths, bond angles, and vibration frequencies were obtained from Johnson, Gill, and Pople.[24]

Values for ionization potential and electron affinity were calculated adiabatically. Hydrogen bonding calculations for the water dimer were carried out using counterpoise corrections.[35]

Previous studies have used molecular geometries obtained at high levels of theory for the calculation of molecular properties at lower levels of theory.[23,36] In this study molecular geometries for all calculated properties were optimized using the basis set and density functional that was being evaluated. Because information based on high levels of theory is not available for large biomolecules, we feel that this is the most appropriate way to conduct our study.

Results and Discussion

Heats of Formation. The optimization of the c-SVWNV correlation scaling factor for the 222 molecular species found within the G3 test set improves the average unsigned error from 110.4 kcal/mol to 19.0 kcal/mol for the 3-21G* basis set and from 109.0 kcal/mol to 11.9 kcal/mol for the 3-21+G* basis set with scaling factors of 0.30 and 0.29, respectively (see Figure 1). The molecule PF_5 was omitted in all calculations of average heats of formation because of its unusually large deviation from experimental values for all combinations of basis sets and functionals.

Table 1. Average Signed and Unsigned Deviations of Calculated Heats of Formation from Experiment for the G3 Test Set[a]

functional	3-21G*	3-21+G*	6-311G**	6-311+G**
	Average Unsigned Deviation			
Slater	46.2	43.6	45.2	47.0
SVWNV	110.4	109.0	115.2	112.1
BLYP	14.6	25.3	16.0	15.0
B3LYP	21.7	31.5	16.1	17.8
c-SVWNV	19.0	11.9	21.4	19.6
	Average Signed Deviation			
Slater	−36.7	−40.4	−36.7	−40.4
SVWNV	110.3	109.0	115.2	112.1
BLYP	−12.4	−24.8	−13.0	−12.6
B3LYP	−21.2	−31.2	−16.0	−17.7
c-SVWNV	7.5	2.7	7.5	6.8
scaling factor	0.30	0.29	0.29	0.31

[a] Deviations in kcal/mol. Deviation = experiment − theory.

Table 1 gives the average signed and unsigned errors for the c-SVWNV, SVWNV, Slater exchange only, BLYP, and B3LYP functionals along with the 3-21G*, 3-21+G*, 6-311G**, and 6-311+G** basis sets. The functional that includes exact exchange, B3LYP, and the Slater and BLYP functionals display underbinding behavior with all basis sets used in this study. The SVWNV functional exhibits significant overbinding, while the c-SVWNV functional slightly overbinds. It is clear that in terms of heat of formation unsigned errors the c-SVWNV functional is very competitive with the more advanced BLYP and B3LYP functionals. The c-SVWNV functional along with the 3-21+G* basis set does especially well in describing heats of formation compared to all other functional/basis set combinations.

Table 2 gives the average signed and unsigned heat of formation errors for the 152 molecules within the G3 set

Table 2. Average Signed and Unsigned Deviations of Calculated Heats of Formation from Experiment for the CHONS Test Set[a]

functional	3-21G*	3-21+G*	6-311G**	6-311+G**
	Average Unsigned Deviation			
Slater	53.9	54.3	52.4	57.4
SVWNV	125.2	127.5	133.7	137.3
BLYP	16.4	28.0	16.8	15.3
B3LYP	24.5	33.8	15.9	17.7
c-SVWNV	13.3	9.1	17.8	16.8
	Average Signed Deviation			
Slater	−53.0	−54.0	−50.1	−55.6
SVWNV	125.2	127.5	133.7	137.3
BLYP	−16.2	−28.0	−14.2	−12.8
B3LYP	−24.5	−33.8	−15.9	−17.7
c-SVWNV	0.1	0.2	4.8	3.3
scaling factor	0.30	0.30	0.30	0.31

[a] Deviations in kcal/mol. Deviation = experiment − theory.

Table 3. Average Signed and Unsigned Deviations of Calculated Ionization Potentials from Experiment[a]

functional	3-21G*	3-21+G*	6-311G**	6-311+G**
	Average Unsigned Deviation			
Slater	35.9	26.3	30.5	28.6
SVWNV	7.5	6.6	5.1	5.2
BLYP	10.3	5.1	6.5	5.4
B3LYP	5.9	6.0	3.8	3.8
c-SVWNV	7.3	5.1	4.8	4.7
	Average Signed Deviation			
Slater	35.9	26.1	30.5	28.6
SVWNV	3.2	−4.7	−0.7	−2.1
BLYP	9.0	0.3	5.0	3.3
B3LYP	2.4	−5.3	−0.5	−1.7
c-SVWNV	1.6	−0.7	0.9	0.0
scaling factor	1.05	0.87	0.95	0.93

[a] Deviations in kcal/mol. Deviation = experiment − theory.

containing only the C, H, O, N, and S atoms. The results obtained for the CHONS subset yield unsigned errors that are larger than those calculated using the entire G3 set for all of the functionals with the exceptions of c-SVWNV, B3LYP/6-311G**, and B3LYP/6-311+G**. The improvements in the unsigned errors for both of the B3LYP functionals are very small (0.2 kcal/mol for 6-311G** and 0.1 kcal/mol for 6-311+G**) compared to the c-SVWNV functional, which displays dramatic improvements for all basis sets when only the CHONS molecules were considered. It is also interesting that with the CHONS test set, the c-SVWNV functional used along with the 3-21G* and 3-21+G* basis set yields average signed errors of −0.1 and −0.2 kcal/mol, respectively. The calculated signed errors for the 6-311G** and 6-311+G** basis sets are also better than those obtained with the BLYP and B3LYP methods. Although the c-SVWNV functional was fitted to the set, the ability of a local only functional to perform at such a high level is not to be overlooked.

Ionization Potentials and Electron Affinities. Table 3 gives the average signed and unsigned ionization potential errors for the 88 atoms and molecules contained within the G3 set. The c-SVWNV scaling factors for all of the basis sets are all very close to one, thus, the effects of the scaling are not nearly as pronounced as in the case of the heat of formation calculations. The c-SVWNV functional outperforms or matches the BLYP functional and obtains errors within 1.5 kcal/mol of the B3LYP results for all basis sets.

Table 4. Average Signed and Unsigned Deviations of Calculated Electron Affinities from Experiment[a]

functional	3-21G*	3-21+G*	6-311G**	6-311+G**
	Average Unsigned Deviation			
Slater	56.5	16.3	34.6	19.7
SVWNV	25.6	8.8	8.8	5.7
BLYP	31.8	5.8	13.7	3.1
B3LYP	26.2	7.3	10.9	3.4
c-SVWNV	14.6	4.8	7.2	2.6
	Average Signed Deviation			
Slater	56.5	16.1	34.6	19.7
SVWNV	25.6	−8.5	6.5	−5.5
BLYP	31.7	−4.1	12.9	−0.3
B3LYP	25.9	−6.6	9.1	−2.3
c-SVWNV	13.1	−2.7	0.9	−0.4
scaling factor	1.40[b]	0.75	1.20	0.80

[a] Deviations in kcal/mol. Deviation = experiment − theory. [b] No true minimum reached.

Table 4 gives the average signed and unsigned electron affinity error for the 58 atoms and molecules in the G3 set. The c-SVWNV functional outperforms both the BLYP and B3LYP functionals in terms of unsigned electron affinity errors for all basis sets. The scaling factor associated with the 3-21G* basis set is not at a minimum; we limited the upper limit to which this parameter could be varied to 1.40 in the case of electron affinity calculations. It should be noted that the standard SVWN functional does better than BLYP and B3LYP with the 3-21G* and 6-311G** basis sets. All of the results obtained using the 3-21G* basis set are very poor compared with the other three basis sets considered in this study.

It is also interesting, but not surprising, that the presence of diffuse functions has a great effect on the quality of the electron affinity and ionization potential calculations. The basis sets with diffuse functions yield much lower values for the average signed errors compared to the basis functions with no diffuse functions.

As expected, the local exchange only Slater functional performs very poorly for both ionization potential and electron affinity calculations.

Ground-State Geometries. Table 5 shows the average signed and unsigned errors for the 16 bond angles (from 12 molecules) considered in this study. For the cases of the 3-21G* and the 3-21+G* basis sets, the minimum in the c-SVWNV functional occurs with a scaling factor of zero, which is merely the Slater exchange only functional. As the larger basis set calculations yield optimum scaling factors of 0.95 in both cases, the errors obtained were very close to those of the standard SVWNV functional.

The inclusion of diffuse functions within the basis sets improves the bond angles for all of the functionals except for B3LYP. With the exception of SVWNV/3-21G*, all calculations using basis sets with no diffuse functions present yield angles that are smaller than experiment. The values

Table 5. Average Signed and Unsigned Deviations of Calculated Bond Angles from Experiment[a]

functional	3-21G*	3-21+G*	6-311G**	6-311+G**
	Average Unsigned Error			
Slater	2.35	1.95	2.05	1.98
SVWNV	2.44	2.40	1.85	1.82
BLYP	2.35	2.08	1.92	1.90
B3LYP	1.85	2.32	1.86	1.94
c-SVWNV	2.35	1.95	1.85	1.82
	Average Signed Error			
Slater	0.97	−0.71	0.68	−0.22
SVWNV	−0.39	−1.60	0.06	0.06
BLYP	1.69	−0.61	0.95	0.25
B3LYP	0.54	−1.45	0.40	−0.18
c-SVWNV	0.97	−0.71	0.09	0.09
scaling factor	0.00[b]	0.00[b]	0.95	0.95

[a] Deviations in degrees. Deviation = experiment − theory. [b] No true minimum reached.

Table 6. Average Signed and Unsigned Deviations of Calculated Bond Distances from Experiment[a]

functional	3-21G*	3-21+G*	6-311G**	6-311+G**
	Average Unsigned Error			
Slater	0.050	0.051	0.029	0.030
SVWNV	0.032	0.033	0.017	0.016
BLYP	0.036	0.038	0.015	0.015
B3LYP	0.024	0.025	0.007	0.008
c-SVWNV	0.025	0.025	0.013	0.013
	Average Signed Error			
Slater	−0.049	−0.051	−0.028	−0.029
SVWNV	−0.028	−0.030	−0.008	−0.009
BLYP	−0.035	−0.038	−0.014	−0.015
B3LYP	−0.021	−0.024	−0.002	−0.003
c-SVWNV	−0.018	−0.020	0.001	0.000
scaling factor	1.50[b]	1.50[b]	1.50[b]	1.50[b]

[a] Deviations in angstroms. Deviation = experiment − theory. [b] No true minimum reached.

for all angles calculated with the 3-21+G* basis set are larger than experiment.

Table 6 gives the average signed and unsigned errors for the 44 bond lengths (from 32 molecules) studied in this work. The scaling of the c-SVWNV functional does not reach a true minimum for any of the basis sets, so the scaling factor was limited to a maximum value of 1.50. The effects of the scaling factor are very small in terms of the bond length errors and typically only gave improvements of a few thousandths of an angstrom.

The c-SVWNV results are comparable to those of BLYP for all basis sets and to B3LYP for the smaller 3-21G* and 3-21+G* basis sets. The B3LYP functional along with the larger 6-311G** and 6-311+G** basis sets yield the best results with errors that are about half those obtained with BLYP and c-SVWN. Interestingly, the presence of diffuse functions in the basis functions seems to have a minimal effect on the bond lengths with all of the functionals used in this study.

Johnson, Gill, and Pople noted that density functional methods typically yield bond lengths that are too long;[24] our studies seem to agree with this observation, with bond lengths being too long for all functional/basis set combinations except c-SVWNV/6-311G**. It is interesting to note that the average bond lengths computed using the 6-311G** and 6-311+G** basis sets are generally shorter than those calculated using the 3-21G* and 3-21+G* basis sets.

Table 7. Average Signed and Unsigned Deviations of Calculated Vibrational Frequencies from Experiment[a]

functional	3-21G*	3-21+G*	6-311G**	6-311+G**
	Average Unsigned Error			
Slater	115	119	69	67
SVWNV	87	84	43	41
BLYP	99	92	37	34
B3LYP	105	103	83	79
c-SVWNV	84	82	40	39
	Average Signed Error			
Slater	99	111	58	61
SVWNV	18	28	−19	−15
BLYP	35	41	−8	−7
B3LYP	−37	−27	−78	−76
c-SVWNV	40	47	0	3
scaling factor	0.75	0.75	0.75	0.75

[a] Deviations in cm^{-1}. Deviation = experiment − theory.

Ground-State Vibration Frequencies. Table 7 gives the average signed and unsigned errors for the 111 vibration frequencies (from 31 molecules) considered in this study. Although the scaling of the c-SVWNV functional yields improvements of only 2 or 3 cm^{-1} over the standard SVWNV functional due to the shallowness of the scaling curve, it is remarkable that the scaling factor is exactly the same (0.75) for all of the basis sets studied. The best vibrational frequency results were obtained with the BLYP, c-SVWNV, and SVWNV functionals along with the 6-311G** and 6-311+G** basis sets. The B3LYP functional performs surprisingly poorly and, when combined with the larger basis sets, is outperformed by the Slater functional.

The presence of diffuse functions in the basis sets does not have a very large effect on the average vibration frequency errors. There is a very marked improvement in the quality of the frequency calculations when we go from using the 3-21G* and 3-21+G* basis sets to the larger 6-311G** and 6-311+G** basis sets.

Model Chemistry for the c-SVWNV Functional (c = 0.30). The average signed and unsigned errors obtained for heats of formation, ionization potentials, electron affinities, bond angles, bond distances, and vibrational frequencies using a c-SVWNV scaling parameter of 0.30 are given in Table 8. The values of the quantities listed above are reasonably good; there is a fairly large decrease in quality in the ionization potential and electron affinity results compared to the optimized parameter results, but the average deviations for diffuse function calculations are still less than 1 eV (23.06 kcal/mol).

It should be noted that the same kind of parametrization presented here could be carried out for other functionals, such as BLYP and B3LYP, with small basis sets. Such studies might improve the small basis set results of atomic and molecular properties for these functionals significantly.

Table 8. Average Signed and Unsigned Deviations from Experiment for Various Atomic and Molecular Properties with a c-SVWNV Scaling Factor of 0.30[a]

	3-21G*	3-21+G*	6-311G**	6-311+G**
Average Unsigned Error				
heat of formation[b]	19.0	11.9	21.4	19.6
heat of formation (CHONS)[b]	13.3	9.1	17.8	17.5
ionization potential[b]	26.2	17.5	23.7	19.6
electron affinity[b]	47.2	11.0	25.9	13.5
bond angle[c]	2.35	2.00	2.01	1.95
bond distance[d]	0.044	0.046	0.025	0.025
vibrational frequency[e]	98	98	56	51
Average Signed Error				
heat of formation[b]	7.5	4.2	9.0	5.3
heat of formation (CHONS)[b]	0.1	0.2	4.8	2.1
ionization potential[b]	26.1	16.9	23.5	19.4
electron affinity[b]	47.2	9.9	25.8	13.4
bond angle[c]	0.54	−0.92	0.48	−0.28
bond distance[d]	−0.044	−0.045	−0.023	−0.023
vibrational frequency[e]	75	82	34	38

[a] Deviation = experiment − theory. [b] kcal/mol. [c] Degrees. [d] Angstroms. [e] cm^{-1}.

Table 9. Conformational Energies[a]

functional	3-21G*	3-21+G*	6-311G**	6-311+G**
Ethane (Staggered vs Eclipsed)				
Slater	2.9	2.7	2.7	2.7
SVWNV	2.9	2.8	2.8	2.8
c-SVWNV(0.3)	2.9	2.7	2.7	2.7
BLYP	2.7	2.5	2.6	2.6
B3LYP	2.7	2.6	2.7	2.7
expt[b]	2.9			
Ammonia (Pyramidal vs Planar)				
Slater	1.1	0	5.1	3.4
SVWNV	0.4	0	4.4	3.1
c-SVWNV(0.3)	0.8	0	4.9	3.3
BLYP	2.1	0.6	5.7	4.2
B3LYP	1.6	0.4	5.4	4
expt[b]	6			
Ethylene (Orthogonal vs Planar)				
Slater	64.2	62.6	62.4	61.6
SVWNV	73.4	71.9	71.5	70.8
c-SVWNV(0.3)	67	65.4	65.1	64.4
BLYP	67.9	66.8	66.2	65.6
B3LYP	66.0	65.3	64.5	64.1
expt[b]	65			

[a] Conformation energies in kcal/mol. [b] Reference 41.

Conformational Energies. The conformational energies for ethane (staggered vs eclipsed), ammonia (pyramidal vs planar), and ethylene (planar vs orthogonal) are given in Table 9.

For the conformational energy of the ethane molecule the SVWN functional yields the best results for all basis sets. The c-SVWNV(0.3) functional and the Slater functional also obtain results that are the same or better than those of the BLYP and B3LYP functionals. The most accurate results were obtained using the SVWNV, c-SVWNV(0.3), and Slater functionals along with the 3-21G* basis set.

Table 10. Interaction Energies[a] and Interoxygen Distances for the Water Dimer[b]

functional	3-21G*	3-21+G*	6-311G**	6-311+G**
Interaction Energy				
Slater	−10.4	−11.6	−7.5	−7.9
SVWN	−10.9	−12.0	−7.9	−8.3
c-SVWNV(0.3)	−12.3	−13.2	−8.7	−9.1
BLYP	−6.6	−7.3	−4.7	−4.6
B3LYP	−7.3	−7.9	−5.1	−5.1
expt[c]	−5.4			
R(O−O)				
Slater	2.782	2.717	2.873	2.806
SVWN	2.762	2.696	2.846	2.782
c-SVWNV(0.3)	2.714	2.654	2.804	2.725
BLYP	2.869	2.846	3.03	2.97
B3LYP	2.826	2.811	2.991	2.938
expt[c]	2.946			

[a] Interaction energies in kcal/mol. [b] Interoxygen distances in angstroms. [c] Reference 42.

The BLYP and B3LYP functionals outperform the Slater, SVWN, and c-SVWNV(0.3) functionals for the conformational energy of the ammonia molecule. For all functionals, calculations made with the 3-21G* and 3-21+G* basis sets yield results that are extremely low; this can be explained by the fact that, with these small basis sets, the pyramidal structure for this molecule is still very flat. The best results were obtained using the 6-311G** basis set for all functionals.

For the conformational energy of the ethylene molecule the SVWNV functional yields results that are too high, while the Slater functional yields results that are too low. The c-SVWNV(0.3), BLYP, and B3LYP functionals obtain very good results for this quantity. The addition of diffuse functions to the basis set does not seem to have a major impact on the overall quality of the calculated conformational energy of this system.

Water Dimer Interaction Energies. Table 10 gives the calculated interaction energies and interoxygen distances, R(O−O), for the water dimer. The interaction energies obtained using the BLYP and B3LYP functionals along with the larger 6-311G** and 6-311+G** basis functions were much better than those obtained with any other functional/basis set combination and were slightly too high. The SVWNV, Slater, and c-SVWNV(0.3) functionals all perform poorly compared to the BLYP and B3LYP functionals in terms of both interaction energies and interoxygen distances and always yield interaction energies that are too low. This is not a surprising result because the LSDA functionals lack the nonlocal terms necessary to describe long-range interactions. Among the local-only functionals the Slater functional yields the best results for both interaction energies and interoxygen distances for all basis sets.

It is interesting to note that when diffuse functions are added into the basis sets the interoxygen distance always decreases. This shortening of the interoxygen distance corresponds to a lowering of the interaction energy for all functional/basis set combinations except BLYP/6-311G** and B3LYP/6-311G**.

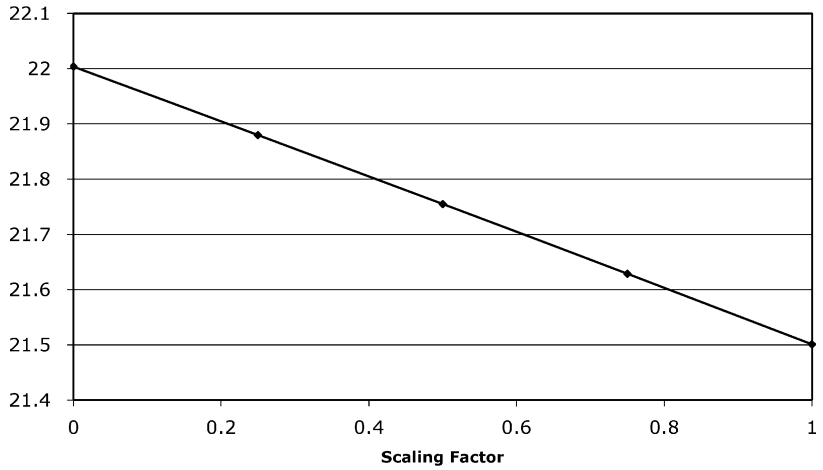

Figure 2. Barrier height of the [1,5]-sigmatropic shift for the 1,3-pentadiene molecule as a function of the c-SVWNV scaling factor (kcal/mol).

Table 11. Barrier Height of the [1,5]-Sigmatropic Shift for the 1,3-Pentadiene Molecule[a]

functional	3-21G*	3-21+G*	6-311G**	6-311+G**
Slater	22.0	23.2	22.9	22.9
SVWNV	21.5	22.6	22.2	22.2
c-SVWNV(0.3)	21.8	23.0	22.7	22.7
BLYP	30.1	31.3	31.6	31.6
B3LYP	33.4	34.4	34.9	34.8
expt[b]	35.4			

[a] Barrier heights in kcal/mol. [b] References 43 and 44.

[1,5]-Sigmatropic Shift Barrier Heights. The experimental and calculated barrier heights of the [1,5]-sigmatropic shift for the 1,3-pentadiene molecule are given in Table 11. All of the density functional methods underestimated the barrier height for this reaction, and all results obtained with the Slater, SVWNV, and c-SVWNV(0.3) methods were off by more than 34%. The B3LYP functional yields the best results with the B3LYP/6-311G** combination coming within 2% of the experimental value.

Figure 2 shows the c-SVWNV/3-21G* barrier height as a function of the scaling factor, *c*. The values for the barrier height are linearly dependent on the scaling factor with the Slater functional ($c=0$) giving the best results. Similar results were obtained with the other three basis sets.

The addition of diffuse functions to the 3-21G* basis set has a significant impact on the quality of the barrier height calculations for all of the functionals and typically bring the DFT results about 1 kcal/mol closer to the experimental value. The effects of introducing diffuse functions to the 6-311G** basis set are negligible.

Conclusions

In summary, we have shown that, by scaling the VWNV part of the SVWNV functional, the quality of LSDA results can be improved significantly. The heats of formation obtained with the c-SVWNV functional were improved by factors of 5.4 (for the 6-311G** basis set) and 9.2 (for the 3-21+G* basis set) compared to the standard SVWNV functional, yielding results comparable to those obtained with BLYP and B3LYP. The electron affinity results obtained using the c-SVWNV functional are generally quite a bit better than those of the SVWNV functional and are better than results obtained using BLYP and B3LYP for all of the basis sets studied here. The ionization potential, vibrational frequency, bond angle, and bond length results are affected very little by the optimization of the scaling parameter and are very similar to the results obtained using the SVWNV functionals. The c-SVWNV (and SVWNV) values of the four aforementioned properties are generally fairly competitive with the BLYP and B3LYP results. The results obtained using the universal scaling parameter of 0.3 are fairly good for all of the properties mentioned above although the electron affinity and ionization potential values are worse than those obtained using the standard SVWNV functional. Nonetheless, the use of the 0.3 scaling factor yields, in general, a model chemistry that is superior to standard SVWNV and is competitive with nonlocal methods such as BLYP and B3LYP at a fraction of the cost.

The conformational energies obtained with the c-SVWNV-(0.3) functional are comparable to those calculated using the BLYP and B3LYP functionals. The small basis results for the ammonia molecule are poor for all functionals. The water dimer interoxygen distances and interaction energies calculated using the c-SVWNV(0.3) functional are poor as expected. The only good results for these quantities are those obtained using the BLYP and B3LYP functionals along with the larger 6-311G** and 6-311+G** basis sets. The [1,5] sigmatropic shift barrier heights are too low except when calculated using the B3LYP functional. Despite these results, for thermochemistry the c-SVWNV(0.3) functional, combined with a 3-21G* basis set, is extremely competitive with more modern functionals, for much lower computational costs. Because of its relative accuracy and low computational cost, the c-SVWNV(0.3) method would be an excellent candidate for the "inexpensive" part of QM/QM[37−40] calculations that use two or more levels of theory to describe a system.

Acknowledgment. We thank the NSF (MCB-0211639) for their generous support of this work.

Supporting Information Available: The deviations from experiment of the heat of formation for the optimized

c-SVWNV, BLYP, and B3LYP functionals along with 3-21G* and 3-21+G* basis sets for each of the molecules in the G3 test set. This material is available free of charge via the Internet at http://pubs.acs.org.

References

(1) Goedecker, S. *Rev. Mod. Phys.* **1999**, *71*, 1085.

(2) Li, X.; Millam, J. M.; Scuseria, G. E.; Frisch, M. J.; Schlegel, H. B. *J. Chem. Phys* **2003**, *119*, 7651.

(3) Improta, R.; Barone, V.; Kudin, K. N.; Scuseria, G. E. *J. Am. Chem. Soc.* **2001**, *123*, 3311.

(4) Van Alsenoy, C.; Yu, C.-H.; Peeters, A.; Martin, J. M. L.; Schafer, L. *J. Phys. Chem. A* **1998**, *102*, 2246.

(5) Challacombe, M.; Schwegler, E. *J. Chem. Phys.* **1997**, *106*, 5526.

(6) Kaschner, R.; Hohl, D. *J. Phys. Chem. A* **1998**, *102*, 5111.

(7) Kohn, W.; Sham, L. J. *Phys. Rev.* **1965**, *140*, A1133.

(8) Hohenberg, P.; Kohn, W. *Phys. Rev.* **1964**, *136*, 864.

(9) Binkley, J. S.; Pople, J. A.; Hehre, W. J. *J. Am. Chem. Soc.* **1980**, *102*, 939.

(10) Gordon, M. S.; Binkley, J. S.; Pople, J. A.; Pietro, W. J.; Hehre, W. J. *J. Am. Chem. Soc.* **1982**, *104*, 2797.

(11) Pietro, W. J.; Franci, M. M.; Hehre, W. J.; DeFrees, D. J.; Pople, J. A.; Binkley, J. S. *J. Am. Chem. Soc.* **1982**, *104*, 5039.

(12) Mole, S. J.; Xuefeng, Z.; Liu, R. *J. Phys. Chem. A* **1996**, *100*, 14665.

(13) Brothers, E. N.; Merz, K. M. *J. Phys. Chem. A* **2004**, *108*, 2904.

(14) Vosko, S. H.; Wilk, L.; Nusair, M. *Can. J. Phys.* **1980**, *58*, 1200.

(15) Slater, J. C. *Quantum Theory of Molecules and Solids. Vol. 4: The Self-Consistent Field for Molecules and Solids*; McGraw-Hill: New York, 1974.

(16) Ceperley, D. M.; Alder, B. J. *Phys. Rev. Lett.* **1980**, *45*, 566.

(17) Proynov, E.; Chermette, H.; Salahub, D. R. *J. Chem. Phys.* **2000**, *113*, 10013.

(18) Chan, G. K.; Handy, N. C. *J. Chem. Phys.* **2000**, *112*, 5639.

(19) Van Voorhis, T.; Scuseria, G. E. *J. Chem. Phys.* **1998**, *109*, 400.

(20) Adamson, R. D.; Gill, P. M. W.; Pople, J. A. *Chem. Phys. Lett.* **1998**, *284*, 6.

(21) Curtiss, L. A.; Raghavachari, K.; Redfern, P. C.; Polple, J. A. *J. Chem. Phys.* **1997**, *106*, 1063.

(22) Curtiss, L. A.; Raghavachari, K.; Redfern, P. C.; V. Rossolov, Pople, J. A. *J. Chem. Phys.* **1998**, *109*, 7764.

(23) Curtiss, L. A.; Raghavachari, K.; Redfern, P. C.; Pople, J. A. *J. Chem. Phys.* **2000**, *112*, 7374.

(24) Johnson, B. G.; Gill, P. M. W.; Pople, J. A. *J. Chem. Phys.* **1993**, *98*, 5612.

(25) Stanton, R. V.; Merz, K. M. *J. Chem. Phys.* **1994**, *100*, 434.

(26) Clark, T.; Chandrasekhar, J.; Spitznagel, G. W.; Schleyer, P. v. R. *J. Comput. Chem.* **1983**, *4*, 294.

(27) Krishnan, R.; Binkley, J. S.; Seeger, R.; Pople, J. A. *J. Chem. Phys.* **1980**, *72*, 650.

(28) Raghavachari, K.; Trucks, G. W. *J. Chem. Phys.* **1989**, *91*, 1062.

(29) Becke, A. D. *Phys. Rev. A* **1988**, *38*, 3098.

(30) Lee, C.; Yang, W.; Parr, R. G. *Phys. Rev. B* **1988**, *37*, 785.

(31) Miehlich, B.; Savin, A.; Stoll, H.; Preuss, H. *Chem. Phys. Lett.* **1989**, *157*, 200.

(32) Becke, A. D. *J. Chem. Phys* **1993**, *98*, 5648.

(33) Frisch, M. J.; Trucks, G. W.; Schlegel, H. B.; Scuseria, G. E.; Robb, M. A.; Chesseman, J. R.; Zakrzewski, V. G.; Montgomery Jr., J. A.; Stratmann, R. E.; Burant, J. C.; Dapprich, S.; Millam, J. M.; Daniels, A. D.; Kudin, K. N.; Strain, M. C.; Farkas, O.; Tomasi, J.; Barone, V.; Cossi, M.; Cammi, R.; Mennucci, B.; Pomelli, C.; Adamo, C.; Clifford, S.; Ochterski, J.; Petersson, G. A.; Ayala, P. Y.; Cui, Q.; Morokuma, K.; Malick, D. K.; Rabuck, A. D.; Raghavachari, K.; Forseman, J. B.; Cioslowski, J.; Ortiz, J. V.; Baboul, A. G.; Stefanov, B. B.; Liu, G.; Liashenko, A.; Piskorz, P.; Komaromi, I.; Gomperts, R.; Martin, R. L.; Fox, D. J.; Keith, T.; AlLoham, M. A.; Peng, C. Y.; Nanayakkara, A.; Gonzalez, C.; Challacombe, M.; Gill, P. M. W.; Johnson, B. G.; Chen, W.; Wong, M. W.; Andres, J. L.; Head-Gordon, M.; Replogle, E. S.; Pople, J. A. *Gaussian 98 (Revision A.9)*, Gaussian Inc.: Pittsburgh, PA, 1998.

(34) Ochterski, J. W. Thermochemistry in Gaussian.

(35) Simon, S.; Duran, M.; Dannenberg, J. J. *J. Phys. Chem.* **1999**, *103*, 1640.

(36) Curtiss, L. A.; Raghavachari, K.; Redfern, P. C.; Polple, J. A. *J. Phys. Chem.* **1996**, *100*, 1063.

(37) Hopkins, B. W.; Tschumper, G. S. *Mol. Phys.* **2005**, *103*, 309.

(38) Cui, Q.; Guo, H.; Karplus, M. *J. Chem. Phys* **2002**, *117*, 5617.

(39) Gogonea, V.; Westerhoff, L. M.; Merz, K. M. *J. Chem. Phys* **2000**, *113*, 5604.

(40) Svensson, M.; Humbel, S.; Froese, R. D.; Matsubara, T.; Sieber, S.; Morokuma, K. *J. Phys. Chem.* **1997**, *100*, 119357.

(41) Repasky, M. P.; Chandrasekhar, J.; Jorgensen, W. L. *J. Comput. Chem.* **2002**, *23*, 1601.

(42) Kim, K.; Jordan, K. D. *J. Phys. Chem.* **1994**, *98*, 10089.

(43) Roth, W. R. *Chimia* **1966**, *229*, 20.

(44) Roth, W. R.; Konig, J. *Liebigs Ann. Chem.* **1966**, *699*, 24.

CT050007C

JCTC Journal of Chemical Theory and Computation

Scanning Reactive Pathways with Orbital Biased Molecular Dynamics

Leonardo Guidoni† and Ursula Rothlisberger*

Ecole Polytechnique Fédérale de Lausanne (EPFL), Institute of Chemical Sciences and Engineering, Laboratory of Computational Chemistry and Biochemistry, BCH - LCBC, CH-1015 Lausanne, Switzerland

Received March 29, 2005

Abstract: To accelerate reactive events in molecular dynamics simulations we introduce a general bias potential scheme which depends only on the electronic degrees of freedom of the reactive system. This electronic reaction coordinate, which is expressed in terms of a penalty function of the one-electron orbital energies, has been applied to study different reaction pathways of *s-cis*-butadiene. Three different reactive channels have been identified: the cis/trans isomerization, the s-cis/s-trans isomerization, and the symmetry allowed cyclization. For the latter, despite the fact that the Woodward−Hoffmann rules are guided by the butadiene frontier orbitals, biasing only these orbitals is not enough to drive the system toward cyclization, but a low-lying valence shell orbital needs to be included.

Introduction

Chemical reactions often have activation barriers that are too high to be observed within the typical picosecond time scale of first-principles Molecular Dynamics (MD) simulations. To investigate the dynamical and thermodynamical properties of these rare events, different methods were developed to overcome the activation barriers within the time scale accessible by computer simulations.[1−9] The most popular and straightforward methodology consists of performing constraint dynamics along an a priori defined partial reaction coordinate that is expressed as a function of the ionic positions.[1,5] Whereas for some chemical reactions the definition of partial reaction coordinates can be a reasonable assumption, for many others involving, for instance, ionic collective motions or dynamic solvent effects, a proper reaction coordinate cannot be easily expressed via a trivial combination of ionic degrees of freedom. Recently, a more general technique, the so-called metadynamics, has been proposed to partially overcome this drawback.[8,9] In this method, a set of different reaction coordinates (that can be either local or collective) are defined, and the free energy landscape of the system is efficiently explored through a Car-Parrinello-type dynamics of this set of variables. However, due to the exponentially growing size of the phase space, the exploration of multiple reaction pathways is usually limited to a small number of local or collective variables.

Both methods cited above are based on the definition of one or more reaction coordinates that are functions of the atomic positions of the system (such as bonds, angles, dihedrals, coordination numbers, etc.). As chemical reactions imply rearrangements of the electronic structure, other quantities, which explicitly depend on electronic instead of ionic properties, might provide helpful information about the reactivity of the system and therefore be useful descriptors for the exploration of reaction pathways.

The idea that the electrons themselves could drive a chemical reaction was developed by Fukui in its work on the role of frontier orbitals in organic reactivity.[10,11] Fukui's investigations revealed the importance of frontier orbitals, namely HOMO and LUMO, in regulating the single molecule reactivity toward external oxidation or reduction. When the analysis is extended to the HOMOs and LUMOs of two reacting molecules, the overlaps between the frontier orbitals of the two molecules becomes the principal indicator to predict probable chemical reactions and stereoselective pathways. In this scheme, the frontier molecular orbitals of the noninteracting reactant species are first considered, and

* Corresponding author e-mail: ursula.roethlisberger@epfl.ch.
† Present address: University of Roma "La Sapienza", Dip. di Fisica, Edificio Fermi, P.le Aldo Moro 5, 00185 Roma, Italy.

10.1021/ct050081v CCC: $30.25
Published on Web 05/12/2005

their interaction is taken into account as a perturbation. Orbital selection rules obtained from these considerations are equivalent to those based on orbital symmetries.[12,13] A quantitative analysis can be carried out with the help of the Fukui functions, namely the derivative of the density with respect to the total number of electrons $f^{\pm}(r) = (\partial\rho(r)/\partial N)^{\pm}$. These functions are sensitive indicators of the most reactive parts of a molecule, and they can designate the atoms which are likely involved in nucleophilic (f^{+}), electrophilic (f^{-}), and radical ($f^{+} - f^{-}$) attacks of an external reagent.[14−16] Further investigation on reactivity in molecular fragment representation has been carried out by Nalewajski using principles based on information theory in order to investigate the equilibrium and nonequilibrium electron distribution between molecular subsystems.[17]

In a paper from the 1970s Nakatsuji made the distinction between ionic movements that are followed by centroids of the electronic clouds and movements where the latter precede the ions.[18] Inspired by this 'electron preceding' picture, we consider the opportunity of forcing the electronic cloud toward certain directions, consequently pushing the ions to follow them, and therefore driving the system to perform a reaction. At variance with the picture emerging from orbital interaction consideration of the single reactants, in this case the reactive electronic quantities refer to the full reactive system (in our case the global one-electron molecular orbitals), without any further partitioning into molecular subsystems.

This type of global electronic variables can also be included as additional collective reaction coordinates within constraint dynamics[1,5] or metadynamics[8,9] schemes. The inclusion of these global electronic descriptors has a 2-fold advantage over standard nuclei-based reaction coordinates. First of all, the introduction of a new type of partial reaction coordinates can help in many cases where an appropriate reaction coordinate is difficult to express in a purely geometrical way. In particular, the approach presented here is specially suitable for introducing collective coordinates, since it is based on one-electron molecular orbitals that can be fully delocalized throughout the reactive system. The second and probably most important issue deals with the possibility to select different reactive channels that could not be easily distinguished by ionic degrees of freedom. Other electronic descriptors, such as the electron density, chemical potential, hardness, softness, and Fukui functions (see refs 16, 19, and 20) can in principle be incorporated in the same way into an electronic constraint. Different reactive channels can be therefore selected and explored by biasing different combinations of these chemically sensitive quantities, without the use of a priori nuclear reaction coordinates.

So far, electronic reaction coordinates have only been applied in a few cases.[21−23] Recently, VandeVondele and Rothlisberger[21] introduced a finite electronic temperature in ab initio MD so that electrons in the HOMOs can be partially excited into unoccupied orbitals, increasing the reactivity of the system. Following a similar approach, Vuilleumier and Sprik[22] have applied an external potential that directly controls the HOMO−LUMO energy gap to explore selected reaction channels. The same idea has been used by Mosey et al. within a MD context.[23]

All these approaches are limited to the exploration of reaction paths that have a decreasing HOMO−LUMO gap towards the transition state. Other reactive channels that do not satisfy this prerequisite are therefore either explicitly or implicitly excluded by these methods.[21] The construction of a more general electronic reaction coordinate would allow a more extensive exploration of the reactivity of the system and, at the same time, allow the selection among different reaction pathways.

To drive the electronic reaction coordinates toward the desired direction we used a bias potential scheme. The general electronic bias potential form we introduce in the present paper depends on the one-electron molecular orbital energies ϵ_i. As a test case we have chosen the *s-cis*-butadiene, a system that is small enough to be fully studied in detail but, at the same time, sufficiently complex to perform different chemical reactions in a rather large energy range (6−55 kcal/mol). Moreover, the reactive channels offered by this system (conrotatory and disrotatory cyclization to cyclobutene, cis−trans isomerization around single and double bonds) can be easily rationalized in terms of orbital correlation diagrams and Woodward−Hoffmann rules. Anticipating our results, we demonstrate that the introduction of a small number of 'critical' molecular orbital energies in the construction of the bias potentials is enough to drive the system towards the different reactions within a picosecond time scale.

Calculations

Methodology. We developed our electronic bias potential scheme in the framework of density functional theory. The additional bias potential depends exclusively on electronic degrees of freedom and is applied during Born−Oppenheimer molecular dynamics to drive the system toward different reactive channels. The electronic bias energy E_{EB} was chosen to be a harmonic function of the one-electron Kohn−Sham orbital energies ϵ_i, which satisfy the Kohn−Sham equations $\hat{H}_{KS}\psi_i = \epsilon_i\psi$. E_{EB} can be written in the following general form:

$$E_{EB} = \left(\frac{1}{2}\right)\alpha\left(\sum_i w_i\epsilon_i - E_T\right)^2$$

The harmonic constant α determines the global strength of the constraint and was chosen as a compromise between a large value, that keeps the system close to the desired target, and a small value, that generates small bias force oscillations, and is thus more easily integrated in molecular dynamics. In test runs with $\alpha = 15$, 30, 60, 120, 200, 300, and 400 a.u. we monitored the fluctuations of the quantity $\sum_i w_i\epsilon_i - E_T$, which turned out to have oscillations of periods ranging from 20 to 6 fs. We have finally chosen the tightest possible value of α which has an oscillation period not smaller than 10 fs, typical of fast molecular vibrational modes such as C−H stretching ($\alpha = 200$ a.u.). The index *i* runs over all the one-electron Kohn−Sham molecular orbitals that are considered in the bias potential, which can be either occupied

or unoccupied states. The weights w_i are the coefficients of the linear combination of the involved orbital energies ϵ_i, and E_T is the target energy which can depend on time. It can be either increased or decreased, starting from its initial value, which is set equal to $\sum_i w_i \epsilon_i$ in the reactants state. These changes can be done in a discrete number of steps, using the umbrella sampling technique (as used for instance in refs 22 and 25) or in a continuous way by changing smoothly $E_T(t) = E_T(0) + t\Delta E$ as a function of the simulation time t up to a final value E_T^*.

The choice of the involved molecular orbitals as well as the weights w_i is quite arbitrary for a general reaction. Anyway, in many cases, molecular orbital correlation diagrams and chemical intuition can help to guess reasonable electronic reaction coordinates (i.e. w_i sets) for a specific reaction. In the case of butadiene, which is the subject of the present paper, we will actually show that it is enough to consider only a restricted group of molecular orbitals to provide a good description of the electronic reaction coordinate for many different reactive channels.

The forces on the nuclei f_{RI} due to the electronic bias potential E_{EB} are given by

$$f_{RI} = -\frac{\partial E_{EB}}{\partial R_I} = -\alpha \sum_i \left(\sum_j w_j \epsilon_j - E_T\right) w_i \frac{\partial \epsilon_i}{\partial R_I}$$

The last term of the above expression, namely the derivative of the Kohn−Sham energy ϵ_i with respect to the ionic coordinates R_I, is calculated in a perturbative approach[26] within the linear response theory using the same scheme as Villeumier and Sprik.[22] In the special case where i is a frontier orbital ($i=F$), $-\partial\epsilon_F/\partial R_I$ coincides with the nuclear Fukui Function $\phi_I = (\partial F_I/\partial N)_V^{\pm}$, namely the response of the force F_I on the nucleus I due to oxidation (−) or reduction (+), as shown in ref 22.

Because of the explicit dependence of the electronic bias on selected Kohn−Sham energies ϵ_i, it turns out to be critical for a proper description to correctly recognize the identity of the orbitals along the entire trajectory. Although the density of states of butadiene in vacuo is not high (only 11 occupied valence states), thermal fluctuations as well as the electronic bias cause the orbital energies to cross during the dynamics. To properly recognize these level crossings and identify the orbitals involved in the bias potential, we adopt the following strategy. The Kohn−Sham orbitals at time step *t+1* are compared with the orbitals at time t by calculating the overlap matrix $O_{ij} = \langle \psi_i(t) | \psi_j(t+1) \rangle$. If no level crossing between orbitals occurred during the time step, the matrix O_{ij} is close to identity. On the contrary, if the orbital order is changed during the time step, the exchanged orbitals are immediately identified by nonzero off-diagonal elements of O_{ij}, and the correct identity of the orbitals can be restored.

Computational Details. The orbital biased Born−Oppenheimer molecular dynamics has been implemented in a modified version of the program CPMD v 3.8 (www.cpmd.org).[27] For the test case studies on butadiene, we used the local density approximation for the exchange and correlation functional. This choice was dictated by the encounter of numerical instabilities in the linear response calculations when GGA functionals are used (see ref 28 for further details). The Kohn−Sham orbitals were expanded in plane waves up to an energy cutoff of 70 Ry, and the interactions with the core electrons were described using Troullier-Martins type pseudopotentials.[29] The temperature was maintained around 300 K by applying a Nose-Hoover thermostat.[30;31] The computation of the Orbital Biased MD is twice more expensive over conventional ab initio MD, due to the additional energy minimization introduced by the linear response part.

The general form of the bias potential provides a large flexibility to select different reactive channels. Few options are tested here for scanning the reactivity of *s-cis*-butadiene. All dynamics started from the geometry optimized structure. The following three variants of bias potentials (BP1−3) were tested:

(BP1). The energies of the HOMO and HOMO-1 orbitals are forced to be exchanged. The corresponding electronic bias is $E_{EB} = (1/2)\alpha(\epsilon_{HOMO} - \epsilon_{HOMO-1} - E_T)$. E_T ranges from the value $E_T(t=0) = (\epsilon_{HOMO} - \epsilon_{HOMO-1})$ to $E_T^* = -(\epsilon_{HOMO} - \epsilon_{HOMO-1})$ calculated on the optimized *s-cis*-butadiene structure.

(BP2). The energies of the Lowest Valence Molecular Orbital + 1 (LVMO+1) is forced to reach the corresponding value of cyclobutene. The electronic bias potential is $E_{EB} = (1/2)\alpha(\epsilon_{LVMO+1} - E_T)$. E_T ranges from the value of ϵ_{LVMO+1} of *s-cis*-butadiene to the corresponding value of cyclobutene.

(BP3). The energies of the HOMO and the LUMO are forced to exchange. The potential $E_{EB} = (1/2)\alpha(\epsilon_{LUMO} - \epsilon_{HOMO} - E_T)$ is applied, where E_T ranges from $(\epsilon_{LUMO} - \epsilon_{HOMO})$ to $-(\epsilon_{LUMO} - \epsilon_{HOMO})$.

Free energies were calculated for the bias potential BP3 using the umbrella sampling technique.[24] We used 16 windows equally spaced between $E_T = -3.82$ eV and $E_T = 0$ eV with $\alpha = 60$ to allow enough overlap between two adjacent windows during the dynamics. To better sample the region close to the transition state, 4 additional windows with $\alpha = 120$ were added close to $E_T = 0$ eV. For each window 1 ps of MD run was performed, 0.7 ps of which were used for data production.

Results

The bias potentials described above are applied to the study of reactive channels of butadiene with different energy barriers E_B: s-cis/s-trans isomerization around the C−C single bond ($E_B \sim 6$ kcal/mol), symmetry allowed cyclization pathway ($E_B \sim 40$ kcal/mol),[32] and cis/trans double-bond isomerization ($E_B \sim 55$ kcal/mol).

To better understand the following results, it is useful to be reminded that the Woodward−Hoffmann rules for butadiene predict that the conversion to cyclobutene follows a conrotatory instead of a disrotatory pathway. Whereas in the case of the symmetry allowed conrotatory pathway correlation occurs between the π-type HOMO of butadiene and the σ-type HOMO-1 of cyclobutene, in the disrotatory (symmetry forbidden) pathway the π-type HOMO of butadiene correlates with the antibonding π^* LUMO of cyclobutene. The latter pathway, which involves an orbital crossing and the closure of the HOMO−LUMO gap, has therefore a higher

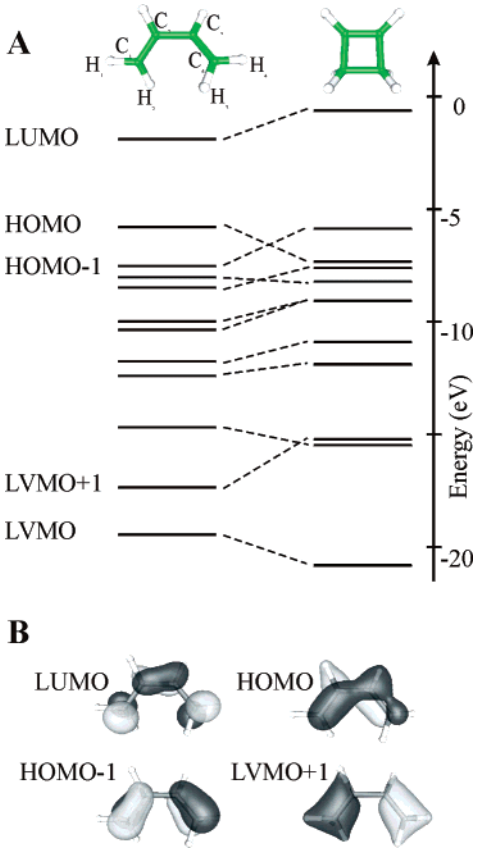

Figure 1. (A) Quantitative orbital correlation diagram for the symmetry allowed conrotatory cyclization pathway of *cis*-butadiene. (B) The Kohn−Sham orbitals of *cis*-butadiene involved in the bias potentials.

activation barrier and is disfavored by thermal activation. A quantitative correlation diagram between butadiene and cyclobutene during conrotatory cyclization is shown in Figure 1.

Reaction 1. Because of the correlation between the two highest occupied orbitals evidenced in Figure 1, it seems, at first glance, reasonable to assume that a bias potential BP1, built from the HOMO and HOMO-1 orbital energies, might be able to drive the reactive butadiene toward conrotatory cyclization. Figure 2 reports the results from a biased dynamics that exchanges ϵ_{HOMO} with ϵ_{HOMO-1}. Surprisingly, although the orbital energy exchange has been achieved, the applied bias potential does not lead to conrotatory cyclization, as testified by the C_1-C_4 distance in Figure 2. Indeed, during the dynamics the $C_1-C_2-C_3-C_4$ dihedral angle shifts to about 180 degrees (Figure 2) by rotating around the single bond, leading to *trans*-butadiene via a s-cis/s-trans isomerization. This reaction channel indeed does require the exchange of ϵ_{HOMO} and ϵ_{HOMO-1}, but it has a much lower activation barrier than cyclization (~6 vs ~40 kcal/mol). The dynamics therefore correctly selected the energy channel with the lowest barrier that is compatible with the applied bias potential.

Reaction 2. As shown in the previous paragraph, the exchange between the two highest occupied molecular orbitals is not a sufficient condition to impose conrotatory cyclization. Other low lying MOs seems to be involved in driving this reaction. According to the correlation diagram

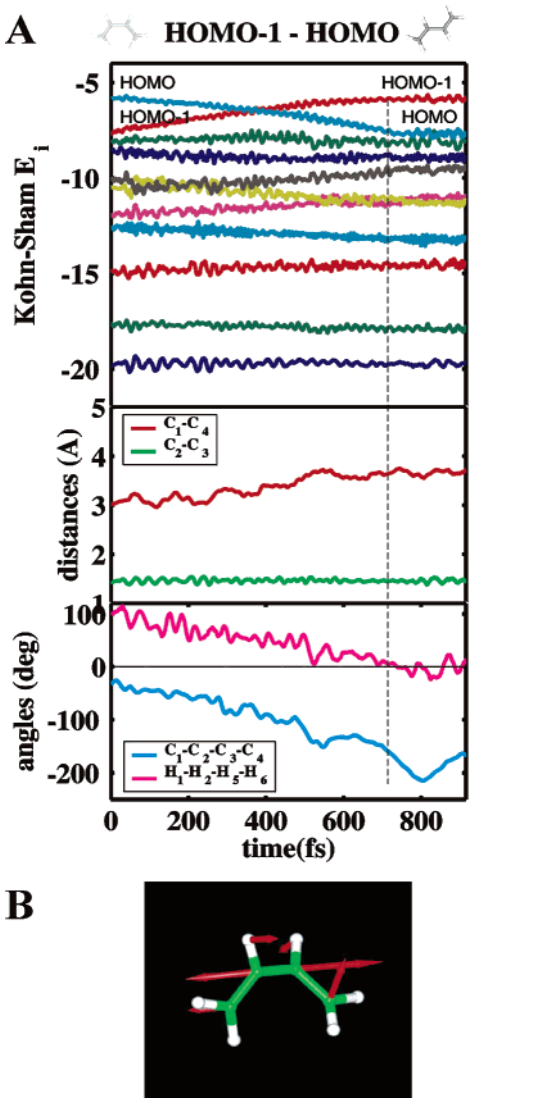

Figure 2. *cis*-Butadiene is driven toward s-*trans*-butadiene by applying a bias potential that exchanges the HOMO and HOMO-1 Kohn−Sham molecular orbital energies. (A) Kohn−Sham eigenvalues (upper panel), relevant distances (middle panel), and dihedral angles (lower panel) are plotted as a function of the simulated time. The vertical dashed line indicates the time when the final value for the target energy E_T^* is achieved. (B) Forces due to the applied bias potential (red arrows) in a representative snapshot from the dynamics evidences both the elongation of the rotating single bond and the torsional component of the gradient.

of Figure 1, the Lowest Valence Molecular Orbital + 1 (LVMO+1) is another orbital that is sensitive to this reactive channel. The shape of this orbital (Figure 1B) explains the reason why the one-particle energy eigenvalue of this low energy orbital is undergoing such a large change during the reaction. The LVMO+1 is indeed a delocalized orbital of σ character, corresponding to the C_1-C_2 and C_3-C_4 bond formation, that is therefore sensitive to both of these bond distances (that undergo elongation during cyclization) and to the newly formed C_1-C_4 bond. Bias potential forces of BP2 in a representative snapshot of the dynamics show how the effect of the applied potential tends to open the two double bonds (Figure 3B). The applied bias potential

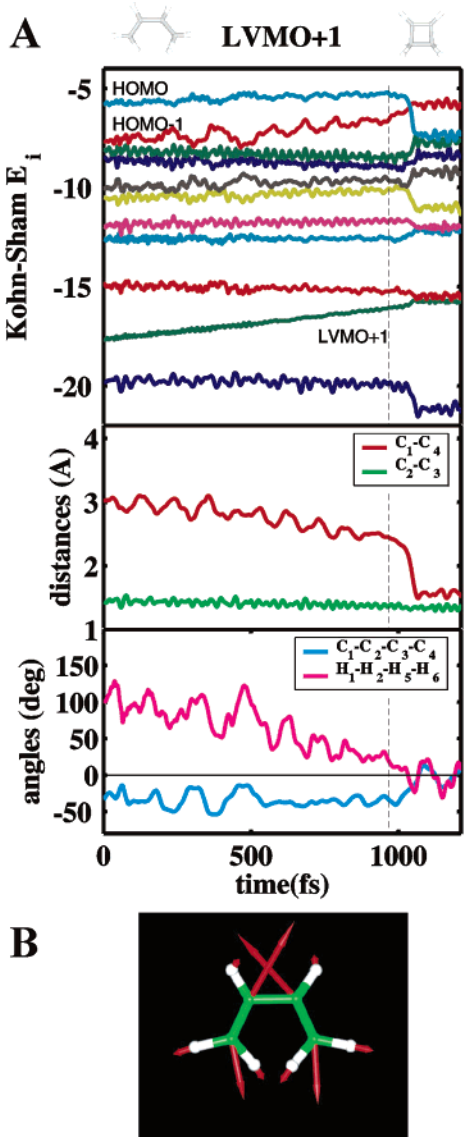

Figure 3. *cis*-Butadiene is driven toward conrotatory cyclization by applying a bias potential that raises the energy of the LVMO+1 Kohn−Sham molecular orbital. (A) Kohn−Sham eigenvalues (upper panel), relevant distances (middle panel), and dihedral angles (lower panel) are plotted as a function of the simulated time. The vertical dashed line indicates the time when the final value for the target energy E_T^* is achieved. (B) Forces due to the bias potential (red arrows) in a representative snapshot from the dynamics shows how the applied potential weakens the C_1-C_2 and C_3-C_4 double bonds while shortening the C_2-C_3 single bond.

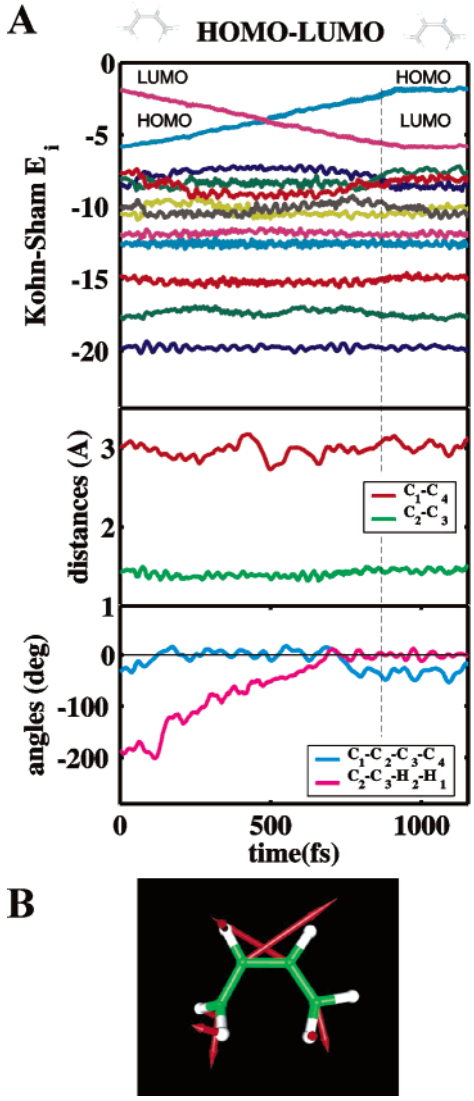

Figure 4. *cis*-Butadiene is driven toward CH_2 rotation around a double bond by applying a bias potential that exchanges the HOMO and LUMO Kohn−Sham molecular orbital energies. (A) Kohn−Sham eigenvalues (upper panel), relevant distances (middle panel), and dihedral angles (lower panel) are plotted as a function of the simulated time. The vertical dashed line indicates the time when the final value for the target energy E_T^* is achieved. (B) Forces due to the bias potential (red arrows) in a representative snapshot from the dynamics. The torsional component of the force is evident on the hydrogens of the rotating $-CH_2$ group.

correctly raises ϵ_{LVMO+1} and leads to the shortening of the distance of the forming C_1-C_4 bond, as shown in Figure 3A. Upon achievement of the target energy E_T, a few steps of room-temperature dynamics were enough to complete the reaction.

Reaction 3. In the symmetry forbidden cyclization pathway a HOMO−LUMO inversion occurs. Molecular dynamics of butadiene biased on the potential BP3 that exchanges ϵ_{LUMO} with ϵ_{HOMO} is reported in Figure 4. Whereas the energies of the frontier orbitals are correctly exchanged, the ϵ_{LVMO+1} is not significantly perturbed during this dynamics, in particular it does not rise in energy as expected in the case of cyclization. The C_1-C_4 distance is not affected by the electronic bias, but the $C_2-C_3-H_2-H_1$ dihedral angle increases to about 180 degrees indicating that the induced reaction is a complete rotation of the $-CH_2$ group around a butadiene double bond. The 90 degree dihedral conformation roughly coincides with the complete closure of the HOMO−LUMO gap.

In addition to the orbital biased dynamics we calculated the free energy profile for the $-CH_2$ rotation using the HOMO−LUMO gap as reaction coordinate. The umbrella sampling results are displayed in Figure 5. The calculated barrier at 0 gap is 68 kcal/mol, ∼15 kcal/mol higher than what was previously proposed.[33] This is due to the use of

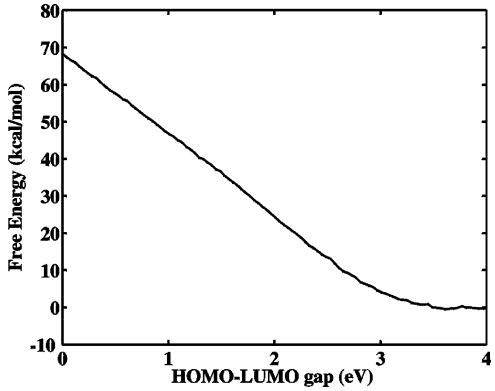

Figure 5. Free energy as a function of the electronic reaction coordinate (HOMO−LUMO gap) for the *cis*-butadiene double bond rotation.

the LDA approximation which is not appropriate to describe the biradicaloïd transition state of the isomerization. As shown by Vuilleumier and Sprik for the ethylene isomerization, the use of local spin density approximation lowers the reaction barrier by as much as 15−20 kcal/mol.

Discussion

The results obtained from the application of the electronic bias potential BP1 show that the system can choose the lowest energy pathway compatible with the imposed electronic constraints. In butadiene, both conrotatory cyclization and s-cis/s-trans isomerization reactions have the common feature of exchanging the two highest occupied orbitals, but the latter occurs spontaneously in our biased dynamics because of the lower activation barrier (∼6 vs ∼40 kcal/mol). To distinguish the two pathways we needed to introduce a low-lying valence molecular orbital in the bias potential BP2 (LVMO+1), which has σ character and is therefore more sensitive to the newly formed C_1-C_4 σ bond. The symmetry allowed cyclization occurred preserving the C_2 symmetry throughout the path, in agreement with previous calculations.[32,34,35]

The HOMO−LUMO inversion experienced by bias potential BP3 drives the system toward double bond rotation and not toward the symmetry forbidden cyclization as suggested by orbital correlation diagrams. At zero HOMO−LUMO gap we found butadiene to assume an asymmetric conformation with one $-CH_2$ group perpendicular to the carbon plane, as identified previously by Vuilleumier and Sprik.[22]

It is interesting to remark that this structure is a transition state of the double bond isomerization and not of the disrotatory cyclization, which is also asymmetric but involves a different geometry.[33,36,37]

We have also shown, using umbrella sampling in the BP3 case, that thermodynamical quantities, such as the free energy profile, can be computed within the Orbital Bias Molecular Dynamics scheme, using purely electronic reaction coordinates. Extension of the method to local spin density approximation is currently under development to better describe biradicaloïd transition states and open shell systems.

The introduction of general electronic reaction coordinates, allows for following different reaction pathways starting from the same reactant, depending on the choice of the bias potential used. Additional improvements can arise using, together with molecular orbitals, other chemical descriptors such as electronegativity, chemical hardness and softness, and population analysis to probe trends in chemical reactivity of large molecular systems.

Conclusions

A bias potential which is an explicit function of the Kohn−Sham molecular orbital energies has been implemented to scan the electronic channels of reactive molecules. The first application to the test case system of *s-cis*-butadiene was able to identify three different independent reactive channels as well as to drive the reactant molecule to the product states.

The proposed methodology was able to extend the electronic control of reactivity to systems where the HOMO−LUMO gap does not significantly change along the reaction, and thus represents a considerable generalization of the electronic bias methods that have been proposed so far.[21,22] The use of such 'electronic reaction coordinates' seems a promising technique to broaden the computational tools for studying reactivity. First of all, the new electronic coordinates, which are of collective nature, can be a useful complement to the ones based on nuclear geometry. Moreover, they offer the opportunity to directly select the electronic channels through descriptors that have a chemical connotation, such as frontier orbitals, HOMO−LUMO gap, chemical potential, and hardness. The resulting dynamics has the ability, as reported here, of selectively accessing high barrier reactions without exploring those with a low energy barrier. Free energy barriers along the desired electronic reaction coordinates can also be calculated.

Further technical improvements are still necessary to provide the Orbital Biased MD with the generalization necessary to study complex (bio)chemical reactions in condensed phase and in mixed QM/MM calculations. For example, the use of more complex chemical descriptors, such as hardness and softness, and the combination with the metadynamics technique developed by Parrinello and coworkers[8,9] can be of valuable help in exploring the phase space in electronic coordinates.

Acknowledgment. We thank D. Sebastiani, R. Vuilleumier, and I. Tavernelli for the precious help for the implementation of the bias potential in CPMD and M. Sprik and G. B. Bachelet for stimulating discussions.

References

(1) Ciccotti, G.; Ferrario, M.; Hynes, J. T.; Kapral, R. *Chem. Phys.* **1989**, *129*, 241−251.

(2) Huber, T.; Torda, A. E.; van Gunsteren, W. F. *J. Comput.-Aided Mol. Des.* **1994**, *8*, 695−708.

(3) Voter, A. F. *Phys. Rev. Lett.* **1997**, *78*, 3908−3911.

(4) Marchi, M.; Ballone, P. *J. Chem. Phys.* **1999**, *110*, 3697−3702.

(5) Sprik, M.; Ciccotti, G. *J. Chem. Phys.* **1998**, *109*, 7737−7744.

(6) VandeVondele, J.; Rothlisberger, U. *J. Chem. Phys.* **2000**, *36*, 4863−4868.

(7) VandeVondele, J.; Rothlisberger, U. *J. Phys. Chem. B* **2002**, *106*, 203−208.

(8) Laio, A.; Parrinello, M. *Proc. Natl. Acad. Sci.* **2002**, *99*, 12562−12566.

(9) Iannuzzi, M.; Laio, A.; Parrinello, M. *Phys. Rev. Lett.* **2003**, *90*, 238302−238306.

(10) Fukui, K. In *Molecular Orbitals in Chemistry, Physics and Biology*; Löwdin, P.-O. a. P. B., Ed.; Academics: New York, 1964.

(11) Fukui, K. *Nobel Lecture;* 1981.

(12) Woodward, R. B.; Hoffmann, R. *J. Am. Chem. Soc*. **1965**, *87*, 395−397.

(13) Woodward, R. B.; Hoffmann, R. *The conservation of orbital symmetry*; Academic Press: New York, 1969.

(14) Parr, R. G.; Yang, W. *J. Am. Chem. Soc*. **1984**, *106*, 4049−4050.

(15) Yang, W.; Parr, R. G.; Pucci, R. *J. Chem. Phys*. **1984**, *81*, 2862−2863.

(16) Chermette, H. *J. Comput. Chem* **1999**, *20*, 129−154.

(17) Nalewajski, R. F. *J. Phys. Chem.* **2003**, *107*, 3792−3802.

(18) Nakatsuji, H. *J. Am. Chem. Soc.* **1974**, *96*, 24−30.

(19) Geerlings, P.; De Proft, F.; Lagenaeker, W. *Chem. Rev.* **2003**, *103*, 1793−1873.

(20) Senet, P. *J. Chem. Phys.* **1997**, *107*, 2516−2524.

(21) VandeVondele, J.; Rothlisberger, U. *J. Am. Chem. Soc.* **2002**, *124*, 8163−8171.

(22) Vuilleumier, R.; Sprik, M. *Chem. Phys. Lett.* **2002**, *365*, 305−312.

(23) Mosey, N. J.; Hu, A.; Woo, T. K. *Chem. Phys. Lett.* **2003**, *373*, 498−505.

(24) Torrie, G. M.; Valleau, J. P. *J. Chem. Phys.* **1977**, *68*, 1402−1408.

(25) Sulpizi, M.; Laio, A.; Rothlisberger, U. to be published **2004**.

(26) Putrino, A.; Sebastiani, D.; Parrinello, M. *J. Chem. Phys.* **2000**, *113*, 7102−7109.

(27) CPMD V3.8 Copyright IBM Corp 1990−2004, Copyright MPI fuer Festkoerperforschung Stuttgart 2004.

(28) Vuilleumier, R.; Sprik, M. *J. Chem. Phys.* **2001**, *115*, 3454−3468.

(29) Troullier, N.; Martins, J. L. *Phys. Rev. B* **1991**, *43*, 1993−2006.

(30) Nose, S. *Mol. Phys.* **1984**, *52*, 255−268.

(31) Hoover, W. G. *Phys. Rev. A* **1985**, *31*, 1695−1697.

(32) Breulet, J.; Shaefer, H. F., III *J. Am. Chem. Soc*. **1984**, *106*, 1221−1226.

(33) Roth, W. R.; Rekowski, V.; Börner, S.; Quast, M. *Liebigs Annalen* **1996**, 409−430.

(34) Hsu, K.; Buenker, R. J.; Peyerimhoff, S. D. *J. Am. Chem. Soc*. **1971**, *93*, 2117−2127.

(35) Spellmeyer, D. C.; Houk, K. N.; Rondan, N. G.; Miller, R. D.; Franz, L.; Fickes, G. N. *J. Am. Chem. Soc*. **1989**, *111*, 5356−5367.

(36) Dewar, M. J. S.; Kirschner, S. *J. Am. Chem. Soc*. **1974**, *96*, 6809−6810.

(37) Sakai, S. *Chem. Phys. Lett.* **1998**, *287*, 263−269.

CT050081V

JCTC Journal of Chemical Theory and Computation

Stabilization of Cylindrical N_{12} and N_{18} by Phosphorus Substitution

Douglas L. Strout*

Department of Physical Sciences, Alabama State University, Montgomery, Alabama 36101

Received March 15, 2005

Abstract: Molecules consisting entirely or predominantly of nitrogen are the subject of much research for their potential as high energy density materials (HEDM). The problem with many such HEDM candidates is their instability with respect to dissociation. For example, a low-energy dissociation path has been shown for a cylindrical cage isomer of N_{12}. The instability is at least partially due to the ease of ring opening at triangles on either end of the molecule. In the current study, nitrogen cage molecules are examined to determine the stabilizing effect of substituting the triangle nitrogens with an element that more naturally forms triangles, namely phosphorus, which is valence isoelectronic with nitrogen. The cylindrical N_{12}, and a larger analogue N_{18}, form the structural basis for cage molecules of N_6P_6 and $N_{12}P_6$. Theoretical calculations using Hartree−Fock theory and perturbation theory (MP2 and MP4), along with the correlation-consistent basis sets of Dunning, have been carried out to determine dissociation energies along various pathways. The energies are discussed in terms of low-energy dissociation and the ability of the molecules to resist dissociation.

Introduction

Nitrogen molecules have been the subject of many recent studies because of their potential as high energy density materials (HEDM). An all-nitrogen molecule N_x can undergo the reaction $N_x \rightarrow (x/2)N_2$, a reaction that can be exothermic by 50 kcal/mol or more per nitrogen atom.[1,2] To be a practical energy source, however, a molecule N_x would have to resist dissociation well enough to be a stable fuel. Theoretical studies[3−7] have shown that numerous N_x molecules are not sufficiently stable to be practical HEDM, including cyclic and acyclic isomers with 8−12 atoms. Cage isomers of N_8 and N_{12} have also been shown[7−10] by theoretical calculations to be unstable. Experimental progress in the synthesis of nitrogen molecules has been very encouraging, with the N_5^+ and N_5^- ions having been recently produced[11,12] in the laboratory. More recently, a network polymer of nitrogen has been produced[13] under very high-pressure conditions. Experimental successes have sparked theoretical studies[14,15] on other potential all-nitrogen molecules. More recent developments include the experimental synthesis of high energy molecules consisting predominantly of nitrogen, including azides[16,17] of various heteroatoms and polyazido isomers[18] of compounds such as 1,3,5-triazine. Future developments in experiment and theory will further broaden the horizons of high energy nitrogen research.

The stability properties of N_x molecules have also been extensively studied in a computational survey[19] of various structural forms with up to 20 atoms. Cyclic, acyclic, and cage isomers have been examined to determine the bonding properties and energetics over a wide range of molecules. A more recent computational study[20] of cage isomers of N_{12} examined the specific structural features that lead to the most stable molecules among the three-coordinate nitrogen cages. Those results showed that molecules with the most pentagons in the nitrogen network tend to be the most stable, with a secondary stabilizing effect due to triangles in the cage structure. A recent study[21] of larger nitrogen molecules N_{24}, N_{30}, and N_{36} showed significant deviations from the pentagon-favoring trend. Each of these molecule sizes has fullerene-like cages consisting solely of pentagons and hexagons, but a large stability advantage was found for molecules with

* Corresponding author phone: (334)229-4718; e-mail: dstraut@alasu.edu.

10.1021/ct050067i CCC: $30.25
Published on Web 05/27/2005

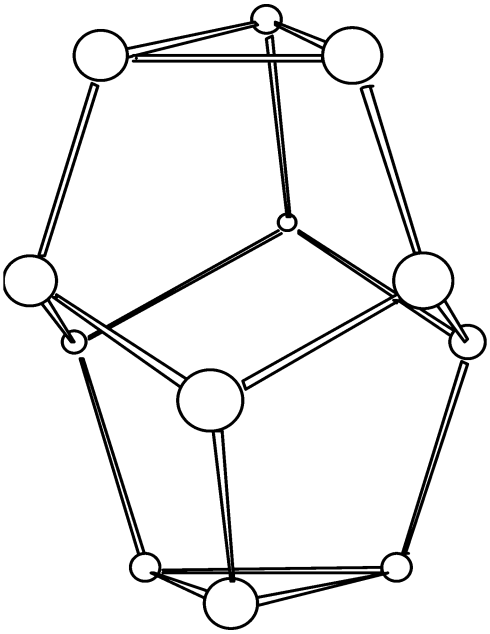

Figure 1. Cage isomer of N_{12} (designated 2060, ref 20). This is the most stable cage isomer of N_{12}.

fewer pentagons, more triangles, and an overall structure more cylindrical than spheroidal. Studies[22,23] of intermediate-sized molecules N_{14}, N_{16}, and N_{18} also showed that the cage isomer with the most pentagons was not the most stable cage, even when compared to isomer(s) containing triangles (which have 60° angles that should have significant angle strain). For each of these molecule sizes, spheroidally shaped molecules proved to be less stable than elongated, cylindrical ones.

However, in terms of absolute stability with respect to dissociation processes, even the most stable N_{12} (see Figure 1) has been shown[7] to have a low-energy path to dissociation. The low-energy dissociation involves the opening of the triangles on each end of the molecule. Nitrogen−nitrogen single bonds become double bonds, which are energetically very favorable compared to single bonds, and become triple bonds (yielding isolated N_2 molecules, the ultimate product of the dissociation processes). In the current study, nitrogen atoms in the triangles are substituted by phosphorus, an element that more naturally forms stable triangles[24] and is valence isoelectronic with nitrogen. This substitution is made on the most stable N_{12} and an analogous N_{18} cage (shown in Figure 2). The resulting molecules have molecular formulas of N_6P_6 and $N_{12}P_6$ and are illustrated in Figures 3 and 4, respectively. The issue to be examined in this study is whether the nitrogen−phosphorus molecules are stable enough to be good candidates for HEDM.

Computational Methods

Geometry optimizations are carried out using Hartree−Fock (HF) theory and perturbation theory[25] (MP2). Single energy points are calculated with fourth-order perturbation theory[25] (MP4(SDQ)). Single energy points for N_6P_6 have also been calculated with coupled-cluster theory[26] (CCSD(T)). Vibrational frequencies and zero-point energies (ZPE) have been calculated for N_6P_6 with MP2 theory. Geometries and

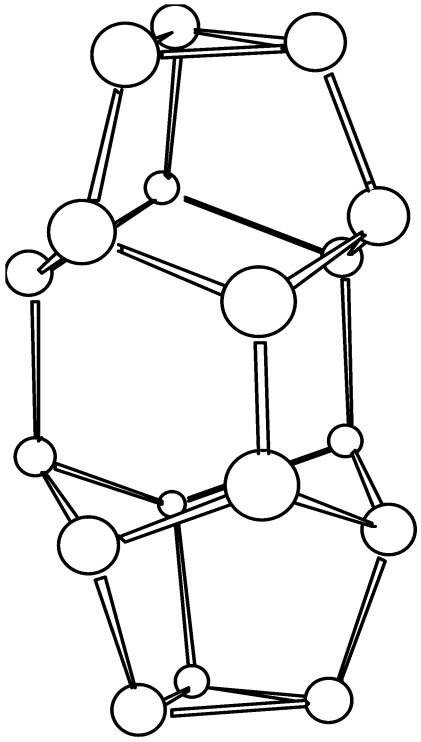

Figure 2. Cage isomer of N_{18} (designated 2063A, ref 22). This is the most stable cage isomer of N_{18}.

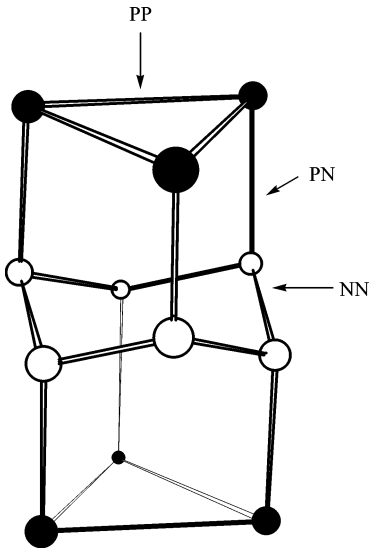

Figure 3. N_6P_6 molecule, with nitrogen atoms in white and phosphorus atoms in black. The molecule has D_{3d} point group symmetry, and symmetry-independent bonds have been labeled.

energies of the intact molecules are calculated in the singlet state, while dissociation intermediates, which have one broken bond, are calculated in the triplet state. The basis sets are the polarized valence double-ζ (cc-pVDZ) and augmented polarized valence double-ζ (aug-cc-pVDZ) sets of Dunning.[27] The Gaussian 03 computational chemistry software package[28] is used for all calculations in this work.

Results and Discussion

The N_6P_6 molecule has D_{3d} point group symmetry and has only three symmetry-independent bonds, marked in Figure

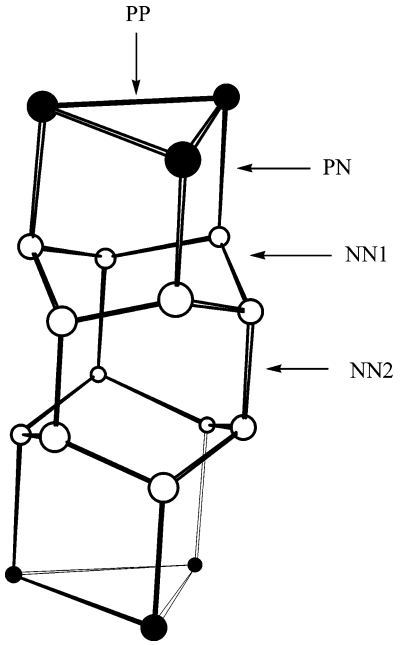

Figure 4. $N_{12}P_6$ molecule, with nitrogen atoms in white and phosphorus atoms in black. The molecule has D_{3h} point group symmetry, and symmetry-independent bonds have been labeled.

Table 1. Dissociation Energies for Each of the Symmetry-Independent Bonds in the N_6P_6 Molecule[a]

	symmetry-independent bonds (Figure 3)		
method/basis set	PP	PN	NN
HF/cc-pVDZ	+26.6	+42.9	+9.5
MP2/cc-pVDZ	+53.9	+68.6	+45.3
MP2 (+ ZPE)/cc-pVDZ	+53.3	+67.5	+44.5
HF/aug-cc-pVDZ	+26.4	+42.6	+10.2
MP2/aug-cc-pVDZ	+54.4	+70.8	+47.2
MP4/cc-pVDZ // MP2/cc-pVDZ	+46.7	+61.1	+34.6
CCSD(T)/cc-pVDZ // MP2/cc-pVDZ	+47.4	+56.2	+32.1

[a] Energies in kcal/mol. Zero-point energies (ZPE) have been calculated at the MP2/cc-pVDZ level of theory.

3 as PP, PN, and NN, denoting the phosphorus−phosphorus, phosphorus−nitrogen, and nitrogen−nitrogen bonds, respectively. Breaking any of these bonds results in a dissociation intermediate whose ground electronic state is a triplet. HOMO−LUMO gaps of the intact molecules and all dissociation intermediates are sufficiently large that there are no other low-lying states, and therefore the use of single-reference methods in this study is justified. The calculated energies of dissociation for each of the three bonds are shown in Table 1; each dissociation energy is the energy difference between the intact molecule and the corresponding dissociation intermediate. The Hartree−Fock numbers are consistently low, with a strong upward correction from MP2 and a moderate lowering effect from MP4. Coupled-cluster theory (CCSD(T)) bond dissociation energies for N_6P_6 are within a few kcal/mol of the MP4 results. Vibrational frequencies with MP2 theory confirm that the N_6P_6 and all of its dissociation intermediates are local minima, and the zero-point corrections to the MP2/cc-pVDZ energies are about 1 kcal/mol. Basis set effects are minimal and tend toward a very slight increase in dissociation energy as the basis set increases.

Table 2. Energies (Relative to the N_6P_6 Molecule) of an Intermediate with Two PN Bonds Broken To Produce an N═N Double Bond[a]

	HF	MP2	MP4//MP2
energy of breaking two PN bonds	+38.3	+61.5	+44.7

[a] Energies in kcal/mol calculated with cc-pVDZ basis set.

Table 3. Energy Releases for N_{12} and N_{18} and the Phosphorus-Substituted Analogues[a]

molecule	reaction	kJ/mol	kJ/g
N_{12}	$N_{12} \rightarrow 6N_2$	2225	13.2
N_{18}	$N_{18} \rightarrow 9N_2$	3449	13.7
N_6P_6	$N_6P_6 \rightarrow 3N_2 + (3/2)P_4$	907	3.4
$N_{12}P_6$	$N_{12}P_6 \rightarrow 6N_2 + (3/2)P_4$	2069	5.8

[a] Calculated at MP2/cc-pVDZ level of theory.

The data suggest that the weakest bond in the molecule is the NN bond; this bond has the lowest dissociation energy at all levels of theory. However, even this bond has a dissociation energy over 30 kcal/mol, which implies that this molecule is stable and could be a viable HEDM. Breaking a bond anywhere in the molecule requires the input of a substantial amount of energy, but what about a concerted dissociation process whereby two or more bonds break simultaneously? Such a process is most likely to proceed at low energy if it leads to the creation of an N═N double bond, because an N═N double bond is an energetically favorable step toward the creation of free N_2. The N_6P_6 has only one pathway whereby the breaking of two bonds leads to an N═N double bond. If two PN bonds are broken such that the two nitrogen atoms are bonded to each other, the two nitrogen atoms will form a double bond. The intermediate with the double bond has a triplet ground state, and its energies are shown in Table 2. The energies are lower than for breaking one PN bond, which is due to the stabilizing effect of the N═N double bond, but the energies are still above 40 kcal/mol. The two-bond-breaking pathway is also a high energy dissociation route for the molecule.

N_6P_6 is a stable molecule, but the loss of half of the nitrogen atoms (relative to N_{12}) would result in a drastic loss of energy production from the molecule. The reaction $N_6P_6 \rightarrow 3N_2 + (3/2)P_4$ would be a great deal less exothermic than $N_{12} \rightarrow 6N_2$. This loss of energy release power is quantified in Table 3. In designing a practical HEDM, maximizing the nitrogen content is a desirable goal. For that reason, calculations are carried out on the $N_{12}P_6$ molecule shown in Figure 4. Its structure is based on the N_{18} shown in Figure 2, with phosphorus substitution similar to the N_6P_6. This molecule has D_{3h} point group symmetry and four symmetry-independent bonds, which are labeled in Figure 4. Two of the bonds are nitrogen−nitrogen and are labeled NN1 and NN2. Dissociation energies for each of the four bonds are shown in Table 4.

The $N_{12}P_6$ molecule is less stable than its N_6P_6 counterpart, due to lesser stability in the NN1 bond. The NN1 bond is the "weakest link" in the $N_{12}P_6$, with a dissociation energy of 25.1 kcal/mol at the MP4/cc-pVDZ level of theory,

Table 4. Dissociation Energies for Each of the Symmetry-Independent Bonds in the $N_{12}P_6$ Molecule[a]

	symmetry-independent bonds (Figure 4)			
method/basis set	PP	PN	NN1	NN2
HF/cc-pVDZ	+27.5	+41.4	+2.4	+41.8
MP2/cc-pVDZ	+55.4	+67.9	+34.7	+58.0
MP4/cc-pVDZ // MP2/cc-pVDZ	+48.1	+59.6	+25.1	+62.1

[a] Energies in kcal/mol.

compared with the 34.6 kcal/mol dissociation energy of the NN bond of N_6P_6. This is an effect that has been previously shown[29] for hexagonal nitrogen tubes, namely a weakening in N−N bonds with increasing length of a nitrogen tube. Further lengthening of the tube to create $N_{18}P_6$, $N_{24}P_6$, etc., by incorporating additional hexagonal "layers" of nitrogen is similarly unlikely to result in strengthening of the molecule. Rather the opposite, not only in the weakening of individual nitrogen−nitrogen bonds but also in the proliferation of multiple-bond-breaking pathways that could expose an N═N double-bonded pair. Even one such low-energy pathway would render the molecule unstable with respect to dissociation. The $N_{12}P_6$ may be more stable than its N_{18} analogue, but the viability of $N_{12}P_6$ as a stable HEDM is questionable.

Conclusion

Nitrogen cages previously shown to be unstable with respect to dissociation can be stabilized with the substitution of appropriate atoms such as phosphorus. Such substitutions can lead to small molecules that are feasible as high energy density materials. It seems, however, that two limitations exist in the utility of phosphorus as a heteroatom: (1) phosphorus substitution on the triangular end-caps does not solve the problem of weakness in the interior of a lengthening nitrogen tube, and (2) the high mass and low energy release properties of phosphorus dilute the energy release properties of the HEDM. While tradeoffs between stability and energy release may be inevitable in HEDM design, other heteroatoms may provide stability with less loss of power. If, in fact, the goal of a 100% nitrogen HEDM is unattainable, then further heteroatom studies will be required to find the optimum balance between stability and energy production.

Acknowledgment. The Alabama Supercomputer Authority is gratefully acknowledged for a grant of computer time on the SGI Altix operated in Huntsville, AL. This work is also supported by the National Institutes of Health (NIH/NCMHD grant 1P20MD000547-01). This work was partially supported by the National Computational Science Alliance under grant number CHE030041 and utilized the IBM p690 cluster in Champaign, IL. The taxpayers of the state of Alabama in particular and the United States in general are also gratefully acknowledged.

References

(1) Fau, S.; Bartlett, R. J. *J. Phys. Chem. A* **2001**, *105*, 4096.

(2) Tian, A.; Ding, F.; Zhang, L.; Xie, Y.; Schaefer, H. F., III *J. Phys. Chem. A* **1997**, *101*, 1946.

(3) Chung, G.; Schmidt, M. W.; Gordon, M. S. *J. Phys. Chem. A* **2000**, *104*, 5647.

(4) Strout, D. L. *J. Phys. Chem. A* **2002**, *106*, 816.

(5) Thompson, M. D.; Bledson, T. M.; Strout, D. L. *J. Phys. Chem. A* **2002**, *106*, 6880.

(6) Li, Q. S.; Liu, Y. D. *Chem. Phys. Lett.* **2002**, *353*, 204. Li, Q. S.; Qu, H.; Zhu, H. S. *Chin. Sci. Bull.* **1996**, *41*, 1184.

(7) Li, Q. S.; Zhao, J. F. *J. Phys. Chem. A* **2002**, *106*, 5367. Qu, H.; Li, Q. S.; Zhu, H. S. *Chin. Sci. Bull.* **1997**, *42*, 462.

(8) Gagliardi, L.; Evangelisti, S.; Widmark, P. O.; Roos, B. O. *Theor. Chem. Acc.* **1997**, *97*, 136.

(9) Gagliardi, L.; Evangelisti, S.; Bernhardsson, A.; Lindh, R.; Roos, B. O. *Int. J. Quantum Chem.* **2000**, *77*, 311.

(10) Schmidt, M. W.; Gordon, M. S.; Boatz, J. A. *Int. J. Quantum Chem.* **2000**, *76*, 434.

(11) Christe, K. O.; Wilson, W. W.; Sheehy, J. A.; Boatz, J. A. *Angew. Chem., Int. Ed.* **1999**, *38*, 2004.

(12) Vij, A.; Pavlovich, J. G.; Wilson, W. W.; Vij, V.; Christe, K. O. *Angew. Chem., Int. Ed.* **2002**, *41*, 3051. Butler, R. N.; Stephens, J. C.; Burke, L. A. *Chem. Commun.* **2003**, *8*, 1016.

(13) Eremets, M. I.; Gavriliuk, A. G.; Trojan, I. A.; Dzivenko, D. A.; Boehler, R. *Nature Mater.* **2004**, *3*, 558.

(14) Fau, S.; Bartlett, R. J. *J. Phys. Chem. A* **2001**, *105*, 4096.

(15) Fau, S.; Wilson, K. J.; Bartlett, R. J. *J. Phys. Chem. A* **2002**, *106*, 4639.

(16) Knapp, C.; Passmore, J. *Angew. Chem., Int. Ed.* **2004**, *43*, 4834.

(17) Haiges, R.; Schneider, S.; Schroer, T.; Christe, K. O. *Angew. Chem., Int. Ed.* **2004**, *43*, 4919.

(18) Huynh, M. V.; Hiskey, M. A.; Hartline, E. L.; Montoya, D. P.; Gilardi, R. *Angew. Chem., Int. Ed.* **2004**, *43*, 4924.

(19) Glukhovtsev, M. N.; Jiao, H.; Schleyer, P.v. R. *Inorg. Chem.* **1996**, *35*, 7124.

(20) Bruney, L. Y.; Bledson, T. M.; Strout, D. L. *Inorg. Chem.* **2003**, *42*, 8117.

(21) Strout, D. L. *J. Phys. Chem. A* **2004**, *108*, 2555.

(22) Sturdivant, S. E.; Nelson, F. A.; Strout, D. L. *J. Phys. Chem. A* **2004**, *108*, 7087.

(23) Strout, D. L. *J. Phys. Chem. A* **2004**, *108*, 10911.

(24) White phosphorus (P_4) consists of tetrahedral molecules, which have triangular faces. See: Chang, R. *Chemistry*, 8th ed.; McGraw-Hill: New York, p 886.

(25) Moller, C.; Plesset, M. S. *Phys. Rev.* **1934**, *46*, 618.

(26) Purvis, G. D.; Bartlett, R. J. *J. Chem. Phys.* **1982**, *76*, 1910. Scuseria, G. E.; Janssen, C. L.; Schaefer, H. F., III. *J. Chem. Phys.* **1988**, *89*, 7382.

(27) Dunning, T. H., Jr. *J. Chem. Phys.* **1989**, *90*, 1007.

(28) Frisch, M. J.; Trucks, G. W.; Schlegel, H. B.; Scuseria, G. E.; Robb, M. A.; Cheeseman, J. R.; Montgomery, J. A., Jr.; Vreven, T.; Kudin, K. N.; Burant, J. C.; Millam, J. M.; Iyengar, S. S.; Tomasi, J.; Barone, V.; Mennucci, B.; Cossi, M.; Scalmani, G.; Rega, N.; Petersson, G. A.; Nakatsuji, H.; Hada, M.; Ehara, M.; Toyota, K.; Fukuda, R.; Hasegawa, J.; Ishida, M.; Nakajima, T.; Honda, Y.; Kitao, O.; Nakai, H.; Klene, M.; Li, X.; Knox, J. E.; Hratchian, H. P.; Cross, J. B.; Bakken, V.; Adamo, C.; Jaramillo, J.; Gomperts, R.; Stratmann, R. E.; Yazyev, O.; Austin, A. J.; Cammi, R.;

Pomelli, C.; Ochterski, J. W.; Ayala, P. Y.; Morokuma, K.; Voth, G. A.; Salvador, P.; Dannenberg, J. J.; Zakrzewski, V. G.; Dapprich, S.; Daniels, A. D.; Strain, M. C.; Farkas, O.; Malick, D. K.; Rabuck, A. D.; Raghavachari, K.; Foresman, J. B.; Ortiz, J. V.; Cui, Q.; Baboul, A. G.; Clifford, S.; Cioslowski, J.; Stefanov, B. B.; Liu, G.; Liashenko, A.; Piskorz, P.; Komaromi, I.; Martin, R. L.; Fox, D. J.; Keith, T.; Al-Laham, M. A.; Peng, C. Y.; Nanayakkara, A.; Challacombe, M.; Gill, P. M. W.; Johnson, B.; Chen, W.; Wong, M. W.; Gonzalez, C.; Pople, J. A. *Gaussian 03*, Revision B.01; Gaussian, Inc., Wallingford CT, 2004.

(29) Sturdivant, S. E.; Strout, D. L. *J. Phys. Chem. A* **2004**, *108*, 4773.

CT050067I

JCTC Journal of Chemical Theory and Computation

Search for the $Li_n^{0/+1/-1}$ ($n = 5-7$) Lowest-Energy Structures Using the ab Initio Gradient Embedded Genetic Algorithm (GEGA). Elucidation of the Chemical Bonding in the Lithium Clusters

Anastassia N. Alexandrova and Alexander I. Boldyrev*

Department of Chemistry and Biochemistry, Utah State University, 0300 Old Main Hill, Logan, Utah 84322-0300

Received April 6, 2005

Abstract: We report the study of small lithium clusters $Li_n^{0/+1/-1}$ ($n = 5-7$), performed via the novel Gradient Embedded Genetic Algorithm (GEGA) technique and molecular orbital analysis. GEGA was developed for searching of the lowest-energy structures of clusters. Results of our search, obtained using this program, have been compared with the previous ab initio calculations, and the efficiency of the developed GEGA method has thus been confirmed. The molecular orbital analysis of the found $Li_n^{0/+1/-1}$ ($n = 5-7$) clusters showed the presence of multiple (σ and π) aromatic character in their chemical bonding, which governs their preferable shapes and special stability.

I. Introduction

The Genetic Algorithm (GA) is an optimization strategy based on the Darwinian evolution process.[1] Genetic Algorithms, simple methods which do not include the calculation of derivatives, were successfully used in many areas of science and technology when global optima for complex, many-parameter functions are needed to be found.[2,3] The search for global minima of chemical systems belongs to this class of problems and has been approached via GA techniques.[4−28] We developed a novel ab initio Gradient Embedded Genetic Algorithm program (GEGA), which combines the efficient features of the ab initio accuracy of obtained relative energies and geometries with a fast convergence rate. This was achieved by the application of the gradient-following technique and implementation of a specific mutation process. The algorithm was illustrated by its application to the search for global minima of small cationic, anionic and uncharged clusters of lithium Li_n ($n = 5-7$). The energies and geometries of the found lowest-energy structures were further refined using more accurate ab initio methods. Finally, analysis of the chemical bonding in the found global minimum species was performed.

The lithium clusters considered in this work have been previously studied experimentally[29,30] and, primarily, theoretically.[29−56] The first ionization potentials of the neutral cluster have been evaluated in photoelectron spectroscopic experiments.[29,30] Most of the authors agree on the structure of the global minima of such small clusters. Thus, the chosen clusters can serve as good testing systems for the developed GEGA program.

After the global minimum structures are found, the chemical bonding within them is analyzed, and the origin of their specific shapes is elucidated. Specifically, we introduce the concepts of aromaticity and antiaromaticity to the description of the chemical bonding in the considered alkali metal clusters. The concept of aromaticity was originally proposed for certain organic compounds possessing high symmetry and planar shape and containing $(4n+2)$ electrons in their π-molecular orbital system (Huckel's rule). Recently, the concept was advanced into organometallic[57−61] and all-metal systems.[62−71] Robinson's aromatic metal clusters[57−61] are only π-aromatic, while the all-metal clusters[62−71] are both π- and σ-aromatic. These examples have already shown the usefulness of the aromaticity concept in metal clusters, and we believe that the advances of the aromaticity concept further into metal and nonmetal clusters

* Corresponding author e-mail: boldyrev@cc.usu.edu.

10.1021/ct050093g CCC: $30.25
Published on Web 06/11/2005

will help us better understand chemical bonding, structure, and stability in these species as well as serve as a better interpretation of spectroscopic data. In our recent work, we presented our interpretation of the chemical bonding in small clusters of lithium and magnesium on the basis of the concept of pure σ-aromaticity.[72] In the current study, we extend the concepts of aromaticity and antiaromaticity of both σ- and π-types to larger lithium clusters, explaining their shape and stability.

II. Theoretical Methods

1. Genetic Algorithm Method. The GA-based search for the global minimum is performed in the 3*N* configurational space with the energy value as a criterion of the fit. Initially, for all individuals (structures) in the population (group of structures), the size of which is user-defined, the random generation of 3*N* Cartesian coordinates in the range [R_{min}; R_{max}] is performed. The R_{max} is calculated on the basis of the average interatomic distance in the cluster, defined by the user, and is adjusted to the dimensionality of the generated cluster. The minimum interatomic distance R_{min} is the smallest allowed interatomic distance, introduction of which prevents the program from generating unphysical solutions. The user can also specify the expected topology of the system ('compact', 'medium', or 'open') in order to adjust the [R_{min}; R_{max}] interval accordingly: the R_{max} evaluated by the program will be the smallest for 'compact' topologies, larger for 'medium', and the largest for 'open' topologies. This rough adjustment at the beginning of the execution allows faster convergence of the algorithm. However, it can only be done if there is some preliminary information available about preferable geometries of the studied type of systems. By default, the topology of the cluster is assumed to be 'open'. For homoatomic systems, such as lithium clusters, the initial generation of the population is performed in two steps. At first, a group of planar individuals, with one linear species included purposely, is randomly created. In the second step, three-dimensional individuals are generated. The two-step generation of the population is introduced, because the chance of planar and especially linear species to be randomly generated in the 3*N* space is very low compared to 3-D species. Our experience showed that such generation procedure guarantees a saturation of the population with planar, linear, and 3-D individuals and accelerates the overall convergence of the algorithm. Employing the Gaussian 03 package,[73] single-point energies are computed for all the species at the chosen level of theory (the user can define the method and the basis set). We used the (U)B3LYP[74−76] level with a small valence-split basis set 3-21G. Our experience showed that even using this level of theory, GEGA can predict the global minimum and the collection of the lowest-energy isomers quite accurately. Although the assignment of the global minimum structure may not always be accurate at this low level of theory in GEGA, we believe that the true global minimum will be among these low-energy isomers and may be identified later on by more sophisticated calculations following the GEGA search. The described meticulous initial selection of individuals is somewhat reminiscent of the Monte Carlo simulation.[77] The size of the population is recommended to be no less than 40 individuals for clusters containing up to seven atoms, in agreement with the previously suggested population size for this type of problem when the gradient-following technique is employed.[5] As we found, larger population size is computationally demanding while not necessary for the systems of such size. The population size should be increased for larger systems. At the moment we do not have detailed information about the performance of the GEGA depending on the population size. The criterion maintained in the code suggests the population size to be equal to or greater than 5*N*, where *N* is the number of atoms in the cluster. If the requested population size is smaller, then the warning message is printed out in the output file.

All the structures of the thus constructed initial population are then optimized to the nearest stationary points on the potential energy surface. If a saddle point is encountered, then the normal mode of the first imaginary frequency is followed until a local minimum is found. Further, the population, composed of the thus selected good individuals, undergoes breeding and mutations. The mating implemented in GEGA is performed on the basis of the robust technique originally proposed in 1995 by Deaven and Ho,[13] in which some of the geometrical features of good individuals in the population (parents) are combined and passed to new individuals (children). Parents are local minimum structures obtained either during the initial or subsequent iterations. Children are new structures made out of two parent structures. Probabilities to be bred (to produce child structures) are assigned to parents according to the best-fit (lowest-energy) criterion. Based on the probabilities, couples of parents are randomly selected. Figure 1A shows a typical breeding procedure on the example of selected structures of the Li_5^- cluster. The geometries of parents are cut by a random cutting plane (XY, YZ, or ZY), and the obtained halves (genes) are then recombined either in a simple or in a head-to-tail manner, forming a child. Figure 1A illustrates the case when the XY plane is chosen, and the recombination of the halves occurs in the simple manner, i.e., the part of geometry of the parent 1 taken from above the cutting plane is recombined with the part of geometry of the parent 2 taken from below the plane. The number of atoms in the newly generated geometry is checked, and the child is optimized to the nearest local minimum. If the number of atoms in the child is incorrect, the cutting plane is shifted so that the correct number of atoms results. After the number of individuals in the population is doubled within the breeding process, the best-fit group is selected and convergence of the algorithm is checked. The GEGA is considered converged if the current lowest-energy species (global minimum or, at least, a very stable local minimum) remains leading for 20 iterations. If the convergence is not yet met, the highest-energy species in the population undergo mutations. The mutation rate is set to 33.33%. Mutations are shifts of random atoms of a species in random directions, with the purpose of changing the initial geometry so as to push the structure out of the current local minimum to another well on the potential energy surface (see Figure 1B). Mutants are

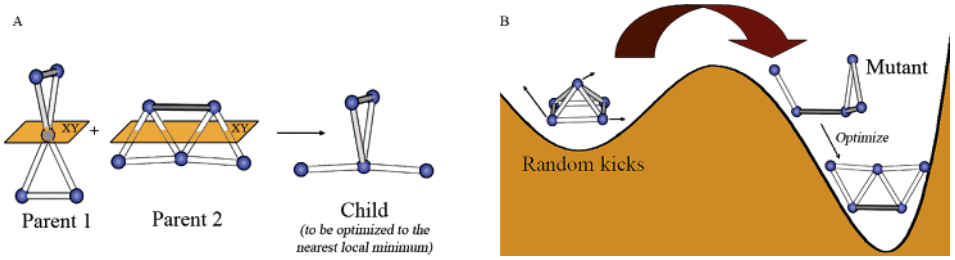

Figure 1. Illustration of the GEGA procedure: A. Breeding, when the XY plane is randomly chosen, geometries of two selected parents are cut by XY, and the parts of parents (the part of the parent 1 from above the plane and the part of the parent 2 from below the plane) are recombined in a simple manner; the obtained child will then be optimized to the nearest local minimum. B. Mutation, when the random number of kicks is introduced to distort the structure strongly enough to cross the barrier on the potential energy surface, the obtained mutant is then optimized to the local minimum.

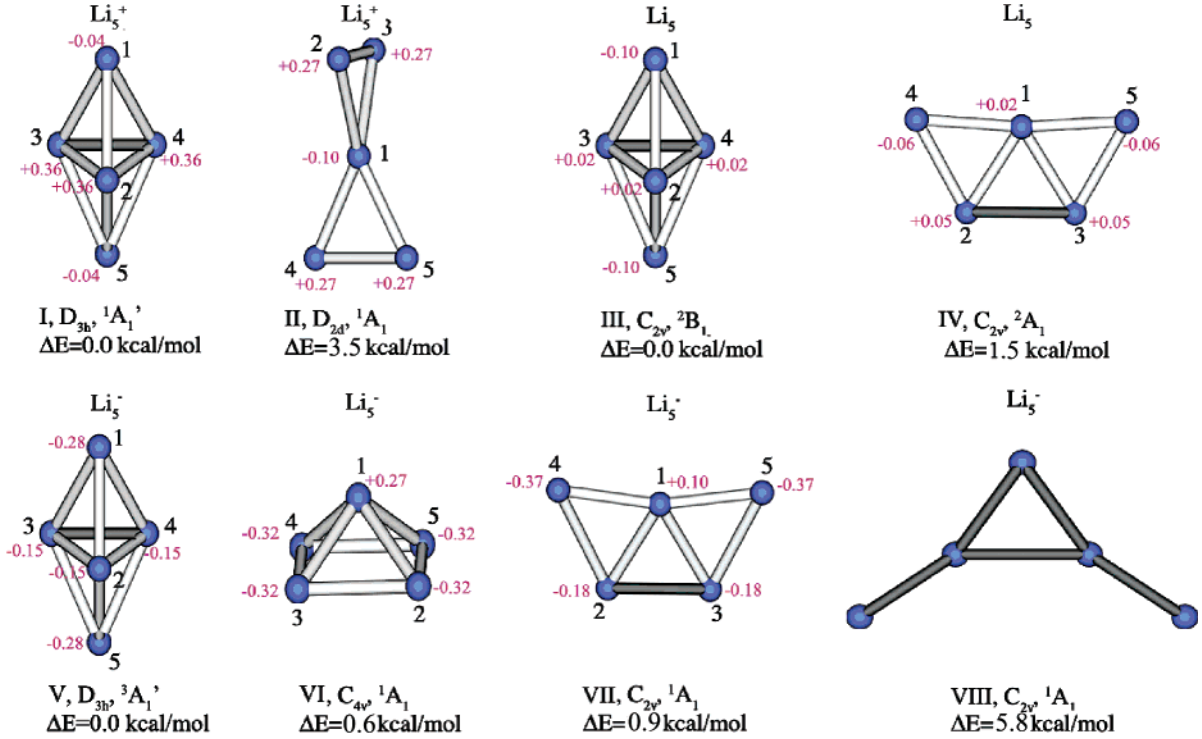

Figure 2. Global minimum and lowest in energy structures of Li_5^+, Li_5, and Li_5^- clusters found using the Genetic Algorithm. Shown geometries are refined at the CCSD(T)/6-311+G* level of theory. CCSD(T)/6-311+G(2df) ΔEs are given with ZPE corrections obtained at the CCSD(T)/6-311+G* level. The NPA atomic charges at the B3LYP/6-311+G* level are shown.

optimized to the nearest local minima. After mutations the algorithm proceeds with a new cycle of breeding. All low-lying isomers are detected and stored throughout the execution, and they are reported to the user at the end of the run. A few runs of GEGA are done on the system in order to confirm the found global minimum structure.

If high multiplicity states can be expected for a certain species, the GEGA search should be performed with different multiplicity values. For simpler systems it may be more reasonable to find the global minimum and isomers with the lowest possible multiplicity value and further manually check the lowest-energy structures with higher multiplicities.

According to our observations, the GEGA performance strongly depends on the calculated [R_{min}; R_{max}] interval. If the R_{max} is too small, imposing an unphysical restraint on the system, the global minimum will not be found. If the R_{max} is chosen to be too large, it is most likely that the convergence will eventually be met, but it will take much longer for the algorithm to converge. In the case of lithium clusters, as will be shown shortly, the geometries of the clusters are rather compact. Thus the specification of topology as 'compact' led to faster convergence to global minima. When 'medium' or 'open' topologies were chosen, the convergence was harder to reach. For example, in the case of the Li_7^+ cluster, 'compact' topology specification permitted the algorithm to converge within 22 iterations, while in the case of 'open' topology, 25 iterations were needed. Accurate average interatomic distance is always necessary for proper R_{max} assignment. On the other hand, if the R_{min} chosen by the user is very large, the performance of the GEGA can slow tremendously. This happens because many randomly generated geometries will have atom−atom distances falling within a large R_{min} and must therefore be discarded. As the number of atoms in the cluster increases, the likelihood of atom−atom distances falling within R_{min} increases, so GEGA can get stuck trying to generate physically eligible geometries. However, if the R_{min} is too

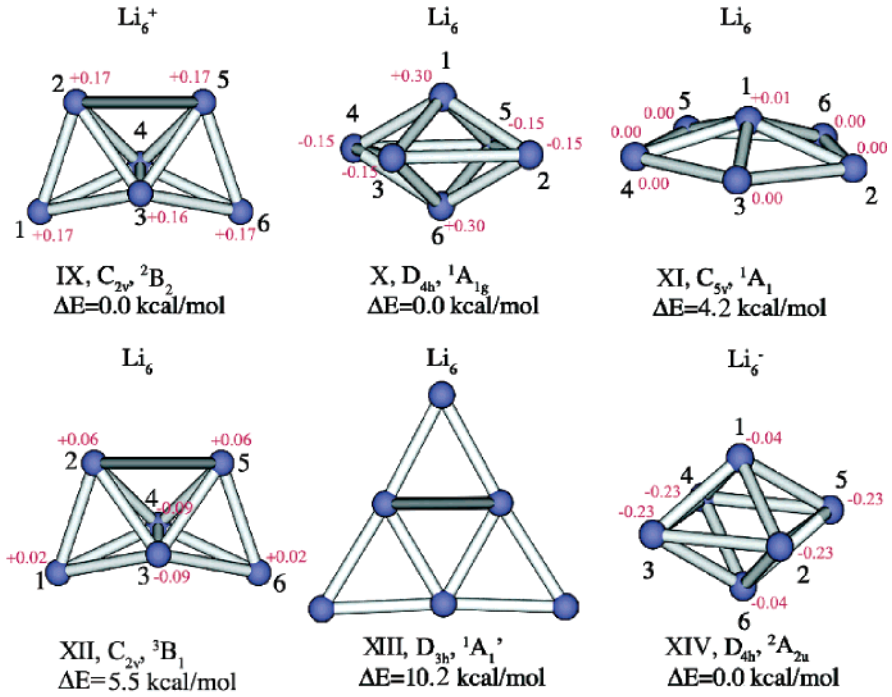

Figure 3. Global minimum and lowest in energy structures of Li_6^+, Li_6, and Li_6^- clusters found using the Genetic Algorithm. Shown geometries are refined at the CCSD(T)/6-311+G* level of theory. CCSD(T)/6-311+G(2df) Δ*E*s are given with ZPE corrections obtained at the CCSD(T)/6-311+G* level. The NPA atomic charges at the B3LYP/6-311+G* level are shown.

small, quantum chemical calculations may not reach SCF-convergence for some of the species.

So far, due to limited computational resources, we were not able to test our program on very large systems. However, the largest clusters to which GEGA was applied contained nine atoms (in the B3LYP/3-21G run) and 13 atoms (in the semiempirical run). With a new computer cluster (128 dual processors) we expect to extend the number of atoms in the GEGA search up to 20 or may be even 30 atoms.

2. Other Methods. After the global minima and lowest-energy isomers are found using the Genetic Algorithm program, geometries and energies of species are refined at the (U)B3LYP[74−76] and the coupled cluster (U)CCSD(T)[78−82] levels of theory with the more extended 6-311+G* basis set. The energies of the species are further refined at the (U)CCSD(T)/6-311+G(2df) + ZPE/CCSD(T)/6-311+G* level of theory. The first vertical and adiabatic ionization potentials were computed for all neutral and anionic global minima and compared to the available experimental data.[29,30] Chemical bonding analysis was performed using molecular orbital pictures (at the (U)HF/6-311+G* level) made with the MOLDEN program,[83] using natural population analysis (NPA)[84] at the (U)B3LYP/6-311+G* level and using the nucleus-independent chemical shifts (NICS)[85] calculated at the (U)B3LYP/6-311+G* level of theory. The diamagnetic and paramagnetic effects of the ring currents, associated with aromatic and antiaromatic compounds (i.e. shielding and deshielding of nuclei), respectively, can be measured by a simple criterion viz. NICS introduced by Schleyer and co-workers in 1996.[85] We employed NICS indices as a probe of aromaticity in our clusters in addition to the MO-analysis. All calculations were done using Gaussian 03 package.

III. Identified Lithium Clusters

We applied the designed GA for the search for the global minima of uncharged, cationic, and anionic small lithium clusters. The global minimum structures of the pentaatomic, hexaatomic, and heptaatomic clusters and their isomers found within 10 kcal/mol above the global minima, elucidated using the GEGA program, are shown in Figure 2−4, respectively. All calculated molecular properties are collected in Tables 1−9. The agreement between computational results obtained at the B3LYP and CCSD(T) methods is noteworthy.

Most of the previous theoretical works on the pentaatomic lithium clusters were devoted to the neutral Li_5 species (see for instance refs 33, 39, 41, and 47). All structures of Li_5 identified in this study have been found before, while their relative energies, depending on the applied computational method, varied.

The bipyramidal D_{3h} ($^1A_1'$) global minimum structure was found by the GEGA to be the global minimum of the Li_5^+ cluster (structure I, Figure 2). Its electronic configuration is $1a_1'^2 1a_2''^2$. The second isomer of the Li_5^+ cluster is the twisted D_{2d} ($^1A_1$) structure. It was found to be 3.5 kcal/mol above the global minimum at the CCSD(T)/6-311+G(2df) + ZPE/CCSD(T)/6-311+G* level of theory (structure II, Figure 2). The electronic configuration of this isomer is $1a_1^2 1b_2^2$.

The C_{2v} ($^2B_1$) isomer III was detected as a global minimum for the neutral Li_5 cluster at the B3LYP/3-21G level during the execution of the GEGA. From the GEGA calculations we found that the neutral Li_5 cluster has two low-lying isomers: the global minimum C_{2v} ($^2B_1$) (structure III, Figure 2) and isomer IV (C_{2v}, $^2A_1$). At the highest CCSD(T)/6-311+G(2df) + ZPE/CCSD(T)/6-311+G* level of theory the energy difference between these two isomers is 1.5 kcal/

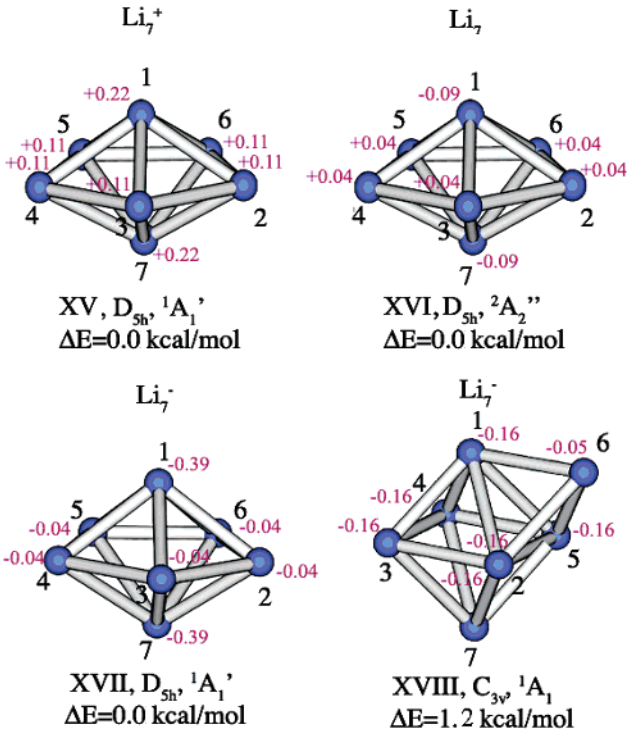

Figure 4. Global minimum and lowest in energy structures of Li_7^+, Li_7, and Li_7^- clusters found using the Genetic Algorithm. Shown geometries are refined at the CCSD(T)/6-311+G* level of theory. CCSD(T)/6-311+G(2df) ΔEs are given with ZPE corrections obtained at the CCSD(T)/6-311+G* level. The NPA atomic charges at the B3LYP/6-311+G* level are shown.

mol. The global minimum species has the $1a_1^2 1b_2^2 1b_1^1$ electronic configuration. The electronic configuration of the C_{2v} ($^2A_1$) species is the following: $1a_1^2 1b_2^2 2a_1^1$.

The GEGA run for the triplet state of the Li_5^- cluster revealed the bipyramidal D_{3h} species V to be the most stable. In the run of the GEGA for the singlet state we found the pyramidal C_{4v} species VI to have the lowest energy and the C_{2v} species VII to be the second isomer. At our highest level of theory (CCSD(T)/6-311+G(2df) + ZPE/CCSD(T)/6-311+G*) the global minimum of the Li_5^- cluster is the bipyramidal D_{3h} ($^3A_1'$) structure V (Figure 2), having the $1a_1'^2 1a_2''^2 1e'^2$ electronic configuration. The CCSD(T) calculation predicts structure VI (Figure 2) to be the second lowest-energy species (0.6 kcal/mol less stable than the global minimum) and structure VII to be 0.9 kcal/mol less stable. At this level of theory we cannot predict with certainty which of the structures V, VI, or VII is more stable. We conclude that the Li_5^- anion has three nearly degenerate most stable structures.

According to GEGA and calculations at higher levels of theory, the global minimum structure of the Li_6^+ cluster has C_{2v} ($^2B_2$) symmetry and the following electronic configuration: $1a_1^2 2a_1^2 1b_2^1$ (structure IX, Figure 3). This structure has also been found previously by Boustani et al.[47]

The neutral Li_6 cluster was found to have two low-energy isomers differing in energy by 4.2 kcal/mol at the CCSD(T)/6-311+G(2df) + ZPE/CCSD(T)/6-311+G* level of theory. The global minimum species (structure X, Figure 3)

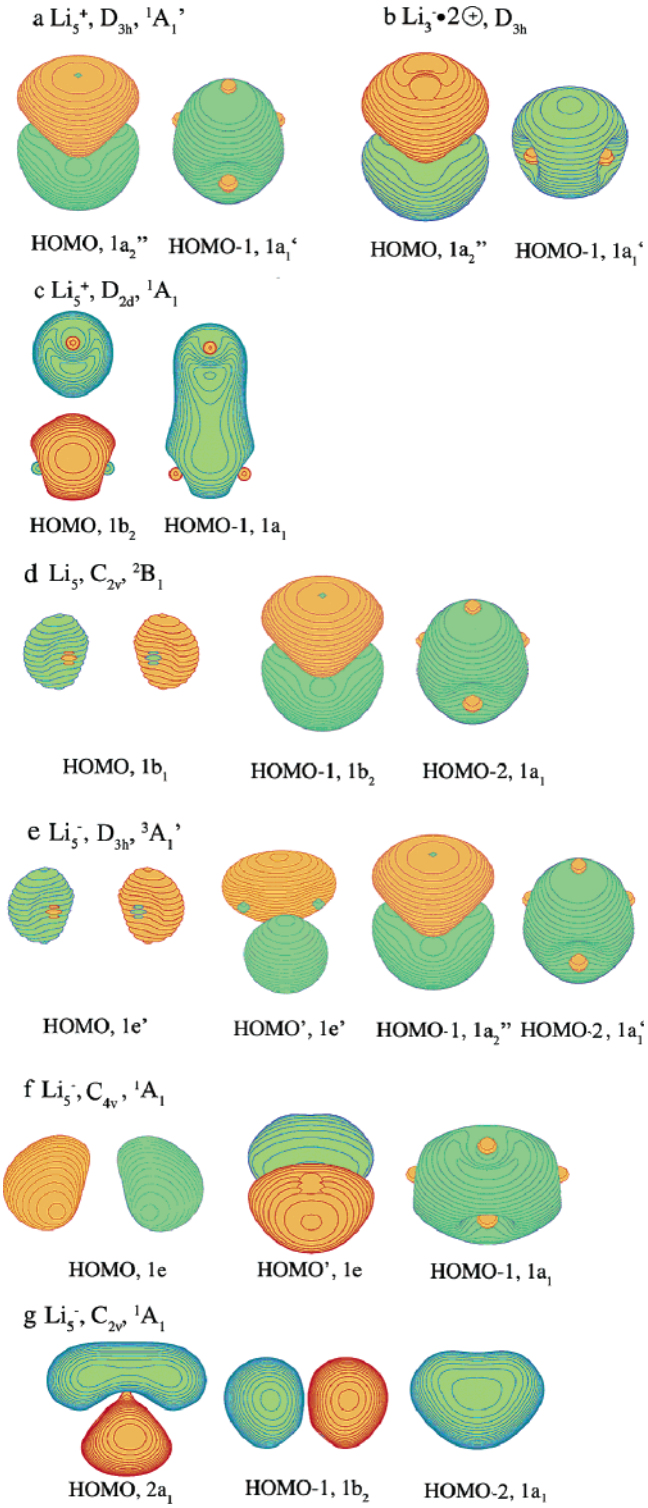

Figure 5. Molecular orbital picture of low-energy pentaatomic lithium clusters.

has D_{4h} ($^1A_{1g}$) symmetry and the $1a_{1g}^2 1e_u^4$ electronic configuration. The second isomer has C_{5v}, $^1A_1$ symmetry and corresponds to structure XI (Figure 3). The triplet species XII (C_{2v}, $^3B_1$) is the third most stable structure of the neutral Li_6 cluster (ΔE = 5.5 kcal/mol at the CCSD(T)/6-311+G(2df) + ZPE/CCSD(T)/6-311+G* level). The planar D_{3h} species XIII was found to be 10.2 kcal/mol (at CCSD(T)/6-311+G(2df) + ZPE/CCSD(T)/6-311+G*) above the global minimum. All detected structures were previously found

Table 1. Molecular Properties of the Li_5^+ Lowest-Energy Isomers

	Li_5^+, D_{3h}, $^1A_1'$		Li_5^+, D_{2d}, $^1A_1$	
level of theory	B3LYP/6-311+G*	CCSD(T)/6-311+G*	B3LYP/6-311+G*	CCSD(T)/6-311+G*
E_{total}, au	−37.428945	−37.145886[a]	−37.425738	−37.13911[b]
ZPE, kcal/mol	2.9	2.9	2.3	2.2
geometry	R(Li1−Li2) = 3.15 Å	R(Li1−Li2) = 3.16 Å	R(Li1−Li2) = 3.07 Å	R(Li1−Li2) = 3.11 Å
	R(Li2−Li3) = 2.69 Å	R(Li2−Li3) = 2.77 Å	R(Li2−Li3) = 2.82 Å	R(Li2−Li3) = 2.85 Å
frequencies	$\omega_1(a_1')$ 350 (0)[c]	$\omega_1(a_1')$ 329	$\omega_1(a_1)$ 318 (0)[c]	$\omega_1(a_1)$ 314
	$\omega_2(a_1')$ 237 (0)	$\omega_2(a_1')$ 236	$\omega_2(a_1)$139 (0)	$\omega_2(a_1)$135
	$\omega_3(a_2'')$ 300 (0)	$\omega_3(a_2'')$ 304	$\omega_3(b_1)$ 30 (0)	$\omega_3(b_1)$ 32
	$\omega_4(e')$ 278 (22)	$\omega_4(e')$ 257	$\omega_4(b_2)$ 329 (1)	$\omega_4(b_2)$ 326
	$\omega_5(e')$ 150 (2)	$\omega_5(e')$ 154	$\omega_5(b_2)$ 271 (60)	$\omega_5(b_2)$ 264
	$\omega_6(e'')$ 136 (0)	$\omega_6(e'')$ 156	$\omega_6(e)$ 219 (28)	$\omega_6(e)$ 208
			$\omega_7(e)$ 41 (4)	$\omega_7(e)$ 44

[a] At the CCSD(T)/6-311+G(2df) level the E_{total} = −37.151522 au. [b] At the CCSD(T)/6-311+G(2df) level the E_{total} = −37.1444574 au. [c] Infrared intensities in km/mol are shown in parentheses.

Table 2. Molecular Properties of the Li_5 Lowest-Energy Isomers

	Li_5, C_{2v}, $^2B_1$		Li_5, C_{2v}, $^2A_1$	
level of theory	B3LYP/6-311+G*	CCSD(T)/6-311+G*	B3LYP/6-311+G*	CCSD(T)/6-311+G*
E_{total}, au	−37.580450	−37.292976[a]	−37.578921	−37.291709[b]
ZPE, kcal/mol	2.7	2.6	2.5	2.5
geometry	R(Li1−Li2) = 2.97 Å	R(Li1−Li2) = 2.98 Å	R(Li2−Li4) = 2.97 Å	R(Li2−Li4) = 2.96 Å
	R(Li1−Li3,4) = 2.63 Å	R(Li1−Li3,4) = 2.72 Å	R(Li1−Li2,3) = 2.85 Å	R(Li1−Li2,3) = 2.94 Å
	R(Li2−Li3) = 3.05 Å	R(Li2−Li3) = 3.07 Å	R(Li1−Li4,5) = 2.98 Å	R(Li1−Li4,5) = 2.99 Å
	R(Li3−Li4) = 3.02 Å	R(Li3−Li4) = 3.07 Å	R(Li2−Li3) = 3.05 Å	R(Li2−Li3) = 3.11 Å
frequencies	$\omega_1(a_1)$ 348 (6)[c]	$\omega_1(a_1)$ 329	$\omega_1(a_1)$ 319 (20)[c]	$\omega_1(a_1)$ 292
	$\omega_2(a_1)$ 245 (1)	$\omega_2(a_1)$ 244	$\omega_2(a_1)$ 289 (0)	$\omega_2(a_1)$ 267
	$\omega_3(a_1)$ 209 (10)	$\omega_3(a_1)$ 205	$\omega_3(a_1)$ 184 (1)	$\omega_3(a_1)$ 185
	$\omega_4(a_2)$ 178 (0)	$\omega_4(a_2)$ 171	$\omega_4(a_1)$ 130 (3)	$\omega_4(a_1)$ 133
	$\omega_5(b_1)$ 160 (19)	$\omega_5(b_1)$ 167	$\omega_5(a_2)$ 69 (0)	$\omega_5(a_2)$ 69
	$\omega_6(b_1)$ 128 (1)	$\omega_6(b_1)$ 96	$\omega_6(b_1)$ 78 (8)	$\omega_6(b_1)$ 65
	$\omega_7(b_2)$ 284 (13)	$\omega_7(b_2)$ 288	$\omega_7(b_2)$ 277 (0)	$\omega_7(b_2)$ 342
	$\omega_8(b_2)$ 183 (1)	$\omega_8(b_2)$ 186	$\omega_8(b_2)$ 224 (5)	$\omega_8(b_2)$ 236
	$\omega_9(b_2)$ 162 (0)	$\omega_9(b_2)$ 161	$\omega_9(b_2)$ 184 (0)	$\omega_9(b_2)$ 182

[a] At the CCSD(T)/6-311+G(2df) level E_{total} =−37.298767 au. [b] At the CCSD(T)/6-311+G(2df) level E_{total} = −37.296434 au. [c] Infrared intensities in Km/mol are shown in parentheses.

by various research groups,[7,33,39,41,50] even though there were some contradictions on which one is the actual global minimum. However, the agreement between results obtained by the B3LYP/3-21G (GEGA run) and other higher levels of theory makes us more confident in our assignment of the relative energies of the Li_6 isomers. As we were about to send this paper to press, an article by Temelso and Sherrill came out.[56] The results of this work on the neutral, anionic, and cationic Li_6 clusters are in almost quantitative agreement with ours. Both cationic C_{2v} and anionic D_{4h} global minimum species found by the authors are the same as in our work. For the neutral Li_6 cluster the authors predicted the D_{4h} bipyramidal structure (analogous to our structure X, Figure 3) to be the most stable. The C_{5v} species was identified as the second isomer being 5.6 kcal/mol above the D_{4h} cluster at the most accurate CCSD(T)/cc-pCVQZ level, which is in good agreement with our number of 4.2 kcal/mol (CCSD(T)/6-311+G(2df) + ZPE/CCSD(T)/6-311+G* level). The planar D_{3h} species was found 7.6 kcal/mol higher in energy than the global minimum compared to our 10.2 kcal/mol (CCSD(T)/6-311+G(2df) + ZPE/CCSD(T)/6-311+G* level).

For the anionic Li_6^- cluster the global minimum structure is a tetragonal bipyramid D_{4h}, $^2A_{2u}$ (structure XIV, Figure 3). The bipyramid D_{4h}, $^2A_{2u}$ structure XIV can be traced to the bipyramid D_{4h}, $^1A_{1g}$ structure X upon addition of an electron to the LUMO of the neutral cluster. As the result of this addition, the tetragonal bipyramid is extended along the C4 axis, and it approaches an octahedral structure.

GEGA identified the global minimum structures of the Li_7^+, Li_7, and Li_7^- clusters all as pentagonal bipyramidals with D_{5h} symmetry (in Figure 4, structures XV, XVI, and XVII, respectively). This result was proved at the B3LYP/6-311G*, CCSD(T)/6-311+G*, and CCSD(T)/6-311+G(2df) + ZPE/CCSD(T)/6-311+G* levels. The electronic configurations of the cationic, neutral, and anionic species are $1a_1'^2 1e_1'^4$, $1a_1'^2 1e_1'^4 1a_2''^1$, and $1a_1'^2 1e_1'^4 1a_2''^2$, respectively. The anionic species also has a low-lying second isomer XVIII (C_{3v}, $^1A_1$) being just 1.2 kcal/mol above the global minimum. Its electronic configuration is $1a_1^2 2a_1^2 1e^4$. The found bipyramidal shape of the species agrees with previous reports.[39,41,47]

We have also calculated various properties of the found species. The predicted first ionization potentials for neutral species were found to be in a good agreement with the experimental photoelectron spectra.[29,30] For the distorted bipyramidal structure of the Li_5 cluster the calculated vertical

Table 3. Molecular Properties of the Li_5^- Lowest-Energy Isomers

	Li_5^-, D_{3h}, $^3A_1'$		Li_5^-, C_{4v}, $^1A_1$		Li_5^-, C_{2v}, $^1A_1$	
level of theory	B3LYP/6-311+G*	CCSD(T)/6-311+G*	B3LYP/6-311+G*	CCSD(T)/6-311+G*	B3LYP/6-311+G*	CCSD(T)/6-311+G*
E_{total}, au	−37.610893	−37.324953[a]	−37.608082	−37.323435[b]	−37.608840	−37.324138[c]
ZPE, kcal/mol	2.8	2.8	2.5	2.4	2.3	2.3
geometry	R(Li1−Li2,3,4) = 2.97 Å	R(Li1−Li2,3,4) = 3.01 Å	R(Li1−Li2) = 2.78 Å	R(Li1−Li2) = 2.84 Å	R(Li2−Li4) = 3.22 Å	R(Li2−Li4) = 3.24 Å
	R(Li2−Li3) = 2.85 Å	R(Li2−Li3) = 2.93 Å	R(Li2−Li3) = 3.21 Å	R(Li2−Li3) = 3.21 Å	R(Li1−Li2,3) = 2.89 Å	R(Li1−Li2,3) = 2.94 Å
					R(Li1−Li4,5) = 2.96 Å	R(Li1−Li4,5) = 2.99 Å
					R(Li2−Li3) = 2.95 Å	R(Li2−Li3) = 2.95 Å
frequencies	$\omega_1(a_1')$ 299 (0)[d]	$\omega_1(a_1')$ 287	$\omega_1(a_1)$ 298 (9)[d]	$\omega_1(a_1)$ 292	$\omega_1(a_1)$ 285 (24)[d]	$\omega_1(a_1)$ 285
	$\omega_2(a_1')$ 226 (0)	$\omega_2(a_1')$ 218	$\omega_2(a_1)$ 150 (4)	$\omega_2(a_1)$ 150	$\omega_2(a_1)$ 219 (4)	$\omega_2(a_1)$ 222
	$\omega_3(a_2'')$ 259 (18)	$\omega_3(a_2'')$ 262	$\omega_3(b_1)$ 180 (0)	$\omega_3(b_1)$ 182	$\omega_3(a_1)$ 182 (19)	$\omega_3(a_1)$ 180
	$\omega_4(e')$ 240 (0)	$\omega_4(e')$ 241	$\omega_4(b_2)$ 221 (0)	$\omega_4(b_2)$ 210	$\omega_4(a_1)$ 121 (0)	$\omega_4(a_1)$ 123
	$\omega_5(e')$ 201 (0)	$\omega_5(e')$ 231	$\omega_5(b_2)$ 73 (0)	$\omega_5(b_2)$ 55	$\omega_5(a_2)$ 93 (0)	$\omega_5(a_2)$ 88
	$\omega_6(e')$ 132 (1)	$\omega_6(e')$ 131	$\omega_6(e)$ 277 (27)	$\omega_6(e)$ 266	$\omega_6(b_1)$ 82 (1)	$\omega_6(b_1)$ 61
			$\omega_7(e)$ 134 (3)	$\omega_7(e)$ 128	$\omega_7(b_2)$ 298 (147)	$\omega_7(b_2)$ 298
					$\omega_8(b_2)$ 200 (3)	$\omega_8(b_2)$ 198
					$\omega_9(b_2)$ 149 (12)	$\omega_9(b_2)$ 144

[a] At the CCSD(T)/6-311+G(2df) level E_{total} = −37.331652 au. [b] At the CCSD(T)/6-311+G(2df) level E_{total} = −37.330154 au. [c] At the CCSD(T)/6-311+G(2df) level E_{total} = −37.329635 au. [d] Infrared intensities in km/mol are shown in parentheses.

ionization potential (IP) is 4.14 eV, and the theoretically predicted adiabatic IP is 4.00 eV. The experimental IP value was reported as 4.02 ± 0.1 eV.[29,30] The VDE_1 of the Li_5^- global minimum isomer V is 0.94 eV and the ADE = 0.87 eV. For the hexaatomic neutral D_{4h} bipyramid Li_6 the calculated vertical IP = 4.44 eV can be compared to the experimental IP = 4.20 ± 0.1 eV.[29,30] The VDE and ADE values for the Li_6^- D_{4h} ($^2A_{2u}$) structure XIV are 1.00 and 0.87 eV, respectively. For the pentagonal bipyramid Li_7 (D_{5h}, $^1A_1'$) the theoretical vertical IP = 4.08 eV and adiabatic IP = 3.95 eV can be compared to the experimental IP = 3.94 ± 0.1 eV.[29,30] Li_7^- (D_{5h}, $^1A_1'$) has VDE = 1.13 eV, and ADE = 0.80 eV.

Our calculated atomization energies per atom of the species are the following: Li_5^+ (D_{3h}, $^1A_1$) − 1.02 eV, Li_5 (C_{2v}, $^2B_1$) − 0.75 eV, Li_5 (C_{2v}, $^2A_1$) − 0.55 eV, Li_5^- (D_{3h}, $^3A_1'$) − 0.85 eV, Li_6^+ (C_{2v}, $^2A_1$) − 1.04 eV, Li_6 (D_{4h}, $^1A_{1g}$) − 0.86 eV, Li_6 (C_{5v}, $^1A_1$) − 0.83 eV, Li_6^- (D_{4h}, $^2A_{2u}$) − 0.92 eV, Li_7^+ (D_{5h}, $^1A_1'$) − 1.12 eV, Li_7 (D_{5h}, $^2A_2''$) − 0.92 eV, and Li_7^- (D_{5h}, $^1A_1'$) − 0.98 eV. These values can be compared to the atomization energy per atom of Li_2 − 0.52 eV.[86] They clearly show the enhanced stability in all clusters.

IV. Chemical Bonding in Lithium Clusters

To elucidate the nature of the chemical bonding in lithium clusters we used the molecular orbital analysis and NICS indices.

$Li_5^{+1/0/-1}$. Figure 5 contains MO pictures of the low-energy pentaatomic lithium clusters. The set of valence molecular orbitals of the bipyramidal D_{3h} global minimum structure of Li_5^+ is shown in Figure 5a. The HOMO-1 ($1a_1$) is a completely bonding σ-molecular orbital composed mostly of 2s-atomic orbitals on all five Li atoms. The HOMO ($1a_2$) is a completely bonding molecular orbital of π-character. It is composed of 2p atomic orbitals of three Li atoms in the base of the pyramid and 2s atomic orbitals of the two apex Li atoms. To prove the π-character of the HOMO, we calculated the cluster composed of three Li atoms in the base of the pyramid and two positive charges substituting the apex Li atoms. The molecular orbitals of this model system are shown in Figure 5b. As one can see the overall look of the molecular orbitals of the Li_3^- triangular base of the pyramid with two positive point-charges above and below the plane is the same as the look of the orbitals of the Li_5^+ pyramidal cluster. Both the π-character of the HOMO and the σ-character of the HOMO-1 are preserved when the contribution from 2s-functions on the apex Li atoms are completely excluded. This fact shows that the chemical bonding in the global Li_5^+ minimum can be described in terms of 2σ and 2π electrons present. Thus, according to the $(4n+2)$ Hückel's rule, the species is both σ- and π-aromatic.[87] The doubly aromatic character[87] of the chemical bonding is responsible for the extra stability of the Li_5^+ global minimum isomer. What is unusual about chemical bonding in this cluster is an early occupation of the π-MO, i.e., the π-MO is occupied before the full set of σ-orbitals, required for the classical 2c-2e bonding among equatorial Li atoms, has been populated. However, such early occupation of π-MO in metal systems was already observed in the Al_4^{2-} cluster.[92]

Molecular orbitals of the second isomer of the Li_5^+ cluster are shown in Figure 5c. Both molecular orbitals of the twisted D_{2d} structure have σ-character. In fact the structure is a result of the fusion of two Li_3^+ triangular motifs sharing one atom. The Li_3^+ cluster has been reported to have only one completely bonding σ-molecular orbital and to be σ-aromatic.[72] The HOMO and HOMO-1 are linear combinations of the two completely bonding σ-molecular orbitals of the Li_3^+ units. Thus, the system can be defined as island aromatic, in the sense that the fusion of the two aromatic fragments is observed, and both individual aromatic units preserve their aromaticity inside the Li_5^+ D_{2d} structure.

Molecular orbitals of the (C_{2v}, $^2B_1$) global minimum isomer of the neutral Li_5 cluster are shown in Figure 5d. Two molecular orbitals (HOMO-1 ($1b_2$) and HOMO-2 ($1a_1$)) are reminiscent to HOMO ($1b_2$) and HOMO-1 ($1a_1$), respectively, of the Li_5^+ D_{3h} pyramidal species. However, the

Table 4. Molecular Properties of the Li_6^+, C_{2v}, $^2B_2$ Global Minimum Structure

level of theory	B3LYP/6-311+G*		CCSD(T)/6-311+G*	
E_{total}, au	−44.960548		−44.618696[a]	
ZPE, kcal/mol	3.6		3.6	
geometry	R(Li1−Li2) = 3.08 Å	R(Li2−Li5) = 3.36 Å	R(Li1−Li2) = 3.10 Å	R(Li2−Li5) = 3.44 Å
	R(Li1−Li3,4) = 3.06 Å	R(Li3−Li4) = 2.53 Å	R(Li1−Li3,4) = 3.00 Å	R(Li3−Li4) = 2.61 Å
	R(Li2−Li3,4) = 2.93 Å		R(Li2−Li3,4) = 3.10 Å	
frequencies	$\omega_1(a_1)$ 349 (4)[b]	$\omega_7(a_2)$ 144 (0)	$\omega_1(a_1)$ 330	$\omega_7(a_2)$ 142
	$\omega_2(a_1)$ 266 (22)	$\omega_8(b_1)$ 176 (6)	$\omega_2(a_1)$ 261	$\omega_8(b_1)$ 175
	$\omega_3(a_1)$ 253 (18)	$\omega_9(b_1)$ 153 (0)	$\omega_3(a_1)$ 251	$\omega_9(b_1)$ 155
	$\omega_4(a_1)$ 190 (0)	$\omega_{10}(b_2)$ 304 (19)	$\omega_4(a_1)$ 187	$\omega_{10}(b_2)$ 305
	$\omega_5(a_1)$ 88 (0)	$\omega_{11}(b_2)$ 212 (1)	$\omega_5(a_1)$ 81	$\omega_{11}(b_2)$ 215
	$\omega_6(a_2)$ 212 (0)	$\omega_{12}(b_2)$ 194 (4)	$\omega_6(a_2)$ 219	$\omega_{12}(b_2)$ 198

[a] At the CCSD(T)/6-311+G(2df) level E_{total} = −44.624912 au. [b] Infrared intensities in km/mol are shown in parentheses.

Table 5. Molecular Properties of the Li_6 Lowest-Energy Isomers

	Li_6, D_{4h}, $^1A_{1g}$		Li_6, C_{5v}, $^1A_1$		Li_6, C_{2v}, $^3B_1$	
level of theory	B3LYP/6-311+G*	CCSD(T)/6-311+G*	B3LYP/6-311+G*	CCSD(T)/6-311+G*	B3LYP/6-311+G*	CCSD(T)/6-311+G*
E_{total}, au	−45.116806	−44.774798[a]	−45.111046	−44.768332[b]	−45.110032	−44.767231[c]
ZPE, kcal/mol	3.8	3.7	3.3	3.2	3.8	3.7
geometry	R(Li1−Li2) = 3.05 Å	R(Li1−Li2) = 3.08 Å	R(Li1−Li2) = 2.79 Å	R(Li1−Li2) = 2.87 Å	R(Li1−Li2) = 2.91 Å	R(Li1−Li2) = 2.95 Å
	R(Li2−Li3) = 2.80 Å	R(Li2−Li3) = 2.81 Å	R(Li2−Li3) = 3.14 Å	R(Li2−Li3) = 3.14 Å	R(Li1−Li3,4) = 2.97 Å	R(Li1−Li3,4) = 3.02 Å
					R(Li2−Li3,4) = 2.86 Å	R(Li2−Li3,4) = 2.92 Å
					R(Li2−Li5) = 3.03 Å	R(Li2−Li5) = 3.11 Å
					R(Li3−Li4) = 2.85 Å	R(Li3−Li4) = 2.94 Å
frequencies	$\omega_1(a_{1g})$ 352 (0)[d]	$\omega_1(a_{1g})$ 326	$\omega_1(a_1)$ 254 (2)[d]	$\omega_1(a_1)$ 257	$\omega_1(a_1)$ 310 (4)[d]	$\omega_1(a_1)$ 302
	$\omega_2(a_{1g})$ 227 (0)	$\omega_2(a_{1g})$ 206	$\omega_2(a_1)$ 85 (4)	$\omega_2(a_1)$ 109	$\omega_2(a_1)$ 277 (14)	$\omega_2(a_1)$ 274
	$\omega_3(a_{2u})$ 205 (5)	$\omega_3(a_{2u})$ 206	$\omega_3(e_1)$ 345 (1)	$\omega_3(e_1)$ 323	$\omega_3(a_1)$ 245 (10)	$\omega_3(a_1)$ 236
	$\omega_4(b_{1g})$ 270 (0)	$\omega_4(b_{1g})$ 263	$\omega_4(e_1)$ 178 (2)	$\omega_4(e_1)$ 182	$\omega_4(a_1)$ 205 (1)	$\omega_4(a_1)$ 197
	$\omega_5(b_{2g})$ 121 (0)	$\omega_5(b_{2g})$ 114	$\omega_5(e_2)$ 203 (0)	$\omega_5(e_2)$ 197	$\omega_5(a_1)$ 97 (0)	$\omega_5(a_1)$ 95
	$\omega_6(b_{2u})$ 179 (0)	$\omega_6(b_{2u})$ 179	$\omega_6(e_2)$ 192 (0)	$\omega_6(e_2)$ 192	$\omega_6(a_2)$ 246 (0)	$\omega_6(a_2)$ 240
	$\omega_7(e_g)$ 254 (0)	$\omega_7(e_g)$ 251	$\omega_7(e_2)$ 58 (0)	$\omega_7(e_2)$ 45	$\omega_8(a_2)$ 125 (0)	$\omega_8(a_2)$ 125
	$\omega_8(e_u)$ 331 (3)	$\omega_8(e_u)$ 328			$\omega_8(b_1)$ 250 (13)	$\omega_8(b_1)$ 244
	$\omega_9(e_u)$ 60 (0)	$\omega_9(e_u)$ 51			$\omega_9(b_1)$ 155 (15)	$\omega_9(b_1)$ 167
					$\omega_{10}(b_2)$ 302 (28)	$\omega_{10}(b_2)$ 309
					$\omega_{11}(b_2)$ 219 (2)	$\omega_{11}(b_2)$ 223
					$\omega_{12}(b_2)$ 197 (0)	$\omega_{12}(b_2)$ 202

[a] At the CCSD(T)/6-311+G(2df) level E_{total} = −44.782932 au. [b] At the CCSD(T)/6-311+G(2df) level E_{total} = −44.774803 au. [c] At the CCSD(T)/6-311+G(2df) level E_{total} = −44.774103 au. [d] Infrared intensities in km/mol are shown in parentheses.

HOMO ($1b_1$) in the C_{2v} global minimum structure of Li_5 is a nonbonding σ-molecular orbital. It belongs to the quasi-degenerate pair of σ-molecular orbitals, with counterpart as the LUMO. A Jahn−Teller distortion, thus imposed, results in the lower C_{2v} symmetry of the cluster. The system contains two π-electrons analogous to the Li_5^+ D_{3h} species, obeys the $(4n+2)$ rule, and, consequently, is π-aromatic. The described partial occupation of the σ-set (the completely bonding HOMO-2 and the nonbonding HOMO) makes the system σ-antiaromatic. Adding an electron leads to the double population of the degenerate HOMO and a gain of σ-aromaticity.

The pattern of the molecular orbitals in the second C_{2v} ($^2A_1$) isomer of Li_5 is very similar to the C_{2v} isomer VII of the Li_5^- cluster, which has an electronic configuration $1a_1^2 1b_2^2 2a_1^2$. The neutral and anionic clusters only differ in the number of electrons occupying the HOMO. Let us first consider the chemical bonding in the closed-shell anionic species.

The planar C_{2v}, $^1A_1$ species is the third lowest-energy isomer of the Li_5^- cluster (structure VII, Figure 2). The molecular orbitals of this cluster are shown in Figure 5g. All three occupied molecular orbitals have σ-character. The HOMO-2 is a completely bonding σ-molecular orbital, while the HOMO and the HOMO-1 are partially bonding σ-MOs. The set of bonding σ-molecular orbitals in this isomer of Li_5^- is completely filled by 6 σ-electrons, which, at first glance, should lead to perfect D_{5h} symmetry and σ-aromaticity due to the $(4n+2)$ rule. However, the perfectly symmetric D_{5h} structure is a second-order saddle point on the potential energy surface, and the imaginary frequency normal mode leads to the found C_{2v} species. This contradiction has been resolved via the analysis of the composition of the molecular orbitals in the species. It showed that all molecular orbitals, although mostly composed of 2s-atomic orbitals of Li atoms, have a significant contribution from 2p-atomic orbitals, and thus should be considered as hybridized. The hybridization enhances the overlap and the overall bonding character of the HOMO and HOMO-1. In the HOMO a large contribution to the bonding comes from the overlap of the σ-cloud on atoms Li2 and Li3 with the p_z-atomic orbital of the Li1 atom perpendicular to this cloud, which can be observed from the molecular orbital picture. If no 2p-contribution would occur, there would be no bonding

Table 6. Molecular Properties of the Li_6^-, D_{4h}, $^2A_{2u}$ Global Minimum Structure

level of theory	B3LYP/6-311+G*	CCSD(T)/6-311+G*
E_{total}, au	−45.147179	−44.806674[a]
ZPE, kcal/mol	3.6	3.6
geometry	R(Li1−Li2) = 2.81 Å	R(Li1−Li2) = 2.88 Å
	R(Li2−Li3) = 3.34 Å	R(Li2−Li3) = 3.35 Å
frequencies	$\omega_1(a_{1g})$ 301 (6)[b]	$\omega_1(a_{1g})$ 301
	$\omega_2(a_{1g})$ 156 (3)	$\omega_2(a_{1g})$ 141
	$\omega_3(a_{2u})$ 191 (2)	$\omega_3(a_{2u})$ 236
	$\omega_4(b_{1g})$ 248 (0)	$\omega_4(b_{1g})$ 286
	$\omega_5(b_{2g})$ 143 (0)	$\omega_5(b_{2g})$ 130
	$\omega_6(b_{2u})$ 166 (0)	$\omega_6(b_{2u})$ 233
	$\omega_7(e_g)$ 254 (0)	$\omega_7(e_g)$ 238
	$\omega_8(e_u)$ 298 (3)	$\omega_8(e_u)$ 292
	$\omega_9(e_u)$ 89 (1)	$\omega_9(e_u)$ 84

[a] At the CCSD(T)/6-311+G(2df) level E_{total} = −44.815330 au. [b] Infrared intensities in km/mol are shown in parentheses.

character between the Li1 atom and the σ-cloud on atoms Li2 and Li3, because in the original σ-molecular orbital they are divided by a nodal plane. Thus, the hybridization brings an additional bonding to the system across the nodal plane of the HOMO and causes a structural distortion from D_{5h} symmetry to C_{2v} by drawing Li1 toward Li2 and Li3. Quantitatively, this phenomenon can be described by the expansion of the HOMO in terms of AOs on atoms. At the RHF/6-311+G* level the portion of the expansion coming from the Li1 atom is the following: $0.002(1s) + 0.028(2s) - 0.046(2p_z) - 0.069(3s) - 0.093(3p_z) - 0.015(4s) - 0.039(4p_z) - 0.199(5s) + 0.109(5p_z) + 0.012(6d_0) + 0.008(6d_{2+})$, which shows that the majority of electron density on Li1 comes from the p_z-originated atomic orbitals. In the HOMO-1, Li1 carries a p_y-contribution across the nodal plane. Li1 brings the following portion to the expansion of the HOMO-1 (RHF/6-311+G* level): $0.07(2p_y) + 0.150(3p_y) - 0.187(4p_y) + 0.081(5p_y) - 0.004(6d_{-1})$. It is important, that if no p-character would exist in HOMO-1, the coefficients in the HOMO-1 expansion, corresponding to the functions on the Li1 atom, would be zero. To check the validity of such an explanation of the chemical bonding in Li_5^- (C_{2v}, $^1A_1$), we artificially removed the p-functions from the atoms and calculated the D_{5h} perfectly symmetric structure. In this case, when there are no p-contributions to molecular orbitals, the Li_5^- D_{5h} species is a true minimum on the potential energy surface.

The chemical bonding in the previously mentioned second C_{2v} isomer of the Li_5 neutral cluster (structure IV, Figure 2), having a similar structure to the third isomer of Li_5^-, can be described in the same manner. The s−p hybridization leads to the strong distortion of the cluster toward C_{2v} symmetry. However, this structural rearrangement is smaller than in the third isomer of Li_5^- (see Tables 2 and 3 to compare geometries), because the HOMO in Li_5 is populated with one electron only, and thus the bonding brought to the system by the HOMO is less.

At the highest applied level of theory (CCSD(T)/6-311+G(2df)) the global minimum of the Li_5^- cluster is a bipyramidal structure V (Figure 2). The $1a_1'^2 1a_2''^2 1e'^2$ electronic configuration of the species corresponds to the population of the σ-bonding set of molecular orbitals (Figure 5e) in the base

Table 7. Molecular Properties of the Li_7^+, D_{5h}, $^1A_1'$ Global Minimum Structure

level of theory	B3LYP/6-311+G*	CCSD(T)/6-311+G*
E_{total}, au	−52.506609	−52.108467[a]
ZPE, kcal/mol	4.7	4.5
geometry	R(Li1−Li2) = 2.78 Å	R(Li1−Li2) = 2.74 Å
	R(Li2−Li3) = 3.06 Å	R(Li2−Li3) = 3.02 Å
frequencies	$\omega_1(a_1')$ 364 (0)[b]	$\omega_1(a_1')$ 338
	$\omega_2(a_1')$ 245 (0)	$\omega_2(a_1')$ 239
	$\omega_3(a_2'')$ 174 (1)	$\omega_3(a_2'')$ 168
	$\omega_4(e_1')$ 304 (37)	$\omega_4(e_1')$ 298
	$\omega_5(e_1')$ 171 (2)	$\omega_5(e_1')$ 168
	$\omega_6(e_2')$ 213 (0)	$\omega_6(e_2')$ 224
	$\omega_7(e_2')$ 198 (0)	$\omega_7(e_2')$ 207
	$\omega_8(e_2'')$ 227 (0)	$\omega_8(e_2'')$ 187
	$\omega_9(e_2'')$ 133 (0)	$\omega_9(e_2'')$ 129

[a] At the CCSD(T)/6-311+G(2df) level E_{total} = −52.116856 au. [b] Infrared intensities in Km/mol are shown in parentheses.

Table 8. Molecular Properties of the Li_7, D_{5h}, $^2A_2''$ Global Minimum Structure

level of theory	B3LYP/6-311+G*	CCSD(T)/6-311+G*
E_{total}, au	−52.652085	−52.253634[a]
ZPE, kcal/mol	4.7	5.7
geometry	R(Li1−Li2,3,4,5) = 2.91 Å	R(Li1−Li2,3,4,5) = 2.97 Å
	R(Li2−Li3) = 3.02 Å	R(Li2−Li3) = 3.06 Å
frequencies	$\omega_1(a_1')$ 301 (0)[b]	$\omega_1(a_1')$ 288
	$\omega_2(a_1')$ 235 (0)	$\omega_2(a_1')$ 218
	$\omega_3(a_2'')$ 165 (28)	$\omega_3(a_2'')$ 217
	$\omega_4(e_1')$ 304 (29)	$\omega_4(e_1')$ 495
	$\omega_5(e_1')$ 184 (4)	$\omega_5(e_1')$ 202
	$\omega_6(e_2')$ 237 (0)	$\omega_6(e_2')$ 231
	$\omega_7(e_2')$ 208 (0)	$\omega_7(e_2')$ 230
	$\omega_8(e_2'')$ 254 (0)	$\omega_8(e_2'')$ 301
	$\omega_9(e_2'')$ 104 (0)	$\omega_9(e_2'')$ 181

[a] At the CCSD(T)/6-311+G(2df) level E_{total} = −52.262340 au. [b] Infrared intensities in km/mol are shown in parentheses.

of the bipyramid. The completely bonding HOMO-2 and the doubly degenerate nonbonding HOMO contain four σ-electrons. The bipyramidal global minimum is σ-aromatic according to the $4n$ rule for triplets.[93] However, this structure is also a π-aromatic system due to the doubly occupied HOMO-1, and thus overall it is a doubly aromatic system. The pyramidal C_{4v} isomer VI (Figure 2) contains six electrons in three σ-molecular orbitals (Figure 5f). Thus this closed-shell cluster is σ-aromatic according to the regular $4n+2$ Hückel's rule.

We also used NICS indices as additional criteria of aromatic or antiaromatic character of the identified global minima. The computed indices are shown in Table 10. However, as one may see, in the case of pentaatomic lithium clusters, our conclusion about the double aromaticity of Li_5^+ (D_{3h}, $^1A_1'$ species I, Figure 2), the σ-antiaromaticity and π-aromaticity of Li_5 (C_{2v}, $^2B_1$ species III, Figure 2), and the double aromaticity of the triplet Li_5^- (cluster V, Figure 2) completely disagrees with the obtained NICS values (negative NICS indices correspond to aromatic character, positive to antiaromatic).

$Li_6^{+1/0/-1}$. MOs of hexaatomic clusters are given in Figure 6. Let us first consider chemical bonding in the neutral Li_6 cluster.

The global minimum of the neutral Li_6 (D_{4h}, $^1A_{1g}$) cluster X has a completely bonding σ-molecular orbital HOMO-1

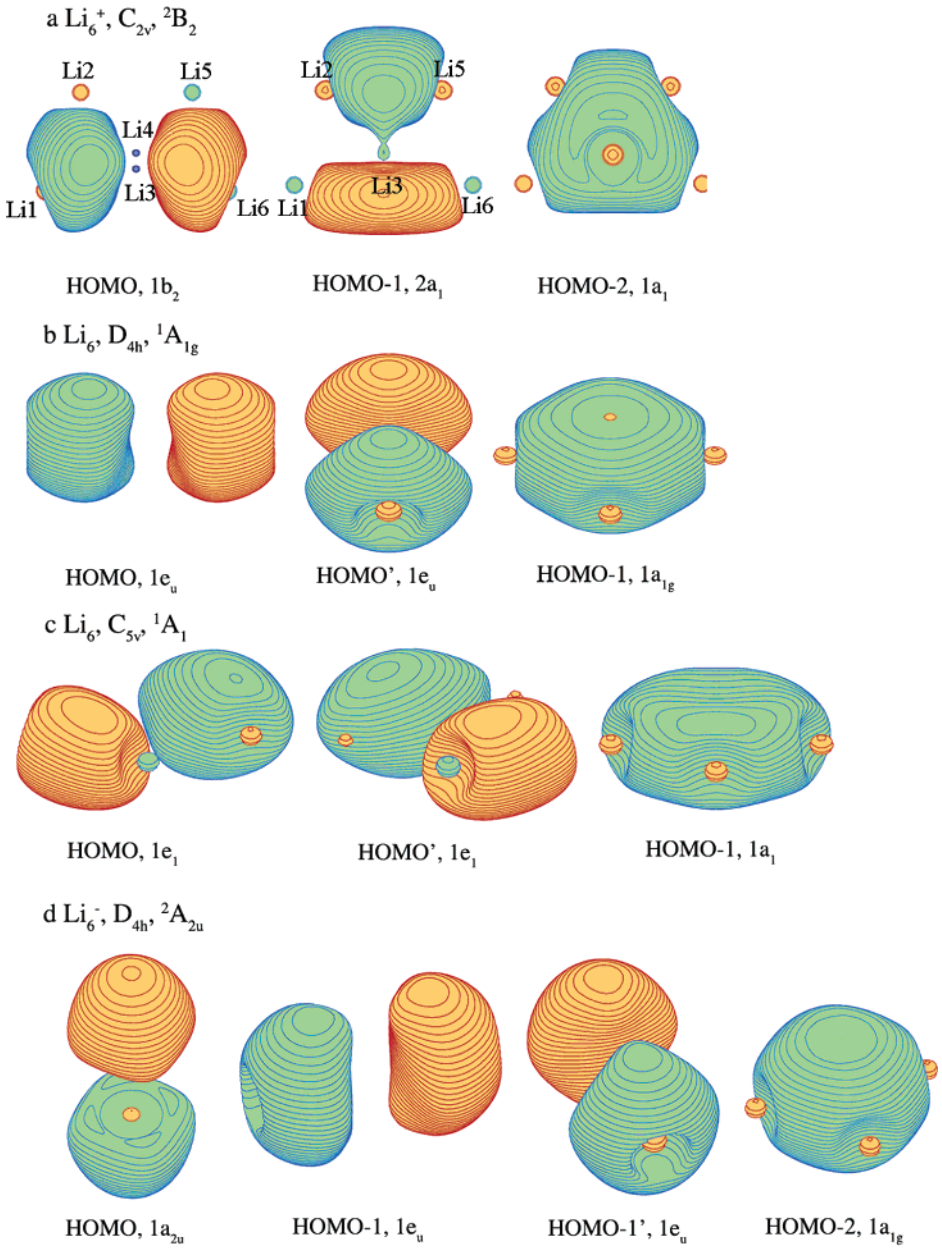

Figure 6. Molecular orbital picture of low-energy hexaatomic lithium clusters.

($1a_{1g}$) (see Figure 6b). The doubly degenerate HOMO has σ-character too with a major contributions from the 2s-functions of the equatorial Li atoms. The system thus contains six σ-electrons and is σ-aromatic.

Figure 6c depicts the molecular orbitals of the second quasi-planar isomer XI (Figure 3) (C_{5v}, $^1A_1$) of the Li_6 cluster. As one may see all electron density in the species is concentrated on the base of the pyramid, while no electron density is observed at the apex Li atom. All molecular orbitals have σ-character and align in the plane of the base of the pyramid. The completely bonding HOMO-1 ($1a_1$) and the partially bonding doubly degenerate HOMO ($1e_1$) form the σ-bonding set. Having six σ-electrons occupying these molecular orbitals the system is σ-aromatic.

Now we can easily interpret molecular orbitals of the global minimum Li_6^+ species (C_{2v}, $^2A_1$ structure IX, Figure 3), which are shown in Figure 6a. We can relate the MOs in Li_6^+ IX to the MOs in Li_6 X. HOMO in Li_6^+ is originated from HOMO in Li_6, HOMO-1 in Li_6^+ is originated from HOMO′ in Li_6, and HOMO-2 in Li_6^+ is originated from HOMO-1 in Li_6. The occupation by three electrons of the doubly degenerate HOMO in the D_{4h} structure leads to a Jahn−Teller distortion toward the C_{2v}, $^2A_1$ structure IX, Figure 3.

The global minimum of Li_6^- has molecular orbitals (shown in Figure 6d) very similar to its neutral structural analogue X (Figure 3). In this case the LUMO in Li_6 (which is the last member of the triply degenerate set of molecular orbitals) is occupied with one electron. The system approaches the perfect octahedral symmetry with atoms Li1 and Li6 being found farther apart than in the neutral species X. The system still possesses σ-aromatic character of the chemical bonding due to the occupation of the HOMO-2 ($1a_{1g}$) and HOMO-1

Table 9. Molecular Properties of the Li_7^- Global Minimum and the Second Lowest-Energy Isomer

	Li_7^-, D_{5h}, $^1A_1'$		Li_7^-, C_{3v}, $^1A_1$	
level of theory	B3LYP/6-311+G*	CCSD(T)/6-311+G*	B3LYP/6-311+G*	CCSD(T)/6-311+G*
E_{total}, au	−52.680731	−52.289214[a]	−52.679888	−52.282973[b]
ZPE, kcal/mol	4.4	4.3	4.3	4.3
geometry	R(Li1−Li2,3,4,5) = 2.98 Å	R(Li1−Li2,3,4,5) = 3.04 Å	R(Li6−Li1,2,5) = 2.94 Å	R(Li6−Li1,2,5) = 2.97 Å
	R(Li2−Li3) = 2.89 Å	R(Li2−Li3) = 2.92 Å	R(Li1−Li2) = 3.03 Å	R(Li1−Li2) = 3.11 Å
			R(Li1−Li3) = 2.88 Å	R(Li1−Li3) = 2.93 Å
			R(Li3−Li4) = 3.08 Å	R(Li3−Li4) = 3.12 Å
frequencies	$\omega_1(a_1')$ 275 (0)[c]	$\omega_1(a_1')$ 269	$\omega_1(a_1)$ 306 (2)[c]	$\omega_1(a_1)$ 302
	$\omega_2(a_1')$ 140 (0)	$\omega_2(a_1')$ 145	$\omega_2(a_1)$ 263 (0)	$\omega_2(a_1)$ 260
	$\omega_3(a_2'')$ 189(12)	$\omega_3(a_2'')$ 197	$\omega_3(a_1)$ 211 (1)	$\omega_3(a_1)$ 212
	$\omega_4(e_1')$ 279 (1)	$\omega_4(e_1')$ 276	$\omega_4(a_1)$ 182 (5)	$\omega_4(a_1)$ 174
	$\omega_5(e_1')$ 191 (1)	$\omega_5(e_1')$ 186	$\omega_5(a_2)$ 188 (0)	$\omega_5(a_2)$ 185
	$\omega_6(e_2')$ 170 (0)	$\omega_6(e_2')$ 166	$\omega_6(e)$ 276 (0)	$\omega_6(e)$ 277
	$\omega_7(e_2')$ 250 (0)	$\omega_7(e_2')$ 269	$\omega_7(e)$ 251 (3)	$\omega_7(e)$ 249
	$\omega_8(e_2'')$ 267 (0)	$\omega_8(e_2'')$ 239	$\omega_8(e)$ 180 (1)	$\omega_8(e)$ 183
	$\omega_9(e_2'')$ 91.(0)	$\omega_9(e_2'')$ 77	$\omega_9(e)$ 131 (2)	$\omega_9(e)$ 129
			$\omega_{10}(e)$ 101 (3)	$\omega_{10}(e)$ 101

[a] At the CCSD(T)/6-311+G(2df) level E_{total} = −52.298875 au. [b] At the CCSD(T)/6-311+G(2df) level E_{total} = −52.296998 au. [c] Infrared intensities in km/mol are shown in parentheses.

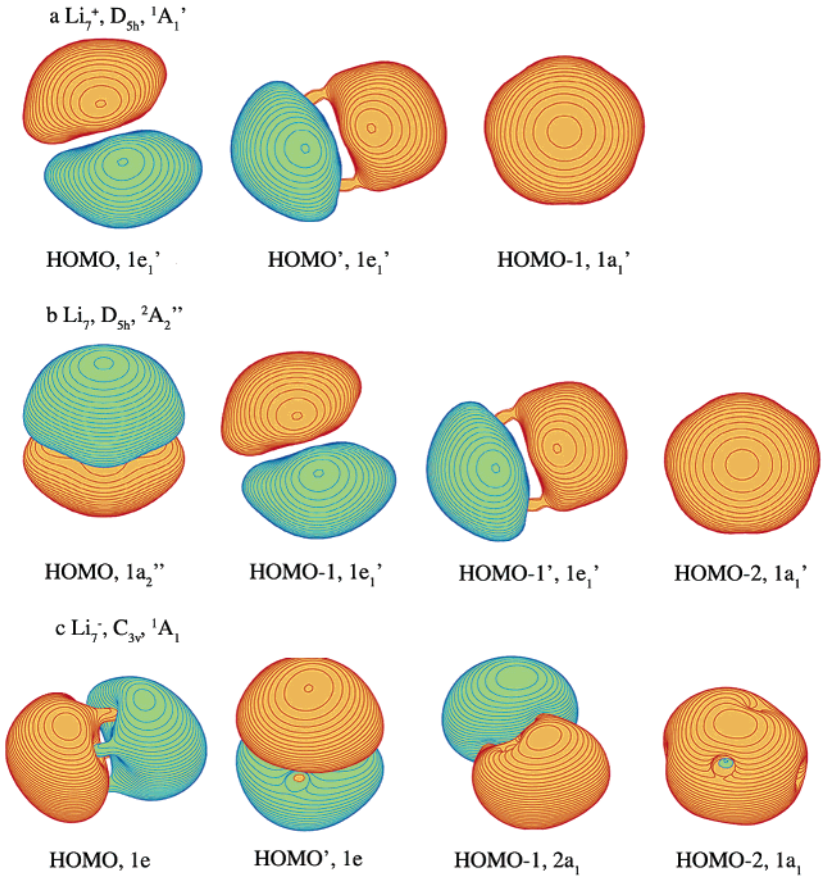

Figure 7. Molecular orbital picture of low-lying heptaatomic lithium clusters.

($1e_u$), and it also has one electron on the π-HOMO ($1a_{2u}$) and thus this anion could be considered as partially π-aromatic.

In the case of charged and neutral Li_6 clusters, the computed NICS indices agree with our interpretation of the chemical bonding. The aromaticity of Li_6 and Li_6^- (negative NICS) and antiaromaticity of Li_6^+ (positive NICS) are identified.

$Li_7^{+1/0/-1}$. MOs of heptaatomic clusters are shown in Figure 7. The molecular orbitals of the Li_7^+ global minimum species are shown in Figure 7a. They have a distinct σ-character. $1a_1'$ HOMO-1 is a completely bonding MO, while the doubly degenerate $1e_1'$ HOMO has one nodal plane and possesses partially bonding character. This provides a sufficient number of electrons for the five-member ring of the system to be σ-aromatic and, consequently, to possess extra stability.

The global minimum isomer of the neutral Li_7 cluster, having D_{5h}, $^2A_2''$ symmetry, is very similar to the cationic

Table 10. Calculated Nucleus-Independent Chemical Shift (NICS) Values for the Global Minima of the $Li_n^{0/+1/-1}$ ($n = 5-7$) Clusters (B3LYP/6-311+G* Level)

	NICS, ppm									
	Li_5^+ D_{3h}, $^1A_1'$	Li_5 C_{2v}, $^2B_1$	Li_5^- D_{3h}, $^3A_1'$	Li_5^- C_{4v}, $^1A_1$	Li_6^+ C_{2v}, $^2A_1$	Li_6 D_{4h}, $^1A_{1g}$	Li_6^- D_{4h}, $^1A_{2u}$	Li_7^+ D_{5h}, $^1A_1'$	Li_7 D_{5h}, $^2A_2''$	Li_7^- D_{5h}, $^1A_1'$
1	15.495[a]	−378.466[b]	37.042[a]	4.846[c]	2.868[d]	−1.522[a]	−10.426[a]	−6.598[a]	−10.336[a]	−27.621[a]
2	14.596	−375.088	37.164	4.820	2.158	−1.450	−10.425	−6.544	−10.506	−27.162
3	12.071	−375.614	37.311	4.663	1.370	−1.165	−10.391	−6.546	−10.726	−25.704
4	8.517	−376.467	37.353	4.395	0.598	−0.765	−10.267	−6.669	−10.671	−23.126
5	4.015	−372.000	36.947	4.013	0.074	−0.656	−10.002	−6.515	−10.079	−19.591
6	0.561	−359.617	35.908	3.486	3.534	−1.048	−9.549	−5.849	−8.968	−15.688
7		−378.466			3.650					
8		−384.207			3.112					
9		−394.547			2.016					
10		−406.860			1.122					
11		−417.223			2.373					
12		−417.144			0.756					
13					−1.396					
14					−3.364					
15					−4.593					

[a] The first index is computed at the center of the symmetry of the polyhedron. The subsequent indices are computed at the points lying equidistantly on the line connecting point 1 and the center of the circle circumscribed around the face of the polyhedron so that points 2−4 are inside of the cluster, point 5 is at the center of the circumscribed circle, and point 6 is outside of the cluster. [b] The first index is computed at the center of the polyhedron. Indices 2−6 and 7−12 are computed at the points lying equidistantly on the lines connecting point 1 and the center of the circle circumscribed around the face Li1−Li2−Li3 and around the face Li1−Li3−Li4, respectively. Points 2−4 and 7−10 are inside of the cluster, points 5 and 11 are at the centers of the circumscribed circles, and points 6 and 12 are outside of the cluster. [c] The first index is computed at the center of the base of the pyramid. The subsequent indices are computed at the points lying equidistantly on the line connecting point 1 and the center of the circle circumscribed around the face of the pyramid so that points 2−4 are inside of the cluster, point 5 is at the center of the circumscribed circle, and point 6 is outside of the cluster. [d] The first index is computed at the point between atoms Li3 and Li4, structure IX, Figure 3. Indices 1−5 are computed at the points lying on the line orienting downward from point 1. Indices 6−10 and 11−15 are computed at the points lying equidistantly on the lines connecting point 1 and the center of the circle circumscribed around the face Li3−Li2−Li5 and around the face Li3−Li5−Li6, respectively. Points 6−8 and 11−13 are inside of the cluster, points 9 and 14 are at the centers of the circumscribed circles, and points 10 and 15 are outside of the cluster.

species XV described above. Out of the four occupied molecular orbitals depicted in the Figure 7b, HOMO-1 ($1e_1'$) and HOMO-2 ($1a_1'$) have the same shapes as the HOMO and HOMO-1, respectively, in the Li_7^+ global minimum moiety. For the reason explained above the species is σ-aromatic. The singly occupied HOMO ($1a_2''$) also contributes to the overall stabilization of the system. This is a completely bonding molecular orbital of π-character. The system, even though having only one π-electron, can be called partially π-aromatic. Thus, the species is doubly aromatic.

The electronic configuration of the global minimum of the Li_7^- (D_{5h}, $^1A_1'$) cluster differs from the Li_7 (D_{5h}, $^2A_2''$) system only by the double population of the HOMO ($1a_2''$). The molecular orbital picture is identical to the one in Figure 7b. Using the same arguments, we conclude that the global minimum of the Li_7^- has doubly aromatic character of the chemical bonding due to the presence of six σ-electrons and two π-electrons. The four valence molecular orbitals in the Li_7^- D_{5h} cluster can also be considered as affective s (HOMO-2, $1a_1'$), p_x (HOMO-1, $1e_1'$), p_y (HOMO-1′, $1e_1'$), and p_z (HOMO, $1a_2''$) orbitals of the superatom, and complete occupation of these orbitals corresponds to major electron-shell closure (compare for example to Ne). And this result is also similar to the jellium model prediction for $n = 8$.[94]

From Figure 7c, where the populated molecular orbitals of the C_{3v}, $^1A_1$ Li_7^- species are shown, one may see that there is no electron density observed on the lithium atom coordinated at the face of the pyramid. The completely bonding HOMO-2 ($1a_1$) contains two σ-electrons and makes the system σ-aromatic according to the ($4n+2$) Hückel's rule. The remaining three molecular orbitals have an obvious triply degenerate nature of the octahedrally symmetric unit, which lost its symmetry due to the presence of the coordinated Li atom changing the point group of the cluster to the C_{3v}. The 1e HOMO and the $2a_1$ HOMO-1 are mostly composed of the 2p-atomic orbitals of the four Li atoms with 2s-contribution from the other two apex Li atoms and have primarily π-character. The complete occupation of this quasi-triply degenerate set leads to the symmetry, stability, and three-dimensional aromaticity of the cluster.

On the basis of negative NICS indices (see Table 10), the assigned aromaticity of all pentagonal bipyramids Li_7^+, Li_7, and Li_7^- receives additional confirmation. Moreover, according to NICS values, the aromatic character of the clusters grows upon addition of electrons to the aromatic π-MO (HOMO in Li_7 and Li_7^-), which is also in accordance with our conclusion about the gain of π-aromaticity.

V. Conclusions

We demonstrated on the small lithium clusters $Li_n^{0/+1/-1}$ ($n = 5-7$) that the novel Gradient Embedded Genetic Algorithm (GEGA) technique can be successfully used for identifying the lowest-energy structures. Results of our search, obtained using this program, have been compared with the previous ab initio calculations and experiments, and

the efficiency of the developed GEGA method has thus been confirmed. We plan to use the GEGA method for search for global minimum and low-lying structures of many main group elements' clusters. From the MO analysis of the chemical bonding in the clusters, found via the novel GEGA program, the significant role of multiple aromaticity as a major stabilizing effect in alkali-metal clusters has been elucidated. Our interpretation of aromatic or antiaromatic character of lithium clusters does not always agree with the assignments based on the computed NICS indices. In our previous work we reported the smaller systems of alkali and alkaline Earth metals and showed the importance of the σ-aromaticity concept in the description of the chemical bonding within them.[72] In this work we extend our knowledge about clusters of alkali metals, increasing the size of the considered systems.

Acknowledgment. This work was supported partially by the donors of the Petroleum Research Fund (ACS-PRF# 38242-AC6), administered by the American Chemical Society and partially by the National Science Foundation (CHE-0404937). The authors express their gratitude to Loren Hasen for discussions on the genetic algorithm technique.

References

(1) Holland, J. H. *Adaptation in Natural and Artificial Systems;* The University of Michigan Press: Ann Arbor, 1975.

(2) Goldberg, D. E. *Genetic Algorithms in Search, Optimization, and Machine Learning*; Addison-Wesley: Reading, MA, 1989.

(3) Davis, L. *Handbook of Genetic Algorithms*; Van Nostrand Reinhold: New York, 1991.

(4) Wang, J. L.; Wang, G. H.; Zhao, J. J. *Rhys. Rev. B* **2002**, *66*, 035418.

(5) Wang, J. L.; Wang, G. H.; Zhao, J. J. *Phys. Rev. A* **2003**, *68*, 013201.

(6) Gregurick, S. K.; Alexander, M. H.; Hartke, B. *J. Chem. Phys*. **1996**, *104(7)*, 2684.

(7) White, R. P.; Niesse, J. A.; Mayne, H. R. *J. Chem. Phys*. **1998**, *108(5)*, 2208.

(8) Marim, L. M.; Lemes, M. R.; Dal Pino, A., Jr. *Phys. Rev. A* **2003**, *67*, 033203.

(9) Ho, K. M.; Shvartsburg, A. A.; Pan, B.; Lu, Z. Y.; Wang, C. Z.; Wacker, J. G.; Fye, J. L.; Jarrold, M. F. *Nature* **1998**, *392*, 582.

(10) Cai, W.; Jiang, H.; Shao, X. *J. Chem. Inf. Comput. Sci*. **2002**, *42*, 1099.

(11) Stucke, D. P.; Crespi, V. H. *Nano Lett.* **2003**, *3*, 9, 1183.

(12) Haupt, R. L.; Haupt, S. E. *Practical Genetic Algorithms;* Wiley-Interscience Publication, John Wiley & Sons: New York, Chichester, Weinheim, Brisbane, Singapore, Toronto, 1998.

(13) Deaven, D. M.; Ho, K. M. *Phys. Rev. Lett*. **1995**, *75*, 2, 288.

(14) Zairi, Y. *Phys. Rev. E* **1995**, *51*, 4, R2769.

(15) Morris, J. R.; Deaven, D. M.; Ho, K. M. *Phys Rev. B* **1996**, *53*, R1740.

(16) Tomasulo, A.; Ramakrishna, M. V. *J. Chem. Phys*. **1996**, *105*, 23, 10449.

(17) Niesse, J. A.; Mayne, H. R. *J. Chem. Phys*. **1996**, *105*, 11, 4700.

(18) Wang, G. M.; Blaisten-Barojas, E.; Roitberg, A. E. *J. Chem. Phys*. **2001**, *115*, 8, 3640.

(19) Iwamatsu, M. *J. Chem. Phys*. **2000**, *112*, 24, 10976.

(20) Yoo, S.; Zeng, X. C. *J. Chem. Phys*. **2003**, *119*, 3, 1442.

(21) Guimaraes, F. F.; Belchior, J. C.; Johnston, R. L.; Roberts, C. *J. Chem. Phys*. **2002**, *116*, 19, 8327.

(22) Hui, L.; Pederiva, F.; Wang, G. H.; Wang, B. L. *J. Chem. Phys*. **2003**, *119*, 18, 9771.

(23) Lai, S. K.; Hsu, P. J.; Wu, K. L.; Liu, W. K.; Iwamatsu, M. *J. Chem. Phys*. **2002**, *117*, 23, 10715.

(24) Bazterra, V. E.; Ferraro, M. B.; Facelli, J. C. *J. Chem. Phys*. **2002**, *116*, 14, 5984.

(25) Bobadovaa-Parvanova, P.; Jackson, K. A.; Srinivas, S.; Horoi, M.; Kohler, C.; Seifert, G. *J. Chem. Phys*. **2002**, *116*, 9, 3576.

(26) Darby, S.; Mortimer-Jones, T. V.; Johnston, R. L.; Roberts, C. *J. Chem. Phys*. **2002**, *116*, 4, 1536.

(27) Kabrede, H.; Hentschke, R. *J. Phys. Chem. B* **2003**, *107*, 3914−3920.

(28) Kabrede, H.; Hentschke, R. *J. Phys. Chem. B* **2002**, *106*, 10089−10095.

(29) Dugourd, P.; Rayane, D.; Labastie, P.; Vezin, B.; Chevaleyre, J.; Broyer, M. *Chem. Phys. Lett*. **1992**, *97*, 433.

(30) Benichou, E.; Allouche, A. R.; Aubert-Frecon, M.; Antoine, R.; Broyer, M.; Dugourd, Ph.; Rayane, D. *Chem. Phys. Lett*. **1998**, *290*, 171.

(31) Bonacic-Koukecky, V.; Pittner, J.; Fuchs, C.; Fantucci, P.; Koutecky, J. *NATO Sci. Ser., Ser. C* **1992**, *372* (Phys. Chem. Finite Syst,: Clusters Cryst., Vol. 2), 899.

(32) Fantucci, P.; Bonacic-Koukecky, V.; Jellinek, J.; Wiechert, M.; Harrison, R. J.; Guest, M. F. *Chem. Phys. Lett*. **1996**, *250*, 47.

(33) Howard, J. A.; Joly, H. A.; Jones, R.; Edwards, P. P.; Singer, R. J.; Logan, D. E. *Chem. Phys. Lett*. **1993**, *204*, 128.

(34) Szaniszlo, J.; Tamassy-Lentei, I. *Acta Phys. Chim. Debrecina* **1994**, *29*, 25.

(35) Rousseau, R.; Marx, D. *Phys. Rev. A* **1997**, *56*, 617.

(36) Gibson, D. A.; Carter, E. A. *Chem. Phys. Lett*. **1997**, *271*, 266.

(37) Chihaia, V.; Sandu, T.; Vass, M. *Rom. J. Phys.* **1998**, *43*, 409.

(38) Fournier, R.; Chang, J. B. Y.; Wong, A. *J. Chem. Phys*. **2003**, *119*, 9444.

(39) de Visser, S. P.; Alpert, Y.; Danovich, D.; Shaik, S. *J. Phys. Chem. A* **2000**, *104*, 11223.

(40) Rousseau, R.; Marx, D. *J. Chem. Phys*. **1999**, *111*, 5091.

(41) Jones, R. O.; Lichtenstein, A. I.; Hutter, J. *J. Chem. Phys*. **1997**, *106*, 4566.

(42) Gardet, G.; Rogemond, F.; Chetmett, H. *Theor. Chim. Acta* **1995**, *91*, 249.

(43) Gardet, G.; Rogemond, F.; Chetmett, H. *J. Chem. Phys*. **1996**, *105*, 9933.

(44) Quassowski, S.; Hermann, K. *Phys. Rev. B* **1995**, *51*, 2457.

(45) Kawai, R.; Tombrello, J. F.; Weare, J. H. *Phys. Rev. A* **1994**, *49*, 4236.

(46) Lin, Z.; Slee, T.; Mingos, D. M. P. *Chem. Phys.* **1990**, *142*, 321.

(47) Ishi, S.; Ohno, K.; Kawazoe, Y.; Louie, S. G. *Phys. Rev. B* **2002**, *65*, 245109.

(48) Blank, J.; Bonacic-Koukecky, V.; Broyer, M.; Chevaleyre, J.; Dugourd, P.; Koutechy, J.; Scheuch, C.; Wolf, J. P.; Woeste, L. *J. Chem. Phys.* **1992**, *96*, 1793.

(49) Boustani, I.; Pewestorf, W.; Fantucci, P.; Bonacic-Koukecky, V.; Koutechy, J. *Phys. Rev. B* **1987**, *35*, 9437.

(50) Bauschlicher, C. W., Jr. *Chem. Phys.* **1996**, *206*, 35.

(51) Maynau, D.; Malrieu, J. P. *J. Chem. Phys.* **1988**, *88*, 3163.

(52) Grassi, A.; Loombardo, G. M.; Angilella, G. G. N.; March, N. H.; Pucci, R. *J. Chem. Phys.* **2003**, *120*, 24, 11615.

(53) de Visser, S. P.; Danovich, D.; Wu, W.; Shaik, S. *J. Phys. Chem. A* **2002**, *106*, 4961.

(54) de Visser, S. P.; Alpert, Y.; Danovich, D.; Shaik, S. *J. Phys. Chem. A* **2000**, *104*, 11223.

(55) Danovich, D.; Wu, W.; Shaik, S. *J. Am. Chem. Soc.* **1999**, *121*, 3165.

(56) Temelso, B.; Sherrill, C. D. *J. Chem. Phys.* **2005**, *122*, 064315.

(57) Li, X. W.; Pennington, W. T.; Robinson, G. H. *J. Am. Chem. Soc.* **1995**, *117*, 7578.

(58) Li, X. W.; Xie, Y.; Schreiner, P. R.; Gripper, K. D.; Crittendon, R. C.; Campana, C. F.; Schaefer, H. F.; Robinson, G. H. *Organometallics* **1996**, *15*, 3798.

(59) Xie, Y.; Schreiner, P. R.; Schaefer, H. F. III; Li, X. W.; Robinson, G. H. *J. Am. Chem. Soc.* **1995**, *117*, 7578.

(60) Li, X.-W.; Xie, Y.; Schreiner, P. R.; Gripper, K. D.; Crittendon, R. C.; Campana, C. F.; Schaefer, H. F.; Li, X. W.; Robinson, G. H. *Organometallics* **1996**, *15*, 3798.

(61) Robinson, G. H. *Acc. Chem. Res.* **1999**, *32*, 773.

(62) Li, X.; Kuznetsov, A. E.; Zhang, H. F.; Boldyrev, A. I.; Wang L. S. *Science* **2001**, *291*, 859.

(63) Li, X.; Zhang, H. F.; Wang, L. S.; Kuznetsov, A. E.; Cannon, N. A.; Boldyrev, A. I. *Angew. Chem., Int. Ed.* **2001**, *40*, 1867.

(64) Kuznetsov, A. E.; Corbett, J. D.; Wang, L. S.; Boldyrev, A. I. *Angew. Chem., Int. Ed.* **2001**, *40*, 3369.

(65) Kuznetsov, A. E.; Boldyrev, A. I.; Li, X.; Wang, L. S. *J. Am. Chem. Soc.* **2001**, *123*, 8825.

(66) Boldyrev, A. I.; Kuznetsov, A. E. *Inorg. Chem.* **2002**, *41*, 532.

(67) Kuznetsov, A. E.; Boldyrev, A. I.; Zhai, H.-J.; Wang, L. S. *J. Am. Chem. Soc.* **2002**, *124*, 11791.

(68) Zhan, C.-G.; Zhan, F.; Dixon, D. A. *J. Am. Chem. Soc.* **2002**, *124*, 14795.

(69) Fowler, P. W.; Havenith, R. W. A.; Steiner, E. *Chem. Phys. Lett.* **2001**, *342*, 85.

(70) Fowler, P. W.; Havenith, R. W. A.; Steiner, E. *Chem. Phys. Lett.* **2001**, *359*, 530.

(71) Juselius, J.; Straka, M.; Sundholm, D. *J. Phys. Chem. A* **2001**, *105*, 9939.

(72) Alexandrova, A. N.; Boldyrev, A. I. *J. Phys. Chem. A* **2003**, *107*, 554−560.

(73) Gaussian 03, Revision C.02, Frisch, M. J.; Trucks, G. W.; Schlegel, H. B.; Scuseria, G. E.; Robb, M. A.; Cheeseman, J. R.; Montgomery, J. A., Jr.; Vreven, T.; Kudin, K. N.; Burant, J. C.; Millam, J. M.; Iyengar, S. S.; Tomasi, J.; Barone, V.; Mennucci, B.; Cossi, M.; Scalmani, G.; Rega, N.; Petersson, G. A.; Nakatsuji, H.; Hada, M.; Ehara, M.; Toyota, K.; Fukuda, R.; Hasegawa, J.; Ishida, M.; Nakajima, T.; Honda, Y.; Kitao, O.; Nakai, H.; Klene, M.; Li, X.; Knox, J. E.; Hratchian, H. P.; Cross, J. B.; Bakken, V.; Adamo, C.; Jaramillo, J.; Gomperts, R.; Stratmann, R. E.; Yazyev, O.; Austin, A. J.; Cammi, R.; Pomelli, C.; Ochterski, J. W.; Ayala, P. Y.; Morokuma, K.; Voth, G. A.; Salvador, P.; Dannenberg, J. J.; Zakrzewski, V. G.; Dapprich, S.; Daniels, A. D.; Strain, M. C.; Farkas, O.; Malick, D. K.; Rabuck, A. D.; Raghavachari, K.; Foresman, J. B.; Ortiz, J. V.; Cui, Q.; Baboul, A. G.; Clifford, S.; Cioslowski, J.; Stefanov, B. B.; Liu, G.; Liashenko, A.; Piskorz, P.; Komaromi, I.; Martin, R. L.; Fox, D. J.; Keith, T.; Al-Laham, M. A.; Peng, C. Y.; Nanayakkara, A.; Challacombe, M.; Gill, P. M. W.; Johnson, B.; Chen, W.; Wong, M. W.; Gonzalez, C.; Pople, J. A. Gaussian, Inc., Wallingford CT, 2004.

(74) Parr, R. G.; Yang, W. *Density-functional theory of atoms and molecules*; Oxford University Press: Oxford, 1989.

(75) Becke, A. D. *J. Chem. Phys.* **1993**, *98*, 5648.

(76) Perdew, J. P.; Chevary, J. A.; Vosko, S. H.; Jackson, K. A.; Pederson, M. R.; Singh, D. J.; Fiolhais, C. *Phys. Rev. B* **1992**, *46*, 6671.

(77) Hammersley, J. M.; Handscomb, D. C. *Monte Carlo Methods*; Methuen: London, 1965; Chapter 9.

(78) Cizek, J. *Adv. Chem. Phys.* **1969**, *14*, 35.

(79) Purvis, G. D, III; Bartlett, R. J. *J. Chem. Phys.* **1982**, *76*, 1910.

(80) Scuseria, G. E.; Janssen, C. L.; Schaefer, H. F., III *J. Chem. Phys.* **1988**, *9*, 7282.

(81) Raghavachari, K.; TrucksJohn, G. W. A.; Pople, J. A.; Head-Gordon, M. *Chem. Phys. Lett.* **1989**, *157*, 479.

(82) Bartlett, R. J.; Watts, J. D.; Kucharski, S. A.; Noga, J. *Chem. Phys. Lett.* **1990**, *165*, 513.

(83) Schaftenaar, G. MOLDEN3.4, CAOS/CAMM Center, The Netherlands 1998.

(84) NPA Version 3.1, Reed, A. E., Carpenter, J. E.; Weinhold, F.; 1998.

(85) Schleyer, P. v. R.; Maerker, C.; Dransfeld, A.; Jiao, H.; van Eikema Hommes, N. J. R. *J. Am. Chem. Soc.* **1996**, *118*, 6317.

(86) Huber, K. P.; Herzberg, G. *Molecular Spectra and Molecular Structure. IV. Constants of Diatomic Molecules*; Van Nostrand: New York, 1979.

(87) While π-aromaticity and π-antiaromaticity, when delocalized bonding occurs due to the π-overlap of atomic orbitals, are well-known, σ-(anti)aromaticity is less known in chemistry. σ-aromaticity occurs when the number of σ-electrons is not sufficient for population of σ-MOs, which could be localized in classical 2c-2e bonds. It has been introduced by Dewar.[88] Double aromaticity (the simultaneous presence of σ- and π-aromaticity) was introduced in chemistry by Schleyer and co-workers[89] in the late 1970s for explaining properties of the 3,5-dehydrophenyl cation. Double aromaticity and anti-aromaticity was first used by Martin-Santamaria and Rzepa[90]

for explaining chemical bonding in small carbon rings. Berndt and co-workers have shown that small carborane molecules containing three- and four-membered rings also exhibit both σ and π aromaticity.[91]

(88) (a) Dewar, M. J. S. *Bull. Soc. Chim. Belg.* **1979**, *88*, 957. (b) Dewar, M. J. S.; McKee, M. L. *Pure Appl.* Chem. **1980**, *52*, 1431. (c) Dewar, M. J. S. *J. Am. Chem. Soc.* **1984**, *106*, 669.

(89) Chandrasekhar, J.; Jemmis, E. D.; Schleyer, P. v. R. *Tetrahedron Lett.* **1979**, *39*, 3707.

(90) Martin-Santamaria, S.; Rzepa, H. S. *Chem. Commun.* **2000**, *16*, 1503.

(91) (a) Präsang, C.; Mlodzianowska, A.; Sahin, Y.; Hofmann. M.; Geiseler. G.; Massa, W.; Berndt. A. *Angew. Chem. Int. Ed.* **2002**, *41*, 3380. (b) Präsang, C.; Hofmann. M.; Geiseler. G.; Massa, W.; Berndt, A. *Angew. Chem. Int. Ed.* **2002**, *41*, 1526. (c) Präsang, C.; Mlodzianowska, A.; Geiseler, G.; Massa, W.; Hofmann, M.; Berndt, A. *Pure Appl. Chem.* **2003**, 75, 1175. (d) Amseis, P.; Mesbah, W.; Präsang, C.; Hofmann, M.; Geiseler, G.; Massa, W.; Berndt, A. *Organometallics* **2003**, *22*, 1594. (e) Mesbah, W.; Präsang, C.; Hofmann, M.; Geiseler, G.; Massa, W.; Berndt, A. *Angew. Chem., Int. Ed.* **2003**, *42*, 1717.

(92) Li, X.; Kuznetsov, A. E.; Zhang, H. F.; Boldyrev, A. I.; Wang, L. S. *Science* **2001**, *291*, 859.

(93) Gogonea, V.; Schleyey, P. v. R.; Scheiner, P. R. *Angew. Chem., Int. Ed.* **1998**, *37*, 1945.

(94) Knigh, W. D.; Clemenger, K.; de Heer, W. A.; Saunders: W. A.; Cho, M. Y.; Cohen, M. L. *Phys. Rev. Lett.* **1984**, *52*, 2141.

CT050093G

JCTC Journal of Chemical Theory and Computation

Anchoring the Torsional Potential of Biphenyl at the ab Initio Level: The Role of Basis Set versus Correlation Effects

J. C. Sancho-García*,†,‡ and J. Cornil†

Laboratory for Chemistry of Novel Materials, Center for Research in Molecular Electronics and Photonics, University of Mons-Hainaut, Place du Parc 20, B-7000 Mons, Belgium, and Departamento de Química-Física, Universidad de Alicante, E-03080 Alicante, Spain

Received February 9, 2005

Abstract: The torsional profile of biphenyl has been calculated by means of quantum-chemical perturbations and coupled-cluster methods of increasing accuracy. The performance of the various theoretical approaches has been assessed through a critical comparison with experimental barrier heights. The theoretical data indicate that the basis set effects become more critical than the correlation effects beyond the perturbational MP4 or variational CCSD(T) levels of theory to obtain the most accurate results. We also discuss the various additional corrections that would be required beyond the scope of our study to provide the best match to the experimental results.

1. Introduction

Considerable efforts have been devoted in recent years to the determination of the torsional potential of biphenyl at various levels of theory.[1−8] Biphenyl is an attractive model compound to study both the conformational changes induced by the interplay between π-conjugation and steric effects and by extension the relationship between conformations and electronic and optical properties. Torsions between conjugated rings dictate the nature of the emission and absorption spectra of many organic conjugated oligomers and polymers;[9,10] a planarization of the backbone, induced for instance by packing effects in the solid state, typically shifts the spectra to the red due to the increased overlap between the π-electronic clouds of the neighboring monomer units. Such torsions also play a significant role in determining the fluorescence quantum yield of conjugated chains[11] and the occurrence of intersystem crossing processes[12] as well as the shape of vibronic progressions in absorption and emission spectra.[13] The torsional potentials obtained by different quantum-chemical approaches may vary significantly depending on the choice of the basis set and the correlation treatment. Severe deviations from experimental data can further be encountered in force fields used for molecular mechanics and molecular dynamics simulations. The torsional terms in current force fields are usually derived from experiment for model systems; the transferability assumption underlying the development of a force field might however fail for related systems, in particular in the presence of small torsional barriers; this has been illustrated in the case of biphenyl.[14,15] The development of a torsional profile for biphenyl fitted from accurate quantum-chemical calculations is thus highly desirable for force field simulations in order to reduce the uncertainties inherent to a large number of modern molecular modeling tools.

It is well-established experimentally[16−18] that the gas-phase barriers (ΔE) separating the global minimum ($\phi = 44.4° \pm 1.2°$) from the planar ($\phi = 0°$) and perpendicular ($\phi = 90°$) conformations are very similar and are on the order of 1−2 kcal/mol. The widely used "chemical accuracy" criterion (defined as ±1 kcal/mol of uncertainty with respect to the experimental results) is clearly not relevant for such small energy barriers. A more stringent "calibration accuracy" (±1 kJ/mol = 0.24 kcal/mol) will thus be sought here by using a well-defined hierarchy of correlated ab initio methods

* Corresponding author e-mail: JC.Sancho@ua.es.
† University of Mons-Hainaut.
‡ Universidad de Alicante.

10.1021/ct0500242 CCC: $30.25
Published on Web 06/01/2005

together with a carefully selected molecular orbital expansion that converges systematically toward the infinite basis set limit. The computational strategy that we have adopted relates somehow to the composite methods recently introduced to provide highly accurate results in the subchemical accuracy range: (i) the Gaussian-n (G-n) family of methods;[19,20] (ii) the focal point analysis (FPA);[21−25] (iii) the Weizmann-n (W-n) protocols;[26−28] and (iv) the HEAT method.[29] The main features of our alternative approach are as follows: (i) the absence of empirical corrections; (ii) the use of extrapolation techniques to reach both the asymptotic basis set and the correlation energy limits; and (iii) the applicability to medium-size conjugated systems without significant loss in accuracy. Density Functional Theory (DFT)[30−33] is known to behave erratically when high accuracy is required for conjugated systems[34−36] due to the fact that current exchange functionals overstabilize π-conjugation in planar conformers and hence provide overestimated energy barriers. A systematic study is thus always recommended when DFT is chosen in view of its reduced computational cost. It is the goal of this contribution to define, on the basis of our previous experience,[37−42] a generally applicable model to calculate accurately the torsional potential of biphenyl. This model could then be applied to other archetypal systems which constitute the building blocks of widely studied conjugated polymers.

2. Theoretical Methods

We have first performed a full optimization of the structure of each conformer for a wide range of dihedral angles, thus dealing explicitly with $3N - 7$ degrees of freedom. A regular and rather tight grid (step of 10° between 0°and 180°) has been considered for the torsion angle ϕ between the two phenyl rings. Hartree−Fock (HF) and Møller−Plesset perturbation theory methods (up to the second order, MP2) involving large basis sets (several hundreds of basis functions) have been employed for these geometry optimizations. The energy of each conformer has been further corrected by applying higher-order valence correlation schemes at the MP4 (Møller−Plesset up to the fourth order), CCSD (Coupled Cluster method with Single and Double excitations), and CCSD(T) (with perturbatively estimated triple excitations) levels with the largest possible basis set. The energy difference E_{CC} between the full configuration interaction limit (FCI) and our most accurate results can be estimated by means of a continued fraction (cf) extrapolation as[43]

$$E_{CC} = \frac{\delta_1}{1 - \dfrac{\dfrac{\delta_2}{\delta_1}}{1 - \dfrac{\delta_3}{\delta_2}}} \quad (1)$$

where $\delta_1 = E_{HF}$, $\delta_2 = E_{CCSD} - E_{HF}$, and $\delta_3 = E_{CCSD(T)} - E_{CCSD}$. CC-based multiplicative approaches[44] are not used here since torsional barriers are derived from energy differences that are better described with continued fractions. The use of MP and CC correlated techniques, although computationally very demanding and strongly basis set dependent, is the only way to ensure the targeted high accuracy.

The infinite basis set limit can be estimated by using the *n*-tuple cc-pV*n*Z basis sets[45] which systematically approaches completeness as *n* grows. The extrapolation of the cc-pV*n*Z sequence (n = double, triple, quadruple, ...) is done with the function

$$E(n) = E(\infty) + Af(n) \quad (2)$$

where $f(n)$ is written as n^{-5} [46,47] or n^{-3} [48] for the HF and for the MP2 correlation energy, respectively; $E(\infty)$ is the corresponding extrapolated energy, and A is the parameter to be fitted. Note that the use of power expansions is nowadays preferred to exponential ones.[49] When the pair of cc-pV*n*Z/cc-pV(n+1)Z results required to eliminate A from eq 2 is not available for computationally demanding systems, the extrapolation can still be applied in the framework of a method-dependent slightly modified model[50]

$$E_c(n) = E_c(\infty)\{1 - 2.4n^{-3}[a + be^{-2.4b} + c]n^{-1}\} \quad (3)$$

where a new set of optimal parameters (a, b, and c) is included; their values can be extracted from ref 50.

Since the zero-point vibrational energies (ZPVE) are different going from the global minimum to the planar or to the perpendicular conformations,[51] such corrections must be explicitly taken into account to estimate the energy barriers. We have thus computed here ZPVE-corrected barriers to allow for the most relevant comparison with the experimental results. Other contributions such as the explicit coupling of vibrational modes, scalar relativistic effects, spin−orbit coupling, or diagonal corrections to the Born−Oppenheimer approximation are not considered in the present work since their impact on the torsional potentials is expected to be negligible.[21,52]

Perturbative approaches or truncated CC methods can fail in producing highly accurate results if the starting single determinant HF wave function is not reliable for the system under study. For the whole range of torsions, the CCSD/cc-pVDZ-calculated low value (0.01) of the T_1 diagnostic,[53−55] which was specifically designed to provide an indication of the quality of the results, did not advise us to use more than a single determinant to generate the manifold of excitations; multireference versions of the CC theory[56] are thus not needed. Moreover, a previous study including nondynamical correlation effects[57] through a multiconfigurational second-order perturbation treatment (CASPT2) provided barrier heights comparable to the monoconfigurational treatment, thus indicating that a single-reference wave function is also an adequate starting point for MP2 calculations. All the results described in this manuscript have been obtained with the Gaussian98[58] and Gaussian03[59] packages.

3. Results and Discussion

3.1. Geometry Optimizations and Zero-Point Vibrational Energy Corrections. Each of the stationary points (i.e., the global twisted minimum as well as the planar and perpendicular conformations) of the torsional profile has been optimized using the HF, MP2, and the B3LYP-based DFT

Table 1. Calculated Bond Lengths (in Å) and Bond Angles (in deg) for Biphenyl[a] as Obtained at Different Levels of Theory and with Different Basis Sets

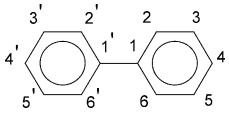

		cc-pVDZ			cc-pVTZ		
	exp[b]	HF	B3LYP	MP2	HF	B3LYP	MP2
$C_1-C_{1'}$	1.507	1.493	1.482	1.485	1.489	1.482	1.473
C_1-C_2	1.404	1.395	1.407	1.413	1.389	1.399	1.400
C_2-C_3	1.395	1.387	1.396	1.404	1.381	1.388	1.392
C_3-C_4	1.396	1.388	1.398	1.406	1.382	1.390	1.394
C−H	1.102	1.082	1.092	1.095	1.073	1.082	1.082
$C_2-C_1-C_6$	119.4	118.3	118.0	118.7	118.3	118.0	118.5
$C_1-C_2-C_3$	119.9	120.9	121.0	120.7	120.9	121.0	120.8
$C_2-C_3-C_4$	120.9	120.3	120.3	120.2	120.3	120.3	120.2
$C_3-C_4-C_5$	119.0	119.4	119.4	119.6	119.4	119.4	119.6
$C_{2'}-C_{1'}-C_1-C_2$	44.4	46.3	39.3	42.1	45.0	39.6	39.7

[a] See chemical structure on top for site labeling. [b] Taken from ref 17.

method[60] with the cc-pVDZ and cc-pVTZ basis sets. The cc-pVQZ basis set could be applied only at the HF level. Table 1 shows the comparison between the geometric parameters experimentally derived from gas-phase electron diffraction data[17] and the corresponding calculated values for the global twisted minimum. Systematic deviations between the vibrationally averaged experimental bond lengths (r_g) and the calculated equilibrium values (r_e) have always to be considered for a detailed comparison: r_g values are about 0.004−0.009 Å and 0.014−0.018 Å longer than r_e for C−C and C−H bonds, respectively.[61] Differences in bond angles are assumed to be negligible. In general, we find that the bond lengths decrease with the extension of the basis set and increase when electron correlation is introduced. This is not the case for the C_1-C_1' bond length for which the largest error is found, as previously reported;[62,63] the experimental uncertainty on this parameter is, however, expected to be large. Very small differences are found for the bond angles among the different methods. All together, the MP2 results can be judged as slightly more accurate than the B3LYP values. Whereas a cc-pVTZ basis set is considered to be converged for a DFT calculation,[64−68] this does not hold true for the MP2 method. A practical scheme for extrapolating the geometric parameters calculated with a sequence of cc-pV*n*Z basis sets has been proposed[69] though being severely questioned.[70] Accordingly, no attempt has been made here to account for this basis set effect, and the MP2/cc-pVTZ-optimized geometries have been used as a starting point for the subsequent energetic corrections. Extrapolated torsional angles are obtained when needed by means of a splines treatment.

In our study, B3LYP was the only affordable technique to calculate with a cc-pVTZ basis set the frequencies of the stationary points and the resulting ZPVE correction. The assignment of the fundamental vibrational frequencies of biphenyl has been, however, repeatedly studied in the literature[71] and will not be discussed here. We have accounted for anharmonic corrections to the harmonic zero-point vibrational energies by scaling them by a factor of 0.985, as suggested in ref 26. The scaled values of the ZPVE for the global minimum and the planar and perpendicular conformations are 112.09, 112.08, and 111.85 kcal/mol, respectively, at the B3LYP-cc-pVTZ level; this leaves almost unaltered the barrier ΔE^0 between the global minimum and the planar conformation and decreases the barrier ΔE^{90} by roughly 0.2 kcal/mol with respect to the ZPVE-uncorrected value. All curves presented in the following will be corrected with this B3LYP/cc-pVTZ-derived values. Note that this correction will also slightly modify the torsion angles with respect to the optimized values listed in Table 1.

3.2. Electron Correlation Effects. One open question in view of the scarcity of literature results is to elucidate whether treatments of the electron correlation beyond the MP2 level may substantially change the barrier heights for a given basis set. We have collected in Table 2 the HF, MP, and CC barriers calculated with the cc-pVDZ basis sets. The MP2 method slightly decreases the ΔE^0 value compared to the uncorrelated HF level (by about 0.1 kcal/mol) but, most importantly, largely increases ΔE^{90} by 0.5 kcal/mol to make it more consistent with the experimental value. MP4 calculations further point to the role of electron correlation effects for the ΔE^0 barrier; the difference between the MP2 and HF values is a few times smaller than between the MP4 and MP2 results. The impact is less pronounced for ΔE^{90} which is very similar at the MP2 and MP4 levels. The CCSD and CCSD(T) calculations provide consistent numbers, with the CCSD(T) value lying close to that obtained with MP4. This nicely reflects the parallel convergence of the two sequences of methods [HF → MP2 → MP4 versus HF → CCSD → and CCSD(T)] toward the exact solution.

The use of the continued fraction technique further demonstrates this convergence process, as illustrated in Table 3. This approach has been recently applied to both thermochemical data[72−76] and rotational barriers[77] but not without warnings about a possible erratic behavior.[28,72] Although the formula given in eq 1 was originally derived to assess the

Table 2. ZPVE-Corrected Relative Energies (in kcal/mol) between the Global Twisted Minimum (Characterized by the Torsion Angle ϕ) and the Planar (ΔE^0) and Perpendicular (ΔE^{90}) Conformations in Biphenyl, as Calculated with Different Approaches

method	ϕ	ΔE^0	ΔE^{90}
HF/cc-pVDZ	48.7	3.10	1.15
HF/cc-pVTZ	47.5	2.97	1.24
HF/cc-pVQZ	47.5	2.99	1.25
HF/cc-pV∞Z	47.5	2.99	1.26
MP2/cc-pVDZ	45.5	3.02	1.63
MP2/cc-pVTZ	41.2	2.39	2.04
MP2/cc-pV∞Z	39.8	2.19	2.26
CCSD/cc-pVDZ[a]	46.6	2.76	1.35
CCSD/cc-pV∞Z[a]	44.3	2.61	1.62
MP4/cc-pVDZ[a]	45.1	2.70	1.59
MP4/cc-pV∞Z[a]	42.1	2.56	1.97
CCSD(T)/cc-pVDZ[a]	45.5	2.67	1.51
CCSD(T)/cc-pV∞Z[a]	42.6	2.51	1.85
exp[b]	44.4 ± 1.2	1.4 ± 0.5	1.6 ± 0.5

[a] From the MP2/cc-pVTZ optimized geometry. [b] Taken from ref 17.

Table 3. ZPVE-Corrected Relative Energies (in kcal/mol) between the Global Twisted Minimum (Characterized by the Torsion Angle ϕ) and the Planar (ΔE^0) and Perpendicular (ΔE^{90}) Conformations in Biphenyl, as Calculated at Different Levels of Theory with the cc-pVDZ Basis Set

method	ϕ	ΔE^0	ΔE^{90}
HF	48.7	3.10	1.15
MP2	45.5	3.02	1.63
MP4	45.1	2.70	1.59
MP-cf	45.0	2.63	1.58
CCSD	46.6	2.76	1.35
CCSD(T)	45.5	2.67	1.51
CC-cf	45.4	2.66	1.53
exp[a]	44.4 ± 1.2	1.4 ± 0.5	1.6 ± 0.5

[a] Taken from ref 17.

difference between CCSD(T) and the full CI limit, it has been also used here to extrapolate the MP4 energies since the MP and CC sequences of methods have much in common. Quadratic approximants of MP series[78] have not been investigated. Moreover, no attempt has been made to justify the validity of eq 1 for the MP sequence; its use appears to be justified on an empirical basis by observing the smooth convergence of the calculated barrier heights. We stress, however, that the prerequisites for a coherent evolution ($\delta_1 \gg \delta_2 + \delta_3$, and $\delta_2 \gg \delta_3$; where $\delta_1 = E_{HF}$, $\delta_2 = E_{MP2} - E_{HF}$, and $\delta_3 = E_{MP4} - E_{MP2}$) are fulfilled by the MP series. Analysis of Table 3 reveals that the impact of the approximations made in our methods on the barrier heights is very small. The approximate FCI/cc-pVDZ values are estimated to be 2.6−2.7 kcal/mol and 1.5−1.6 kcal/mol for ΔE^0 and ΔE^{90}, respectively, while the corresponding experimental values are around 1.4 and 1.6 kcal/mol. Basis set effects thus appear to be the root of the well-documented problem of obtaining highly accurate barrier heights with ab initio methods.

3.3. Basis Set Effects. The previous section suggests that augmenting the size of the basis set is more crucial than going beyond MP4 or CCSD(T) for the correlation treatment. However, the computational limits are easily reached if no restrictions are imposed on the number of unoccupied orbitals involved to generate the manifold of excitations (N_u). Since the MP4 and CCSD(T) methods scale as $N_o^3 \times N_u^4$ (with N_o being the number of occupied orbitals), the extension of the basis set size typically leads to a strong increase in N_u and hence to unaffordable computational requirements. Accordingly, we will exploit in the following the systematic convergence of correlation consistent basis sets with the help of eqs 2 and 3 to overcome this problem. Other extrapolation schemes have been proposed[79−81] but usually yield marginal improvements in the torsional potentials and energy barriers.[40,41]

The corresponding extrapolated results are reported in Table 2 where cc-pV∞Z refers to HF, MP, or CC results after estimation of the basis set limit. The extrapolated energy associated with a given correlation treatment has been added here to the separately extrapolated HF/cc-pV∞Z energy. The ΔE^0 and ΔE^{90} barriers calculated at the HF level do not largely depend on the basis set; the cc-pVTZ results can be actually be considered as nearly converged. The well-known slower convergence of correlated electronic structure calculations is clearly observed at the MP2 level where both energy barriers markedly evolve with the size of the basis set; ΔE^0 decreases from 2.39 to 2.19 kcal/mol, whereas ΔE^{90} increases from 2.04 to 2.25 kcal/mol going from cc-pVTZ to the basis set limit. These results are in good agreement with those previously reported by Tsuzuki et al.[2] The same trends are also observed with the MP4, CCSD, and CCSD(T) results; this gives us confidence in the fitting procedure done in eq 2 and shows uniformly the slightly larger dependence of ΔE^{90} with respect to the size of the basis set. Considering the residual effects associated with the truncation of the MP or CC series, as detailed in the previous section, optimal FCI/cc-pV∞Z values of 2.5 kcal/mol and 1.9−2.0 kcal/mol are obtained for the ΔE^0 and ΔE^{90} barriers, respectively. Unexpectedly, the "calibration accuracy" is still not matched for the ΔE^0 barrier. Additional possible contributions to the torsional potentials will thus be carefully explored in the next section to try and solve this discrepancy. Figures 1 and 2 display the CC and MP torsional energy profiles obtained when the above-mentioned corrections (continued fraction extrapolation to the FCI limit and basis set extrapolation to the infinite basis set limit) are included. The cc-pVDZ curves are also illustrated for sake of completeness.

3.4. Additional Factors. The MP and CC calculations described so far have been routinely performed within the frozen-core approximation, i.e., the lower lying 1s orbitals of carbon were not correlated. Although core correlation effects are expected to modify the barriers by less than 0.1 kcal/mol, it is necessary to account for both core−core (intrashell 1s) and core-valence (intershell 1s − 2s2p) correlation effects to attain a definitive set of results. We have thus investigated the impact of the highly computationally expensive inner-shell correlation effects at the MP2 level by using the recently introduced weighted core-valence

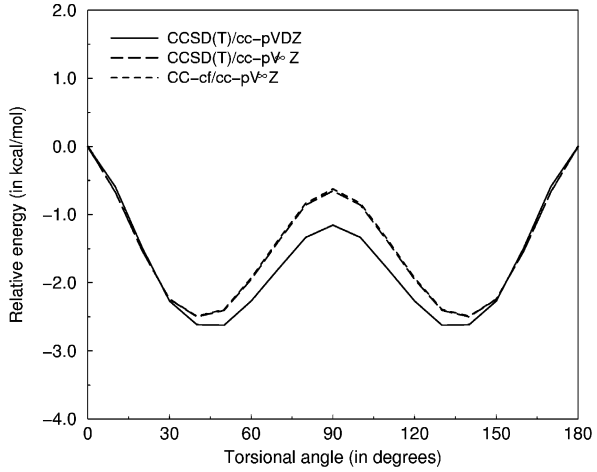

Figure 1. Torsion potential of biphenyl calculated at different levels of CC theory.

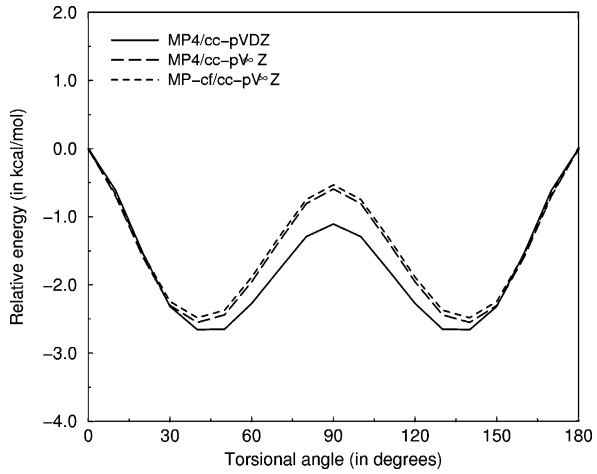

Figure 2. Torsion potential of biphenyl calculated at different levels of MP theory.

Table 4. ZPVE-Corrected Relative Energies (in kcal/mol) between the Global Twisted Minimum (Characterized by the Torsion Angle ϕ) and the Planar (ΔE^0) and Perpendicular (ΔE^{90}) Conformations in Biphenyl, as Calculated at the MP2 Level with Different Basis Sets

method	ϕ	ΔE^0	ΔE^{90}
MP2/cc-pVDZ	45.5	3.02	1.63
MP2/cc-pwCVDZ	45.8	3.10	1.60
MP2/aug-cc-pVDZ	46.4	2.46	1.52
MP2/cc-pVTZ	41.2	2.39	2.04
exp[a]	44.4 ± 1.2	1.4 ± 0.5	1.6 ± 0.5

[a] Taken from ref 17.

basis set (cc-pwCVDZ[82] compared to the former cc-pCVDZ[83]). Table 4 reports the corresponding results. The difference between the all-electron (cc-pwCVDZ) and valence-only (cc-pwCVDZ) energy barriers provides an estimate of the amplitude of the core correlation effects for a given basis set. The extrapolation of these results provides barrier heights that are negligibly modified compared to the extrapolated frozen core value: both barriers are increased by less than 0.01 kcal/mol. When this correction is taken into account, all-electrons FCI/cc-pV∞Z barrier heights of 2.5 kcal/mol and 1.9−2.0 kcal/mol are still obtained for ΔE^0 and ΔE^{90}, respectively.

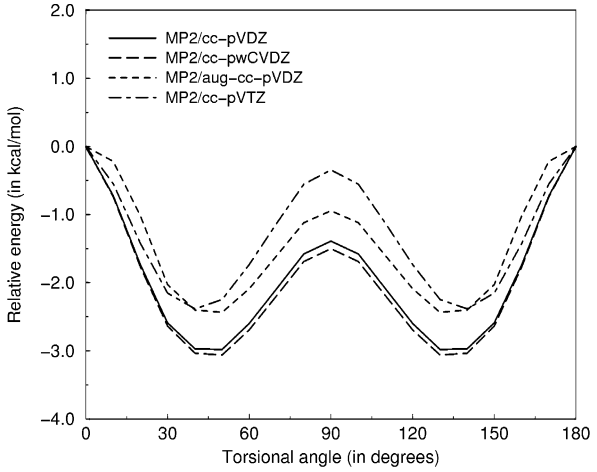

Figure 3. Torsion potential of biphenyl calculated at the MP2 level with different basis sets.

On the other hand, the use of diffuse functions (aug-cc-pVDZ) helps the ΔE^0 barrier to converge toward the higher levels of the hierarchy, as evidenced in Table 4. However, the dihedral angle is found to increase and the ΔE^{90} barrier to be reduced in this case, in marked contrast with the trends found when a complete set of polarization functions is added (going for instance from cc-pVDZ to cc-pVTZ). The C_1-C_1' distances in the 90° conformer (1.4915, 1.4924, and 1.4802 Å for the cc-pVDZ, aug-cc-pVDZ, and cc-pVTZ basis set, respectively) demonstrate that the underestimation of the π-conjugation effects by the aug-cc-pVDZ basis set is at the origin of this discrepancy, in agreement with the results obtained for other conjugated molecules.[41] The aug-cc-pVTZ basis set should probably improve the description of these effects; however, the requested compromise between accuracy and computational cost precludes the use of the aug-cc-pVnZ extension, thus favoring the cc-pVnZ sequence in conjunction with the extrapolation scheme. The deviations between these various approaches are further illustrated through the corresponding torsional profiles depicted in Figure 3.

It has also been suggested that the cc-pVDZ basis set underestimates the dispersion interactions and hence the stability of the coplanar conformer of biphenyl;[2] this translates into an overestimation of ΔE^0 compared to ΔE^{90}. The employed extrapolation technique can hardly overcome this intrinsic deficiency of the cc-pVDZ basis functions. To evaluate the amplitude of this effect, the impact of an additional set of polarization d-type functions on the hydrogen atoms[84] has been analyzed; the imposed contraction [C/H] scheme thus becomes at this stage [3s2p/2s1p1d] instead of the standard one. As expected, multiple polarization functions on the hydrogen atoms reduce ΔE^0 (ΔE^{90}) by 0.4 (0.2) kcal/mol, while the dihedral angle increases by a few degrees due to the exaltation of nonbonding interactions. All-electrons hydrogen d-polarized FCI/cc-pV∞Z values of 2.1−2.2 kcal/mol and 1.7−1.8 kcal/mol are obtained for the

Table 5. Expansion Coefficients (in kcal/mol) for the Analytical Torsional Potential of Biphenyl Fitted from the Extrapolated HF/cc-pV∞Z and the Most Accurate MP and CC Results[a]

method	V_2	V_4	V_6	V_8	V_{10}	V_{12}
HF	−1.301	−2.096	−0.3760	−0.1575	−0.0464	−0.0251
MP[b]	0.0332	−2.142	−0.3938	−0.2462	−0.1193	−0.0945
CC[c]	−0.0923	−2.112	−0.3916	−0.2428	−0.1174	−0.0931

[a] The odd terms are zero for symmetry reasons. [b] All-electrons MP-cf/cc-pV∞Z results. [c] All-elecontrs CC-cf/cc-pV∞Z results.

ΔE^0 and ΔE^{90} barriers. This basis set engineering should be treated however with much caution.[85]

3.5. Analytical Torsional Functions. The point-wise calculated torsion energies can be fitted to a Fourier-like expansion of the form

$$V(\phi) = \frac{1}{2}\sum_{n=1}^{m} V_n[1 - \cos n(180 - \phi)] \qquad (4)$$

where V_n are the expansion coefficients to be determined. Since such a potential energy function $V(\phi)$ is virtually included in all current force fields, it is of interest to determine the coefficients required to best match our ab initio results. This has been done for an expansion up to the sixth order from HF/cc-pV∞Z and all-electrons basis set extrapolated MP-cf and CC-cf results (see Table 5).

4. Summary and Perspectives

A thorough study of the gas-phase torsional potential of biphenyl has been performed at the ab initio level to determine the role of correlation versus basis set effects in the search of the most accurate results. Our approach involves primarily hierarchical calculations at the MP or CC levels, followed by an extrapolation procedure of the results to the infinite basis set limit and the highest order of MP or CC, and finally a set of small but non-negligible additive corrections to the energy (among them, core correlation effects and the impact of including an additional set of polarization functions on the hydrogen atoms were explicitly evaluated). The degree of sophistication of the most advanced theoretical approaches used here fulfills the constraints of "calibration accuracy". The best predictions achieved in our work for ΔE^0 (ΔE^{90}) amount to 2.1 (1.7) and 2.2 (1.8) kcal/mol at the corrected CC and MP doubly extrapolated levels, respectively.

Ingredients are still missing in the protocol to predict with higher accuracy the torsional potentials of medium-size conjugated molecules. We discuss below some of these factors and their possible impact at a quantitative level:

(a) Improved extrapolation to the infinite basis set limit. Although modern extrapolation techniques[50] allow for the use of only one basis set from the cc-pV*n*Z sequence, they might provide in some cases a rough estimate of the extrapolated energies if the lowest cc-pVDZ level is used. In this context, the application of the dual-level scheme of Halkier et al.[48] or Schwenke[86] relying on the cc-pVDZ and cc-pVTZ basis sets could shed light on the quality of the extrapolation schemes performed at the MP or CC level. This is expected to be the main source of error in our approach. A separate extrapolation of the singlet-coupled and triplet-coupled CCSD pair correlation energies has also been proposed based on the fact that their convergence appears to be different.[87] Moreover, the (T) contribution is known to converge more rapidly with the basis set than the CCSD correlation energy;[88] particular attention should therefore be paid to the extrapolation of CCSD energies. Nevertheless, it is generally accepted that an extrapolated value obtained with the cc-pV*n*Z member of the hierarchy usually compares qualitatively with at least a cc-pV(n+2)Z result. Moreover, since the number of paired electrons remain unchanged during the rotation, the basis set convergence is expected to be very fast;[89] previously published nonextrapolated results can thus hardly compete in terms of accuracy with the CC extrapolated values presented in this work.

(b) Iterative treatment of T_3 contributions at the CCSDT level. The explicit treatment of triple excitations is not expected to significantly change barrier heights with respect to the CCSD(T) values, as suggested by the results of the continued-fraction approximation and by previous studies.[90] The error introduced in the CCSD(T) perturbed method is relatively large (about 10% of the full contribution arising from triple excitations)[91] but is partly canceled by the neglect of quadruple excitations; thus, the CCSDT method might only account for the possibly remaining nondynamical correlation effects,[92] which are expected to affect the barrier by less than 0.01 kcal/mol.

(c) Improved core correlation contribution. The use of all-electron CCSD(T) instead of MP2 should also be tested to evaluate the inner-shell correlation effects and their extrapolation to the asymptotic limit. Since the basis set incompleteness errors are expected to be much larger than the core-valence effects,[93] this correction is expected to be also negligible.

(d) The impact of performing the geometry optimizations beyond the MP2/cc-pVTZ level employed here may also be explored; the correction is, however, expected to be very small.[40,94]

We do not know at this stage to which extent these different factors might fill the gap between the experimental and theoretical value obtained for the ΔE^0 barrier. Both barriers were experimentally estimated from the analysis of Raman spectra of the torsional mode[16] or from electron diffraction measurements.[17,18] The periodic potential function extracted from the experimental analysis is essentially accurate in the region around the potential minimum. However, the barrier heights might be affected to a large extent[18] by the severely truncated mathematical expression which was selected to describe the potential. Further confirmations of the experimental number reported in the literature are seen as a prerequisite to solve this apparent discrepancy since the aforesaid corrections are expected to be very small and possibly of different signs.

Acknowledgment. The work in Mons was partly supported by the Belgian Federal Government "Service des Affaires Scientifiques, Techniques et Culturelles (SSTC)" in the framework of the "Pôle d'Attraction Interuniversitaire

en Chimie Supramoléculaire et Catalyse Supramoléculaire (PAI 5/3)", the Belgian National Fund for Scientific Research (FNRS/FRFC), and by the Directorate of General Research of the EC, RTN NANOCHANNEL (Grant No. HPRN-CT-2002-00323). J.C. is an FNRS research associate. Part of the calculations has been performed at the Interuniversity Scientific Computing Facility (ISCF) installed at the "Facultés Universitaires Notre-Dame de la Paix" (FUNDP, Namur, Belgium), which is supported by FNRS/FRFC and the "Loterie Nationale" under the convention no. 2.4578.02. The work in Alicante is supported by the project CTQ2004-06519/BQU ("Ministerio de Educación y Ciencia" of Spain) and by the "Vicerrectorado de Investigación" of the University of Alicante (VIGROB2004-36). We thank Prof. A. Karpfen (Universität Wien, Austria) for his critical reading of the manuscript.

References

(1) Karpfen, A.; Choi, C. H.; Kertesz, M. *J. Phys. Chem. A* **1997**, *101*, 7426.

(2) Tsuzuki, S.; Uchimaru, T.; Matsumura, K.; Mikami, M.; Tanabe, K. *J. Chem. Phys.* **1999**, *110*, 2858.

(3) Göller, A.; Grummt, U.-W. *Chem. Phys. Lett.* **2000**, *321*, 399.

(4) Pan, J.-F.; Chua, S.-J.; Huang, W. *Thin Solid Films* **2000**, *363*, 1.

(5) Arulmozhiraja, S.; Fujii, T. *J. Chem. Phys.* **2001**, *115*, 10589.

(6) Grein, F. *J. Phys. Chem. A* **2002**, *106*, 3823.

(7) Grein, F. *J. Mol. Struct. (THEOCHEM)* **2003**, *624*, 23.

(8) Grein, F. *Theor. Chem. Acc.* **2003**, *109*, 274.

(9) Salaneck, W. R.; Inganäs, O.; Nilsson, J.-O.; Österholm, J.-E.; Thémans, B.; Brédas, J. L. *Synth. Metals* **1989**, *28*, 451.

(10) Zhang, H.; Yang, B.; Zheng, Y.; Yang, G.; Ye, L.; Ma, Y.; Chen, X. *J. Phys. Chem. B* **2004**, *108*, 9571.

(11) Gierschner, J.; Lüer, L.; Oelkrug, D.; Musluoglu, E.; Behnisch, B.; Hanack, M. *Adv. Mater.* **2000**, *12*, 757.

(12) Beljonne, D.; Shuai, Z.; Pourtois, G.; Brédas, J. L. *J. Phys. Chem. A* **2001**, *105*, 3899.

(13) Gierschner, J.; Mack, H.-G.; Lüer, L.; Oelkurg, D. *J. Chem. Phys.* **2002**, *116*, 8596.

(14) Jaime, C.; Font, J. *J. Mol. Struct.* **1989**, *195*, 103.

(15) Cheung, D. L.; Clark, S. J.; Wilson, M. R. *Phys. Rev. E* **2002**, *65*, 051709.

(16) Carreira, L. A.; Towns, T. G. *J. Mol. Struct.* **1977**, *41*, 1.

(17) Almenningen, A.; Bastiansen, O.; Fernholt, L.; Cyvin, B. N.; Cyvin, S. J.; Samdal, S. *J. Mol. Struct.* **1985**, *128*, 59.

(18) Bastiansen, O.; Samdal, S. *J. Mol. Struct.* **1985**, *128*, 115.

(19) Curtiss, L. A.; Raghavachari, K. In *Encyclopedia of Computational Chemistry*; von Ragué Schleyer, P., Ed.; Wiley: New York, 1998; p 1104.

(20) Raghavachari, K.; Curtiss, L. A. In *Quantum Mechanical Prediction of Thermochemical Data*; Cioslowski, J., Ed.; Kluwer: Dordrecht, 2001; p 67.

(21) Császár, A. G.; Allen, W. D.; Schaefer, H. F. *J. Chem. Phys.* **1998**, *108*, 9751.

(22) Tarczay, G.; Császár, A. G.; Klopper, W.; Szalay, V.; Allen, W. D.; Schaefer, H. F. *J. Chem. Phys.* **1999**, *110*, 11971.

(23) Tschumper, G. S. *J. Chem. Phys.* **2001**, *114*, 225.

(24) Tschumper, G. S.; Leininger, M. L.; Hoffman, B. C.; Valeev, E. F.; Schaefer, H. F.; Quack, M. *J. Chem. Phys.* **2002**, *116*, 690.

(25) Kahn, K.; Bruice, T. C. *Theor. Chem. Acc.* **2004**, *111*, 18.

(26) Martin, J. M. L.; De Oliveira, G. *J. Chem. Phys.* **1999**, *111*, 1843.

(27) Martin, J. M. L.; Parthiban, S. In *Quantum Mechanical Prediction of Thermochemical Data*; Cioslowski, J., Ed.; Kluwer: Dordrecht, 2001; p 31.

(28) Boese, A. D.; Oren, M.; Atasoylu, O.; Martin, J. M. L.; Kállay, M.; Gauss, J. *J. Chem. Phys.* **2004**, *120*, 4129.

(29) Tajti, A.; Szalay, P. G.; Császár, A. G.; Kállay, M. Gauss, J.; Valeev, E. F.; Howers, B. A.; Vázquez, J.; Stanton, J. F. *J. Chem. Phys.* **2004**, *121*, 11599.

(30) Hohenberg, P.; Kohn, W. *Phys. Rev. B* **1964**, *136*, 864.

(31) Kohn, W.; Sham, L. J. *Phys. Rev. A* **1965**, *140*, 1133.

(32) Lieb, E. *Int. J. Quantum Chem.* **1983**, *24*, 243.

(33) Koch, H.; Holthausen, M. C. *A Chemist's Guide to Density Functional Theory*; Wiley-VCH: Weinheim, 2000.

(34) Sancho-García, J. C.; Pérez-Jiménez, A. J.; Moscardó, F. *J. Phys. Chem. A* **2001**, *105*, 11541.

(35) Sancho-García, J. C.; Brédas, J. L.; Cornil, J. *Chem. Phys. Lett.* **2003**, *377*, 63.

(36) Sancho-García, J. C.; Cornil, J. *J. Chem. Phys.* **2004**, *121*, 3096.

(37) Sancho-García, J. C.; Pérez-Jiménez, A. J.; Pérez-Jordá, J. M.; Moscardó, F. *Mol. Phys.* **2001**, *99*, 47.

(38) Sancho-García, J. C.; Pérez-Jiménez, A. J.; Pérez-Jordá, J. M.; Moscardó, F. *Chem. Phys. Lett.* **2001**, *342*, 452.

(39) Sancho-García, J. C.; Pérez-Jiménez, A. J.; Pérez-Jordá, J. M.; Moscardó, F. *J. Chem. Phys.* **2001**, *115*, 3698.

(40) Sancho-García, J. C.; Pérez-Jiménez, A. J. *J. Phys. B: At., Mol. Opt. Phys.* **2002**, *35*, 1509.

(41) Sancho-García, J. C.; Pérez-Jiménez, A. J. *J. Chem. Phys.* **2003**, *119*, 5121.

(42) Sancho-García, J. C.; Pérez-Jiménez, A. J. *Recent Res. Dev. Chem. Phys.* **2004**, *5*, 157.

(43) Goodson, D. Z. *J. Chem. Phys.* **2002**, *116*, 6948.

(44) Császár, A. G.; Leininger, M. L. *J. Chem. Phys.* **2001**, *114*, 5491.

(45) Dunning, T. H.; Peterson, K. A.; Woon, D. E. In *Encyclopedia of Computational Chemistry*; von Ragué Schleyer, P., Ed.; Wiley: New York, 1998; p 88.

(46) Parthiban, S.; Martin, J. M. L. *J. Chem. Phys.* **2001**, *114*, 6014.

(47) Parthiban, S.; Martin, J. M. L. *J. Chem. Phys.* **2001**, *115*, 2051.

(48) Halkier, A.; Helgaker, T.; Jørgensen, P.; Klopper, W.; Koch, H.; Olsen, J.; Wilson, A. K. *Chem. Phys. Lett.* **1998**, *286*, 243.

(49) Klopper, W.; Bak, K. L.; Jørgensen, P.; Olsen, J.; Helgaker, T. *J. Phys. B: At. Mol. Opt. Phys.* **1999**, *32*, R103.

(50) Varandas, A. J. C. *J. Chem. Phys.* **2000**, *113*, 8880.

(51) Haaland, P. D.; Pachter, R.; Adams, W. W. *Polymer* **1994**, *35*, 300.

(52) Császár, A. G.; Szalay, V.; Senent, M. L. *J. Chem. Phys.* **2004**, *120*, 1203.

(53) Lee, T. J.; Taylor, P. R. *Int. J. Quantum Chem. Symp*. **1989**, *23*, 199.

(54) Lee, T. J.; Scuseria, G. E. In *Quantum Mechanical Electronic Structure Calculations with Chemical Accuracy*; Langhoff, S. R., Ed.; Kluwer: Dordrecht, 1995; p 47.

(55) Lee, T. J. *Chem. Phys. Lett.* **2003**, *372*, 362.

(56) Pittner, J. *J. Chem. Phys.* **2003**, *118*, 10876.

(57) Rubio, M.; Merchán, M.; Ortí, E. *Theor. Chim. Acta* **1995**, *91*, 17.

(58) Gaussian 98, Revision A.11, Frisch, M. J.; Trucks, G. W.; Schlegel, H. B.; Scuseria, G. E.; Robb, M. A.; Cheeseman, J. R.; Zakrzewski, V. G.; Montgomery, J. A.; Stratmann, R. E.; Burant, J. C.; Dapprich, S.; Millam, J. M.; Daniels, A. D.; Kudin, K.; Strain, M. C.; Farkas, O.; Tomasi, J.; Barone, V.; Cossi, M.; Cammi, R.; Mennucci, B.; Pomelli, C.; Adamo, C.; Clifford, S.; Ochterski, J.; Petersson, J. A.; Ayala, P. Y.; Cui, Q.; Morokuma, K.; Salvador, P.; Dannenberg, J. J.; Malick, D. K.; Rabuck, A. D.; Raghavachari, K.; Foresman, J. B.; Cioslowski, J.; Ortiz, J. V.; Baboul, A. G.; Stefanov, B. B.; Liu, G.; Liashenko, A.; Piskorz, P.; Komaromi, I.; Gomperts, R.; Martin, R. L.; Fox, D. J.; Keith, T.; Al-Laham, M. A.; Peng, C. Y.; Nanayakkara, A.; Gonzalez, C.; Challacombe, M.; Gill, P. M. W.; Johnson, B. G.; Chen, W.; Wong, M. W.; Andres, J. L.; Head-Gordon, M.; Replogle, E. S.; Pople, J. A.; Gaussian, Inc., Pittsburgh, PA, 2002.

(59) Gaussian 03, Revision B.04, Frisch, M. J.; Trucks, G. W.; Schlegel, H. B.; Scuseria, G. E.; Robb, M. A.; Cheeseman, J. R.; Montgomery, Jr., J. A.; Vreven, T.; Kudin, K. N.; Burant, J. C.; Millam, J. M.; Iyengar, S. S.; Tomasi, J.; Barone, V.; Mennucci, B.; Cossi, M.; Scalmani, G.; Rega, N.; Petersson, G. A.; Nakatsuji, H.; Hada, M.; Ehara, M.; Toyota, K.; Fukuda, R.; Hasegawa, J.; Ishida, M.; Nakajima, T.; Honda, Y.; Kitao, O.; Nakai, H.; Klene, M.; Li, X.; Knox, J. E.; Hratchian, H. P.; Cross, J. B.; Bakken, V.; Adamo, C.; Jaramillo, J.; Gomperts, R.; Stratmann, R. E.; Yazyev, O.; Austin, A. J.; Cammi, R.; Pomelli, C.; Ochterski, J. W.; Ayala, P. Y.; Morokuma, K.; Voth, G. A.; Salvador, P.; Dannenberg, J. J.; Zakrzewski, V. G.; Dapprich, S.; Daniels, A. D.; Strain, M. C.; Farkas, O.; Malick, D. K.; Rabuck, A. D.; Raghavachari, K.; Foresman, J. B.; Ortiz, J. V.; Cui, Q.; Baboul, A. G.; Clifford, S.; Cioslowski, J.; Stefanov, B. B.; Liu, G.; Liashenko, A.; Piskorz, P.; Komaromi, I.; Martin, R. L.; Fox, D. J.; Keith, T.; Al-Laham, M. A.; Peng, C. Y.; Nanayakkara, A.; Challacombe, M.; Gill, P. M. W.; Johnson, B.; Chen, W.; Wong, M. W.; Gonzalez, C.; Pople, J. A. Gaussian, Inc., Wallingford CT, 2004.

(60) Becke, A. D. *J. Chem. Phys.* **1993**, *98*, 5648.

(61) Oberhammer, H. *J. Comput. Chem.* **1998**, *19*, 123.

(62) Lee, S. Y. *Korean Bull. Chem. Soc.* **1998**, *19*, 93.

(63) Furuya, K.; Torii, H.; Furukawa, Y.; Tasumi, M. *J. Mol. Struct. (THEOCHEM)* **1998**, *424*, 225.

(64) Martin, J. M. L. In *Density Functional Theory: a Bridge between Chemistry and Physics*; Geerlings, P., De Proft, F., Langenaeker, W., Eds.; VUB University Press: Brussels, 1999; p 111.

(65) Lynch, B. J.; Zhao, Y.; Truhlar, D. G. *J. Phys. Chem. A* **2003**, *107*, 1384.

(66) Boese, A. D.; Martin, J. M. L.; Handy, N. C. *J. Chem. Phys.* **2003**, *119*, 3005.

(67) Swart, M.; Snijders, J. G. *Theor. Chem. Acc.* **2003**, *110*, 34.

(68) Wang, N. X.; Wilson, A. K. *J. Chem. Phys.* **2004**, *121*, 7632.

(69) Chuang, Y.-Y.; Truhlar, D. G. *J. Phys. Chem. A* **1999**, *103*, 691.

(70) Halkier, A.; Helgaker, T.; Klopper, W.; Jorgensen, P.; Császár, A. G. *Chem. Phys. Lett.* **1999**, *310*, 385.

(71) Dorofeeva, O. V.; Moiseeva, N. F.; Yungman, V. S.; Novikov, V. P. *Thermochim. Acta* **2001**, *374*, 7.

(72) Feller, D.; Peterson, K. A.; de Jong, W. A.; Dixon, D. A. *J. Chem. Phys.* **2003**, *118*, 3510.

(73) Feller, D.; Dixon, D. A.; Francisco, J. S. *J. Phys. Chem. A* **2003**, *107*, 1604.

(74) Keeny, J. P.; Allen, W. D.; Schaefer, H. F. *J. Chem. Phys.* **2003**, *118*, 7353.

(75) Feller, D.; Dixon, D. A. *J. Phys. Chem. A* **2003**, *107*, 9641.

(76) Feller, D.; Dixon, D. A. *J. Phys. Chem. A* **2003**, *107*, 10419.

(77) Halpern, A. M.; Glendening, E. D. *J. Chem. Phys.* **2003**, *119*, 11186.

(78) Goodson, D. Z. *Int. J. Quantum Chem.* **2003**, *92*, 35.

(79) Feller, D. *J. Chem. Phys.* **1992**, *96*, 6104.

(80) Peterson, K. A.; Woon, D. E.; Dunning, T. H. *J. Chem. Phys.* **1994**, *100*, 7410.

(81) Martin, J. M. L. *Chem. Phys. Lett.* **1996**, *259*, 669.

(82) Peterson, K. A.; Dunning, T. H. *J. Chem. Phys.* **2002**, *117*, 10548.

(83) Woon, D. E.; Dunning, T. H. *J. Chem. Phys.* **1995**, *103*, 4572.

(84) The Extensible Computational Chemistry Environment Basis Set Database, Version 02/25/04, as developed and distributed by the Molecular Science Computing Facility, Environmental and Molecular Sciences Laboratory which is part of the Pacific Northwest Laboratory, P.O. Box 999, Richland, WA 99352, U.S.A., and funded by the U.S. Department of Energy. The Pacific Northwest Laboratory is a multiprogram laboratory operated by Battelle Memorial Institute for the U.S. Department of Energy under contract DE-AC06-76RLO 1830. Contact David Feller or Karen Schuchardt for further information.

(85) Mintz, B.; Lennox, K. P.; Wilson, A. K. *J. Chem. Phys.* **2004**, *121*, 5629.

(86) Schwenke, D. W. *J. Chem. Phys.* **2005**, *122*, 014107.

(87) Klopper, W. *Mol. Phys.* **2001**, *99*, 481.

(88) Klopper, W.; Noga, J.; Koch, H.; Helgaker, T. *Theor. Chim. Acta* **1997**, *97*, 164.

(89) Helgaker, T.; Ruden, T. A.; Jørgensen, P.; Olsen, J.; Klopper, W. *J. Phys. Org. Chem.* **2004**, *17*, 913.

(90) Sancho-García, J. C.; Pérez-Jiménez, A. J. *Chem. Phys. Lett.* **2000**, *318*, 649.

(91) Gauss, J. In *Encyclopedia of Computational Chemistry*; von Ragué Schleyer; P., Ed.; Wiley: New York, 1998; p 615.

(92) Sancho-García, J. C.; Pittner, J.; Cársky, P.; Hubac, I. *J. Chem. Phys.* **2000**, *112*, 8785.

(93) Partridge, H. In *Encyclopedia of Computational Chemistry*; von Ragué Schleyer, P., Ed.; Wiley: New York, 1998; p 581.

(94) Kahn, K.; Bruice, T. *Chem. Phys. Chem.* **2005**, *6*, 487.

CT0500242

JCTC Journal of Chemical Theory and Computation

Density-Functional-Based Determination of Vibrational Polarizabilities in Molecules within the Double-Harmonic Approximation: Derivation and Application

Mark R. Pederson,*,† Tunna Baruah,†,‡ Philip B. Allen,§ and Christian Schmidt§

Center for Computational Materials Science, Code 6390, Naval Research Laboratory, Washington, DC 20375, Department of Electrical and Computer Engineering, Howard University, Washington, DC 20059, and Department of Physics and Astronomy, State University of New York, Stony Brook, New York 11794-3800

Received March 9, 2005

Abstract: We present a nonperturbative derivation for the primary contribution to the vibrational polarizability for molecules, clusters, and other finite systems. Using a double-harmonic approximation and a finite-field approach the vibrational polarizability is calculated within the generalized gradient approximation to the density functional theory for a variety of molecules and clusters. The agreement between theory and experiment is quite good. The results show that for small ionic molecules and clusters, inclusion of the vibrational polarizability is necessary to achieve agreement with experiment.

I. Introduction

Materials with high dielectric constants have many important technological applications. Predicting the *total* second-order molecular polarizability is one capability that is required for the computational design of materials with high dielectric constants. The second largest contribution to the static second-order polarizability tensor is usually due to field-induced atomic relaxation. As the effect is of interest to several fields of research, a common terminology is lacking. This effect has been referred to as the displacement-, atomic-, nuclear-, relaxation-, or vibrational polarizability. Here we adopt the latter term and determine this effect within the double harmonic approximation.[1−4] For an in-depth review of recent efforts related to many aspects of polarizability calculations the interested reader is especially referred to ref 1. As discussed below, this effect is governed by the dynamic effective charge tensor which is known to account for infrared intensities of vibrational modes in molecules and clusters. The goal of this paper is to provide a database of calculations on the vibrational polarizability on small, medium, and large molecules. In doing so, we hope to show that DFT provides an excellent and efficient means for identifying molecules for which the vibrational polarizability may be important and worthy of study within higher level quantum mechanical treatments. Also through these examples we compare to other calculations and experiment and attempt to identify some of the other competing factors that affect the total polarizability of a molecule. Also, through comparison between DFT and HF we identify some cases where reasonably large deviations between the two approaches appear. We note that there has been a significant amount of work aimed at in-depth studies of polarizabilities and vibrational polarizabilities on particular molecules. These careful studies have examined the accuracy as a function of basis sets and level of correlation and have been largely focused on conventional (Hartree−Fock and beyond) quantum-chemistry approaches rather than density-functional approaches.[5−7]

The dynamic effective charge tensor describes how the total dipole moment of a molecule or other finite system changes due to an atomic displacement. For a simple dipole consisting of two point charges $\pm Q$, the change of the dipole per unit change of the separation is just Q. For crystals, the local dipole is not necessarily a well-defined notion, and effective charge tensors come in multiple forms.[8] However, the lowest nonzero moment of a finite system is a well-

* Corresponding author e-mail: mark.pederson@nrl.navy.mil.
† Naval Research Laboratory.
‡ Howard University.
§ State University of New York.

10.1021/ct050061t CCC: $30.25
Published on Web 06/03/2005

defined quantity. For a neutral molecule with N atoms, both the electrical dipole moment $\vec{p}$ and the derivative of the dipole moment with respect to the ith atomic position $\vec{u}_i$ are well defined. Only the latter quantity is uniquely defined for a charged molecule. These derivatives may be expressed as a $3 \times 3N$ tensor $\mathbf{Z}$ which has units of charge and is written

$$Z_{\alpha,i\mu} = \partial p_\alpha / \partial u_{i\mu} \tag{1}$$

This tensor is also sometimes called the "polar tensor"[9], and it is used for the calculation of the infrared intensity.[9−11] The infrared intensities are also related to the vibrational component of the *dc* molecular polarizability,[12] and a simple proof of this is included below.

By vibrational polarizability, we refer to the following physics. When a molecule is placed in a static electric field, it can lower its energy through several mechanisms. First, the electronic clouds rearrange themselves in response to the field which leads to an induced electronic dipole moment given by $p_{\mathrm{el},x} = \Sigma_y \alpha_{\mathrm{el},xy} E_y$. This is usually the largest linear effect. Second, this induced dipole moment is further modified since the atomic positions rearrange themselves in response to the forces caused by the direct application of a field and the subsequent electronic rearrangement. The tensor that describes the portion of the induced dipole moment due to atomic rearrangement is what we refer to as the double harmonic vibrational polarizability.

To concentrate on effects due to vibrational polarizability, we ignore molecular rotation and assume the molecule to be oriented in the lab frame. Equivalently, we work in a frame which is tied to the molecule, so that there is a fixed dipole moment. The polarizability α is then a 3×3 tensor which reduces to a scalar for symmetrical molecules such as CH_4 or SF_6. The molecular vibrations within the harmonic approximation correspond to the classical normal modes of a coupled system of oscillators

$$M_i \frac{\mathrm{d}^2 u_{i\mu}}{\mathrm{d}t^2} = -\sum_{j\nu} K_{i\mu,j\nu} u_{j\nu} \tag{2}$$

where the $3N \times 3N$ force constant tensor K is defined as

$$K_{i\mu,j\nu} = \frac{\partial^2 \mathcal{E}}{\partial u_{i\mu} \partial u_{j,\nu}} \tag{3}$$

and $\mathcal{E}$ is the total energy of the molecule at zero field.

The dipole moment $\vec{p}$ is a first derivative of the energy ($\mathcal{E}$), and the dynamical charge tensor and the electronic polarizability tensor are second partial derivatives given by

$$p_\alpha = -\partial \mathcal{E} / \partial E_\alpha \tag{4}$$

$$Z_{\alpha,i\mu} = -\partial^2 \mathcal{E} / \partial E_\alpha \partial u_{i\mu} = \partial F_{i\mu} / \partial E_\alpha \tag{5}$$

$$\alpha_{\mathrm{el},\alpha\beta} = -\partial^2 \mathcal{E} / \partial E_\alpha \partial E_\beta \tag{6}$$

In eqs 4−6, the electronic degrees of freedom must be relaxed in response to changes of the independent variables ($\vec{E}$, $\vec{u}_1$, ..., $\vec{u}_N$), and the derivatives are evaluated at zero field and displacement ($\vec{E} = \vec{u}_i = 0$). Equation 5 also shows that the dynamical charge tensor determines how the Hellmann−Feynman force ($F_{i\mu} = -\partial \mathcal{E} / \partial u_{i\mu}$) changes due to the application of an external electric field. As discussed in ref 11, the relationship between the dynamic effective charge tensor and the derivative of the Hellmann−Feynman force is both instructive and optimal for efficient determination of infrared and Raman intensities.

Now the total energy of the molecule may be expanded as a Taylor series in powers of both the atomic displacements and applied electric fields according to

$$\mathcal{E} = \mathcal{E}_0 - \vec{p}\cdot\vec{E} - \frac{1}{2}\vec{E}\cdot\alpha_{\mathrm{el}}\cdot\vec{E} - \vec{E}\cdot\mathrm{Z}\cdot\mathbf{u} + \frac{1}{2}\mathbf{u}\cdot\mathrm{K}\cdot\mathbf{u} \tag{7}$$

In the above equation $\vec{p}$ and α are the zero-field values of the dipole moment and polarizability, respectively. The tensor notation is fairly obvious except perhaps for the asymmetrical tensor Z whose transpose Z^{T} is defined by

$$\vec{E}\cdot\mathrm{Z}\cdot\mathbf{u} = \mathbf{u}\cdot\mathrm{Z}^{\mathrm{T}}\cdot\vec{E} \tag{8}$$

Now if a static external field $\vec{E}$ is applied, the atomic coordinates $\mathbf{u}$ will relax to new positions to minimize the energy according to

$$\mathbf{u} = \mathrm{K}^{-1}\cdot\mathrm{Z}^{\mathrm{T}}\cdot\vec{E} \tag{9}$$

The force-constant matrix K operates in the $3N$-dimensional displacement space, which can be divided into two subspaces: the null space (spanned by the translational and rotational degrees of freedom ($L = 6$ in general $L = 5$ for a linear molecule) and the $3N-L$ dimension space that is orthogonal to it. The 3-vector $\mathrm{Z}\cdot\mathbf{u}$ is the displacive electrical dipole caused by the displacement $\mathbf{u}$. It clearly vanishes when $\mathbf{u}$ lies in the null space. Taking the gradient of eq 9 by $\mathbf{u}$, the new equilibrium displacement in an external field is given by $\mathrm{K}\cdot\mathbf{u} - \mathrm{Z}^{\mathrm{T}}\cdot\mathbf{u} = 0$. This $3N$-vector lies in the $3N-L$-dimensional positive space, and the force constant matrix can be inverted in this space, giving for the induced displacement the $3N-L$-vector. The corresponding energy of the relaxed molecule is then determined to be

$$\mathcal{E} = \mathcal{E}_0 - \vec{p}\cdot\vec{E} - \frac{1}{2}\vec{E}\cdot[\alpha_{\mathrm{el}} + \alpha_{\mathrm{vib}}]\cdot\vec{E} \tag{10}$$

In the above, the vibrational part of the polarizability is given by

$$\alpha_{\mathrm{vib}} = \mathrm{Z}\cdot\mathrm{K}^{-1}\cdot\mathrm{Z}^{\mathrm{T}} \tag{11}$$

In fully indexed Cartesian form, the polarizability matrix is

$$\alpha_{\mathrm{vib},\alpha\beta} = \sum_{i\mu,j\nu} Z_{\alpha,i\mu} (K^{-1})_{i\mu,j\nu} Z^{\mathrm{T}}_{j\nu,\beta} \tag{12}$$

While the above expression clearly exhibits the isotopic independence of this part of the polarizability tensor, a simpler expression, directly comparable to experimental observables, is possible by rewriting this energy in terms of the normal modes of vibration. Let $|\upsilon\rangle$ denote the eigenvector and ω_υ the corresponding eigenfrequency, which satisfies the Newtonian equations

$$\mathrm{K}|\upsilon\rangle = \omega_\upsilon{}^2 \mathrm{M}|\upsilon\rangle \tag{13}$$

where M is the mass tensor which in the atom displacement basis ($i\mu$) is

$$M_{i\mu,j\nu} = M_i \delta_{ij} \delta_{\mu\nu} \tag{14}$$

The orthogonality and completeness relations are

$$\langle v|\mathrm{M}|v'\rangle = \delta_{vv'} \tag{15}$$

$$\sum_v |v\rangle\langle v| = \mathrm{M}^{-1} \tag{16}$$

The force constant matrix can be written as

$$\mathrm{K} = \sum_v \mathrm{M}|v\rangle\, \omega_v^{\,2}\, \langle v|\mathrm{M} \tag{17}$$

$$\mathrm{K}^{-1} = \sum_v |v\rangle\, \omega_v^{\,-2}\, \langle v| \tag{18}$$

The effective charge tensor can now be written in the eigenvector basis as the charge vector for each normal mode

$$Z_{\beta,v} = \hat{\beta}\cdot\mathrm{Z}|v\rangle \tag{19}$$

Then the vibrational polarizability can be written as a sum of contributions from the normal modes

$$\alpha_{\mathrm{vib},\alpha\beta} = \sum_v Z_{\alpha,v} \omega_v^{\,-2} Z^{\mathrm{T}}_{v,\beta} \tag{20}$$

The above expression is easier to work with than eq 12 since it is clear that the five or six zero-frequency modes are to be excluded in the sum. While both eqs 12 and 20 give the same answer, it is necessary to invert within a $3N-L$ dimensional subspace when working with eq 12. However, it is also worthwhile noting that, in principle, eq 20 allows one to determine the double-harmonic vibrational polarizability from *measured* infrared spectra. Equation 12 is not directly useful for extracting second-harmonic vibrational polarizabilities from an experiment.

This equation is a generalization of a known relation[12] between infrared intensities and static polarizability. In the past, this equation has been used to determine vibrational polarizabilities from experimental IR data and from calculations.[13] We include our derivation here because it appears to be rather simple in comparison to previous derivations that appear in the literature. Equation 20 follows immediately from eq 17.29 of Born and Huang.[14] It has also been derived by Flytzanis.[15] Probably the earliest modern discussion of vibrational polarizabilities using quantum-mechanical derivations can be found in refs 16 and 17 where applications to $CHCl_3$ and CHF_3 are discussed and the above formula is derived within a sum over states method within the clamped nucleus approximation. Equations 1 and A5 of ref 16b lead to our eq 20. However, as noted in refs 16 and 17, one of the earliest discussions dates back to 1924.[18]

In addition to the interaction discussed above, there are other smaller vibrational effects that modify the polarizability of a molecule. The presence of the field modifies the spring constant matrix which changes the zero-point energy of the molecule. Also, the occurrence of anharmonicity, both diagonal and off-diagonal, leads to further corrections. We are unaware of discussions on the role of off-diagonal anharmonicity, but discussion of the zero-point effect and diagonal anharmonicity may be found in ref 19. In the notation of the work of Marti and Bishop, the above term is equivalent to $[\mu^2]^{0,0}$ in their paper.

II. Computational Details

The calculations presented below have been performed using the NRLMOL suite of density-functional-based cluster codes.[20] The Perdew-Burke-Ernzerhof (PBE) energy functional has been used in all calculations.[21] The Kohn−Sham equations are solved self-consistently for each electron in the problem. Then the HF forces are calculated, and the geometries are updated using standard force optimization methods. Geometries were considered converged when the force on each atom fell below 0.001 Hartree/Bohr. However, for the Na and H_2O clusters we used a tighter force convergence criteria of 0.0001 Hartree/Bohr. The numerical integration mesh was also significantly more dense for our calculations on the water molecules. The method for generating the basis sets used for these calculations is discussed in ref 22. These basis sets have been specifically optimized for the PBE-GGA functional using a total-energy minimization criteria for the isolated atoms. A unique feature of these basis sets is that they satisfy a theorem, proved in ref 22, that the shortest-range Gaussian function must scale as $Z^{10/3}$ in order to have the same uniform accuracy in the total energy as a function of atomic charge. This feature aids in eliminating basis-set superposition error between weakly interacting atoms.[23] For an entirely typical example we discuss fluorine in some detail. For the fluorine atom we use 14-single Gaussian exponents that range between 1.2317422×10^5 and 0.11818616 Bohr^{-2}. These are contracted to 5 s-type functions, 4 p-type functions, and 3 d-type functions. In addition the r^2 s-types derived from the d-functions are also used in the basis set. This leads to a total of 35 basis functions on the fluorine atom. Two of the contracted s-states and one of the contracted p-states are chosen so the energy of the spin-unpolarized atom is the same as the result obtained from a calculation using 14 single Gaussian for the s and p manifolds. Basis sets and the unpublished geometries are available upon request. For further discussion about how the basis-set construction method used here performs relative to large single-Gaussian basis sets, the interested reader is referred to ref 11 which discusses the calculation of electronic polarizabilities, dipole moments, and vibrational frequencies, and infrared and Raman intensities for CH_4, H_2O, C_2H_2, C_2H_4, and C_2H_6. Once the optimized geometries[24−26] are obtained, the vibrational frequencies, eigenvectors, and dynamical charge tensors ($Z_{\alpha,i\mu}$) are determined using the method discussed in ref 11. We then use eq 20 to determine the vibrational component of the polarizability. As discussed in ref 11, the infrared and Raman spectra showed some sensitivity to the inclusion of longer range polarization functions. We have used such polarization functions for the calculations displayed in Table. 1.

For a few cases where agreement between PBE-GGA, Hartree−Fock (HF), and/or experiment seems uncharacteristic, we have performed Hartree−Fock calculations using

Table 1: Calculated and Experimental Vibrational Polarizabilities (Å^3) for Molecules[d]

	vibrational		electronic	
molecule	theory	expt	theory	expt
H_2O	0.04	0.04	1.57	1.45
$(H_2O)_2$	23.30		3.19	
$(H_2O)_3$	13.50		4.82	
$(H_2O)_5$	14.52		8.13	
NF_3	1.15	0.70	3.07	2.81
HCCH	0.48	0.45	3.56	3.40
CH_4	0.04	0.03	2.63	2.60
$TiCl_4$	2.04	>1.68	15.03	15.0
SF_6	2.29	2.29	5.15	4.49
SiF_4	2.09	1.75	3.72	3.32
HCN	0.21	0.14	2.62	2.59
H_3CNC	0.07		4.87	
H_3CCN	0.03	0.04	4.59	4.28
C_{60}@Kr[a]	0.55		83.3	
C_{60}	0.58	2.0	82.9	79 ± 4
Na_2	0.00		35.91	37.91−40.0[*]
Na_3	1.72		60.89	69.8[*]
Na_8	0.63		116.2	133.5[*]
NaF	0.29		2.71	
$(NaF)_2$	9.08		3.94	20.7 ± 3.1[*]
$(NaCl)_2$	8.94		13.06	23.4 ± 2.5[*]
Ti_8C_{12} [b]	3.72		56.40	
As@Ni_{12}@As_{20} [c]	4.56		140.86	

[a] Reference 24. [b] Reference 25. [c] Reference 26. [d] This is one-third of the trace of the polarizability tensor. Unless otherwise stated the experimental values are taken from ref 12. Experimental data for C_{60} is from refs 28−31 and references therein. For the pure sodium clusters, the experimental values are total polarizabilities (denoted with an *) which have been taken from refs 51, 52, and 54.

a new exact-exchange option that we have implemented into the NRLMOL code. Unless stated otherwise, these calculations have been performed using the default PBE-GGA basis sets at the PBE-GGA geometry. We have performed these calculations to eliminate the possibility that the deviation between the methods is due to an underlying numerical, geometrical, or basis-set completeness issue. For the Hartree−Fock calculations discussed here we have converged the total energy to 10^{-9} Hartree and used the same finite field approach as for the case of the PBE-GGA calculations.

III. Results

Table 1 presents calculations on several molecular systems which include both covalent, ionic bonding, and hydrogen bonding. It also include calculations on systems with both loosely and tightly bound electrons. We have calculated both the electronic and vibrational contributions to the polarizability tensor. Agreement is generally good.

Fullerene Molecule. The polarizability of the Fullerene molecules has been well studied both theoretically and experimentally.[27−31] Here we calculate the electronic polarizability to be 82.9 Å^3 which is in good agreement with one of the earliest density-functional calculations[27] of 83.5 Å^3. This earlier calculation used the same code, a slightly different version of DFT, slightly smaller basis sets, and geometries that were not as well converged.[27] The good agreement between the early and most recent calculations indicate that the electronic part of the neutral fullerene polarizability is rather robust, and the experimental polarizability[28−31] is known to be very close to this number as shown in Table 1 (79 ± 4). Within HF, Fowler, Lazzeretti, and Zanasi have calculated the electronic polarizability of the fullerene molecule to be 65.6 Å^3. Their method is an iterative AO-based version of the coupled HF procedure due to McWeeny and Diercksen.[33] Fowler et al. point out that their result (65.6 Å^3) is protected by the Hylleraas variation principle and is guaranteed to be a *lower bound* to the coupled HF value provided the unperturbed wave function is close enough to the HF ground state. More recently Perpete, Champagne, and Kirtman[34] have improved upon the earlier HF calculation by including vibrational contributions within the double-harmonic and "infinite optical frequency" (e.g. static field) approximation. Their vibrational contributions used DFT-based normal coordinates. In this work they find an electronic polarizability of 63.4 Å^3. Their calculated vibrational polarizability (0.78 Å^3) is in reasonably good agreement with the value obtained here (0.58 Å^3.) Most importantly, the uncertainty in calculated linear polarizabilities is at least as large as these numbers. Whitehouse and Buckingham[35] have also calculated the static polarizability of the C_{60} molecule as a function of basis set with the Hartree−Fock approximation. They have confirmed the earlier results showing a polarizability of 65.5 Å^3 for their largest basis sets. It appears that there are definitely deviations between HF and PBE-GGA for the linear polarizability of the C_{60} molecule.

Based on experiments, it has also been suggested that the polarizability due to lattice relaxation is 2 Å^3 (see ref 28) which is small but still four times larger than the value calculated here. In a recent letter Munn et al.[36] have suggested that the polarizability per fullerene molecule in a lattice may exhibit further enhancements over the isolated fullerene molecule and that the total polarizability associated with a fullerene molecule in a lattice is deduced to be closer to 89.9 Å^3. In ref 27 it has been shown that the polarizability of an anion would indeed increase relative to the neutral which lends some support to the their discussion.

The deviation could also be due to the lower T_h symmetry that occurs when the icosahedral C_{60} molecules are placed on a cubic lattice. Such a symmetry lowering would cause some of the optically silent G_u and H_u modes to split and partially fall into the IR active T_{1u} manifold which in turn could lead to additional vibrational polarizability. There will also be weak IR activity due to weak intermolecular vibrations activated by weakly broken translational symmetry.[37] Also included in Table 1 are the electronic and vibrational polarizabilities of a C_{60} molecule with an endohedral Kr atom. The addition of the Kr atom adds another infrared mode due to a rattling motion of Kr inside the C_{60} cage. The low-frequency Kr rattling mode is found to be at 88 cm^{-1}, but the IR intensity associated with this mode is 1000 times smaller than the four T_{1u} modes associated with the fullerene cage. Because of this the vibrational polarizabilities are unchanged due to the addition of an inert endohedral atom. More interesting, albeit beyond double-harmonic, polarization effects do appear in alkali-doped

fullerene molecules which have been shown to relax off-center,[38] create the potential for Jahn−Teller distortions,[38,39] and exhibit interesting polarization effects, within the molecule and when exposed to an external field. Temperature-dependent model calculations, based upon HF-based energetics of the rattling ion, of this effect have been investigated by Whitehouse and Buckingham.[35]

Acetylene. The acetylene molecule provides an interesting test case because the anisotropy of the polarizability tensor is reversed significantly by the inclusion of the vibrational terms. For example, in Å^3 the electronic and vibrational polarizability tensors have been measured to be (2.43, 2.43, 5.12) and (0.667, 0.667, 0.027), respectively. Density functional theory yields (2.96, 2.96, 4.78) and (0.71, 0.71, 0.030) Å^3 which is in reasonably good agreement with experiment. In ref 7, careful studies on the acetylene molecule have been performed as a function of basis set and level of correlation. They point out that their calculated vibrational polarizabilities are not very sensitive to either basis set choice or level of correlation. Russell and Spackman find an average vibrational polarizability of 0.41 Å^3 which is slightly less than the experimental polarizability of Gussoni (0.45 Å^3 and the PBE-GGA values of 0.48 Å^3 reported here.

Halogen Containing Ionic Molecules. Halogen containing compounds are known to exhibit high vibrational polarizabilities as would be expected since they make very good ionic systems.[16,17] We have performed calculations on NaF, Na_2F_2, Na_2Cl_2, SF_6, SiF_4, and $TiCl_4$. Of the molecules in this size regime listed in the large database of Gussoni, the latter three stand out as having very large vibrational contributions. The agreement between theory and experiment is in the neighborhood of 15% for these systems.

In a recent letter, Andrade et al.[40] have calculated the vibrational polarizability for NaF with HF. The calculated double-harmonic vibrational polarizability (labeled nuclear relaxation term in their work) is 0.35 Å^3 (HF) and in relatively good agreement with our PBE-GGA calculation of 0.29 Å^3. Andrade et al. find that higher levels of theory do not change their result significantly. However, agreement between HF and PBE-GGA is not good for the electronic polarizibility. They find an average electronic polarizability of 1.34 Å^3 which is in good agreement with the work of Pluta[41] (1.32 Å^3) but roughly half the size of what we have calculated for NaF. To eliminate the possibility that this deviation is due to the basis set employed here, we have repeated our PBE-GGA calculation (bond length is 1.950 Å) for NaF using a very large basis set. For fluorine, we have used 14-single s-Gaussians ($1.232 \times 10^5 \leq \alpha_i \leq 0.118$), 14-single p-Gaussians ($1.232 \times 10^5 \leq \alpha_i \leq 0.118$), and 6-single d-Gaussians ($10.03 \leq \alpha_i \leq 0.118$). For sodium, we have 14-single s-Gaussians ($2.515 \times 10^5 \leq \alpha_i \leq 0.0269$), 14-single p-Gaussians ($2.515 \times 10^5 \leq \alpha_i \leq 0.0269$), and 6-single d-Gaussians ($3.998 \leq \alpha_i \leq 0.0.0269$). We find transverse and longitudinal polarizabilities of 2.379 and 3.298 Å^3 leading to an isotropic electronic polarizability of 2.685 in good agreement with the answer obtained from our default-DFT basis sets in Table 1. We have also repeated a HF calculation for NaF using the same default-DFT basis set and for applied electric fields of 0.0001, 0.0002, 0.0004, 0.0008, and 0.0016 atomic units. We find longitudinal and transverse polarizabilities of 1.30 and 1.24 Å^3, respectively, leading to an average polarizability of 1.26 Å^3 which is slightly smaller than that of Pluta and Andrade and once again significantly smaller than our PBE-GGA result. Thus it appears that there is, again, a real difference between PBE-GGA and Hartree−Fock for the case of the NaF molecule.

While we have been unable to find experimental work on the NaF monomer, Guella et al.[42] have measured the polarizability for many alkali-halide dimers so we have performed calculations on some of these structures to make contact with experiment. Our calculated total values for $(NaF)_2$ and $(NaCl)_2$ polarizabilities are 13.12 and 22 Å^3 respectively. While the $(NaCl)_2$ is in good agreement with the $T = 1030$ K experimental value (23.4 ± 2.5 Å^3) a significantly large deviation is observed for the seemingly simpler case of $(NaF)_2$ which has a $T = 1221$ K experimental value of 20.7 ± 3.4 Å^3.

Isomeric Dependencies. Acetonitrile (CH_3CN) and methylisonitrile (CH_3NC) have the same chemical composition. However, the former has the two carbon atoms bound to one another, while the latter has the nitrogen bound to the methyl radical. This causes a 5% difference in the electronic polarizability and a factor of 2 difference in the vibrational polarizability. The source of the deviation in the vibrational polarizability is clearly due to changes in the spring constant matrix since eq 11 shows that changes of mass cannot perturb the vibrational contributions within the double harmonic approximation.[4] There is a 1-fold mode at 2269 cm^{-1} for acetonitrile that is reduced to 2149 cm^{-1} for methylisonitrile. In addition to a reduction in the vibrational frequency, the infrared intensity of the methylisonitrile is 2.57 compared to 0.227 in the case of acetonitrile. This mode accounts for about 75% of the difference in the vibrational polarizability. The large change in infrared intensity in this frequency range should be a clear indicator of methylisonitrile isomerization to acetonitrile at higher temperatures.

Sodium Clusters. In two recent papers[43] Blundell, Guet, and Zope and Kronik, Vasiliev, and Chelikowsky[44] have calculated the temperature dependence of polarizabilities in sodium clusters. They show that temperature effects enhance the apparent polarizability at 300 K. This temperature enhancement appears to account for most of the difference between experiment and the calculated electronic polarizabilities from many different theoretical calculations.[45−50] Our results show that the vibrational contribution to the polarizability is indeed small for the sodium clusters which supports the assertion that temperature effects are important in these systems.

To make contact with other works we note that Maroulis[6] has performed benchmark calculations on the Na_2 as a function of basis set and level of correlation. For Hartree−Fock (HF) his results are essentially converged as a function of basis set, and an average value of 40.35 Å^3 has been found. As noted by Maroulis, this value is larger than the DFT value of 35.91 Å^3. The experimental values range between 37.91[51,52] and 40.00[53,54] with the larger value corresponding to the more recent experimental work. According to the CRC, the small and large values are low- and high-temperature

values, respectively.[55] To ensure that the deviation is indeed a HF vs GGA-PBE we have repeated the HF calculation for the Na_2 polarizability with NRLMOL. Using default DFT basis sets and the PBE-GGA bond length, we find transverse and longitudinal polarizabilities of 32.8 Å^3 and 52.2 Å^3 at the PBE-GGA geometry in very good agreement with the large-basis-set calculations of Maroulis (34.07 Å^3 and 52.92 Å^3, respectively).

Weakly Bound Molecules. As mentioned in our discussion of fullerene molecules the vibrational polarizability between two weakly bound molecules could be enhanced if the weak intermolecular vibrations are IR active. As discussed in ref 56 the water dimer represents an extreme example of this case. As shown in Table 1, we find the electronic polarizability of this molecule (3.19 Å^3) to be approximately twice that of a water monomer. The electronic polarizabilities obtained for the water trimer and pentamer also show a linear scaling as a function of the number of molecules. This result is in good agreement with the work of Maroulis[5] (2.90 Å^3) and Eckart et al. (2.48 Å^3).[56] Maroulis[5] have carefully studied the electronic polarizability as a function of both basis set and level of correlation. The uncertainties due to these effects are at most 12.5% indicating that large deviations from these values must be due to other effects. Our calculated double-harmonic vibrational polarizability of 23.30 Å^3 is indeed a factor of 7 times larger than the electronic polarizability. Eckart et al. find this term to be even larger (39.2 Å^3) and further demonstrate that anharmonic corrections enhance the vibrational component of the dimer by an additional factor of 3. The large vibrational enhancement in polarizability in going from the monomer to dimer is indeed interesting. In particular, the scaling of this term as a function of system size is impossible to guess based upon the results of the monomer and dimer. It is reasonable to expect that this large result should be an upper limit since a dielectric medium that is coupled to an IR active mode should counteract the IR activity and thus the vibrational polarizability. So the presence of more water molecules should lead to a vibrational polarizability that is eventually sublinear in the total number of molecules. To partially address this point we have performed additional calculations on the trimer and pentamer. Our results show a decrease in the total vibrational polarizability in going from the dimer to the trimer and a flattening of the total vibrational polarizability for the pentamer. For the pentamer the ratio of the vibrational to electronic polarizability has decreased significantly from seven for the dimer to slightly less than two for the pentamer. Overall, these results show that weak intermolecular vibrations can enhance the vibrational polarizability over what is determined from intramolecular vibrations.

IV. Summary

We have used the PBE-GGA functional to calculate electronic polarizabilities and vibrational polarizabilities using a finite-field method and NRLMOL on a relatively large collection of small to intermediate size clusters and molecules. The double-harmonic approximation has been employed here which allows, in principle, direct comparison to experiment through accurate measurements of infrared spectra. We have compared our electronic and vibrational polarizabilities to experiment and other theoretical calculations. For the most part, the PBE-GGA vibrational polarizabilities are in good agreement with both experiment and the work here suggests that DFT will be a good computational tool for the study of vibrational polarizabilities of clusters and molecules especially for systems where where the vibrational polarizability is known to be large.

However, there are a few notable exceptions where the results exhibit rather large dependencies upon method. For the fullerene molecule, the vibrational polarizabilities, as calculated here and elsewhere within Hartree−Fock, are in relatively close agreement with one another but are a factor of 3−4 smaller than experiment. For the electronic polarizability, where experiment and PBE-GGA agree quite well, the HF result is significantly smaller. For NaF, Hartree−Fock (three different calculations) and PBE-GGA differ by a factor of 2 on the electronic polarizability but are within 17% for the vibrational polarizability. An experimental value for the electronic polarizability of NaF is unavailable. The combined PBE-GGA electronic and vibrational polarizability values for $(NaF)_2$ is significantly smaller than the experimental result; however, agreement between experiment and PBE-GGA returns for the isoelectronic $(NaCl)_2$ molecule.

Acknowledgment. The work was supported in part by NSF grants NIRT-0304122, HRD-0317607, ONR, and the HPCMO CHSSI program. We thank Drs. R. Zope, D. M. Bishop, and J. L. Feldman for helpful advice.

References

(1) For a recent survey on many aspects of polarizabilities in molecules and clusters, see: Computational aspects of electric polarizability calculations: Atoms, Molecules and Clusters. *J. Comput. Methods Sci. Eng.* **2004**, *4*(3 and 4); Ed. by G. Maroulis.

(2) Bishop, D. M. *J. Chem. Phys.* **1987**, *86*, 5613−5616.

(3) Bishop, D. M. *Rev. Mod. Phys.* **1990**, *62*, 343−374.

(4) Bishop, D. M.; Kirtman, B. *J. Chem. Phys.* **1991**, *95*, 2646−2658. Bishop, D. M.; Kirtman, B. *J. Chem. Phys.* **1992**, *97*, 5255−5256.

(5) Maroulis, G. *J. Chem. Phys.* **2000**, *113*, 1813−1820.

(6) Maroulis, G. *J. Chem. Phys.* **2004**, *121*, 10519−10524.

(7) Russell, A. J.; Spackman, M. A. *Mol. Phys.* **1996**, *88*, 1109−1136).

(8) Ghosez, Ph.; Michenaud, P.-P.; Gonze, X. *Phys. Rev. B* **1998**, *58*, 6224−6240.

(9) Biarge, J. F.; Herranz, J.; Morcillo, J. *An. R. Soc. Esp. Fix. Quim. A* **1961**, *57*, 81.

(10) Person, W. B.; Newton, J. H. *J. Chem. Phys.* **1974**, *61*, 1040−1049.

(11) Porezag, D.; Pederson, M. R. *Phys. Rev. B* **1996**, *54*, 7830−7836.

(12) Gussoni, M.; Rui, M.; Zerbi, G. *J. Mol. Struct.* **1998**, *447*, 163−215.

(13) Jug, K.; Chiodo, S.; Calaminici, P.; Avramopoulos, A.; Papadopoulos, M. G. *J. Phys. Chem. A* **2003**, *107*, 4172−4183.

(14) Born and Huang note that when a molecule is viewed as a collection of normal modes with a linear perturbation of the form $\Sigma_j a_j q_j$ that the energy decreases as $(1/2)\Sigma_j(a_j^2/\omega_j^2)$. In an actual molecule with an electric field the coupling constant a_j would be determined from the $\mathbf{E}\cdot(d\bar{p}/dq_j)$ which would also lead to eq 20 of this paper.

(15) Flytzanis, C. In *Quantum Electronics, a Treatise*; Rabin, H., Tang, C. L. Eds.; Academic: New York, 1975; Vol. 1 *Nonlinear Optics, Park A*, Chapter 2, pp 9−207.

(16) Bishop, D.; Cheung, L. M.; Buckingham, A. D. *Mol. Phys.* **1980**, *41*, 1225−1226. Bishop, D. *Mol. Phys.* **1981**, *42*, 1219−1232.

(17) Bishop, D. M.; Cheung, L. M. *J. Phys. Chem. Ref. Data* **1982**, *11*, 119−133.

(18) Ebert, L. *Z. Phys. Chem.* **1924**, *113*, 1−4.

(19) Marti, J.; Bishop, D. M. *J. Chem. Phys.* **1993**, *99*, 3860−3864.

(20) Pederson, M. R.; Jackson, K. A. *Phys. Rev. B* **1990**, *41*, 7453−7461. Jackson, K. A.; Pederson, M. R. *Phys. Rev. B* **1991**, *42*, 3276−3281. Pederson, M. R. *Phys. Stat. Solidi* **2000**, *217*, 197−218.

(21) Perdew, J. P.; Burke, K.; Ernzerhof, M. *Phys. Rev. Lett.* **1996**, *77*, 3865−3868.

(22) Porezag, D.; Pederson, M. R. *Phys. Rev. A* **1999**, *60*, 2840−2847.

(23) Patton, D. C.; Porezag, D. V.; Pederson, M. R. *Phys. Rev. B* **1997**, *55*, 7454−7459; Patton, D. C.; Pederson, M. R. *Int. J. Quantum Chem.* **1998**, *69*, 619−627.

(24) Baruah, T.; Pederson, M. R. To be published.

(25) Baruah, T.; Pederson, M. R.; Lyn, M. L.; Castleman, A. W., Jr. *Phys. Rev. A* **2002**, *66*, 053201−053206.

(26) Baruah, T.; Zope, R.; Richardson, S. L.; Pederson, M. R. *Phys. Rev. B* **2003**, *68*, 241404−241408 (R).

(27) Pederson, M. R.; Quong, A. A. *Phys. Rev. B* **1992**, *46*, 13584−13591.

(28) Eklund, P. C.; Rao, A. M.; Wang, Y.; Zhou, P.; Wang, K. A.; Holden, J. M.; Dresselhaus, M. S.; Dresselhaus, G. *Thin Solid Films* **1995**, *257*, 211−232.

(29) Bonin, K. D.; Kresin, V. V. *Electric-Dipole Polarizabilities in Atoms, Molecules and Clusters*; World Scientific: Singapore, 1997.

(30) Antoine, P.; Dugourd, Ph.; Rayane, D.; Benichou, E.; Broyer, M.; Chandezon, F.; Guet, C. *J. Chem. Phys.* **1999**, *110*, 9771−9772.

(31) Ballard, A.; Bonin, K.; Louderback, J. *J. Chem. Phys.* **2000**, *113*, 5732−5735.

(32) Fowler, P. W.; Lazzeretti, P.; Zanasi, R. *Chem. Phys. Lett.* **1990**, *165*, 79−86.

(33) McWeeny, R.; Diercksen, G. H. F. *J. Chem. Phys.* **1966**, *44*, 3554−3560.

(34) Perpete, E. A.; Champagne, B.; Kirtman, B. *Phys. Rev. B* **2000**, *61*, 13137−13143.

(35) Whitehouse, D. B.; Buckingham, A. D. *Chem. Phys. Lett.* **1993**, *207*, 332−337.

(36) Munn, R. W.; Petelenz, P. *Chem. Phys. Lett.* **2004**, *392*, 7−10.

(37) Horoyski, P. J.; Thewalt, M. L. W. *Phys. Rev. B* **1993**, *48*, 11466−11449. Huant, S.; Robet, J. B.; Chouteau, G.; Bernier, P.; Fabre, C.; Rassat, A. *Phys. Rev. Lett.* **1992**, *69*, 2666−2669.

(38) Schmidt, P. P.; Dunlap, B. I.; White, C. T. *J. Phys. Chem.* **1991**, *95*, 10537−10541. Dunlap, B. I.; Ballester, J. L.; Schmidt, P. P. *J. Phys. Chem.* **1992**, *96*, 9781−9787.

(39) Pederson, M. R.; Jackson, K. A.; Boyer, L. L. *Phys. Rev. B* **1992**, *45*, 6919−6922.

(40) Andrade, O. P.; Aragao, A.; Amaral, O. A. V.; Fonseca, T. L.; Castro, M. A. *Chem. Phys. Lett.* **2004**, *392*, 270−275.

(41) Pluta, T. *Mol. Phys.* **2001**, *99*, 1535−1547.

(42) Guella, T.; Miller, T. M.; Stockdale, J. A. D.; Bederson, B.; Vuskovic, L. *J. Chem. Phys.* **1991**, *94*, 6857−6861.

(43) Blundell, S. A.; Guet, C.; Zope, R. *Phys. Rev. Lett.* **2000**, *84*, 4826−4829.

(44) Kronik, L.; Vasiliev, I.; Chelikowsky, J. R. *Phys. Rev. B* **2000**, *62*, 9992−9995.

(45) Moullet, I.; Martins, J. L.; Reuse, F.; Buttet, J. *Phys. Rev. Lett.* **1990**, *65*, 476−479. *Phys. Rev. B* **1990**, *42*, 11598−11609.

(46) Guan, J.; Casida, M. E.; Koester, A. M.; Salahub, D. R. *Phys. Rev. B* **1995**, *52*, 2184−2200.

(47) Rubio, A.; Alonso, J. A.; Blase, X.; Balbas, L. C.; Louie, S. G. *Phys. Rev. Lett.* **1996**, *77*, 247−250.

(48) Pacheco, J. M.; Martins, J. L. *J. Chem. Phys.* **1997**, *106*, 6039−6044.

(49) Vasiliev, I.; Ogut, S.; Chelikowsky, J. R. *Phys. Rev. Lett.* **1999**, *82*, 1919−1922.

(50) Caliminici, P.; Jug, K.; Koester, A. M. *J. Chem. Phys.* **1999**, *111*, 4613−4620.

(51) Knight, W. D.; Clemenger, K.; de Heer, W. A.; Saunders, W. A. *Phys. Rev. B* **1985**, *31*, 2539−2540.

(52) Molof, R. W.; Schwartz, H. L.; Miller, T. M.; Bederson, B. *Phys. Rev. A* **1974**, *10*, 1131−1140.

(53) Antione, R.; Rayane, D.; Allouche, A. R.; Aubert-Frecon, M.; Benichou, E.; Dalby, F. W.; Dugourd, Ph.; Broyer, M. *J. Chem. Phys.* **1999**, *110*, 5568−5577.

(54) Tarnovsky, V.; Bunimovicz, M.; Vuskovic, L.; Stumpf, B.; Bederson, B. *J. Chem. Phys.* **1993**, *98*, 3894−3904.

(55) *CRC Handbook of Chemistry and Physics*, LLC 85th ed.; CRC Press: 2004−2005.

(56) Eckart, U.; Sadlej, A. *J. Mol. Phys.* **2001**, *99*, 735−743.

CT050061T

JCTC Journal of Chemical Theory and Computation

Iron(IV) Porphyrin Difluoride Does Not Exist: Implications for DFT Calculations on Heme Protein Reaction Pathways

Abhik Ghosh*,† and Peter R. Taylor*,‡

Department of Chemistry, University of Tromsø, N-9037 Tromsø, Norway, and Department of Chemistry, University of Warwick, Coventry CV4 7AL, United Kingdom

Received April 4, 2005

Abstract: DFT (B3LYP as well as a number of common exchange-correlation functionals) predicts a low-spin Fe(IV) ground state for $Fe(P)F_2$ (P = porphyrinato), whereas electrochemical evidence has apparently indicated an Fe(III) porphyrin π-cation radical formulation for such a species. Ab initio CASPT2 calculations favor a high-spin porphyrin π-cation radical as the ground state by a significant energetic margin, thus dramatically overturning the DFT results. In contrast, both DFT and CASPT2 calculations correctly indicate a true Mn(IV) ground state for $Mn(P)F_2$. The remarkable failure of DFT to correctly predict the metal- versus ligand-oxidized nature of $Fe(P)F_2$ may have significant ramifications for the theoretical modeling of heme protein reaction pathways where until now the performance of DFT has raised little concern.

Introduction

It is not often that the nonexistence of something makes an interesting story, but in this case we believe that it does. In a narrow sense, our main conclusion here is that difluoroiron porphyrins do not exist as ground-state Fe(IV) species.[1] However, the wider implications of our results *potentially* impact many theoretically derived insights into the reaction pathways of iron enzymes such as cytochrome P_{450}.[2] One such insight is that a particular heme protein-mediated oxidation may involve multiple electronic states of a high-valent iron (compound I) intermediate[3] or even multiple reactive oxygen species,[4] such as a compound I *and* an Fe(III) hydroperoxide. Clearly, it would be of interest to evaluate the energetics of the different conceivable reaction pathways by means of high-quality quantum chemical methods, and, indeed, DFT calculations have already resulted in significant progress in this area.[2b,3] Unfortunately, there has been little calibration of the quality of the DFT energetics results against more reliable methods such as CASPT2 and CCSD(T),[5] which should not be particularly surprising, given that any even moderately realistic models of heme protein intermediates are plainly beyond the reach of current implementations of high-level ab initio correlated methods. A key problem with DFT is that most, if not all, currently available functionals provide an unreliable description of the energetics of the low-lying spin states of open-shell transition-metal complexes. In particular, for high-valent transition-metal complexes,[6] DFT does not always correctly describe the relative energetics of metal- versus ligand-centered oxidation.[7] For example, for one-electron-oxidized five-coordinate iron(III) porphyrin derivatives, DFT unduly favors low-spin Fe(IV) oxidized states relative to high-spin Fe(III) porphyrin π-cation radical states.[7a]

To calibrate the performance of DFT vis-à-vis these problems, we have investigated the energetics of the low-lying states of the highly symmetric (D_{4h}) species, $Fe(P)F_2$ (P = porphyrinato), the point being to determine whether it is an Fe(IV) species or an Fe(III) porphyrin "π-cation" radical. While DFT calculations— regardless of the functional (for a number of common functionals tested)—prefer an S = 1 Fe(IV) ground state, electrochemical evidence[1a] suggests the latter description. The authors of a DFT study suggested that solvent effects such as hydrogen bonding interactions involving the axial fluorides might destabilize the Fe(IV) states in the electrochemical studies, favoring instead an Fe-

* Corresponding author e-mail: abhik@chem.uit.no (A.G.), P.R.Taylor@warwick.ac.uk (P.R.T.).

† University of Tromsø.

‡ University of Warwick.

10.1021/ct050086s CCC: $30.25
Published on Web 06/03/2005

Table 1. B3LYP, CASPT2(AS1), and CASPT2(AS2) Energies (eV) for Selected Low-Lying States of $Fe(P)F_2$, $Mn(P)F_2$, and $[Zn(P)]^+$[a]

		occupations								
		metal d				porphyrin		relative energy (eV)		
molecule; electronic configuration	S	d_{xy} (b_{2g})	d_{xz},d_{yz} (e_g)	d_{z2} (a_{1g})	d_{x2-y2} (b_{1g})	a_{1u}	a_{2u}	B3LYP	CASPT2 (AS1)	CASPT2 (AS2)
					$Fe(P)F_2$					
S = 1 Fe(IV); $d_{xy}^2(d_{xz}d_{yz})^2$	1	2	2	0	0	2	2	**0.00**	**0.00**	**0.00**
S = 2 Fe(IV); $d_{xy}^1(d_{xz}d_{yz})^2d_{x2-y2}^1$	2	1	2	0	1	2	2	0.95	0.57	0.47
S = 2 Fe(IV); $d_{xy}^1(d_{xz}d_{yz})^2d_{z2}^1$	2	1	2	1	0	2	2	1.07	1.01	
S = 5/2 Fe(III); a_{1u} radical; ferro	3	1	2	1	1	1	2	0.59	0.47	0.16
S = 5/2 Fe(III); a_{1u} radical; antiferro	2	1	2	1	1	1	2	0.59	0.47	
S = 5/2 Fe(III); a_{2u} radical; ferro	3	1	2	1	1	2	1	0.30	−0.31	−0.42
S = 5/2 Fe(III); a_{2u} radical; antiferro	2	1	2	1	1	2	1	0.35	−0.27	
					$Mn(P)F_2$					
S = 3/2 Mn(IV); $d_{xy}^1(d_{xz}d_{yz})^2$	3/2	1	2	0	0	2	2	**0.00**	**0.00**	**0.00**
S = 2 Mn(III); a_{1u} radical; ferro	5/2	1	2	0	1	1	2	1.02	1.31	1.19
S = 2 Mn(III); a_{1u} radical; antiferro	3/2	1	2	0	1	1	2	1.03	1.32	
S = 2 Mn(III); a_{2u} radical; ferro	5/2	1	2	0	1	2	1	0.75	0.59	0.60
S = 2 Mn(III); a_{2u} radical; antiferro	3/2	1	2	0	1	2	1	0.75	0.61	
S = 2 Mn(III); a_{1u} radical; ferro	5/2	1	2	1	0	1	2	1.55	2.05	
S = 2 Mn(III); a_{1u} radical; antiferro	3/2	1	2	1	0	1	2	1.58	2.06	
S = 2 Mn(III); a_{2u} radical; ferro	5/2	1	2	1	0	2	1	1.35	1.22	
S = 2 Mn(III); a_{2u} radical; antiferro	3/2	1	2	1	0	2	1	1.34	1.23	
					$[Zn(P)]^{0,+}$					
Zn(P)	0	2	4	2	2	2	2	**0.00**	**0.00**	**0.00**
$[Zn(P)]^+$; a_{2u} radical	1/2	2	4	2	2	2	1	6.75	6.27	6.29
$[Zn(P)]^+$; a_{1u} radical	1/2	2	4	2	2	1	2	6.77	6.78	6.59

[a] D_{4h} irreps are used throughout. Energy zero levels are indicated in bold. Abbreviations: ferro = ferromagnetic coupling; antiferro = antiferromagnetic coupling.

(III) π-cation radical.[1a] In light of our recent critical evaluations of DFT,[5,7] we entertained an alternative explanation for this apparent discrepancy between theory and experiment: we surmised that perhaps a nonradical Fe(IV) species is not observed simply because it does not exist! We present here ab initio multiconfiguration reference second-order perturbation theory (CASPT2) calculations with large basis sets and different active spaces (denoted below as AS1 and AS2) that lend support to our suspicion. As control studies, similar calculations were also carried out for the low-lying electronic states of $Mn(P)F_2$, where a true Mn(IV) ground state seems well-established[8,9] as well as for the two lowest π-cation radicals of zinc porphine, Zn(P).[10]

Methods

DFT geometry optimizations for different electronic configurations of $Fe(P)F_2$, $Mn(P)F_2$, and $[Zn(P)]^{+,0}$ were carried out with the B3LYP functional, D_{4h} symmetry constraints, and default grids and convergence criteria implemented in the TURBOMOLE program system.[11] The basis sets used in these calculations were of TZP quality, with an extra diffuse sp set on Cl and an extra d and an f function on the transition metal.

CASSCF and CASPT2 calculations were carried out on the B3LYP optimized structures with the MOLCAS 5.1 program system.[12] (Attempts were also made to perform coupled-cluster calculations, but these proved too computationally demanding.) The basis sets used in the CASPT2 calculations comprised correlation-consistent polarized valence double-ζ (cc-pVDZ) basis sets on H, C, and N,[13] the augmented aug-cc-pVDZ set on Cl,[14] and a new [6s 5p 4d 3f 2g] atomic natural orbital (ANO) basis on Mn.[15] The latter basis set is designed to properly account for 3s3p correlation. The zeroth-order Hamiltonian for the CASPT2 calculations was the g3 choice suggested by Andersson[16] and an imaginary level shift of 0.3 au (based on exhaustive investigation of smaller transition-metal-containing molecules) as proposed by Forsberg and Malmqvist[17] was used to ensure convergence of the CASPT2 iterative equations. In the CASPT2 calculations, all valence electrons were correlated, including the iron 3s and 3p electrons.

For Zn(P), the smaller active space AS1 comprised the four porphyrin frontier MOs, viz. the highest occupied a_{1u} and a_{2u} MOs and the lowest unoccupied e_g MOs. However, although this active space is adequate for describing the absorption spectrum, it is less satisfactory for ionization potentials, for which it was necessary to extend the active space (now called AS2) by adding four more MOs, namely the highest occupied e_g MOs and the lowest empty a_{1u} and a_{2u} MOs.

For $Fe(P)F_2$ and $Mn(P)F_2$, the smaller AS1 active space comprised the four porphyrin frontier MOs mentioned above, the five metal 3d orbitals, the highest metal-F bonding MO (a_{1g}) and its antibonding counterpart (a_{1g}). The larger active space AS2 included the extra four porphyrin MOs mentioned above for Zn(P). These active spaces were chosen by detailed consideration of CASPT2 natural orbital occupation numbers.

Table 2. Selected CASSCF Atomic Spin Populations for $Fe(P)F_2$, $Mn(P)F_2$, and $[Zn(P)]^+$

molecule; electronic configuration	S	M	F	C_α	C_β	C_{meso}	N
			$Fe(P)F_2$				
S = 1 Fe(IV); $d_{xy}^2(d_{xz}d_{yz})^2$	1	2.1676	−0.0087	0.0000	−0.0003	−0.0012	−0.0356
S = 2 Fe(IV); $d_{xy}^1(d_{xz}d_{yz})^2d_{x2-y2}^1$	2	4.1051	−0.0882	0.0070	0.0024	0.0068	−0.0078
S = 2 Fe(IV); $d_{xy}^1(d_{xz}d_{yz})^2d_{z2}^1$	2	4.2287	−0.1051	0.0006	−0.0001	0.0000	−0.0054
S = 5/2 Fe(III); a_{1u} radical; ferro	3	4.9584	0.0157	0.1187	0.0272	−0.0302	−0.0090
S = 5/2 Fe(III); a_{1u} radical; antiferro	2	4.6312	0.0141	−0.0621	−0.0173	−0.0037	−0.0021
S = 5/2 Fe(III); a_{2u} radical; ferro	3	4.9561	0.0182	−0.0112	0.0008	0.2005	0.0694
S = 5/2 Fe(III); a_{2u} radical; antiferro	2	4.6291	0.0127	−0.0046	−0.0027	−0.1024	−0.0460
			$Mn(P)F_2$				
S = 3/2 Mn(IV); $d_{xy}^1(d_{xz}d_{yz})^2$	3/2	3.2168	−0.0207	0.0006	−0.0004	−0.0020	−0.0422
S = 2 Mn(III); a_{1u} radical; ferro	5/2	4.0204	−0.0160	0.1188	0.0269	−0.0307	−0.0079
S = 2 Mn(III); a_{1u} radical; antiferro	3/2	3.6138	−0.0142	−0.0559	−0.0154	−0.0028	−0.0007
S = 2 Mn(III); a_{2u} radical; ferro	5/2	4.0185	−0.0136	−0.0114	0.0005	0.2006	0.0721
S = 2 Mn(III); a_{2u} radical; antiferro	3/2	3.6160	−0.0174	−0.0039	−0.0021	−0.0913	−0.0410
S = 1 Mn(III); a_{1u} radical; ferro	5/2	3.6056	−0.0186	−0.0039	−0.0022	−0.0888	−0.0407
S = 1 Mn(III); a_{1u} radical; antiferro	3/2	1.3373	0.0043	−0.0312	−0.0090	−0.0010	−0.0050
S = 1 Mn(III); a_{2u} radical; ferro	5/2	3.6051	−0.0145	−0.0544	−0.0167	−0.0024	0.0007
S = 1 Mn(III); a_{2u} radical; antiferro	3/2	1.3380	0.0027	−0.0027	−0.0015	−0.0495	−0.0276
			$[Zn(P)]^{0,+}$				
Zn(P)	0	0		0	0	0	0
$[Zn(P)]^+$; a_{1u} radical	1/2	0.0000		0.0949	0.0262	0.0056	0.0018
$[Zn(P)]^+$; a_{2u} radical	1/2	0.0195		0.0102	0.0092	0.1508	0.0544

[a] D_{4h} irreps are used throughout. Abbreviations: ferro = ferromagnetic coupling; antiferro = antiferromagnetic coupling; M = metal.

Because the two S = 2 Fe(IV) states studied (shown in Table 1) are of different symmetries — $^5B_{1g}$ and $^5A_{1g}$ — they were optimized separately with B3LYP calculations, exploiting full D_{4h} point group symmetry. However, the CASSCF/CASPT2 calculations could only be performed with D_{2h} symmetry where both Fe(IV) quintet states fall in the same irreducible representation. We therefore performed a two-root CASSCF/CASPT2 calculation for the two quintet states; such a calculation produces a slightly different energy for the lower state relative to what is obtained in a single-root calculation. For the best estimate for the energy of the higher S = 2 Fe(IV) state, we combined the calculated (two-root) energy difference between the two states with the single-root energy for the lower state.

Results and Discussion

Table 1 presents B3LYP and CASPT2 energies for the B3LYP optimized geometries of a number of Fe(P)F2, Mn(P)F2, and $[Zn(P)]^{0,+}$.

With the B3LYP functional (as well as with most other common functionals), generally believed to be one of the best for transition-metal calculations, the low-spin Fe(IV) ground state is clearly indicated for $Fe(P)F_2$. In contrast, at the CASPT2 level with the smaller AS1 active space, the ground state is a high-spin Fe(III) porphyrin A_{2u} radical; as expected on the basis of orthogonality of the metal d and porphyrin a_{1u} and a_{2u} MOs, ferromagnetic versus antiferromagnetic coupling between the metal and the radical does not seem to significantly affect the energy of the species. At the CASPT2(AS1) level, the low-spin Fe(IV) state is about 0.3 eV above the ground state, while the lower of two high-spin Fe(IV) states studied (see Table 1) is about 0.8 eV above the ground state. In addition, a high-spin Fe(III) porphyrin A_{1u} radical is also about 0.8 eV above the ground state at the CASPT2(AS1) level.

CASPT2 calculations with the larger active space AS2 essentially confirm the above picture: the ground state is a high-spin Fe(III) porphyrin A_{2u} radical, while the low-spin Fe(IV) state and a high-spin Fe(III) A_{1u} radical state are about 0.5 and 0.6 eV, respectively, higher in energy. In other words, the CASPT2 calculations are consistent with the experimental observation of an electrooxidized porphyrin radical state.

To what extent should we believe the CASPT2 results? To explore this issue, we turn to our controls, $Mn(P)F_2$ and $[Zn(P)]^{0,+}$. Consistent with experimental evidence[8] and earlier DFT(PW91/TZP) calculations,[9] CASPT2(AS1) calculations clearly indicate an S = 3/2 Mn(IV) ground state, while high-spin Mn(III) porphyrin π-cation radical states are several tenths of an eV above the ground state (see Table 2).

For a particular metal electronic configuration, the CASPT2-(AS1) energy difference between the A_{1u} and A_{2u} radicals may seem excessive, in view of the four-orbital model, which stipulates near-degenerate porphyrin HOMOs. However, the larger active space AS2 results in comparatively smaller differences in the A_{1u} and A_{2u} radical energies, e.g., as shown in Table 1, the A_{1u} π-cation radical of Zn(P) is only 0.3 eV higher in energy than the A_{2u} radical, which is reasonably in line with the four-orbital model.

Table 2 presents the CASSCF Mulliken spin populations for the various open-shell species studied. In general, these do not warrant much comment. The various A_{1u} and A_{2u} radicals exhibit their typical and well-known spin density profiles.[9,10] For the S = 1 Fe(IV) and S = 3/2 Mn(IV) states, note the significant minority spin populations on the por-

phyrin nitrogens, something that has also been observed in DFT calculations on a number of other metalloporphyrins.[9,18]

The reasonableness of the CASPT2 results for Mn(P)F_2 and Zn(P) lends credence to our conclusions regarding Fe(P)F_2, where CASPT2 results in a major upheaval of the DFT energetics of the low-lying spin states. Hence, we feel comfortable concluding that Fe(P)F_2 probably does not exist as a ground-state Fe(IV) species. The broader implications of our results may be illustrated with reference to the following mechanistic and electronic-structural problems: (a) describing the relative energetics of alkene epoxidation by a compound I (typically an $Fe^{IV}O$ porphyrin π-cation radical) versus an $Fe^{III}OOH$ intermediate; (b) describing the relative energetics of homolysis versus heterolysis of an $Fe^{III}OOH$ intermediate (Both pathways have been proposed for heme oxygenase.);[19] and (c) describing the issue of metal- versus ligand-oxidized nature of Fe(corrolato)Cl complexes.[20] To reliably address these problems, we need to accurately calculate the relative energetics of different Fe spin and oxidation states. As shown above, this is clearly a problem for DFT. There can be little doubt that the importance of these and other problems will spur continued development of high-quality exchange-correlation functionals as well as efforts to expand the range of application of high-level correlated ab initio methods to larger, more biologically relevant systems.

Acknowledgment. This work was supported by grants from the Research Council of Norway (A.G.) and the Wolfson Foundation (through the Royal Society) (P.R.T.).

Supporting Information Available: Optimized B3LYP Cartesian coordinates. This material is available free of charge via the Internet at http://pubs.acs.org.

References

(1) (a) Jones, D. H.; Hinman, A. S.; Ziegler, T. *Inorg. Chem*. **1993**, *32*, 2092−2095. (b) See, also: Nanthakumar, A.; Goff, H. *J. Am. Chem. Soc*. **1990**, *112*, 4047−4049. Unfortunately, ref (a) merely mentions the electrochemical evidence but refers to an unpublished cross-reference for details. However, one may conjecture that the evidence consists of a porphyrin π-cation-like electronic spectrum for the species in question.

(2) Reviews: (a) Groves, J. T. In *Cytochrome P450: Structure, Mechanism, and Biochemistry*, 3rd ed.; Ortiz de Montellano, P. R., Ed.; Kluwer/Plenum: New York, 2005; pp 1−43. (b) Shaik, S.; de Visser, S. P. In *Cytochrome P450: Structure, Mechanism, and Biochemistry*, 3rd ed.; Ortiz de Montellano, P. R., Ed.; Kluwer/Plenum: New York, 2005; pp 45−85.

(3) Reviews: (a) Shaik, S.; de Visser, S. P.; Kumar, D. *J. Biol. Inorg. Chem*. **2004**, *9*, 661−668. (b) Shaik, S. Cohen, S.; de Visser, S. P.; Kumar, D.; Kozuch, S.; Ogliaro, F.; Danovich, D. *Eur. J. Inorg. Chem*. **2004**, 207−226. (c) Hlavica, P. *Eur. J. Biochem*. **2004**, *271*, 4335−4360.

(4) Review: Jin, S.; Bryson, T. A.; Dawson, J. H. *J. Biol. Inorg. Chem*. **2004**, *9*, 644−653.

(5) Ghosh, A.; Taylor, P. R. *Curr. Opin. Chem. Biol*. **2003**, *7*, 113−124.

(6) (a) For an overview of DFT calculations on high-valent metalloporphyrins, see: Ghosh, A.; Steene, E. *J. Biol. Inorg. Chem*. **2001**, *6*, 739−752. (b) For a survey of the experimental scenario, see: Weiss, R.; Bulach, V.; Gold, A.; Terner, J.; Trautwein, A. X. *J. Biol. Inorg. Chem*. **2001**, *6*, 831−845.

(7) (a) Ghosh, A.; Persson, B. J.; Taylor, P. R. *J. Biol. Inorg. Chem*. **2003**, *8*, 507−511. (b) For a CASPT2 study on nonheme high-valent Fe, see: Ghosh, A.; Tangen, E.; Ryeng, H.; Taylor, P. R. *Eur. J. Inorg. Chem*. **2004**, 4555−4560.

(8) Kaustov, L.; Tal, M. E.; Shames, A. I.; Gross, Z. *Inorg. Chem*. **1997**, *36*, 3503−3511.

(9) (a) Ghosh, A.; Vangberg, T.; Gonzalez, E.; Taylor, P. *J. Porphyrins Phthalocyanines* **2001**, *5*, 345−356. (b) Ghosh, A.; Gonzalez, E. *Israel J. Chem*. **2000**, *40*, 1−8.

(10) (a) Vangberg, T.; Lie, R.; Ghosh, A. *J. Am. Chem. Soc*. **2002**, *124*, 8122−8130. (b) Ghosh, A.; Vangberg, T. *Theor. Chem. Acc*. **1997**, *97*, 143−149.

(11) Ahlrichs, R.; Bär, M.; Häser, M.; Horn, H.; Kölmel, C. *Chem. Phys. Lett*. **1989**, *162*, 165−169.

(12) (a) Information on MOLCAS: http://www.teokem.lu.se/MOLCAS/. (b) Applications of MOLCAS: Roos, B. *Acc. Chem. Res*. **1999**, *32*, 137−144.

(13) Dunning, T. H. *J. Chem. Phys*. **1989**, *90*, 1007−1023.

(14) Woon, D. E.; Dunning, T. H. *J. Chem. Phys*. **1993**, *99*, 3730−3737.

(15) Persson, B. J.; Taylor, P. R. unpublished results.

(16) Andersson, K. *Theor. Chim. Acta* **1995**, *91*, 31−46.

(17) Forsberg, N.; Malmquist, P.-Å. *Chem. Phys. Lett*. **1997**, *274*, 196−204.

(18) Johansson, M. P.; Sundholm, D.; Gerfen, G.; Wikström, M. *J. Am. Chem. Soc*. **2002**, *124*, 11771−11780.

(19) (a) Review: Rivera, M.; Zeng, Y. H. *J. Inorg. Biochem*. **2005**, *99*, 337−354. (b) Sharma, P. K.; Kevorkiants, R.; de Visser, S. P.; Kumar, D.; Shaik, S. *Angew. Chem., Int. Ed*. **2004**, *43*, 1129−1132.

(20) (a) Steene, E.; Wondimagegn, T.; Ghosh, A. *J. Phys. Chem. B* **2001**, *105*, 11406−11413; Addition/Correction: *J. Phys. Chem. B* **2002**, *106*, 5312−5312. (b) Zakharieva, O.; Schunemann, V.; Gerdan, M.; Licoccia, S.; Cai, S.; Walker, F. A.; Trautwein, A. X. *J. Am. Chem. Soc*. **2002**, *124*, 6636−6648. (c) Steene, E.; Dey, A.; Ghosh, A. *J. Am. Chem. Soc*. **2003**, *125*, 16300−16309. (d) Simkovich, L.; Gross, Z. *Inorg. Chem*. **2004**, *43*, 6136−6138, and references therein.

CT050086S

JCTC Journal of Chemical Theory and Computation

Density Functional Study of H−D Coupling Constants in Heavy Metal Dihydrogen and Dihydride Complexes: The Role of Geometry, Spin−Orbit Coupling, and Gradient Corrections in the Exchange-Correlation Kernel

Boris Le Guennic,[†] Serguei Patchkovskii,[‡] and Jochen Autschbach*,[†]

Department of Chemistry, 312 Natural Sciences Complex, State University of New York at Buffalo, Buffalo, New York 14260-3000, and Theory and Computation Group, Steacie Institute for Molecular Sciences, National Research Council Canada, 100 Sussex Drive, Ottawa, Ontario K1A 0R6, Canada

Received February 25, 2005

Abstract: The H−D nuclear spin−spin coupling constants J(H−D) of 14 heavy transition-metal dihydrogen and dihydride complexes were calculated with density functional theory using the "zeroth-order regular approximation" (ZORA) for the one-electron operators. The applied gradient-corrected density functional was able to achieve an average agreement with experimental data that is almost comparable to what has been obtained recently with hybrid functionals [*J. Am. Chem. Soc.* **2004**, *126*, 14249]. However, a systematic overestimation of J(H−D) for complexes with short H−D distances was obtained, which could be traced back to problems of the gradient functional to describe the H−D coupling in free dihydrogen well. We implemented gradient corrections for the exchange-correlation (XC) kernel and employed a basis sets with high-exponent 1s function for the coupled hydrogens. The gradient terms in the XC kernel turned out to be very important in order to achieve reasonable agreement with experimental coupling constants. On the other hand, our study reveals that spin−orbit relativistic corrections on the H−D coupling constants are comparatively small and need not to be considered at the accuracy level of currently available "standard" density functionals. The discussion of the results highlights the strong dependence of the coupling constants on the H−D distance and the possibility of large vibrational contributions to them. We also discuss the coupling constant for the hydrogen molecule in detail because of its relevance to the coupling in dihydrogen and dihydride complexes.

1. Introduction

A number of authors have pointed out the sensitivity of H−D nuclear spin−spin coupling constants with respect to the H−D distance in η^2-dihydrogen[1] and dihydride complexes of transition metals.[1−6] Of particular interest is the relationship between J(H−D) and the H−D distance. Its knowledge allows for estimating the H−D distance in such complexes in solution from NMR measurements of J(H−D). This has been recently emphasized again in ref 7. For instance, dihydrogen complexes can be classified as "elongated" based on solution NMR measurements. A recent example can be found in ref 8 which reported the synthesis and properties of iridium bis(phosphinite) pincer complexes. Elongated dihydrogen complexes afford H−H distances between 1.0 and 1.6 Å, whereas the H−H distance in true dihydrogen complexes is close to the 0.74 Å found for H_2 itself. Typically, H−H distances in dihydrogen complexes range from about 0.8 to 1.0 Å. Once the H−H distance increases to 1.6 Å, the complex is classified as a dihydride instead. From the shape of the potential energy surface (PES) in the H−H stretch region, Gelabert et al. have also identified

* Corresponding author e-mail: jochena@buffalo.edu.
[†] State University of New York at Buffalo.
[‡] National Research Council Canada.

10.1021/ct050042j CCC: $30.25
Published on Web 05/21/2005

"compressed dihydride" complexes. The classification depends on whether the deepest minimum of the PES of elongated complexes is rather in the dihydrogen or in the dihydride regime.[4] Due to the small mass of the hydrogen isotopes, the measured H−D coupling constant might be strongly influenced by stretching and bending motions of the H−Me−D subsystem. Thus, elongated dihydrogen and compressed dihydride complexes can be expected to exhibit different temperature dependence of J(H−D).[4]

Besides structural information for newly synthesized metal complexes, an important application of NMR measurements on complexated H_2 is related to the safe storage and handling of hydrogen, which represents one of the challenges for use of hydrogen in mobile energy generation.[12,15,17] In this context, nuclear magnetic resonance has established itself as one of the most powerful, nondestructive techniques for the analysis of structure, composition, and dynamics of guest molecules in microporous materials.[10,13] NMR spin−spin coupling constants provide a sensitive probe of the interactions of the H_2 guests with transition-metal centers in such systems, particularly because of their sensitivity to the H−H distance. As a result, NMR can be used to follow the transition between physisorption and chemisorption regimes in a hydrogen storage system. In such situations, first-principle calculations might permit discrimination between different possible structural interpretations of the experimental data.

From a theoretical/computational viewpoint, the prediction or verification of NMR parameters for transition-metal complexes, in particular with heavy metals, is not unproblematic.[20−23] The reason is the sensitivity of NMR parameters to internal and external influences. It is necessary to treat electron correlation, relativistic effects, but also the influence from the complexes' chemical environment (usually solvent molecules) simultaneously at a high level. Prior experience with density functional theory (DFT) calculations of metal chemical shifts has shown that hybrid functionals such as B3LYP perform quite well for 3d metals[24] (in particular for Fe chemical shifts[25] where nonhybrid DFT was shown to fail spectacularly). However, a reinvestigation of Fe shifts has recently shown that the hybrid DFT results might deteriorate in case this functional is used also for the geometry optimizations.[26] Ligand chemical shifts in metal complexes, on the other hand, are often well described at the nonhybrid DFT level. Similar conclusions were drawn for metal−ligand nuclear spin−spin coupling constants.[20]

Somewhat surprisingly, for spin−spin coupling constants between ligands in metal complexes there are only a few computational data available in the literature. For a survey of DFT studies published up to late 2003 we refer the reader to ref 20. Acceptable agreement with experimental results and, more importantly, the observed trends could, for example, be achieved in studies of two-bond P−P couplings in Cp*(L)M=PAr (M = Co, Rh, Ir, L = PR_3 or CO, Ar = Mes*)[27] and group VI metal carbonyl phosphines $M(CO)_4(PH_3)_2$ (M = Cr, Mo, W),[28,29] for the Si−H coupling constant in $(\eta^5\text{-}C_5H_5)(CO)_2MnHSiCl_3$,[30] for the three-bond C−C coupling in $[(NC)_5Pt-Tl(CN)]^-$,[31] and for H−D coupling in Os dihydride complexes.[32,33] So far, the small number of computational studies of ligand−ligand coupling constants in metal complexes does not permit the drawing of general conclusions as to which computational model generally performs best.

A first-principles computational study of η^2-dihydrogen complexes of Os(II) of the form $[\eta^2\text{-}H_2Os(NH_3)_4L]$ was carried out by Hush et al. already in 1994.[32] Hartree−Fock and MP2 methods were employed but neither did yield acceptable agreement with the experimentally observed trends for different ligands L. A follow-up study using DFT, on the other hand, was able to achieve a much improved agreement between theory and experiment,[33] though for some ligands L (Cl^-, acetate) sizable differences between the calculated and measured values of J(H−D) remained. The success of DFT was attributed to the treatment of electron correlation, which is certainly an important aspect in NMR calculations in general[34] and for transition-metal systems in particular.[20] More recent computational studies of J(H−D) in η^2-dihydrogen complexes can be found in refs 7, 3, and 4. A comparatively large number of complexes with different metals were optimized in ref 7 using the mPW1PW91 hybrid density functional. The same functional was applied in subsequent computations of nuclear spin−spin coupling constants. Good agreement with experimental data was obtained. The calculations also showed that the coupling constants for the most elongated systems have negative signs. All previous computational studies of H−D coupling constants were considered relativistic effects by using scalar relativistic effective core potentials (ECPs).

So far, the question of whether spin−orbit coupling at the metal center has any influence on J(H−D) has not been addressed, though such an influence might be important in particular for strongly elongated H−D bonds with concomitant small coupling constants. A part of the coupling could be mediated and influenced by the metal's valence orbitals in this case. Further, the influence of the density functional on the combined geometry optimization/coupling constant calculation is unclear. In the present work we address these issues. We have recently implemented gradient corrections for the exchange-correlation (XC) kernel in calculations of spin−spin coupling constants. Thus, we have in addition taken the opportunity to investigate the question of their importance in nuclear spin−spin coupling constant calculations as part of the present study. As it turned out, their influence is large for J(H−D) and improves the agreement with experiment and hybrid DFT calculations substantially for complexes with medium to large H−D internuclear distances.

This work is organized as follows: In section 2 we summarize the computational details. The results of our computations in comparison with experimental data and the computations of ref 7 are presented and discussed in section 3. We conclude this work with a short summary in section 4.

2. Computational Details

We have performed the computations for the present study with the spin−orbit relativistic DFT approach for nuclear spin−spin coupling constants developed by Autschbach and Ziegler[37,38] and implemented in the Amsterdam Density

Functional (ADF) program package.[41−43] It is based on the two-component zeroth-order regular approximate (ZORA) relativistic one-electron Hamiltonian.[39,40] DFT exchange-correlation contributions in the calculations are based on nonrelativistic density functional expressions evaluated with the relativistic electron density obtained from the ZORA Fock operator.

The spin−spin coupling constant within the relativistic ZORA formalism consists of four terms that we denote by Fermi-contact (FC), spin-dipole (SD), and the paramagnetic and diamagnetic orbital terms (OP and OD). As in previous work,[31,44−47] we have chosen the well-known nonrelativistic nomenclature[48,49] for the four terms because, first, they yield the respective FC, SD, OP, and OD terms of Ramsey's nonrelativistic theory in the nonrelativistic limit (speed of light $c \rightarrow \infty$), and, second, they can be interpreted in a similar way.[37,50] In most scalar relativistic calculations, we have omitted the expensive computation of the SD contribution after test calculations had shown that its magnitude is small for all complexes. The SD term has been included in all spin−orbit calculations since there it leads only to a marginal increase in computational time. The spin−orbit results also contain important cross terms between OP and FC and OP and SD, respectively.[44]

In ref 7, geometry optimizations of the metal−dihydrogen complexes were performed using the mPW1PW91 hybrid density functional which includes modified Perdew-Wang exchange and Perdew-Wang 91 correlation terms.[51−53] Relativistic corrections were included in the computations via a scalar relativistic effective core potentials (ECPs) for the metal. In the present work, we have employed these geometries. Additionally, geometry optimizations were carried out with the Vosko-Wilk-Nusair (VWN)[54] local density approximation (LDA) functional as well as with the Becke-Perdew (BP)[55,56] and the revised Perdew-Burke-Ernzerhof (revPBE)[57−60] generalized gradient approximated (GGA) density functionals. The NMR H−D spin−spin coupling constants have been computed using the same functionals in order to analyze the sensitivity of the results to approximations in the (nonhybrid) density functionals. We have also applied the "statistical average of orbital-dependent model potentials" (SAOP) Kohn−Sham potential[61] to the calculation of the NMR coupling constants. It has been previously designed for, and successfully applied to, excitation energies and frequency dependent response properties.[62−65] Poater et al. have subsequently reported that for a range of light-nucleus chemical shifts the SAOP potential shows considerable improvement over other nonhybrid potentials, such as VWN or BP.[66] Our own work on heavy-metal−heavy-metal nuclear spin−spin coupling constants as well as heavy nucleus chemical shifts has also shown marked improvements of results obtained with SAOP as compared to standard GGAs in some cases,[47] though not consistently so[67] (however, in the case where large disagreement between theory and experiment occurred it is unclear whether the discrepancies are due to the Kohn−Sham potential or neglected solvent effects and other more "chemical" influences).

In our original implementation of ZORA spin−spin coupling calculations[37,38] a LDA XC kernel was applied to evaluate the linear response of the Kohn−Sham DFT potential due to the Fermi-contact (FC) perturbation operator. The FC perturbation does not cause a density but just a spin-density response. Consequently, there is no Coulomb contribution in the response of the Kohn−Sham potential when using nonhybrid functionals. Major improvements for spin−spin coupling calculations might thus be expected from considering GGA terms in the XC kernel, in particular for coupling constants involving light atoms. For the present work, we have implemented such terms based on the revPBE functional. Evaluation of GGA contributions to the matrix elements of the DFT response kernel $\hat{k}[\rho^{(0)}; \rho^{(1)}]$ employed the standard symmetric expression[9] for the second variation of the exchange-correlation energy to yield

$$\begin{aligned}\langle\phi_i|\hat{k}[\rho^{(0)};\rho^{(1)}]|\phi_j\rangle = &\sum_{\gamma,\,\delta=\alpha,\beta}\int f_{\gamma,\delta}\phi^*_{i,\gamma}\phi_{j,\gamma}\rho^{(1)}_\delta + \\ &\sum_{\gamma,\,\delta=\alpha,\beta}\sum_{b=x,y,z}\int f_{\gamma,\delta b}\phi^*_{i,\gamma}\phi_{j,\gamma}\frac{\partial}{\partial b}(\rho^{(1)}_\delta) + \\ &\sum_{\gamma,\,\delta=\alpha,\beta}\sum_{a=x,y,z}\int f_{\gamma a,\delta}\frac{\partial}{\partial a}(\phi^*_{i,\gamma}\phi_{j,\gamma})(\rho^{(1)}_\delta) + \\ &\sum_{\gamma,\,\delta=\alpha,\beta}\sum_{a,b=x,y,z}\int f_{\gamma a,\delta b}\frac{\partial}{\partial a}(\phi^*_{i,\gamma}\phi_{j,\gamma})\frac{\partial}{\partial b}(\rho^{(1)}_\delta) \quad (1)\end{aligned}$$

Here, ϕ_i and ϕ_j are combined spatial and spin basis functions (molecular orbitals in the algorithm that we have implemented), with the spatial components corresponding to α and β spins given respectively by $\phi_{i,\alpha}$ and $\phi_{i,\beta}$. Further, $\rho^{(0)}$ is the unperturbed electron spin-density, and $\rho^{(1)}$ is the first-order response of the spin density. The α and β components are indicated by the subscripts α and β.

The quantities $f_{\gamma,\delta}$, $f_{\gamma,\delta b}$, $f_{\gamma a,\delta}$, and $f_{\gamma a,\delta b}$ are explicit functions of the unperturbed electron density and its Cartesian gradients. They are given by the corresponding derivatives of the exchange-correlation energy density $\rho\cdot\epsilon_{XC}[\rho]$, for example

$$f_{\gamma,\delta} = \frac{\partial^2(\rho\cdot\epsilon_{XC}[\rho])}{\partial\rho_\gamma\partial\rho_\delta} \quad (2)$$

Expression (1) has the practical advantage of requiring at most the first derivatives of the unperturbed densities, first-order densities, and the basis functions. As a consequence, it is straightforward to implement in any DFT code which already includes gradient-corrected exchange-correlation potentials. A computationally more efficient asymmetric expression,[19] which does not require derivatives of the basis functions, would be somewhat more difficult to implement.

The expressions for the derivatives $f_{\gamma,\delta}$, $f_{\gamma,\delta b}$, $f_{\gamma a,\delta}$, and $f_{\gamma a,\delta b}$ are XC functional-specific (and often quite lengthy). These expressions, together with the computer code used to evaluate them, were derived and implemented using a computer algebra system, as will be discussed elsewhere.[19]

Full geometry optimizations of all metal dihydrogen complexes were carried out employing valence triple-ζ Slater-type basis sets with polarization functions for all atoms (TZP) from the ADF basis set library. Inner shells up to, but not including 5spd and 6sp for W, Os, Re, and Ta and 4spd and 5sp for Ru and Nb, were kept as frozen cores. Inner shells up to 1s for C, N and O, 2p for P, and 3d for Br were also kept frozen in the geometry optimizations. All electron Slater-type basis sets with two polarization functions (TZ2P) were used for the computations of NMR spin−spin coupling constants. Since it turned out that the H−D coupling is very sensitive to the description of the FC term we have also carried out NMR calculations where the TZ2P basis for the two coupled hydrogens has been augmented with four additional high exponent 1s functions. The additional exponents were chosen as $\zeta_{max}{}^{1.4 \cdot n}$, $n = 1...4$, where ζ_{max} is the highest 1s exponent of the unmodified TZ2P basis. We will denote this locally dense basis by TZ2P+steep.

3. Results and Discussion

The Hydrogen Molecule. Before we present the computed results for our set of 14 transition-metal complexes, it is beneficial to discuss the calculated indirect spin−spin coupling constant for the hydrogen molecule itself. The experimental value for the *J*-coupling constant is 42.9 ± 0.1 Hz for the HD isotopomer,[68] which corresponds to a *reduced* coupling constant K(H−H) of $23.3 \cdot 10^{19} T^2 J^{-1}$. Further, this corresponds to a *J*-coupling of 279.5 Hz for H_2. Here, and throughout the rest of this paper we have used a factor of 1.844 to convert the reduced coupling in 10^{19} SI units to the HD coupling constant in Hz and a factor of 12.01 to convert from K to J for H_2. The conversion factor from J(H−D) to J(H−H) is 6.514. All values for K coupling constants quoted in the following are understood to be in 10^{19} SI units.

The calculated value for K of H_2 at the TZP/revPBE(LDA) density functional level (i.e. using the revPBE XC potential but the LDA kernel) is 32.8 when the SD term is excluded, and 33.0 when the SD term is included. These results are for the experimental equilibrium distance of 0.741 Å and do not change substantially when the TZP/revPBE optimized geometry of 0.747 Å is used instead (33.0 excluding the SD term, 33.2 when the SD term is included). Dickson and Ziegler have in 1996 reported a calculated value of 28.2 (excluding the SD term) obtained with the VWN LDA functional, the TZ2P basis set, and a finite-perturbation approach. The additional *d* polarization functions of the TZ2P vs the TZP basis are not the reason for the large difference between the Dickson and Ziegler value and our result. We obtain a TZ2P/revPBE(LDA) value of 33.0 at the experimental bond distance (SD excluded), which is just 0.2 larger than the result with the TZP basis. The main effect stems from the functional. Indeed, when calculating the H−D coupling with the VWN functional and the TZ2P basis instead, the computed value drops to 28.6 which compares well with the literature value of 28.2, taking into account that the finite-perturbation approach used by Dickson and Ziegler might have introduced some numerical errors.

The coupling constant for H_2 at the equilibrium H−H distance is largely caused by the FC mechanism. An improvement of the calculated results toward the experimental coupling constant can be obtained by adding additional high-exponent 1s basis functions to the Slater-type basis sets. It is well-known that such additional basis functions are necessary to correctly describe the response of the electron density to the FC perturbation. The highest 1s exponent in the TZ2P basis for H is 1.580. We have added four 1s functions with exponents of 6.070, 4.336, 3.097, and 2.212, respectively, to the TZ2P basis for H as well as five density fit functions with exponents between 4.4 and 23.8 (from now on referred to as "TZ2P+steep"). The coupling constants of 24.2 (VWN) and 26.9 (revPBE(LDA)) obtained with the TZ2P+steep basis agree much better with the experimental value of 23.3 than those obtained with the unmodified TZ2P basis. The agreement is best for the VWN functional, which is obviously due to some fortuitous error cancellation.

The influence of the LDA approximation in the revPBE-(LDA) result is large. With the XC kernel of the revPBE functional, we obtain reduced coupling constants of 36.5 (TZ2P) and 29.6 (TZ2P+steep) at the experimental internuclear distance instead; i.e., the GGA contributions in the XC kernel cause an increase of the coupling constant by 11 and 10%, respectively. Thus, our "best" nonhybrid DFT result obtained at the TZ2P+steep/revPBE level including gradient corrections in the XC kernel overestimate the experimental value by 27%.

We have averaged the coupling constant with the ground-state nuclear vibrational wave functions for H_2, HD, and D_2, respectively, that were calculated in a discrete variable representation (DVR)[70] based on the TZ2P+steep/revPBE potential curve, using an approach similar to one reported in ref 71. With 23 points we obtain zero-point vibration corrected reduced couplings of 31.3 for H_2, 31.1 for HD, and 30.9 for D_2, at the TZ2P+steep/revPBE level, i.e., an additional 5% increase over the equilibrium value of 29.9. The vibrational correction of $1.2 \cdot 10^{19} T^2 J^{-1}$ corresponds to 2.2 Hz for HD. This is in good agreement with a value of 2.8 Hz ($1.5 \cdot 10^{19} T^2 J^{-1}$) recently calculated by Ruden et al.[69] with the B3-LYP hybrid functional. Vibrational corrections of at least the same order of magnitude (percentage-wise) might be expected in the metal complexes.

Unfortunately, in ref 69, only the B3-LYP vibrational correction but not the HD coupling constant itself was tabulated. In 2002, Sychrovsky et al. reported equilibrium nuclear spin−spin coupling constants calculated at the hybrid functional level, with a B3-LYP value of 23.0 for K(H−H).[36] In the same paper, the B3PW91 functional yielded a coupling of 21.1. When subtracting the vibrational correction of ref 69 from the experimental value to obtain an empirical experimental equilibrium coupling of 21.8, the B3PW91 agrees with an experiment slightly better than B3-LYP. The authors of ref 36 have also investigated the influence of Hartree−Fock (HF) exchange in the hybrid functional on the coupling constant by replacing a fraction x of the BLYP XC potential with HF exchange. For H_2, values of 0.1, 0.5, and 0.9 for x lead to a change of the coupling constant by only $1.3 \cdot 10^{19} T^2 J^{-1}$, from 24.1 for $x = 0.1$ to 25.4 for $x = 0.9$. A TZ2P+steep/BLYP(LDA)

Table 1. Calculated J_{HD} in Dihydrogen Complexes Using the TZ2P+steep Basis Set for the Hydrogen Atoms Bonded to the Metal (in Hz)

				ref 7	
	dist.[a]	VWN	revPBE[b]	calc.	exp.
$WH_2(CO)_3(P^iPr_3)_2$ (**1**)	0.84	38.4	47.3	34.8	34
$[RuH_2Cp(CO)(PCy_3)]^+$ (**2**)	0.93	27.2	33.9	27.2	22.3
$[RuH_2Cp(dmpe)]^+$ (**3**)	0.99	24.4	29.8	24.6	22.1
$[RuH_2Cp^*(dppm)]^+$ (**4**)	0.98	27.4	33.6	25.2	22.3
$[OsH_2(en)_2(OAc)]^+$ (**5**)	1.28	9.5	9.7	6.8	9
$ReH_2Br_2(NO)(P^iPr_3)_2$ (**6**)	1.33	11.0	11.8	9.8	12.8
$[TaH_2Cp_2(P(OMe)_3)]^+$ (**7**)	1.64	3.0	2.1	0.4	1.5
$OsH_2Cl[CH(C_2H_4P^tBu_2)_2]$ (**8**)	1.63	0.6	−0.1	−0.1	0
$[IrH_3Cp(PMe_3)]^+$ (**9**)	1.71	3.3	3.3	2.4	3.9
$[IrH_3Cp^*(PMe_3)]^+$ (**10**)	1.74	2.9	2.9	2.0	3.3
NbH_3Cp_2 (**11**)	1.76	0.6	−0.2	−1.1	−0.9
TaH_3Cp_2 (**12**)	1.82	0.0	−1.0	−2.0	−1.5
$TaH_2Cp_2(BO_2C_6H_4)$ (**13**)	2.03	0.1	−0.5	−1.2	−0.9
$ReH_2(CO)(NO)(PMe_3)_2$ (**14**)	2.22	−0.1	−0.8	−1.0	−1.0

[a] d(H−D) in angstroms from ref 7. [b] With revPBE XC potential and kernel.

result calculated by us is 26.5, with an expected increase of roughly 3.0 when the correct BLYP XC kernel would be used instead. This leads to a rough estimate of 29.5 for $x = 0$. This might indicate that the difference between $x = 0$ and $x = 0.1$ is extremely vital to obtain results close to experiment and that choosing $x = 0.1$ instead of 0.0 leads to a very significant reduction of the H−H coupling by about 20−25%. The use of different basis sets (IGLO-III in ref 36 vs TZ2P+steep here) could lead to different results at $x = 0$. Regarding the basis set convergence for the FC term, it has previously been pointed out in ref 72 that the polarized Slater-type basis sets employed here (even without additional high-exponent functions) are quite well suited to give a faithful description of the FC mechanism. We did not attempt to reach complete convergence of the results with respect to the number of high-exponent functions on the hydrogens. The errors resulting from the approximations in the density functional, neglect of vibrational corrections, solvent effects, etc. in the calculations on the metal complexes (see below) are expected to outweigh improvements from a basis for the hydrogens that is better than the TZ2P+steep basis employed here.

Our ZORA relativistic method for spin−spin coupling constants is currently restricted to nonhybrid functionals. We have obtained essentially the same H−D coupling constants (based on the LDA XC kernel) when using gradient functionals other than revPBE. Thus, it should be kept in mind in the following sections that for all GGA calculations of J(H−D) in metal dihydrogen complexes a pronounced overestimation of J(H−D) might be expected for complexes with H−D distances near the H_2 equilibrium bond length of 0.741 and large H−D coupling constants.

Computational Results for 14 Dihydrogen Metal Complexes. Table 1 lists the calculated H−D J-coupling constants for 14 transition-metal complexes with experimentally determined H−D distances between 0.84 and 2.25 Å. The data were obtained at the scalar ZORA level with the TZ2P+steep basis, using the optimized geometries of ref 7.

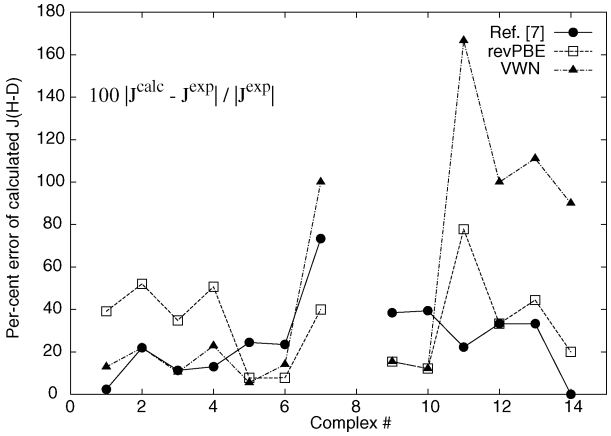

Figure 1. Relative deviations from experiment for the calculated H−D coupling constants obtained with the different methods listed in Table 1. See text for details. For complex **8**, the exp. value is 0.0; thus, no relative error is given. The lines were added to guide the eye.

Table 1 contains results obtained with the VWN and the revPBE functionals (both for XC potential and kernel).

Further, Table 1 lists the computational results of ref 7 which were obtained with a hybrid functional as well as the experimental coupling constants. The expected overestimation of J(H−D) for the complexes with short H−D distance is indeed visible in the revPBE results. One might take the fact that the calculated coupling in free hydrogen and in the dihydrogen complexes afford similar errors as an indication that the electronic structure of the H_2 moiety in complexes **1**−**4** is very similar to free H_2.

Whereas the calculated values using the VWN functional agree quite well with the experimental as well as with the hybrid functional data for the complexes **1**−**6** with short H−D distances, the accuracy of the VWN calculations deteriorates as d(H−D) increases. On the other hand, the revPBE results agree better with experiment for the elongated dihydrogen and the hydride complexes than for the complexes with short d(H−D).

For data sets such as the one in Table 1 where the elements differ by orders of magnitude, absolute unsigned differences do not allow for an easy comparison of different methods. For a small coupling constant, a deviation of 1 Hz would not be acceptable, whereas the same deviation would be considered acceptable or small for complexes where J(H−D) is of the order of 10 Hz. In Figure 1, we have therefore compared the relative unsigned errors of each computation.

The graphics reveals that the hybrid DFT method used in ref 7 performs best overall, even though some significant deviations between theory and experiment are visible. The largest relative deviations are obtained for the complexes with the largest H−H distances and the VWN functional. It should also be noted that the signs of the VWN results for these complexes do not agree with the revPBE and the hybrid DFT results (except for **14**; however, the calculated VWN value is much too small in magnitude). A disadvantage of using relative deviations is that they tend to inflate where the reference value is close to zero. Nevertheless, it can be

Table 2. Relative Deviation (in Percent) of the Computational Results of Table 1 from Experiment[a]

complex	Δ ref 7	Δ revPBE	Δ VWN	Δ revPBE[c]
1	2.4	39.1	12.9	38.8
2	22.0	52.0	22.0	45.7
3	11.3	34.8	10.4	18.6
4	13.0	50.7	22.9	42.6
5	24.4	7.8	5.6	31.1
6	23.4	7.8	14.1	43.8
7	73.3	40.0	100.0	0.0
8[b]				
9	38.5	15.4	15.4	17.9
10	39.4	12.1	12.1	18.2
11	22.2	77.8	166.7	44.4
12	33.3	33.3	100.0	20.0
13	33.3	44.4	111.1	33.3
14	0.0	20.0	90.0	20.0
average	25.9	33.5	52.5	28.8
median	23.4	34.8	22.0	31.1

[a] Mean unsigned relative deviation Δ calculated as $\Delta = 100|J^{calc} - J^{exp}|/|J^{exp}|$. [b] For complex **8**, the exp. value is 0.0; thus, no relative error is given. [c] For geometry optimized with the revPBE functional. See Table 6.

seen that the hybrid functional of ref 7 and the revPBE functional used here yield absolute deviations from experiment that decrease along with a decrease of the coupling constants' magnitudes. Hence, the accuracy does not deteriorate for complexes with large H−D distances (as seen in the relative deviations) and meaningful calculations are possible over the whole range of distances.

The good agreement between revPBE and hybrid DFT regarding the negative signs of the coupling constants for complexes **11**−**14** strongly supports the tentative conclusion of ref 7 that these coupling constants are negative. We will see later that the sign is not affected by the inclusion of spin−orbit coupling.

The deviations between calculated and experimental H−D couplings relative to the experimental value that are displayed in Figure 1 are collected in Table 2 (the last column is for revPBE optimized geometries which will be discussed later).

The median deviation for the VWN functional is small and does not reflect the poor overall performance of this functional. The small median stems from its good performance for the complexes with short d(H−D). The fact that the median and the average are very different indicates that the VWN functional causes a lot of outliers with large deviations from experiment. For the other two methods, the average and median agree well. The somewhat worse performance of the GGA functional compared to the hybrid is seen to result mainly from the overestimation of J(H−D) at short H−D distances that was also found for free H_2. For complex **8**, no relative error is listed because the experimental value is 0.0 Hz. Both the hybrid and the revPBE functional perform equally well for this complex whereas VWN is far off.

It should be noted that the equilibrium coupling constants (i.e. at R_e(H−H)) are not expected to agree well with the experimental values even at low temperature in case the PES is very anharmonic or in case the coupling constant surface has a large curvature around the equilibrium geometry. A recent paper has shown that for the complex [Cp*Ir(dmpm)-H_2]$^{2+}$, d(H−D) might be strongly temperature dependent and that the PES is indeed very anharmonic regarding the H−D stretching motion.[3] Increasing the temperature would lead to a shortened average H−D distance and thus likely to larger coupling constants. The opposite behavior might occur as well, depending on the shape of the PES and the *J*-coupling surface. Thus, the deviations displayed in Table 2 do not truly reflect the ability of the computations to accurately predict solution measurements at room temperature (for which solvent effects might also be important). The calculations afford systematic deviations from experiment due to the missing vibrational corrections. It might be the case that for the complexes with a significantly weakened, but still intact, H−D bond (i.e. for the elongated dihydrogen complexes) the magnitudes of the vibrational corrections *relative* to the equilibrium coupling constants are significantly larger than for the hydrogen molecule itself.

The Influence of Spin−Orbit Coupling on the H−D Coupling Constants. Table 3 lists computed results including the SD mechanism and/or spin−orbit coupling induced mechanisms on the H−D coupling, most notably from the FC/OP cross term. Included are also indirect effects on the FC, SD, OP, and OD mechanisms due to the change on the molecular orbitals when spin−orbit coupling is included variationally in the calculation. Most of the spin−orbit calculations have been carried out with the VWN functional and the TZ2P basis but without the additional steep functions. The scalar ZORA BP and SAOP calculations presented in Table 3 have been performed with the same basis. They are provided in order to demonstrate the influence of omitting the steep functions on the hydrogens in the coupling constant calculations (by comparison with Table 1) and to allow, for a select case, to verify that the magnitude of the spin−orbit contributions are the same in LDA and GGA calculations. All results were obtained using the optimized geometries of ref 7.

It is clear from the results that neither the inclusion of the SD term nor the inclusion of spin−orbit coupling causes dramatic changes to the H−D coupling constants. The changes to J(H−D) are 0.1 Hz in magnitude throughout the test set. Obviously, for coupling constants near zero, 0.1 Hz represents a substantial change. However, upon inspection of the results it can be seen that the VWN results for complexes with large H−D distances are still far off from experiment. Neither inclusion of spin−orbit coupling and/or the SD term would reconcile theory and experiment at the VWN level.

From these results we conclude that at the present level of accuracy (i.e. when considering the differences between theory and experiment) for local density functionals, gradient functionals, and hybrid functionals, relativistic spin−orbit corrections to the H−D coupling constant are not particularly significant, i.e., their negligence does not represent a major source of error in the computations. For more accurate computations that would deliver an accuracy of the order of 0.1 Hz it will be necessary to include all spin−orbit coupling effects. However, though highly accurate ab initio methods

Table 3. Calculated J_{HD} (in Hz) in Dihydrogen Complexes Using Optimized Geometries from Ref 7

		VWN	Becke-Perdew	SAOP
$WH_2(CO)_3(P^iPr_3)_2$	scal.	44.4	49.8	50.9
(**1**) *(0.89[a] − 0.84[b])*	scal.[c]	44.3		
	scal.[f]	41.1		
	s.o.	44.3		
$[RuH_2Cp(CO)(PCy_3)]^+$	scal.	28.8	32.7	32.9
(**2**) *(0.97[a] − 0.93[b])*	scal.[c]	28.7		
	s.o.	28.7		
$[RuH_2Cp(dmpe)]^+$	scal.	24.2	26.4	27.3
(**3**) *(1.02[a] − 0.99[b])*	scal.[c]	24.1		
	s.o.	24.1		
$[RuH_2Cp^*(dppm)]^+$	scal.	28.0	31.4	31.9
(**4**) *(1.10[d] − 0.98[b])*	scal.[c]			
	s.o.	28.0		
$[OsH_2(en)_2(OAc)]^+$	scal.	8.4	8.8	9.4
(**5**) *(1.34[d] − 1.28[b])*	scal.[c]	8.5		
	s.o.	8.6		
$ReH_2Br_2(NO)(P^iPr_3)_2$	scal.	9.9	10.4	11.0
(**6**) *(1.27[a] − 1.33[b])*	scal.[c]	10.0		
	s.o.	10.0		
$[TaH_2Cp_2(P(OMe)_3)]^+$	scal.	2.4	2.0	2.0
(**7**) *(1.67[a] − 1.64[b])*	scal.[c]	2.4		
	s.o.	2.4		
$OsH_2Cl[CH(C_2H_4P^tBu_2)_2]$	scal.	0.4	0.2	0.2
(**8**) *(1.57[e] − 1.68[a] − 1.63[b])*	scal.[c]	0.5		
	s.o.			
$[IrH_3Cp(PMe_3)]^+$	scal.	2.9	3.1	3.4
(**9**) *(1.69[d] − 1.71[b])*	scal.[c]	3.0		
	s.o.	3.0		
$[IrH_3Cp^*(PMe_3)]^+$	scal.	2.6	2.7	3.0
(**10**) *(1.73[a] − 1.74[b])*	scal.[c]	2.6		
	s.o.	2.7		
NbH_3Cp_2	scal.	0.4	0.1	0.2
(**11**) *(1.76[e] − 1.76[b])*	scal.[c]	0.4		
	s.o.	0.4		
TaH_3Cp_2	scal.	−0.4	−0.8	−0.8
(**12**) *(1.85[d] − 1.82[b])*	scal.[c]	−0.4	−0.7	−0.7
	s.o.	−0.4	−0.8	−0.8
$TaH_2Cp_2(BO_2C_6H_4)$	scal.	−0.1	−0.2	−0.3
(**13**) *(2.3[e] − 2.03[b])*	scal.[c]	−0.1		
	s.o.	−0.1		
$ReH_2(CO)(NO)(PMe_3)_2$	scal.	0.0	−0.1	−0.1
(**14**) *(2.25[a] − 2.22[b])*	scal.[c]	0.0		
	scal.[f]	0.0		
	s.o.	0.1		

[a] d(H−D) measured by solid-state NMR. See ref 7 and references therein. [b] d(H−D) obtained by DFT. [c] Including SD term. [d] d(H−D) measured by single-crystal neutron diffraction.[7] [e] d(H−D) measured by X-ray diffraction.[7] [f] TZP basis instead of TZ2P.

exist for calculations of spin−spin coupling, reproducing the experimental value to such accuracy would be a formidable task since there are many influences (solvent, temperature) in addition to electron correlation that would need to be considered also.

A comparison between the revPBE and the SAOP results shows that the SAOP potential does not improve upon the revPBE functional. In particular, it also yields the strong overestimation of J(H−D) at short H−D distances. Both the revPBE and SAOP results in Table 3 were calculated using the LDA XC kernel since a XC kernel consistent with the SAOP potential is not yet available. Thus, only the difference in the shapes and energies of the unperturbed molecular orbitals in the revPBE and SAOP calculations, respectively, is responsible for the slightly different J(H−D) when comparing the two methods. Whether both methods would yield similar results also if the respective XC kernels were employed in the calculations is unclear.

Table 4. Calculated J_{HD} in Dihydrogen Complexes Using the revPBE Functional with and without GGA Corrections in the XC Kernel (in Hz)[c]

	dist.[a]	revPBE(LDA)	revPBE
$WH_2(CO)_3(P^iPr_3)_2$ (**1**)	0.84	50.5	53.6
$[RuH_2Cp(CO)(PCy_3)]^+$ (**2**)	0.93	33.0	35.9
$[RuH_2Cp(dmpe)]^+$ (**3**)	0.99	27.3	29.6
	1.08[b]	23.3	25.3
$[RuH_2Cp^*(dppm)]^+$ (**4**)	0.98	31.7	34.1
$[OsH_2(en)_2(OAc)]^+$ (**5**)	1.28	8.7	8.6
$ReH_2Br_2(NO)(P^iPr_3)_2$ (**6**)	1.33	10.4	10.3
$[TaH_2Cp_2(P(OMe)_3)]^+$ (**7**)	1.64	2.0	1.3
$OsH_2Cl[CH(C_2H_4P^tBu_2)_2]$ (**8**)	1.63	0.2	−0.4
$[IrH_3Cp(PMe_3)]^+$ (**9**)	1.71	3.1	2.9
$[IrH_3Cp^*(PMe_3)]^+$ (**10**)	1.74	2.7	2.5
NbH_3Cp_2 (**11**)	1.76	0.0	−0.7
TaH_3Cp_2 (**12**)	1.82	−0.8	−1.5
$TaH_2Cp_2(BO_2C_6H_4)$ (**13**)	2.03	−0.3	−0.7
$ReH_2(CO)(NO)(PMe_3)_2$ (**14**)	2.22	−0.1	−0.5

[a] d(H−D) in angstroms from ref 7. [b] Optimization with the GGA revPBE functional. [c] Calculations based on geometries from ref 7, TZ2P basis.

The Influence of the GGA XC Kernel. In Table 4, calculated results at the revPBE(LDA) and the full revPBE level (where the XC kernel is consistent with the potential) are compared. Again, the TZ2P basis without the additional steep functions and the geometries from ref 7 have been used for this comparison.

As might have already been expected from the preceding discussion of the H_2 molecule, the influence of the GGA corrections in the XC kernel is sizable. For the short H−D distance dihydrogen complexes the increase in J(H−D) worsens the agreement with experiment, but this can be traced back to the problem of calculating H_2 itself. In particular for the complexes with large H−D distances, the inclusion of the GGA corrections in the kernel systematically improves the agreement with experiment as well as with the hybrid functional data. For example, for complexes **13** and **14**, a decrease of J(H−D) of as much as 0.4 Hz is obtained. This number is to be compared to experimental values of −0.9 and −1.0 Hz, respectively. The GGA terms in the XC kernel are obviously highly important to obtain the correct H−D coupling constants for these complexes.

By comparing the results in Table 4 with those in Table 1, the influence of the addition of steep 1s functions in the hydrogen basis can again be seen. In several cases, the presence of these functions reduces the magnitude of the coupling constant but consistently so only for the complexes with the shortest H−D distances. There are many other examples where the magnitude is increased instead; therefore, a general trend cannot be observed. Apparently, "cross terms"

Table 5. Calculated J_{HD} in Optimized Dihydrogen Complexes (in Hz)[a]

					ref 7	
	dist.[b]	VWN	Becke-Perdew (LDA)[j]	SAOP (LDA)	calc.	exp.
$WH_2(CO)_3(P^iPr_3)_2$	0.87[g]	43.5	48.8	49.8	34.8	34
(**1**) *(0.89[c] − 0.84[d])*	0.92[h]	41.0	45.8	46.8	34.8	34
	0.86[i]	43.7	49.1	50.2	34.8	34
$[RuH_2Cp(CO)(PCy_3)]^+$	0.99[g]	26.5	30.1	30.4	27.2	22.3
(**2**) *(0.97[c] − 0.93[d])*	1.32[h]	12.0	13.2	13.8	27.2	22.3
	0.98[i]	27.2	30.9	31.2	27.2	22.3
$[RuH_2Cp(dmpe)]^+$	1.41[g]	8.4	9.1	9.6	24.6	22.1
(**3**) *(1.02[c] − 0.99[d])*	1.43[h]	8.4	9.0	9.5	24.6	22.1
	1.08[i]	20.7	23.2	23.6	24.6	22.1
$[OsH_2(en)_2(OAc)]^+$	1.40[g]	5.6	5.8	6.3	6.8	9
(**5**) *(1.34[e] − 1.28[d])*	1.37[h]	6.3	6.5	7.1	6.8	9
	1.40[i]	5.7	5.8	6.4	6.8	9
$ReH_2Br_2(NO)(P^iPr_3)_2$	1.48[g]				9.8	12.8
(**6**) *(1.27[c] − 1.33[d])*	1.48[h]	6.5	6.8	7.2	9.8	12.8
NbH_3Cp_2	1.78[g]	0.2	−0.2	0.0	−1.1	−0.9
(**11**) *(1.76[f] − 1.76[d])*	1.76[h]	0.6	0.3	0.4	−1.1	−0.9
	1.79[i]	0.1	−0.2	−0.1	−1.1	−0.9
TaH_3Cp_2	1.83[g]	−0.5	−0.9	−0.9	−2.0	−1.5
(**12**) *(1.85[e] − 1.82[d])*	1.80[h]	−0.2	−0.5	−0.5	−2.0	−1.5
	1.84[i]	−0.6	−0.9	−1.0	−2.0	−1.5
$ReH_2(CO)(NO)(PMe_3)_2$	2.21[g]	0.0	−0.1	−0.1	−1.0	−1.0
(**14**) *(2.25[c] − 2.22[d])*	2.16[h]	0.1	0.0	0.0	−1.0	−1.0
	2.22[i]	0.0	−0.1	−0.1	−1.0	−1.0

[a] The geometry optimizations have been performed with ADF. [b] d(H−D) in Å. [c] d(H−D) measured by NMR. [d] d(H−D) obtained by DFT. [e] d(H−D) measured by single-crystal neutron diffraction. [f] d(H−D) measured by X-ray diffraction. [g] Optimization with the GGA Becke-Perdew functional. [h] Optimization with the LDA VWN functional. [i] Optimization with the GGA rev-PBE functional. [j] (LDA) indicated the use of the LDA XC kernel in the calculation of the H−D coupling.

of varying sign occur between the basis size and the quality of the functional. The resulting effect on the H−D coupling constant is balanced by such competing effects.

To summarize this paragraph, we find that the GGA corrections in the XC kernel are much more important than spin−orbit effects for predicting the correct sign and magnitude of the H−D coupling constant in our samples. The changes in the coupling constants can amount to several times the coupling constant calculated without a GGA XC kernel for complexes with large H−D distances. They are still of the order of 10% for those complexes with the largest H−D couplings among our samples. Further improvement can obviously be obtained with a hybrid functional, which is not surprising taking their known good performance for couplings between light nuclei into consideration.[35,36] This result is in marked contrast to calculations of ligand chemical shifts and metal−ligand coupling constants in transition-metal systems, where often nonhybrid functionals were found to yield excellent agreement with experiment.[20]

The Influence of the Optimized Geometry and Other DFT Potentials. The large difference between the experimental (22.3 Hz) and the GGA coupling constant for complex **3** in Table 4 based on the optimized geometry of ref 7 suggests that the optimized geometry of the complexes might be a source of error. The question arises whether the performance of any of the density functionals might change if geometries are obtained in consistency with the spin−spin coupling calculations. A marked improvement for complex **3** upon optimization with the revPBE functional, as seen in Table 4, has motivated us to investigate this issue in more detail. For Table 5, we have optimized the geometries of the complexes with the VWN, the Becke-Perdew (BP), and the revPBE functional. The coupling constants listed in Table 5 were subsequently calculated with the TZ2P, using the VWN and the BP functionals as well as the SAOP potential (unfortunately, SAOP optimizations could not be carried out because of the lack of a SAOP energy expression). We have not optimized all complexes at all DFT levels but restricted the investigation to a representative subset. Table 6, on the other hand, lists results obtained for all complexes. The data are based on a consistent treatment at the revPBE level which includes the geometry optimization. The results of Table 6 were calculated with the TZ2P+steep basis and the revPBE XC kernel in order to facilitate a direct comparison with Table 1.

Table 6. Calculated J_{HD} in Dihydrogen Complexes Using the TZ2P+steep Basis Set for the Hydrogen Atoms Bonded to the Metal (in Hz), revPBE Optimized Geometries

			ref 7	
	dist.[a]	revPBE	calc.	exp.
$WH_2(CO)_3(P^iPr_3)_2$ (**1**)	0.86	47.2	34.8	34
$[RuH_2Cp(CO)(PCy_3)]^+$ (**2**)	0.98	32.5	27.2	22.3
$[RuH_2Cp(dmpe)]^+$ (**3**)	1.08	26.2	24.6	22.1
$[RuH_2Cp^*(dppm)]^+$ (**4**)	1.02	31.8	25.2	22.3
$[OsH_2(en)_2(OAc)]^+$ (**5**)	1.40	6.2	6.8	9
$ReH_2Br_2(NO)(P^iPr_3)_2$ (**6**)	1.47	7.2	9.8	12.8
$[TaH_2Cp_2(P(OMe)_3)]^+$ (**7**)	1.68	1.5	0.4	1.5
$OsH_2Cl[CH(C_2H_4P^tBu_2)_2]$ (**8**)	1.66	−0.3	−0.1	0
$[IrH_3Cp(PMe_3)]^+$ (**9**)	1.72	3.2	2.4	3.9
$[IrH_3Cp^*(PMe_3)]^+$ (**10**)	1.76	2.7	2.0	3.3
NbH_3Cp_2 (**11**)	1.79	−0.5	−1.1	−0.9
TaH_3Cp_2 (**12**)	1.84	−1.2	−2.0	−1.5
$TaH_2Cp_2(BO_2C_6H_4)$ (**13**)	2.04	−0.6	−1.2	−0.9
$ReH_2(CO)(NO)(PMe_3)_2$ (**14**)	2.22	−0.8	−1.0	−1.0

[a] d(H−D) in Å, optimized with the revPBE functional.

From the data in Table 5 one can see that, as one might expect, the calculated coupling constants are sensitive to changes in the geometries upon optimization. For the VWN functional it is known that it strongly overbinds but tends to yields quite accurate geometries. Thus, the VWN functional is often used for geometry optimizations along with subsequent energy or property calculations at formally more accurate DFT levels. However, for example for complexes **2** and **3**, and to some extent for **1**, the optimized H−D distances are much too long (more than 0.3 Å) as compared to the experimental values (from solid-state NMR measurements) and the hybrid DFT results of ref 7. For complex **3**, also the Becke-Perdew functional fails to predict the H−D distance correctly. For complex **3**, the overestimation of d(H−D) by the VWN and the BP functionals leads to an underestimation of J(H−D) by almost a factor of 3. On the other hand, in all cases the revPBE functional yields H−D

distances that are similar to the hybrid-DFT results of ref 7 and the experimental values. Both LDA and the BP functional work best for the solid state[60] or for "classical" bonds, while the PBE family (and particularly revPBE and RPBE) gives a somewhat better balance for weak(er) interactions (for an application to transition-metal structures see, e.g., ref 73). Because the structures of the dihydrogen/dihydride complexes are a compromise between several competing weak interactions, revPBE might be expected to be more reliable on general principles.

Our most consistent results at the gradient DFT level are obtained with the revPBE functional. This functional also appears to yield consistently reliable geometries for our samples, whereas the other nonhybrid functionals fail spectacularly in some cases. In Table 6 we have therefore collected the H−D coupling constants similar to Table 2 (i.e. including GGA corrections in the XC kernel as well as the TZ2P+steep basis for the coupled hydrogens) but with geometries optimized at the ZORA-revPBE level instead of using the geometries of ref 7. The relative deviations from experiment are listed in the last column of Table 2 along with the average and the median. The average and median deviation are lower than those in the "Δ revPBE" column. This indicates that better agreement with experiment is obtained for the geometries optimized with the revPBE functional, in particular for complexes with medium to large H−D distances. The problem of overestimating the free dihydrogen coupling is still visible in the complexes with short H−D distances. It should be kept in mind that our data set is small. Therefore, small differences in the averages are statistically not significant. The average is now comparable to the hybrid functional data of ref 7, but the median is still noticeably larger. In two cases the deviation from experiment increases strongly (complexes **5** and **6**). In fact, the change in the results due to the different geometry is larger than what the data in Table 2 suggest since the computed results now under—instead of overestimate the experimental value. The revPBE calculations now predict an equilibrium coupling constant similar to the hybrid-DFT results of ref 7. It is possible that the experimental H−D coupling constants of complexes **5** and **6** include large positive vibrational effects which would cause the calculated equilibrium values to deviate substantially from experiment.

4. Summary and Conclusions

For the H_2 molecule, the calculated nuclear spin−spin coupling constant including gradient corrections both in the potential and in the kernel is about 30% too large in comparison with experiment. Therefore, most of the complexes with short H−D distances are not so well described at the GGA DFT level and exhibit a similar overestimation of J(H−D). For complexes with larger H−D distances, however, good agreement with experiment can be achieved. It turns out that the gradient corrections in the XC kernel are sizable. They are vital for obtaining the correct sign and magnitude of J(H−D) for the complexes with the largest H−D distance.

With the VWN functional, on the other hand, good agreement with experiment is obtained for complexes with short d(H−D). However, this functional fails completely for the dihydride complexes and also leads to extremely poor geometries for some of the complexes. In some cases, the BP GGA functional also yields poor geometries.

The calculations of H−D coupling constants based on geometries that were optimized with the revPBE functional and that were including high exponent 1s functions for the coupled hydrogens as well as GGA corrections in the XC kernel agree best with experiment among the calculations performed in this study. The average relative unsigned deviation from experiment obtained with this approach is similar to the hybrid DFT results of ref 7. The median deviations are larger because of the systematic overestimation of J(H−D) for complexes with short H−D distances. We have traced this overestimation back to problems of the GGA functional to describe the coupling constant for the free hydrogen molecule.

Basis sets with additional high-exponent s-functions are required for a faithful description of the Fermi-contact coupling mechanism. It is the dominant term at short d(H−D), whereas the long-range coupling constants are determined by a sensitive balance of all coupling mechanisms (see Supporting Information).

Spin−orbit corrections for calculations of H−D coupling constants in heavy metal dihydrogen and dihydride complexes are not required at the present level of computational accuracy but will become important for computational methods that are able to deliver one more digit of accuracy. In selected cases, spin−orbit terms might be crucial in order to obtain the correct magnitude for small J(H−D) in heavy metal complexes even with methods of the same accuracy as employed here and in related studies.

In contrast to the rather small spin−orbit coupling effects, vibrational corrections should be included in all calculations of J(H−D) at the present level of accuracy to achieve a more realistic comparison with experiments. Vibrational corrections will also give access to the temperature dependence of the coupling constants. Work along these lines is currently pursued in our group.

Acknowledgment. We thank Dr. D. G. Gusev for making his optimized geometries for the metal complexes available to us prior to publication of ref 7. We thank the Center for Computational Research (CCR) at the University of Buffalo for support. J.A. acknowledges the donors of the American Chemical Society Petroleum Research Fund and the CAREER program of the National Science Foundation (CHE-0447321) for financial support of his research.

Supporting Information Available: Expanded versions of the data tables where the FC, PSO, and DSO contributions to the spin−spin coupling constants are listed separately. This material is available free of charge via the Internet at http://pubs.acs.org.

References

(1) Kubas, G. J. *J. Organomet. Chem.* **2001**, *635*, 37−68.

(2) Heinekey, D. M.; Luther, T. A. *Inorg. Chem.* **1996**, *35*, 4396−4399.

(3) Gelabert, R.; Moreno, M.; Lluch, J. M.; Lledos, A. *J. Am. Chem. Soc.* **1997**, *119*, 9840−9847.

(4) Gelabert, R.; Moreno, M.; Lluch, J. M.; Lledos, A.; Pons, V.; Heinekey, D. M. *J. Am. Chem. Soc.* **2004**, *126*, 8813−8822.

(5) Maltby, P. A.; Schlaf, M.; Steinbeck, M.; Lough, A. J.; Morris, R. H.; Klooster, W. T.; Koetzle, T. F.; Srivastava, R. C. *J. Am. Chem. Soc.* **1996**, *118*, 5396−5407.

(6) Gründemann, S.; Limbach, H.-H.; Buntkowsky, G.; Sabo-etienne, S.; Chaudret, B. *J. Phys. Chem. A* **1999**, *103*, 4752−4754.

(7) Gusev, D. *J. Am. Chem. Soc.* **2004**, *126*, 14249−14257.

(8) Göttger-Schnetmann, I.; White, P. S.; Brookhart, M. *Organometallics* **2004**, *23*, 1766−1776.

(9) Gelfand, I. M.; Fomin, S. V. *Calculus of Variations*; Dover: Mineola, NY, 2000.

(10) Ripmeester, J. A.; Ratcliffe, C. I. *Solid-state NMR studies of inclusion compounds*; National Research Council of Canada, Ottawa 1989.

(11) Conner Jr., W. C.; Falconer, J. L. *Chem. Rev.* **1995**, *95*, 759−788.

(12) Mao, W. L.; Mao, H.-K.; Goncharov, A. F.; Struzhkin, V. V.; Guo, Q.; Hu, J.; Shu, J.; Hemley, R. J.; Somayazulu, M.; Zhao, Y. *Science* **2002**, *297*, 2247−2249.

(13) Shen, K.; Pietrass, T. *Appl. Phys. Lett.* **2004**, *84*, 1567−1569.

(14) Züttel, A.; Wenger, P.; Sudan, P.; Mauron, P.; Orimo, S.-I. *Mater. Sci. Eng. B* **2004**, *108*, 9−18.

(15) Schlapbach, L.; Züttel, A. *Nature* **2001**, *414*, 353−358.

(16) Lueking, A. D.; Yang, R. T. *App. Catal. A* **2004**, *265*, 259−268.

(17) Rosi, N. L.; Eckert, J.; Eddaoudi, M.; Vodak, D. T.; Kim, J.; Keeffe, M. O.; Yaghi, O. M. *Science* **2003**, *300*, 1127−1129.

(18) Schreckenbach, G. *J. Chem. Phys.* **1999**, *110*, 11936−11949.

(19) Patchkovskii, S.; Autschbach, J. Manuscript in preparation.

(20) Autschbach, J. The calculation of NMR parameters in transition metal complexes. In *Principles and Applications of Density Functional Theory in Inorganic Chemistry I*; Kaltsoyannis, N., McGrady, J. E., Eds.; Springer: Heidelberg, 2004; Vol. 112.

(21) Autschbach, J. Calculation of heavy-nucleus chemical shifts: Relativistic all-electron methods. In *Calculation of NMR and EPR Parameters. Theory and Applications*; Kaupp, M., Bühl, M., Malkin, V. G., Eds.; Wiley-VCH: Weinheim, 2004.

(22) Autschbach, J.; Ziegler, T. Relativistic calculation of spin−spin coupling constants. In *Calculation of NMR and EPR Parameters. Theory and Applications*; Kaupp, M., Bühl, M., Malkin, V. G., Eds.; Wiley-VCH: Weinheim, 2004.

(23) Autschbach, J.; Ziegler, T. Relativistic Computation of NMR shieldings and Spin−spin Coupling Constants. In *Encyclopedia of Nuclear Magnetic Resonance*; Grant, D. M., Harris, R. K., Eds.; John Wiley & Sons: Chichester, 2002; Vol. 9.

(24) Bühl, M.; Kaupp, M.; Malkina, O. L.; Malkin, V. G. *J. Comput. Chem.* **1999**, *20*, 91−105.

(25) Bühl, M. *Chem. Phys. Lett.* **1997**, *267*, 251−257.

(26) Hieringer, W.; Görling, A.; Arbouznikov, A.; Kaupp, M. Manuscript to be submitted.

(27) Termaten, A. J.; Aktas, H.; Schakel, M.; Ehlers, A. W.; Lutz, M.; Spek, A. L.; Lammertsma, K. *Organometallics* **2003**, *22*, 1827−1834.

(28) Kaupp, M. Untersuchung der Strukturen, Energien und NMR-Eigenschaften von Übergangsmetallverbindungen mit Hilfe quantenchemischer Methoden, 1996 Habilitationsschrift, Universität Stuttgart, Germany.

(29) Kaupp, M.; Malkin, V. G.; Malkina, O. L. NMR of transition metal compounds. In *Encyclopedia of Computational Chemistry*; von Ragué Schleyer, P., Ed.; John Wiley & Sons: Chichester, 1998.

(30) Lichtenberger, D. L. *Organometallics* **2003**, *22*, 1599−1602.

(31) Autschbach, J.; Ziegler, T. *J. Am. Chem. Soc.* **2001**, *123*, 5320−5324.

(32) Craw, J. S.; Bacskay, G. B.; Hush, N. S. *J. Am. Chem. Soc.* **1994**, *116*, 5937−5948.

(33) Bacskay, G. B.; Bytheway, I.; Hush, N. S. *J. Am. Chem. Soc.* **1996**, *118*, 3753−3756.

(34) Helgaker, T.; Jaszuński, M.; Ruud, K. *Chem. Rev.* **1999**, *99*, 293−352.

(35) Helgaker, T.; Watson, M.; Handy, N. C. *J. Chem. Phys.* **2000**, *113*, 9402−9409.

(36) Sychrovský, V.; Gräfenstein, J.; Cremer, D. *J. Chem. Phys.* **2000**, *113*, 3530−3547.

(37) Autschbach, J.; Ziegler, T. *J. Chem. Phys.* **2000**, *113*, 936−947.

(38) Autschbach, J.; Ziegler, T. *J. Chem. Phys.* **2000**, *113*, 9410−9418.

(39) van Lenthe, E.; Baerends, E. J.; Snijders, J. G. *J. Chem. Phys.* **1993**, *99*, 4597−4610.

(40) van Lenthe, E. *The ZORA Equation*; Thesis, Vrije Universiteit Amsterdam, Netherlands, 1996.

(41) Fonseca Guerra, C.; Visser, O.; Snijders, J. G.; te Velde, G.; Baerends, E. J. Parallelisation of the Amsterdam Density Functional Program. In *Methods and Techniques for Computational Chemistry*; STEF: Cagliari, 1995.

(42) te Velde, G.; Bickelhaupt, F. M.; Baerends, E. J.; van Gisbergen, S. J. A.; Fonseca Guerra, C.; Snijders, J. G.; Ziegler, T. *J. Comput. Chem.* **2001**, *22*, 931−967.

(43) Baerends, E. J. et al. Amsterdam Density Functional, Theoretical Chemistry, Vrije Universiteit, Amsterdam, URL http://www.scm.com.

(44) Autschbach, J.; Ziegler, T. *J. Am. Chem. Soc.* **2001**, *123*, 3341−3349.

(45) Autschbach, J.; Igna, C. D.; Ziegler, T. *J. Am. Chem. Soc.* **2003**, *125*, 1028−1032.

(46) Autschbach, J.; Igna, C. D.; Ziegler, T. *J. Am. Chem. Soc.* **2003**, *125*, 4937−4942.

(47) Autschbach, J.; Le Guennic, B. *J. Am. Chem. Soc.* **2003**, *125*, 13585−13593.

(48) Ramsey, N. F. *Phys. Rev.* **1953**, *91*, 303−307.

(49) Pyykkö, P. *Theor. Chem. Acc.* **2000**, *103*, 214−216.

(50) Wolff, S. K.; Ziegler, T.; van Lenthe, E.; Baerends, E. J. *J. Chem. Phys.* **1999**, *110*, 7689−7698.

(51) Adamo, C.; Barone, V. *J. Chem. Phys.* **1998**, *108*, 664−675.

(52) Perdew, J. P.; Burke, K.; Wang, Y. *Phys. Rev. B* **1996**, *54*, 16533−16539.

(53) Burke, K.; Perdew, J. P.; Wang, Y. Derivation of a generalized gradient approximation: the PE91 density functional. In *Electronic density functional theory. Recent progress and new directions*; Dobson, J. F., Vignale, G., Das, M. P., Eds.; Plenum Press: New York, 1998.

(54) Vosko, S. H.; Wilk, L.; Nusair, M. *Can. J. Phys.* **1980**, *58*, 1200−1211.

(55) Becke, A. D. *Phys. Rev. A* **1988**, *38*, 3098−3100.

(56) Perdew, J. P. *Phys. Rev. B* **1986**, *33*, 8822−8824.

(57) Perdew, J. P.; Burke, K.; Ernzerhof, M. *Phys. Rev. Lett.* **1996**, *77*, 3865−3868.

(58) Zhang, Y.; Yang, W. *Phys. Rev. Lett.* **1998**, *80*, 890.

(59) Perdew, J. P.; Burke, K.; Ernzerhof, M. *Phys. Rev. Lett.* **1998**, *80*, 891.

(60) Hammer, B.; Hansen, L. B.; Norskov, J. K. *Phys. Rev. B* **1999**, *59*, 7413−7421.

(61) Schipper, P. R. T.; Gritsenko, O. V.; van Gisbergen, S. J. A.; Baerends, E. J. *J. Chem. Phys.* **2000**, *112*, 1344−1352.

(62) Gritsenko, O. V.; Schipper, P. R. T.; Baerends, E. J. *Int. J. Quantum Chem.* **2000**, *76*, 407−419.

(63) Chong, D. P.; Gritsenko, O. V.; Baerends, E. J. *J. Chem. Phys.* **2002**, *116*, 1760−1772.

(64) Grüning, M.; Gritsenko, O. V.; van Gisbergen, S. J. A.; Baerends, E. J. *J. Chem. Phys.* **2002**, *116*, 9591−9601.

(65) van Gisbergen, S. J. A.; Pacheco, J. M.; Baerends, E. J. *Phys. Rev. A* **2001**, *63*, 63201.

(66) Poater, J.; van Lenthe, E.; Baerends, E. J. *J. Chem. Phys.* **2003**, *118*, 8584−8593.

(67) Le Guennic, B.; Matsumoto, K.; Autschbach, J. *Magn. Res. Chem.* **2004**, *42*, S99−S116.

(68) Kowalewski, J. *Annu. Rep. NMR Spectrosc.* **1982**, *12*, 81−176.

(69) Ruden, T. A.; Lutnæs, O. B.; Helgaker, T.; Ruud, K. *J. Chem. Phys.* **2003**, *118*, 9572−9581.

(70) Light, J. C.; Hamilton, I. P.; Lill, J. V. *J. Chem. Phys.* **1985**, *82*, 1400−1409.

(71) Witek, H. A.; Fedorov, D. G.; Hirao, K.; Viel, A.; Widmark, P.-O. *J. Chem. Phys.* **2002**, *116*, 8396−8406.

(72) Koch, W.; Holthausen, M. C. *A Chemist's Guide to Density Functional Theory*, 2nd ed.; Wiley-VCH: Weinheim, 2001.

(73) Matveev, A.; Staufer, M.; Mayer, M.; Rösch, N. *Int. J. Quantum Chem.* **1999**, *75*, 863.

CT050042J

JCTC Journal of Chemical Theory and Computation

All-Electron Hybrid Density Functional Calculations on UF_n and UCl_n ($n = 1-6$)

Juan E. Peralta,[‡] Enrique R. Batista,[†] Gustavo E. Scuseria,*[,‡] and Richard L. Martin[†]

Department of Chemistry, Rice University, Houston, Texas 77005-1892, and Los Alamos National Laboratory, Theoretical Division, MS B268, Los Alamos, New Mexico 87545

Received February 28, 2005

Abstract: We calculate the bond dissociation energies of the series UF_n and UCl_n ($n = 1-6$) using the all-electron third-order Douglas-Kroll-Hess approximation in combination with hybrid density functionals. The spin−orbit (SO) operator is included self-consistently using the nuclear-only SO and the screened-nuclear SO approximations. Results are in very good agreement with experimental values, with the exception of the smallest molecules of each series, UF and UCl. By shifting the one-electron orbital energies of UF_6 and UCl_6 to match the HOMO level with the ΔSCF calculated value of the first ionization energy, we are able to reproduce the main features of the photoelectron spectrum of these two molecules.

1. Introduction

The uranium hexafluoride molecule (UF_6) has been a prototype to test computational electronic structure methods for actinide complexes for a quarter of a century.[1,2] The reasons are that experimental data for UF_6 is abundant, and, in addition, UF_6 presents a closed shell electronic ground state, which simplifies the calculations. The rest of the fluoride series, UF_n ($n = 1-5$), and the uranium chlorides, UCl_n ($n = 1-6$), are by far less studied from a computational point of view, even though similar experimental data exists for most of the species on both series.[3−8]

In a recent paper,[9] we have studied the structural properties of UF_6 and UF_5 and the bond dissociation energy (BDE) of UF_6 ($UF_6 \rightarrow UF_5 + F$) using density functional theory (DFT) in combination with both relativistic effective core potentials (RECPs) and an all-electron approach based on the Douglas-Kroll-Hess (DKH) approximation.[10−14] In that study, the hybrid density functionals (i.e., those containing a portion of Hartree−Fock type exchange) B3LYP[15,16] and PBEh (hybrid PBE, also refer to as PBE0[17] and PBE1PBE[18] in the literature) were found to perform notably better than the local spin-density approximation (LSDA), the generalized-gradient approximation (GGA), and the Hartree−Fock approximation. In the same paper,[9] the calculated spin−orbit (SO) effect to the BDE of UF_6 using the all-electron approach was found to be approximately −4 kcal/mol. In a subsequent paper, Batista et al.[19] performed a systematic study of structural properties and BDEs of the series UF_n and UCl_n ($n = 1-6$) using hybrid DFT and RECPs.

In this work, we complete the study of the BDEs of UF_n and UCl_n ($n = 1-6$) using the all-electron DKH approximation and hybrid density functionals. To this end, we analyze three different levels of approximation: the scalar-relativistic (i.e., without the SO operator), including the nuclear-only SO operator, and including the screened-nuclear spin−orbit approximation (SNSO).[20] In the latter two cases, the corresponding SO operator is fully included in the self-consistent procedure by using a generalized Kohn−Sham approach (GKS).

2. Computational Details

Relativistic effects are taken into account through the third-order DKH (DKH3) approximation. Using a fourth-order Hamiltonian (DKH4) does not change the calculated BDEs in the first decimal figure. Scalar relativistic calculations are carried out using the unrestricted Kohn−Sham approximation, i.e., the electronic ground state is represented by a single unrestricted determinant. When the spin−orbit operator is included in the calculation, we have used the GKS approach. In this scheme, the electronic ground state is represented by

* Corresponding author e-mail: guscus@rice.edu.
† Los Alamos National Laboratory.
‡ Rice University.

10.1021/ct050047g CCC: $30.25
Published on Web 05/17/2005

a single determinant built up from two-component spinors. To guarantee the rotational invariance of the total energy we have employed a noncollinear generalization of the spin-density functional energy and potential.[21] Two flavors of the SO operator are considered: the third-order nuclear-only (denoted as SO) and the SNSO operator, which includes the electron−electron SO interaction in an approximate way.[20] The SNSO approximation has been shown to effectively take into account the electron−electron interaction in atoms and molecules with a marginal increase in computational cost.[22] For more details on the implementation the reader is referred to ref 21.

Two different hybrid density functionals are employed: PBEh[17,18] and the B3LYP functional.[16,15] The equilibrium molecular structures are taken from ref 19. We have employed the universal Gaussian basis set (UGBS) of Malli and co-workers[23] for the U atom, which consists of an uncontracted (32*s*29*p*20*d*17*f*) set, and the 6-31+G* basis for fluorine and chlorine. We have checked the impact of using a larger triple-ζ basis set for F and Cl and the basis set superposition error (BSSE) in our results (see next section). The BDEs at the equilibrium geometries are calculated as

$$E(UX_n) = E(UX_{n-1}) + E(X) - E(UX_n) \qquad (1)$$

Finite temperature effects and zero-point energy correction are rather small[19] and not included in this study.

The population analysis reported here has been carried out using the scalar relativistic DKH3 Hamiltonian and the PBEh functional. The presence of the SO operator (either nuclear-only or SNSO) as well as the choice of the functional produces only minor changes in the population analysis, and therefore its qualitative meaning remains the same.

All calculations were carried out with the development version of the *Gaussian*[24] suite of codes.

3. Results and Discussion

As pointed out in ref 19, the bonding in UF_n and UCl_n can be approximately seen as $U^{+n}F_n^-$ and $U^{+n}Cl_n^-$, respectively. This ionic picture arises from the ionization of the U valence orbitals to the 2*p* orbitals of F or 3*p* orbitals of Cl. To obtain a more accurate picture of the bonding nature of the UF_n and UCl_n complexes, we have performed an atomic electron population analysis of the U atom using the natural population analysis (NPA).[25] The NPA has recently been shown to achieve the best performance among several orbital based partitioning schemes.[26]

In Table 1, we show the natural valence electron configuration and the natural charge of the U center for the series UF_n and UCl_n. As suggested by Clark and co-workers, the NPA of the U orbitals is chosen such that the valence space is composed of the 5*f*, 6*d*, and 7*s* orbitals.[26] Inspection of the U electron configuration of the UF_n indicates that the electron donation from the U to the F atoms is not uniform along the series. For UF, the total charge donated by the U center is $+0.74e^-$, indicating a strong ionic character. The total charge donated, per fluorine atom, systematically decreases as the number of F atoms increases: $+0.69e^-$ (UF_2), $+0.66e^-$ (UF_3), $+0.59e^-$ (UF_4), $+0.46e^-$ (UF_5), and $+0.35e^-$ (UF_6). It is worth commenting that the total charge on U increases from $+0.74e^-$ for UF to $+2.35e^-$ for UF_4, mainly due to changes in the population of the 6*d* and 7*s* orbitals, while the population of the 5*f* remains unchanged. Further fluorination, $UF_4 \rightarrow UF_5 \rightarrow UF_6$, leads to a redistribution of the charge among the U orbitals, with very little decrease of the total charge of the U atom.

Table 1: Natural Electron Configuration and Natural Charge of the Uranium Atom from Natural Population Analysis

	configuration			U		configuration			U
molecule	5*f*	6*d*	7*s*	charge	molecule	5*f*	6*d*	7*s*	charge
UF	2.94	0.47	1.85	+0.74	UCl	3.07	0.40	1.87	+0.65
UF_2	3.09	0.67	0.84	+1.38	UCl_2	3.14	0.77	0.84	+1.21
UF_3	3.04	0.69	0.28	+1.97	UCl_3	3.18	0.92	0.23	+1.62
UF_4	2.55	0.99	0.05	+2.35	UCl_4	2.69	1.58	0.23	+1.38
UF_5	2.36	1.17	0.09	+2.29	UCl_5	2.91	1.98	0.30	+0.65
UF_6	2.31	1.42	0.14	+2.08	UCl_6	3.39	2.41	0.38	−0.24

Table 2: All-Electron Bond Dissociation Energies for the UF_n Series (in kcal/mol)

	B3LYP			PBEh			
	scalar	SO	SNSO	scalar	SO	SNSO	exp[5]
UF	165.1	168.5	172.7	164.1	166.1	172.7	154.9
UF_2	142.3	142.6	143.6	146.1	145.2	146.4	135.0
UF_3	148.3	147.3	148.2	146.5	146.7	147.2	147.9
UF_4	139.0	137.8	139.9	140.8	138.7	140.5	147.0
UF_5	99.7	94.7	98.6	98.2	92.5	96.8	98.0
UF_6	76.0	72.2	75.7	74.5	70.8	74.4	71.0

Table 3: All-Electron Bond Dissociation Energies for the UCl_n Series (in kcal/mol)

	B3LYP			PBEh			
	scalar	SO	SNSO	scalar	SO	SNSO	exp[6]
UCl	121.0	124.8	129.2	123.8	126.0	132.9	104.9
UCl_2	106.3	105.1	105.1	115.2	114.3	114.7	115.1
UCl_3	114.7	111.5	113.0	116.6	113.2	113.8	116.3
UCl_4	89.3	91.3	92.7	92.7	94.7	96.4	100.9
UCl_5	46.7	44.7	48.6	49.6	47.3	51.3	50.4
UCl_6	48.5	37.9	41.0	51.1	40.4	43.6	

The picture that emerges for the first 3 molecules of the UCl_n series ($n = 1-3$) is similar to that of their analogues UF_n (Table 1), although the total charge on U is slightly smaller, indicating a weaker charge donation to the Cl atoms. Addition of more Cl atoms, $UCl_3 \rightarrow UCl_6$, yields a different situation when compared with UF_n; the total charge on U decreases from $+1.62e^-$ for UCl_3, to $+1.38e^-$ for UCl_4, to $+0.65e^-$ for UCl_5, and to $-0.24e^-$ for UCl_6. If we express this decrease in terms of the charge per Cl atom, we obtain $+0.54e^-$ for UCl_3, $+0.35e^-$ for UCl_4, $+0.13e^-$ for UCl_5, and $-0.04e^-$ for UCl_6, which represents a progressive loss of the ionic character of the U−Cl bonds.

In Tables 2 and 3 we show the all-electron BDEs calculated using the B3LYP and the PBEh functionals and three different relativistic Hamiltonians: scalar, SO, and SNSO, as described above, as well as the experimental

Table 4: One-Electron Enery Levels of the Highest Occupied Molecular Orbitals of UF_6 Using the All-Electron DKH3 Hamiltonian and the PBEh Functional[b]

scalar relativistic		spinor	SO	SNSO[a]
t_{1u}	−12.18	γ_{8u}	−11.80	−13.95
		γ_{6u}	−12.94	−15.09
t_{1g}	−12.79	γ_{8g}	−12.79	−14.94
		γ_{6g}	−12.80	−14.95
t_{2u}	−13.70	γ_{8u}	−13.70	−15.85
		γ_{7u}	−13.70	−15.85
a_{1g}	−13.75	γ_{6g}	−13.76	−15.91
t_{1u}	−14.18	γ_{8u}	−14.17	−16.32
		γ_{6u}	−14.20	−16.35
t_{2g}	−14.59	γ_{7g}	−14.55	−16.70
		γ_{8g}	−14.62	−16.77
e_g	−15.19	γ_{8g}	−15.19	−17.34
t_{1u}	−27.40	γ_{8u}	−25.43	−27.58
		γ_{6u}	−31.73	−33.88
a_{1g}	−33.77	γ_{6g}	−33.77	−35.92
e_g	−34.30	γ_{8g}	−34.31	−36.46
t_{1u}	−35.81	γ_{8u}	−35.44	−37.59
		γ_{6u}	−38.47	−40.62

[a] The orbital energy levels are shifted by 2.15 eV to match the HOMO with the ΔSCF calculated value of the first ionization energy. [b] All values in eV.

Table 5: One-Electron Enery Levels of the Highest Occupied Molecular Orbitals of UCl_6 Using the All-Electron DKH3 Hamiltonian and the PBEh Functional[b]

scalar relativistic		spinor	SO	SNSO[a]
t_{1g}	−9.46	γ_{8g}	−9.44	−11.08
		γ_{6g}	−9.49	−11.13
t_{1u}	−10.22	γ_{8u}	−10.00	−11.64
		γ_{6u}	−10.63	−12.27
t_{2u}	−10.43	γ_{7u}	−10.40	−12.04
		γ_{8u}	−10.42	−12.06
t_{1u}	−10.76	γ_{8u}	−10.49	−12.13
		γ_{6u}	−10.84	−12.48
t_{2g}	−11.56	γ_{7u}	−11.50	−13.14
		γ_{8u}	−11.60	−13.24
a_{1g}	−11.72	γ_{6g}	−11.73	−13.37
e_g	−12.10	γ_{8g}	−12.10	−13.74
t_{1u}	−22.56	γ_{8u}	−22.01	−23.65
		γ_{6u}	−23.21	−24.85
e_g	−23.72	γ_{8g}	−23.72	−25.36
a_{1g}	−23.85	γ_{6g}	−23.85	−25.49
t_{1u}	−29.52	γ_{8u}	−27.65	−29.29
		γ_{6u}	−35.91	−37.55

[a] The orbital energy levels are shifted by 1.64 eV to match the HOMO with the ΔSCF calculated value of the first ionization energy. [b] All values in eV.

values. The two hybrid functionals employed here give similar BDEs; the largest difference (10 kcal/mol) occurs for the UCl_2 molecule.

We have tested the effect of BSSE on our results. Using the counterpoise method, the effect of BSSE on calculated BDEs (with PBEh and the scalar relativistic Hamiltonian) is −0.9 kcal/mol for UF_6 and −0.5 kcal/mol for UCl_6. We have also tested the quality of the basis chosen for F and Cl. Using the larger triple-ζ 6-311+G(3df) basis, the BDEs for UF_6 and UCl_6 change by 0.5 and 1.2 kcal/mol, respectively.

The effect of the nuclear-only SO on the BDEs (columns labeled as "SO" in Tables 2 and 3) is rather small for UF_n. For instance, using PBEh, the SO contribution to the BDEs is about +2 kcal/mol for UF, and decreasing when increasing n, with a SO effect on the BDE of UF_6 of −4 kcal/mol. On the other hand, the effect of the electron−electron SO interaction included through the SNSO approximation (columns labeled as "SNSO" in Tables 2 and 3) is positive along the series. The SNSO tends to compensate the effect of the nuclear-only SO for $n = 2-6$, while for UF they operate in the same direction.

The effect of the nuclear-only SO on the UCl_n BDEs follows the same trend as for UF_n, although its magnitude for UCl_6 is larger (approximately 10 kcal/mol). The SNSO correction to the BDEs of UCl_n is similar to that of the UF_n series. As a consequence, we obtain a SO effect for UCl_6 of about −7 kcal/mol, while for the rest of the series ($n = 2-6$), the effect increases when decreasing n up to +9 kcal/mol for UCl.

It is interesting to relate the trend in the BDEs along both series of UF_n and UCl_n to the change of the ionic character (as reflected by the NPA charge on the U atom). According to our calculations, the larger the ionic character is, the larger the BDE. This suggests that even though the nature of the U−F and U−Cl bonds is a mixture of ionic and covalent character, the trend in the BDEs is given mainly by its ionic component.

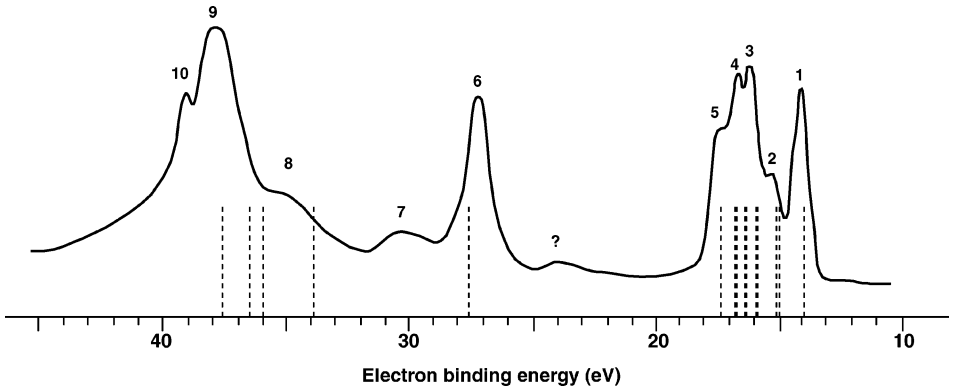

Figure 1. Photoelectron spectrum of UF_6 from ref 29 (solid line) and calculated orbital energies (dashed lines). The orbital energies have been shifted so that the HOMO matches the ΔSCF calculation of the first ionization potential.

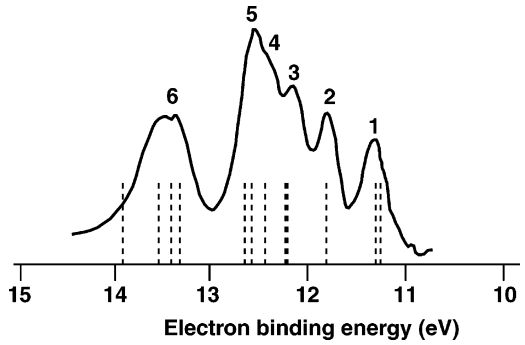

Figure 2. Photoelectron spectrum of UCl_6 from ref 31 and calculated orbital energies. The orbital energies have been shifted so that the HOMO matches the ΔSCF calculation of the first ionization potential.

Our scalar relativistic BDE are in fairly good agreement with those from ref 19 using scalar relativistic effective core potentials. The largest discrepancy corresponds to UCl_6, where the difference is approximately 7 kcal/mol.

There is an overall good performance of both hybrid functionals for $n = 2-6$, although there is a noticeable worse performance for the BDEs of UF and UCl. This could be attributed to the unsuitability of the approximation employed here to describe systems with a large number of unpaired electrons.[27] This observation is in line with the findings of a previous paper.[19] It is worth mentioning that although the total SO effect for UF and UCl is the largest along both series it does not improve the agreement with experiment, making the error associated with the neglect of multiplet interaction in DFT even more dramatic.

There are also large spin−orbit effects on the first ionization energy (IE) of these systems. For example, at the ΔSCF level of approximation, the scalar relativistic first IE of UF_6 is 14.30 eV with PBEh, and 13.96 eV when the SNSO is included. The experimental value is 14.14 eV.[28,29] This error is of the order of the mean absolute error in the predicted IEs in the G3 data set (0.20 eV).[30] A similar analysis for UCl_6 yields a first IE of 11.08 eV, also in good agreement with the experimental value, 11.26 eV.[31] Tables 4 and 5 present the valence orbital symmetries, the Kohn−Sham orbital eigenvalues, and a set of adjusted energies where the first eigenvalue has been adjusted to the ΔSCF value and the remaining shifted accordingly. The latter are compared with experimental photoemission spectra in Figures 1 and 2. The agreement with experiment is quite good. In fact, the calculation helps identify the features labeled as 7 and "?"[29] in UF_6 as artifacts not associated with the molecular ionization spectrum. Our assignments for UF_6 are consistent with previous studies,[1,32,33] and those for UCl_6 differ only slightly from the pioneering work of Thornton et al.[31] (the order of the a_{1g} and t_{2g} states in the 11 eV range differs in the present work).

4. Conclusions

The BDEs of the series UF_n and UCl_n ($n = 1-6$) have been calculated using the all-electron third-order DKH approximation in combination with the hybrid density functionals PBEh and B3LYP. The spin−orbit operator is included self-consistently using the nuclear-only and the SNSO approximation. Results are in very good agreement with experimental values, with the exception of the smallest molecules of each series, UF and UCl, where the deviation from experiment is 18 and 28 kcal/mol, respectively. These systems represent a challenge for computational methods, and they may need to be studied using accurate multireference approaches.

Population analysis reveals a larger ionic character for the U−F bonds than for the U−Cl bonds as well as an increase of the ionicity when decreasing the number of halogen atoms.

The ΔSCF first ionization energies of UF_6 and UCl_6 calculated using PBEh and the SNSO approximation are in good agreement with available experimental data. By shifting the one-electron orbital energies to match the HOMO level with the ΔSCF calculated value of the first ionization energy, we are able to reproduce the main features of the UF_6 and UCl_6 photoelectron spectrum.

Acknowledgment. The work at Rice University was supported by the Department of Energy grant DE-FG02-04ER15523. The work at Los Alamos National Laboratory was supported by the Division of Chemical Sciences, Office of Basic Energy Sciences, U.S. Department of Energy under the Heavy Element Chemistry program at Los Alamos National Laboratory. J.E.P. thanks A. E. Clark and P. J. Hay.

References

(1) Hay, P. J.; Wadt, W. R.; Kahn, L. R.; Phillips, D. H. *J. Chem. Phys.* **1979**, *71*, 1767.

(2) Case, D. A.; Yang, C. Y. *J. Phys. Chem.* **1979**, *72*, 3443.

(3) Hildenbrand, D. L.; Gurvich, L. B.; Yungman, V. S. *The Chemical Thermodynamics of Actinide Elements and Compounds, Part 13, The Gaseous Actinide Ions;* International Atomic Energy Agency: Vienna, 1985.

(4) Fuger, J.; Parker, V. B.; Hubbard, W. N.; Oetting, F. L. *The Chemical Thermodynamics of Actinide Elements and Compounds, Part 8, The Actinide Halides;* International Atomic Energy Agency: Vienna, 1983.

(5) Hildenbrand, D. L.; Lau, K. H. *J. Chem. Phys.* **1991**, *94*, 1420.

(6) Hildenbrand, D. L.; Lau, K. H. *Pure Appl. Chem.* **1992**, *64*, 87.

(7) Cordfunke, E. H. P.; Ouweltjes, W.; Prins, G. *J. Chem. Thermodyn.* **1982**, *14*, 495.

(8) Cordfunke, E. H. P.; Ouweltjes, W.; Prins, G.; Vlaanderen, P. V. *J. Chem. Thermodyn.* **1983**, *15*, 1103.

(9) Batista, E. R.; Martin, R. L.; Hay, P. J.; Peralta, J. E.; Scuseria, G. E. *J. Chem. Phys.* **2004**, *121*, 2144.

(10) Douglas, M.; Kroll, N. M. *Ann. Phys.* **1974**, *82*, 89.

(11) Hess, B. A. *Phys. Rev. A* **1985**, *32*, 756, **1986**, *33*, 3742.

(12) Nakajima, T.; Hirao, K. *J. Chem. Phys.* **2000**, *113*, 7786.

(13) van Wüllen, C. *J. Chem. Phys.* **2004**, *120*, 7307.

(14) Wolf, A.; Reiher, M.; Hess, B. E. *J. Chem. Phys.* **2002**, *117*, 9215.

(15) Becke, A. D. *J. Chem. Phys.* **1993**, *98*, 5648.

(16) Stephens, P. J.; Devlin, F. J.; Chabalowski, C. F.; Frisch, M. J. *J. Chem. Phys.* **1994**, *98*, 11623.

(17) Adamo, C.; Barone, V. *J. Chem. Phys.* **1999**, *110*, 6158.

(18) Ernzerhof, M.; Scuseria, G. E. *J. Chem. Phys.* **1999**, *110*, 5029.

(19) Batista, E. R.; Martin, R. L.; Hay, P. J. *J. Chem. Phys.* **2004**, *121*, 11104.

(20) Boettger, J. C. *Phys. Rev. B* **2000**, *62*, 7809.

(21) Peralta, J. E.; Scuseria, G. E. *J. Chem. Phys.* **2004**, *120*, 5875.

(22) Majumder, S.; Matveev, A. V.; Rösch, N. *Chem. Phys. Lett.* **2003**, *382*, 186.

(23) Malli, G. L.; Da Silva, A. B. F.; Ishikawa, Y. *Phys. Rev. A* **1993**, *47*, 143.

(24) Gaussian Development Version, Revision B.07, Frisch, M. J.; Trucks, G. W.; Schlegel, H. B.; Scuseria, G. E.; Robb, M. A.; Cheeseman, J. R.; Montgomery, J. A., Jr.; Vreven, T.; Kudin, K. N.; Burant, J. C.; Millam, J. M.; Iyengar, S. S.; Tomasi, J.; Barone, V.; Mennucci, B.; Cossi, M.; Scalmani, G.; Rega, N.; Petersson, G. A.; Nakatsuji, H.; Hada, M.; Ehara, M.; Toyota, K.; Fukuda, R.; Hasegawa, J.; Ishida, M.; Nakajima, T.; Honda, Y.; Kitao, O.; Nakai, H.; Klene, M.; Li, X.; Knox, J. E.; Hratchian, H. P.; Cross, J. B.; Bakken, V.; Adamo, C.; Jaramillo, J.; Gomperts, R.; Stratmann, R. E.; Yazyev, O.; Austin, A. J.; Cammi, R.; Pomelli, C.; Ochterski, J. W.; Ayala, P. Y.; Morokuma, K.; Voth, G. A.; Salvador, P.; Dannenberg, J. J.; Zakrzewski, V. G.; Dapprich, S.; Daniels, A. D.; Strain, M. C.; Farkas, O.; Malick, D. K.; Rabuck, A. D.; Raghavachari, K.; Foresman, J. B.; Ortiz, J. V.; Cui, Q.; Baboul, A. G.; Clifford, S.; Cioslowski, J.; Stefanov, B. B.; Liu, G.; Liashenko, A.; Piskorz, P.; Komaromi, I.; Martin, R. L.; Fox, D. J.; Keith, T.; Al-Laham, M. A.; Peng, C. Y.; Nanayakkara, A.; Challacombe, M.; Gill, P. M. W.; Johnson, B.; Chen, W.; Wong, M. W.; Gonzalez, C.; Pople, J. A. Gaussian, Inc., Wallingford, CT, 2004.

(25) Reed, A. E.; Curtiss, L. A.; Weinhold, F. *Chem. Rev.* **1988**, *88*, 893.

(26) Clark, A. E.; Sonnenberg, J. L.; Hay, P. J.; Martin, R. L. *J. Chem. Phys.* **2004**, *121*, 2563.

(27) Gagliardi, L.; Roos, B. O. *Nature* **2005**, *433*, 848.

(28) Karlsson, L.; Mattsson, L.; Jadrny, R.; Bergmark, T.; Siegbahn, K. *Phys. Scr.* **1976**, *14*, 230.

(29) Mårtensson, N.; Malmquist, P.-Å.; Svensson, S.; Johansson, B. *J. Chem. Phys.* **1984**, *80*, 5458.

(30) Staroverov, V. N.; Scuseria, G. E.; Tao, J.; Perdew, J. P. *J. Chem. Phys.* **2003**, *119*, 12129.

(31) Thornton, G.; Edelstein, N.; Rösch, N.; Egdel, R. G.; Woodwark, D. R. *J. Chem. Phys.* **1979**, *70*, 5218.

(32) Koelling, D. D.; Ellis, D. E.; Bartlett, R. J. *J. Chem. Phys.* **1976**, *65*, 3331.

(33) deJong, W. A.; Nieuwpoort, W. C. *Int. J. Quantum Chem.* **1996**, *58*, 203.

CT050047G

JCTC Journal of Chemical Theory and Computation

Effects of Arg90 Neutralization on the Enzyme-Catalyzed Rearrangement of Chorismate to Prephenate

Cristiano Ruch Werneck Guimarães,* Marina Udier-Blagović, Ivan Tubert-Brohman, and William L. Jorgensen*

Department of Chemistry, Yale University, 225 Prospect Street, New Haven, Connecticut 06520-8107

Received March 28, 2005

Abstract: Chorismate mutase (CM) is an enzyme that catalyzes the Claisen rearrangement of chorismate to prephenate. In a recent effort to understand the basis for catalysis by CM, Kienhöfer and co-workers (*J. Am. Chem. Soc.* **2003**, *125*, 3206−3207) reported results on the mutation of Arg90 in *Bacillus subtilis* CM (BsCM) to citrulline (Cit), an isosteric but neutral arginine analogue. An ca. 10^4-fold decrease in k_{cat} or 5.9 kcal/mol increase in the free-energy barrier ($\Delta G^{\ddagger}$) for the overall catalysis was observed upon mutation. In this work, attention is turned to determining the key factors that contribute to the reduced catalytic efficiency of Arg90Cit BsCM. Using a combined QM/MM Monte Carlo/Free-Energy Perturbation method, a $\Delta\Delta G^{\ddagger}$ value of 3.3 kcal/mol is obtained. The higher free-energy barrier for the mutant is exclusively related to inferior stabilization of the TS, particularly one of its carboxylate groups, by neutral Cit. In addition, the reaction becomes 2.0 kcal/mol more exergonic. As BsCM is limited by product release, this step contributes to the remainder of the 10^4-fold decrease in the rate constant in going from Arg90 to Cit.

Introduction

Chorismate mutase (CM) is an enzyme that catalyzes the Claisen rearrangement of chorismate to prephenate, a key step in the shikimate pathway for generating aromatic amino acids in plant, fungal, and bacterial systems.[1−3] The reaction, which proceeds via a chairlike transition state (TS) with the C−O cleavage preceding the C−C bond formation (Scheme 1), is a relatively rare example of a chemical transformation that occurs via an identical mechanism in various solvents as well as within the enzymatic environment provided by CM.[4]

This system has been the subject of a variety of experimental[5] and theoretical[6] investigations over the last 20 years. Despite the great attention, the origins of the rate enhancement by CM still remain controversial. Preferential stabilization of the highly polarized TS in the enzyme environment,[7] favorable formation of near attack conformations (NACs)[8] in the active site,[9] and destabilization of the reactant caused by a protein-driven conformational compression[6g,10] have all been presented as possibilities.

Scheme 1. The Chorismate to Prephenate Rearrangement and the Transition State Analogue

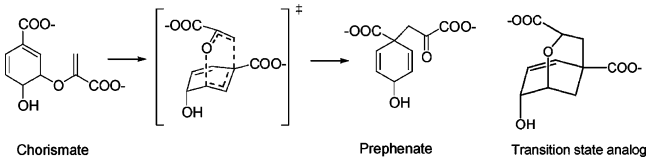

In two recent works,[11] the origins of solvent effects and rate enhancement provided by the *Bacillus subtilis* CM (BsCM) for the rearrangement of chorismate to prephenate were examined using mixed quantum mechanics and molecular mechanics (QM/MM)[12] combined with Monte Carlo[13]/Free-Energy Perturbation[14] (MC/FEP) simulations and the NAC concept.[9] Scheme 2 illustrates the important steps in the NAC-based model for the chorismate to prephenate rearrangement. The first component of the free energy of activation ($\Delta G^{\ddagger}$), the preequilibrium free energy (ΔG_{preq}), is the free energy associated with the process of orienting

* Corresponding author e-mail: cris@ramana.chem.yale.edu (C.R.W.G.) william.jorgensen@yale.edu (W.L.J.).

10.1021/ct0500803 CCC: $30.25
Published on Web 06/04/2005

Scheme 2. NAC-Based Model for the Chorismate to Prephenate Rearrangement

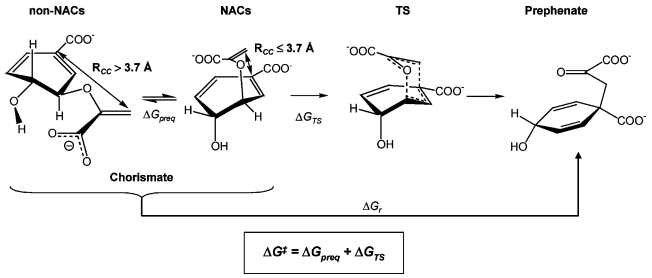

chorismate in appropriate conformations, NACs, that are well disposed to lead directly to the TS of the reaction. This step substitutes the former pseudodiequatorial/pseudodiaxial preequilibrium, which provides a less general and more restrictive definition of a reactive conformer.[15] Chorismate conformers with the forming C−C bond (R_{CC}) less than or equal to 3.70 Å, a distance shorter than the van der Waals distance between vinyl carbons, are considered as NACs. The second component of $\Delta G^{\ddagger}$ is the free energy associated with the conversion of the NACs into the TS (ΔG_{TS}), leading ultimately to the formation of prephenate, and ΔG_r is the free-energy change for the reaction. The QM/MM MC/FEP results suggested that the rate enhancement by CM over the aqueous phase arises primarily from conformational compression of NACs by the enzyme, in agreement with the work of Lyne et al.[6g] and Khanjin et al.[10]

In one of the latest efforts to understand the basis for catalysis by CM, Kienhöfer and co-workers[16] reported results on the mutation of Arg90 in BsCM to citrulline (Cit), an isosteric but neutral arginine analogue. In doing that, the authors aimed at investigating the effects of neutralization of a critical cationic group in the selective stabilization of the TS. An ca. 10^4-fold decrease in k_{cat} or a 5.9 kcal/mol increase in the free-energy barrier for the overall catalysis was observed. A more modest 2.7-fold increase in the K_m value, which corresponds to a 0.6 kcal/mol less favorable free energy of binding for chorismate, indicated only minor perturbation of the ground-state Michaelis complex upon mutation. Therefore, the results show that the binding of the TS to BsCM is considerably affected by the Arg90Cit mutation, becoming 6.5 kcal/mol less favorable. Interestingly, the inhibition constant for Bartlett's transition state analogue (TSA)[17] (Scheme 1) increases only 5.7-fold upon mutation, which corresponds to a 1.1 kcal/mol less favorable free energy of binding; this contrasts dramatically with the 6.5 kcal/mol for the TS. Kienhöfer and co-workers[16] suggest that the TS is more affected by the neutralization of Arg90 due to greater anionic character for the ether oxygen in the TS than in the TSA.

In this work, further attention is turned to determining the key factors that contribute to the reduced catalytic efficiency of Arg90Cit BsCM. To accomplish that, QM/MM MC/FEP simulations were carried out to compute the effects of the Arg90→Cit transformation on ΔG_{preq}, ΔG_{TS}, and ΔG_r. This work also aims at understanding the different decrease in affinity upon mutation for the binding of the TS and TSA to BsCM.

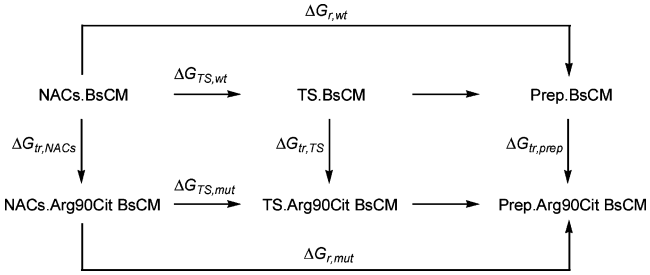

Figure 1. Thermodynamic cycles used for the calculation of relative free energies between the mutant and wild-type BsCMs for the conversion of NACs into the TS ($\Delta\Delta G_{TS}$) and for the reaction ($\Delta\Delta G_r$). $\Delta G_{tr,TS}$, $\Delta G_{tr,NACs}$, and $\Delta G_{tr,prep}$ are the free-energy changes associated with the Arg90→Cit transformation for the TS, NACs, and prephenate bound to the enzyme environments.

Computational Details

NACs vs non-NACs (ΔG_{preq}). Since non-NACs are in equilibrium with NACs, ΔG_{preq} can be estimated by counting the number of NACs and non-NACs sampled in molecular dynamics or Monte Carlo simulations using eq 1, where P_{NACs} and $P_{non-NACs}$ are the probabilities of sampling NACs and non-NACs.

$$\Delta G_{preq} = -RT \ln \frac{P_{NACs}}{P_{non-NACs}} \quad (1)$$

Alternatively, ΔG_{preq} can be derived from a potential of mean force (pmf)[14b] that is computed for the reaction coordinate that converts non-NACs into NACs (R_{CC}) in Scheme 2. The latter approach was followed in this work, and ΔG_{preq} was obtained by computing pmf curves for R_{CC}, $G(R_{CC})$, in BsCM and Arg90Cit BsCM. The lower limit for R_{CC} was taken as the value of R_{CC} in which the ether C−O linkage begins to break in order to form the transition state. The upper limit for R_{CC} was determined as the value of R_{CC} in which the chorismate structure begins to deform from a normal geometry for a ground state. The radial distribution function for R_{CC} ($g(R_{CC})$) in each environment was obtained from $G(R_{CC})$. The probability of sampling R_{CC} ($P(R_{CC})$) was obtained as a product of the respective $g(R_{CC})$ and the volume element of the configuration space corresponding to the coordinate R_{CC}. The volume element can be interpreted as a quantity proportional to the probability of sampling R_{CC} with the potential function set to zero.[14b] In the present case, the volume element is $4\pi R_{CC}^2$.

$\Delta\Delta G_{TS}$, $\Delta\Delta G_r$, and TS vs TSA. Since the free energy is a thermodynamic state function, the cycles shown in Figure 1 give the relative free energies between the mutant and wild-type BsCMs for the conversion of NACs into the TS ($\Delta\Delta G_{TS}$) (eq 2) and for the reaction ($\Delta\Delta G_r$) (eq 3). In eqs 2 and 3, $\Delta G_{TS,mut}$ and $\Delta G_{r,mut}$ are the free-energy changes for the conversion of NACs into the TS and prephenate in the mutant BsCM, while $\Delta G_{TS,wt}$ and $\Delta G_{r,wt}$ are the corresponding quantities for the wild-type BsCM. $\Delta G_{tr,TS}$, $\Delta G_{tr,NACs}$, and $\Delta G_{tr,prep}$ are the free-energy changes associated with the Arg90→Cit transformation for the TS, chorismate NACs, and prephenate bound to the active site of the enzyme, respectively. It is important to note that formally ΔG_r is the

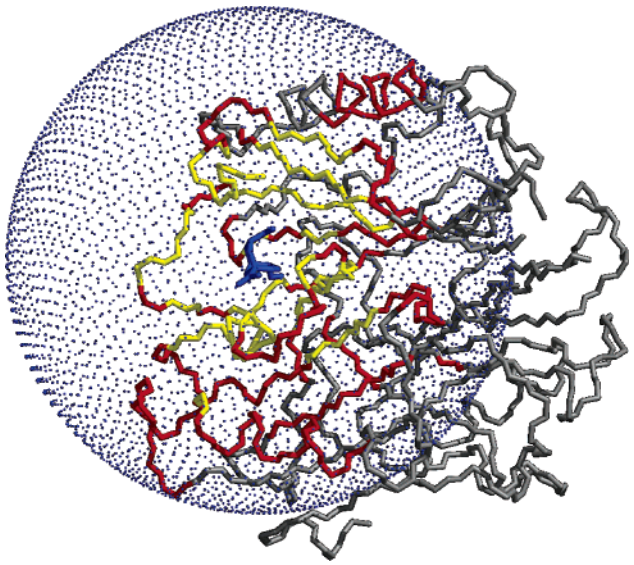

Figure 2. Chorismate mutase with Bartlett's inhibitor (shown in blue). The blue dots represent the 22-Å radius water cap of 766 molecules. Residues with any atom within 15 Å of the center of the reacting system were retained in the simulations (residues in yellow and red).

free-energy change for the conversion of chorismate to prephenate. However, as almost 100% of the chorismate conformers in the active site of both the wild-type and mutant BsCMs are NACs, as described in the Results section, $\Delta\Delta G_r$ can be written as the difference between $\Delta G_{tr,prep}$ and $\Delta G_{tr,NACs}$.

$$\Delta\Delta G_{TS} = \Delta G_{TS,mut} - \Delta G_{TS,wt} = \Delta G_{tr,TS} - \Delta G_{tr,NACs} \quad (2)$$

$$\Delta\Delta G_r = \Delta G_{r,mut} - \Delta G_{r,wt} = \Delta G_{tr,prep} - \Delta G_{tr,NACs} \quad (3)$$

The different decrease in affinity upon mutation for the binding of the TS and TSA to BsCM was also investigated. To accomplish that, QM/MM MC/FEP simulations for the Arg90→Cit transformation with the TSA bound to the active site of the enzyme were also performed.

QM/MM System. Coordinates for the 2.2 Å *Bacillus subtilis* crystal structure complexed with the TSA (2cht from the Brookhaven Protein Data Bank) were employed.[18] Of the four homotrimers of chorismate mutase in the 2cht structure, only the first was retained (Figure 2). A single active site was taken as the center of the reacting system. Residues with any atom within 15 Å of the center of the reacting system were retained in the simulations (residues in yellow and red), and any clipped residues were capped with acetyl and *N*-methylamine groups. The enzymatic system then has 2249 atoms, consisting of 149 amino acid residues and a single substrate or the TSA (shown in blue). In the QM/MM calculations, degrees of freedom for the protein backbone atoms were not sampled. Only the bond angles and dihedral angles for the side chains of residues with any atom within 10 Å from the center of the reacting system were varied (residues in yellow). The substrate and TSA are fully flexible except where specified below. Charge neutrality for the wild-type BsCM was imposed by having a total protein charge of 2 e; charged residues near the active

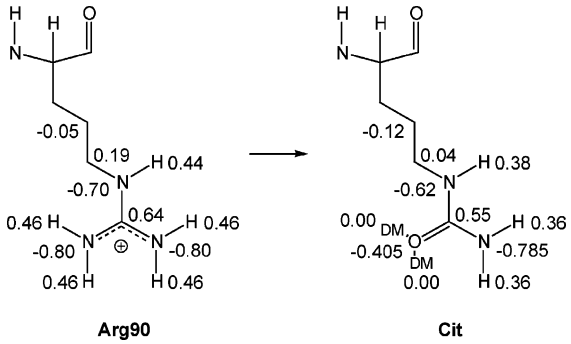

Figure 3. The Arg90→Cit transformation and the change in the charge distribution. DM is a dummy atom.

site were assigned normal protonation states for physiological pH, and the adjustments for neutrality were made to the most distant residues. Each protein-solute system was solvated with a 22-Å radius water cap of 766 molecules, and a half-harmonic potential with a 1.5 kcal/mol·Å^2 force constant was applied to water molecules at distances greater than 22 Å from the center of the solute. The preparation of the enzymatic systems was much facilitated by use of the chop delegate and MidasPlus 2.1.[19]

Arg90→Cit Transformations. Initial geometries for the Arg90→Cit simulations with the TS, chorismate, and prephenate bound to the BsCM active site were obtained from the previous study with the wild-type enzyme.[11a] The R_{CO} (1.86 Å) and R_{CC} (2.20 Å) distances obtained by the TS search in BsCM were assumed to be the same for the mutant. This is reasonable based on previous findings that showed that the TS geometry in the gas-phase, water, methanol, and in BsCM are essentially the same, being little affected by the environment.[11] The R_{CO} and R_{CC} distances were fixed during the simulations with the TS bound to the active site; however, they were fully sampled for chorismate and prephenate in the active site. The initial geometry for the Arg90→Cit simulations with the TSA bound to BsCM was built by adding two hydrogen atoms to the initial geometry for the TS and by reducing R_{CO} and R_{CC} to the values in the 2cht crystal structure. The R_{CO} and R_{CC} distances were sampled with the TSA bound in the active site.

The Arg90→Cit transformations were performed using the single topology approach by melding the force field parameters for bond angles, torsions, and nonbonded interactions. To keep the number of atoms fixed, two guanidinium hydrogens were mutated to dummy atoms (DM) (Figure 3). The bond angles involving dummy atoms have the same parameters as their counterparts in the initial state. Associated unphysical contributions to the free-energy differences cancel in a thermodynamic cycle.[20] Since the bond lengths for the side chains were not sampled in the QM/MM simulations, they were treated as geometrical variables in the Arg90→Cit transformation; the C−N equilibrium distance in Arg90 was perturbed from 1.34 to 1.23 Å, the C═O equilibrium distance in Cit. The N−H distances were perturbed from 1.01 Å to the value of 0.5 Å for the O−DM distances. Shrinking the bond length for dummy atoms is a common practice to improve convergence in FEP simulations.[20−22] Finally, Figure 3 illustrates how the charge distribution is changed by the transformation.

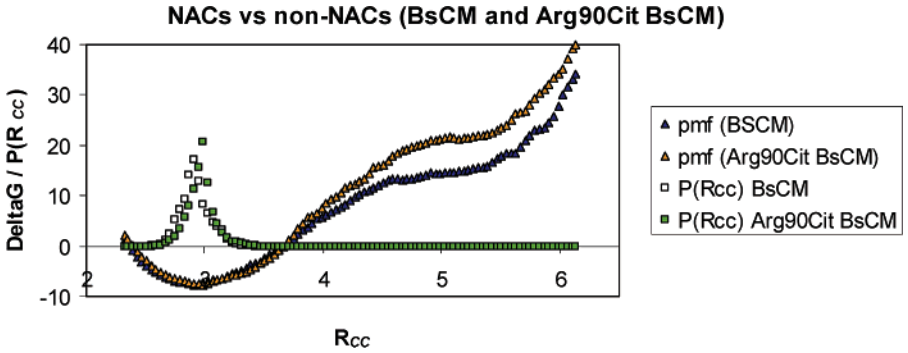

Figure 4. Plots of the one-dimensional potentials of mean force following R_{CC} (the reaction coordinate that converts non-NACs into NACs) and the probability of sampling it in the wild-type and mutant BsCMs.

MC Simulations Protocol. Pmf curves following R_{CC}, computed using increments of 0.02 Å, were obtained via MC statistical mechanics in conjunction with FEP calculations at 25 °C using double-wide sampling. To ensure convergence, each MC/FEP simulation was extensive. Initial reorganization of the solvent was performed for 5×10^6 configurations. This was followed by 30×10^6 configurations of full equilibration and 30×10^6 configurations of averaging for each window. The Arg90→Cit transformations were also performed via MC/FEP calculations at 25 °C using double-wide sampling. The initial and final states were coupled using 20 windows with values for the coupling parameter (λ) evenly distributed between 0 and 1 (0.025, 0.075, 0.125, ..., 0.875, 0.925, 0.975). In this case, initial reorganization of the solvent was performed for 5×10^6 configurations, followed by 30×10^6 configurations of full equilibration and 100×10^6 configurations of averaging for each window.

The combined QM/MM method as implemented in MCPRO 2.1[23] was used to perform all calculations. Established procedures including Metropolis and preferential sampling and the Zwanzig equation were employed.[13,24] Statistical uncertainties were obtained from the batch means procedure with batch sizes of 1×10^6 configurations.[13] The present QM/MM calculations used AM1[25] for the solute intramolecular energy. Computation of the QM energy and atomic charges is required for every attempted move of the QM region, which occurred every 200 configurations. Intermolecular interactions ($E_{QM/MM}$) of the QM solute with the MM region are given by eq 4 as the sum of all interactions between the QM and MM atoms, where q_i and q_j are the partial atomic charges and σ_{ij} and ϵ_{ij} are Lennard-Jones (LJ) parameters.

$$E_{QM/MM} = \sum_{i}^{\text{on QM}} \sum_{j}^{\text{on MM}} [q_i q_j e^2/r_{ij} + 4\epsilon_{ij}(\sigma_{ij}^{12}/r_{ij}^{12} - \sigma_{ij}^{6}/r_{ij}^{6})] \quad (4)$$

Partial atomic charges for the solutes were obtained from the CM1A procedure,[26] while standard Lennard-Jones parameters were assigned for solute atoms [for C, $\sigma = 3.550$ Å, $\epsilon = 0.070$ kcal/mol; for H on C, $\sigma = 2.460$ Å, $\epsilon = 0.030$ kcal/mol; for hydroxyl H, $\sigma = \epsilon = 0.000$; for O, $\sigma = 3.000$ Å, $\epsilon = 0.170$ kcal/mol]. The choice of partial charges is important in the present context, and the AM1-based CM1A charges have been shown to perform well in studies of medium effects on reaction rates and for free energies of hydration.[11,27]

The protein was represented with the OPLS-AA force field,[28] and the TIP4P model was used for water.[29] Residue-based cutoffs of 10 Å were employed. However, as the Arg90→Cit transformation involves a charge mutation, no cutoffs were applied for the mutating residue. In this manner, the missing long-range electrostatic interactions between Arg90 and the residues and solvent molecules outside the finite spherical system would likely cancel when computing double free-energy differences.

Results and Discussion

NACs vs non-NACs. Figure 4 shows the computed pmf curves ($G(R_{CC})$) and the probability of sampling R_{CC} ($P(R_{CC})$) in the mutant and wild-type BsCMs. All chorismate conformations with R_{CC} less than or equal to 3.70 Å are characterized as NACs. It should be noted that ΔG_{preq} only contributes to $\Delta G^{\ddagger}$ in the case of an unfavorable preequilibrium step; the number of non-NACs is greater than the number of NACs. Figure 4 shows that when chorismate is bound to either the mutant or wild-type BsCM, the population of NACs is almost 100%, which makes ΔG_{preq} very favorable, −9.0 kcal/mol in BsCM and −9.3 kcal/mol in Arg90Cit BsCM. In other words, the preequilibrium step is unimportant to the kinetics for both enzymes and thus is not responsible for the 10^4-fold decrease in the rate constant in going from Arg90 to Cit.

Average R_{CC} distances of 3.08 and 3.04 Å were obtained for the complexes between fully flexible chorismate and the wild-type and mutant BsCMs. The average distances agree with the R_{CC} distribution profiles extracted from the pmf curves obtained in both environments and show once again that the chorismate conformers in the active site with either Arg90 or Cit are essentially NACs.

Arg90→Cit Transformations. The Arg90→Cit transformation was performed for the TS, TSA, chorismate (or NACs), and prephenate bound to the active site. Long MC/FEP simulations generated smooth free-energy curves in all cases (Figure 5). The neutralization of the cationic Arg90 is uniformly unfavorable as the solutes have a charge of −2; $\Delta G_{tr,TS}$, $\Delta G_{tr,TSA}$, $\Delta G_{tr,NACs}$, and $\Delta G_{tr,prep}$ were computed to be 68.2 ± 0.1, 70.0 ± 0.1, 64.9 ± 0.1, and 62.9 ± 0.1 kcal/mol, respectively.

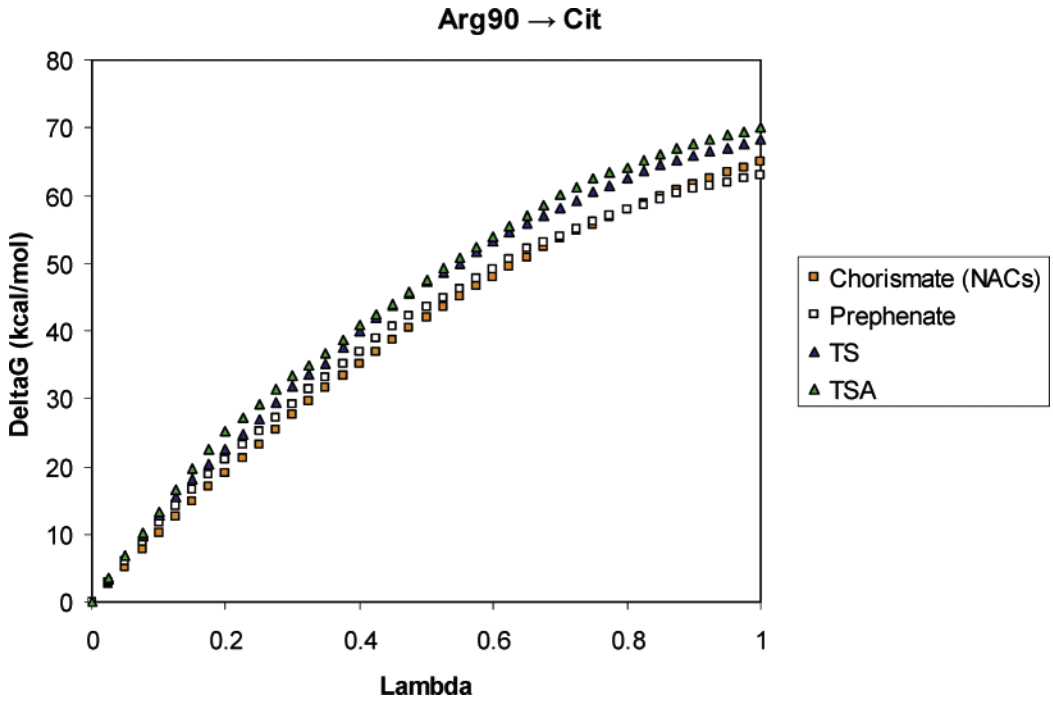

Figure 5. Free-energy curves associated with the Arg90→Cit transformation for the TS, TSA, chorismate, and prephenate bound to the active site. $\Delta G_{tr,TS}$, $\Delta G_{tr,TSA}$, $\Delta G_{tr,NACs}$, and $\Delta G_{tr,prep}$ values of 68.2, 70.0, 64.9, and 62.9 kcal/mol were obtained.

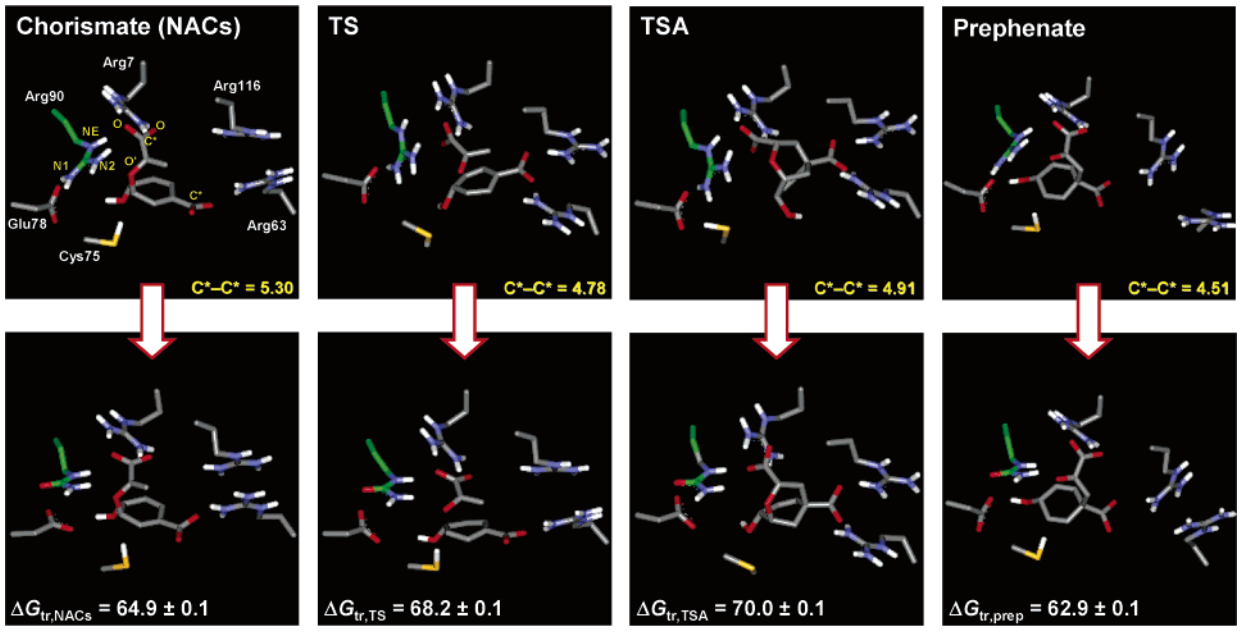

Figure 6. Snapshots illustrating key interactions between each solute and selected residues from the active site. The carbon atoms of Arg90 and Cit are colored green. C*−C* is the average distance between the carbon atoms of the carboxylate groups.

To investigate the effects of the Arg90→Cit transformation for all complexes, the interaction mode between each compound and selected residues from the active site was analyzed (Figure 6). It can be seen that the carboxylate groups of the TS and TSA closely interact with all arginine residues (Arg7, Arg63, Arg90, and Arg116) in the pocket for the wild-type enzyme, whereas chorismate and prephenate interact with only three; chorismate loses the interaction with Arg116 and prephenate with Arg63. The TS and TSA appear to have optimal arrangement of the carboxylate groups to maximize their interactions with the cationic residues. The average distance between the carbon atoms of the carboxylate groups (C*−C*) for the TS and TSA is very similar, 4.78 Å for the TS and 4.91 Å for the TSA. However, the average C*−C* distance for chorismate is too long (5.30 Å), while for prephenate it is too short (4.51 Å).

In the specific case of the interactions with Arg90, Table 1 shows that the average distances between its guanidinium nitrogens (NE, N1, and N2) and the oxygens (O) of the carboxylate group closely interacting with the cationic residue are shorter for the TS and TSA than for chorismate and prephenate. On the other hand, the average distances between the ether oxygen (O′; carbonyl oxygen for prephenate) and the Arg90 guanidinium nitrogens are shorter overall for

Table 1. Average Distances between the Arg90 Guanidinium Nitrogens and Pyruvyl and Ether Oxygens for All Solutes[a]

	chorismate	TS	TS*[b]	TSA	prephenate
O−NE	3.65	3.22	2.94	2.87	3.78
O−N1	5.86	4.15	4.18	4.22	5.94
O−N2	4.56	3.46	3.23	3.16	4.98
O′-NE	3.31	4.75	4.66	4.59	3.03
O′-N1	4.61	4.47	4.73	4.86	4.24
O′-N2	2.96	3.29	3.15	3.12	2.99

[a] Obtained with the Mok program.[30] [b] TS* has R_{CO} and R_{CC} increased to 2.16 and 2.50 Å from the values of 1.86 and 2.20 Å for the TS.

Table 2. Computed and Experimental Free-Energy Changes for the Claisen Rearrangement of Chorismate Catalyzed by the Wild-Type and Mutant BsCMs[a]

	BsCM	Arg90Cit BsCM
ΔG_{preq}	−9.0	−9.3
ΔG_{TS}[b]	26.9 ± 0.5	30.2 ± 0.5
$\Delta G^{\ddagger}_{calc}$	26.9 ± 0.5	30.2 ± 0.5
$\Delta G^{\ddagger}_{exp}$	15.4[c]	21.3[d]
$\Delta\Delta G^{\ddagger}_{calc}$	0.0	3.3 ± 0.1
$\Delta\Delta G^{\ddagger}_{exp}$	0.0	5.9
ΔG_r[b]	−40.7 ± 0.6	−42.7 ± 0.6

[a] Values in kcal/mol. [b] The error in ΔG_{TS} and ΔG_r were calculated by propagating the standard deviation (σ_i) on the individual ΔG_i used to obtain the pmf curve. The equation

$$\sqrt{\sum_{i}^{N}\sigma_i^2}$$

was used, where N is the number of ΔG_i values. [c] Reference 31. [d] Reference 16.

chorismate and prephenate than for the TS and TSA. The latter pattern is at odds with the ΔG_{tr} values. Thus, the results indicate that the ΔG_{tr} values are dominated by the proximity of Arg90 and the carboxylate group; the complex between the TSA and BsCM, which has the closest proximity to the carboxylate group (Table 1), is the most affected by the neutralization followed by the TS, chorismate, and prephenate.

$\Delta\Delta G_{TS}$ and $\Delta\Delta G_r$. As ΔG_{preq} is negative for the wild-type and mutant BsCMs, the preequilibrium step does not contribute to the free energies of activation in both environments; $\Delta G^{\ddagger}$ is equal to ΔG_{TS}. In the prior work,[11a] ΔG_{TS} and, consequently, $\Delta G^{\ddagger}$ were computed to be 26.9 ± 0.5 kcal/mol for BsCM (Table 2). Then, insertion of the computed $\Delta G_{tr,TS}$ and $\Delta G_{tr,NACs}$ values in eq 2 leads to a $\Delta\Delta G_{TS}$ value of 3.3 ± 0.1 kcal/mol. Thus, a $\Delta G^{\ddagger}$ value of 30.2 ± 0.5 kcal/mol is obtained for the mutant. The calculated barriers are larger than the experimental $\Delta G^{\ddagger}$ of 15.4 and 21.3 kcal/mol for BsCM and Arg90Cit BsCM, respectively.[16,31] This difference arises from the previously described deficiency in the AM1 activation barriers.[11b] However, in examining the difference in the free energy of activation between the mutant and wild-type BsCMs, $\Delta\Delta G^{\ddagger}$, errors from the QM method are mostly expected to cancel. Indeed, the calculated $\Delta\Delta G^{\ddagger}$ (3.3 kcal/mol) compares favorably to the experimental value (5.9 kcal/mol).

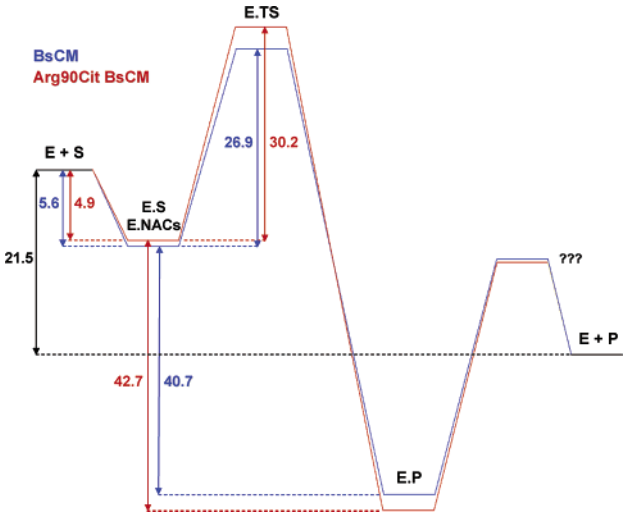

Figure 7. Free-energy diagram for the wild-type and mutant BsCMs. The free energies of binding between chorismate and the enzymes were estimated using the K_m values reported by Kienhöfer and co-workers.[16] The TS for the product release step was assumed not to be affected by mutation (see text for details). The more stable complex between prephenate and Arg90Cit BsCM would increase the barrier and retard product release for the mutant.

Mattei et al. have shown that BsCM is limited by product release at high substrate concentrations.[32] Analysis of the kinetic data indicated that the diffusive transition state for product release is 40% rate-determining in this concentration regime. Calculation of $\Delta\Delta G_r$ (eq 3) shows that the reaction becomes 2.0 ± 0.1 kcal/mol more exergonic with the Arg90→Cit transformation (Table 2), which should make the mutant less efficient in catalyzing the rearrangement due to slower product release. This, obviously, assumes that the TS for the product release step is not affected by mutation. This assumption is supported by the experimental work of Mattei et al.,[32] which indicates that the product release step is controlled by conformational changes observed on the C-terminal tail of BsCM; this region does not contain Arg90. Finally, if the computed $\Delta\Delta G^{\ddagger}$ included not only the chemical step but also the product release step, the calculated value should be more positive than 3.3 kcal/mol. This would bring the experimental and calculated values into closer agreement.

Figure 7 summarizes the free-energy results for the wild-type and mutant BsCMs. The free energies of binding of chorismate to the wild-type and mutant BsCMs were taken from the experimental work of Kienhöfer et al.[16] The calculated ΔG_r value of −21.5 ± 0.6 kcal/mol obtained in water[11b] is significantly more negative than the experimental value of −13.4 ± 2.2 kcal/mol,[5c] while it is close to other theoretical predictions ranging from −20.5 to −22.0 kcal/mol.[7f] However, ΔG_r in BsCM (Table 2) was computed to be more favorable than other theoretical estimations.[6b,7f]

Our previous QM/MM MC/FEP calculations indicated that the rate enhancement by BsCM over the aqueous phase resulted primarily from conformational compression of NACs by the enzyme and that the selective stabilization of the TS in the enzyme environment relative to water played a

secondary role in the catalysis.[11a] More specifically, conformational compression was estimated to lower the free-energy barrier by 7.9 kcal/mol of a total $\Delta\Delta G^{\ddagger}$ of 11.2 kcal/mol, while the remaining 3.3 kcal/mol is due to preferential TS stabilization. This conflicts with other QM/MM calculations which showed significant TS stabilization by the enzyme.[7a,7d] One possible explanation for this is the use of a different thermodynamic analysis to estimate the contributions for the lowering of the barrier in BsCM. While in our work[11a] conformational compression (or substrate preorganization) was defined as unfavorable intramolecular contributions due to geometrical changes of the substrate upon binding to the enzyme, other QM/MM calculations defined substrate preorganization as the free energy cost of forming the same distribution in solution as observed in the enzyme. An alternative source of discrepancy might be associated with energetic deficiencies of AM1 in reproducing the activation barrier.[11b] This could potentially lead to an overestimation of the conformational compression contributions for the binding of NACs to BsCM and consequently for the lowering of the free-energy barrier in BsCM relative to water.

The calculations show that the free energy of activation for the mutant is increased by 3.3 kcal/mol relative to the wild-type BsCM; the slower product release step should contribute to the remaining of the 10^4-fold decrease in the rate constant in going from Arg90 to Cit. Also, the average R_{CC} distance for chorismate changes from 3.5 Å in water[11a] to ca. 3.0 Å in the complex with either Arg90 or Cit in the active site. These results suggest that the mutation completely abolishes the preferential TS stabilization in the enzyme, particularly due to loss of the salt-bridge with the pyruvyl carboxylate group by neutral Cit, while giving similar conformational compression of NACs. In other words, the reaction in the mutant is faster than in water due exclusively to conformational compression of the substrate.

TS Geometry. The R_{CO} (1.86 Å) and R_{CC} (2.20 Å) distances obtained previously by the TS search in BsCM[11a] using AM1 for the solute were found to be more compact than those obtained by higher levels of QM theory.[4a,6a,6c,7b,7f,7g] This is consistent with a previous study which examined the Claisen rearrangements of allyl vinyl ether and allyl phenyl ether, where AM1 transition structures were found to be tighter with greater 1,4-diyl character than various ab initio structures.[33] Thus, the effects of different geometries for the TS on $\Delta G_{tr,TS}$ were examined by perturbing R_{CO} and R_{CC} from 1.86 and 2.20 Å to 2.16 and 2.50 Å, respectively, with increments of 0.05 Å for Arg90 and Cit in the active site. The elongated TS is referred to here as the TS*, and its values for the reaction coordinate were estimated by averaging the R_{CO} and R_{CC} values obtained with higher levels of QM theory.[4a,6a,6c,7b,7f,7g]

Figure 8 shows that the neutralization of Arg90 to Cit becomes increasingly unfavorable as R_{CO} and R_{CC} are elongated; $\Delta G_{tr,TS}$ changes from 68.2 to 70.9 kcal/mol when the TS is transformed to the TS* in the active site. The results in Table 1 once again suggest that the ΔG_{tr} values are largely dominated by the proximity of Arg90 to the pyruvyl carboxylate group; the complexes between the TSA and BsCM and the TS* and BsCM, which have similar values

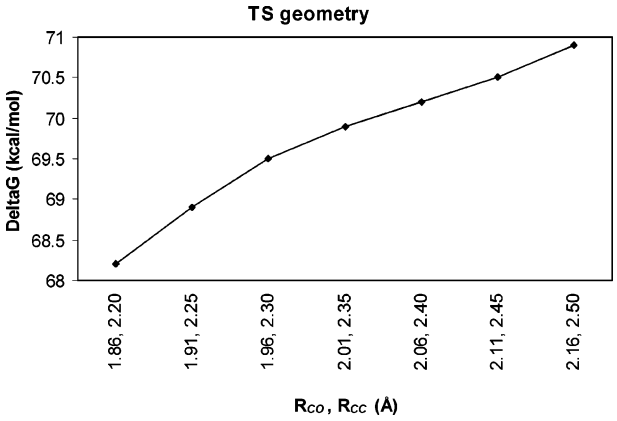

Figure 8. Effects of modification of the TS geometry on $\Delta G_{tr,TS}$ from MC/FEP calculations. The neutralization of Arg90 to Cit becomes increasingly unfavorable as R_{CO} and R_{CC} are elongated.

for the average distances between Arg90 and the carboxylate oxygens (O), are expected to be the most affected by the neutralization followed by the TS. Contributions from the interaction between Arg90 and the ether oxygen (O′) should also be relevant. Figure 9 shows that the average charge distributions for the TSA, TS, and TS* are very similar, except that the latter has more negative charge on the ether oxygen (O′). Finally, if the more dissociated TS* is considered, the increased $\Delta G_{tr,TS}$ value in eq 2 yields a $\Delta\Delta G^{\ddagger}$ value of 6.0 ± 0.1 kcal/mol. This is the same as the experimental value (5.9 kcal/mol) without consideration of the effect of the mutation on product release.

TS vs TSA. The experimental results of Kienhöfer and co-workers[16] show that the binding of the TS to BsCM is significantly affected by the Arg90Cit mutation, becoming 6.5 kcal/mol less favorable. This contrasts dramatically with the effects of mutation on the binding of the TSA, which becomes less favorable by only 1.1 kcal/mol. In other words, the mutation diminishes the binding of the TS to BsCM by 5.4 kcal/mol more than it does for the binding of the TSA. Kienhöfer and co-workers[16] suggest that this is due to greater anionic character for the ether oxygen in the TS. This pattern is not well reproduced here. If the TS and TSA are compared, the TS is less destabilized by the Arg90Cit mutation than the TSA by 1.8 kcal/mol (Figure 5). However, if the TS* is used, it is more destabilized than the TSA but by only 0.9 kcal/mol.

As mentioned above, the ether oxygen is more negative by 0.05 and 0.11 e in the TS and TS* than in the TSA (Figure 9); however, the FEP calculations predict similar effects for the mutation on binding of all three. The more dominant interaction in the computations is between Arg90 and the proximal carboxylate group, which has a similar disposition and charge distribution for the TS, TS*, and TSA (Figures 6 and 9). A possible source of the discrepancy between the computations and the experiment for the TSA vs TS or TS* is the lack of backbone sampling in the calculations. The TSA is more compact and might benefit more from relaxation of the protein backbone upon Arg90 neutralization. Another explanation might be related to the much closer proximity between Arg90 and the pyruvyl carboxylate group of the

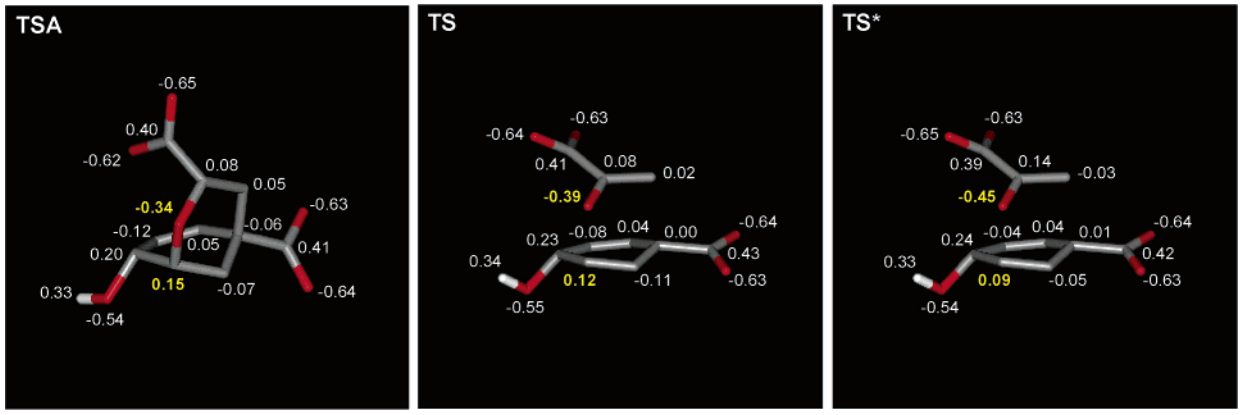

Figure 9. Charge distribution for the TSA, TS, and TS*. The atomic charges with hydrogens were summed onto the carbon atoms.

TSA obtained by the MC simulations. The calculated O−NE, O−N1, and O−N2 distances of 2.87, 4.22, and 3.16 Å (Table 1) compare to experimental values of 4.43, 5.31, and 5.53 Å, obtained by averaging the distances for 12 independent active sites in the BsCM crystal structure complexed with the TSA. However, the experimental distances should be taken with caution as they have considerable noise; the O−NE, O−N1, and O−N2 distances range from 3.84 to 5.66, 3.83 to 6.33, and 4.60 to 7.01 Å with standard deviations of 0.66, 1.02, and 0.75 Å, respectively. This contrasts dramatically with the good agreement between experimental and calculated distances obtained for the complex between prephenate and BsCM. The calculated O−NE, O−N1, and O−N2 distances of 3.78, 5.94, and 4.98 Å (Table 1) compare to experimental values of 3.91, 6.16, and 5.05 Å, obtained by averaging the distances for 9 independent active sites in the BsCM crystal structure complexed with prephenate (1com from the Brookhaven Protein Data Bank).[34] In this case, the experimental distances are much more precise; O−NE, O−N1, and O−N2 range from 3.70 to 4.13, 5.90 to 6.43, and 4.64 to 5.53 Å with standard deviations of 0.14, 0.19, and 0.27 Å, respectively.

Conclusions

Bacillus subtilis chorismate mutase (BsCM) catalyzes the Claisen rearrangement of chorismate to prephenate. In this work, the key factors that contribute to the reduced catalytic efficiency upon mutation of Arg90 to citrulline (Cit), an isosteric but neutral arginine analogue, were investigated. The differential effects on affinity upon Arg90 neutralization for the binding of the transtition state (TS) and the transition state analogue (TSA) to BsCM were also studied. Using a combined QM/MM Monte Carlo/Free-Energy Perturbation method, an increase in the free-energy barrier upon mutation ($\Delta\Delta G^{\ddagger}$) of 3.3 kcal/mol was obtained. The computations have provided extensive structural details, as in Table 1 and Figure 6, and the higher free-energy barrier for the mutant is ascribed to inferior stabilization of the TS, particularly the pyruvyl carboxylate group, by neutral Cit. The calculated $\Delta\Delta G^{\ddagger}$ can be compared to an experimental value of 5.9 kcal/mol for the overall catalysis. However, in addition to the increase in the free-energy barrier, the reaction is computed to be 2.0 kcal/mol more exergonic for the mutant according to the QM/MM simulations. Consideration of the associated retardation of the product release should bring the experimental and calculated values into even closer agreement. Alternatively, it was also shown that if a more dissociative transition state (TS*) is considered, the calculated $\Delta\Delta G^{\ddagger}$ value increases to 6.0 kcal/mol.

Finally, the experimental results of Kienhöfer and coworkers[16] indicate that the mutation diminishes the binding of the TS to BsCM by 5.4 kcal/mol more than it does for the binding of the TSA, and they suggested that this is due to greater anionic character for the ether oxygen in the TS. The charge shift is supported here; however, similar effects of the mutation are predicted for the TS and TSA. Further computational exploration on this point is warranted using alternative QM methodology and allowing relaxation of the protein backbone.

Acknowledgment. Gratitude is expressed to the National Institutes of Health (GM032136) for support.

References

(1) Ganem, B. *Angew. Chem., Int. Ed. Engl.* **1996**, *35*, 936−945.

(2) Haslam, E. *Shikimic Acid: Metabolism and Metabolites*; John Wiley & Sons: New York, 1993.

(3) Conn, E. E. In *The Shikimic Acid Pathway*; Conn, E. E., Ed.; Recent Advances in Phytochemistry; Plenum Press: New York, 1986.

(4) (a) Wiest, O.; Houk, K. N. *J. Am. Chem. Soc.* **1995**, *117*, 11628−11639. (b) Wiest, O.; Houk, K. N. *J. Org. Chem.* **1994**, *59*, 7582−7584. (c) Copley, S. D.; Knowles, J. R. *J. Am. Chem. Soc.* **1985**, *107*, 5306−5308. (d) Addadi, L.; Jaffe, E. K.; Knowles, J. R. *Biochemistry* **1983**, *22*, 4494−4501.

(5) (a) Kast, P.; Grisostomi, C.; Chen, I. A.; Li, S.; Krengel, U.; Xue, Y.; Hilvert, D. *J. Biol. Chem.* **2000**, *275*, 36832−36838. (b) Meyer, M. P.; DelMonte, A. J.; Singleton, D. A. *J. Am. Chem. Soc.* **1999**, *121*, 10865−10874. (c) Kast, P.; Tewari, Y. B.; Wiest, O.; Hilvert, D.; Houk, K. N.; Goldberg, R. N. *J. Phys. Chem. B* **1997**, *101*, 10976−10982. (d) Kast, P. M.; Ullah, A.; Hilvert, D. *Tetrahedron Lett.* **1996**, *37*, 2691−2694. (e) Copley, S. D.; Knowles, J. R. *J. Am. Chem. Soc.* **1987**, *109*, 5008−5013.

(6) (a) Ruiz-Pernia, J. J.; Silla, E.; Tunon, I.; Marti, S.; Moliner, V. *J. Phys. Chem. B* **2004**, *108*, 8427−8433. (b) Woodcock, H. L.; Hodoscek, M.; Sherwood, P.; Lee, Y. S.; Schaefer, H. F., III; Brooks, B. R. *Theor. Chem. Acc.* **2003**, *109*, 140−148. (c) Worthington, S. E.; Roitberg, A. E.; Krauss, M. *J. Phys. Chem. B* **2001**, *105*, 7087−7095. (d) Marti, S.; Andres, J.; Moliner, V.; Silla, E.; Tunon, I.; Bertran, J. *Theor. Chem. Acc.* **2001**, *105*, 207−212. (e) Marti, S.; Andres, J.; Moliner, V.; Silla, E.; Tunon, I.; Bertran, J.; Field, M. J. *J. Am. Chem. Soc.* **2001**, *123*, 1709−1712. (f) Marti, S.; Andres, J.; Moliner, V.; Silla, E.; Tunon, I.; Bertran, J. *J. Phys. Chem. B* **2000**, *104*, 11308−11315. (g) Lyne, P. D.; Mulholland, A. J.; Richards, W. G. *J. Am. Chem. Soc.* **1995**, *117*, 11345−11350.

(7) (a) Ranaghan, K. E.; Mulholland, A. J. *Chem. Commun.* **2004**, *10*, 1238−1239. (b) Ranaghan, K. E.; Ridder, L.; Szefczyk, B.; Sokalski, W. A.; Hermann, J. C.; Mulholland, A. *Org. Biomol. Chem.* **2004**, *2*, 968−980. (c) Marti, S.; Andres, J.; Moliner, V.; Silla, E.; Tunon, I.; Bertran, J. *J. Am. Chem. Soc.* **2004**, *126*, 311−319. (d) Štrajbl, M.; Shurki, A.; Kato, M.; Warshel, A. *J. Am. Chem. Soc.* **2003**, *125*, 10228−10237. (e) Ranaghan, K. E.; Ridder, L.; Szefczyk, B.; Sokalski, W. A.; Hermann, J. C.; Mulholland, A. J. *Mol. Phys.* **2003**, *101*, 2695−2714. (f) Crespo, A.; Scherlis, D. A.; Marti, M. A.; Ordejon, P.; Roitberg, A. E.; Estrin, D. A. *J. Phys. Chem. B* **2003**, *107*, 13728−13736. (g) Hall, R. J.; Hindle, S. A.; Burton, N. A.; Hillier, I. H. *J. Comput. Chem.* **2000**, *21*, 1433−1441.

(8) NACs possess the proper geometric juxtaposition of groups for a reaction to proceed directly to a transition state without significant bond stretching/contraction, angle bending, or torsional motion.

(9) (a) Hur, S.; Bruice, T. C. *J. Am. Chem. Soc.* **2003**, *125*, 10540−10542. (b) Hur, S.; Bruice, T. C. *Proc. Natl. Acad. Sci. U.S.A.* **2003**, *100*, 12015−12020. (c) Hur, S.; Bruice, T. C. *Proc. Natl. Acad. Sci. U.S.A.* **2002**, *99*, 1176−1181.

(10) Khanjin, N. A.; Snyder, J. P.; Menger, F. M. *J. Am. Chem. Soc.* **1999**, *121*, 11831−11846.

(11) (a) Guimarães, C. R. W.; Repasky, M. P.; Tirado-Rives, J.; Chandrasekhar, J.; Jorgensen, W. L. *J. Am. Chem. Soc.* **2003**, *125*, 6892−6899. (b) Repasky, M. P.; Guimarães, C. R. W.; Tirado-Rives, J.; Chandrasekhar, J.; Jorgensen, W. L. *J. Am. Chem. Soc.* **2003**, *125*, 6663−6672.

(12) Warshel, A.; Levitt, M. *J. Mol. Biol.* **1976**, *103*, 227−249.

(13) Allen, M. P.; Tildesley, D. J. *Computer Simulations of Liquids*; Clarendon Press: Oxford, U.K., 1987.

(14) (a) Kollman, P. A. *Chem. Rev.* **1993**, *93*, 2395−2417. (b) Beveridge, D. L.; DiCapua, F. M. *Annu. Rev. Biophys. Biophys. Biochem.* **1989**, *18*, 431−492. (c) Jorgensen, W. L. *Acc. Chem. Res.* **1989**, *22*, 184−189.

(15) Carlson, H. A.; Jorgensen, W. L. *J. Am. Chem. Soc.* **1996**, *118*, 8475−8484.

(16) Kienhöfer, A.; Kast, P.; Hilvert, D. *J. Am. Chem. Soc.* **2003**, *125*, 3206−3207.

(17) Bartlett, P. A.; Nakagawa, Y.; Johnson, C. R.; Reich, S. H.; Luis, A. *J. Org. Chem.* **1988**, *53*, 3195−3210.

(18) Chook, Y. M.; Ke, H.; Lipscomb, W. N. *Proc. Natl. Acad. Sci. U.S.A.* **1993**, *90*, 8600−8603.

(19) (a) Tirado-Rives, J. *Chop*, Yale University, New Haven, CT, 2002. (b) Huang, C.; Pettersen, E.; Couch, G.; Ferrin, T. *MidasPlus 2.1*, University of California, San Francisco, CA, 1994.

(20) Boresch, S.; Karplus, M. *J. Phys. Chem. A* **1999**, *103*, 103−118.

(21) Pearlman, D. A.; Kollman, P. A. *J. Chem. Phys.* **1991**, *94*, 4532−4545.

(22) Price, D. J.; Jorgensen, W. L. *J. Comput.-Aided Mol. Des.* **2001**, *15*, 681−695.

(23) Jorgensen, W. L.; Tirado-Rives, J. *MCPRO, Version 2.1*, Yale University, New Haven, CT, 2004.

(24) Zwanzig, R. *J. Chem. Phys.* **1954**, *22*(8), 1420−1426.

(25) Dewar, M. J. S., Zoebisch, E. G.; Healy, E. F.; Stewart, J. J. P. *J. Am. Chem. Soc.* **1985**, *107*, 3902−3909.

(26) Storer, J. W.; Giesen, D. J.; Cramer, C. J.; Truhlar, D. G. *J. Comput.-Aided Mol. Des.* **1995**, *9*, 87−109.

(27) (a) Chandrasekhar, J.; Shariffskul, S.; Jorgensen, W. L. *J. Phys. Chem. B* **2002**, *106*, 8078−8085. (b) Udier-Blagović, M.; Morales de Tirado, P.; Pearlman, S. A.; Jorgensen, W. L. *J. Comput. Chem.* **2004**, *25*, 1322−1332.

(28) Jorgensen, W. L.; Maxwell, D. S.; Tirado-Rives, J. *J. Am. Chem. Soc.* **1996**, *118*, 11225−11236.

(29) Jorgensen, W. L.; Chandrasekhar, J.; Madura, J. D.; Impey, W.; Klein, M. L. *J. Chem. Phys.* **1983**, *79*, 926−935.

(30) Average values for the distances were obtained with the Mok program (www.perlmol.org/pod/mok.html).

(31) Galopin, C. C.; Zhang, S.; Wilson, D. B.; Ganem, B. *Tetrahedron Lett.* **1996**, *37*, 8675−8678.

(32) Mattei, P.; Kast, P.; Hilvert, D. *Eur. J. Biochem.* **1999**, *261*, 25−32.

(33) Meyer, M. P.; DelMonte, A. J.; Singleton, D. A. *J. Am. Chem. Soc.* **1999**, *121*, 10865−10874.

(34) Chook, Y. M.; Gray, J. V.; Ke, H.; Lipscomb, W. N. *J. Mol. Biol.* **1994**, *240*, 476−500.

CT0500803

JCTC Journal of Chemical Theory and Computation

Frequency-Dependent Polarizabilities of Amino Acids as Calculated by an Electrostatic Interaction Model

Thorsten Hansen,[†] Lasse Jensen,*[,‡] Per-Olof Åstrand,[§] and Kurt V. Mikkelsen[†]

Department of Chemistry, University of Copenhagen, Universitetsparken 5, DK-2100 Copenhagen Ø, Denmark, Department of Chemistry, Northwestern University, 2145 Sheridan Road, Evanston, Illinois 60208-3113, and Department of Chemistry, Norwegian University of Science and Technology (NTNU), NO-7491 Trondheim, Norway

Received March 4, 2005

Abstract: The frequency-dependent polarizability of the 20 essential amino acids has been calculated by an electrostatic interaction model where an Unsöld-type of model has been adopted for the frequency dependence. The interaction model has previously been parametrized from Hartree−Fock calculations on a set of molecules, and the model is in this work extended by sulfur parameters by including a set of 18 small sulfur compounds. The results for the amino acids by using the interaction model compare well with Hartree−Fock calculations with deviations of around 5% for the isotropic polarizability. Furthermore, the intrinsic (or optical) dielectric constant related to the polarizability has been calculated for three small proteins, ribonuclease inhibitor, lysozyme, and green fluorescent protein, adopting the interaction model. The results are consistent with the intrinsic dielectric constants found for proteins in the literature.

I. Introduction

Molecular models of polarization are of importance in many aspects of computational molecular sciences. For example, when molecules interact with each other, they are polarized by the electric field of the surroundings.[1−3] In many cases, explicit polarization has also been included in force fields,[4−17] and its relevance for protein simulations has also been discussed.[4−21] In addition, the frequency-dependent polarizability also describes the response to an external electric field.[1,22,23] The polarizability is thus the microscopic counterpart to the macroscopic refractive index and dielectric constant, which are of fundamental importance in the design of new electro-optical materials.[24−26]

The modeling of molecular polarizabilities is thus of fundamental importance in molecular sciences. They may be calculated in quantum chemical calculations, but even though the method development has been substantial over the last years including new density functional theory (DFT) methods,[27,28] these methods are restricted to rather small systems. On the other hand, in simulations of molecular liquids, the polarization energy is calculated repeatedly for systems with a large number of molecules.[15,29,30] In a force field, atom-type parameters are used to model the molecular charge distribution, and consequently the molecular polarizability is in most cases described in terms of atomic or bond polarizabilities.[15,19,31−33]

We have developed a molecular mechanics model for molecular polarizabilities,[34−37] which is based on the point-dipole interaction (PDI) model originally suggested by Silberstein,[38−40] and to a large extent exploited by Applequist.[41,42] The model is based on the fact that a molecule is regarded as a set of (isotropic) atomic polarizabilities. In an external electric field, atomic dipole moments are induced which results in an additional electric field on the surrounding atoms. A set of coupled equations is obtained, where the solution gives the molecular polarizability tensor. The model includes a set of atom-type polarizabilities which may be parametrized from known molecular polarizabilities. In our work, the model has been parametrized from quantum chemical calculations, and the frequency-dependence has

* Corresponding author phone: (847)491-2793; fax: (847)491-7713; e-mail: l.jensen@chem.northwestern.edu.

[†] University of Copenhagen.

[‡] Northwestern University.

[§] Norwegian University of Science and Technology (NTNU).

10.1021/ct050053c CCC: $30.25
Published on Web 06/04/2005

been included as an Unsöld model.[34] The model for including the damping of the interatomic interactions at short distances has been improved,[37] and the model has been extended by boron parameters.[36] The model has also been extended to second hyperpolarizabilities.[43−46]

The polarizabilities of the essential amino acids are studied in this work. It may be regarded as a first step toward a polarizable force field for peptides and proteins, but peptide systems are also strong candidates for materials in nonlinear optics.[47,48] To include also the sulfur-containing amino acids, the model has to be extended with sulfur parameters. The work is thus divided into three parts: a parametrization of sulfur, calculations on amino acids, and calculations on three small proteins.

II. Theoretical Background

Considering a set of N interacting atomic polarizabilities, the atomic induced dipole moment, μ_I^{ind}, of atom I due to an external electric field, E^{ext}, is given by

$$\mu_{I,\alpha}^{\text{ind}} = \alpha_{I,\alpha\beta}\left(E_\beta^{\text{ext}} + \sum_{J\neq I}^{N} T_{IJ,\beta\gamma}^{(2)}\,\mu_{J,\gamma}^{\text{ind}}\right) \tag{1}$$

where $T_{IJ,\beta\gamma}^{(2)}$ is the dipole interaction tensor given as

$$T_{IJ,\beta\gamma}^{(2)} = \frac{3R_{IJ,\beta}R_{IJ,\gamma}}{R_{IJ}^5} - \frac{\delta_{\beta\gamma}}{R_{IJ}^3} \tag{2}$$

The Greek subscripts, α, β, ..., denote the Cartesian coordinates x, y, or z. In eq 1 the Einstein summation convention for repeated Greek subscripts has been employed, and it is used throughout this work. The molecular polarizability is obtained as[41]

$$\alpha_{\alpha\beta}^{\text{mol}} = \sum_{I,J}^{N} B_{IJ,\alpha\beta} \tag{3}$$

here **B** is the relay matrix defined as

$$\mathbf{B} = (\alpha^{-1} - \mathbf{T}^{(2)})^{-1} \tag{4}$$

An improved model is obtained if the contributions from a smeared-out charge distribution is included in terms of a damping of the interaction in eq 1 by modifying the $T_{IJ,\alpha\beta}$ tensor.[49,50] The damping of the interactions arises from the overlap of the smeared-out charge distributions, and the model used here is obtained by considering the overlap between two Gaussian charge distributions.[37] We obtain the damped interaction by modifying the interaction tensors

$$T_{IJ,\alpha_1\ldots\alpha_n}^{(n)} = \nabla_{\alpha_1}\ldots\nabla_{\alpha_n}\left(\frac{1}{S_{IJ}}\right) \tag{5}$$

which is equivalent to replacing R_{IJ} by S_{IJ} and $R_{IJ,\alpha}$ by $S_{IJ,\alpha}$ in the regular formulas for the interaction tensor. We utilize the following "scaled distance"[37]

$$S_{IJ} = \sqrt{R_{IJ}^2 + \frac{\pi}{4a_{IJ}}} \tag{6}$$

where a_{IJ} is given by $a_{IJ} = \Phi_I\Phi_J/(\Phi_I + \Phi_J)$, and Φ_I is the damping parameter (the width of a Gaussian charge distribution) of atom I.

Well below the first electronic absorption, the frequency-dependence of the molecular polarizability is often approximated with an Unsöld-type of expression.[22] Here we assume that the atomic polarizability has a similar frequency-dependence[34]

$$\alpha_I(-\omega;\omega) = \alpha_I(0;0) \times \left[\frac{\bar{\omega}_I^2}{\bar{\omega}_I^2 - \omega^2}\right] \tag{7}$$

where $\bar{\omega}_I$ is an atom-type parameter and ω is the frequency.

For a given polarizability tensor $\alpha_{\alpha\beta}$, the *isotropic* (or mean) polarizability is defined as

$$\bar{\alpha} = \frac{1}{3}\alpha_{\alpha\alpha} \tag{8}$$

and here the *anisotropic* polarizability is calculated as

$$(\Delta\alpha)^2 = \frac{1}{2}\sum_{\alpha\beta}(3\alpha_{\alpha\beta}\alpha_{\alpha\beta} - \alpha_{\alpha\alpha}\alpha_{\beta\beta}) \tag{9}$$

III. Calculational Details

For the quantum chemical computations of frequency-dependent polarizabilities we use the Dalton program package[51] as described in refs 52−54 using linear response functions at the SCF level. The basis set of Sadlej[55] was employed since it has been shown previously that it gives good results for polarizabilities considering its limited size.[56] The following frequencies have been used: ω(au)/λ(nm) = 0.0/∞, 0.02389/1907, 0.04282/1064, and 0.0774/589 (1 au = 27.21 eV). For the parametrization of sulfur, a series of 18 molecules[57] containing S atoms has been added to the original set of 187 molecules used in our previous study.[37] The geometries of the new molecules containing S atoms have been optimized at the PM3 level with the Gaussian 98 program package.[58] The geometries of the amino acids have been generated in a similar manner, but these molecules were not included in the trial set. The choice of basis set and optimization level is dictated by our previous work.[37] Although optimizing the geometries at a higher level of theory, like DFT, would be preferable, it is not deemed necessary for the present work since the geometry dependence of the molecular polarizability may be assumed to be modeled by the $T^{(2)}$ tensor.

The structures for the three proteins ribonuclease inhibitor (RNI), lysozyme (LYS), and green fluorescent protein (GFP), were taken as the crystal structures from the Protein Data Bank with entry code 1BTA, 135L, and 1GFL, respectively. For LYS hydrogen atoms were added, and the water molecules were removed using PyMol.[59] For GFP only the monomer (chain A) was used, and again hydrogen atoms were added, and water molecules were removed using PyMol. Besides this no other refinements of the stuctures have been done in this work. Cartoon models of RNI, LYS, and GFP are displayed in Figures 1−3, respectively.

IV. Parametrization of Sulfur

We adopt the same scheme as used in our previous work to optimize the parameters describing the frequency-dependent

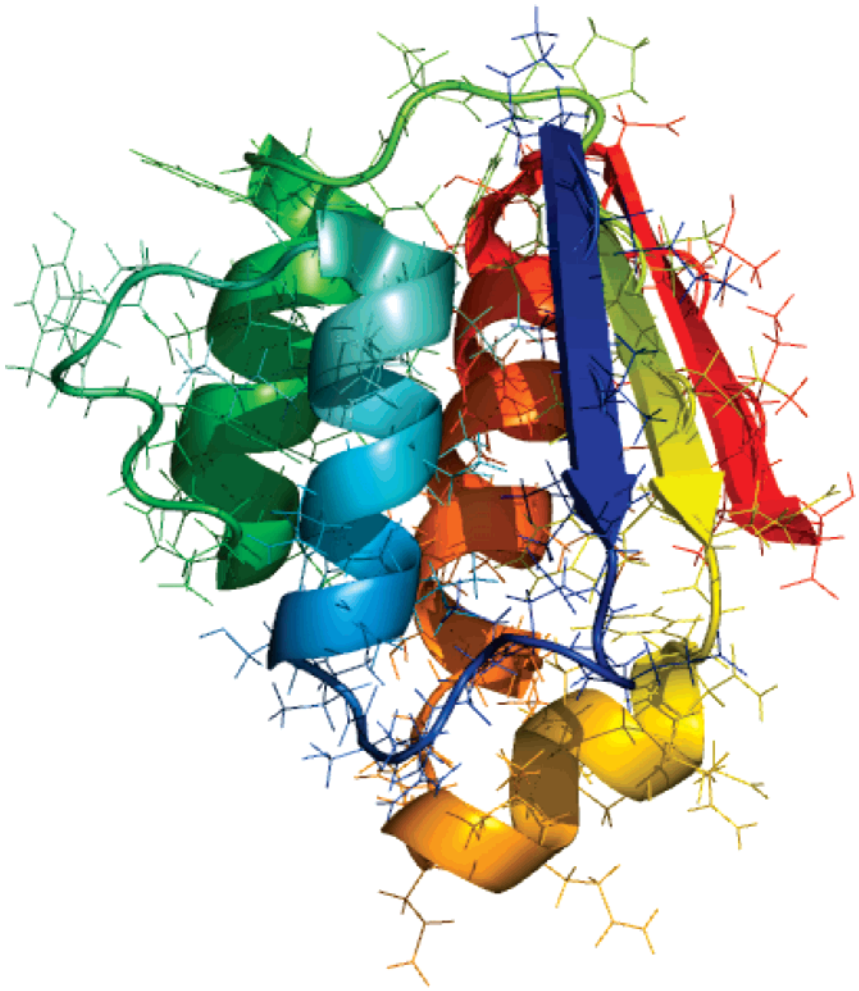

Figure 1. Cartoon of the ribonuclease inhibitor protein made using PyMol.[59]

polarizabilities.[37] For the static polarizability, the root-mean-square (rms) of the differences between the quantum chemical molecular polarizability tensors, $\alpha_{\alpha\beta,i}^{QC}$, and the model molecular polarizability tensors, $\alpha_{\alpha\beta,i}^{model}$, have been minimized as

$$\mathrm{rms} = \sqrt{\frac{\sum_{i=1}^{N}\sum_{\alpha,\beta=1}^{3}(\alpha_{\alpha\beta,i}^{model} - \alpha_{\alpha\beta,i}^{QC})^2}{N-1}} \tag{10}$$

where N is the number of molecules.

In a similar manner, the parameters describing the frequency-dependence of the molecular polarizability have been optimized by minimizing

$$\mathrm{rms} = \sqrt{\frac{\sum_{i=1}^{N}\sum_{\alpha,\beta=1}^{3}[(\alpha_{\alpha\beta,i}^{model}(\omega) - \alpha_{\alpha\beta,i}^{model}(0)) - (\alpha_{\alpha\beta,i}^{QC}(\omega) - \alpha_{\alpha\beta,i}^{QC}(0))]^2}{N-1}} \tag{11}$$

i.e. we parametrize the frequency-dependence only and do not attempt to correct for errors introduced in the parametrization of the static polarizability.

Since we already have obtained parameters for the elements H, B, C, N, O, F, and Cl in our previous work on a trial set of 187 molecules,[37] only the S parameters have been optimized, and the parameters for the other elements have been kept fixed. The optimized parameters are collected in Table 1 together with the obtained rms. The rms for the static polarizability is only 2.47 au considerably lower than the rms of 5.29 au found previously.[37] Therefore, we conclude that it is not needed to perform a refit of all parameters. This illustrates that the inclusion of new elements in the optimization can be performed by only optimizing the parameters for the new elements, at least as long as the new molecules included in the trial set are similar to the existing molecules. One would expect on the basis of atomic numbers that the "atomic" polarizability of S would be lower than that of Cl; however, we find the opposite to be the case. However, a better measure is the radius of the atoms since the classical polarizability of a conducting sphere (CS) is given by $\bar{\alpha}^{CS} = R^3$ where R is the radius of the sphere. Using this criteria we would expect an ordering of the atomic polarizability as H < F < O < N < C < B < Cl < S, if we use the covalent atomic radius adopted from WebElements.[60] If we compare with the polarizability in Table 1, this ordering is in agreement with our results. A similar trend has also been found in the work by Swart et al.[33] using the PDI model by Thole. The rms of 0.77 au found for the frequency-

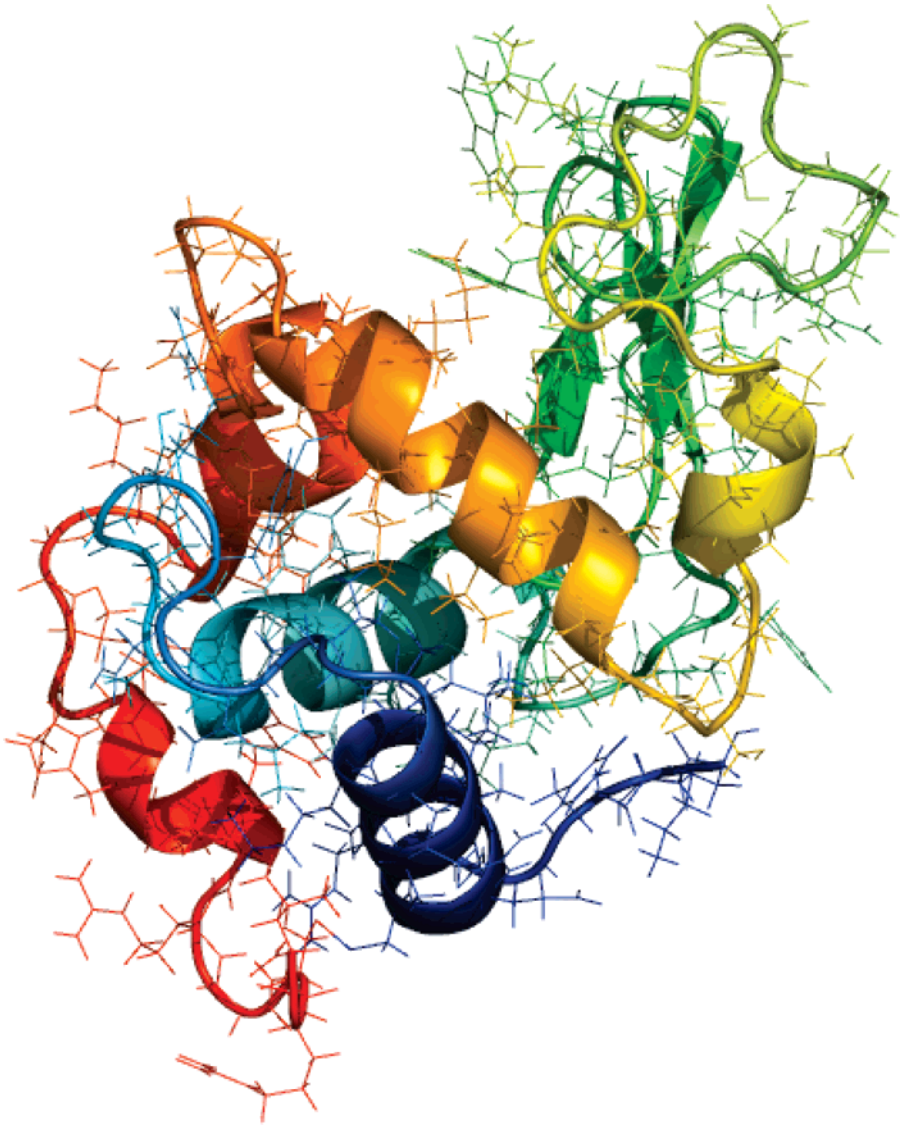

Figure 2. Cartoon of the lysozyme protein made using PyMol.[59]

dependence is larger than the value of 0.37 au that was obtained previously. Due to the very different frequency-dependence of the molecules containing B atoms, we found in our previous work a significant improvement by adopting a separate set of ω_p parameters for the boron molecules.[37] This may also be the case for the molecules containing S atoms. However, the frequency-dependence is in general very modest, and, therefore, we will keep the more general set of parameters.

V. Calculations on Amino Acids

The essential amino acids have not been included in the trial set and will therefore allow us to test the accuracy of the PDI model with the parameters adopted from Table 1. The frequency-dependent mean polarizabilities of the amino acids calculated with the PDI model, $\bar{\alpha}^{PDI}$, have been plotted versus the polarizabilities obtained using the SCF method, $\bar{\alpha}^{SCF}$, in Figure 4. In Figure 5, the corresponding plot is presented for the anisotropic polarizabilities. Furthermore, the static mean and anisotropic polarizabilities for the amino acids have been collected in Table 2.

In Table 2 and Figure 4, a good agreement is found for the mean polarizability between the PDI model and SCF results. The deviation in the static mean polarizability is on average 4.9% with the largest deviations of 8.5% for aspartic acid and 8.3% for glutamic acid. Among the 20 amino acids, it is only cysteine and methionine which contain an S atom, and the mean polarizability of these molecules is well described with the PDI model again illustrating the accuracy of the new S parameters. For all amino acids, the mean polarizability calculated with PDI is larger than the SCF polarizability.

In general, it is expected that the inclusion of electron correlation in the quantum chemical calculations will increase the values of the polarizabilities since the SCF method is known to underestimate the polarizability. If we compare our SCF values for the polarizability with the DFT results of Swart et al.[61] we find that this is indeed the case. Swart et al.[61] also presented a parametrization of the original Thole PDI model for the 20 amino acids against polarizabilities calculated using DFT. If we compare our results with both their reported DFT results and the Thole PDI model results we find a good agreement.

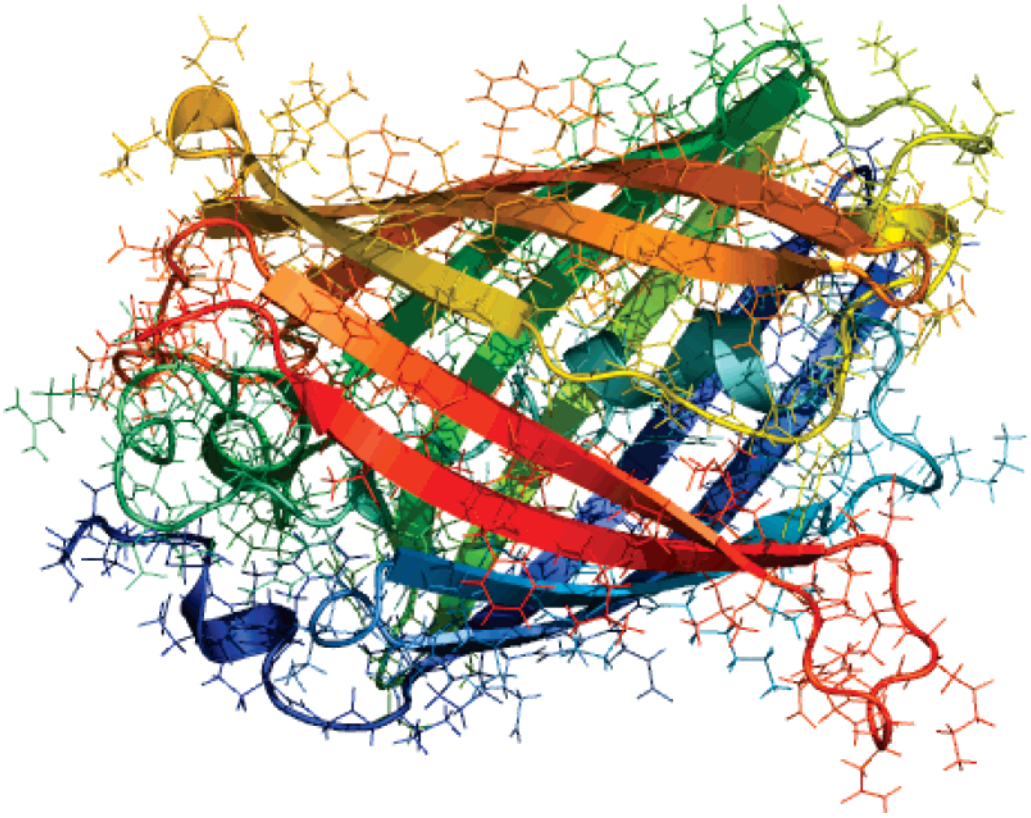

Figure 3. Cartoon of the green fluorescent protein made using PyMol.[59]

Table 1: Atomic Parameters Fitted To Model the Frequency-Dependent Polarizability Using the PDI-SQRT Unsöld Model[a]

atom	α_p	Φ_p	ω_p
H	1.280	0.358	0.413
B	8.649	0.074	-
C	8.465	0.124	0.784
N	6.169	0.268	0.658
O	3.754	4.103	0.493
F	1.907	1.468	0.896
Cl	13.081	0.453	0.375
S	19.617	0.120	0.534
rms[b]	2.47		0.77

[a] In au, 1 au = 0.1482 Å^3. The parameters for the elements H, B, C, N, O, F, and Cl have been taken from ref 37, and only the S parameters have been optimized in this work. [b] Optimized error, see eqs 10 and 11.

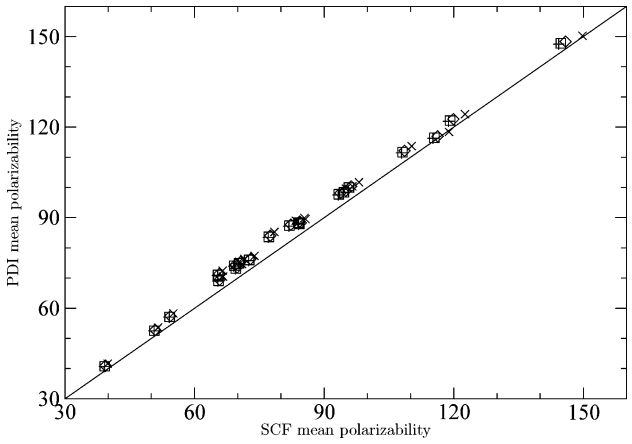

Figure 4. The isotropic polarizability in au calculated using PDI vs SCF for the frequencies ω(au) = 0.0 (+), 0.02389 (□), 0.04282 (◇), and 0.0774 (×).

For the anisotropies in Figure 5 and Table 2, a larger deviation is found between the PDI model and the SCF results. The average deviation is 25.9% with the largest deviation of 64.1% for isoleucine. In general, anisotropies are much more difficult to model than the mean polarizability, and it is therefore not surprising that the deviation is larger in this case. Furthermore, according to eq 10 the absolute error of the tensor components is minimized, which may result in large relative errors in cases where the absolute values are small. For the aromatic amino acids, phenylalanine, tyrosine, and trypthophan, we see that not only the anisotropy is modeled accurately but also the anisotropy of arginine is modeled successfully by the PDI model. These molecules have a large polarizability as compared with the other amino acids, and also the mean polarizability of these molecules are modeled very well with the PDI model. We note that in all cases the PDI model predicts anisotropic polarizabilities which are larger than the corresponding SCF value.

In Figures 4 and 5, a similar accuracy is obtained for the frequency-dependent polarizabilities of the amino acids. This is expected due to the small dispersion in the frequency range investigated here. Again the amino acids containing S atoms give similar results to the other amino acids.

VI. Calculations on Proteins

To illustrate the usefulness of the PDI model to calculate the polarizability of large systems where quantum chemical

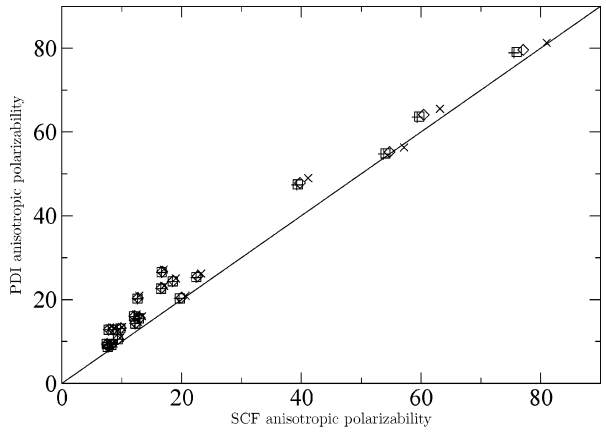

Figure 5. The anisotropic polarizability in au calculated using PDI vs SCF for the frequencies ω(au) = 0.0 (+), 0.02389 (□), 0.04282 (◇), and 0.0774 (×).

Table 2

amino acid	$\bar{\alpha}^{SCF}$	$\bar{\alpha}^{PDI}$	dev[a] (%)	$\Delta\alpha^{SCF}$	$\Delta\alpha^{PDI}$	dev[b] (%)
alanine (A)	50.59	52.46	3.7	9.32	10.52	12.9
arginine (R)	107.90	111.47	3.3	19.62	20.23	3.1
asparagine (N)	70.16	74.79	6.6	12.87	15.47	20.2
aspartic acid (D)	65.34	70.89	8.5	8.54	12.76	49.5
cysteine (C)	69.41	73.07	5.3	7.65	8.66	13.2
glutamine (Q)	81.84	87.18	6.5	16.52	22.58	36.6
glutamic acid (E)	77.09	83.48	8.3	12.62	20.17	59.8
glycine (G)	39.16	40.70	3.9	12.22	14.25	16.7
histidine (H)	95.49	99.80	4.5	39.23	47.37	20.7
isoleucine (I)	83.89	88.16	5.1	7.79	12.79	64.1
leucine (L)	84.12	87.78	4.4	9.76	13.10	34.2
lysine (K)	93.25	97.59	4.7	16.65	26.48	59.1
methionine (M)	94.37	98.26	4.1	22.40	25.27	12.8
phenylalanine (F)	115.16	116.30	1.0	53.76	54.73	1.8
proline (P)	69.05	73.94	7.1	18.45	24.28	31.6
serine (S)	54.13	57.02	5.4	8.25	9.22	11.8
threonine (T)	65.44	68.98	5.4	12.03	15.95	32.6
tryptophan (W)	144.28	147.52	2.2	75.54	78.88	4.4
tyrosine (Y)	118.79	121.95	2.7	59.38	63.51	7.0
valine (V)	72.54	75.82	4.5	7.51	9.39	25.0

[a] Deviation of $\bar{\alpha}^{PDI}$ from $\bar{\alpha}^{SCF}$. [b] Deviation of $\Delta\alpha^{PDI}$ from $\Delta\alpha^{SCF}$.

calculations are unfeasible, PDI calculations have been performed for the static polarizability of three proteins. The three proteins are ribonuclease inhibitor (RNI) which contains 89 residues (1434 atoms), lysozyme (LYS) which contains 129 residues (1950 atoms), and green fluorescent protein (GFP) which contains 230 residues (3604 atoms). Cartoons of the proteins are presented in Figures 1−3, respectively. For RNI, we obtain a mean polarizability of $\bar{\alpha}$ = 6903.64 au and an anisotropy of $\Delta\alpha$ = 667.62 au. The mean polarizability for LYS is $\bar{\alpha}$ = 9506.30 au with an anisotropy of $\Delta\alpha$ = 1344.43 au. For the largest protein studied here, GFP, we obtain a mean polarizability of $\bar{\alpha}$ = 17443.98 au and an anisotropy of $\Delta\alpha$ = 2300.4 au

The mean polarizability obtained with the PDI model is compared with an additive model for the polarizability, $\bar{\alpha}^{add}$, i.e., the sum of the polarizability of the residues in the protein. This simple additive model does not take into account the differences due to the peptide bond formations in the proteins and will therefore only be able to give a rough estimate of the polarizability. For RNI we get an additive polarizability of $\bar{\alpha}^{add}$ = 7344.77 au, for LYS $\bar{\alpha}^{add}$ = 10220.65 au, and for GFP $\bar{\alpha}^{add}$ = 18844.68 au. For these proteins, the simple additive model overestimates the mean polarizability by 6.3% for RNI, 7.5% for LYS, and 8% for GFP. Although the additive model seems to be reasonable for the mean polarizability, the model is trivially unable to describe the anisotropic polarizability since this is not related to the sum of the residues.

Dielectric properties of proteins are important for their structural and functional characteristics.[18,62−71] The concept of a dielectric constant of a protein depends on the model in which it is used, and the value therefore varies in different applications.[68] However, in general it is agreed on that the intrinsic dielectric constant of proteins are in the range 2−4 which is consistent with measurements on dry proteins.[72,73] The intrinsic (or optical) dielectric constant means here the part which is related to the polarizability or induced polarization. The contribution to the dielectric constant arising from the permanent polarization (the static dielectric constant) is not considered here.

The intrinsic dielectric constant is related to the susceptibility, i.e., polarizability per volume, by[74]

$$\epsilon = 1 + 4\pi\chi^{(1)} = 1 + 4\pi\frac{\bar{\alpha}}{V} \qquad (12)$$

where $\chi^{(1)}$ is the susceptibility or polarizability per volume V. The volume of the proteins may be estimated by using an average van der Waals radius of 1.5 Å for the atoms, which gives the following volumes $V^{RNI} = 1.04 \times 10^4$ Å^3, $V^{LYS} = 1.46 \times 10^4$ Å^3, and $V^{GFP} = 2.69 \times 10^4$ Å^3. Using these estimates and the mean polarizability calculated for the proteins, an intrinsic dielectric constant may be obtained for the proteins. For RNI we get ϵ = 2.24, for LYS ϵ = 2.21, and for GPL we get ϵ = 2.21. This estimate for the intrinsic dielectric constant is in good agreement with both measurements on dry proteins and the values generally adopted. It is noted that the value of the intrinsic dielectric constants for the three proteins investigated are very similar.

VII. Discussion and Conclusions

The focus of this work has been to study the polarizability of the amino acids by means of a PDI model. Therefore, to also study the sulfur containing amino acids we extended our existing PDI model to also include the sulfur atom. It was shown that this was straightforward by adopting the parameters obtained previously for the PDI model and only optimize the S parameters to a small set of molecules. The PDI model with the new parameters was subsequently tested on the amino acids. We compared the results from the PDI model with SCF calculations. This comparison showed that the PDI model is capable of reproducing the SCF polarizabilities to an accuracy of 5% for the mean polarizability. The description of its anisotropy is reproduced within 25%. Although accurate calculations of the polarizability requires the inclusion of electron correlation, especially for the anisotropic polarizability, it is clear that the PDI model reproduces the polarizability accurately enough for many

purposes. We also showed that a similar accuracy can be obtained for the frequency-dependent polarizability well below any electronic transitions. Therefore, we conclude that the PDI model produces an accurate description of the polarizability for the amino acids. Since the PDI model represents an atomistic model for the polarization, it is well suited for adoption in classical force field see e.g. refs 6, 13, 21, and 75−77 or combined quantum mechanics and molecular mechanics (QM/MM) models, see e.g. refs 4 and 78−82.

To test the PDI model on systems for which quantum chemical calculations would be unfeasible, the static polarizability has been calculated for three proteins. The polarizability obtained with the PDI model has been compared to an additive model, i.e., the sum of the polarizability of the amino acids residues. This showed that the simple additive model is good to within 10%. We have also calculated the intrinsic dielectric constant for the three proteins. For all three proteins, we found an intrinsic dielectric constant of 2.2 which is in good agreement with measurement on dry proteins.

Acknowledgment. P.-O.Å. has received support from the Norwegian Research Council (NFR) through a Strategic University Program (Grant no 154011/420), a NANOMAT program (Grant no 158538/431), and a grant of computer time from the Norwegian High Performance Computing Consortium (NOTUR). K.V.M. thanks the Danish Natural Science Research Council, the Danish Technical Research Council, the Carlsberg Foundation, the Danish Center for Scientific Computing, and the EU-network NANOQUANT for support.

References

(1) Buckingham, A. D. *Adv. Chem. Phys.* **1967**, *12*, 107.

(2) Buckingham, A. D. Basic Theory of Intermolecular Forces: Application to Small Molecules. In *Intermolecular Interactions: From Diatomics to Biopolymers*; Pullman, B., Ed.; Wiley: New York, 1978.

(3) Stone, A. J. *The theory of intermolecular forces*; Clarendon Press: Oxford, 1996.

(4) Warshel, A.; Levitt, M. *J. Mol. Biol.* **1976**, *103*, 227.

(5) Warshel, A. *J. Phys. Chem.* **1979**, *83*, 1640.

(6) Rullmann, J. A. C.; van Duijnen, P. T. *Mol. Phys.* **1988**, *63*, 451.

(7) Ahlström, P.; Wallqvist, A.; Engström, S.; Jönsson, B. *Mol. Phys.* **1989**, *68*, 563.

(8) Rullman, J. A. C.; van Duijnen, P. T. *Rep. Mol. Theory* **1990**, *1*, 1−21.

(9) Kuwajima, S.; Warshel, A. *J. Phys. Chem.* **1990**, *94*, 460.

(10) Dang, L. X. *J. Chem. Phys.* **1992**, *97*, 2183.

(11) Soetens, J.-C.; Milot, C. *Chem. Phys. Lett.* **1995**, *235*, 22.

(12) Dang, L. X.; Chang, T.-M. *J. Chem. Phys.* **1997**, *106*, 8149.

(13) Burnham, C. J.; Li, J.; Xantheas, S. S.; Leslie, M. *J. Chem. Phys.* **1999**, *110*, 4566.

(14) Halgren, T. A.; Damm, W. *Curr. Opin. Struct. Biol.* **2001**, *11*, 236.

(15) Engkvist, O.; Åstrand, P.-O.; Karlström, G. *Chem. Rev.* **2000**, *100*, 4087.

(16) Rick, S. W.; Stuart, S. J. *Rev. Comput. Chem.* **2002**, *18*, 89−146.

(17) Ren, P.; Ponder, J. W. *J. Comput. Chem.* **2002**, *23*, 1497−1506.

(18) Warshel, A.; Russel, S. *Quart. Rev. Biophys.* **1984**, *17*, 283.

(19) Voisin, C.; Cartier, A. *J. Mol. Struct. (THEOCHEM)* **1993**, *286*, 35−45.

(20) van der Vaart, A.; Bursulaya, B. D.; Brooks, C. L., III; Merz, K. M., Jr. *J. Phys. Chem. B* **2000**, *104*, 9554−9563.

(21) Ponder, J. W.; Case, D. A. *Adv. Protein Chem.* **2003**, *66*, 27.

(22) Bishop, D. M. *Adv. Quantum Chem.* **1994**, *25*, 1.

(23) Bishop, D. M.; Norman, P. Calculation of dynamic hyperpolarizabilities for small and medium sized molecules. In *Handbook of Advanced Electronic and Photonic Materials*; Nalwa, H. S., Ed.; Academic Press: San Diego, 2000.

(24) Prasad, P. N.; Williams, D. J. *Introduction to nonlinear optical effects in molecules and polymers*; Wiley: New York, 1991.

(25) Kanis, D. R.; Ratner, M. A.; Marks, T. J. *Chem. Rev.* **1994**, *94*, 195−242.

(26) *Molecular Electronics*; Jortner, J., Ratner, M., Eds.; Blackwell Science: Oxford, 1997.

(27) van Gisbergen, S. J. A.; Snijders, J. G.; Baerends, E. J. *J. Chem. Phys.* **1998**, *109*, 10644.

(28) van Faassen, M.; de Boeij, P. L.; van Leeuwen, R.; Berger, J. A.; Snijders, J. G. *Phys. Rev. Lett.* **2002**, *88*, 186401.

(29) Allen, M. P.; Tildesley, D. S. *Computer Simulations of Liquids*; Clarendon: Oxford, 1987.

(30) Genzer, J.; Kolafa, J. *J. Mol. Liquids* **2004**, *109*, 63−72.

(31) Stone, A. J. *Mol. Phys.* **1985**, *56*, 1065−1082.

(32) Åstrand, P.-O.; Karlström, G. *Mol. Phys.* **1992**, *77*, 143−155.

(33) van Duijnen, P. T.; Swart, M. *J. Phys. Chem. A* **1998**, *102*, 2399.

(34) Jensen, L.; Åstrand, P.-O.; Sylvester-Hvid, K. O.; Mikkelsen, K. V. *J. Phys. Chem. A* **2000**, *104*, 1563.

(35) Jensen, L.; Schmidt, O. H.; Mikkelsen, K. V.; Åstrand, P.-O. *J. Phys. Chem. B* **2000**, *104*, 10462.

(36) Kongsted, J.; Osted, A.; Jensen, L.; Åstrand, P.-O.; Mikkelsen, K. V. *J. Phys. Chem. B* **2001**, *105*, 10243.

(37) Jensen, L.; Åstrand, P.-O.; Osted, A.; Kongsted, J.; Mikkelsen, K. V. *J. Chem. Phys.* **2002**, *116*, 4001.

(38) Silberstein, L. *Philos. Mag.* **1917**, *33*, 92.

(39) Silberstein, L. *Philos. Mag.* **1917**, *33*, 215.

(40) Silberstein, L. *Philos. Mag.* **1917**, *33*, 521.

(41) Applequist, J.; Carl, J. R.; Fung, K. F. *J. Am. Chem. Soc.* **1972**, *94*, 2952.

(42) Applequist, J. *Acc. Chem. Res.* **1977**, *10*, 79.

(43) Jensen, L.; Sylvester-Hvid, K. O.; Mikkelsen, K. V.; Åstrand, P.-O. *J. Phys. Chem. A* **2003**, *107*, 2270.

(44) Jensen, L.; Åstrand, P.-O.; Mikkelsen, K. V. *Nano Lett.* **2003**, *3*, 661.

(45) Jensen, L.; Åstrand, P.-O.; Mikkelsen, K. V. *J. Phys. Chem. B* **2004**, *108*, 8226.

(46) Jensen, L.; Åstrand, P.-O.; Mikkelsen, K. V. *J. Phys. Chem. A* **2005**, *108*, 8795.

(47) Birge, R. R.; Parsons, B.; Song, Q. W.; Tallent, J. R. Protein-based three-dimensional memories and associative processors. In *Molecular Electronics*; Jortner, J., Ratner, M., Eds.; Blackwell Science: Oxford, 1997.

(48) Salafsky, J. S. *Chem. Phys. Lett.* **2001**, *342*, 485−491.

(49) Birge, R. R. *J. Chem. Phys.* **1980**, *72*, 5312−5319.

(50) Thole, B. T. *Chem. Phys.* **1981**, *59*, 341.

(51) Helgaker, T. et al. Release 1.2, 2001.

(52) Olsen, J.; Jørgensen, P. *J. Chem. Phys.* **1985**, *82*, 3235−3264.

(53) Jensen, H. J. AA.; Koch, H.; Jørgensen, P.; Olsen, J. *Chem. Phys.* **1988**, *119*, 297.

(54) Jensen, H. J. AA.; Jørgensen, P.; Olsen, J. *J. Chem. Phys.* **1988**, *89*, 3654.

(55) Sadlej, A. J. *Collect. Czech. Chem. Commun.* **1988**, *53*, 1995−2015.

(56) Sylvester-Hvid, K. O.; Åstrand, P.-O.; Ratner, M. A.; Mikkelsen, K. V. *J. Phys. Chem. A* **1999**, *103*, 1818.

(57) The 18 molecules are as follows: methylthioethane ($C_2H_5SCH_3$), ethanethiol (C_2H_5SH), 1-propanethiol (C_3H_7SH), trichloromethanethiol (CCl_3SH), methyl(trifluoromethyl) sulfide (CF_3SCH_3), trifluoromethanethiol (CF_3SH), chloromethyl sulfide (CH_2ClSCH_3), chloromethanethiol (CH_2ClSH), fluoromethyl sulfide (CH_2FSCH_3), fluoromethanethiol (CH_2FSH), dimethyl sulfide (CH_3SCH_3), methanesulfenylchloride (CH_3SCl), methanesulfenylfluoride (CH_3SF), methanethiol (CH_3SH), dichloromethyl sulfide ($CHCl_2SCH_3$), dichloromethanethiol ($CHCl_2SH$), difluoromethyl sulfide (CHF_2SCH_3), defluoromethanethiol (CHF_2SH).

(58) Frisch, M. J. et al. Gaussian, Inc. Pittsburgh, PA, 1998.

(59) Delano, W. L. The PyMOL Molecular Graphics System, http://www.pymol.org, 2002.

(60) WebElements, http://www.webelements.com, 2005.

(61) Swart, M.; Snijders, J. G.; van Duijnen, P. T. *J. Comput. Methods Sci. Eng.* **2004**, *4*, 419−425.

(62) Matthew, J. B. *Annu. Rev. Biophys. Biomol. Chem.* **1985**, *14*, 387.

(63) King, G.; Lee, F. S.; Warshel, A. *J. Chem. Phys.* **1991**, *95*, 4366.

(64) Laberge, M. *Biochim. Biophys. Acta* **1998**, *1386*, 305.

(65) Voges, D.; Karshikoff, *J. Chem. Phys.* **1998**, *108*, 2219.

(66) Havranek, J. J.; Harbury, P. B. *Proc. Natl. Acad. Sci. U.S.A.* **1999**, *96*, 11145.

(67) Simonson, T. *Int. J. Quantum Chem.* **1999**, *73*, 45.

(68) Schutz, C. N.; Warshel, A. *Proteins* **2001**, *44*, 400.

(69) Archontis, G.; Simonson, T. *J. Am. Chem. Soc.* **2001**, *123*, 11047.

(70) Song, X. *J. Chem. Phys.* **2002**, *116*, 9359.

(71) Rubinstein, A.; Sherman, S. *Biophys. J.* **2004**, *87*, 1544.

(72) Takashima, S.; Schwan, H. P. *J. Phys. Chem.* **1965**, *69*, 4176.

(73) Pennock, B. E.; Schwan, H. P. *J. Phys. Chem.* **1969**, *73*, 2600.

(74) Böttcher, C. J. F. *Theory of Electric Polarization*, 2nd ed.; Elsevier: Amsterdam, 1973; Vol. 1.

(75) Chialvo, A. A.; Cummings, P. T. *Fluid Phase Equilibria* **1998**, *150−151*, 73.

(76) Ren, P. Y.; Ponder, J. W. *J. Phys. Chem. B* **2003**, *107*, 5933.

(77) Burnham, C. J.; Xantheas, S. S. *J. Chem. Phys.* **2002**, *116*, 1500.

(78) Thole, B. T.; van Duijnen, P. T. *Theor. Chim. Acta* **1980**, *55*, 307.

(79) van Duijnen, P. T.; de Vries, A. H. *Int. J. Quantum Chem.* **1996**, *60*, 1111.

(80) Jensen, L.; van Duijnen, P. T.; Snijders, J. G. *J. Chem. Phys.* **2003**, *118*, 514.

(81) Poulsen, T. D.; Ogilby, P. R.; Mikkelsen, K. V. *J. Chem. Phys.* **2001**, *115*, 7843.

(82) Kongsted, J.; Osted, A.; Mikkelsen, K. V.; Christiansen, O. *Mol. Phys.* **2002**, *100*, 1813.

CT050053C

JCTC Journal of Chemical Theory and Computation

A Simple Method for Improving Torsion Optimization of Ligand Molecules in Receptor Binding Sites

Jianwei Che*

Genomics Institute of the Novartis Research Foundation, 10675 John Jay Hopkins Drive, San Diego, California 92121

Received September 7, 2004

Abstract: A simple but effective method is introduced for optimizing ligand molecules in torsion space within receptor binding sites. The algorithm makes use of geometric constraints of ligand molecules to search for energetically favorable conformations. It is applied to a conjugate gradient (CG) method as an example. During conformational energy optimization, new line search directions are modified according to the spatial span of rotational groups in ligand molecules. Significant improvements were observed in terms of the abilities both to recover global optimal structures and to obtain lower energy ensembles. This simple algorithm allows rapid implementation and can be incorporated into other conformational energy optimization techniques.

I. Introduction

Energy minimization has been a common and powerful tool in molecular modeling. While global optimization is extremely difficult and rare to achieve except for simple systems, local optimization has been quite useful for studying the properties of a molecular system. For example, it is very important to predict the correct binding configuration of ligand−receptor complexes for rational drug design and lead optimization in the pharmaceutical industry, and one important technique is through multiple conformational energy minimizations of ligand molecules.[1−7] Because of the relative stiffness of bond stretching and angle bending modes, the conformational variation of a ligand molecule mainly comes from the changes of dihedral angles of rotatable bonds (e.g. simple σ bond in a chain). A typical small molecule ligand has several to more than a dozen such rotatable bonds, so its conformational space can be very large and consist of many local energy minimum states. Furthermore, as the number of rotatable bonds increases, the complexity of the system increases exponentially and results in a rough energy landscape, and the energy surface becomes even more complex and rough in a protein binding site.

In classical molecular modeling, energy optimization is normally treated as an applied mathematical problem.[8−11] For example, conjugate gradient (CG) and Monte Carlo (MC) methods are two popular techniques. Other more advanced techniques have been developed, such as truncated Newton conjugate gradient method[12,13] and convex global underestimation (CGU) method.[14] Within the CG framework, different versions have also been developed based on different approaches of updating the line search directions.[15−20] Optimizing a molecular structure is generally done in Cartesian coordinates (CC) (i.e. x, y, and z) or internal coordinates (IC) (e.g. bond length, bond angle, and dihedral angle). They have been implemented in various molecular mechanics and dynamics software.[8−11] Upon noncovalent binding with receptors, it is often convenient to constrain ligand bond lengths and angles at equilibrium positions. This can be done easily in IC but more complicated in CC.

Torsion (i.e. dihedral angle) optimization of ligand molecules is usually efficient because of soft modes of torsional motions. In addition, it has less number of degrees of freedom (DOF) than all atom CC optimization does. Its effectiveness, however, is reduced when applied to ligand molecules in receptor binding sites, because many rotations are restricted by the presence of receptor atoms. The rotation about some ligand rotatable bonds, in particular bonds close to the central core structure, is likely to cause steric clashes. Consequently, only very small steps of rotation can be taken during optimization. To improve torsional optimization under these circumstances, we present here a modified version of this method that considers the geometric structure of biomolecular

* Corresponding author e-mail: jche@gnf.org.

10.1021/ct0499433 CCC: $30.25
Published on Web 05/26/2005

complexes. The modified algorithm was able to obtain global optimal configuration much easier than conventional torsional optimization. In addition to the example application of improving conventional CG, this method can be easily integrated with other existing optimization algorithms such as steepest descent, Powell's method,[17] etc. to increase their performance, particularly for flexible ligand docking. The paper is organized into following sections. In section II, we describe the algorithm in detail. In section III, numerical examples and discussions are presented, and we summarize in section IV.

II. Algorithm

In torsion optimization only dihedral angles are free variables. The system potential energy can be written as

$$U = U(\{\tau_i\}|\{r_j,\theta_k\},i,j,k = 1,2,3...) \quad (1)$$

where τ_i is the ith torsion angle, and r_j and θ_k are jth bond length and kth bond angle, respectively. Note that all rs and θs are fixed parameters in the potential function. Equation 1 can also be written in CC with constraints of fixed bond lengths and angles. It is known that the potential surface in receptor binding sites is very rough, and energy barriers between local minima are often high compared to room temperature. Conventional energy minimization easily gets trapped in local minimum close to initial condition. To overcome the difficulty, soft core potentials (e.g. reduced van der Waals radii) are often used in docking program to ease the steric clashes. Although it introduces softness to the rotation modes restricted by receptor atoms, a drawback is that more false positives can squeeze into the sites, and it is difficult to discriminate between them. Other methods to level off potential barriers[21,22] have also been used.

To further improve the effectiveness of energy minimization with or without modifying potential, we introduce a simple scaling technique that can be combined with many optimization methods. As a demonstration, we will limit our discussion to the CG method, since CG requires a bit more attention in implementation than other simpler methods such as steepest descent. The general principle of torsional scaling, however, is applicable to other algorithms with little modification. In the CG algorithm, a new coordinate that minimizes a given function is generated from an iterative sequence[17]

$$\mathbf{x}_{i+1} = \mathbf{x}_i + \alpha_i \mathbf{d}_i \quad (2)$$

where $\mathbf{x}_i$ is the coordinate vector at ith iteration, $\mathbf{d}_i$ is the direction vector, and α_i is a scalar of the step length. After each iteration, the new coordinate (e.g. $\mathbf{x}_{i+1}$) locally minimizes the given function along the given search direction (e.g. $\mathbf{d}_i$). The important quantity in CG method is the generation of the direction vector sequence. A simple form is given by[20]

$$\mathbf{d}_{i+1} = -\mathbf{K}\mathbf{g}_{i+1} + \beta_i \mathbf{d}_i \quad (3)$$

where matrix $\mathbf{K}$ is normally chosen to be identity matrix, $\beta_i = \mathbf{g}_{i+1}{}^T\mathbf{K}(\mathbf{g}_{i+1} - \mathbf{g}_i)/\mathbf{d}_i{}^T(\mathbf{g}_{i+1} - \mathbf{g}_i)$, and $\mathbf{g}_i$ is the gradient of the potential function at position $\mathbf{x}_i$. The direction vector sequence must satisfy the conjugacy relation

$$\mathbf{d}^T{}_i\mathbf{A}\mathbf{d}_j = 0, \textit{ for } i \neq j \quad (4)$$

$\mathbf{A}$ is the Hessian matrix of the given potential function, though in practice, most CG implementations avoid explicit or direct calculation of the Hessian matrix.[17,23] In CG, a central step is to calculate the successive conjugate directions $\mathbf{d}_i$, which is determined by β_i. Many variations of CG (e.g. Fletcher-Reeves,[15] Polak-Ribiere,[18] and Shanno's[19,20] CG) differ only by the method of updating line search directions. In the case of exact quadratic functions, they yield identical results. However, because of the nonquadratic nature of molecular potential functions, computer round-off error, and inexact line minimization, they can and normally do give different convergence performance and final results.

Besides many improvements in optimization procedures from mathematic perspectives, less attention has been given to the molecular nature of the problem. When only dihedral angles are free variables, a molecule closely resembles a kinematical system. In fact, this analogy has been used in molecular dynamics and mechanics in torsion space.[24−26] Because torsion movements can introduce nonlocal structural changes for ligand−receptor systems, it limits the optimization step length in line minimization along certain directions. To reduce the limitation, we need to consider the molecular geometric property. It is known from basic mechanics that the corresponding general forces for dihedral angles are torques

$$\mathbf{T}_i = -\nabla_{\tau_i} U = \sum_{j\in D_i} \mathbf{r}_j \times \mathbf{f}_j \quad (5)$$

where τ_i is the rotation vector for dihedral angle i that has the direction of rotation in right-handed convention and magnitude of rotation angle. $\mathbf{T}_i$ is the corresponding torque, which can be calculated from forces and coordinates in CC. D_i denotes the set of all atoms involved in the rotation of torsion angle CC. $\mathbf{f}_j$ is the force acting on atom j, and $\mathbf{r}_j$ is the vector of atom j in the local coordinate frame where ith rotation center vector $\mathbf{O}_i$ is the origin. $\mathbf{r}_j$ can then be calculated from space fixed frame coordinates $\mathbf{R}_j$

$$\mathbf{r}_j = \mathbf{R}_j - \mathbf{O}_i \quad (6)$$

Substitute eq 6 into eq 5, we have

$$\mathbf{T}_i = \sum_{j\in D_i} \mathbf{R}_j \times \mathbf{f}_j - \mathbf{O}_i \times \sum_{j\in D_i} \mathbf{f}_j \quad (7)$$

For a branched molecule, D_i can be partitioned into subgroups if it has additional rotatable bonds. The rotation about the main rotatable bond changes all the atomic positions in the group, and the rotation about a subrotatable bond modifies only the atomic positions within the subgroup. The hierarchical relation forms a tree topology and each branch forms a "cluster". At each level, a cluster can have sublevel clusters if it has rotatable bonds. Otherwise, the cluster is called a leaf. In our present treatment, a rotatable bond is defined as a nonterminal σ bond that does not participate in a ring structure. In principle, the definition can be extended to include double bond and ring bonds. For

computational convenience, we chose the atom that connected to its parent cluster as the rotation center $\mathbf{O}_i$. The overall molecule is treated as a grand cluster, and its center of mass (COM) is the rotation center $\mathbf{O}_{\text{grand}}$. For a given cluster, its torque in the local coordination frame is calculated using eq 5. Therefore, we can rewrite the total torque of a cluster in its local frame in terms of the local torques of its subclusters

$$\mathbf{T}_i = \sum_{D_j \in D_i} [\mathbf{T}_j + (\mathbf{O}_j - \mathbf{O}_i) \times \mathbf{F}_j] \tag{8}$$

where D_j runs through all subclusters of D_i, and $\mathbf{F}_j$ and $\mathbf{O}_j$ are the total force and position of subcluster j. For leaf clusters, only the second terms in the summation survive, and eq 8 recovers eq 5. Similarly, $\mathbf{T}_j$ is also zero for single atoms in cluster i, where $\mathbf{O}_j$ are atomic coordinates and $\mathbf{F}_j$ is its force. Equation 8 clearly illustrates a recursive nature of the torque calculation for the tree topology clusters. In actual implementation, a sweep from tip to base is carried out to calculate $\mathbf{T}_i$ for each cluster using eq 8. Each cluster stored its torque $\mathbf{T}_i$, total force $\mathbf{F}_i$, and rotation center $\mathbf{O}_i$ as its C++ class attributes. As total torque can be calculated recursively from the sweep, the actual gradient along each rotatable bond is the projection of torque. The projection step is trivial and can be carried out after the sweep. We also want to mention that Jain et al.[24] developed a very efficient recursive method for solving equation of motion in IC without explicit inversion of mass matrix. The difference here is that there is no mass matrix in the optimization procedure. Energy minimization in IC is fortunately simpler than the dynamics in this respect. Therefore, we can avoid many matrix operation steps in Jain's[24,25] algorithm. As we can see from eq 8, large clusters tend to have large torques because of their large radius of gyration even if they experience a similar amount of force as smaller ones, and rotation of large clusters will likely create more serious steric clashes with receptor atoms than smaller ones. Because large clusters extend further away from the rotation axis, atomic displacements are amplified for atoms at the tip. It renders line minimization for dihedral angles much less effective if the search direction is dictated by local gradients (e.g. starting direction, and restarting direction), because only a small step length can be taken in each iteration. Therefore, direct optimization of torsion angles (re)started with torques given by eq 5 more likely gets trapped in a local optimal structure close to the initial starting point.

Here, we introduce a novel way of defining initial and restart line search direction in the CG procedure according to the size of each cluster to reduce the restraining effects induced by large clusters. The quantity to characterize the size of a cluster rotating about a given axis is the radius of gyration, defined as l_i for cluster i at a given conformation. When a molecule changes its conformation, the radii of gyration for some or all clusters will also change their values. For a given rotation axis, the radius of gyration of the ith cluster is calculated through the projection of its inertia tensor $\mathbf{I}_i$ with respect to the rotation center

$$\mu_i l_i^2 = \mathbf{i}^T \mathbf{I}_i \mathbf{i}, i = 1,2, \cdots \tag{9}$$

where $\mathbf{i}$ is the unit vector of rotation axis for cluster i. The inertial tensor at any given rotation center is evaluated from the inertia tensor in its COM frame

$$\mathbf{I}_i = \mathbf{I}_i^{\text{com}} + \mu_i(a_i^2 \mathbf{1} - \mathbf{a}_i \mathbf{a}_i^T), i = 1,2, \cdots \tag{10}$$

where $\mathbf{1}$ is the unit tensor, $\mathbf{a}_i$ is the displacement vector from the rotation center to the COM, $a_i^2 = \mathbf{a}_i^T \mathbf{a}_i$, and μ_i is the total mass of cluster i. Similar to eq 8, the inertia tensor of parent cluster is also obtained from their subclusters

$$\mathbf{I}_i^{\text{COM}} = \sum_{D_j \in D_i} \lfloor \mathbf{I}_j^{\text{COM}} + \mu_j(a_{ij}^2 \mathbf{1} - \mathbf{a}_{ij} \mathbf{a}_{ij}^T) \rfloor, i = 1,2, \cdots \tag{11}$$

where $\mathbf{a}_{ij} = \mathbf{R}_j^{\text{COM}} - \mathbf{R}_i^{\text{COM}}$. This is done during the same sweep as torque collection. Inertia tensor $\mathbf{I}_i^{\text{COM}}$ and $\mathbf{R}_i^{\text{COM}}$ are also attributes of cluster class. It is also worth pointing out that normal radius of gyration is not the only choice for characterizing the size of a cluster. For instance, substituting all atomic masses by corresponding van der Waals radii in above equations or simply choosing the largest atomic distance away from the rotation axis in each cluster can all be used to define a cluster size.

Instead of using the negative gradient as initial and restarting direction vectors in conventional CG, we define the initial and restarting direction vectors according to scaled gradients. First, we scale the torque as the following

$$\mathbf{T}_i^s = \mathbf{T}_i / l_i, i = 1,2, \cdots \tag{12}$$

where the superscript s indicates the scaled torque. Define a diagonal scaling matrix $\mathbf{S}$ as

$$\mathbf{S} = \begin{bmatrix} 1/l_1 & & & \\ & 1/l_2 & & \\ & & 1/l_3 & \\ & & & \vdots \end{bmatrix} \tag{13}$$

The scaled initial and restarting direction vectors $\mathbf{g}_t^s$ are obtained from original gradients

$$\mathbf{g}_t^s = \mathbf{S}\mathbf{g}_t \tag{14}$$

Because the scaling factor l_i can be very different for different clusters, the newly constructed line search direction is normally different from the direction used in conventional CG. Note that for a given sequence of CG minimization steps, the subsequent line search directions are determined by conjugacy condition governed by eq 4, applying eq 14 to each iteration will normally break the conjugacy. Therefore, in CG implementation, eq 14 is applied to initial and restarting directions only. Other methods, such as steepest descent, can use eq 14 at each step of minimization. As the result, the scaling transformation chooses a direction that limits the amplification of torques for a large cluster, improving CG optimization to a local/global optimum. Also as expected, the scaling becomes less important when the conformation gets closer to the converged structure.

The first step for torsion optimization is to divide a ligand molecule into clusters. Figure 1 illustrates how a ligand molecule is partitioned. The partition process starts by choosing a base atom, and all atoms that connect to the base

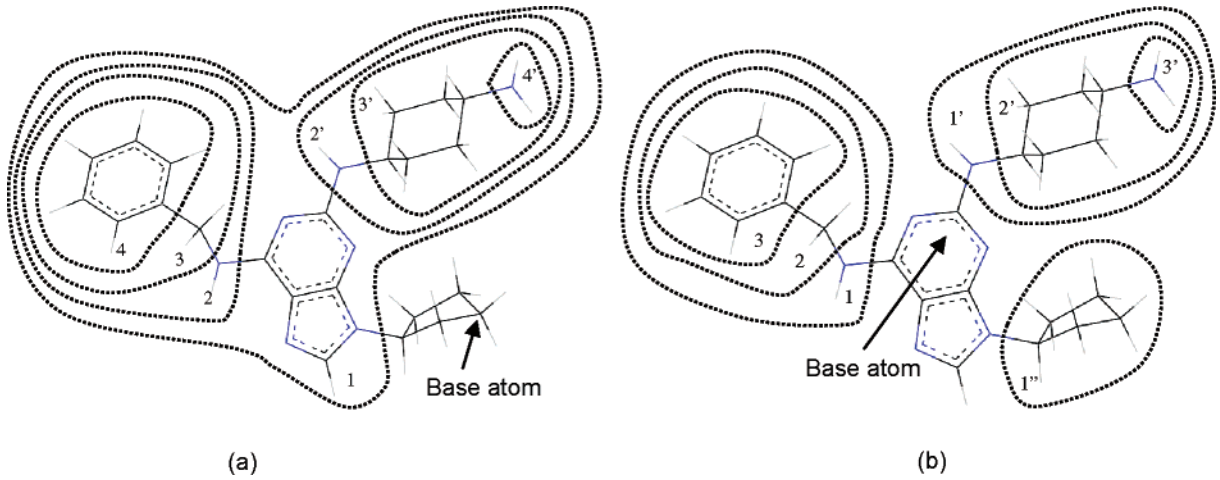

Figure 1. Schematic clustering of molecule, 2-[trans-(4-aminocyclohexyl)amino]-6-(benzyl-amino)-9-cyclopentylpurine. (a) Clusters obtained by choosing a tip atom as the starting root atom. (b) Clusters obtained by choosing the atom closest to COM as the starting root atom.

atom through nonrotatable bonds belong to the base group. When an atom connects to the base group by a rotatable bond, this atom is placed into a subcluster. The base group is always in the grand cluster (i.e. overall molecule). This process is carried out recursively until all atoms are put into proper clusters. In principle, any atom can be a base atom. For instance in Figure 1 (a), a tip atom is the base atom, while in (b) the atom closest to the COM is the base atom. In practice, we found that it was more efficient when the tree structure was balanced in terms of radii of gyration of clusters, for a reason similar to what was previously discussed for large clusters. When a molecule is properly clusterized, the sizes of clusters are kept as small and balanced as possible to reduce the large swinging of tip atoms. Although not rigorously proved, simply choosing the atom closest to COM as the base atom normally gives a satisfactory partition of clusters. Once a ligand molecule is partitioned, energy minimization can be carried out in a straightforward manner. In the next section, we demonstrate that this simple torsion scaling modification can improve the effectiveness of optimizing ligand molecules in binding sites.

III. Numerical Results and Discussion

To study the performance of the modified algorithm, we implemented it in an existing structure optimization module.[27,28] No modification was necessary to the existing module except the initial and restarting directions were recalculated according to eq 14. In our comparitive studies, the exact same multidimensional CG optimization routine was used to carry out three variations of energy minimization: scaled torsion, direct torsion, and all atom minimizations in CC. In all atom CC optimization, line search directions were calculated from atomic forces directly. The inter- and intramolecular interactions were modeled by Merck Molecular Force Field (MMFF94).[29−35] Interactions between ligand and receptor molecules were precalculated on a rectangular grid box that encompassed the whole binding site. The grid spacing is 0.5 Å, and three-dimensional cubic spline interpolation was used to calculate the energy between grid points. In order for the interpolation to give accurate values, we limited the extremely large repulsive pair wise energy by the following equation[36]

$$V_i' = \begin{cases} V_i, & \text{if } V_i < U_s \\ U_s + \dfrac{U_m(V_i - U_s)}{U_m + V_i - U_s}, & \text{if } V_i \geq U_s \end{cases} \quad (15)$$

where V_i is the interaction energy between the ith ligand atom and the receptor molecule, and U_s and U_m are user defined parameters. In our calculations, we use large values $U_s =$ 120 kcal/mol and $U_m =$ 240 kcal/mol in our calculations to maintain the "original" form the potential surface. Although whether this potential accurately represented the molecular system is another question and beyond the scope of this study, our intention was to test the optimization procedure itself even in the very extreme condition. The main purpose for eq 15 in our calculation is for the accuracy of interpolation rather than optimization itself. Equation 15 leveled off only the very top portion of the energy surface (>120 kcal/mol) without any modifications to the lower energy surface. In contrast, conventional potential softening (e.g. reducing van der Waals radii) alters the overall energy surface including the shapes and perhaps the positions of energy minima. To keep the ligand molecule from moving out of binding sites, a harmonic restraint potential is imposed outside the binding box.

Figure 2 depicts the 3D structures of four ligand molecules among those that we used as examples. Our examples included additional 31 ligand−receptor complexes randomly chosen from PDB database, so that they represented a variety of protein−ligand complex structures. These four structures shown here represented very typical ligands and systems from very simple (i.e. few rotatable bonds in 1E1X) to more complicated ones (i.e. more than a dozen rotatable bonds in 1KV2). Their cocrystal PDB codes are labeled above each molecule.

As shown in Figure 1, clusters can have very different sizes. Consequently, the scaling factor can be quite different for different clusters. More importantly, if a cluster contains several levels of subclusters, its radius of gyration l_i (i.e. the

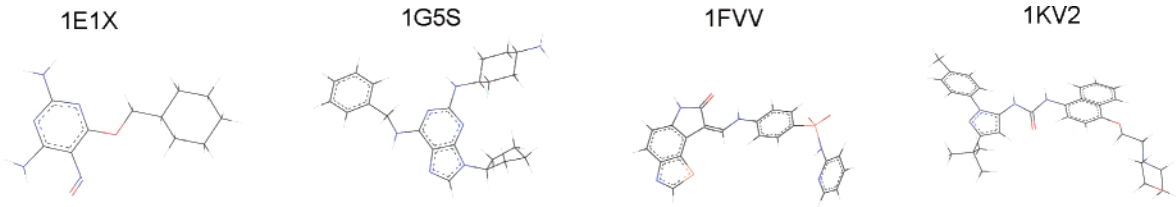

Figure 2. 3D structures of four inhibitor molecules for CDK2. Cocrystal PDB codes are labeled above each structure. Color coding for elements: C: black, H: gray, N: blue, F: green, S: orange, O: red.

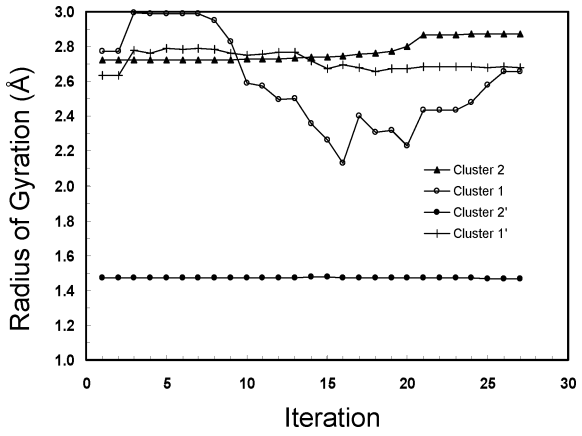

Figure 3. Variation of radius of gyration of all clusters during an optimization for the ligand molecule in Figure 1. The cluster hierarchical structure in Figure 1 (b) is used.

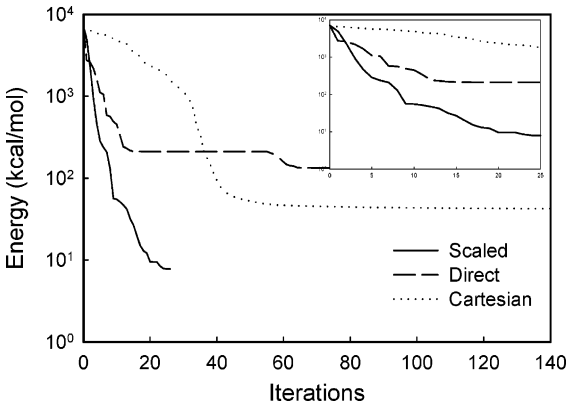

Figure 4. The optimization results of three energy minimization algorithm. The solid line is for scaled torsion optimization, the dashed line is for directed torsion optimization, and the dotted line is for all atom optimization in CC. The inset shows the zoom-in view of the first 25 iterations. The vertical axis for the main graph is in logarithm scale, and it is in linear scale in the inset graph. 100 kcal/mol had been added to the energy values in order to show logarithm scale.

scaling factor) may change significantly during the minimization process. It requires consistent updates of the radius of gyration of all clusters whenever a restarting vector is constructed in CG. The "dynamic" behavior of the radius of gyration during optimization is shown in Figure 3 for a minimization run.

The radii of gyration of some clusters did not change appreciably while others varied significantly during the minimization process. Obviously, the ones that belong to the leaf clusters (omitted in Figure 3) did not change at all (i.e. cluster 1″, 3, and 3′ in Figure 1(b)), and the ones whose subclusters had relatively high symmetry also did not change much (i.e. cluster 2 and 2′ in Figure 1(b)). If l_i of a cluster changed significantly (e.g. cluster 1 had a range of 1 Å variation), it indicated that the cluster conformation has been altered dramatically. The energy changes for this particular minimization process are depicted in Figure 4 for the three optimization algorithms. It shows that the scaled torsion optimization led to a much lower energy state. The inset shows the zoom-in view of the first 25 steps.

Interestingly, while the direct torsion optimization reduced the energy most rapidly in the first few steps, the scaled torsion optimization converged on a lower energy state. The reason is that the direct optimization chose the negative gradients as initial line search direction and therefore was able to go downhill more rapidly than scaled version. However, the initial rapid downhill movement trapped the conformation in a local minimum, so it ended up with a higher energy state. In contrast, the scaled torsion optimization chose the direction that allowed the molecule to have larger configuration change without being pulled into nearby local minima so quickly. This property is particularly appropriate when minimizing ligand molecules in receptors. The variation of l of cluster 1 and the total energy indicated that the final structure was quickly approached in about 25 iterations. To assess the quality of the final converged structures, we compared them to the global optimized crystal structure, which was obtained from all atom minimization of the experimental X-ray structure. Its energy value was −94 kcal/mol and had an RMSD of 0.55 Å with respect to the experimental X-ray structure. More importantly, it had the lowest energy among all configurations studied in our calculations. We believed that this structure could be used as a standard to gauge the performance of the 3 different optimization procedures. As mentioned earlier, direct torsion optimization is more likely to get trapped in a nearby local minimum because of the larger motion of tip atoms. This behavior is quite evident in Figure 4, where all three different methods arrived at different energy states. Each minimization was carried out until gradient RMS was below 0.1 kJ/mol or it reached 500 iterations. Both direct torsion and all atom optimization had difficulties escaping from the local minimum near the initial structure. When the CG (re)started with scaled directions, the molecule was able to find a path to reach the global optimal. The final structure had an energy of −93 kcal/mol and an RMSD of 0.6 Å with respect to the global optimal, and the final energies from direct torsion and all atom CC optimizations were 32 kcal/mol and −60 kcal/mol, respectively. Since each CG minimization iteration finds the local minimum in a particular search direction, it usually

requires multiple (e.g. 3−4) energy updates (i.e. energy evaluations) to bracket and locate the coordinate that minimizes the energy function. In our calculations, normal Amijo and Goldstein criteria[37] were used to terminate each iteration. After an iteration was finished, a new search direction was generated, and the minimization was resumed along the new direction. Here, we gave both iteration and energy update numbers for detailed comparisons. In Figure 4, the scaled method reached the final structure in 26 iterations with energy updates of 109 times, while Cartesian optimization used 406 iterations with energy updates of 1304 times and direct torsion optimization used 76 iterations with energy updates of 285 times to reach their final structures. Although the scaled torsion optimization converged more quickly than direction torsion algorithm in Figure 4, it cannot be generalized. Although the behavior in Figure 4 is not rare, it is not a common phenomenon for a scaled optimization to be significantly faster than direct torsion optimization and achieving much lower energy than CC at the same time. On average, the speed of the scaled method is comparable to direct torsion optimization. Usually, it is very slow for all atom CC optimizations to converge, while the direct torsion optimization often ends with high energy final structures. The whole purpose of the scaled method is to have the advantages from both all atom and direct torsion optimizations while avoiding their major drawbacks. In other words, it is a method able to find low energy structures like all atom CC optimization and as efficiently as the conventional torsion method.

It is usually less meaningful to judge an optimization method for rugged potential functions based on one or a few calculations. A good energy minimization algorithm should consistently produce a lower energy ensemble for a set of random initial conditions, provided that the set is made without biases. To get a global picture of how the scaled torsion optimization can improve an existing direct optimization algorithm for ligand configuration energy minimization, 300 initial configurations for each of the 35 ligand molecules were generated by randomly rotating the rotatable bonds and an overall random rotation translation of the optimized cocrystal structure. The resulting initial structures all had very large RMSD with respect to the global optimal (4 Å−8 Å) and high initial energy (above several thousands kcal/mol). Each configuration was then optimized directly by the three different procedures. Although the initial configurations were far away from global optimal structures and inappropriate for direct molecular dynamics simulations, they were quite relevant in studies that searched for global optima such as docking studies. Unlike molecular dynamics studies of a particular binding configuration, where most conformations in an initial ensemble are generated around the configuration, docking finds the correct one without prior knowledge how a ligand binds. In other words, a much larger configuration space has to be searched to find the best possible binding mode. For any local optimization method, this also means that many calculations are done in a physically irrelevant configuration space. However, whether a given initial configuration leads to a meaningful final state is generally not known a priori. This is particularly true for rugged energy surfaces such as the ones in protein binding sites. Therefore, the initial configurations generated here are very relevant to many practical applications.

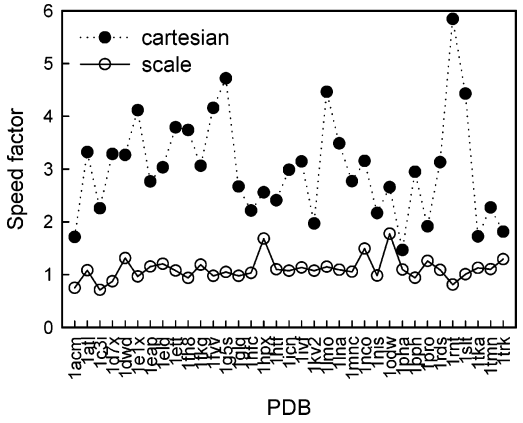

Figure 5. The computational speed factors all-atom Cartesian and scale torsion optimizations scaled by direct torsion method. The dotted line is for Cartesian coordinate optimization, and the solid line is for scaled torsion optimization.

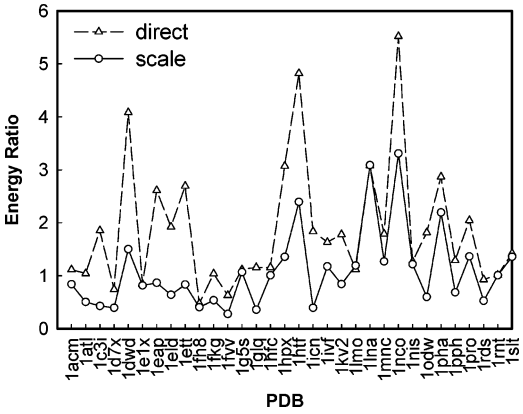

Figure 6. The average energy ratio of direct and scale torsion optimizations measured by all atom CC minimization method. The dashed line is for direct torsion, and the solid line is for scaled torsion optimization.

As we briefly mentioned previously, the scaled method is expected to be as fast as the conventional direct torsion optimization due to its intrinsic similarity. In Figure 5, the computational speed performances of all atom CC and scaled torsion optimizations were illustrated by the ratio between their average iterations and the ones from direct torsion minimization for each system. The larger the factors are, the slower the method is. As we expected, the efficiency of direct torsion optimization was well maintained in the scaled method, and both optimizations were significantly faster than all atom CC optimization.

It is known that all atom optimizations in many cases can achieve energetically more favorable structures than direct torsion optimization, even though it may take significantly longer computing time. The results in Figures 5 and 6 also indicated this behavior. In Figure 6, we plotted the ratios of average energies of all minimized structures from scaled and direct torsion optimizations to the all atom CC method. The ratio was calculated by $(\bar{E} - E_{\min}^{\text{global}})/(\bar{E}_{CC} - E_{\min}^{\text{global}})$, where $\bar{E}$ is the average energy given by a particular method,

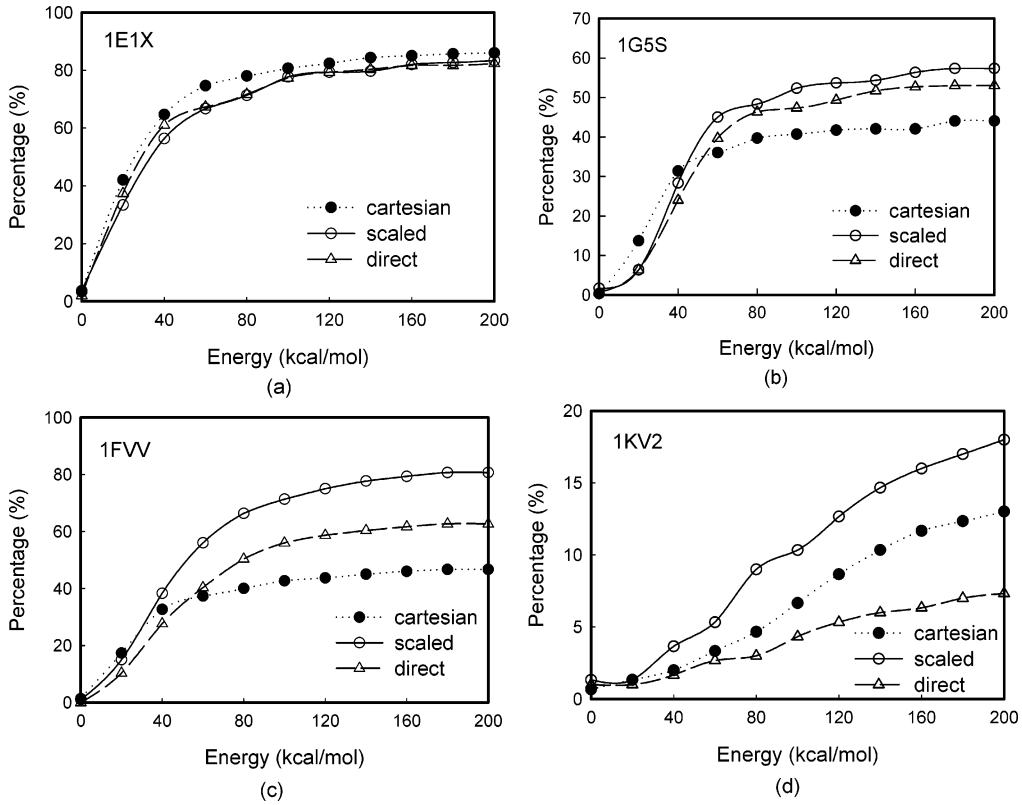

Figure 7. Energy distribution of conformational ensembles obtained from three different optimization procedures for (a) 1E1X, (b) 1G5S, (c) 1FVV, and (d) 1KV2. The initial energy distributions are not shown because they have extremely high energies far beyond the scale of the figure. The first 200 kcal/mol energy window is shown against the accumulate percentage of conformers in each energy bin of 20 kcal/mol. The solid line is for scaled torsion optimization, the dashed line is for direction torsion optimization, and the dotted line is for all atom CC optimization.

$\bar{E}_{CC}$ is the average energy by all atom CC minimization, and E_{min}^{global} is the global minimum energy. Obviously, the scaled optimization consistently outperformed the direct torsion method and gave comparable energies as all atom CC optimizations on average.

Since the scaling is a simple step on top of a conventional optimization algorithm, its overall performance inherits the intrinsic property of the specific optimizer with which it is combined. CG is a local optimization algorithm, and so is the scaled CG optimizer. The added benefit is that it can find better local energy minima more effectively, but it does not guarantee to locate the global optimal. It is also common that different versions of the optimizer result in different final structures from an identical initial structure. It should be noted that effective rotation barriers in torsion optimization are systematically higher than those in all atom optimization because of less flexible molecular structures.[38] We expect the success rate will be further improved if the effective rotational barriers were made consistent with all atom optimization. Although it is not exactly equivalent, a way of estimating it is to further minimize the final structures after torsion optimizations with all atom CC minimization. Our calculations showed that the average energies from both direct and scaled torsion optimization were further reduced significantly and became much lower than the ones given by an all atom CC method alone. The final energy difference between the two torsion methods, however, became much smaller. They were normally within a few to tens kcal/mol. The energies from the scaled method were consistently lower (about 22 kcal/mol on average). Since the combination of optimization methods is not the main subject in the paper, the properties and results will be studied elsewhere. The results shown in subsequent sections were all from a single optimization method unless otherwise specified.

Besides the comparison of the average energies of distributions, it is also important to check the energy distributions resulting from different optimizers. As an example, Figure 7 shows the accumulative percentage of conformers within the lowest 200 kcal/mol for the four systems in Figure 2.

As shown in Figure 7, scaled torsion optimization consistently recovers more low energy structures than direct torsion algorithm and most all atom CC optimization. The higher rate over all atom CC optimization is much less obvious because molecules had higher flexibility and greater numbers of DOF in all atom CC optimization. For 1E1X, scaled method, direct torsion, and all atom CC optimization behaved similarly. This can be explained by the simplicity of the ligand structure. Because most clusters are similar in size and there is only 1 rotatable bond that can affect its radius of gyration, the benefit of scaling torque is substantially reduced. However, the scaled method still recovered the global optimal structures almost twice as frequently as the direct torsion method, and its average total energy was also slightly lower than direct method. The difference between the methods is most evident for more complex

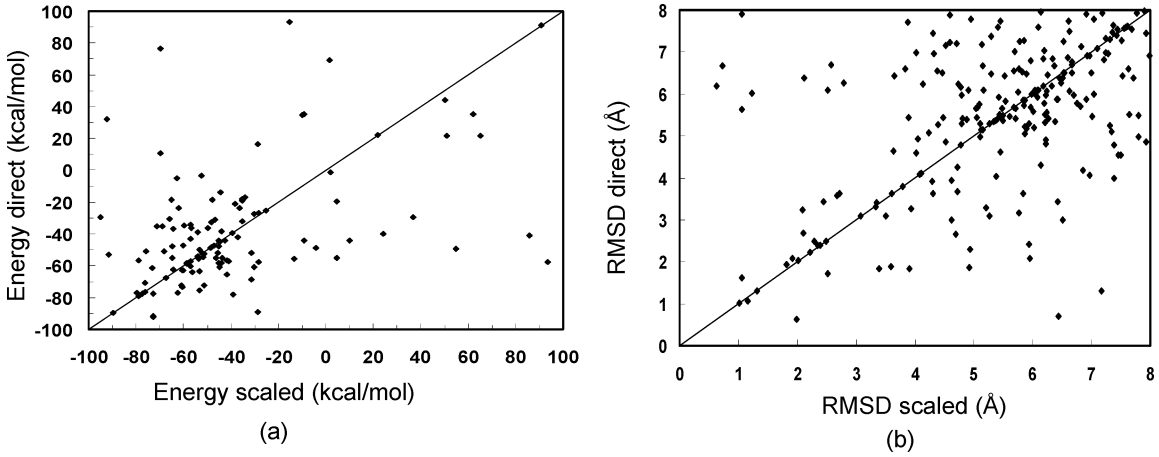

Figure 8. (a) Final energies obtained from direct torsion optimization against the ones from scaled torsion optimization. (b) RMSDs of final structures obtained from direct torsion optimization against the ones from scaled method.

Table 1. Number of Configurations that Reached Global Minima

	scaled torsion minimization	direct torsion minimization	all atom CC minimization
single optimization	69	47	60
reoptimized by all atom CC minimization	219	191	60

structures such as in Figure 7(d) for 1KV2, which showed the greatest advantage among the four examples. The comparison clearly demonstrated that the simple scaling improved the effectiveness of direct torsion optimization particularly for complicated ligand molecules. This trend was also evident in all 35 test cases that we studied here. Overall, the scaled torsion optimization found 34% more structures than the conventional torsion method and 16% more than the all atom CC method within the lowest 90 kcal/mol window. The numbers of structures that reached global optima showed similar behavior as well. In Table 1, we listed the total numbers of final structures that reached global optima for all 35 cases. These structures were chosen based on energies that were within 3 kcal/mol relative to the global optima. Their RMSDs were generally less than 1 Å relative to the global optimal structure. The numbers in the first row were from straightforward optimizations by three methods, respectively. The numbers in the second row were from further optimization by an all atom CC method after torsion optimization. It clearly showed that scaled torsion optimizer was able to recover more global minima structures than direct torsion minimization, particularly when only one level of optimization could be used due to other constraints (e.g. resources, time).

It is also interesting to compare how different the final structures were due to different optimization algorithms. In Figure 8(a), we showed the energy correlation for the lowest 200 kcal/mol window between the direct and scaled methods for complex 1G5S. Although there is a trend of positive correlation between the two methods, the correlation is very weak. This relation is also clear in the RMSD correlation plot of Figure 8(b).

Also, the initial structures that were able to reach the global optimal had very little overlap between all three methods. This behavior is the direct result of the rough energy surface. However, different algorithms have different levels of tolerance for starting structures from which the global optimal can be obtained. This can be inferred from Table 1. Clearly, the combination of the three methods achieved the best energy ensembles. It indicated that none of the optimization methods should be used exclusively. All three methods can be combined to maximize the likelihood of finding the global minimum. Nevertheless, if only one method can be used (e.g. due to the limitation of computing resource), we believe that the scaled torsion optimization is an optimal choice among the three.

IV. Summary

We have introduced a very simple and effective scaling step to improve torsion minimization of ligand molecules inside receptor binding sites. Unlike conventional torsion optimizations that directly use gradients from eq 5 as initial and restarting line search directions in CG, our method takes into account the molecule's 3-dimensional structural properties. This enhancement improved the effectiveness of an existing optimization program. The method can be combined with other functional optimization algorithms such as steepest descent or other versions of CG methods such as TNCG to further improve their performance. We demonstrated that the scaled torsion optimization was able to reach a lower energy ensemble than both direct torsion like all atom CC optimization while still maintaining the computational efficiency of direct torsional optimization. The scaling can also be applied to nongradient based optimization such as dihedral angle MC. It improves the efficiency of the MC algorithm by increasing the acceptance rate of dihedral angle movements.[28] Besides optimization, the principle is applicable to conformational sampling. In our docking software,[28] we found the scaling improved the quality of the conformational distributions.

Although the scaling method generally improves direct torsion optimization, it does not intend to replace existing optimization algorithms. The new method is optimally used in conjunction with other methods to improve the overall results of molecular modeling as we can see from Table 1. In summary, the scaling method is a simple but powerful algorithm that has many applications in molecular modeling.

We specifically emphasize the method for ligand molecules in receptor binding sites because of the roughness of the energy surface in general binding sites. For free small ligand molecules, there is no significant advantage. However, we believe that the scaled method can improve the optimization for large ligand molecules as well as proteins or polymers. It is also useful when simultaneously optimizing protein residues and ligand molecules.

Acknowledgment. This research was funded by the Novartis Research Foundation. We have made use of biochemical algorithm library (BALL) in our implementation.[27] The author especially thanks Dr. Andrew Su for the critical reading of the manuscript.

References

(1) Leach, A. R. *A Survey of Methods for Searching the Conformational Space of Small and Medium-Sized Molecules*; VCH Publishers: New York, 1991.

(2) Blaney, J. M.; Dixon, J. S. *Perspect. Drug Discovery Des.* **1993**, *1*, 301.

(3) Rarey, M.; Kramer, B.; Lengauer, T.; Klebe, G. *J. Mol. Biol.* **1996**, *261*, 470.

(4) Meng, E. C.; Schoichet, B. K.; Kuntz, I. D. *J. Comput. Chem.* **1992**, *13*, 380.

(5) Friesner, R. A.; Banks, J. L.; Murphy, R. B.; Halgren, T. A.; Klicic, J. J.; Mainz, D. T.; Repasky, M. P.; Knoll, E. H.; Shelly, M.; Perry, J.; Shaw, D. E.; Francis, P.; Shenkin, P. S. *J. Med. Chem.* **2004**, *47*, 1739.

(6) Totrov, M.; Abagyan, R. *Proteins: Struct., Funct., Genet., Suppl.* **1997**, *1*, 215.

(7) Jones, G.; Willett, P.; Glen, R. C.; Leach, A. R.; Taylor, R. *J. Mol. Biol.* **1997**, *267*, 727.

(8) Weiner, P. K.; Kollman, P. A. *J. Comput. Chem.* **1981**, *2*, 287.

(9) Brooks, B.; Bruccoleri, R. E.; Olafson, B. D.; States, O. J.; Swiminathan, S.; Karplus, M. *J. Comput. Chem.* **1983**, *4*, 187.

(10) van Gunsteren, W. F.; Berendsen, H. J. C. *Angew. Chem., Int. Ed. Engl.* **1990**, *29*, 992.

(11) Mohamadi, F.; Richards, N. G. J.; Guida, W. C.; Liskamp, R.; Lipton, M.; Caufield, C.; Chang, G.; Hendrickson, T.; Still, W. C. *J. Comput. Chem.* **1990**, *11*, 440.

(12) Xie, D.; Schlick, T. *SIAM J. Optim.* **1999**, 9.

(13) Derreumaux, P.; Zhang, G.; Brooks, B.; Schlick, T. *J. Comput. Chem.* **1994**, *15*, 532.

(14) Phillipss, A. T.; Rosen, J. B.; Walke, V. H. *Dimacs Ser. Discrete Math. Theor. Comput. Sci.* **1995**, *23*, 181.

(15) Fletcher, R.; Reeves, C. M. *Comput. J.* **1964**, *7*, 149.

(16) Nocedal, J.; Wright, S. J. *Numerical Optimization*; Springer: New York, 1999.

(17) Press: W. H.; Teukolsky, S. A.; Vetterling, W. T.; Flannery, B. P. *Numerical Recipes in C++: The art of scientific computing*; Cambridge University Press: 2002.

(18) Polak, E. *Computational Methods in Optimization*; Academic Press: New York, 1971.

(19) Shanno, D. F. *Math. Oper. Res.* **1978**, *3*, 244.

(20) Watowich, S. J.; Meyer, E. S.; Hagstrom, R.; Josephs, R. *J. Comput. Chem.* **1988**, *9*, 650.

(21) Wenzel, W.; Hamacher, K. *Phys. Rev. Lett.* **1999**, 3003.

(22) Merlitz, H.; Wenzel, W. *Chem. Phys. Lett.* **2002**, *362*, 271.

(23) Schlick, T. In *Encyclopedia of Computational Chemistry*; Schleyer, P. v. R., Allinger, N. L., Clark, T., Gasteiger, J., Kollman, P. A., Schaefer III, H. F., Eds.; John Wiley & Sons: 1997.

(24) Jain, A.; Vaidehi, N.; Rodriguez, G. *J. Comput. Phys.* **1993**, *106*, 258.

(25) Vaidehi, N.; Jain, A.; Goddard, W. A. *J. Phys. Chem.* **1996**, *100*, 10508.

(26) Schwieters, C. D.; Clore, M. G. *J. Magn. Reson.* **2001**, *152*, 288.

(27) Kohlbacher, O.; Lenhof, H. P. *Bioinformatics* **2000**, *16*, 815.

(28) Che, J. to be published.

(29) Halgren, T. A. *J. Comput. Chem.* **1996**, *17*, 490.

(30) Halgren, T. A. *J. Comput. Chem.* **1996**, *17*, 520.

(31) Halgren, T. A. *J. Comput. Chem.* **1996**, *17*, 553.

(32) Halgren, T. A. *J. Comput. Chem.* **1996**, *17*, 587.

(33) Halgren, T. A. *J. Comput. Chem.* **1996**, *17*, 616.

(34) Halgren, T. A. *J. Comput. Chem.* **1999**, *20*, 720.

(35) Halgren, T. A. *J. Comput. Chem.* **1999**, *20*, 730.

(36) Cavasotto, C. N.; Abagyan, R. *J. Mol. Biol.* **2004**, *337*, 209.

(37) Dennis, J. E.; Schnabel, R. B. *Numerical Methods for Unconstrained Optimization and Nonlinear Equations*; Prentice Hall: Englewood Cliffs, NJ, 1983.

(38) Katritch, V.; Totrov, M.; Abagyan, R. *J. Comput. Chem.* **2002**, *24*, 254.

CT0499433

JCTC Journal of Chemical Theory and Computation

From Hydrophobic to Hydrophilic Solvation: An Application to Hydration of Benzene

Pim Schravendijk and Nico F. A. van der Vegt*

Max-Planck-Institute for Polymer Research, Ackermannweg 10, D-55128 Mainz, Germany

Received December 23, 2004

Abstract: We report a computer simulation study on the hydration of benzene, which, despite being hydrophobic, is a weak hydrogen bond acceptor. The effect of benzene−water hydrogen bonding on the hydration free energy has been analyzed in terms of solute−solvent energies and entropies. Our calculations show that benzene−water hydrogen bonding restricts the number of arrangements possible for the water molecules resulting in a more unfavorable (negative) solute−solvent entropy change than observed for a 'nonpolar benzene' not capable of accepting water hydrogen bonds. More favorable hydration free energies of aromatic hydrocarbons in comparison with aliphatic hydrocarbons observed experimentally as well as in our calculations must therefore be a result of more favorable solute−solvent interaction energies. This result supports the view that lower aqueous solubilities of nonpolar molecules compared to polar molecules are due to a lack of favorable electrostatic interactions with water molecules. The calculated hydration free energy, enthalpy, entropy, and hydration heat capacity of benzene are in good agreement with experimentally reported values.

1. Introduction

A detailed molecular understanding of hydration of hydrophobic and hydrophilic molecules is of prime importance in physical chemistry and biology. Most studies reported in the literature are devoted to hydrophobic hydration, which is believed to play an important role in protein folding and other self-assembly processes in water.[1−5] Hydrophobic hydration of nonpolar solutes (i.e. aliphatic hydrocarbons), defined as the process of transferring the solute molecule from the gas phase into room-temperature water, is characterized by unfavorable (negative) hydration entropies and favorable, but smaller in magnitude, hydration enthalpies (negative). In room-temperature water, first shell water molecules form a hydrogen bonded cage structure surrounding the nonpolar solute. In a cage structure, the water molecules do not "waste" hydrogen bonds by pointing them at the solute; instead they orient their O−H bonds tangential to the solute surface in order to maximize hydrogen bonding with vicinal water molecules.[5] Historically, Frank and Evans[6] proposed that the large entropy that opposes solute transfer into water arises from the cost of ordering the waters in this way.

The mechanism causing hydrophobicity of aromatic hydrocarbons (i.e. benzene, toluene) has a different nature than that causing the hydrophobicity of aliphatic hydrocarbons. In the case of aromatic hydrocarbons the enthalpic contribution predominates over the entropic contribution to the Gibbs energy of hydration.[7] This results in a negative value of the hydration Gibbs energy of aromatic hydrocarbons, in contrast to the positive values obtained in the case of aliphatic hydrocarbons. In terms of aqueous solubilities, these differences cause the solubility of, e.g., *n*-hexane being almost 20 times lower than the solubility of benzene, although these hydrocarbons have similar molecular weight.[8] Moreover, the heat capacity change upon transfer into aqueous solution (the thermodynamic hallmark that indicates the presence of structured hydration water), normalized to the water accessible surface area, is smaller for the aromatic hydrocarbons than the aliphatic ones.[9,10]

Benzene is a slightly polar molecule due to the nature of its π-electron system that acts as a weak hydrogen bond acceptor.[11−14] It has been argued that higher aqueous

* Corresponding author phone: +49 6131 379 245; fax: +49 6131 379 340; e-mail: vdervegt@mpip-mainz.mpg.de.

10.1021/ct049841c CCC: $30.25
Published on Web 05/17/2005

solubilities of aromatic hydrocarbons are probably due to formation of energetically favorable hydrogen bonds between the aromatic hydrocarbons and water.[7] This explanation is in accord with the results of computer simulation studies using semiempirical force fields that showed that the hydration Gibbs energy of benzene can only be reproduced when adopting a model that includes a permanent charge distribution of benzene, which can be expressed by an electrostatic multipole expansion where the quadrupole moment is the first nonzero term.[15] A consequence of this charge distribution is that the benzene−water potential energy is strongly dependent on the mutual orientation thereby accounting for weak hydrogen bonding interactions. Using available experimental and computer simulation data, Graziano and Lee[16] however argued that the formation of weak O−H$\cdots\pi$ hydrogen bonds between water and benzene is likely to be largely enthalpy−entropy compensating therefore not explaining the higher solubility of aromatic hydrocarbons. Instead they argue that the large van der Waals interaction energy overwhelms the Gibbs energy cost of cavity formation at room temperature in contrast to aliphatic hydrocarbons where the Gibbs energy cost of cavity creation dominates.

In this paper, we report the hydration thermodynamics of benzene obtained by classical molecular dynamics simulations of benzene in simple point charge (SPC) water. To quantify how benzene−water hydrogen bonding changes the hydration thermodynamics, we studied a benzene model that favors formation of weak water−benzene hydrogen bonds ("real benzene") as well as a "van der Waals benzene" model obtained by removing all partial charges of the first model while keeping the exchange repulsion and dispersion interaction terms unaffected. In addition to calculating the Gibbs energy of hydrating the real benzene and van der Waals benzene models, we calculated the enthalpy, entropy, and heat capacity of hydration. To understand the difference in aqueous solubility between the two benzene models better, we also studied contributions to the hydration enthalpy and entropy arising from benzene−water interactions (the solute−solvent interaction energy and solute−solvent entropy) and reorganization of the solvent.

2. Thermodynamics

The solute hydration free energy (the Ben-Naim pseudo-chemical potential[17] $\mu_{ex,S}$) and the corresponding hydration enthalpy ($h_{ex,S}$) and entropy ($s_{ex,S}$) have been theoretically analyzed by Yu and Karplus[18] who showed that

$$\mu_{ex,S} = \Delta u_{SW} - T\Delta s_{SW} \quad (1)$$

$$(h_{ex,S})_P = \Delta u_{SW} + (\Delta h_{WW})_P \quad (2)$$

$$(s_{ex,S})_P = \Delta s_{SW} + (\Delta h_{WW})_P/T \quad (3)$$

In eqs 1−3, Δu_{SW} denotes the energy of solute−water interaction (the solute−solvent energy), Δs_{SW} denotes the entropy change of solute−water interaction (the solute−solvent entropy), and $(\Delta h_{WW})_P$ denotes the (constant pressure) water−water enthalpy change (solvent reorganization enthalpy). The derivation of eqs 1−3 and a discussion of the solute−solvent entropy are presented in more detail in the Appendix. Whereas $\mu_{ex,S}$ is ensemble independent, $h_{ex,S}$ and $s_{ex,S}$ do depend on the insertion condition (constant P,T; constant V,T) with the ensemble dependence occurring in the Δh_{WW} term.[19,20] Here we restrict ourselves to conditions of constant pressure and temperature at which experiments are usually performed and drop the subscript $(\cdots)_P$. In computer simulation studies, $\mu_{ex,S}$ may be obtained by thermodynamic integration (TI), perturbation (TP), or related methods.[20] Since Δu_{SW} is obtained straightforwardly by keeping an average of the solute−water interaction energy at the end-point simulation ($\lambda=1$) in TI/TP, Δs_{SW} follows directly from eq 1. We note that both Δu_{SW} and Δs_{SW} are negative (see the Appendix), while Δh_{WW} is positive. Eqs 1−3 have several important consequences:

(i) The water−water enthalpy change has no impact on $\mu_{ex,S}$. In hydrophobic hydration, Δh_{WW} is usually small (in comparison to solvent reorganization energies in organic solvents) and positive[21] because water hydrates nonpolar solutes without significantly sacrificing hydrogen bonding.

(ii) Cancellation of Δh_{WW} in $\mu_{ex,S}(= h_{ex,S} - Ts_{ex,S})$ does not mean that the extent to which water−water hydrogen bonds are disrupted is irrelevant in understanding $\mu_{ex,S}$ because Δu_{SW} and Δs_{SW} are defined as ensemble averages containing the water−water interaction implicitly.[18] The solute−solvent entropy change ($-T\Delta s_{SW}$) can conceptually be interpreted as the free energy to create a solute cavity that has all solvent molecules properly oriented to accommodate all chemical moieties of the solute,[22] while the solute−solvent energy (Δu_{SW}) may be interpreted as the remaining solute−cavity interaction contribution to $\mu_{ex,S}$. In hydrophobic hydration, first shell water molecules orient to minimize their loss of H-bonds. Any reduction of orientational entropy associated with preferred water orientations (driven by W−W interactions) therefore appears in Δs_{SW}. The cavity formation work ($-T\Delta s_{SW}$) also increases with the excluded volume radius (i.e. loss of translational entropy).

(iii) In hydrophilic hydration, polar solute−solvent interactions (e.g. dipolar interactions, dipole−quadrupole interactions) bias orientations of hydration waters, too. This process may in fact reduce the solute−solvent entropy stronger than the biasing of water orientations close to nonpolar solutes. In that case, lower aqueous solubilities of nonpolar molecules over polar molecules result from a lack of favorable electrostatic interactions with the solvent.

3. Computational Details

Thermodynamic Calculations. Excess chemical potentials were calculated by TI using at least 50 λ-values. At each new λ, the system was first equilibrated for 50 ps after which the free energy derivative was sampled for 500 ps. A soft-core λ scaling was used[23] to avoid singularities of the derivative at the end-points. The excess partial molar enthalpy was calculated using the expression

$$h_{ex,S} = \langle U_{SW} + U_{WW} + PV\rangle_{\text{solution}} - \langle U_{WW} + PV\rangle_{\text{pure}H_2O} \quad (4)$$

where U_{SW} denotes the solute−water interaction energy, U_{WW} denotes the sum of interaction energies of the water

Table 1. Nonbonded Interaction Parameters[a]

atom	$C_{12}(i,i)$ (10^{-6} kJ mol^{-1} nm^{12})	$C_6(i,i)$ (10^{-3} kJ mol^{-1} nm^6)	q_i (e)
	Benzene (GROMOS 43A1)[26]		
C	3.374569	2.340624	−0.10
H	0.015129	0.084640	0.10
	Benzene (GROMOS 53A6)[27]		
C	4.937284	2.340624	−0.14
H	0.015129	0.084640	0.14
	SPC Water[25]		
O	2.634129	2.617346	−0.82
H	0.00	0.00	0.41

[a] Nonbonded interaction function: $V(r_{ij}) = C_{12}(i,j)/r_{ij}^{12} - C_6(i,j)/r_{ij}^6 + q_iq_j/4\pi\epsilon_0[1/r_{ij} + (\epsilon_{RF} - 1)r_{ij}^2/(2\epsilon_{RF} + 1)R_C^3 - 3\epsilon_{RF}/(2\epsilon_{RF} + 1)R_C]$. R_c: long-range cutoff radius. ϵ_{RF}: reaction field relative dielectric permittivity. Combination rules: $C_6(i,j) = C_6(i,i)^{1/2}\, C_6(j,j)^{1/2}$; $C_{12}(i,j) = C_{12}(i,i)^{1/2}C_{12}(j,j)^{1/2}$.

molecules with all other water molecules, and PV denotes a pressure−volume work term. The brackets denote a constant pressure−temperature ensemble average. Two constant pressure−temperature simulations, one of the aqueous solution (1 solute, N solvent molecules) and one of the neat solvent (N solvent molecules), are performed, and the average potential energies are subtracted (the $P\Delta V$ term is usually small). Because both terms on the right-hand side of eq 4 are of $O(N)$ whereas $h_{ex,S}$ is of $O(1)$, the statistical accuracy obtained in MD runs of several hundreds of picoseconds is usually poor. We produced long (90 ns) trajectories to sample the two averages in eq 4 resulting in statistical inaccuracies of $h_{ex,S}$ smaller than 0.3 kJ/mol. Excess partial molar entropies were obtained from the calculated excess chemical potential and enthalpy using $Ts_{ex,S} = h_{ex,S} - \mu_{ex,S}$. Solute−solvent entropies were obtained from the calculated excess chemical potential and solute−solvent energy using $T\Delta s_{SW} = \Delta u_{SW} - \mu_{ex,S}$ (eq 1). The solute−solvent energy was obtained from the simulations by taking the average benzene−water interaction energy. Heat capacities of hydration were calculated from the temperature dependence of $h_{ex,S}$ using the finite difference expression

$$c_{P,ex,S}(T) = \frac{h_{ex,S}(T + \Delta T) - h_{ex,S}(T - \Delta T)}{2\Delta T} \qquad (5)$$

A temperature difference $\Delta T = 20$ K was chosen in our simulations. The excess partial molar enthalpies $h_{ex,S}(T + \Delta T)$ and $h_{ex,S}(T - \Delta T)$ were calculated using eq 4 based on 90 ns trajectories. The statistical inaccuracy of $c_{P,ex,S}$ is determined by that of $h_{ex,S}$ and amounts to 15−20 J mol^{-1} K^{-1}.

Simulation Details. All simulations were performed using the Gromacs 3.2.1 simulation package[23,24] and were based on an equilibrated cubic, periodic simulation box containing 1500 water molecules and 1 benzene molecule. The simple point charge (SPC) model of water was used.[25] Benzene was modeled using the GROMOS 43A1 force field parameters.[26] For reasons of comparison, we used the recent GROMOS 53A6 parameters as well.[27] The nonbonded force field parameters are summarized in Table 1. For the bonded parameters, which are identical in the 43A1 and 53A6 GROMOS force fields, we refer to refs 26 and 27. Intramolecular Lennard-Jones and electrostatic interactions were accounted for between atom pairs separated by more than 3 bonds. The simulation temperature was kept constant at 302 K by weakly coupling to a temperature bath with a relaxation time of 0.1 ps.[28] The pressure was maintained at 1 atm by also applying the weak coupling algorithm with a relaxation time of 0.5 ps and an isothermal compressibility of 45.75×10^{-5} (kJ mol^{-1} nm^{-3})$^{-1}$. The equilibrated box length was 3.592 nm. For nonbonded interactions, a twin-range method with cutoff radii of 0.8 and 1.4 nm was used. Outside the longer cutoff radius a reaction field correction was applied with a relative dielectric permittivity of 54.0. The integration time step was 2 fs, and the pairlist for pairs within the inner cutoff and the energies and forces for pairs between the inner and outer cutoff radii were updated every 10 fs. All bond lengths were kept constant using the SHAKE algorithm[29] using a relative geometrical tolerance of 10^{-4}.

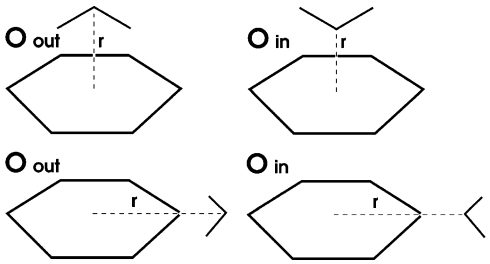

Figure 1. Relative orientations used for calculating the water−benzene interaction. The distance r is defined between the water oxygen and the ring center of mass. In orientation O_{out}, the water dipole moment is pointing toward the solute, in orientation O_{in} the water dipole moment is oriented outward.

Benzene−Water Interaction. The benzene−water interaction potential is strongly orientation dependent. Based on the relative orientations shown in Figure 1, we calculated the interaction energy between a benzene−water (SPC) pair as a function of the distance r defined in Figure 1 (using the GROMOS 43A1 parameters in Table 1). Figure 2 shows the corresponding potential energy curves (denoted "real O in" and "real O out"), which also includes the interactions obtained when not accounting for the electrostatic part of the interaction (denoted "van der Waals O in & O out"). The interaction energies for a water molecule oriented perpendicular to the aromatic plane (Figure 2a) are in good agreement with the energies reported by Linse,[30,31,12] which are based on ab initio quantum chemical calculations using a Hartree−Fock self-consistent-field approximation combined with a second-order perturbation procedure to account for the dispersion energy. The dashed line in Figure 2a ("real O out"; benzene−water hydrogen bonding) shows a minimum at approximately 3.0 Å with a corresponding energy between 13 and 14 kJ/mol. In the ab initio study,[30,31,12] the minimum is found at the same distance with an energy of 12−13 kJ/mol. The configuration with the oxygen pointing inward (dotted curve in Figure 2a) is repulsive and is also in good agreement with the corresponding ab initio benzene−water interaction reported in ref 12. For conformations where the water is aligned in the benzene plane (Figure 2b), the agreement between our data and those from the work of

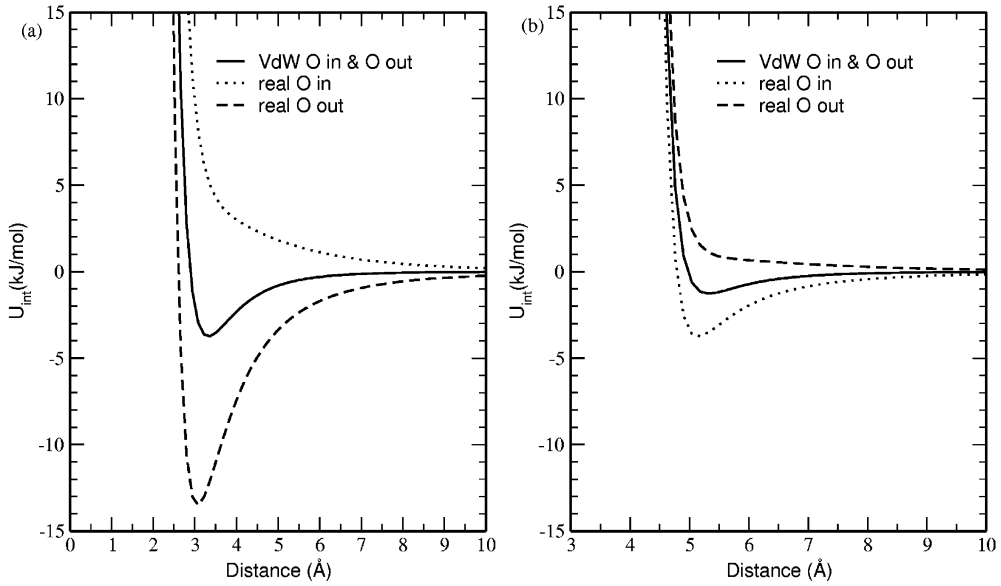

Figure 2. Potential energy curve for SPC water−benzene interaction. (a) The water molecule is located above the benzene plane. (b) The water molecule is located in the plane of the benzene ring (see Figure 1). Solid line, van der Waals benzene (the quadrupole−dipole interaction is omitted); dashed line, water having its dipole pointing inward; and dotted line, water having its dipole pointing outward (see Figure 1).

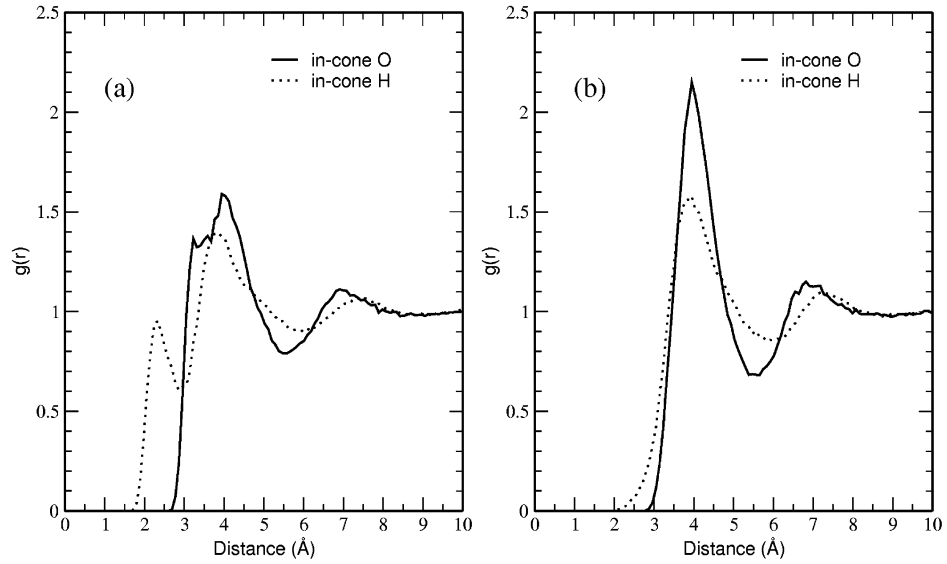

Figure 3. In-cone benzene−water radial distribution functions. Solid line, benzene center-of-mass-to-water oxygen RDF and dashed line, benzene center-of-mass-to-water hydrogen RDF. (a) Real benzene. (b) van der Waals benzene.

Linse et al. is less satisfactory. In the ab initio study, the energy minimum for the oxygen-inward conformation is found around 4.5 Å with a corresponding energy of 7−8 kJ/mol, while with the GROMOS 43A1 force field this minimum is located at 5.2 Å with a corresponding energy of 3.6 kJ/mol. For the configuration with the oxygen pointing outward, the ab initio data show a slightly stronger repulsion than our data.

4. Results and Discussion

4.1. Hydration Structure. Radial Distribution Functions. Due to the anisotropic benzene−water interaction potential, the benzene hydration structure should preferably be characterized by distinguishing water molecules inside the volume above the benzene plane from water molecules located elsewhere. We adopted the approach of Linse et al.[31] to subdivide the space around the benzene. Water molecules inside the conical volumes above and below the benzene plane and remaining water molecules were considered separately. The cones make a 45° angle with the benzene symmetry axis. Water molecules located inside the conical volumes are hydrogen bonded to benzene more likely than molecules located outside. Figure 3 shows the incone water−benzene center of mass radial distribution function (RDF) for real benzene (Figure 3a), modeled with the GROMOS 43a1 parameters, and the van der Waals benzene model (Figure 3b). For the case of the real benzene, the first peak of the hydrogen at 2.25 Å clearly indicates that water donates hydrogen bonds to benzene. The peak area up to 3 Å corresponds to 1.0 benzene−water hydrogen bonds. The

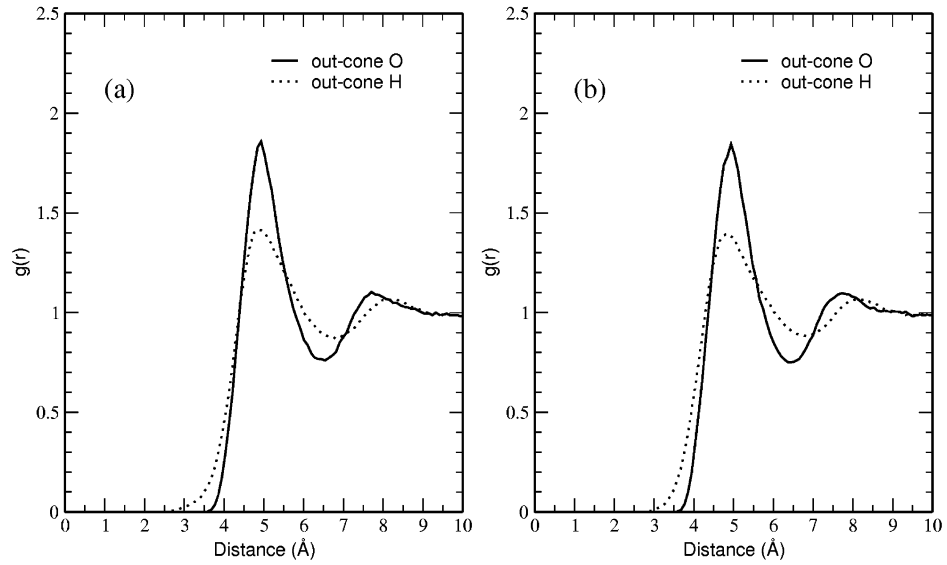

Figure 4. Out-of-cone benzene−water radial distribution functions. Solid line, benzene center-of-mass-to-water oxygen RDF and dashed line, benzene center-of-mass-to-water hydrogen RDF. (a) Real benzene. (b) van der Waals benzene.

larger oxygen peak is split in two parts. The first maximum occurs at 3.25 Å and corresponds to the water molecule donating a hydrogen bond to benzene (i.e. the distance between the first maximum of the hydrogen RDF and that of the oxygen RDF is exactly a OH bond length). The second oxygen peak at 4 Å corresponds to water not directly hydrogen bonded to benzene. The incone RDFs for the van der Waals benzene (Figure 3b) are typical of hydrophobic hydration. The peaks are narrower and the maxima are higher compared to the real benzene system, indicating significantly more structured hydration water. Moreover, the first maximum for the oxygen and hydrogen RDFs is located at the same distance, which suggests that water orients one of its OH bonds parallel to the surface of the nonpolar solute. The first peak of the hydrogen RDF has a broad shoulder extending to larger distances, which arises from the second OH bond that orients toward the bulk where it donates a hydrogen bond to water molecules in the second solvation shell. The latter becomes apparent from the second maximum of the oxygen RDF being located closer to the solute than the second maximum of the hydrogen RDF. The out-of-cone RDFs for real benzene and van der Waals benzene are shown in Figure 4 (parts a and b, respectively). For both systems the observed structure is typical of hydrophobic hydration with no significant differences between the realistic and van der Waals benzene models.

Orientational Distributions. The probability density of orientation of the water OH bonds with respect to the vector connecting the benzene center of mass and the water oxygen is shown in Figure 5. The data apply to water molecules in the first shell (r<6 Å), which on average contains 26.5 molecules. No distinction is made here between water molecules located inside or outside the conical volumes. The distribution $P'(\theta)$ obtained just from the statistical sampling of the angles was rescaled according to $P(\theta) = P'(\theta)/\sin\theta$, accounting for the volume elements associated with the angle θ. For the GROMOS 43A1 van der Waals model, we observe a higher occurrence of OH orientation at both 0° (radially outward) and 110−120°. Postma et al.[32] made similar

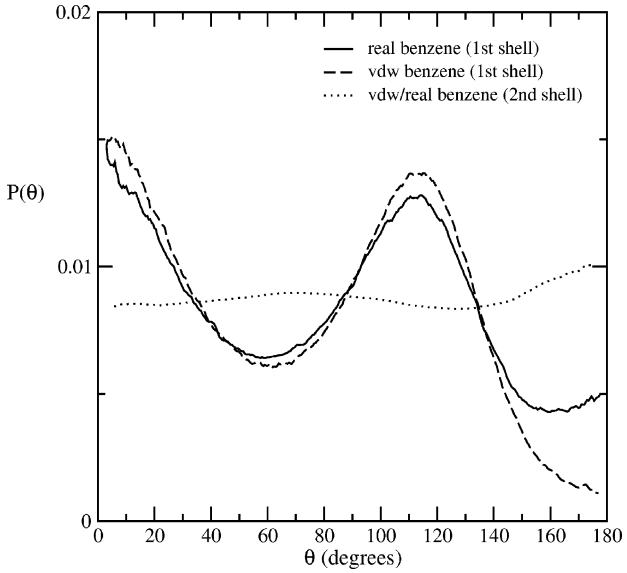

Figure 5. Probability density of orientation of the OH direction with respect to the vector connecting the benzene center of mass and water oxygen (normalization: $\int P(\theta)\sin\theta d\theta = 1$). Data apply to molecules in the first shell (r<6 Å) or second shell (6<r<9 Å). Solid line, real benzene (first shell); dashed line, van der Waals benzene (first shell); and dotted line, benzene (second shell).

observations in a study of the hydration of spherical cavities with a thermal radius of 3 Å (the orientationally averaged cavity radius of van der Waals benzene equals ∼3.5 Å). They showed that water molecules may have one OH-bond directed toward the bulk, whereas the other OH bond is directed parallel to the cavity surface, but may also have both of their OH-bonds parallel to the cavity surface. The water orientational distribution corresponding to real benzene shows somewhat weaker maxima at 0° and 110° and has an additional weak maximum at 180° (OH radially inward), which arises from benzene−water hydrogen bonding. The orientational distribution of second shell hydration waters (dotted line in Figure 5) neither reveals strong preferential

Table 2. Hydration Thermodynamics of Benzene and "van der Waals Benzene"[a]

T (K)	$\mu_{ex,S}$ (kJ/mol)	$h_{ex,S}$ (kJ/mol)	$s_{ex,S}$ (J/mol/K)	$c_{p,ex,S}$ (J/mol/K)
		Experimental[b]		
278		−35.7	−108.4	318.8
298	−3.6	−29.6	−87.2	291.6
323		−22.6	−64.6	268.1
		43A1 Benzene		
282		−32.7		
302	−4.8	−29.3	−82.2	277.5
322		−21.6		
		53A6 Benzene		
282		−34.5		
302	−6.7	−31.1	−81.8	217.5
322		−25.8		
		43A1 Benzene, van der Waals Only		
282		−29.7		
302	1.0	−24.8	−86.5	327.5
322		−16.6		

[a] The excess chemical potentials ($\mu_{ex,S}$) were computed by thermodynamic integration, and the excess partial molar enthalpies ($h_{ex,S}$) were computed using eq 4 in which total potential energies of the solution (water + benzene) and solvent (water) MD simulations were averaged over 90 ns time periods. The excess partial molar entropies ($s_{ex,S}$) were obtained from $Ts_{ex,S} = h_{ex,S} - \mu_{ex,S}$. Heat capacity changes ($c_{p,ex,S}$) were calculated by finite difference (eq 5). [b] Experimental values were from ref 7.

OH directions nor does it show differences for the real and van der Waals solutes.

4.2. Hydration Thermodynamics. In Table 2 all thermodynamic hydration quantities are summarized. For real benzene, the calculations were performed using the 43A1[26] and 53A6[27] GROMOS parameters (see Table 1). The thermodynamic quantities for van der Waals benzene were obtained from simulations using 12−6 Lennard-Jones parameters from the 43A1 force field. The best agreement with the experimental data is found for the 43A1 GROMOS parameter set and will be discussed here. Not only the benzene excess chemical potential agrees satisfactorily with the experimentally reported value but also the excess partial molar enthalpy and entropy are closely reproduced. Especially the latter quantities provide a good test of the quality of a particular force field. Although the excess chemical potential can be predicted correctly, it may happen for the wrong reason because errors in the energy may cancel out against errors in the entropy. The isobaric heat capacity of benzene hydration is predicted most accurately as well with the GROMOS 43A1 force field. The hydration thermodynamics of the van der Waals benzene model differs from the real model and is typical of hydrophobic hydration: the excess chemical potential is positive and also the isobaric heat capacity of hydration is significantly more positive than for real benzene. The excess partial molar entropies of van der Waals and real benzene do not significantly differ. The excess partial molar enthalpy of real (43A1) benzene is however −4.5 kJ/mol more favorable compared to that of van der Waals benzene, hence the larger negative excess chemical potential of real benzene is mainly enthalpic. This enthalpy difference compares with a value of −5.4 kJ/mol predicted by Makhatadze and Privalov[7] based on combining experimental data for benzene and aliphatic hydrocarbons, the latter corrected for the benzene accessible surface area. Based on a similar calculation, Makhatadze and Privalov predict a change of the excess chemical potential and excess partial molar entropy of −13.4 kJ/mol and +26.8 J/mol/K, respectively, which our calculations do not reproduce.

Table 3. Solute−Solvent Energy Change (Δu_{SW}), Solute−Solvent Entropy Change ($T\Delta s_{SW}$), and Solvent Reorganization Energies (Δh_{WW}) for Hydrating Real Benzene and van der Waals Benzene

T (K)	Δu_{SW} (kJ/mol)	$T\Delta s_{SW}$ (kJ/mol)	Δh_{WW} (kJ/mol)
	43A1 Benzene		
282	−61.2		28.5
302	−59.4	−54.6	30.1
322	−57.5		35.9
	43A1 Benzene, van der Waals Only		
282	−47.1		17.4
302	−45.6	−46.6	20.8
322	−43.9		27.3

Solute−Solvent Contributions. The solute−solvent energies, Δu_{SW}, solute−solvent entropies, $T\Delta s_{SW}$, and water reorganization enthalpies, Δh_{WW}, are shown in Table 3 for the 43A1 real benzene and the 43A1 van der Waals benzene models. The benzene−water energy is −13.8 kJ/mol more favorable than the van der Waals benzene−water energy (T = 302 K). Because benzene on average accepts one hydrogen bond from water and the benzene−water hydrogen bond energy equals approximately 13 kJ/mol (Figure 2a), this result is expected.

The enthalpy change of water reorganization was calculated based on eq 4, which can also be written as

$$h_{ex,S} = \langle U_{SW}\rangle_{\text{solution}} + [\langle U_{WW} + PV\rangle_{\text{solution}} - \langle U_{WW} + PV\rangle_{\text{pure}H_2O}] = \Delta u_{SW} + \Delta h_{WW} \quad (6)$$

The water reorganization enthalpies (Δh_{WW}) are large and positive contributing significantly to the excess partial molar enthalpies. For dissolving a solute in its own pure liquid at constant P and T, the solvent reorganization enthalpy equals the average potential energy of the liquid.[33] Transferring for example a SPC water molecule from the saturated vapor phase into the liquid SPC water phase involves a solvent reorganization enthalpy of 41.5 kJ/mol at 298 K. For benzene (43A1 model) in its own liquid this enthalpy is 33.2 kJ/mol. If one compares these numbers to the reorganization enthalpies in Table 3 it shows that, in particular for van der Waals benzene, the water reorganization enthalpy is small. For the real benzene model, Δh_{WW} is larger because benzene−water hydrogen bonding happens at the expense of water−water hydrogen bonding.

The temperature dependencies of Δu_{SW} and Δh_{WW} are interesting because they provide further clues on the different heat capacity changes of real and van der Waals benzene (Table 2). In the 40 K temperature interval, Δu_{SW} increases with 3.7 and 3.2 kJ/mol for real and van der Waals benzene,

respectively. For the real benzene model we found that this energy change was almost exclusively due to a reduction of the benzene−water van der Waals energy with increasing temperature. The benzene−water electrostatic interactions changed only little (+0.7 kJ/mol) in this temperature interval. Interestingly, in the same temperature interval, Δh_{WW} increases with 7.4 kJ/mol (real benzene) and 9.9 kJ/mol (van der Waals benzene). Based on these energy changes it can be concluded that the larger positive heat capacity change of hydrating van der Waals benzene is entirely due to an increase of the water−water enthalpy, which occurs upon "melting" the cagelike water structure surrounding the nonpolar solute. We note that under conditions of constant pressure, theoretical work[19] and experimental data[34] have suggested that the mechanism of enthalpy absorption may indeed be localized in the solute hydration shell (whereas under conditions of constant volume, the excess partial molar energy contains a nonlocal, bulk response contribution).[19]

It is interesting to address in some detail the question to what extent reorganization of the solvent occurring in response to introducing solute−solvent electrostatic interactions is enthalpy−entropy compensating in the free energy. Because the solute molecule considered here is rigid all the entropy change of this process is due to the rearrangement of solvent molecules. Thus, as originally proposed by Lee,[35] the total entropy change can be considered as the solvent reorganization entropy. We will refer to this quantity as Δs^{reo} (= $s_{ex,S}$(real) − $s_{ex,S}$(vanderWaals)). The corresponding solvent reorganization enthalpy we refer to as Δh^{reo}(= Δh_{WW}(real) − Δh_{WW}(vanderWaals)). The free energy change of introducing solute−solvent electrostatic interactions contains the free energy of solvent reorganization ($\Delta h^{reo} - T\Delta s^{reo}$) in addition to the change of solute−solvent interaction energy. In case perfect enthalpy−entropy compensation occurs ($T\Delta s^{reo} = \Delta h^{reo}$), the free energy change of introducing the electrostatic interactions will only be determined by the change of the solute−solvent interaction energy. The solute−solvent energy change (Table 3) amounts to $-59.4 + 45.6 = -13.8$ kJ mol^{-1}. The free energy change (43A1 benzene, Table 2) is however smaller and amounts to $-4.8 - 1.0 = -5.8$ kJ mol^{-1} indicating that solvent reorganization contributes unfavorably to the free energy change. From Table 2 we see that introducing benzene−water electrostatic interactions causes an entropy change $T\Delta s^{reo} = 1.3$ kJ mol^{-1} (302 K). The reorganization enthalpy (Table 3) is significantly larger and amounts to $\Delta h^{reo} = 9.3$ kJ mol^{-1}. Solvent reorganization thus causes an (small) increase of the entropy, which is however overcompensated by a much larger unfavorable increase of the solvent reorganization enthalpy. In this view, the presence of weak solute−solvent hydrogen bonds forces the solvent to assume strained, less stable, conformations relative to the pure solvent leading to a free energy change smaller than the energy gained by solute−solvent hydrogen bonding.

Although we may just have reached a satisfactory conclusion, the microscopic significance of the reorganization entropy remains problematic. An alternative way exists to arrive the same conclusion based on a discussion of the solute−solvent entropy and the solute−solvent energy whose microscopic significance is discussed in the Appendix. We start out by noting that a zero change of the solute−solvent entropy is the condition for perfect enthalpy−entropy compensation of the solvent reorganization process discussed above (i.e. $\Delta h^{reo} - T\Delta s^{reo} = T(\Delta s_{SW}$(real) − Δs_{SW}(vander-Waals)). In the Appendix we show[37]

$$T\Delta s_{SW} = k_B T \ln P_{ins} - [(\langle\psi^2\rangle - \langle\psi\rangle^2)\beta/2 + \cdots]_a \qquad (7)$$

The solute−solvent entropy is determined by (1) the probability (P_{ins}) that in a system of only solvent molecules a cavity is found where the solute−solvent interaction energy (ψ) is attractive and (2) the fluctuations of the solute−solvent energy in configurations of the solute−solvent system where $\psi < 0$. The second contribution reflects the fact that fluctuations in positions and orientations of solvent molecules vicinal to the solute are biased by attractive solute−solvent interactions resulting in a reduction of configuration space and thus a reduction of the entropy. The process of introducing the electrostatic interactions leads to favorable change of Δu_{SW} of −13.8 kJ mol^{-1} while causing a compensating unfavorable change of $T\Delta s_{SW}$ of $-54.6 + 46.6 = -8.0$ kJ mol^{-1} (see Table 3). We note that this observed change of $T\Delta s_{SW}$ results from changes in the second term on the right-hand side of eq 7, not from changes in the first term: calculations of $(\langle\psi^2\rangle - \langle\psi\rangle^2)_a\beta/2$, using the 90 ns trajectories of hydrated real benzene and van der Waals benzene, resulted in 12.8 (±0.2) kJ mol^{-1} for real benzene and 3.9 (±0.2) kJ mol^{-1} for van der Waals benzene, thus contributing −8.9 kJ mol^{-1} to the change of $T\Delta s_{SW}$. Benzene−water hydrogen bonding thus introduces a stronger bias on the orientations sampled by hydration waters than the bias introduced in hydrating nonpolar van der Waals benzene. The formation of weak benzene−water hydrogen bonds, which energetically favors the hydration of real benzene, happens in competition with solvent−solvent interactions that favor water−water hydrogen bonding. In creating these energetically favorable benzene−water hydrogen bonds, the solvent is forced to sacrifice some of its own hydrogen bonds. The corresponding water configurations will have a potential energy significantly larger than configurations representative of pure water and configurations compatible with hydrating van der Waals benzene (i.e. the solvent reorganization enthalpy is positive). Clearly, due to its attempt to maintain hydrogen bonds, pure water will with lower probability sample configurations representative for the hydration structure of real benzene than for van der Waals benzene. The probability $\exp[\Delta s_{SW}/k_B]$ to successfully insert real benzene in pure water configurations with an appropriately formed cavity (that satisfies benzene−water hydrogen bonding) will therefore be lower than the probability to successfully insert van der Waals benzene. We thus see that the reduction of the solute−solvent entropy arising by introducing electrostatic benzene−water interactions originates from less stable configurations that water has to adopt in order to donate hydrogen bonds to benzene. This automatically implies that the solvent reorganization process is noncompensating and the solvent reorganization enthalpy is positive.

We conclude by noting that moderately polar, real benzene dissolves better than van der Waals benzene due to energetically favorable electrostatic interactions with the solvent. Although here we have only shown that the hydration entropies of van der Waals and realistic benzene do not significantly differ, we more generally believe that lower aqueous solubilities of nonpolar compared to polar molecules are not due to the entropy differences but due to the lack of favorable electrostatic interactions with the solvent. This view, advocated earlier by Gallicchio et al.,[33] is supported by the Monte Carlo simulations of Stone et al.[36] based on which the authors conclude that poor aqueous solubilities correlate with poor solute−solvent interaction.

5. Conclusions

In this study we have used MD simulations to make a detailed comparison of the hydration structure and thermodynamics of a realistic benzene model capable of forming weak hydrogen bonds with water and a nonrealistic (van der Waals) benzene model incapable of accepting H-bonds. Calculations were performed using an all-atom benzene model taken from the GROMOS force field and the SPC water model. The benzene excess chemical potential and excess partial molar enthalpy and entropy as well as the hydration heat capacity change were calculated and showed good overall agreement with the corresponding experimental values. Our calculations indicate that a favorable hydration free energy of benzene compared to "van der Waals benzene" is due to favorable electrostatic (H-bonding) interactions with the solvent. The solvation entropies of the realistic and van der Waals benzene models were found to be not significantly different. The hydration heat capacity change of the van der Waals model was found larger than that of the realistic model, which could be assigned to a larger enthalpy absorbed by the hydration water of the van der Waals model. Although changes of water−water interactions greatly affect the hydration enthalpy, entropy, and heat capacity, they have no impact on the benzene solubilily due to exact enthalpy−entropy compensation of the solvent reorganization enthalpy. Therefore, we also studied the solute−solvent energy and solute−solvent entropy, which are the pertinent quantities determining the chemical potential of the solute. The solute−solvent entropy of the van der Waals benzene model is larger (more favorable) than that of the realistic benzene model. This result indicates that restrictions in water orientations due to benzene−water hydrogen bonding are larger than restrictions in water orientations close to the van der Waals (hydrophobic) benzene. The low solubility of the nonpolar van der Waals benzene relative to real benzene therefore cannot be explained in terms of the entropy change but is due to lack of favorable electrostatic interactions with the solvent water molecules.

Acknowledgment. The authors thank Luigi Delle Site, Berk Hess, Kurt Kremer, and Christine Peter for useful discussions and comments regarding the manuscript.

Appendix: The Solute−Solvent Entropy

The solute−solvent terms in eq 1 have been analyzed by Sanchez et al.[37] whose treatment we briefly summarize below. The reader is referred to ref 37 for the derivation of eq 12, which we do not repeat here. The solute (S) excess chemical potential ($\mu_{ex,S}$) can be defined using Widom's potential distribution theorem[38]

$$\mu_{ex,S} = -\beta^{-1}\ln\langle e^{-\beta\psi}\rangle_0 = \beta^{-1}\ln\langle e^{\beta\psi}\rangle \quad (8)$$

In eq 8, ψ denotes the interaction energy of the solute molecule with the other (solvent) molecules, $\beta = (k_BT)^{-1}$ with k_B the Boltzmann constant, and the angular brackets denote a constant volume−temperature ensemble average. The subscript zero indicates that the average is taken under the condition that the other molecules in the system do not sense the presence of the "test molecule". The average without subscript indicates a normal ensemble average where the solute molecule interacts and influences the other system molecules. The excess chemical potential of molecules S (eq 8) is defined relative to an ideal gas with a number density of molecules S equal to the number density of the solution. Eq 8 can be decomposed in an energetic and entropic contribution

$$\mu_{ex,S} = \beta^{-1}\ln\langle e^{\beta\psi}\rangle = \langle\psi\rangle + \beta^{-1}\ln\langle e^{\beta(\psi-\langle\psi\rangle)}\rangle \equiv \Delta u_{SW} - T\Delta s_{SW} \quad (9)$$

In eq 9, $\Delta u_{SW} = \langle\psi\rangle$ and $\Delta s_{SW} = -k_B\ln\langle e^{\beta(\psi-\langle\psi\rangle)}\rangle$. Using the inequality $\langle e^{\beta\psi}\rangle \geq e^{\beta\langle\psi\rangle}$ one sees that Δs_{SW} is always negative or zero, and thus $-T\Delta s_{SW}$ adds positively to $\mu_{ex,S}$. For molecules with attractive interactions Δu_{SW} is always negative. Negative values of $\mu_{ex,S}$ therefore always result from favorable solute−solvent interactions $\Delta u_{SW} < 0$ overriding the solute−solvent entropy. We note that $-T\Delta s_{SW}$ may be interpreted as the work of creating a cavity that has the solvent molecules in the appropriate positions and orientations to accommodate all chemical moieties of the solute; Δu_{SW} is the interaction energy of the solute with the properly formed cavity. The quantity $\exp[\Delta s_{SW}/k_B]$ is the probability to observe the above cavity in configurations of the pure solvent.

The (constant pressure) excess partial molar enthalpy $(h_{ex,S})_P$ contains, in addition to the solute−solvent energy Δu_{SW}, a contribution arising from changes of solvent−solvent interactions. This contribution is different depending on whether the pressure or volume is kept fixed.[19,20] At constant pressure, the solvent−solvent energy (enthalpy) change is denoted $(\Delta h_{WW})_P = (\Delta u_{WW})_P + p\Delta v \approx (\Delta u_{WW})_P$. This energy change is localized in the solute hydration shell unlike in the constant volume case where it includes a nonlocal bulk response contribution.[19,20] Below we will drop the subscript $(\cdots)_P$. One should keep in mind that in this paper excess partial molar enthalpies and entropies are evaluated at constant pressure. Assuming the energies Δu_{SW} and Δh_{WW} are additive yields

$$h_{ex,S} = \Delta u_{SW} + \Delta h_{WW} \quad (10)$$

Because the excess chemical potential is defined as $\mu_{ex,S} = h_{ex,S} - Ts_{ex,S}$, the excess partial molar entropy is given by

$$s_{ex,S} = \Delta s_{SW} + \Delta h_{WW}/T \quad (11)$$

Hence, $h_{ex,S}$ and $Ts_{ex,S}$ contain a contribution (Δh_{WW}) which never impacts $\mu_{ex,S}$ (exact energy-entropy compensation). Although the definitions of Δu_{SW} and Δs_{SW} (eq 9) take slightly different forms in the constant $P-T$ and constant $V-T$ ensembles their values are ensemble-independent.

From eq 9 it can be seen that energy fluctuations $\psi - \langle\psi\rangle > 0$ contribute most significantly to the solute−solvent entropy. To better understand the physics inherent in Δs_{SW} it is useful to think of it as having two contributions of which both are negative. First, Δs_{SW} has a cavity contribution that arises from repulsive solute−solvent interaction energies ($\psi > 0$) with corresponding solvent configurations that violate the excluded volume constraint imposed by the solute. This contribution reflects the tendency of the solvent to close the solute cavity (or "squeeze-out" the solute). The second contribution arises from fluctuations of the interaction energy in configurations where the interaction is attractive ($\psi \leq 0$). Sanchez et al.[37] derived

$$\Delta s_{SW}/k_B = \ln P_{ins} - \ln\langle e^{\beta(\psi-\langle\psi\rangle)}\rangle_a - \ln P_a$$
$$= \ln P_{ins} - [(\langle\psi^2\rangle - \langle\psi\rangle^2)\beta^2/2 + \cdots]_a - \ln P_a \quad (12)$$

where the subscript 'a' indicates that the average is taken under the condition that the solute−solvent interaction energy is attractive ($\psi < 0$). The quantity P_{ins} is the probability that a randomly inserted solute molecule into a system of only solvent molecules will experience an attractive or zero interaction ($\psi \leq 0$). P_a is the probability that the solute molecule in the fluid will have an attractive energy. Because P_a will be very close to unity the $\ln P_a$ term can be ignored. The second term on the right-hand side of eq 12 will always be zero in case ψ is independent of the positions and orientations sampled by solvent molecules vicinal to the solute. In a mean field approximation, where fluctuations in the energy are ignored, this term would actually be set to zero and $\Delta s_{SW}(= k_B \ln P_{ins})$ would then be determined by the cavity contribution only. Thus, in a mean field approximation, one would only account for excluded volume effects and the corresponding loss of solvent translational entropy. In eq 12, the fluctuation term $(\langle\psi^2\rangle - \langle\psi\rangle^2)\beta^2/2$ expresses the fact that the available configuration space is biased by attractive interactions (i.e. solute−solvent attractive interactions bias positions and orientations of the vicinal solvent molecules). The corresponding loss of configuration space causes a loss of entropy.

References

(1) Murphy, K. P.; Privalov, P. L.; Gill, S. J. *Science* **1990**, *247*, 559.

(2) Hummer, G.; Garde, S.; García, A. E.; Paulaitis, M. E.; Pratt, L. R. *J. Phys. Chem. B* **1998**, *102*, 10469.

(3) Dill, K. A. *Biochemistry* **1990**, *29*, 7133.

(4) Hummer, G.; Garde, S.; García, A. E.; Paulaitis, M. E. *Proc. Natl. Acad. Sci. U.S.A.* **1998**, *95*, 1552.

(5) Southall, N. T.; Dill, K. A.; Haymet, A. D. J. *J. Phys. Chem. B* **2002**, *106*, 521.

(6) Frank, H. S.; Evans, M. E. *J. Chem. Phys.* **1945**, *13*, 507.

(7) Makhatadze, G. I.; Privalov, P. L. *Biophys. Chem.* **1994**, *50*, 285.

(8) McAuliffe, C. *J. Phys. Chem.* **1966**, *70*, 1267.

(9) Makhatadze, G. I.; Privalov, P. L. *J. Solution Chem.* **1989**, *18*, 1267.

(10) Makhatadze, G. I.; Privalov, P. L. *J. Mol. Biol.* **1990**, *213*, 375.

(11) Levitt, M.; Perutz, M. F. *J. Mol. Biol.* **1988**, *201*, 751.

(12) Linse, P. *J. Am. Chem. Soc.* **1990**, *112*, 1744.

(13) Atwood, J. L.; Hamada, F.; Robinson, K. D.; Orr, G. W.; Vincent, R. L. *Nature* **1991**, *349*, 683.

(14) Suzuki, S.; Green, P. G.; Bumgarner, R. E.; Dasgupta, S.; Goddard, W. A., III; Blake, G. A. *Science* **1992**, *257*, 942.

(15) Jorgenson, W. L.; Severance, D. L. *J. Am. Chem. Soc.* **1990**, *112*, 4768.

(16) Graziano, G.; Lee, B. *J. Phys. Chem. B* **2001**, *105*, 10367.

(17) Ben-Naim, A.; Marcus, Y. *J. Chem. Phys.* **1984**, *81*, 2016.

(18) Yu, H.-A.; Karplus, M. *J. Chem. Phys.* **1988**, *89*, 2366.

(19) Matubayasi, N.; Reed, L. H.; Levy, R. M. *J. Phys. Chem.* **1994**, *98*, 10640.

(20) Levy, R. M.; Gallicchio, E. *Annu. Rev. Phys. Chem.* **1998**, *49*, 531.

(21) Lee, B. *Biopolymers* **1985**, *24*, 813.

(22) Brooks, C. L., III; Karplus M.; Pettitt, B. M. In *Advances in Chemical Physics*; Prigogine, I., Rice S. A., Eds.; 1988; Vol. 71.

(23) Lindahl, E.; Hess, B.; van der Spoel, D. *J. Mol. Model.* **2001**, *7*, 306.

(24) Berendsen, H. J. C.; van der Spoel, D.; van Drunen, R. *Comput. Phys. Commun.* **1995**, *91*, 43.

(25) Berendsen, H. J. C.; Postma, J. P. M.; van Gunsteren, W. F.; Hermans, J. in *Intermolecular Forces*; Pullman, B., Ed.; Reidel: Dordrecht, 1981; pp 331−342.

(26) van Gunsteren, W. F.; Billeter, S. R., Eising, A. A.; Hünenberger, P. H.; Krüger, P.; Mark, A. E.; Scott, W. R. P.; Tironi, I. G. *Biomolecular Simulation: The GROMOS96 Manual and User Guide*; vdf Hochschulverslag: ETH Zürich, Switzerland, 1996.

(27) Oostenbrink, C.; Villa, A.; Mark, A. E.; Van Gunsteren, W. F. *J. Comput. Chem.* **2004**, *25*, 1656.

(28) Berendsen, H. J. C.; Postma, J. P. M.; van Gunsteren, W. F.; DiNola, A.; Haak, J. R. *J. Chem. Phys.* **1984**, *81*, 3684.

(29) Ryckaert, J.-P.; Ciccotti, G.; Berendsen, H. J. C. *J. Comput. Phys.* **1977**, *23*, 327.

(30) Karlström, G.; Linse, P.; Wallqvist, A.; Jönsson, B. *J. Am. Chem. Soc.* **1983**, *105*, 3777.

(31) Linse, P.; Karlström, G.; Jönsson, B. *J. Am. Chem. Soc.* **1984**, *106*, 4096.

(32) Postma, J. P. M.; Berendsen, H. C.; Haak, J. R. *Faraday Symp. Chem. Soc.* **1982**, *17*, 55.

(33) Gallicchio, E.; Kubo, M. M.; Levy, R. M. *J. Phys. Chem. B* **2000**, *104*, 6271.

(34) Gill, S. J.; Dec, S. F.; Olofsson, G.; Wadsö, I. *J. Phys. Chem.* **1985**, *89*, 3758.

(35) Lee B. *Biophys. Chem*. **1994**, 51, 271.

(36) Stone, M. T.; In ‘t Veld, P. J.; Lu, Y.; Sanchez, I. C. *Mol. Phys*. **2002**, *100*, 2773.

(37) Sanchez, I. C.; Truskett, T. M.; In ‘t Veld, P. J. *J. Phys. Chem. B* **1999**, *103*, 5106.

(38) Widom, B. *J. Chem. Phys*. **1963**, *39*, 2808.

CT049841C

JCTC Journal of Chemical Theory and Computation

Modeling Nitrogen Adsorption in Spherical Pores of Siliceous Materials by Density Functional Theory

E. A. Ustinov,[§] D. D. Do,*[,†] and M. Jaroniec[‡]

Department of Chemical Engineering, University of Queensland, St. Lucia, Queensland 4072, Australia, and Department of Chemistry, Kent State University, Kent, Ohio 44242

Received November 2, 2004

Abstract: Adsorption of nitrogen in spherical pores of FDU-1 silica at 77 K is considered by means of a nonlocal density functional theory (NLDFT) accounting for a disordered structure of pore walls. Pore size distribution analysis of various FDU-1 samples subject to different temperatures of calcination revealed three distinct groups of pores. The principal group of pores is identified as ordered spherical mesopores connected with each other by smaller interconnecting pores and irregular micropores present in the mesopore walls. To account for the entrances (connecting pores) into spherical mesopores, a concept of solid mass distribution with respect to the apparent density was introduced. It is shown that the introduction of the aforementioned distribution was sufficient to quantitatively describe experimental adsorption isotherms over the entire range of relative pressures spanning six decades.

1. Introduction

Over the past decades we have witnessed a markedly increasing interest in the analysis of adsorption phenomena in mesoporous materials. This was stimulated by discovery of highly ordered mesoporous materials such as MCM-41, SBA-15, SBA-16, and FDU-1 having cylindrical or spherical pores of controlled size. Adsorption isotherms for such adsorbents give scientists an opportunity to verify the capability of different theories to describe the hysteresis phenomena and properly characterize porous structure of solid materials. Analysis of adsorption in cylindrical pores is considered by means of continuum and molecular approaches. Examples of the former approaches are the Barret, Joyner, and Halenda (BJH) method,[1] the modified BJH method of Kruk, Jaroniec, and Sayari (KJS),[2] and the Broekhoff and de Boer (BdB) theory[3,4] and its many modified versions (modifications accounting for the solid−fluid potential dependence on the pore size,[5−7] dependence of the surface tension on the meniscus curvature,[8−12] and surface roughness[13]). Among molecular approaches applied for the analysis of adsorption in cylindrical pores the most frequently used are the nonlocal density functional theory (NLDFT)[14−22] and Monte Carlo technique.[17,23−25] The comparison of results obtained with the original BdB theory and the NLDFT[26] showed that they are close to each other for pores having a diameter greater than 7 nm. In general, the molecular approaches adequately represent features of adsorption in mesopores; however, some unresolved problems still remain. For example, the diameter of cylindrical pore determined with NLDFT is less than that determined with the X-ray diffraction technique (XRD) about 0.3−0.7 nm.[26] The lower closure point of the hysteresis is underestimated by the NLDFT (compared to 0.4 for nitrogen at 77 K and 0.34 for argon at 87.3 K[27] observed experimentally). The critical hysteresis diameter determined with the NLDFT for nitrogen adsorption at 77 K is 2 nm[15] (compared to 4 nm observed experimentally[28−30]). This difference is explained by the density fluctuations leading to nucleation via formation of bumps and bridges if the potential barrier is less than

* Corresponding author e-mail: duongd@cheque.uq.edu.au.
† University of Queensland.
‡ Kent State University.
§ On leave from Saint Petersburg State Technological Institute (Technical University), 26 Moskovsky Prospect, St. Petersburg 198013, Russia.

10.1021/ct049903z CCC: $30.25
Published on Web 05/04/2005

approximately 20 kT.[21,23,24,31] Another reason for an experimentally observed higher value of the critical hysteresis pore diameter could be energetic heterogeneity[32] or intrinsic pore size distribution.[33] Another unresolved issue is that which branch of the isotherm is equilibrium. According to the classical scenario of adsorption in cylindrical pores capillary evaporation occurs at equilibrium via receding menisci from the open ends of the pore, while the capillary condensation pressure corresponds to the limiting case of mechanical stability of metastable segment of adsorption branch of the isotherm (vaporlike spinodal point).[34] Nevertheless, some experimental investigations do not seem to support this scenario,[2,30,35−37] but instead they suggested that the adsorption branch of the isotherm corresponds to the true equilibrium. Our NLDFT analysis of condensation pressure for nitrogen and argon adsorption in MCM-41 samples in comparison with the XRD data also shows that the experimental condensation pressure−diameter dependence can be quantitatively matched only by the theoretical dependence obtained for the equilibrium transition pressure.[38]

Theoretical investigation of adsorption in spherical pores is very scarce in the literature. A comprehensive NLDFT analysis of nitrogen and argon adsorption in spherical pores of different siliceous adsorbents was recently presented by Ravikovitch et al.[21,39] The present paper is devoted to further development and refinement of the NLDFT method of analysis of adsorption isotherms in spherical pores. Our aim is to quantitatively describe nitrogen adsorption isotherms at 77 K in spherical pores of FDU-1 materials[40] over the entire range of relative pressures. We analyze a number of samples obtained at different temperatures of calcinations and derive their pore size distribution (PSD) functions. We proceed from the assumption that the average density of the solid constituting the pore wall is less than that for the reference nonporous silica due to the fraction of the surface of spherical pores is taken up by channels connecting spherical pores with each other. This average density is shown to be determined by the PSD analysis of the samples, which disclose important additional information on the pore structure of adsorbents.

2. Model

2.1. Nonlocal Density Functional Theory in the Case of Disordered Solids. In the present paper we use the Tarazona's smoothed density approximation[41,42] in our NLDFT formulation. The density distribution of a fluid confined in an open pore (grand canonical ensemble) corresponds to the minimum of the following grand thermodynamic potential

$$\Omega = \int \rho(\mathbf{r})[f(\mathbf{r}) - \mu]d\mathbf{r} \tag{1}$$

Here ρ is the local density in the pore; f is the molecular Helmholtz free energy; and μ is the chemical potential. The molecular Helmholtz free energy can be represented as a sum of four terms, representing the ideal, excess, attractive, and external part of the Helmholtz free energy, respectively

$$f(\mathbf{r}) = k_B T[\ln(\Lambda^3 \rho(\mathbf{r})) - 1] + f_{ex}[\bar{\rho}(\mathbf{r})] + u^{int}(\mathbf{r}) + u^{ext}(\mathbf{r}) \tag{2}$$

where Λ is the thermal de Broglie wavelength and k_B is the Boltzmann's constant. The excess Helmholtz free energy, $f_{ex}(\bar{\rho})$, accounts for the repulsive part of the interaction potential and is defined in the form of the Carnahan−Starling (CS) equation[43] derived for the equivalent hard sphere fluid:

$$f_{ex}(\bar{\rho}) = k_B T \frac{4\bar{\eta} - 3\bar{\eta}^2}{(1-\bar{\eta})^2},\ \bar{\eta} = \frac{\pi}{6} d_{HS}{}^3 \bar{\rho} \tag{3}$$

Here d_{HS} is the equivalent hard sphere diameter, and the smoothed density $\bar{\rho}$ is given by

$$\bar{\rho}(\mathbf{r}) = \int \rho(\mathbf{r}')\omega(|\mathbf{r} - \mathbf{r}'|;\bar{\rho}(\mathbf{r}))d\mathbf{r}' \tag{4}$$

The function $\omega(|\mathbf{r} - \mathbf{r}'|;\bar{\rho}(\mathbf{r}))$ in the integrand of the above equation is approximated by the following polynomial[42]

$$\bar{\rho}(\mathbf{r}) = \bar{\rho}_0(\mathbf{r}) + \bar{\rho}_1(\mathbf{r})\bar{\rho}(\mathbf{r}) + \bar{\rho}_2(\mathbf{r})(\bar{\rho}(\mathbf{r}))^2 \tag{5}$$

where

$$\bar{\rho}_i(\mathbf{r}) = \int \rho(\mathbf{r}')\omega_i(|\mathbf{r} - \mathbf{r}'|)d\mathbf{r}',\ i = 0,1,2 \tag{6}$$

The weight functions $\omega_0(r)$, $\omega_1(r)$, and $\omega_2(r)$ are defined as functions of the distance r in the region $0 < r < 2\ \sigma_{ff}$.[42] It is relevant to point here that the excess Helmholtz free energy may be interpreted as a function of the smoothed void volume $\bar{v} = 1 - \bar{\eta}$. The decrease of the void volume leads to the increase of repulsive forces. In the limiting case of zero value of the void volume there is no space to insert an additional molecule, which means infinite repulsive forces. This limiting case corresponds to the maximum possible value of the fluid density $\rho_m = 6/(\pi d_{HS}{}^3)$. The concept of the void volume is from a mathematical viewpoint exactly an equivalent way of the definition of the excess Helmholtz free energy of a homogeneous or inhomogeneous fluid far away from solid walls confining the fluid. However, the advantage of such a representation is that it accounts for the decrease in the void volume (that is the volume fraction available to fluid molecules) due to the increase in the fluid density as well as due to the presence of the solid wall. In this case repulsive forces acting between the wall and fluid molecules are also accounted for. The replacement of the density by the void volume allows us to consider the combined solid−fluid system from the same viewpoint as that developed for the inhomogeneous fluid. Such a consideration is justified for the case of amorphous solids because those could be treated as 'frozen' liquids and be a part of the system. This concept has been successfully applied to analysis of nitrogen and argon adsorption on nonporous silica[44] and in cylindrical pores of MCM-41 samples.[45,46] Below we briefly reproduce some basic points of this approach. Thus, in terms of void volume the excess Helmholtz free energy may be rewritten as follows:

$$f_{ex}(\bar{\rho}) = k_B T \frac{1 + 2\bar{v} - 3\bar{v}^2}{\bar{v}^2},\ \bar{v} = 1 - \bar{\rho}/\rho_m \tag{7}$$

In the above equation $\bar{v}$ is the smoothed void volume, which can be determined from the distribution of local void volume $v(\mathbf{r}) = 1 - \rho/\rho_m$ using the following equivalent form

of eqs 5 and 6

$$\bar{v}(\mathbf{r}) = \bar{v}_0(\mathbf{r}) + \rho_m \bar{v}_1(\mathbf{r})[1 - \bar{v}(\mathbf{r})] + \rho_m{}^2 \bar{v}_2(\mathbf{r})[1 - \bar{v}(\mathbf{r})]^2 \quad (8)$$

where

$$\bar{v}_i(\mathbf{r}) = \int v(\mathbf{r}')\omega_i(|\mathbf{r} - \mathbf{r}'|)d\mathbf{r}',\ i = 0,1,2 \quad (9)$$

The integration in the RHS of eq 9 has taken over the region of two fluid collision diameters. If the distance from the center of a given molecule to the pore wall surface is less than two collision diameters, the integral has taken over the space outside of the solid volume. It means that the local void volume inside the solid is zero, i.e., no one fluid molecule could reside inside the solid constituted the pore wall. Strictly speaking, such an assumption is not completely correct, as some molecules could penetrate to the solid and localize between solid atoms. Nevertheless, in the case of amorphous solids this assumption is more plausible compared to the formal application of the CS equation coupled with the Tarazona's prescription (5) and (6) to the solid−fluid interface. Indeed, in the latter case the local density of the fluid inside the solid is zero, which in accordance with eqs 3−6 is formally equivalent to the misleading statement that the void volume reaches maximum in the solid. In reality the replacement of the fluid molecules by the solid atoms never leads to the increase in the void volume (available to fluid molecules) up to its maximum value.

Contribution of the attractive potential to the Helmholtz free energy is usually modeled using the mean field approximation as follows:

$$u^{int}(\mathbf{r}) = \frac{1}{2}\int \rho(\mathbf{r}')\phi_{ff}(|\mathbf{r} - \mathbf{r}'|)d\mathbf{r}' \quad (10)$$

The pairwise potential ϕ_{ff} of two molecules is defined by the Weeks−Chandler−Andersen (WCA) scheme:[47]

$$\phi_{ff}(r) = \begin{bmatrix} -\epsilon_{ff} & r < r_m \\ 4\epsilon_{ff}[(\sigma_{ff}/r)^{12} - (\sigma_{ff}/r)^6] & r_m < r < r_c \\ 0 & r > r_c \end{bmatrix} \quad (11)$$

Here r and r_c are the distance between the molecules and the cutoff distance, respectively; ϵ_{ff} is the potential well depth; σ_{ff} is the collision diameter; $r_m = 2^{1/6}\,\sigma_{ff}$ is the distance at which the potential is minimum.

In the case of crystalline solids the external potential u^{ext} could be determined by integration of the 12-6 Lennard−Jones pairwise solid−fluid potential over the solid volume or surface, which for a flat interface results in the 9-3 or 10-4 potential, respectively. The resulting potential exerted by the solid has a form of the potential well, having minimum at a distance of about one solid−fluid collision diameter from the surface. The locus of the potential minimum is a two-dimensional plane parallel to the solid surface. Consequently, adsorption occurs as a sequential molecular layering, which is often reflected in highly undulated predicted adsorption isotherms, especially at low temperatures. In the case of disordered materials such as silica the centers of the outermost solid atoms are not located on a 2D surface. Therefore one could expect that the solid−fluid potential minimum is not as sharp as that observed with a crystalline surface but rather significantly dispersed. It is this dispersed minimum that prevents 2D condensation of the adsorbed fluid. There are approaches dealing with binary systems (so-called quenched−annealed (QA) systems), one part of which is a fluid (annealed) allowed to equilibrate, and the other one is the solid (quenched or frozen liquid).[48,49] Physical quantities of such systems are defined as double ensemble averages. The QA theory is quite involved. Therefore we apply an approach, which is simple in its description, but elegant enough to account for the dispersed minimum, and most importantly it is able to quantitatively describe nitrogen adsorption on amorphous surface of siliceous adsorbents.

Since repulsive forces arising between solid atoms and fluid molecules are already accounted for in the excess Helmholtz free energy using the concept of void volume, the only attractive term for the solid−fluid interaction is needed to be added. This could be done in a similar way used for the fluid−fluid interaction via the WCA perturbation scheme. For the system amorphous solid−fluid the WCA equation can be rewritten as follows

$$\phi_{sf}^{(j)}(r) = \begin{bmatrix} -\epsilon_{sf}^{(j)} & r < r_m^{(s)} \\ 4\epsilon_{sf}^{(j)}[(\sigma_{sf}/r)^{12} - (\sigma_{sf}/r)^6] & r_m^{(s)} < r < r_c^{(s)} \\ 0 & r > r_c^{(s)} \end{bmatrix} \quad (12)$$

where ϵ_{ff}, σ_{ff}, and $r_c^{(s)}$ are the solid−fluid potential well depth, the solid−fluid collision diameter, and the cutoff distance for the solid−fluid interaction, respectively. The superscript j at the pairwise potential and the potential well depth is 1 or 2 and is introduced to account for the distinction between atoms inside the solid ($j = 1$) and those on the solid surface ($j = 2$). It is important because in the general case the difference between the two can be very significant due to the surface functional groups such as silanols on the silica surface. Thus, the resulting external potential may be expressed as follows

$$u^{ext}(\mathbf{r}) = \int_V \rho_V^{(s)}\,\phi_{sf}^{(1)}(|\mathbf{r} - \mathbf{r}'|)d\mathbf{r}' + \int_S \rho_S^{(s)}\,\phi_{sf}^{(2)}(|\mathbf{r} - \mathbf{r}'|)d\mathbf{r}' \quad (13)$$

where $\rho_V^{(s)}$ and $\rho_S^{(s)}$ are the solid and surface density, respectively. The corresponding integrals are taken over the solid volume and surface.

2.1.1. Henry Law Limit. There could be a question as to whether the method of application of NLDFT to amorphous solids leads to the Henry law at low densities. At the limiting case of zero loading the fluid−fluid interaction potential vanishes. In this case the minimization of the grand thermodynamic potential leads to the following equation

$$k_B T \ln[\Lambda^3 \rho(\mathbf{r})] + f_{ex}[\bar{v}(\mathbf{r})] + u^{ext}(\mathbf{r}) = \mu \quad (14)$$

At negligibly small bulk pressure p and, as a consequence, the adsorbed fluid density and the smoothed void volume are a function of only the distance from the surface, and the chemical potential is proportional to $k_B T \ln p$. It means that

Table 1. Molecular Parameters for the System N_2 − Silica at 77 K

fluid − fluid			solid − fluid			
σ_{ff} (nm)	ϵ_{ff}/k_B (K)	d_{HS} (nm)	σ_{sf} (nm)	$\rho_V^{(s)}\,\epsilon_{sf}^{(1)}/k_B$ (K nm^{-3})	$\rho_S^{(s)}\,\epsilon_{sf}^{(2)}/k_B$ (K nm^{-2})	$r_c^{(s)}/\sigma_{sf}$
0.3575	94.45	0.3575	0.2988	6406	640.1	4.4

the fluid density is proportional to the bulk pressure at a specified point of space near the surface:

$$\rho(\mathbf{r}) = \frac{p}{k_B T} \exp\left[-\frac{f_{ex}[\bar{v}(\mathbf{r})] + u^{ext}(\mathbf{r})}{k_B T}\right] \qquad (15)$$

The proportionality between the density and the pressure results in linear dependence of the amount adsorbed on the bulk pressure, i.e., the adsorption isotherm reduces to the Henry law at a sufficiently low-pressure region, which confirms the correctness of the method under consideration. Our observation is that the Henry law region in the case of amorphous solids corresponds to much lower pressures compared to that for the conventional NLDFT. Some additional features of the adsorption isotherm on a nonporous amorphous solid under the monolayer coverage will be discussed in the next subsection.

It should be noted that the proposed approach is an extension of the conventional NLDFT to a binary system of fluid−amorphous solid, rather than its alternative. The reason this method as applied to amorphous solids works much better than the formal application of NLDFT to crystalline surfaces (it is shown below) is apparently associated with a smoother repulsive term of the solid−fluid potential due to random dispersion of solid atoms relative to the surface, which prevents artificial layering of the adsorbed fluid. Viewing fluid−fluid and fluid−solid interactions from the same standpoint seems to be justified in the case of amorphous solids despite some simplifications such as the neglect of the nonzero transition zone at the surface, thermodynamic inertness of the solid (the excess free energy of solid atoms in the vicinity of the surface is assumed to not be affected by the fluid molecules), and impermeability of the solid to fluid molecules. A more rigorous approach requires further investigations.

2.2. Adsorption on Nonporous Reference Material. The fluid−fluid molecular parameters are determined from the bulk properties (the saturation pressure and the liquid density at the saturation pressure) and surface tension. These parameters were taken from the paper of Neimark et al.[50] The solid−fluid parameters were determined by the least squares procedure from the nitrogen adsorption isotherm on nonporous silica LiChrospher Si-1000 at 77 K.[51] All molecular parameters are listed in Table 1.

Nitrogen adsorption isotherm on nonporous silica is presented in Figure 1 in logarithmic and linear scales. The solid line is plotted with the described above method of application of NLDFT to disordered solids using the parameters listed in Table 1. As one can see from the figure, the experimental isotherm is excellently fitted by the theoretical curve over the entire relative pressure range by six decades, which confirms the adequacy of the NLDFT approach. For comparison the dashed line in the figure shows the result of conventional NLDFT application, in which the solid is not a part of the binary solid−fluid system and is considered solely as a source of the external 10-4 LJ potential. The dashed line is calculated for the solid−fluid parameters presented in refs 18, 20, and 50. The Henry law region corresponding to our approach is not seen in Figure 1, but it exists in the lower pressure range. Interestingly, according to experimental data and the developed version of NLDFT there is a broad region between the Henry law and the monolayer coverage where the amount adsorbed increases gradually with pressure. This indirectly points to the energetic heterogeneity of silica surface, which formally could be described in the framework of the Langmuir model of adsorption on isolated sites distributed over their energy. It means that the proposed algorithm of NLDFT application to the amorphous surface implicitly accounts for its energetic heterogeneity at the microscopic level (as opposed to the patchwise model having macroscopic origin) caused by random spatial distribution of solid atoms in the vicinity of the surface.

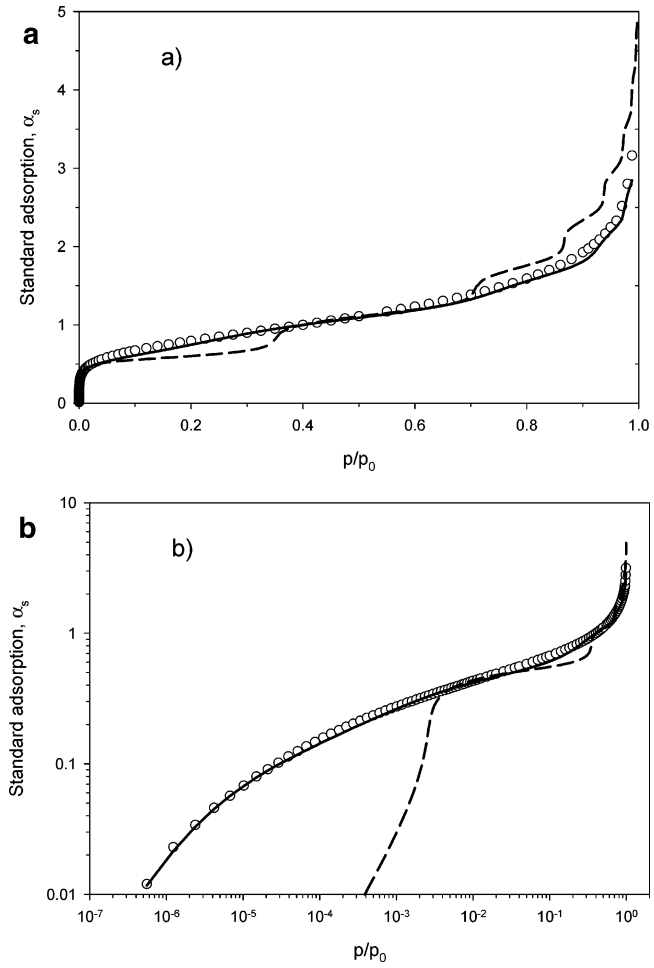

Figure 1. Nitrogen standard reduced adsorption isotherm on silica LiChrospher Si-1000 at 77.3 K in linear scale (a) and logarithmic scale (b). (Circles) experimental data,[51] (solid line) the developed version of NLDFT for amorphous surface, and (dashed line) conventional NLDFT with molecular parameters listed in Table 1.

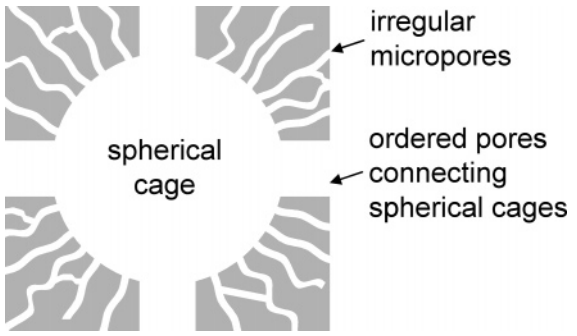

Figure 2. Illustration of a spherical cage with neighboring connecting pores and irregular micropores. Spherical cages together with connecting pores form a three-dimensional system of ordered mesopores, which in the case of FDU-1 has *Fm*3*m* symmetry.

2.3. Application of the NLDFT to Spherical Pores. In the present paper we considered a spherically symmetrical density distribution inside a spherical pore. This is a quite strong assumption since each spherical mesopore of FDU-1 silica has 12 windows connecting this pore with the neighboring pores. The two-dimensional diagram of a spherical pore with connecting channels as well as micropores is shown in Figure 2. The rigorous way is to solve the 3D task; however, this task is highly time-consuming, so the 1D spherically symmetrical model seems to be a reasonable simplification. In this 1D representation, the spherical pore is modeled as one without any connecting pores, and therefore the average density of solid atoms of this model pore would be less than the solid skeleton density of a real pore. We shall denote hereafter this average density as the apparent density. Since we do not exactly know the shape and volume of the connecting pores it makes sense to consider the average pore wall density as an adjustable parameter. The spherical pore volume was divided into the set of concentric spheres having radii incremented by 1/30 fluid−fluid collision diameter. For each pair of spherical surfaces the Tarazona's weight function and the WCA attractive potential were determined. Minimization of the functional (1) results in the set of equations relative to the set of local densities defined at the spherical surfaces at a given chemical potential. This set of equations is solved by a standard iteration procedure producing a density profile corresponding to the thermodynamic equilibrium. Having determined the density profile, one can easily calculate the apparent density at a given bulk phase pressure. In doing so, we determined a set of local isotherms for a set of pore size ranging from 0.72 to 21 nm at a specified apparent density of the pore wall. Note that the capillary rise that we refer to is the equilibrium transition pressure, rather than the vaporlike spinodal pressure. Besides we generated 60 sets of local isotherms, each of which corresponds to a specified pore wall density in the region from 0.88 to 2.2 g/cm^3.

We applied the NLDFT extended to amorphous solids to the adsorption branch of isotherms assuming that like in the case of cylindrical pores the adsorption branch for spherical pores is close to the true equilibrium.[36−38] Besides the pore size distribution the distribution function of mass of adsorbent with respect to the average pore wall density (MDF) was introduced in the following form

$$\xi(\rho_V^{(s)}) = \frac{d(m/m_0)}{d\rho_V^{(s)}} \tag{16}$$

where m/m_0 is the fraction of mass of adsorbent having apparent density of the pore wall less than $\rho_V^{(s)}$ and m_0 is the total mass of the sample. Note that the function ξ is normalized. For the sake of simplicity we assume that $\rho_S^{(s)}/\rho_V^{(s)}$ is constant. With the above definition the amount adsorbed can be expressed as follows:

$$a(p/p_0) = \int\int f(D)\xi(\rho_V^{(s)})\rho^a(p/p_0,D,\rho_V^{(s)})d(\rho_V^{(s)})d\log D \tag{17}$$

Here ρ^a is the density of adsorbed fluid at a relative pressure p/p_0 in the pore having diameter D and average pore wall density $\rho_V^{(s)}$; $f(D)$ is the pore size distribution function, that is

$$f(D) = \frac{dV}{d\log D} \tag{18}$$

The PSD and MDF were determined using the Tikhonov regularization method.[52,53] Details of application of the regularization method can be found elsewhere.[54,55]

3. Results

In the present paper we analyze nitrogen adsorption isotherms for a series of ordered mesoporous silica samples, FDU-1, having a cagelike structure.[40] Adsorption branches of isotherms for five samples calcined at different temperatures are presented in Figure 3. Pore size distribution functions determined for these isotherms are shown in Figure 4 in logarithmic and linear scales. It is seen from the figure that there are three distinct peaks in the PSDs. The first one in the region of equivalent spherical pore diameters from 0.8 to approximately 1.3 nm is associated with micropores in the pore walls. The second peak in the pore size region from 1.3 to 3 nm may be attributed to connecting pores between neighboring larger spherical pores, which are represented by the third peak in the PSD. The increase of the temperature of calcination leads to a decrease in the pore volume of all groups of pores as well as their sizes due to the shrinkage of the silica framework. In the case of micropores their average size does not change much because calcination may cause elimination of fine micropores[56] and/or substantial reduction of their size, making them inaccessible for adsorbate molecules.

Figure 5 shows the distribution of mass of the adsorbent with respect to the average pore wall density. The mass distribution functions (MDF) can be interpreted by considering the hypothetical case of ordered adsorbent having spherical pores of equal size connected with each other by channels whose surfaces are treated as hard walls (i.e., adsorption does not occur). With this hypothetical case, its MDF is a Dirac delta function at a density of the solid, and this density is less than the density of nonporous silica (2.2 g/cm^3). This is because the pore wall of the spherical pores is not continuum due to hollows, occupied by the connecting channels. Since the model considers the pore surface as a

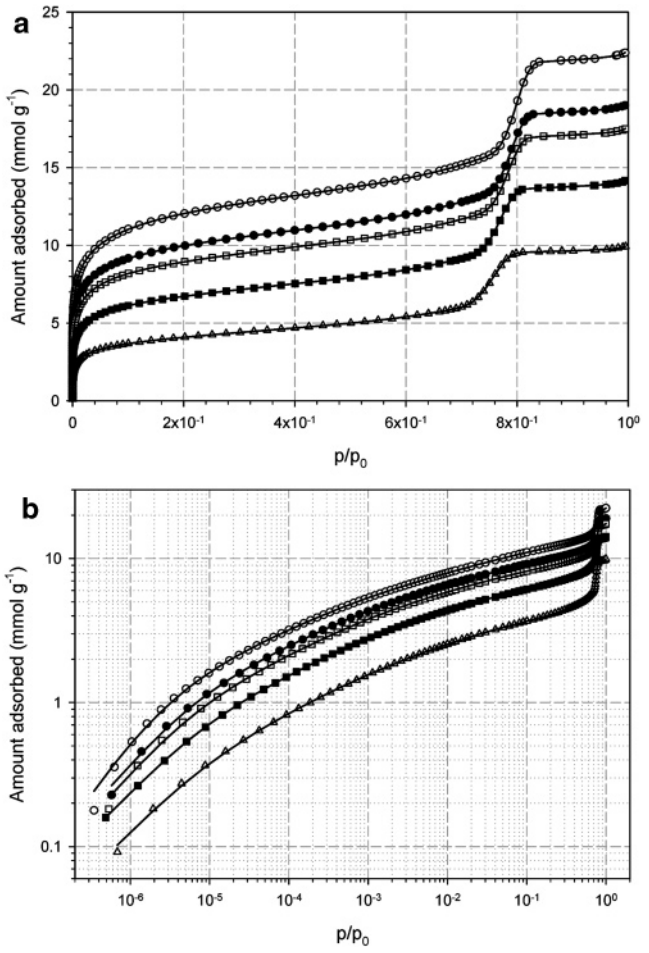

Figure 3. Nitrogen adsorption isotherm for FDU-1 samples at 77 K at linear scale (a) and in logarithmic scale (b). Temperature of calcinations (K): ○ − 813, ● − 973, □ − 1073, ■ − 1173, △ − 1273. Solid lines are correlated by the NLDFT version for amorphous solids.

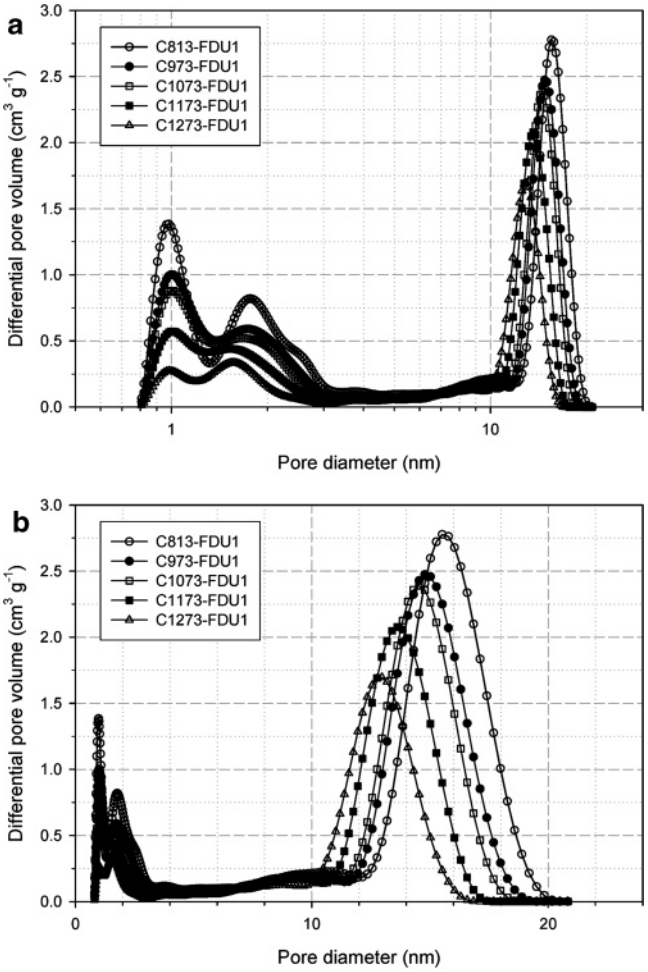

Figure 4. Pore size distributions for FDU-1 samples calcined at different temperature in logarithmic (a) and linear (b) scale obtained with the developed NLDFT version for amorphous solids. Three peaks from left to right correspond to micropores in pore walls, connecting pores, and spherical mesopores, respectively.

contiguous spherical wall, the apparent density of the solid constituting the wall must be decreased. Now let the connecting channels be adsorbing pores. In this case we have to account for two kinds of pores (main spherical mesopores and connecting pores) having a different size and, most importantly, a different apparent density of the pore walls. The latter is due to the different geometry of those pores and numbers of windows. It leads us to the conclusion that the MDF should consist of at least two peaks. This is exactly what we observe on the MDF in Figure 5. However, any further geometrical considerations should be done with reservations for the following reasons. First, the model is one-dimensional, while the pore has a number of hollows, which destroys the spherical symmetry. Second, little is known about the geometry of connecting pores, though we model them as spherical pores (as well as micropores) the same way as we do for the main pores. Third, the PSD function and MDF are uncorrelated, which is generally not correct. Any attempts to correlate these are bound to great complication, due to the ill-posed nature of the task under consideration. It is interesting to note that the MDF is nearly the same for all samples despite the significant decrease in the pore volume with the temperature of calcination. It could be explained by a proportional shrinkage of solid and pore volume, which keeps unchanged the relation between pore size and windows for each group of pores. There is some uncertainty about which peak corresponds to larger spherical pores and that to connecting pores, but it is likely that the average pore wall density for the main spherical pores is about 0.75 $\rho_{V0}^{(s)}$, i.e., 1.65 g/cm^3 since the right peak is larger compared to the left one, which is in agreement with the PSD functions.

All characteristics of the porous structure of analyzed samples are summarized in Table 2.

The subscripts 'me', 'con', and 'mi' denote (spherical) mesopores, connecting pores, and micropores, respectively. Corresponding volumes were determined by integration of the PSD function in the regions of size 10−21, 1.3−3, and 0.8−1.3 nm, respectively. The pore diameters were determined using the maximum of the corresponding peak. The surface area is determined only for the main spherical pores, S_{me}, as the physical shape of micropores and connecting pores is not known exactly. Besides, we also determined the external surface S_{ex}, whose contribution to the amount adsorbed was accounted for by using the *t*-curve for nitrogen

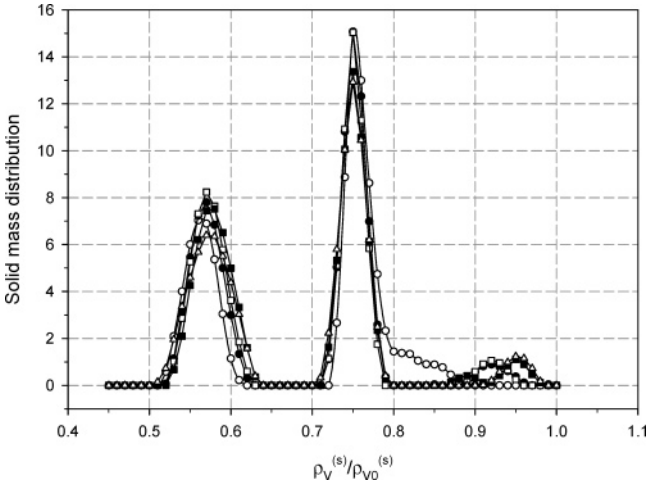

Figure 5. Mass distribution of silica $\rho_{V0}^{(s)}\xi(\rho_V^{(s)})$ with respect to the average pore wall density for series of FDU1 silica samples calcined at different temperatures (K): ○ − 813, ● − 973, □ − 1073, ■ − 1173, △ − 1273. $\rho_{V0}^{(s)}$ is the density of continuous nonporous silica (2.2 g/cm^3). The area under each curve is unity.

Table 2. Structural Parameters for the Series of FDU1 Samples

sample	D_{me} (nm)	D_{con} (nm)	D_{mi} (nm)	V_{me} (nm)	V_{con} (nm)	V_{mi} (nm)	S_{me} (m^2/g)	S_{ex} (m^2/g)
C-813	15.5	1.77	0.98	0.31	0.19	0.18	124	12
C-973	14.8	1.74	1.00	0.27	0.15	0.15	112	11
C-1073	14.5	1.68	1.00	0.26	0.13	0.13	108	10
C-1173	13.6	1.53	1.01	0.22	0.10	0.09	100	10
C-1273	13.0	1.55	0.99	0.18	0.06	0.04	86	7

adsorption on nonporous silica LiChrospher Si-1000.[51] Analysis of the data presented in Table 2 shows that the increase of the temperature of calcination decreases the size of spherical mesopores and connecting pores but does not affect the size of micropores. The surface of mesopores and their diameter both decrease with the increase of calcination temperature. It raises the question whether the number of (available) pores is affected by the temperature. Figure 6 gives one more piece of information on this matter. In this figure we present the distribution function of number of pores with respect to the pore size defined as

$$\varphi(D) = \left(\frac{\pi D^3}{6}\right)^{-1} \frac{dV}{d\log D} \tag{19}$$

Figure 6a shows the distribution in the whole region of pore size. Due to the relatively small size of micropores their number is very large compared to mesopores, so the distribution function in the region above 2 nm is not seen. One can see from the figure that the increase of the calcination temperature does not change the pore size of micropores but substantially decreases their number. It could mean that calcination leads to progressive blocking of micropores and/or their elimination.[56] The situation is different if this figure is plotted in a small scale for the region of pores larger than 5 nm (Figure 6b). It is seen from the figure that all distribution functions related to the main

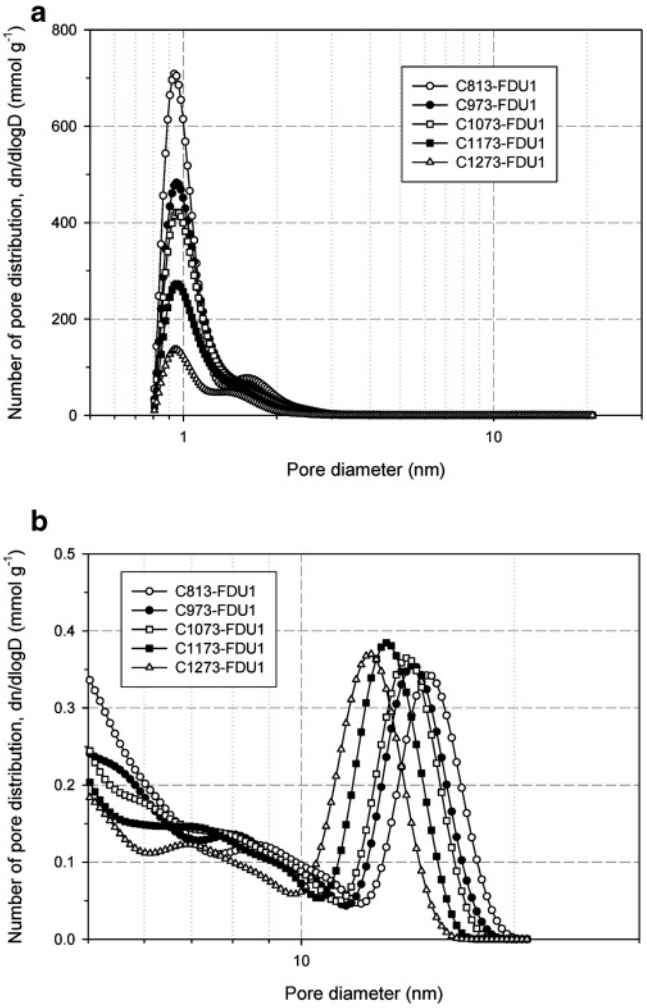

Figure 6. Distribution of number of pores of FDU-1 samples calcined at different temperatures: (a) the whole region of pores and (b) the region of spherical mesopores.

spherical mesopores are nearly the same, but the increase of the temperature of calcination just shifts them toward smaller pore size. It confirms the conclusion that geometrical mesopore structure remains the same during calcination, but the pore size and the pore wall thickness decrease in the same proportion, i.e., the adsorbent shrinks isotropically. The external surface, as is seen from Table 2, also decreases with the increase of the temperature.

4. Conclusion

The nonlocal density functional theory extended for the case of amorphous surfaces is presented. We demonstrated results of the application of the new version of NLDFT to spherical pores of a series of silica FDU-1 samples obtained with a progressive increase in the temperature of calcination. The model quantitatively describes nitrogen adsorption isotherms at 77 K over the entire pressure range. It was found that the apparent density of the pore wall is smaller than that for the nonporous silica due to intermediate pores connecting spherical mesopores. The increase of the calcination temperature leads to blocking micropores and shrinkage of mesopores; however, the geometrical structure of the adsorbent remains the same. The proposed model and method

of simultaneous pore size and mass distribution analysis is a convenient tool for characterization of amorphous porous solids.

Acknowledgment. Support from the Australian Research Council is gratefully acknowledged. M.J. acknowledges NSF for a partial support of this research (grant CHE-0093707).

References

(1) Barrett, E. P.; Joyner, L. G.; Halenda, P. P. *J. Am. Chem. Soc.* **1951**, *73*, 373−380.

(2) Kruk, M.; Jaroniec, M.; Sayari, A. *Langmuir* **1997**, *13*, 6267−6273.

(3) Broekhoff, J. C. P.; de Boer, J. H. *J. Catal.* **1967**, *9*, 8−14, 15−27.

(4) Broekhoff, J. C. P.; de Boer, J. H. *J. Catal.* **1968**, *10*, 368−376, 377−390, 391−400.

(5) Zhu, H. Y.; Lu, G. Q.; Zhao, X. S. *J. Phys. Chem. B* **1998**, *102*, 7371−7376.

(6) Qiao, S. Z.; Bhatia, S. K.; Zhao, X. S. *Microporous Mesoporous Mater.* **2003**, *65*, 287−298.

(7) Qiao, S. Z.; Bhatia, S. K.; Nicholson, D. *Langmuir* **2004**, *20*, 389−395.

(8) Sonwane, C. G.; Bhatia, S. K. *Chem. Eng. Sci.* **1998**, *53*, 3143−3156.

(9) Bhatia, S. K.; Sonwane, C. G. *Langmuir* **1998**, *14*, 1521−1524.

(10) Sonwane, C. G.; Bhatia, S. K. *Langmuir* **1999**, *15*, 5347−5354.

(11) Sonwane, C. G.; Bhatia, S. K.; Calos, N. *Ind. Eng. Chem. Res.* **1998**, *37*, 2271−2283.

(12) Sonwane, C. G.; Bhatia, S. K. *J. Phys. Chem. B* **2000**, *104*, 9099−9110.

(13) Inoue, S.; Hanzawa, Y.; Kaneko, K. *Langmuir* **1998**, *14*, 3079−3081.

(14) Ravikovitch, P.; Domhnaill, S.; Neimark, A.; Schuth, F.; Unger, K. *Langmuir* **1995**, *11*, 4765−4772.

(15) Ravikovitch, P. I.; Wei, D.; Chueh, W. T.; Haller, G. L.; Neimark, A. V. *J. Phys. Chem. B* **1997**, *101*, 3671−3679.

(16) Ravikovitch, P. I.; Neimark, A. V. *Stud. Surf. Sci., Catal.* **2000**, *129*, 597−606.

(17) Neimark, A. V.; Ravikovitch, P. I.; Vishnyakov, A. *Phys. Rev. E* **2000**, *62*, 1493−1496.

(18) Ravikovitch, P. I.; Vishnyakov, A.; Neimark, A. V. *Phys. Rev. E* **2001**, *64*, 011602/1−011602/20.

(19) Ravikovitch, P. I.; Neimark, A. V. *Colloids Surf., A* **2001**, *187−188*, 11−21.

(20) Neimark, A. V.; Ravikovitch, P. I. *Microporous Mesoporous Mater.* **2001**, *44−45*, 697−707.

(21) Ravikovitch, P. I.; Neimark, A. V. *Langmuir* **2002**, *18*, 9830−9837.

(22) Cao, D.; Shen, Z.; Chen, J.; Zhang, X. *Microporous Mesoporous Mater.* **2004**, *67*, 159−166.

(23) Gelb, L. D. *Mol. Phys.* **2002**, *100*, 2049−2057.

(24) Vishnyakov, A.; Neimark, A. V. *J. Chem. Phys.* **2003**, *119*, 9755−9764.

(25) Coasne, B.; Pellenq, R. J.-M. *J. Chem. Phys.* **2004**, *120*, 2913−2922.

(26) Neimark, A. V.; Ravikovitch, P. I.; Vishnyakov, A. *J. Phys.: Condens. Matter* **2003**, *15*, 347−365.

(27) Kruk, M.; Jaroniec, M. *Chem. Mater.* **2001**, *13*, 3169−3183.

(28) Kruk, M.; Jaroniec, M.; Sayari, A. *J. Phys. Chem. B* **1997**, *101*, 583−589.

(29) Franke, O.; Schulz-Ekloff, G.; Rathousky, J.; Starek, J.; Zukal, A. *J. Chem. Soc., Chem. Commun.* **1993**, 724−726.

(30) Branton, P. J.; Hall, P. G.; Sing, K. S. W. *J. Chem. Soc., Chem. Commun.* **1993**, 1257−1258.

(31) Vishnyakov, A.; Neimark, A. V. *J. Phys. Chem. B* **2001**, *105*, 7009−7020.

(32) Maddox, M. W.; Olivier, J. P.; Gubbins, K. E. *Langmuir* **1997**, *13*, 1737−1735.

(33) Kruk, M.; Jaroniec, M.; Sayari, A. *Adsorption* **2000**, *6*, 47−51.

(34) Everett, D. H. In *The Solid−Gas Interface*; Flood, E. A., Ed.; Marcel Dekker: New York, 1967; Vol. 2, Chapter 36, p 1055.

(35) Kruk, M.; Jaroniec, M. *J. Phys. Chem. B* **2002**, *106*, 4732−4739.

(36) Morishige, K.; Ito, M. *J. Chem. Phys.* **2002**, *117*, 8036−8041.

(37) Morishige, K.; Nakamura, Y. *Langmuir* **2004**, *20*, 4503−4506.

(38) Ustinov, E. A.; Do, D. D. Capillary phenomena in the framework of the two-dimensional density functional theory. *Fundamentals of Adsorption 8.* Sedona, Arizona, U.S.A. May 23−28 2004.

(39) Ravikovitch, P. I.; Neimark, A. V. *Langmuir* **2002**, *18*, 1550−1560.

(40) Kruk, M.; Celer, E. B.; Jaroniec, M. *Chem. Mater.* **2004**, *16*, 698−707.

(41) Tarazona, P. *Phys. Rev. A* **1985**, *31*, 2672−2679.

(42) Tarazona, P.; Marconi, U. M. B.; Evans, R. *Mol. Phys.* **1987**, *60*, 573−595.

(43) Carnahan, N. F.; Starling, K. E. *J. Chem. Phys.* **1969**, *51*, 635−636.

(44) Ustinov, E. A.; Do, D. D.; Jaroniec, M. Application of density functional theory to equilibrium adsorption of argon and nitrogen on amorphous silica surface. *Appl. Surf. Sci.* **2005**, in press.

(45) Ustinov, E. A.; Do, D. D.; Jaroniec, M. Adsorption of argon and nitrogen in cylindrical pores of MCM-41 materials: Application of density functional theory. *Appl. Surf. Sci.* **2005,** in press.

(46) Ustinov, E. A.; Do, D. D.; Jaroniec, M. *J. Phys. Chem. B* **2005**, *109*, 1947−1958.

(47) Weeks, J. D.; Chandler, D.; Andersen, H. C. *J. Chem. Phys.* **1971**, *54*, 5237−5247.

(48) Madden, W. G. *J. Chem. Phys.* **1992**, *96*, 5422−5432.

(49) Given, J. A. *J. Chem. Phys.* **1995**, *102*, 2934−2945.

(50) Neimark, A. V.; Ravikovitch, P. I.; Grün, M.; Schüth, F.; Unger, K. K. *J. Colloid Interface Sci.* **1998**, *207*, 159−169.

(51) Jaroniec, M.; Kruk, M.; Olivier, J. P. *Langmuir* **1999**, *15*, 5410−5413.

(52) Tikhonov, A. N. *Dokl. AN SSSR* **1943**, *39*, 195−198.

(53) Tikhonov, A. N. *Dokl. AN SSSR* **1963**, *153*, 49−52.

(54) Ustinov, E. A.; Do, D. D. *Langmuir* **2003**, *19*, 8349−8357.

(55) Ustinov, E. A.; Do, D. D. *Langmuir* **2004**, *20*, 3791−3797.

(56) Matos, J. R.; Mecuri, L. P.; Kruk, M.; Jaroniec, M. *Chem. Mater.* **2001**, *13*, 1726−1731.

CT049903Z

JCTC Journal of Chemical Theory and Computation

Computational Free Energy Studies of a New Ice Polymorph Which Exhibits Greater Stability than Ice I_h

Christopher J. Fennell and J. Daniel Gezelter*

Department of Chemistry and Biochemistry, University of Notre Dame, Notre Dame, Indiana 46556

Received January 7, 2005

Abstract: The absolute free energies of several ice polymorphs were calculated using thermodynamic integration. These polymorphs are predicted by computer simulations using a variety of common water models to be stable at low pressures. A recently discovered ice polymorph that has as yet *only* been observed in computer simulations (Ice-*i*) was determined to be the stable crystalline state for *all* the water models investigated. Phase diagrams were generated, and phase coexistence lines were determined for all of the known low-pressure ice structures. Additionally, potential truncation was shown to play a role in the resulting shape of the free energy landscape.

1. Introduction

Water has proven to be a challenging substance to depict in simulations, and a variety of models have been developed to describe its behavior under varying simulation conditions.[1−12] These models have been used to investigate important physical phenomena-like phase transitions, transport properties, and the hydrophobic effect.[13−15] With the choice of models available, it is only natural to compare them under interesting thermodynamic conditions in an attempt to clarify the limitations of each.[4,16−18] Two important properties to quantify are the Gibbs and Helmholtz free energies, particularly for the solid forms of water, as these predict the thermodynamic stability of the various phases. Water has a particularly rich phase diagram and takes on a number of different and stable crystalline structures as the temperature and pressure are varied. It is a challenging task to investigate the entire free energy landscape;[19] and ideally, research is focused on the phases having the lowest free energy at a given state point, because these phases will dictate the relevant transition temperatures and pressures for the model.

The high-pressure phases of water (ice II−ice X as well as ice XII) have been studied extensively both experimentally and computationally. In this paper, standard reference state methods were applied in the *low* pressure regime to evaluate the free energies for a few known crystalline water polymorphs that might be stable at these pressures. This work is unique in that one of the crystal lattices was arrived at through crystallization of a computationally efficient water model under constant pressure and temperature conditions. Crystallization events are interesting in and of themselves;[13,20] however, the crystal structure obtained in this case is different from any previously observed ice polymorphs in experiment or simulation.[12] We have named this structure Ice-*i* to indicate its origin in computational simulation. The unit cell of Ice-*i* and an axially elongated variant named Ice-*i*′ both consist of eight water molecules that stack in rows of interlocking water tetramers as illustrated in Figure 1A,B. These tetramers form a crystal structure similar in appearance to a recent two-dimensional surface tessellation simulated on silica.[21] As expected in an ice crystal constructed of water tetramers, the hydrogen bonds are not as linear as those observed in ice I_h; however, the interlocking of these subunits appears to provide significant stabilization to the overall crystal. The arrangement of these tetramers results in octagonal cavities that are typically greater than 6.3 Å in diameter (Figure 2). This open structure leads to crystals that are typically 0.07 g/cm^3 less dense than ice I_h.

Results from our previous study indicated that Ice-*i* is the minimum energy crystal structure for the single point water models investigated (for discussions on these single point dipole models, see our previous work and related articles).[5,8,12] Our earlier results considered only energetic stabilization and neglected entropic contributions to the overall free energy. To address this issue, we have calculated

10.1021/ct050005s CCC: $30.25
Published on Web 04/30/2005

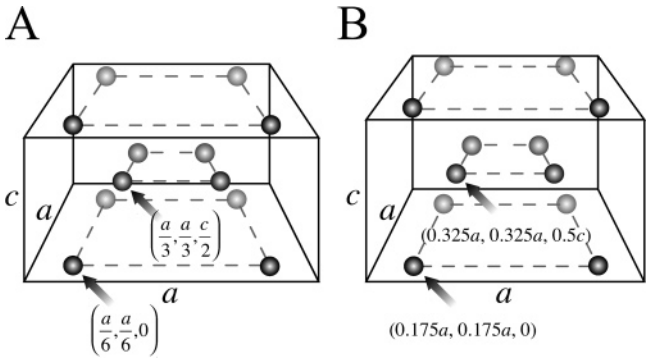

Figure 1. (A) Unit cells for Ice-*i* and (B) Ice-*i′*. The spheres represent the center-of-mass locations of the water molecules. The *a* to *c* ratios for Ice-*i* and Ice-*i′* are given by 2.1214 and 1.785, respectively.

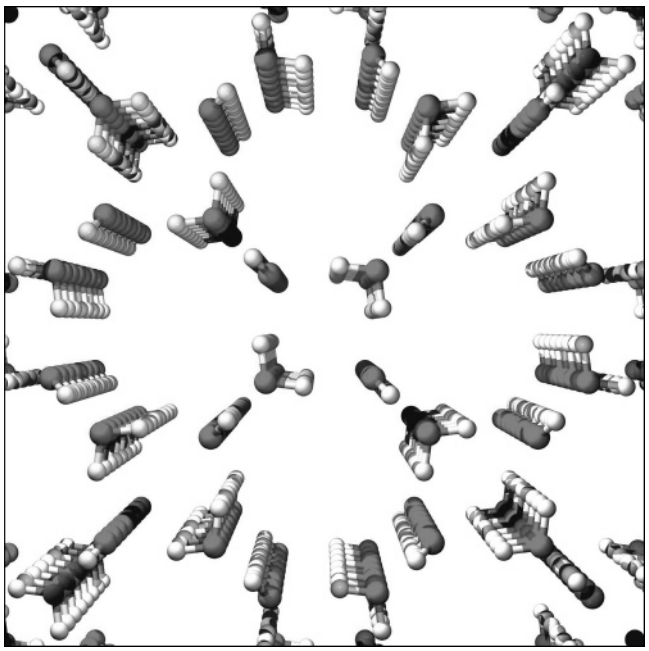

Figure 2. A rendering of a proton ordered crystal of Ice-*i* looking down the (001) crystal face. The presence of large octagonal pores leads to a polymorph that is less dense than ice I_h.

the absolute free energy of this crystal using thermodynamic integration and compared it to the free energies of ice I_c and ice I_h (the common low-density ice polymorphs) and ice B (a higher density but very stable crystal structure observed by Bàez and Clancy in free energy studies of SPC/E).[22] This work includes results for the water model from which Ice-*i* was crystallized (SSD/E) in addition to several common water models (TIP3P, TIP4P, TIP5P, and SPC/E) and a reaction field parametrized single point dipole water model (SSD/RF). The axially elongated variant, Ice-*i′*, was used in calculations involving SPC/E, TIP4P, and TIP5P. The square tetramers in Ice-*i* distort in Ice-*i′* to form a rhombus with alternating 85 and 95 degree angles. Under SPC/E, TIP4P, and TIP5P, this geometry is better at forming favorable hydrogen bonds. The degree of rhomboid distortion depends on the water model used but is significant enough to split a peak in the radial distribution function which corresponds to diagonal sites in the tetramers.

2. Methods

Canonical ensemble (NVT) molecular dynamics calculations were performed using the OOPSE molecular mechanics program.[23] The densities chosen for the simulations were taken from isobaric−isothermal (NPT) simulations performed at 1 atm and at 200 K. Each model (and each crystal structure) was allowed to relax for 300 ps in the NPT ensemble before averaging the density to obtain the volumes for the NVT simulations. All molecules were treated as rigid bodies, with orientational motion propagated using the symplectic DLM integration method. Details about the implementation of this technique can be found in a recent publication.[24]

Thermodynamic integration was utilized to calculate the Helmholtz free energies (A) of the listed water models at various state points. Thermodynamic integration is an established technique that has been used extensively in the calculation of free energies for condensed phases of materials.[25−29] This method uses a sequence of simulations during which the system of interest is converted into a reference system for which the free energy is known analytically (A_0). The difference in potential energy between the reference system and the system of interest (ΔV) is then integrated in order to determine the free energy difference between the two states:

$$A = A_0 + \int_0^1 \langle \Delta V \rangle_\lambda d\lambda \qquad (1)$$

Here, λ is the parameter that governs the transformation between the reference system and the system of interest. For crystalline phases, an harmonically restrained (Einstein) crystal is chosen as the reference state, while for liquid phases, the ideal gas is taken as the reference state.

In an Einstein crystal, the molecules are restrained at their ideal lattice locations and orientations. Using harmonic restraints, as applied by Bàez and Clancy, the total potential for this reference crystal (V_{EC}) is the sum of all the harmonic restraints

$$V_{EC} = \sum_i \left[\frac{K_v}{2}(r_i - r_i^0)^2 + \frac{K_\theta}{2}(\theta_i - \theta_i^0)^2 + \frac{K_\omega}{2}(\omega_i - \omega_i^0)^2 \right] \qquad (2)$$

where K_v, K_θ, and K_ω are the spring constants restraining translational motion and deflection of and rotation around the principal axis of the molecule, respectively. These spring constants are typically calculated from the mean-square displacements of water molecules in an unrestrained ice

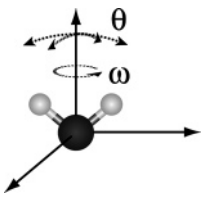

Figure 3. Possible orientational motions for a restrained molecule. θ angles correspond to displacement from the body-frame *z*-axis, while ω angles correspond to rotation about the body-frame *z*-axis. K_θ and K_ω are spring constants for the harmonic springs restraining motion in the θ and ω directions.

Table 1. Calculated Free Energies for Several Ice Polymorphs along with the Calculated Melting (or Sublimation) and Boiling Points for the Investigated Water Models[a]

water model	I_h	I_c	B	Ice-*i*	Ice-*i′*	T_m (*T_s)	T_b
TIP3P	−11.41(2)	−11.23(3)	−11.82(3)	−12.30(3)		269(7)	357(4)
TIP4P	−11.84(3)	−12.04(2)	−12.08(3)		−12.33(3)	262(6)	354(4)
TIP5P	−11.85(3)	−11.86(2)	−11.96(2)		−12.29(2)	266(7)	337(4)
SPC/E	−12.87(2)	−13.05(2)	−13.26(3)		−13.55(2)	299(6)	396(4)
SSD/E	−11.27(2)	−11.19(4)	−12.09(2)	−12.54(2)		*355(4)	
SSD/RF	−11.96(2)	−11.60(2)	−12.53(3)	−12.79(2)		278(7)	382(4)

[a] All free energy calculations used a cutoff radius of 9.0 Å and were performed at 200 K and 1 atm. Units of free energy are kcal/mol, while transition temperature are in Kelvin. Calculated error of the final digits is in parentheses.

crystal at 200 K. For these studies, $K_\nu = 4.29$ kcal mol^{-1} Å^{-2}, $K_\theta = 13.88$ kcal mol^{-1} rad^{-2}, and $K_\omega = 17.75$ kcal mol^{-1} rad^{-2}. It is clear from Figure 3 that the values of θ range from 0 to π, while ω ranges from $-\pi$ to π. The partition function for a molecular crystal restrained in this fashion can be evaluated analytically, and the Helmholtz Free Energy (A) is given by

$$\frac{A}{N} = \frac{E_m}{N} - kT\ln\left(\frac{kT}{h\nu}\right)^3 - kT\ln\left[\pi^{1/2}\left(\frac{8\pi^2 I_A kT}{h^2}\right)^{1/2}\left(\frac{8\pi^2 I_B kT}{h^2}\right)^{1/2}\left(\frac{8\pi I_C kT}{h^2}\right)^{1/2}\right] - kT\ln\left[\frac{kT}{2(\pi K_\omega K_\theta)^{1/2}}\exp\left(-\frac{kT}{2K_\theta}\right)\int_0^{(kT/2K_\theta)^{1/2}}\exp(t^2)\mathrm{d}t\right] \quad (3)$$

where $2\pi\nu = (K_\nu/m)^{1/2}$, and E_m is the minimum potential energy of the ideal crystal.[28] The choice of an Einstein crystal reference state is somewhat arbitrary. Any ideal system for which the partition function is known exactly could be used as a reference point as long as the system does not undergo a phase transition during the integration path between the real and ideal systems. Nada and van der Eerden have shown that the use of different force constants in the Einstein crystal does not affect the total free energy,[30] and Gao et al. have shown that free energies computed with the Debye crystal reference state differ from the Einstein crystal by only a few tenths of a kJ mol^{-1}.[31] These free energy differences can lead to some uncertainty in the computed melting point of the solids.

In the case of molecular liquids, the ideal vapor is chosen as the target reference state. There are several examples of liquid-state free energy calculations of water models present in the literature.[22,26,32,33] These methods typically differ in regard to the path taken for switching off the interaction potential to convert the system to an ideal gas of water molecules. In this study, we applied one of the most convenient methods and integrated over the λ^4 path, where all interaction parameters are scaled equally by this transformation parameter. This method has been shown to be reversible and provide results in excellent agreement with other established methods.[22]

Near the cutoff radius ($0.85*r_{cut}$), charge, dipole, and Lennard-Jones interactions were gradually reduced by a cubic switching function. By applying this function, these interactions are smoothly truncated, thereby avoiding the poor energy conservation which results from harsher truncation schemes. The effect of a long-range correction was also investigated on select model systems in a variety of manners. For the SSD/RF model, a reaction field with a fixed dielectric constant of 80 was applied in all simulations.[34] For a series of the least computationally expensive models (SSD/E, SSD/RF, TIP3P, and SPC/E), simulations were performed with longer cutoffs of 10.5, 12, 13.5, and 15 Å to compare with the 9 Å cutoff results. Finally, the effects of using the Ewald summation were estimated for TIP3P and SPC/E by performing single configuration Particle-Mesh Ewald (PME) calculations[35] for each of the ice polymorphs. The calculated energy difference in the presence and absence of PME was applied to the previous results in order to predict changes to the free energy landscape.

3. Results and Discussion

The calculated free energies of proton-ordered variants of three low-density polymorphs (I_h, I_c, and Ice-*i* or Ice-*i′*) and the stable higher density ice B are listed in Table 1. Ice B was included because it has been shown to be a minimum free energy structure for SPC/E at ambient conditions.[22] In addition to the free energies, the relevant transition temperatures at standard pressure are also displayed in Table 1. These free energy values indicate that Ice-*i* is the most stable state for all of the investigated water models. With the free energy at these state points, the Gibbs−Helmholtz equation was used to project to other state points and to build phase diagrams. Figure 4 is an example diagram built from the results for the TIP3P water model. All other models have similar structure, although the crossing points between the phases move to different temperatures and pressures as indicated from the transition temperatures in Table 1. It is interesting to note that ice I_h (and ice I_c for that matter) do not appear in any of the phase diagrams for any of the models. For purposes of this study, ice B is representative of the dense ice polymorphs. A recent study by Sanz et al. provides details on the phase diagrams for SPC/E and TIP4P at higher pressures than those studied here.[19]

We note that all of the crystals investigated in this study are ideal proton-ordered antiferroelectric structures. All of the structures obey the Bernal-Fowler rules[36] and should be able to form stable proton-*disordered* crystals which have the traditional $k_B\ln(3/2)$ residual entropy at 0 K.[37] Simulations of proton-disordered structures are relatively unstable with all but the most expensive water models.[30] Our simulations have therefore been performed with the ordered antiferroelectric structures which do not require the residual entropy term to be accounted for in the free energies. However, this

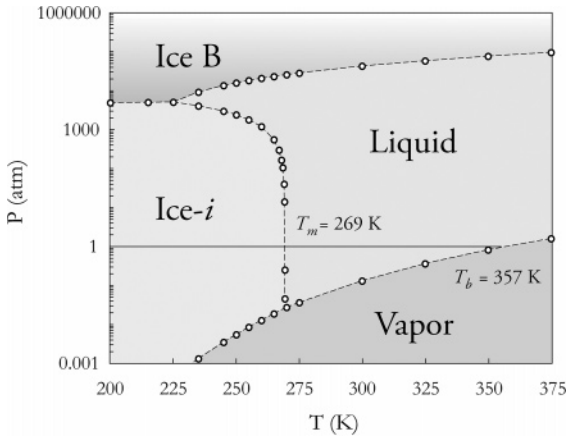

Figure 4. Phase diagram for the TIP3P water model in the low-pressure regime. The displayed T_m and T_b values are good predictions of the experimental values; however, the solid phases shown are not the experimentally observed forms. Both cubic and hexagonal ice *I* are higher in energy and do not appear in the phase diagram.

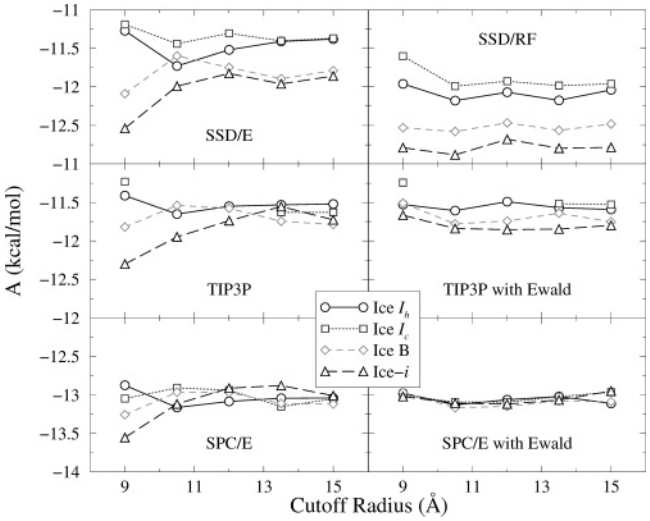

Figure 5. Free energy as a function of cutoff radius for SSD/E, TIP3P, SPC/E, SSD/RF with a reaction field and the TIP3P and SPC/E models with an added Ewald correction term. Error for the larger cutoff points is equivalent to that observed at 9.0 Å (see Table 1). Data for ice I_c with TIP3P using both 12 and 13.5 Å cutoffs were omitted because the crystal was prone to distortion and melting at 200 K. Ice-*i*′ is the form of Ice-*i* used in the SPC/E simulations.

may result in some discrepancies when comparing our melting temperatures to the melting temperatures that have been calculated via thermodynamic integrations of the disordered structures.[19]

Most of the water models have melting points that compare quite favorably with the experimental value of 273 K. The unfortunate aspect of this result is that this phase change occurs between Ice-*i* and the liquid-state rather than ice I_h and the liquid state. These results do not contradict other studies which predict a range of 191 to 238 K for the melting temperature of ice I_h using TIP4P. The range in temperatures can be attributed to choice of interaction truncation and proton ordering.[19,29−31] If the presence of ice B and Ice-*i* were omitted, a T_m value around 200 K would be predicted from this work. However, the T_m from Ice-*i* is calculated to be 262 K, indicating that these simulation based structures ought to be included in studies probing phase transitions with this model. Also of interest in these results is that SSD/E does not exhibit a melting point at 1 atm but does sublime at 355 K. This is due to the significant stability of Ice-*i* over all other polymorphs for this particular model under these conditions. While troubling, this behavior resulted in the spontaneous crystallization of Ice-*i* which led us to investigate this structure. These observations provide a warning that simulations of SSD/E as a "liquid" near 300 K are actually metastable and run the risk of spontaneous crystallization. However, when a longer cutoff radius is used, SSD/E prefers the liquid state under standard temperature and pressure.

For the more computationally efficient water models, we have also investigated the effect of potential trunctaion on the computed free energies as a function of the cutoff radius. As seen in Figure 5, the free energies of the ice polymorphs with water models lacking a long-range correction show significant cutoff dependence. In general, there is a narrowing of the free energy differences while moving to greater cutoff radii. As the free energies for the polymorphs converge, the stability advantage that Ice-*i* exhibits is reduced. Adjacent to each of these plots are results for systems with applied or estimated long-range corrections. SSD/RF was parametrized for use with a reaction field, and the benefit provided by this computationally inexpensive correction is apparent. The free energies are largely independent of the size of the reaction field cavity in this model, so small cutoff radii mimic bulk calculations quite well under SSD/RF.

Although TIP3P was paramaterized for use without the Ewald summation, we have estimated the effect of this method for computing long-range electrostatics for both TIP3P and SPC/E. This was accomplished by calculating the potential energy of identical crystals both with and without particle mesh Ewald (PME). Similar behavior to that observed with reaction field is seen for both of these models. The free energies show reduced dependence on cutoff radius and span a narrower range for the various polymorphs. Like the dipolar water models, TIP3P displays a relatively constant preference for the Ice-*i* polymorph. Crystal preference is much more difficult to determine for SPC/E. Without a long-range correction, each of the polymorphs studied assumes the role of the preferred polymorph under different cutoff radii. The inclusion of the Ewald correction flattens and narrows the gap in free energies such that the polymorphs are isoenergetic within statistical uncertainty. This suggests that other conditions, such as the density in fixed-volume simulations, can influence the polymorph expressed upon crystallization.

4. Conclusions

In this work, thermodynamic integration was used to determine the absolute free energies of several ice polymorphs. The new polymorph, Ice-*i*, was observed to be the stable crystalline state for *all* the water models when using a 9.0 Å cutoff. However, the free energy partially depends on simulation conditions (particularly on the choice of long-

range correction method). Regardless, Ice-*i* was still observed to be either the stable polymorph or one of a set of metastable polymorphs for *all* of the studied water models.

So what is the preferred solid polymorph for simulated water? As indicated above, the answer appears to be dependent both on the conditions and the model used. In the case of short cutoffs without a long-range interaction correction, Ice-*i* and Ice-*i*′ have the lowest free energy of the studied polymorphs with all the models. Ideally, crystallization of each model under constant pressure conditions, as was done with SSD/E, would aid in the identification of their respective preferred structures. This work, however, helps illustrate how studies involving one specific model can lead to insight about important behavior of others.

The stability of Ice-*i* in the SSD models is probably due to wide conical angle over which the short-range sticky potential is attractive. This allows added stability from hydrogen bonding at unrealistic O−H−O angles. The tetramers present in the Ice-*i* structure are *not* in particularly favorable arrangements for the dipolar interactions, so it is unlikely that the dipolar strength of the SSD family is helping to stabilize this structure. Increasing the angular specificity of the attractive portion of the sticky potential by using higher powers of the spherical harmonic term (i.e. $(Y_3^2 + Y_3^{-2})^3$) would be a simple way to destabilize the Ice-*i* structure.

It is possible that one of the newer parametrizations of the point-charge models such as the Nada and van der Eerden six-site model,[30] or the Ewald-corrected versions of the TIP models (e.g. TIP4P-Ew,[38] and TIP5P-E[39]), would also destabilize this structure relative to the correct ice structures. We also note that none of the water models used in this study are polarizable or flexible models. It is entirely possible that the polarizability of real water makes Ice-*i* substantially less stable than ice I_h. However, the calculations presented above seem interesting enough to communicate before the role of polarizability (or flexibility) has been thoroughly investigated.

Finally, due to the stability of Ice-*i* in the investigated simulation conditions, the question arises as to possible experimental observation of this polymorph. The rather extensive past and current experimental investigation of water in the low-pressure regime makes us hesitant to ascribe any relevance to this work outside of the simulation community. It is for this reason that we chose a name for this polymorph which involves an imaginary quantity. That said, there are certain experimental conditions that would provide the most ideal situation for possible observation. These include the negative pressure or stretched solid regime, small clusters in vacuum deposition environments, and in clathrate structures involving small nonpolar molecules. For the purpose of comparison with experimental results, we have calculated the oxygen−oxygen pair correlation function, $g_{OO}(r)$, and the structure factor, $S(\vec{q})$, for the two Ice-*i* variants (along with example ice I_h and I_c plots) at 77 K, and they are shown in Figures 6 and 7 respectively. It is interesting to note that the structure factors for Ice-*i*′ and Ice-I_c are quite similar. The primary differences are small peaks at 1.125, 2.29, and 2.53 Å^{-1}, so particular attention to these regions would be needed to identify the new *i*′ variant from the I_c variant.

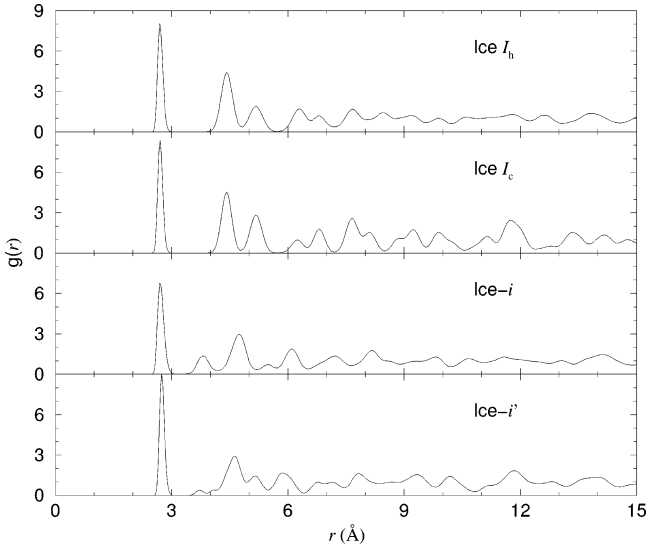

Figure 6. Radial distribution functions of ice I_h, I_c, and Ice-*i* calculated from simulations of the SSD/RF water model at 77 K. The Ice-*i* distribution function was obtained from simulations composed of TIP4P water.

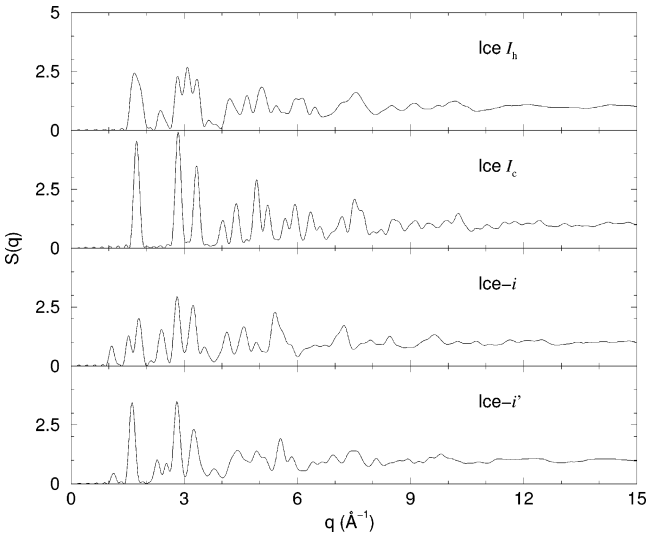

Figure 7. Predicted structure factors for ice I_h, I_c, Ice-*i*, and Ice-*i*′ at 77 K. The raw structure factors have been convoluted with a Gaussian instrument function (0.075 Å^{-1} width) to compensate for the trunction effects in our finite size simulations.

Acknowledgment. Support for this project was provided by the National Science Foundation under grant CHE-0134881. Computation time was provided by the Notre Dame High Performance Computing Cluster and the Notre Dame Bunch-of-Boxes (B.o.B) computer cluster (NSF grant DMR-0079647).

Supporting Information Available: PDB files containing 1024-molecule example structures of proton-ordered Ice-*i* and Ice-*i*′. This material is available free of charge via the Internet at http://pubs.acs.org.

References

(1) Stillinger, F. H.; Rahman, A. *J. Chem. Phys.* **1974**, *60*, 1545−1557.

(2) Rahman, A.; Stillinger, F. H.; Lemberg, H. L. *J. Chem. Phys.* **1975**, *63*, 5223−5230.

(3) Berendsen, H. J. C.; Postma, J. P. M.; van Gunsteren, W. F.; Hermans, J. Simple Point Charge Water. In *Intermolecular Forces*; Pullman, B., Ed.; Reidel: Dordrecht, 1981.

(4) Jorgensen, W. L.; Chandrasekhar, J.; Madura, J. D.; Impey, R. W.; Klein, M. L. *J. Chem. Phys.* **1983**, *79*, 926−935.

(5) Bratko, D.; Blum, L.; Luzar, A. *J. Chem. Phys.* **1985**, *83*, 6367−6370.

(6) Berendsen, H. J. C.; Grigera, J. R.; Straatsma, T. P. *J. Phys. Chem.* **1987**, *91*, 6269−6271.

(7) Caldwell, J. W.; Kollman, P. A. *J. Phys. Chem.* **1995**, *99*, 6208−6219.

(8) Liu, Y.; Ichiye, T. *J. Phys. Chem.* **1996**, *100*, 2723−2730.

(9) van der Spoel, D.; van Maaren, P. J.; Berendsen, H. J. C. *J. Chem. Phys.* **1998**, *108*, 10220−10230.

(10) Urbič, T.; Vlachy, V.; Kalyuzhnyi, Y. V.; Southall, N. T.; Dill, K. A. *J. Chem. Phys.* **2000**, *112*, 2843−2848.

(11) Mahoney, M. W.; Jorgensen, W. L. *J. Chem. Phys.* **2000**, *112*, 8910−8922.

(12) Fennell, C. J.; Gezelter, J. D. *J. Chem. Phys.* **2004**, *120*, 9175−9184.

(13) Yamada, M.; Mossa, S.; Stanley, H. E.; Sciortino, F. *Phys. Rev. Lett.* **2002**, *88*, 195701.

(14) Marrink, S. J.; Berendsen, H. J. C. *J. Phys. Chem.* **1994**, *98*, 4155−4168.

(15) Gallagher, K. R.; Sharp, K. A. *J. Am. Chem. Soc.* **2003**, *125*, 9853.

(16) Jorgensen, W. L.; Jenson, C. *J. Comput. Chem.* **1998**, *19*, 1179−1186.

(17) Báez, L. A.; Clancy, P. *J. Chem. Phys.* **1994**, *101*, 9837−9840.

(18) Mahoney, M. W.; Jorgensen, W. L. *J. Chem. Phys.* **2001**, *114*, 363−366.

(19) Sanz, E.; Vega, C.; Abascal, J. L. F.; MacDowell, L. G. *Phys. Rev. Lett.* **2004**, *92*, 255701.

(20) Matsumoto, M.; Saito, S.; Ohimine, I. *Nature (London)* **2002**, *416*, 409−413.

(21) Yang, J.; Meng, S.; Xu, L. F.; Wang, E. G. *Phys. Rev. Lett.* **2004**, *92*, 146102.

(22) Bàez, L. A.; Clancy, P. *J. Chem. Phys.* **1995**, *103*, 9744−9755.

(23) Meineke, M. A.; II, C. F. V.; Lin, T.; Fennell, C. J.; Gezelter, J. D. *J. Comput. Chem.* **2005**, *26*, 252−271.

(24) Dullweber, A.; Leimkuhler, B.; McLachlan, R. *J. Chem. Phys.* **1997**, *107*, 5840−5851.

(25) Frenkel, D.; Ladd, A. J. C. *J. Chem. Phys.* **1984**, *81*, 3188−3193.

(26) Hermans, J.; Pathiaseril, A.; Anderson, A. *J. Am. Chem. Soc.* **1988**, *110*, 5982−5986.

(27) Meijer, E. J.; Frenkel, D.; LeSar, R. A.; Ladd, A. J. C. *J. Chem. Phys.* **1990**, *92*, 7570−7575.

(28) Bàez, L. A.; Clancy, P. *Mol. Phys.* **1995**, *86*, 385−396.

(29) Vlot, M. J.; Huinink, J.; van der Eerden, J. P. *J. Chem. Phys.* **1999**, *110*, 55−61.

(30) Nada, H.; van der Eerden, J. P. J. M. *J. Chem. Phys.* **2003**, *118*, 7401−7413.

(31) Gao, G. T.; Zeng, X. C.; Tanaka, H. *J. Chem. Phys.* **2000**, *112*, 8534−8538.

(32) Quintana, J.; Haymet, A. D. J. *Chem. Phys. Lett.* **1992**, *189*, 273−277.

(33) Mezei, M. *J. Comput. Chem.* **1992**, *13*, 651.

(34) Onsager, L. *J. Am. Chem. Soc.* **1936**, *58*, 1486-1493.

(35) Ponder, J. W.; Richards, F. M. *J. Comput. Chem.* **1987**, *8*, 1016−1024.

(36) Bernal, J. D.; Fowler, R. H. *J. Chem. Phys.* **1933**, *1*, 515−548.

(37) Pauling, L. *J. Am. Chem. Soc.* **1935**, *57*, 2680−2684.

(38) Horn, H. W.; Swope, W. C.; Pitera, J. W.; Madura, J. D.; Dick, T. J.; Hura, G. L.; Head-Gordon, T. *J. Chem. Phys.* **2004**, *120*, 9665−9678.

(39) Rick, S. W. *J. Chem. Phys.* **2004**, *120*, 6085−6093.

CT050005S

JCTC Journal of Chemical Theory and Computation

Control of the Barrier in Cyanide Based Single Molecule Magnets $Mn(III)_2Mn(II)_3$: Theoretical Analysis

Boris S. Tsukerblat,*,† Andrew V. Palii,*,‡ Sergei M. Ostrovsky,‡ Sergei V. Kunitsky,‡ Sophia I. Klokishner,‡ and Kim R. Dunbar*,§

Chemistry Department, Ben-Gurion University of the Negev, Beer-Sheva 84105, Israel, Institute of Applied Physics, Academy of Sciences of Moldova, Academy Str. 5, MD 2028 Kishinev, Moldova, and Department of Chemistry, Texas A&M University, College Station, Texas 77842-3012

Received February 22, 2005

Abstract: The aim of this communication is to probe the possibility of increasing the barrier for reversal of magnetization in the family of new cyano-bridged pentanuclear $Mn(III)_2Mn(II)_3$ clusters in which single molecule magnet behavior has been recently discovered. In this context, we analyze the global magnetic anisotropy arising from the unquenched orbital angular momenta of ground terms $^3T_1(t_2^4)$ of the two apical Mn(III) ions. The model takes into account the trigonal component of the crystal field, spin−orbit interaction in $^3T_1(t_2^4)$, and an isotropic exchange interaction between Mn(III) and Mn(II) ions. The height of the barrier is shown to be sensitive to the change of the trigonal field stabilizing orbital doublet ^3E, which carries the first-order orbital magnetic contribution and enhances with an increase of the trigonal field. This result is expected to be useful for the more rational design of new cyano-bridged SMMs with high blocking temperatures.

1. Introduction

The existence of the phenomenon of single-molecule magnetism was first noted in the family of clusters of general formula $[Mn_{12}O_{12}(O_2CR)_{16}(H_2O)_4]$.[1−3] These systems show very slow relaxation of magnetization and quantum tunneling effects at low temperatures. One of the most important characteristics of single molecule magnets (SMM) is the blocking temperature, which is closely related to the magnitude of the spin reorientation barrier. The blocking temperature for existing magnetic clusters with SMM properties is still not high enough to be used in applications. In fact, the highest blocking temperature observed to date is 3 K (for the Mn_{12}*acetate* cluster having a barrier of about 60 K). This corresponds to a relaxation time of about 10^8 s in Mn_{12}*acetate*; a relaxation time acceptable for applications should be at least 15 years at room temperature.[4] Therefore, the increase of the spin reversal barrier remains the central problem in the design of SMMs with higher blocking temperatures.

The magnitude of the barrier is closely related to the global magnetic anisotropy of the system that can arise from single ion anisotropy or/and anisotropic exchange interactions. If the ionic ground states are orbital singlets, both types of anisotropic interactions are relatively small. This is peculiar for most of the known SMMs based on oxo-bridged clusters, in which the orbital angular momenta of the constituent metal ions are quenched by the local low-symmetry crystal fields. Under these conditions, a large spin S of the ground state and the axial global magnetic anisotropy described by the Hamiltonian $D_S S_Z^2$ with $D_S < 0$ are the basic ingredients of SMM behavior. The magnitude of the barrier in the oxo-bridged clusters can be increased either by increasing the spin of the ground state or the axial zero field splitting parameter D_S. However, the $D_S S_Z^2$ term represents a second-order correction with respect to the spin−orbit coupling, and hence D_S is usually small. This fact essentially constrains

* Corresponding authors phone: 972-8-647 93 61; e-mail: tsuker@bgumail.bgu.ac.il (B.T.); e-mail: andrew.palii@uv.es (A.P); e-mail: dunbar@mail.chem.tamu.edu (K.R.D.).

† Ben-Gurion University of the Negev.

‡ Academy of Sciences of Moldova.

§ Texas A&M University.

10.1021/ct0500343 CCC: $30.25
Published on Web 05/04/2005

the possibility to increase the barrier exhibited by oxo-bridged molecules even if the sizes of the spin clusters are made much larger.

If the ground terms of the ions are orbitally degenerate, the unquenched orbital angular momenta give rise to a strong (first order) anisotropy. The orbitally dependent exchange in this case has been considered in detail in the series of articles,[5−9] in which the exchange Hamiltonian in the most general form has been constructed, the idea about strong exchange anisotropy was developed, and the magnetic anisotropy has been analyzed. Within this approach the anisotropic pseudo-spin-1/2 Hamiltonian for the Kramers doublet ions in the case of strong spin−orbit interaction has been deduced. The parameters of the anisotropic interaction in a Mo(III)−CN−Mn(II) pair in the case of strong spin−orbit interaction have been evaluated in ref 10. The unquenched orbital angular momentum also promotes a strong (first-order) single ion anisotropy. In general, both types of the anisotropy (single-ion and exchange) contribute to the global magnetic anisotropy of the system, with the relative importance of these two contributions being dependent on the electronic and geometrical structure of the cluster.

As distinguished from the oxo-bridged clusters the highly symmetric ligand network in the metal−cyanide complexes can give rise to the unquenched orbital angular momenta of the constituent metal ions and hence to the strong global magnetic anisotropy. Such a situation takes place in the trigonal bipyramidal cyano-bridged cluster $[Mn^{III}(CN)_6]_2$-$[Mn^{II}(tmphen)_2]_3$ (tmphen = 3,4,7,8-tetramethyl-1,10-phenanthroline) exhibiting SMM properties.[11] Due to a strong cubic crystal field produced by six carbon ions, the ground term of each Mn(III) ion is orbitally degenerate being the low spin−orbital triplet $^3T_1(t_2^4)$. Under this condition the Mn^{III} ions carry a first-order magnetic contribution that is sensitive to the local crystal fields. This leads to a significant single ion anisotropy governed by the combined action of spin−orbit coupling and trigonal component of the crystal field, which splits the ground orbital triplet of the Mn(III) ion. Such anisotropy represents a first-order effect with respect to the named interactions and thus cannot be described by the term $D_S S_Z^2$. Recently we have shown[12] that strong single ion anisotropy of this type is able to create a barrier for the reversal of magnetization. At the same time the anisotropic terms in the exchange Hamiltonian have been neglected. In this way the experimental data on the static magnetic susceptibility of the Mn_5-cyanide cluster have been explained, and the proposed model has been shown to be in accordance with the observed SMM properties of the system. The analysis of the model proposed in ref 12 argues hints at future prospects for the design of new cyano-bridged SMMs with higher blocking temperatures. In this paper we show that the barrier in the family of Mn_5-cyanide clusters should be able to be significantly increased by ligand substitutions that result in the variation of the trigonal crystal field.

2. Hamiltonian of the Mn_5-Cyanide Cluster

The model for the interpretation of the observed temperature dependence of the static magnetic susceptibility has been considered in detail in our paper,[12] so here we briefly describe only the Hamiltonian of the system. The molecular structure of the Mn_5-cyanide cluster is shown in Figure 1. The metal skeleton represents a trigonal bipyramid containing two Mn(III) ions (1 and 2) in the apical positions and three Mn(II) ions (3, 4, and 5) in the equatorial positions. Each Mn(III) ion is in an almost perfect octahedral surrounding of the carbon atoms (strong cubic crystal field), and the ground term of this ion possesses a fictitious orbital angular momentum $l = 1$, and spin $s = 1$ associated with the low spin cubic term $^3T_1(t_2^4)$. This state is split into the orbital singlet $^3A_2$ (orbital basis $m_l = 0$) and the orbital doublet $^3E(m_l = \pm 1)$ due to slight distortions of the carbon octahedra along the common C_3 axis of the molecule. On the contrary, the ground state of each Mn(II) ion coordinated by the nitrogen atoms (weak cubic crystal field) is the orbital singlet $^6A_1$-$(t_2^3e^2)$. The effective Hamiltonian of the system operating within the ground $(^3T_1)_1 \otimes (^3T_1)_2 \otimes (^6A_1)_3 \otimes (^6A_1)_4 \oplus (^6A_1)_5$ manifold is as follows:

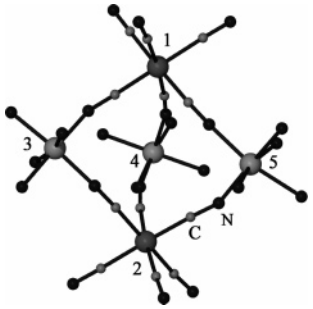

Figure 1. Molecular structure of $\{[Mn^{II}(tmphen)_2]_3[Mn^{III}(CN)_6]_2\}$: 1,2-Mn(III), 3,4,5-Mn(II).

$$H = -\kappa\lambda(\boldsymbol{s}_1\boldsymbol{l}_1 + \boldsymbol{s}_2\boldsymbol{l}_2) + \Delta({l_{1Z}}^2 + {l_{2Z}}^2 - 4/3) - 2J_{ex}(\boldsymbol{s}_1 + \boldsymbol{s}_2)(\boldsymbol{s}_3 + \boldsymbol{s}_4 + \boldsymbol{s}_5) \quad (1)$$

Here the first two terms describe the intracenter interactions for the Mn(III) ions including the spin−orbit (SO) coupling and the trigonal component of the crystal field, with λ, κ, and Δ being the many-electron SO coupling parameter, the orbital reduction factor, and the trigonal field parameter, respectively. The trigonal field parameter Δ is defined in such a way that $^3A_2$ becomes the ground term providing $\Delta > 0$. Finally, the last term in eq 1 describes the isotropic Heisenberg superexchange between Mn(II) and Mn(III) ions through the cyanide bridges. The results of paper[12] indicate that, in the Mn_5-cyanide cluster, the superexchange is antiferromagnetic, so we will consider only negative values of J_{ex}. From now on, for the spin−orbit coupling parameter and orbital reduction factor we use the values $\lambda \approx -180$ cm^{-1} and $\kappa \approx 0.8$ used in the previous simulations (see ref 12 and references therein).

3. Results and Discussion

The sign of the local magnetic anisotropy is determined by the sign of the trigonal component of the crystal field. Providing relatively strong positive trigonal field ($\Delta > 0$) each Mn(III) behaves as a spin $s = 1$ ion with the quenched (to a second order) orbital angular momentum so in this case the Mn_5-cyanide cluster can be considered as a spin-system containing two spins $s_1 = s_2 = 1$ and three spins $s_3 = s_4 =$

$s_5 = 5/2$. Since the exchange interaction is antiferromagnetic, the spin of the ground state of the whole cluster is $S = 11/2$, and the global magnetic anisotropy can be described by the second-order zero-field splitting Hamiltonian $D(s_{1Z}^2 + s_{2Z}^2)$, where D is the single ion zero-field splitting parameter. By considering the combined action of SO coupling and trigonal crystal field one obtains the following approximate result for the parameter D (that is valid in the strong trigonal field limit and accurate within λ^3/Δ^2) for a Mn(III) ion:[12]

$$D = \frac{\kappa^2\lambda^2}{\Delta} - \frac{2\kappa^3\lambda^3}{\Delta^2}$$

Providing $\Delta > 0$ the parameter D proves to be positive. Since the anisotropy of the Mn(II) ions is negligible, the molecular D_S value for the isolated ground multiplet with $S = 11/2$ (in which two spins of Mn(III) $s_1 = s_2 = 1$ are parallel being antiparallel to three spins of Mn(II) $s_3 = s_4 = s_5 = 5/2$) is also positive, thus precluding the formation of the barrier for the reversal of magnetization in the case of large positive Δ. This conclusion is valid for any positive value of Δ.

A qualitatively different situation occurs when the trigonal crystal field is negative, and the ground state of each Mn(III) ion is the trigonal ^3E term that carries first-order orbital magnetism. This orbital magnetism was shown to result in the barrier for the reversal of magnetization.[12] A satisfactory explanation of the observed temperature dependence of the static magnetic susceptibility of the Mn_5-cyanide cluster has been obtained with the best fit parameters $\Delta = -251$ cm^{-1}, $J_{ex} = -3.8$ cm^{-1}. The results demonstrate that the trigonal field plays a crucial role in the formation of the barrier in the Mn_5-cyanide cluster. From this point of view the idea to control the SMM properties by changing the crystal field appears attractive. Such a change in the crystal field is expected to be achieved by substituting ligands on the Mn(III) ions to create a mixed-ligand environment in which the terminal ligands are changed meanwhile the bridging ones remain the same in the series of new hypothetic compounds. Provided that such a substitution does not affect the CN-bridges mediating the superexchange between the Mn(II) and Mn(III), one can use the fixed value of the exchange parameter $J_{ex} = -3.8$ cm^{-1} as a starting point in the subsequent consideration. The role of the exchange will be revealed later.

To clarify the role of the trigonal field in the formation of the barrier we will first discuss the limit of strong negative trigonal field ($|\Delta| \gg \kappa|\lambda|, J_{ex}$), a case for which the ground orbital doublet is well separated from the excited orbital singlet thus preventing spin−orbital and exchange mixing of the ground $(^3E)_1 \otimes (^3E)_2 \otimes (^6A_1)_3 \otimes (^6A_1)_3 \otimes (^6A_1)_5$ manifold of the system with the excited states. In this limit the effective SO coupling operator acting within the $^3E(m_1 = \pm 1)$ term proves to be axial

$$H_{SO}(^3E) = -\kappa\lambda s_Z l_Z \qquad (2)$$

so the low-lying part of the energy pattern of a single Mn(III) ion contains three equidistant levels with the energies $-\kappa|\lambda|$, 0, and $\kappa|\lambda|$ as shown in Figure 2.

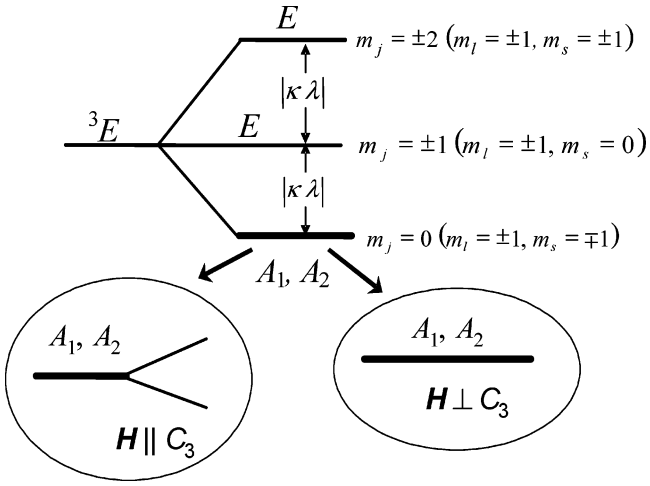

Figure 2. Spin-orbit splitting of the trigonal ^3E term and Zeeman splitting of the ground A_1, A_2 doublet.

This set of levels includes the ground accidentally degenerate level A_1, A_2 possessing the total angular momentum projection of the Mn(III) ion $m_j = 0$ ($m_l = \pm 1$, $m_s = \mp 1$) and two non-Kramers doublets E with $m_j = \pm 1$ ($m_l = \pm 1$, $m_s = 0$ and $m_j = \pm 1$, $m_s = \pm 1$). At low temperatures, when only the ground non-Kramers doublets of the Mn(III) ions are populated, one can restrict the exchange problem by considering only the ground $(A_1, A_2)_2 \otimes (A_1, A_2)_2 \otimes (^6A_1)_4 \otimes (^6A_1)_5$ manifold of the Mn_5-cyanide cluster. Moreover, since $\kappa|\lambda| \gg J_{ex}$ one can take into account only the matrix elements of the exchange interaction between the states belonging to the ground manifold thus neglecting the mixing of these states with the excited ones. This corresponds to the first order of perturbation theory with respect to the exchange coupling. A remarkable feature of the ground non-Kramers doublet of the Mn(III) ion is that this state is magnetic. In fact, in a magnetic field parallel to C_3 axis the A_1, A_2 level is split into two Zeeman sublevels with the energies

$$\langle m_l = \pm 1, m_s = \mp 1, m_j = 0|\beta(g_e s_Z - \kappa l_Z)H_Z|m_l = \pm 1, m_s \mp 1, m_j = 0\rangle = \mp\beta(g_e + \kappa)\, H_Z \quad (3)$$

This splitting is shown schematically in Figure 2. At the same time, this level is nonmagnetic in a perpendicular magnetic field because all matrix elements of the operators s_X, s_Y and l_X, l_Y vanish within the A_1, A_2 level. To describe the exchange interaction between the Mn(III) ion in the ground non-Kramers doublet state and the spin-ion Mn(II) (let us say, ions 1 and 3) one can use the following effective Hamiltonian:

$$H_{ex}^{eff}(1,3) = -4J_{ex}\tau_{1Z}\, s_{3Z} \qquad (4)$$

Here $\tau_{1Z} = (1/2)\sigma_Z$ (σ_Z is a Pauli matrix defined in a basis $|\pm 1/2\rangle$), so that eq 4 defines a pseudo-spin-1/2 Hamiltonian. The two basis states $|+1/2\rangle$ and $|-1/2\rangle$ correspond to the two components $|m_l = +1, m_s = -1\rangle$ and $|m_l = -1, m_s = +1\rangle$ of the ground non-Kramers doublet. Equation 4 shows that the initial isotropic Heisenberg exchange Hamiltonian is reduced to the fully anisotropic Ising one that is operative within the ground manifold.

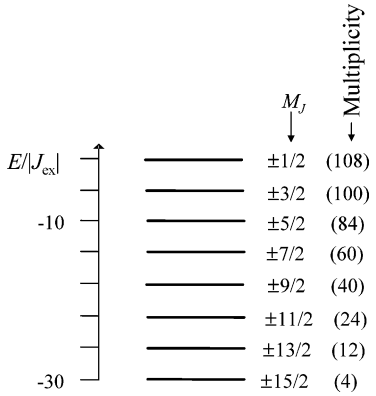

Figure 3. Eight low-lying energy levels of the Mn_5-cyanide cluster calculated with the aid of eq 7.

To find the principal values of *g*-tensor for the ground A_1, A_2 doublet one must compare the matrix of the Zeeman operator $\beta(-\kappa \boldsymbol{l} + g_e \boldsymbol{s})\boldsymbol{H}$ defined in the $m_l = \pm 1$, $m_s = \mp 1$, $m_j = 0$ basis with the matrix of the effective Zeeman operator $\beta\, \tau\, \boldsymbol{g}\, \boldsymbol{H}$ in the pseudo-spin-1/2 basis. Using eq 3 we obtain

$$g_{\parallel} = 2(\kappa + g_e),\ g_{\perp} = 0 \tag{5}$$

Then the full effective Hamiltonian of the Mn_5-cyanide cluster is given by

$$H_{\text{eff}} = -4J_{\text{ex}}(\tau_{1Z} + \tau_{2Z})(s_{3Z} + s_{4Z} + s_{5Z}) + \beta\, g_{\parallel}(\tau_{1Z} + \tau_{2Z})H_Z + g_e\beta(\boldsymbol{s_3} + \boldsymbol{s_4} + \boldsymbol{s_5})\boldsymbol{H} \tag{6}$$

The most suitable choice of the effective basis is the following: $|\sigma_1\ \sigma_2\ m_{3s}\ m_{4s}\ m_{5s}\rangle$, where σ_1, $\sigma_2 = \pm 1/2$, and m_{3s}, m_{4s}, m_{5s} take on the values $\pm 1/2$, $\pm 3/2$, $\pm 5/2$. The eigenvalues of the exchange part of the Hamiltonian, eq 6, are the following:

$$E(\sigma_{12}, M_S^{345}) = -4J_{\text{ex}}(\sigma_1 + \sigma_2)(m_{3s} + \mathrm{m}_{4s} + m_{5s}) = -4J_{\text{ex}}\sigma_{12}M_S^{345} \tag{7}$$

The corresponding eigenvectors are characterized by the total angular momentum projection defined as $M_J = M_S^{345}$, because the effective $|\sigma\rangle$ states correspond to the true $|m_j = 0\rangle$ states of the Mn(III) ions and hence the total angular momentum projection is composed of the spin projection of three Mn(II) ions. The eight low-lying energy levels calculated with the use of eq 7 are shown in Figure 3. The main feature of this energy pattern is that the absolute value of the total angular momentum projection decreases with the increase in energy, so these levels form the barrier for the reversal of magnetization. Each level is 4-fold degenerate over the signs of M_J and σ_{12}, additional factors of multiplicity are related to the spin projection $M_S^{345} = m_{3S} + m_{4S} + m_{5S}$ that can be achieved at different sets of $m_{3S} + m_{4S} + m_{5S}$. Full multiplicities increase with the decrease of M_J as indicated in Figure 3. It is also notable that these levels are equidistant, and in this aspect the present energy pattern is drastically different from that described by the zero-field splitting Hamiltonian $D_S S_Z^2$. Setting $J_{\text{ex}} = -3.8$ cm^{-1} one can roughly estimate the magnitude of the barrier as $\Delta_b = E(|M_J| = 1/2) - E(|M_J| = 15/2) = 106.4$ cm^{-1}. This value is approximately 3.5 times larger than the value $\Delta_b \approx 30$ cm^{-1} calculated in ref 12 with the set of the parameters that provide the best fit to the static magnetic susceptibility data. Although the magnitude of the barrier calculated within the simple model operating with the only non-Kramers doublet on each Mn(III) ion proves to be overestimated, the results reported here clearly indicate that the barrier can be significantly increased by variation of the strength of the trigonal crystal field.

One comment should be made concerning the possibility to regard the value Δ_b as the effective height of the barrier. Indeed this definition is approximate because it does not take into account the fact that the degeneracy of the levels rapidly increases with the decrease of $|M_J|$. The increase of degree of degeneracy leads to the population of excited levels at lower temperatures thus facilitating a more rapid magnetic moment reorientation. Despite this the value Δ_b (and especially the ratio between the Δ_b values related to different values of the trigonal field) seems to be useful as a qualitative measure of the barrier.

Now we turn from the above approximate consideration to the analysis of the results obtained by means of the diagonalization of the matrix of the initial Hamiltonian, eq 1 within the full basis set that includes the wave functions:

$$|s_1 l_1(j_1) s_2 l_2(j_2)(J_{12})\ s_3 s_4(S_{34})\ s_5(S_{345}) J M_J\rangle \tag{8}$$

This basis is defined in such a way that the orbital angular momentum of each Mn(III) ion is coupled with its spin to give the total angular momentum of the ion, the total angular momenta of two Mn(III) ions are coupled to give the total angular momentum J_{12} of the Mn(III) pair, and finally J_{12} is added to the spin S_{345} of the Mn(II) triad leading to the total angular momentum*J* of the cluster. The matrix elements are calculated with the aid of the irreducible tensor operator technique, and the details are given in ref 12.

Figure 4 demonstrates the low-lying energy levels calculated with three different values of the parameter Δ. The energies depend on the absolute value of the total angular momentum projection $M_J = m_{1j} + m_{2j} + M_S^{345}$ that reflects the axial magnetic symmetry of the system. The level with $|M_J| = 15/2$ is always the ground one, and then M_J is decreased (in general, nonmonotonically) with the increase of the energy and reaches its minimum value $|M_J| = 1/2$. This energy pattern can be associated with the barrier for the reversal of magnetization. One sees that the increase of the negative trigonal field from $\Delta = -250$ cm^{-1} to $\Delta = -10\,000$ cm^{-1} nearly triples the barrier (from 30 cm^{-1} up to 87 cm^{-1}). An additional illustration of this fact is provided by Figure 5, where the effective magnitude of the barrier defined as $\Delta_b = E(|M_J| = 1/2) - E(|M_J| = 15/2)$ is shown as a function of the parameter Δ.

At $\Delta = 0$ (isotropic limit) the energies depend on *J* rather than on M_J, and no barrier appears ($\Delta_b = 0$); on the contrary, at $\Delta \neq 0 (\Delta < 0)$ we obtain a barrier that monotonically increases with the increase of $|\Delta|$. This can be realized by inspecting two low-lying energy levels of the Mn(III) ion (the levels A_1 and A_2 with $m_j = 0$). In the limit of strong negative field when these two levels are merged into an accidentally degenerate level (Figure 2) we are dealing with the first-order angular momentum contribution to the mag-

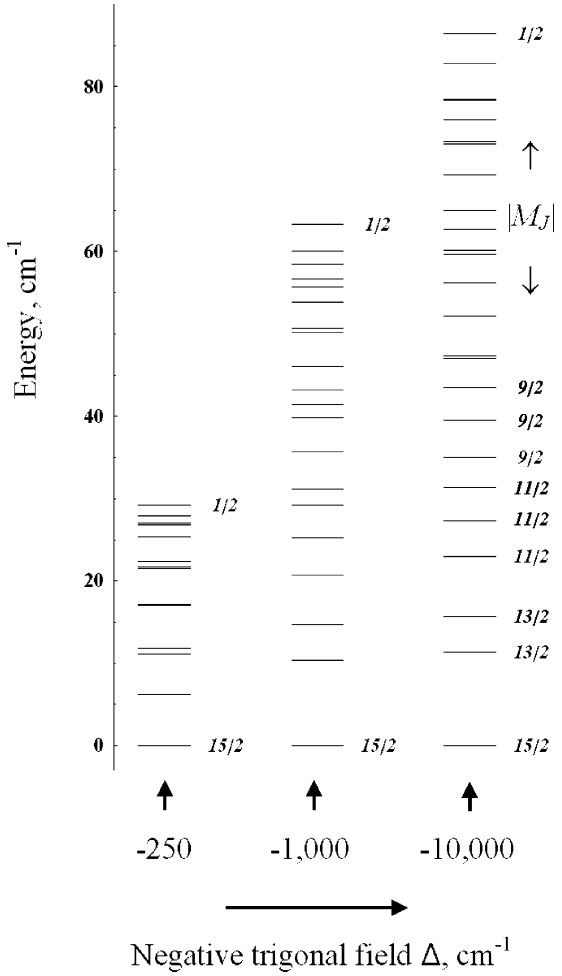

Figure 4. Low-lying energy levels calculated with $J_{ex} = -3.8$ cm^{-1} and three different values of Δ.

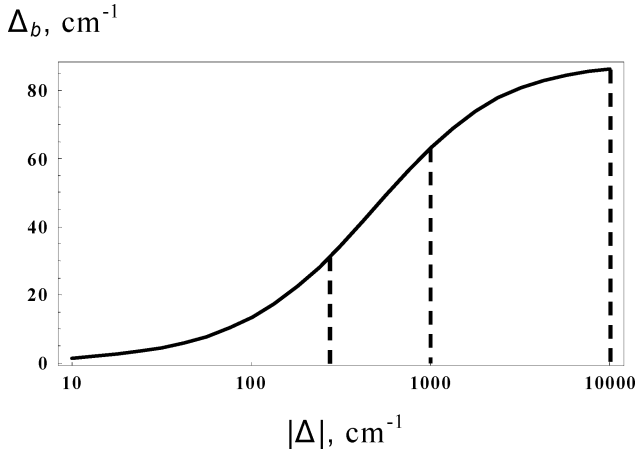

Figure 5. Magnitude of the barrier vs trigonal crystal field.

netic moment that appears due to the mixing of states A_1 and A_2 by the operator $\hat{l}_Z(A_2)$. When we pass from this axial limit toward the more symmetric case (smaller $|\Delta|$ values), this level is split into two singlets, and the first-order effect is transformed into the second-order one thus reducing the single ion anisotropy and hence the global anisotropy. Note in this context that the value $-10\,000$ cm^{-1} for the trigonal crystal field parameter does not appear to be too high as compared to the cubic one. In fact, the latter reaches the value $10\,Dq = 30\,000$ cm^{-1} in cyanide complexes.

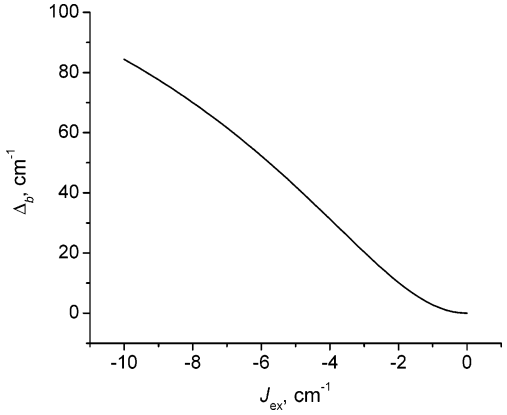

Figure 6. Magnitude of the barrier vs exchange parameter calculated with $\Delta = -250$ cm^{-1}.

The possibility to significantly increase the barrier by varying $|\Delta|$ seems to be a specific feature of cyano-bridged SMMs containing metal ions with unquenched orbital angular momenta thus distinguishing such systems from the traditional oxo-bridged SMMs. The variation of the crystal field can be achieved by substitution of the terminal ligands in a controllable way with the aid of cyanide chemistry in order to increase the barrier for magnetization reversal and the blocking temperature.

Although the magnitude of the exchange interaction Mn(II)-Mn(III) is mainly determined by the cyano bridging ligands, the variation of the terminal ligands can also be appreciable. In fact, the substitution of three ligands on the same magnetic center can change metal−metal distances and angles in the first coordination sphere and for this reason influence the exchange interaction through the bridging ligands. This influence can be especially significant when the exchange interaction is relatively small. As it follows from the approximate Hamiltonian, eq 7, the value of the plateau in the dependence height of the barrier vs trigonal field is influenced by the exchange interaction. The magnitude of the barrier as a function of the exchange coupling is shown in Figure 6 providing that the trigonal field is fixed to the value -250 cm^{-1}. One can see that the height of the barrier enhances with the increase of the antiferromagnetic exchange and thus the variation of the exchange (along with the trigonal field) can be also used to increase the barrier, although the electronic factors controlling the exchange are less evident.

Finally, a remark regarding the vibronic interaction is to be made. The adopted model is dealing with the orbitally degenerate ($^3T_{1g}$) terms of Mn(II) ions for which the vibronic Jahn−Teller (JT) interaction could be active. Accordingly to the JT theorem[13] the vibronic interaction with the nonsymmetric (JT) vibrations stabilizes the nuclear configuration corresponding to the ground orbital singlet. As it follows from the previous arguments the magnetic anisotropy in this case would be positive precluding thus the formation of the barrier. On the contrary, the orbital doublet ground state that gives the negative magnetic anisotropy cannot be achieved through the JT distortion in the adiabatic limit that justifies the employed static crystal field model. To develop and to justify a more general model that would take into

account both static crystal field and pseudo JT vibronic interaction one needs more experimental data (temperature variable single crystal EPR and magnetic data) that are presently unavailable.

Acknowledgment. B.S.T. thanks the Council for Higher Education of Israel for the financial support. Financial support of U.S. Civilian Research & Development Foundation for the Independent States of the Former Soviet Union (CRDF, award MOC2-2611-CH-04) and Moldovan Research and Development Association (MRDA, award No. MTFP-04-07 under funding from CRDF) is appreciated. K.R.D. gratefully acknowledges the Department of Energy (DOE-FG03-02ER45999).

References

(1) Awschalom, D. D.; Di Vencenzo, D. P. *Physics Today* **1995**, 43−48.

(2) Sessoli, R.; Gatteschi, D.; Caneschi, A.; Novak, M. A. *Nature* **1993**, *365*, 141−143.

(3) Gatteschi, D.; Sessoli, R. *Angew. Chem. Int. Ed.* **2003**, *42*, 268−297.

(4) Barbara, B.; Gunter, L. *Physics World* **1999**, *12*, 35−39.

(5) Borrás-Almenar, J. J.; Clemente-Juan, J. M.; Coronado, E.; Palii, A. V.; Tsukerblat, B. S. *Chem. Phys*. **2001**, *274*, 131−144; *Chem. Phys*. **2001**, *274*, 145−163.

(6) Borrás-Almenar, J. J.; Clemente-Juan, J. M.; Coronado, E.; Palii, A. V.; Tsukerblat, B. S. *J. Sol. State Chem.* **2001**, *159*, 268−280.

(7) Borrás-Almenar, J. J.; Clemente-Juan, J. M.; Coronado, E.; Palii, A. V.; Tsukerblat, B. S. *J. Chem. Phys.* **2001**, *114*, 1148−1164.

(8) Palii, A. V.; Tsukerblat, B. S.; Coronado, E.; Clemente-Juan, J. M.; Borrás-Almenar, J. J. *Inorg. Chem.* **2003**, *42*, 2455−2458.

(9) Palii, A. V.; Tsukerblat, B. S.; Coronado, E.; Clemente-Juan, J. M.; Borrás-Almenar, J. J. *J. Chem. Phys.* **2003**, *118*, 5566−5581.

(10) Mironov, V. S.; Chibotaru, L. F.; Ceulemans, A. *J. Am. Chem. Soc.* **2003**, *125*, 9750−9760.

(11) Berlinguette, C. P.; Vaughn, D.; Cañada-Vilalta, C.; Galán-Mascarós, J.-R.; Dunbar, K. R. *Angew. Chem. Int. Ed.* **2003**, *42*, 1523−1526.

(12) Palii, A. V.; Ostrovsky, S. M.; Klokishner, S. I.; Tsukerblat, B. S.; Galán-Mascarós, J. R.; Berlinguette, C. P.; Dunbar, K. R. *J. Am. Chem. Soc.* **2004**, *126*, 16860−16867.

(13) Bersuker, I. B.; Polinger, V. Z. *Vibronic Interaction in Molecules and Crystals*; Springer-Verlag: Berlin, 1989.

CT0500343

JCTC Journal of Chemical Theory and Computation

QM/MM Study of the NMR Spectroscopy of the Retinyl Chromophore in Visual Rhodopsin

José A. Gascón, Eduardo M. Sproviero, and Victor S. Batista*

Department of Chemistry, Yale University, P.O. Box 208107, New Haven, Connecticut 06520-8107

Received April 4, 2005

Abstract: The ^{1}H and ^{13}C nuclear magnetic resonance (NMR) spectra of the retinyl chromophore in rhodopsin are investigated by using quantum mechanics/molecular mechanics (QM/MM) hybrid methods at the density functional theory (DFT) B3LYP/6-31G*:Amber level of theory, in conjunction with the gauge independent atomic orbital (GIAO) method for the ab initio self-consistent-field (SCF) calculation of NMR chemical shifts. The study provides a first-principle interpretation of solid-state NMR experiments based on recently developed QM/MM computational models of rhodopsin and bathorhodopsin [Gascón, J. A.; Batista, V. S. *Biophys. J.* **2004**, *87*, 2931−2941]. The reported results are particularly relevant to the development and validation of atomistic models of prototypical G-protein-coupled receptors which regulate signal transduction across plasma membranes.

1. Introduction

G-protein-coupled membrane receptors (GPCRs) are macromolecules of great biological interest,[1−5] since they regulate signal transduction from the extracellular environment to the interior of every cell. The membrane glycoprotein rhodopsin is a prototypical GPCR present in rod cells of the retina.[4,6] Rhodopsin is particularly important in studies of GPCRs since it is the only member of the GPCR family whose crystal structure has been resolved at high-resolution. This paper investigates the ^{1}H NMR and ^{13}C NMR spectra of rhodopsin by using quantum mechanical/ molecular mechanics hybrid methods,[7−13] in conjunction with the gauge independent atomic orbital (GIAO) approach.[14,15] The study builds upon structural models recently developed in an effort to advance our understanding of the ligand binding site in a prototypical GPCR.[16]

Rhodopsin consists of 348-aa residues forming a bundle of seven transmembrane α-helices surrounding the 11-*cis* retinyl prosthetic group, a chromophore that is bound to Lys-296 via a protonated Schiff base (pSB) linkage,[17] stabilized by electrostatic interactions with the negatively charged Glu-113 counterion. Rhodopsin is responsible for triggering a signal transduction mechanism, through 11-cis/all-trans-isomerization of the retinyl ligand (see Figure 1), upon light absorption during the primary photochemical event.[17−20] The reaction produces bathorhodopsin in the ground electronic state,[21,22] with a high quantum yield within 200 fs, making it one of the fastest and most efficient photoreactions in nature.[1−3] The formation of the product bathorhodopsin is endothermic and stores approximately 50% of the photon energy.[20,23−25] The energy storage is required to promote thermal reactions in the protein bleaching sequence and in the subsequent transducin cycle. The underlying molecular rearrangements responsible for energy storage have been recently analyzed in terms of rigorous DFT QM/MM (molecular orbitals: molecular mechanics) (QM/MM-(MO:MM)) hybrid methods as applied to the refinement of high-resolution X-ray structures of bovine rhodopsin.[16]

There are currently four high-resolution structures of rhodopsin in the literature. The original 2.8 Å structure (PDB identifier 1F88)[26] is the first high-resolution structure of a GPCR revealing all the major features of the protein previously obtained from a variety of experimental data, including cryomicroscopy.[27] A refined model (PDB identifier 1HZX)[28] adds some amino acid residues not identified from the original work. A more recent structure (PDB identifier 1L9h) improves the resolution to 2.6 Å and resolves essential structural components of the chromophore binding site,

* Corresponding author e-mail: victor.batista@yale.edu.

10.1021/ct0500850 CCC: $30.25
Published on Web 06/03/2005

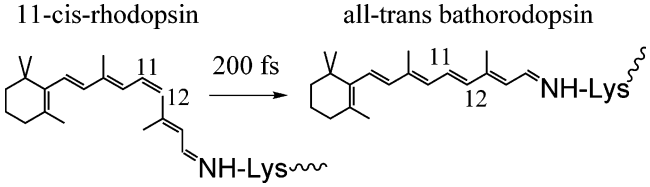

Figure 1. Photoisomerization of the retinyl chromophore in rhodopsin.

including two bound-water molecules next to the retinyl chromophore.[29] Finally, the most recent structure (PDB identifier 1U19) completely resolves the polypeptide chain at 2.2 Å resolution and provides further conformational details of the retinyl chromophore.[30] However, even with these breakthroughs in X-ray spectroscopy, the crystallographic resolution obtained so far remains insufficient to unequivocally define the parts functionally important to the chromophore binding site.[30] The reason for this seems to be that the refinement software for X-ray structures does not include parameters for chemically unusual structures such as the twisted extended π-system of the retinyl chromophore or the carboxylate group of Glu-113 interacting with the delocalized charge in the chromophore.

In the absence of an unequivocal X-ray definition of the chromophore-binding site, the elucidation of the orientation and conformation of the pSB retinyl chromophore in rhodopsin continues to be the subject of much spectroscopic analysis, including rather heroic efforts in NMR spectroscopy[21,31−44] as well as FTIR[45−47] and resonance Raman spectroscopic studies.[48−51] While the experimental data reported in these studies have been reproduced and are considered unambiguous, the theoretical interpretation of the data does not yet lead to a fully consistent molecular picture in terms of the spatial, electronic, and vibrational structure of the system.[52]

The problem to be solved involves a challenging chromophore with a polarizable π-system embedded in a classical protein environment, an ideal system for applications of quantum mechanical/molecular mechanics (QM/MM) hybrid methods. QM/MM hybrid methods,[7−12] originally due to Warshel,[53] presently offer the most rigorous available methodologies to develop atomistic models from high-resolution X-ray structures and to investigate the electronic, vibrational, and nuclear magnetic resonance (NMR) properties of challenging chromophore prosthetic groups embedded in biological molecules.[54] This paper is focused on the application of DFT QM/MM hybrid methods, in an effort to provide rigorous interpretations of NMR experiments and fundamental insight on how the structure of the ligand-binding pocket determines the spectroscopic properties and functionality of the chromophore.

Many theoretical studies on rhodopsin were performed long before the high-resolution crystallographic X-ray structures were available.[25,55−72] The early studies by Warshel and co-workers[56−58] were focused on the analysis of the photoisomerization process in terms of the semiempirical QCFF/PI method for the description of the chromophore and a description of the protein environment based on a surface of closed-packed spheres with adjustable parameters. The QCFF/PI surfaces have been recalibrated[71] on the basis of ab initio studies of the isolated chromophore[66,67] and applied to studies of bacteriorhodopsin.[71] Further, the MNDO/AM1 and INDO-PSDCI procedures have been implemented by Birge and co-workers[59,61,64] to describe the photoisomerization dynamics in terms of a one-dimensional potential model with an arbitrary rate constant for the dissipation of internal energy. However, rigorous molecular models and simulations of NMR spectroscopy were not possible since the protein structure was not known.

The availability of high-resolution X-ray structures, combined with advances in the development of QM/MM hybrid methods,[7−12] offers a great opportunity to develop rigorous atomistic models. High-resolution X-ray structures have already motivated theoretical work focused on the analysis of the geometry and electronic excitation of the retinyl chromophore. The reported studies include calculations based on classical molecular dynamics simulations,[73−75] ab initio restricted Hartree−Fock (RHF) calculations of reduced-model systems,[76,52] and QM/MM computations.[16,30,77−80]

The ^{1}H and ^{13}C NMR spectra reported in this paper are based on the atomistic computational models of rhodopsin and bathorhodopsin developed in previous work,[16] in an effort to provide an explicit and rigorous description of the influence of the opsin environment on the ^{1}H and ^{13}C NMR chemical shifts of the retinyl chromophore. The models are able to predict the energy storage and electronic excitation energies for the dark and product states in very good agreement with experimental data.[16] However, there is the nontrivial question as to whether simulations of NMR spectroscopy, based on these computational models, are able to reproduce experimental data. This paper shows the affirmative, that such models predict NMR chemical shifts in very good agreement with solid-state NMR spectra of the retinyl chromophore in rhodopsin and bathorhodopsin. In addition to the obvious advance associated with validating prototypical GPCR models, these calculations show that QM/MM geometry optimization of high-resolution structural data provides a rigorous technique to overcome the limitations of traditional refinement methods and a general approach for simulating the spectroscopy of prosthetic groups embedded in biological molecules.

The paper is organized according to the following sections. Section 2 outlines the preparation of computational models of the 11-*cis*-retinyl chromophore in rhodopsin and in chloroform solution. Section 3 outlines the computational approach, including a description of the implementation of the ONIOM electronic-embedding hybrid method for computations of ^{1}H and ^{13}C NMR chemical shifts according to the GIAO acpproach. Section 4 presents the computational results organized in five subsections: Section 4.1 reports the computed ^{1}H NMR chemical shifts of rhodopsin and the comparison to solid-state NMR data. Section 4.1 also reports the computed ^{1}H NMR chemical shifts of the pSB 11-*cis*-retinyl chromophore in chloroform solution and the comparison to the corresponding experimental data. Section 4.2 discusses the conformation of the retinyl chromophore, with emphasis on the 6s-cis and 6s-trans configurations about the C6−C7 single bond. Section 4.3 reports ^{13}C NMR chemical

shifts of the 11-*cis*-retinyl chromophore in rhodopsin and in chloroform solution as well as the corresponding comparisons to experimental data. Section 4.4 compares the computed ^{13}C NMR chemical shifts of the *all-trans*-retinyl chromophore in bathorhodopsin with available solid-state NMR data. Finally, section 4.5 compares the rhodopsin computational model investigated in this paper to other structures of bovine visual rhodopsin available in the literature. Section 5 summarizes the computational findings and concludes.

2. Computational Models

Rhodopsin. A detailed description of the computational models and methods implemented in the present QM/MM study can be found in our recent work.[16] Here, we briefly summarize the underlying methodology as follows. The rhodopsin models are based on the refinement of the crystal structure of bovine rhodopsin (Protein Data Bank (PDB) accession code 1F88, monomer A), solved at 2.8 Å resolution.[26] Starting from the 1F88 PDB crystal structures, hydrogen atoms are added by using the molecular modeling program TINKER.[81] The protonation of all titratable groups is standard. The rhodopsin cavity is set neutral, consistently with FTIR experiments.[45] The pSB linkage between Lys-296 and the chromophore bears a net positive charge NH(+) that forms a salt-bridge with the Glu-113 negative counterion.[82,83] Amino acid residues Glu-122, Asp-83, and Glu-181, all within the protein core, are assumed to be neutral, as indicated by FTIR experiments[45] and UV−vis spectroscopic measurements of site-directed mutants.[84] Finally, the regular ends of the protein and the artificial ends due to the missing or incomplete amino acids from the X-ray structures in the third cytoplasmic loop (236−239) and in the C-terminal tail (328−348) are capped with NH_3^+ and CO_2^-. The complete model system in the present calculations contains 5170 atoms with a total charge of $+4e$.

Model systems based on the crystal structure with PDB accession code 1L9H, monomer A, solved at 2.6 Å resolution[29] have also been prepared. A crucial difference between the 1F88 and 1L9H crystal structures is the presence of two water molecules next to the retinyl chromophore in the 1L9H structure not observed at the lower resolution. These two water molecules are included in the computational model investigated in this paper, since they are important to the stabilization of the chromophore inside the protein cavity. Specifically, according to the computational models implemented in this paper, these two water molecules participate in an extended hydrogen-bonding network (see Figure 2), that involves both water molecules and polar residues Glu-181, Cys-187, Ser-186, and Glu-113.[16] This structural feature associated with the extracellular loop II (EII), folded next to the chromophore, is consistent with a recently proposed counterion switch mechanism associated with a subsequent step in the rhodopsin photobleaching sequence.[85,86]

The geometry of the resulting protein model is relaxed at the ONIOM-EE (B3LYP/6-31G*:Amber) level of theory by using Gaussian G03,[87] including the retinyl chromophore, bound water molecules, and all residues within a 20 Å radius from the chromophore. The remaining environment is subject to harmonic constraints in order to preserve the overall shape of the protein.

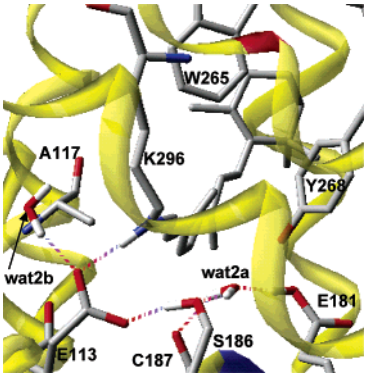

Figure 2. QM/MM optimized structure of the rhodopsin binding site, including the retinyl chromophore, the residues referenced in the text and the hydrogen bond network extending from E181 to E113.

The construction of the activated state is based on the assumption that the isomerization dynamics of the retinyl chromophore is much faster than protein relaxation. This assumption is consistent with the experimental 200 fs reaction time[21,22] as well as with the observation that the isomerization coordinate is mainly coupled to the vibrational modes of the retinyl chromophore.[50] It is also assumed that the molecular structure of the *all-trans*-retinyl chromophore in the ground-electronic state, produced by the underlying curve-crossing dynamics after photoexcitation of the system, *relaxes to the same minimum* energy configuration as when the chromophore is isomerized along the ground-state minimum energy path (MEP) subject to the constraint of fixed protein environment.[16] These assumptions are consistent with the recent observation of thermal activation of visual pigments,[88] indicating that activation by light and by heat may in fact follow the same molecular route.

The reactant and product minimum energy configurations are subsequently used for generating an ensemble of thermally accessible configurations according to importance sampling Monte Carlo, with umbrella sampling functions defined in terms of the DFT QM/MM minimum energy configurations. An ensemble of 1000 thermal configurations are generated at 300 K from a Markov chain of 900 000 configurations generated by importance sampling Monte Carlo, using Boltzmann sampling functions defined by the classical energy (e.g., the standard Amber-MM force field with additional soft-harmonic constraints relative to the QM/MM equilibrium geometries). The statistical factors (weights) of the subset of 1000 importance sampled configurations are subsequently reweighted by performing single point calculations at the ONIOM-EE(B3LYP/6-31G*:Amber) level and computing the corresponding Boltzmann factors defined by the difference of ONIOM-EE (B3LYP/6-31G*:Amber) and classical energies. The equilibrium geometry as well as the thermal fluctuations for the 11-cis conformation at 300 K compare very favorably to recently reported results of Molecular Dynamics (MD) simulations at the QM/MM(SCC-DFTB:CHARMM) level of theory,

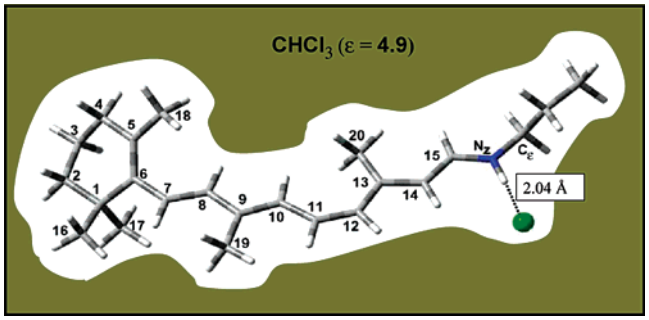

Figure 3. Optimized structure of the 11-*cis*-retinyl propylinium chloride complex embedded in a PCM solvent with $\epsilon = 4.9$ (chloroform).

where in agreement with our work, all simulated annealing minimizations converged to the same minimum energy structure.[30] Considering the usual symmetry of magnetic shielding matrix elements, relative to fluctuations around equilibrium configurations, it is therefore natural to expect that such a minimum energy configuration provides the dominant contribution to thermal ensemble averages.

pSB Model. To compare changes in the NMR spectroscopy of the retinyl chromophore inside the protein, relative to the corresponding spectrum of the chromophore in solution,[31] computational models of the 11-*cis*-retinyl propylinium−chloride complex in chloroform solution are constructed by geometry optimization at the DFT B3LYP/6-31G* level of theory of the complex embedded in a polarizable continuum model (PCM) solvent ($\epsilon_{sol} = 4.9$). Figure 3 shows the optimized configuration of the complex, where the chloride ion is located in the C=NH+plane at 2.09 Å from the proton of the Schiff-base linkage.

3. Methods

The QM/MM(MO:MM) calculations reported in this paper are based on the ONIOM two-layer hydrogen link-atom scheme.[7−13] The full system of 5170 atoms is partitioned into two layers by imposing a frontier, between the QM and MM layers, at the $C_\delta-C_\epsilon$ bond of the Lys-296 side chain (i.e., two bonds beyond the C−NH(+) linkage). The quantum mechanical (QM) layer includes 48 atoms of the retinyl chromophore, five atoms of Lys-296 (NH^+, CH_2), and a link hydrogen atom that saturates the extra valence of the terminal $-C-H_2$ at the boundary. While a QM layer that includes only the retinyl chromophore is sufficient to describe the optimum geometry of the system as well as conformational changes due to 11-cis/all-trans isomerization, the analysis of numerical convergence with respect to the size of the QM layer indicates that precise calculations of ^{1}H and ^{13}C NMR chemical shifts require a more extended QM layer. Thus single point calculations of chemical shifts explicitly consider extended QM layers including amino acid residues with significant steric interactions with the chromophore as well as nearby residues with aromatic functional groups, including Trp-265, Tyr-268, Ser-186, Cys-187, and Gly-188. Inclusion of these extra residues results in a QM layer with 80 additional atoms, including the six link-hydrogen atoms placed at the C−N bonds connecting these five residues with their neighbors. The remainder of the protein defines the MM layer.

The total energy of the system E is obtained according to the *ONIOM electronic-embedding* (ONIOM-EE) approach

$$E = E^{MM,full} + E^{QM,red} - E^{MM,red} \quad (1)$$

where $E^{MM,full}$ is the energy of the full system computed at the MM level of theory, $E^{QM,red}$ is the energy of the reduced system computed at the QM level of theory, and $E^{MM,red}$ is the energy of the reduced system computed at the MM level of theory. Electrostatic interactions between the two layers are included in the calculation of both $E^{QM,red}$ and $E^{MM,red}$ at the QM and MM levels, respectively. Therefore, the electrostatic interactions included at the MM level in both terms $E^{MM,red}$ and $E^{MM,full}$ cancel. The resulting QM description includes polarization of the reduced system as induced by the surrounding protein environment.

All calculations reported in this paper involve a description of the MM layer modeled by the standard Amber force field.[89] Shielding constants (i.e., chemical shifts) are obtained according to the GIAO method at the DFT ONIOM-EE (B3LYP/6-31G*:Amber) level of theory. The ability of the B3LYP hybrid density functional to reproduce experimental NMR shielding constants with similar basis sets is well documented.[90] Details concerning the calculation of shielding constants are not discussed in this paper since they have already been extensively reviewed in the literature.[91] However, it is important to mention that in order to facilitate the comparison between theoretical and experimental values of shielding constants, often reported relative to various different internal or external references, ab initio chemical shifts are reported relative to the reference value that minimizes the overall root-mean-squared deviation between the ab initio and experimental NMR spectra. All chemical shifts are expressed as usual in parts per million (ppm). Therefore, a chemical shift at δ ppm indicates that the nucleus responsible for the signal is magnetically unshielded relative to the reference and requires a magnetic field δ millionths less than the field needed by the reference to produce resonance.

4. Results and Discussion

4.1. Rhodopsin ^{1}H NMR. Figure 4 and Table 1 (columns 2 and 3) compare the calculated ^{1}H NMR chemical shifts of the 11-*cis*-retinyl chromophore in rhodopsin and the chemical shifts of the 11-*cis*- retinyl propylinium−chloride complex in chloroform solution to the corresponding values of experimental data. The agreement between ab initio and experimental values indicates that the computational models are able to reproduce the ^{1}H NMR spectroscopy of the chromophore in both the rhodopsin and solution environments, including the significant differences in chemical shifts between the more unshielded H atoms attached to sp^2 carbon atoms in the C7−C15 segment ($\sigma^P = 6-7$ ppm range) and the more protected sp^3 carbon atoms ($\sigma^C = 0.3-2$ ppm range) in the methyl substituent groups and the β-ionone ring.

Figure 5 and Table 1 (column 4) present the theoretical and experimental values of *changes* in the chromophore ^{1}H NMR chemical shifts, $\Delta\sigma^H = \sigma^H_{rhod} - \sigma^H_{sol}$, due to the influence of the rhodopsin environment (i.e., the opsin effects

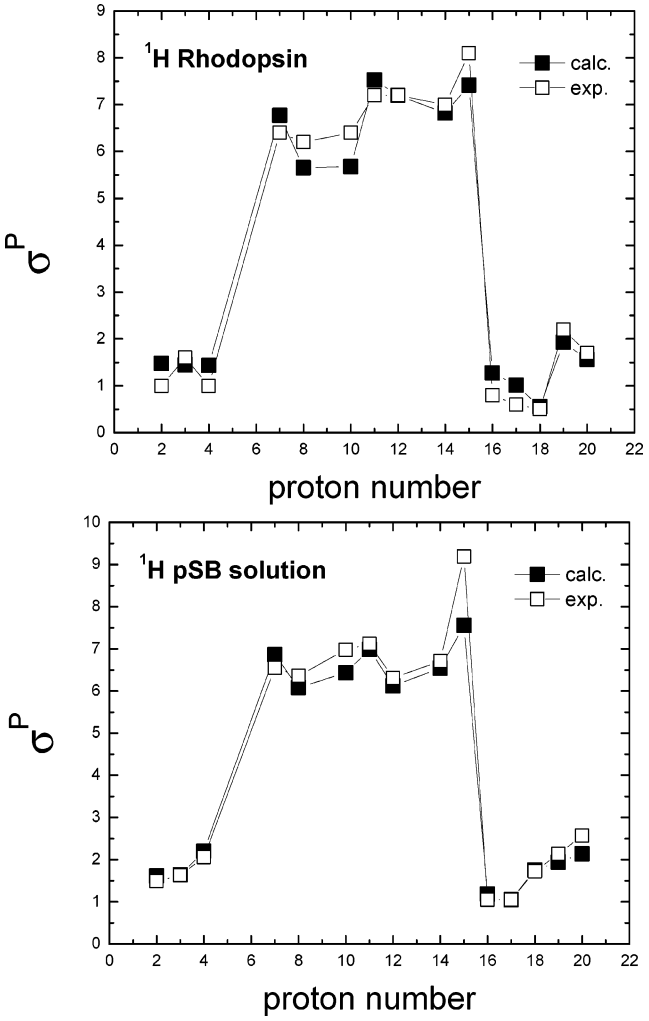

Figure 4. Comparison of ^{1}H NMR chemical shifts (in ppm) of the 11-*cis*-retinyl chromophore in rhodopsin σ^H_{rhod} (upper panel) and 11-*cis*-retinyl propylinium chloride complex in chloroform σ^H_{sol} (lower panel). H atoms are labeled as indicated in Figure 3.

on ^{1}H NMR chemical shifts). In semiquantitative agreement with the experimental data, the ab initio calculations predict that the most significant influence of the protein environment is to unshield H atoms in the C11−C14 segment, while nearby residues partially shield protons in the β-ionone ring, including H-4 and H-18. The theoretical predictions, however, underestimate changes in chemical shifts of H-15 and H-20 probably due to the oversimplified description provided by the reaction field of the PCM dielectric solvent, as indicated by the numerical deviations in Table 1 (column 3).

4.2. C6−C7 Bond Conformation. The configuration about the C6−C7 single bond of the 11-*cis* retinyl chromophore defines the orientation of the β-ionone ring relative to the polyene chain and has been the subject of debate in the literature.[32,40,42,72,92] In particular, NMR studies by Watts and co-workers[40] as well as theoretical work by Birge and co-workers[72] concluded that the chromophore geometry is 6s-trans at the C6−C7 bond, in contrast to the 6s-cis conformation assumed by earlier NMR and optical studies.[32,42,93−96] It is therefore of interest to analyze this

Table 1: Comparison of ^{1}H NMR Chemical Shifts (in ppm) of the 11-*cis*-Retinyl Chromophore in Rhodopsin σ^H_{rhod}, the 11-*cis*-Retinyl Propylinium−Chloride Complex in Chloroform Solution σ^H_{sol}, and Opsin Effects on ^{1}H NMR Chemical Shifts as Defined by $\Delta\sigma^H = \sigma^H_{rhod} - \sigma^H_{sol}$[a]

position	σ^H_{rhod}	σ^H_{sol}	$\Delta\sigma^H$
H-2	1.18 (1.0)[b]	1.61 (1.49)[c]	−0.43 (−0.49)
H-3	1.00 (1.6)[b]	1.64 (1.63)[c]	−0.64 (−0.03)
H-4	0.97 (1.0)[b]	2.20 (2.06)[c]	−1.23 (−1.06)
H-7	6.81 (6.4)[b]	6.86 (6.55)[d]	−0.05 (−0.15)
H-8	6.11 (6.2)[b]	6.09 (6.36)[d]	0.02 (−0.16)
H-10	6.19 (6.4)[b]	6.44 (6.98)[d]	−0.25 (−0.58)
H-11	7.62 (7.2)[b]	6.99 (7.12)[d]	0.63 (0.08)
H-12	7.26 (7.2)[b]	6.13 (6.31)[d]	0.13 (0.89)
H-14	6.85 (7.0)[b]	6.54 (6.71)[d]	0.31 (0.29)
H-15	7.35 (8.1)[b]	7.55 (9.19)[d]	−0.20 (−1.09)
H-16	0.89 (0.8)[b]	1.18 (1.05)[d]	−0.29 (−0.25)
H-17	0.84 (0.6)[b]	1.05 (1.05)[d]	−0.21 (−0.45)
H-18	0.28 (0.5)[b]	1.76 (1.73)[d]	−1.48 (−1.23)
H-19	2.05 (2.2)[b]	1.94 (2.14)[d]	0.11 (0.06)
H-20	1.98 (1.7)[b]	2.14 (2.57)[d]	−0.16 (−0.87)

[a] Experimental values are reported between parentheses. H atoms are labeled as indicated in Figure 3. [b] Data from ref 42. [c] Data from ref 99. [d] Data from ref 31.

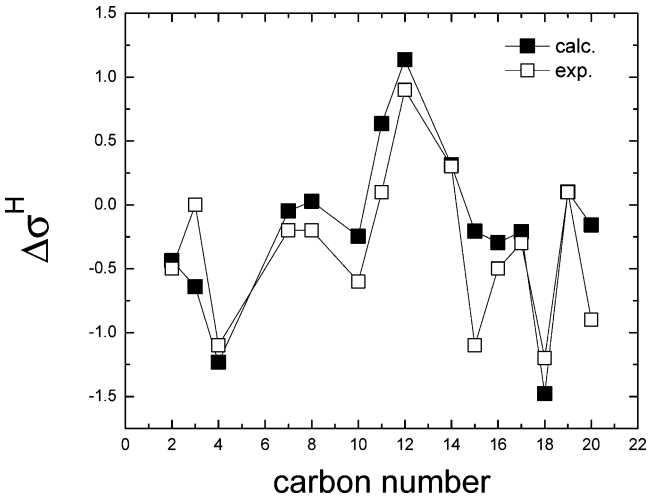

Figure 5. Comparison of theoretical and experimental values of *changes* in the ^{1}H NMR chemical shifts of the 11-*cis*-retinyl chromophore (in ppm), $\Delta\sigma^H = \sigma^H_{rhod} - \sigma^H_{sol}$, due to the influence of the rhodopsin environment (i.e., the opsin effects on ^{1}H NMR chemical shifts as described in the text).

controversial aspect by simulating the ^{1}H NMR spectra for the retinyl chromophore in rhodopsin for both the 6s-cis and 6s-trans conformations and comparing these theoretical predictions to the ^{1}H NMR experimental spectrum.

To perform these calculations, a computational model of the 6s-trans isomer was constructed by geometry relaxation of the system after rotation of the β-ionone ring around the C6−C7 bond. The resulting 6s-trans structure, obtained at the ONIOM electronic-embedding (B3LYP/6-31G*:Amber) level of theory, was found to be as stable as the 6s-cis isomer for most thermally accessible configurations and about 8 kcal/mol less stable than the 6s-cis structure when comparing minimum energy geometries. In addition, the ^{1}H NMR spectrum of the 6s-trans isomer compares much less favor-

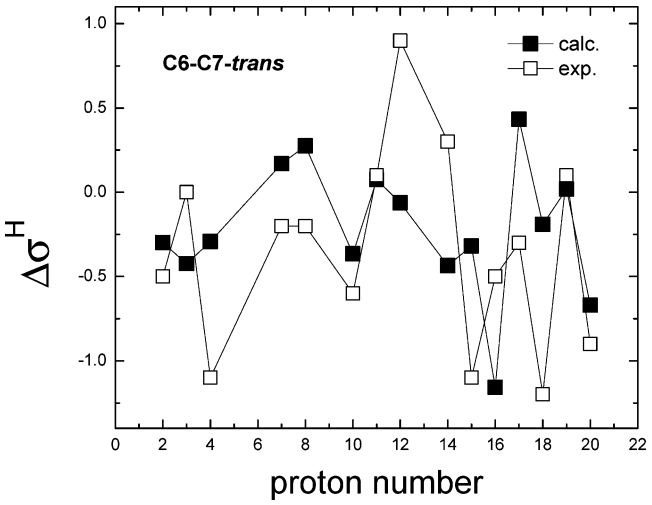

Figure 6. Changes in the ^{1}H NMR chemical shifts of the 6*s-trans*-retinyl chromophore, $\Delta\sigma^H = \sigma^H_{rhod} - \sigma^H_{sol}$, due to the influence of the rhodopsin environment. Theoretical values are compared to experimental data.

ably to experiments than the spectrum of the 6s-cis isomer, as shown in Figures 6 and 5. Figure 6 compares the opsin effects on the ^{1}H NMR chemical shifts of the 6s-trans chromophore ($\Delta\sigma^H = \sigma^H_{rhod} - \sigma^H_{sol}$) to experimental data, indicating that the 6s-trans isomer compares less favorably to experiments than the 6s-cis isomer analyzed in Figure 5.

The comparison of theoretical and experimental ^{1}H NMR chemical shifts presented in Figures 6 and 5, in conjunction with the analysis of relative stabilities, indicates that the orientation of the β-ionone ring relative to the polyene chain is consistent with the 6s-cis configuration of the retinyl chromophore at the C6−C7 single bond. The QM/MM computational models reported in this paper thus support the 6s-cis form, with substantial negative (−44°) twist of the C6−C7 bond in the minimum energy configuration.[16] These computational results are partially consistent with recent NMR studies[42,92] and with the analysis of the recently resolved X-ray structure at 2.2 Å resolution.[30]

4.3. Rhodopsin ^{13}C NMR. Figure 7 and Table 2 (columns 2 and 3) compare theoretical and experimental values of ^{13}C NMR chemical shifts of the 11-*cis*-retinyl chromophore in rhodopsin as well as the corresponding chemical shifts of the 11-*cis*-retinyl propylinium−chloride complex in chloroform solution. The agreement, shown in Figure 7, indicates that the computational models are able to reproduce the ^{13}C NMR spectroscopy of the chromophore in both rhodopsin and solution environments, including the description of significant differences in chemical shifts between the unshielded carbon atoms with sp^2 hybridization in the C7−C15 segment (σ^C = 115−160 ppm range) and the more protected sp^3 carbon atoms (σ^C = 20−40 ppm range).

A common feature of the ^{13}C NMR spectra of the pSB in rhodopsin (Figure 7, upper panel) and in solution (Figure 7, lower panel) is the zigzag alternation of chemical shifts in the C9−C15 segment of the polyene chain, where the displacement maxima at C15, C13, C11, and C9 are alternated with the minima at C14, C12, and C10. Such an alternation pattern is partially correlated with a corresponding

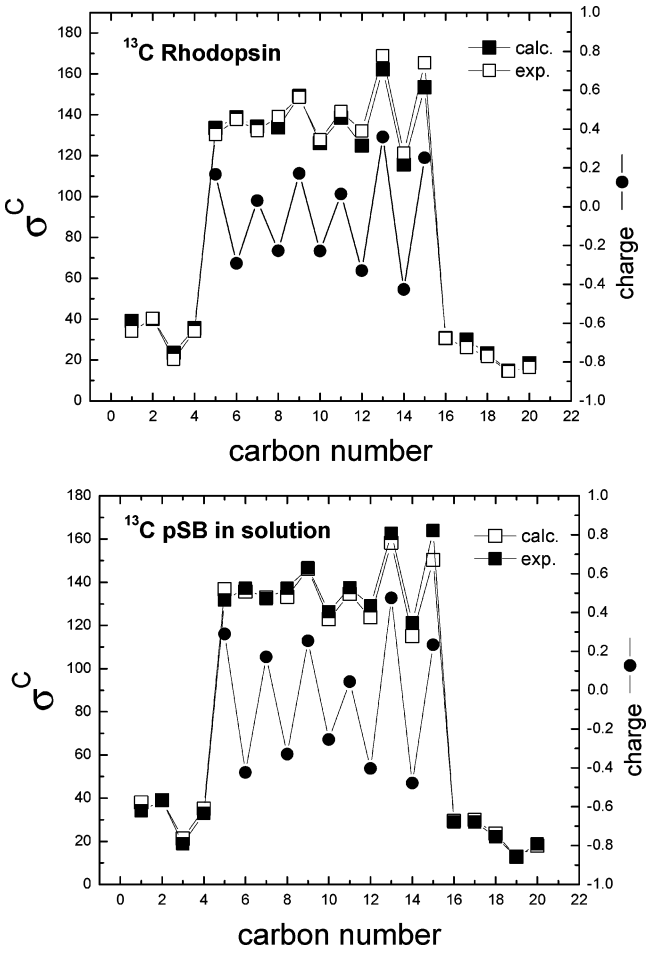

Figure 7. Comparison of ^{13}C NMR chemical shifts (in ppm) of the 11-*cis*-retinyl chromophore in rhodopsin σ^C_{rhod} (upper panel) and the 11-*cis*-retinyl propylinium−chloride complex in chloroform σ^C_{sol} (lower panel). ESP atomic charges of carbon atoms with sp^2 hybridization are reported in solid circles.

alternation of the atomic charges of carbon atoms with sp^2 hybridization along the polyene chain (see solid circles in Figure 7).

Figure 8 and Table 2 (column 4) compare theoretical and experimental values of *changes* in the chromophore ^{13}C NMR chemical shifts, $\Delta\sigma^C = \sigma^C_{rhod} - \sigma^C_{sol}$, due to the influence of the rhodopsin environment (i.e., the opsin effects on ^{13}C NMR chemical shifts). Considering that the reported experimental errors of ^{13}C NMR chemical shifts can be as large as ±1 ppm,[32,42] and larger when comparing different studies, the overall semiquantitative agreement with experimental data is quite satisfactory. The theoretical predictions, however, seem to underestimate changes in chemical shifts of C17 and C20. This is due to an overestimation of the chemical shifts of the corresponding methyl substituent groups in rhodopsin, as indicated by the numerical deviations in Table 2 (column 2). In agreement with experimental data, these results predict that the protein environment unshields all C atoms but C5 in the retinyl chromophore polyene chain.

The upfield of σ^C at C5 has been assigned to the interaction between C5 and the carboxylic group of Glu-122.[42] The calculations reported in this paper, however, indicate that the electrostatic influence of Glu-122 is negligible when such

Table 2: Comparison of ^{13}C NMR Chemical Shifts (in ppm) of the 11-*cis*-Retinyl Chromophore in Rhodopsin σ^{C}_{rhod}, the 11-*cis*-Retinyl Propylinium−Chloride Complex in Chloroform Solution σ^{C}_{sol}, and Opsin Effects on ^{13}C NMR Chemical Shifts as Defined by $\Delta\sigma^{C} = \sigma^{C}_{rhod} - \sigma^{C}_{sol}$[a]

position	σ^{C}_{rhod}	σ^{C}_{sol}	$\Delta\sigma^{C}$
C1	39.06 (34.0)[b]	37.97 (34.1)[b]	1.09 (−0.1)
C2	40.08 (40.3)[b]	39.03 (38.9)[b]	1.05 (1.4)
C3	23.45 (20.3)[b]	21.23 (18.8)[b]	2.22 (1.5)
C4	35.52 (34.0)[b]	35.13 (33.0)[b]	0.39 (1.0)
C5	133.43 (130.3)[c]	136.66 (131.7)[d]	−3.23 (−1.4)
C6	138.77 (137.7)[c]	135.69 (137.2)[d]	3.08 (0.5)
C7	134.21 (132.3)[c]	132.89 (132.3)[d]	1.32 (0.0)
C8	133.78 (139.2)[c]	133.27 (137.2)[d]	0.51 (2.0)
C9	149.09 (148.5)[c]	146.20 (146.6)[d]	2.89 (1.9)
C10	126.11 (127.8)[c]	122.94 (126.4)[d]	3.17 (1.4)
C11	138.55 (141.6)[c]	134.61 (137.5)[d]	3.94 (4.1)
C12	124.89 (132.1)[c]	123.70 (129.0)[d]	1.19 (3.1)
C13	162.18 (168.9)[c]	158.28 (162.7)[d]	3.90 (6.2)
C14	115.60 (121.2)[c]	115.04 (121.3)[d]	0.56 (−0.1)
C15	153.49 (165.4)[c]	150.31 (163.9)[d]	3.18 (1.5)
C16	30.60 (30.6)[b]	29.47 (28.9)[b]	1.13 (1.7)
C17	29.96 (26.1)[b]	29.91 (28.9)[b]	0.05 (−2.8)
C18	23.28 (21.7)[b]	23.54 (22.1)[b]	−0.26 (−0.4)
C19	14.73 (14.4)[b]	12.81 (12.6)[b]	1.92 (1.8)
C20	18.42 (16.3)[b]	17.88 (18.8)[b]	0.54 (−2.5)

[a] Experimental values are reported between parentheses. [b] Data from ref 42. [c] Data from ref 32. [d] Data from ref 31.

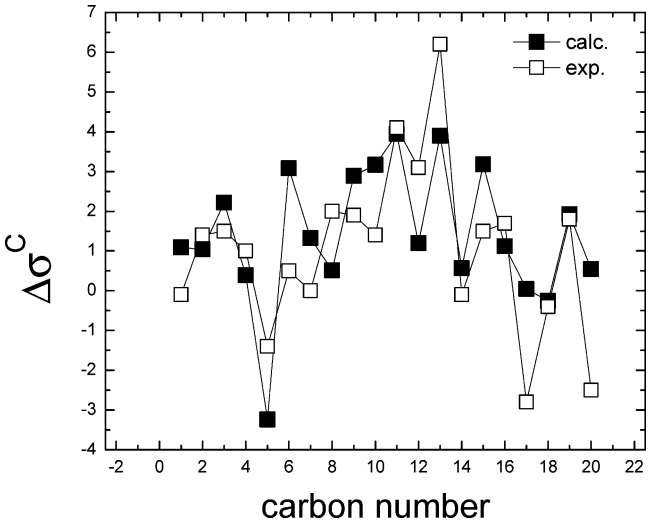

Figure 8. Comparison of theoretical and experimental values of *changes* in the ^{13}C NMR chemical shifts of the 11-*cis*-retinyl chromophore (in ppm), $\Delta\sigma^{H} = \sigma^{C}_{rhod} - \sigma^{C}_{sol}$, due to the influence of the rhodopsin environment (i.e., the opsin effects on ^{13}C NMR chemical shifts).

a residue is protonated as suggested by FTIR experiments.[45] Instead, Table 3 shows that the most important upfield effect on C5 is due to Trp-265, with an upfield of −2.0 ppm. This effect, however, is almost completely canceled by the 1.8 ppm downfield due to Asp-190. It is, therefore, concluded that the net upfield of σ^{C} at C5 is not determined by the nearby residue with the largest upfield contribution but rather by the overall polarization of the π-system, predominantly modulated by the counterion Glu-113. Further, it is predicted

Table 3: List of Residues with Significant Contribution on the Opsin Shift, $\Delta\sigma^{Ca}$

	upfield		downfield	
position	residue	$\Delta\sigma^{C}$ (ppm)	residue	$\Delta\sigma^{C}$ (ppm)
C1	Glu-122	−0.2	His-211	0.1
C2	Asp-190	−0.1	Phe-212	0.6
C3	Tyr-268	−0.2	Glu-122	0.2
C4	Leu-125	−0.2	Glu-122	0.3
C5	Trp-265	−2.0	Asp-190	1.8
C6	Glu-201	−1.0	Trp-265	0.9
C7	Tyr-191	−1.6	Cys-187	1.7
C8	Asp-190	−0.3	Trp-265	0.5
C9	Thr-118	−2.3	Cys-187	2.2
C10	Tyr-268	−1.2	Tyr-191	1.2
C11	Thr-118	−1.8	Gly-188	2.2
C12	Cys-187	−2.2	Ala-117	1.7
C13	Wat2a	−2.7	Tyr-191	0.6
C14	Cys-187	−3.0	Wat2a	3.0
C15	Ala-292	−1.6	Glu-181	0.5
C16	His-211	−0.1	Met-207	0.5
C17	Tyr-268	−0.4	Tyr-191	0.3
C18	Thr-118	−0.2	Gly-121	1.3
C19	Thr-118	−0.9	Glu-122	0.1
C20	Wat2a	−0.5	Tyr-268	0.3

[a] This table quantifies the effect on the ^{13}C NMR chemical shifts as described in the text.

that mutations of either Trp-265 or Asp-190 are expected to produce a significant effect on the ^{13}C NMR spectrum at the C5 position.

For completeness, Table 3 presents the quantitative analysis of the electrostatic influence of nearby amino acid residues on the ^{13}C NMR chemical shifts of the retinyl chromophore. Individual contributions are estimated as the difference in chemical shifts after and before zeroing the atomic charges of specific residues. For clarity, only the residues with the largest upfield and downfield effects are listed. Table 3 thus identifies the specific residues responsible for producing the most significant influence, indicating that nearby residues can cause $\Delta\sigma^{C}$ values as large as ±3 ppm for carbon atoms in the conjugate π-system (i.e., carbon atoms with sp^2 hybridization). In contrast, chemical shifts of carbon atoms with sp^3 hybridization (e.g., carbon atoms in methyl substituent groups) are found to be significantly less sensitive to the electrostatic influence of nearby polar residues (e.g., $|\Delta\sigma^{C}| < 1$ ppm).

4.4. Bathorhodopsin ^{13}C NMR. Figure 9 (upper panel) and Table 4 (second column) compare the calculated ^{13}C NMR chemical shifts of the *all-trans*-retinyl chromophore in bathorhodopsin to readily available experimental data, including ^{13}C NMR chemical shifts for C8, C10, C11, C12, C13, C14, and C15.[33] In addition, Table 4 (third column) and Figure 9 (lower panel) present theoretical and experimental values of *changes* in the chromophore ^{13}C NMR chemical shifts, $\Delta\sigma^{C} = \sigma^{C}_{batho} - \sigma^{C}_{rhod}$, due to the 11-cis/all-trans isomerization. The comparison presented in Figure 9 shows good qualitative agreement between theoretical and existing experimental data, supporting the underlying molecular rearrangements due to the primary photochemical event reported in previous work.[16]

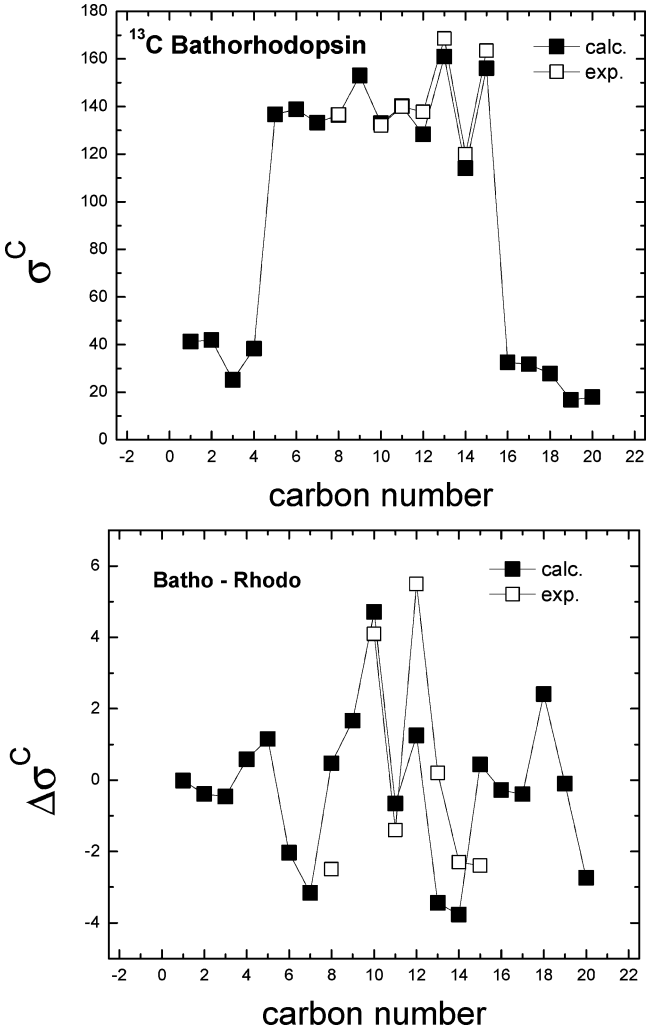

Figure 9. Comparison of ^{13}C NMR chemical shifts (in ppm) of the *all-trans*-retinyl chromophore in bathorhodopsin σ^{C}_{rhod} (upper panel) and the difference between ^{13}C NMR chemical shifts in bathorhodopsin and rhodopsin (lower panel).

The favorable comparison of theoretical and experimental values of changes in ^{13}C NMR chemical shifts, due to the cis/trans isomerization, is consistent with the agreement between theoretical and experimental values of other observables determined by the molecular rearrangements, including the endothermicity of the cis/trans isomerization as compared to calorimetry measurements and the $S_0 \rightarrow S_1$ electronic excitation energies for the dark and product states as compared to readily available spectroscopic data. It is therefore concluded that the ϕ(C11−C12) dihedral angle changes from −11° in the 11-cis isomer to −161° in the all-trans product during the primary event, as predicted in previous work,[16] where the preferential sense of rotation along negative angles is determined by steric interactions between Ala-117 and the polyene chain at the C13 position. The isomerization also induces torsion of the polyene chain due to other steric constraints in the binding pocket and stretching of the salt-bridge between the protonated Schiff-base and the Glu-113 counterion. The salt-bridge stretching is stabilized by the formation of a hydrogen bond between the protonated Schiff-base and Wat2b,[16] involving reorientation of the polarized NH+ and CH bonds localizing part of the net positive charge at the Schiff-base linkage.

Table 4: Comparison of ^{13}C NMR Chemical Shifts (in ppm) of the *all-trans*-Retinyl Chromophore in Bathorhodopsin σ^{C}_{batho} and *Changes* in the Chromophore ^{13}C NMR Chemical Shifts, $\Delta\sigma^{C} = \sigma^{C}_{batho} - \sigma^{C}_{rhod}$, Due to the 11-Cis/All-Trans Isomerization[a]

position	σ^{C}_{batho}	$\Delta\sigma^{C}$
C1	39.05	−0.01
C2	39.69	−0.39
C3	22.98	−0.46
C4	36.10	0.58
C5	134.58	1.15
C6	136.73	−2.04
C7	131.05	−3.17
C8	134.25 (136.6)[b]	0.47 (−2.5)[c]
C9	150.76	1.67
C10	130.82 (132.0)[b]	4.71 (4.1)[c]
C11	137.90 (140.0)[b]	−0.65 (−1.4)[c]
C12	126.14 (137.7)[b]	1.25 (5.5)[c]
C13	158.74 (168.5)[b]	−3.44 (0.2)[c]
C14	111.83 (120.0)[b]	−3.77 (−2.3)[c]
C15	153.92 (163.4)[b]	0.43 (−2.4)[c]
C16	30.32	−0.28
C17	29.56	−0.40
C18	25.69	2.41
C19	14.63	−0.10
C20	15.68	−2.74

[a] Experimental values are reported between parentheses. [b] Data from ref 33. [c] Data from ref 32.

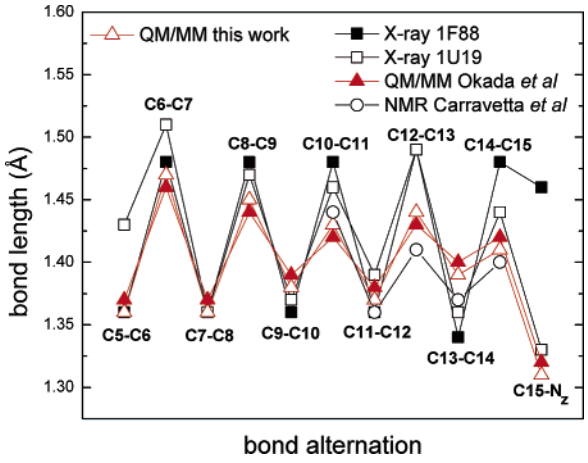

Figure 10. Bond length alternation along the polyene chain of the 11-*cis*-retinyl chromophore in rhodopsin.

4.5. Comparative Structural Analysis. After the computational studies reported in the previous sections were completed, the latest refinement of the rhodopsin crystal structure was published at 2.2 Å resolution,[30] together with a QM/MM structural analysis based on the self-consistent charge density functional tight binding (SCC-DFTB) method[97] and the CHARMM force field.[98] Therefore, it is of interest to compare the structural properties of the rhodopsin computational model analyzed in this paper to the more recently published molecular structures.

Figure 10 and Table 5 compare the chromophore bond lengths in readily available X-ray structures and QM/MM

Table 5: Comparison of the Retinyl Chromophore Bond Lengths in Readily Available X-ray Structures and QM/MM Computational Models, Including the Crystal Structures with PDB Access Code 1F88,[26] 1HZX,[28] 1L9H,[29] and 1U19,[30] the QM/MM-MD (SCC-DFTB:CHARMM) Structure,[30] and the QM/MM ONIOM-EE (B3LYP:Amber) Structure Analyzed in This Paper and in Previous Work[16]

	1F88	1HZX	1L9H	1U19	QM/MM[a]	QM/MM[b]	NMR[c]
C5−C6	1.36	1.36	1.41	1.43	1.37	1.36	
C6−C7	1.48	1.51	1.50	1.51	1.46	1.47	
C7−C8	1.36	1.38	1.37	1.36	1.37	1.36	
C8−C9	1.48	1.49	1.47	1.47	1.44	1.45	
C9−C10	1.36	1.36	1.35	1.37	1.39	1.38	
C10−C11	1.48	1.48	1.49	1.46	1.42	1.43	1.44
C11−C12	1.36	1.37	1.37	1.39	1.38	1.37	1.36
C12−C13	1.49	1.50	1.48	1.49	1.43	1.44	1.41
C13−C14	1.34	1.36	1.36	1.36	1.40	1.39	1.37
C14−C15	1.48	1.50	1.51	1.44	1.42	1.41	1.43
C15−N(Lys-296)	1.46	1.36	1.36	1.33	1.32	1.31	
N(Lys-296)−O(Glu-113)	3.28	3.58	3.08	3.36	2.60	2.74	

[a] Reference 30. [b] This work and ref 16. [c] Reference 43.

computational models, including the 1F88, 1HZX, 1L9H, and 1U19 X-ray structures, the QM/MM-MD (SCC-DFTB:CHARMM) structure,[30] and the QM/MM ONIOM-EE (B3LYP:Amber) rhodopsin model[16] considered in this paper. The comparison includes bond lengths along the polyene chain and the salt-bridge between the protonated Schiff-base and the negative counterion Glu-113. All distances but those in the last two columns are averaged over both monomers. The comparison shows that the rhodopsin computational model investigated in this work is consistent with the QM/MM-MD (SCC-DFTB:CHARMM) structure.[30] However, when QM/MM models are compared to X-ray structures, both computational models show a weaker alternation of CC bond lengths along the polyene chain (see zigzag of red triangles in Figure 10), although in partial agreement with the chromophore bond lengths predicted by a recent double-quantum solid-state NMR study (see last column of Table 5 and open circles in Figure 10).[43] Furthermore, both QM/MM models predict a shorter N(Lys-296)−O(Glu-113) distance between the Schiff-base linkage and the counterion Glu-113.

The structural differences between X-ray and QM/MM structures seem to result from difficulties faced by the X-ray refinement software when dealing with chemically unusual structures, including the twisted and extended π-system and the carboxylate group interacting with the delocalized charge of the extended chromophore. Further, the X-ray structures show significant dispersion in the reported values of bond lengths and C11−C12 dihedral angles. The latter ranges from −36° in the 1U19 crystal structure,[30] to −1° in 1F88, 8° in 1HZX, and 0° in 1L9H. In contrast, the ONIOM-EE and SCC-DFTB QM/MM models have a smaller dispersion and predict the C11−C12 dihedral angle to be −11°[16] and −18° ± 9,[30] respectively, in reasonable agreement with the value −13° suggested by molecular dynamics simulations.[74]

An important difference between the QM/MM-MD (SCC-DFTB:CHARMM) structure[30] and the QM/MM ONIOM-EE (B3LYP:Amber) rhodopsin model analyzed in this paper[16] concerns the assignment of interactions responsible for twisting the extended π-system. Okada et. al. suggested, from simple inspection of neighboring residues, that the C11−C12 negative twist is due to interactions with the Trp-265 residue.[30] In contrast, the QM/MM ONIOM-EE model predicts that the torque responsible for the C11−C12 dihedral twist is mainly due to steric interactions between the methyl group of Ala-117 and the polyene chain at the C13 position.[16] These results are obtained from an analysis of the decomposition of forces acting on the chromophore at its equilibrium configuration in the binding site.

5. Concluding Remarks

We have shown how to investigate the ^{1}H NMR and ^{13}C NMR spectra of the retinyl chromophore in rhodopsin by using recently developed QM/MM computational models, in conjunction with the GIAO method for ab initio SCF calculations of NMR chemical shifts at the DFT (B3LYP/6-31G*:Amber) level of theory. The reported results indicate that the QM/MM models describe the NMR spectroscopy of the retinyl chromophore in rhodopsin in very good agreement with solid-state NMR experiments, including opsin effects on NMR chemical shifts and *changes* in the chromophore chemical shifts due to 11-cis/all-trans isomerization in rhodopsin. These findings are particularly relevant to the development and validation of fully atomistic models of prototypical G-protein-coupled receptors.

We have demonstrated that the 6s-cis/6s-trans configurational change, about the C6−C7 single bond of the 11-cis retinyl chromophore, significantly affects the ^{1}H NMR chemical shifts of the chromophore. The comparison of theoretical and experimental ^{1}H NMR spectra indicates that the 6s-cis isomer is the most likely structure in the dark state of rhodopsin. This conclusion is consistent with the analysis of relative stabilities, indicating that the 6s-cis configuration is 8 kcal/mol more stable than the 6s-trans configuration when comparing minimum energy structures.

We have shown that the QM/MM computational models reveal significant bond length alternation in the C5−C9 segment of the polyene chain. Such a bond length alternation pattern becomes weaker along the π-system near the Schiff-base linkage, in partial agreement with the chromophore bond lengths predicted by double-quantum solid-state NMR experiments.[43]

We found that ^{1}H NMR chemical shifts are considerably more sensitive than ^{13}C NMR chemical shifts to changes in the chromophore environment (e.g., from solution to the protein environment). In particular, the ^{1}H NMR spectra is found to be significantly influenced by nearby polar residues and residues with aromatic functional groups (e.g., Trp-265 and Tyr-268). Reliable QM/MM simulations of NMR chemical shifts thus require including these crucial residues in the QM layer, predicting specific phenotypes that affect the magnetic environment of the retinyl chromophore in rhodopsin.

Finally, we conclude that the QM/MM refinement of high-resolution structural data provides a rigorous technique to overcome limitations of traditional X-ray refinement methods

and a general approach to simulate the NMR spectroscopy of challenging prosthetic groups embedded in biological molecules.

Acknowledgment. V.S.B. acknowledges supercomputer time from the National Energy Research Scientific Computing (NERSC) Center and financial support from Research Corporation, Research Innovation Award # RI0702, a Petroleum Research Fund Award from the American Chemical Society PRF # 37789-G6, a junior faculty award from the F. Warren Hellman Family, the National Science Foundation (NSF) Career Program Award CHE # 0345984, the NSF Nanoscale Exploratory Research (NER) Award ECS # 0404191, the Alfred P. Sloan Fellowship from the Sloan Foundation, and start-up package funds from the Provost's office at Yale University. The authors are grateful to Mr. Sabas Abuabara for proofreading the manuscript.

References

(1) Ji, T.; Grossmann, M.; Ji, I. *J. Biol. Chem.* **1998**, *273*, 17299−17302.

(2) Gether, U.; Kobilka, B. *J. Biol. Chem.* **1998**, *273*, 17979−17982.

(3) Marinissen, M.; Gutkind, J. *Trends. Pharmacol. Sci.* **2001**, *22*, 368−376.

(4) Meng, E.; Bourne, H. *Trends. Pharmacol. Sci.* **2001**, *22*, 587−593.

(5) Baldwin, J.; Schertler, G.; Unger, V. *J. Mol. Biol.* **1997**, *272*, 144−164.

(6) Hamm, H. *Proc. Natl. Acad. Sci. U.S.A.* **2001**, *98*, 4819−4821.

(7) Maseras, M.; Morokuma, K. *J. Comput. Chem.* **1995**, *16*, 1170−1179.

(8) Svensson, M.; Humbel, S.; Froese, R.; Matsubara, T.; Sieber, S.; Morokuma, K. *J. Phys. Chem.* **1996**, *100*, 19357−19363.

(9) Humbel, S.; Sieber, S.; Morokuma, K. *J. Chem. Phys.* **1996**, *105*, 1959−1967.

(10) Dapprich, S.; Komaromi, K.; Byun, K.; Morokuma, K.; Frisch, M. *J. Mol. Struct. (THEOCHEM)* **1999**, *461*, 1−21.

(11) Vreven, T.; Morokuma, K. *J. Comput. Chem.* **2000**, *16*, 1419−1432.

(12) Vreven, T.; Mennucci, B.; daSilva, C.; Morokuma, K.; Tomasi, J. *J. Chem. Phys.* **2001**, *115*, 62−72.

(13) Vreven, T.; Morokuma, K. *Theor. Chem. Acc.* **2003**, *109*, 125−132.

(14) Ditchfield, R. *Mol. Phys.* **1974**, *27*, 789−807.

(15) Wolinski, K.; Hinton, J. F.; Pulay, P. *J. Am. Chem. Soc.* **1990**, *112*, 8251−8260 (and references therein).

(16) Gascon, J. A.; Batista, V. S. *Biophys. J.* **2004**, *87*, 2931−2941.

(17) Wald, G. *Science* **1968**, *162*, 230−239.

(18) Goldschmidt, C.; Ottolenghi, M.; Rosenfeld, T. *Nature* **1976**, *263*, 169−171.

(19) Rosenfeld, T.; Honig, B.; Ottolenghi, M.; Hurley, J.; Ebrey, T. *Pure Appl. Chem.* **1977**, *49*, 341−351.

(20) Honig, B.; Ebrey, T.; Callender, R.; Dinur, U.; Callender, R. *Proc. Natl. Acad. Sci. U.S.A.* **1979**, *76*, 2503−2507.

(21) Schoenlein, R.; Peteanu, L.; Mathies, R.; Shank, C. *Science* **1991**, *254*, 412−415.

(22) Wang, Q.; Schoenlein, R.; Peteanu, L.; Mathies, R.; Shank, C. *Science* **1994**, *266*, 422−424.

(23) Cooper, A. *FEBS Lett.* **1979**, *100*, 382−384.

(24) Cooper, A. *Nature* **1979**, *282*, 531−533.

(25) Schick, G.; Cooper, T.; Holloway, R.; Murray, L.; Birge, R. *Biochem.* **1987**, *26*, 2556−2562.

(26) Palczewski, K.; Kumasaka, T.; Hori, T.; Behnke, C.; Motoshima, H.; Fox, B.; Le Trong, I.; Teller, D.; Okada, T.; Stenkamp, R.; Yamamoto, M.; Miyano, M. *Science* **2000**, *289*, 739−745.

(27) Schertler, G.; Hargrave, P. *Methods Enzymol.* **2000**, *315*, 91−107.

(28) Teller, D.; Okada, T.; Behnke, C.; Palczewki, K.; Stenkamp, R. *Biochemistry* **2001**, *40*, 7761−7772.

(29) Okada, T.; Yoshinori, Y.; Silow, M.; Navarro, J.; Landau, J.; Schichida, Y. *Proc. Natl. Acad. Sci.* **2002**, *99*, 5982−5987.

(30) Okada, T.; Sugihara, M.; Bondar, A.; Elstner, M.; Entel, P.; Buss, V. *J. Mol. Biol.* **2004**, *342*, 571−583.

(31) Shriver, J. W.; Mateescu, G. D.; Abrahamson, E. W. *Biochemistry* **1979**, *18*, 4785−4792.

(32) Smith, S. O.; Palings, I.; Miley, M. E.; Courtin, J.; de Groot, H.; Lugtenburg, J.; Mathies, R. A.; Griffin, R. G. *Biochemistry* **1990**, *29*, 8158−8164.

(33) Smith, S. O.; Courtin, J.; de Groot, H.; Gebhard, R.; Lugtenburg, J. *Biochemistry* **1991**, *30*, 7409−7415.

(34) Wang, Q.; Kochendoerfer, G.; Schoenlein, R.; Verdegem, P.; Lugtenburg, J.; Mathies, R.; Shank, C. *J. Phys. Chem.* **1996**, *100*, 17388−17394.

(35) Feng, X.; Verdegem, P. J. E.; Lee, Y. K.; Sandström, D.; Edén, M.; Bovee-Geurts, P. H. M.; de Grip, W. J.; Lugtenburg, J.; Levitt, M. H. *J. Am. Chem. Soc.* **1997**, *119*, 6853−6857.

(36) Gröbner, G.; Choi, G.; Burnett, I. J.; Glaubitz, C.; Verdegem, P. J. E.; Lugtenburg, J.; Watts, A. *FEBS Lett.* **1998**, *422*, 201−204.

(37) Creemers, A. F. L.; Klaasen, C. H. W.; Bovee-Geurts, P. H. M.; Kelle, R.; Kragl, U.; Raap, J.; de Grip, W. J.; Lugtenburg, J.; de Groot, H. J. M. *Biochemistry* **1999**, *38*, 7195−7199.

(38) Verdegem, P. J. E.; Bovee-Geurts, P. H. M.; de Grip, W. J.; Lugtenburg, J.; de Groot, H. J. M. *Biochemistry* **1999**, *38*, 11316−11324.

(39) Feng, X.; Verdegem, P. J. E.; Eden, M.; Sandström, D.; Lee, Y. K.; Bovee-Geurts, P. H. M.; de Grip, W. J.; Lugtenburg, J.; de Groot, H. J. M.; Levitt, M. H. *J. Biomol. NMR* **2000**, *16*, 1−8.

(40) Gröbner, G.; Burnett, I. J.; Glaubitz, C.; Choi, G.; Mason, A. J.; Watts, A. *Nature* **2000**, *405*, 810−813.

(41) Verhoeven, M.; Creemers, A.; Bovee-Geurts, P. H. M.; deGrip, W.; Lugtenburg, J.; de Groot, H. J. M. *Biochemistry* **2001**, *40*, 3282−3288.

(42) Creemers, A. F. L.; Kiihne, S.; Bovee-Geurts, P. H. M.; DeGrip, W. J.; Lugtenburg, J.; de Groot, H. J. M. *Proc. Natl. Acad. Sci.* **2002**, *99*, 9101−9106.

(43) Carravetta, M.; Zhao, X.; Johannessen, O. G.; Lai, W. C.; Verhoeven, M. A.; Bovee-Geurts, P. H. M.; Verdegem, P. J. E.; Kiihne, S.; Luthman, H.; de Groot, H. J. M.; deGrip, W. J.; Lugtenburg, J.; Levitt, M. H. *J. Am. Chem. Soc.* **2004**, *126*, 3948−3953.

(44) Crocker, E.; Patel, A.; Eilers, M.; Jayaraman, S.; Getmanova, E.; Reeves, P.; Ziliox, M.; Khorana, H.; Sheves, M.; Smith, S. *J. Biomol. NMR* **2004**, *29*, 11−20.

(45) Fahmy, K.; Jäger, F.; Beck, M.; Zvyaga, T. A.; Sakmar, T. P.; Siebert, F. *Proc. Natl. Acad. Sci.* **1993**, *90*, 10206−10210.

(46) Fahmy, K.; Zvyaga, T.; Sakmar, T.; Siebert, F. *Biochemistry* **1996**, *35*, 15065−15073.

(47) Zvyaga, T.; Fahmy, K.; Siebert, F.; Sakmar, T. *Biochemistry* **1996**, *35*, 7536−7545.

(48) Deng, H.; Callender, R.; Rodman, H.; Honig, B. *Biophys. J.* **2001**, *51*, A268−A268.

(49) Eyring, G.; Curry, B.; Broek, A.; Lugtenburg, J.; Mathies, R. A. *Biochemistry* **1982**, *21*, 384−394.

(50) Palings, I.; Pardoen, J.; Van den Berg, E.; Winkel, C.; Lugtenburg, J.; Mathies, R. *Biochemistry* **1987**, *26*, 2544−2556.

(51) Lin, S. W.; Groesbeek, M.; van der Hoef, I.; Verdegem, P.; Lugtenburg, J.; Mathies, R. A. *J. Phys. Chem. B* **1998**, *102*, 2787−2806.

(52) Touw, S.; de Groot, H. J. M.; Buda, F. *J. Phys. Chem. B* **2004**, *108*, 13560−13572.

(53) Warshel, A.; Levitt, M. *J. Mol. Biol.* **1976**, *103*, 227−249.

(54) Karadakov, P.; Morokuma, K. *Chem. Phys. Lett.* **2000**, *317*, 589−596.

(55) Warshel, A.; Karplus, M. *J. Am. Chem. Soc.* **1974**, *96*, 5677−5689.

(56) Warshel, A. *Nature* **1976**, *260*, 679−683.

(57) Weiss, R.; Warshel, A. *J. Am. Chem. Soc.* **1979**, *101*, 6131−6133.

(58) Warshel, A.; Barboy, N. *J. Am. Chem. Soc.* **1982**, *104*, 1469−1476.

(59) Birge, R.; Hubbard, L. *J. Am. Chem. Soc.* **1980**, *102*, 2195−2205.

(60) Birge, R. *Annu. Rev. Biophys. Bioeng.* **1981**, *10*, 315−354.

(61) Birge, R.; Cooper, T. *Biophys. J.* **1983**, *42*, 61−69.

(62) Car, R.; Parrinello, M. *Phys. Rev. Lett.* **1985**, *55*, 2471−2474.

(63) Pastore, G.; Smargiassi, E.; Buda, F. *Phys. Rev. A* **1991**, *44*, 6334−6347.

(64) Tallent, J.; Hyde, E.; Findsen, L.; Fox, G.; Birge, R. *J. Am. Chem. Soc.* **1992**, *114*, 1581−1592.

(65) Bifone, A.; de Groot, H. J. M.; Buda, F. *J. Phys. Chem. B* **1997**, *101*, 2954−2958.

(66) Vreven, T.; Bernardi, F.; Garavelli, M.; Olivucci, M.; Robb, M.; Schlegel, H. B. *J. Am. Chem. Soc.* **1997**, *119*, 12687−12688.

(67) Garavelli, M.; Vreven, T.; Celani, P.; Bernardi, F.; Robb, M.; Olivucci, M. *J. Am. Chem. Soc.* **1998**, *120*, 1285−1288.

(68) La Penna, G.; Buda, F.; Bifone, A.; de Groot, H. J. M. *Chem. Phys. Lett.* **1998**, *294*, 447−453.

(69) Molteni, C.; Frank, I.; Parrinello, M. *J. Am. Chem. Soc.* **1999**, *121*, 12177−12183.

(70) Birge, R.; Vought, B. *Method. Enzymol.* **2000**, *315*, 143−163.

(71) Warshel, A.; Chu, Z. *J. Phys. Chem. B* **2001**, *105*, 9857−9871.

(72) Singh, D.; Hudson, B. S.; Birge, R. R. *Biochemistry* **2001**, *40*, 4201−4204.

(73) Rohrig, U.; Guidoni, L.; Rothlisberger, U. *Biochemistry* **2002**, *41*, 10799−10809.

(74) Saam, J.; Tajkhorshid, E.; Hayashi, S.; Schulten, K. *Biophys. J.* **2002**, *83*, 3097−3112.

(75) Furutani, Y.; Shichida, Y.; Kandori, H. *Biochemistry* **2003**, *42*, 9619−9625.

(76) Yamada, A.; Kakitani, T.; Yamamoto, S.; Yamato, T. *Chem. Phys. Lett.* **2002**, *366*, 670−675.

(77) Sugihara, M.; Buss, V.; Entel, P.; Elstner, M.; Frauenheim, T. *Biochemistry* **2002**, *41*, 15259−15266.

(78) Sugihara, M.; Entel, P.; Buss, V. *Phase Transit.* **2002**, *75*, 11−17.

(79) Ferre, N.; Olivucci, M. *J. Am. Chem. Soc.* **2003**, *125*, 6868−6869.

(80) Andruniow, T.; Ferre, N.; Olivucci, M. *Proc. Natl. Acad. Sci.* **2004**, *101*, 17908−17913.

(81) Ponder, J. W. *Tinker, version 3.9*; Washington University School of Medicine, St. Louis, MO, 2001.

(82) Sakmar, T.; Franke, R.; Khorana, H. *Proc. Natl. Acad. Sci. U.S.A.* **1989**, *86*, 8309−8313.

(83) Zhukovsky, E.; Oprian, D. *Science* **1989**, *246*, 928−930.

(84) Yan, E.; Kazmi, M.; De, S.; Chang, B.; Seibert, C.; Marin, E.; Mathies, R.; Sakmar, T. *Biochemistry* **2002**, *41*, 3620−3627.

(85) Birge, R. R.; Knox, B. E. *Proc. Natl. Acad. Sci.* **2003**, *100*, 9105−9107.

(86) Yan, E. C. Y.; Kazmi, M. A.; Ganim, Z.; Hou, J.; Pan, D.; Chang, B. S. W.; Sakmar, T. P.; Mathies, R. A. *Proc. Natl. Acad. Sci.* **2003**, *100*, 9262−9267.

(87) Frisch, M. J. et al. *Gaussian 03, Revision A.1*; Gaussian, Inc., Pittsburgh, PA, 2003.

(88) Ala-Laurila, P.; Donner, K.; Koskelainen, A. *Biophys. J.* **2004**, *86*, 3653−3662.

(89) Cornell, W. D.; Cieplak, P.; Bayly, C. I.; Gould, I. R.; Merz, K. M.; Ferguson, D. M.; Spellmeyer, D. C.; Fox, T.; Caldwell, J. W.; Kollman, P. A. *J. Am. Chem. Soc.* **1995**, *117*, 5179−5197.

(90) Wiberg, K. *J. Comput. Chem.* **1999**, *20*, 1299−1303.

(91) Helgaker, T.; Jaszuriski, M.; Ruud, K. *Chem. Rev.* **1999**, *99*, 293−352.

(92) Spooner, P. J. R.; Sharples, J. M.; Goodall, S. C.; Seedorf, H.; Verhoeven, M. A.; Lugtenburg, J.; Bovee-Geurts, P. H. M.; DeGrip, W. J.; Watts, A. *Biochemistry* **2003**, *42*, 13371−13378.

(93) Smith, S. O.; Palings, I.; Copie, V.; Raleigh, D.; Courtin, J.; Pardoen, J.; Lugtenburg, J.; Mathies, R.; Griffin, R. G. *Biochemistry* **1987**, *26*, 1606−1611.

(94) Tan, Q.; Lou, J.; Borhan, B.; Karnaukhova, E.; Berova, N.; Nakanishi, K. *Angew. Chem., Int. Ed. Engl.* **1997**, *36*, 2089−2093.

(95) Jäger, S.; Lewis, J.; Zvyaga, T.; Szundi, I.; Sakmar, T.; Kliger, D. *Proc. Natl. Acad. Sci.* **1997**, *94*, 8557−8562.

(96) Buss, V.; Kolster, K.; Terstegen, F.; Vahrenhorst, R. *Angew. Chem., Int. Ed. Engl.* **1998**, *37*, 18893−18895.

(97) Elstner, M.; Porezag, D.; Jungnickel, G.; Elsner, J.; Haugk, M.; Frauenheim, T.; Suhai, S.; Seifert, G. *Phys. Rev. B* **1998**, *58*, 7260−7268.

(98) MacKerell, A. D. et al. *J. Phys. Chem. B* **1998**, *102*, 3586−3616.

(99) Elia, G. R.; Childs, R. F.; Britten, J. F.; Yang, D. S. C.; Santarsiero, B. D. *Can. J. Chem.* **1996**, *74*, 591−601.

CT0500850

JCTC Journal of Chemical Theory and Computation

Catalytic Reaction Mechanism of Oxalate Oxidase (Germin). A Hybrid DFT Study

Tomasz Borowski,*,† Arianna Bassan,† Nigel G. J. Richards,# and Per E. M. Siegbahn†

Department of Physics, Stockholm Center for Physics, Astronomy and Biotechnology, Stockholm University, S-106 91, Stockholm, Sweden, and Department of Chemistry, University of Florida, Gainesville, Florida 32611-7200

Received February 25, 2005

Abstract: The mechanism of the catalytic reaction for oxalate oxidase has been investigated with the hybrid density functional method B3LYP. The models used in the calculations comprise of the manganese ion, three imidazoles, and one acetate, which model the active-site Mn(II) and its first-shell protein ligands. Moreover, the reactants, i.e., singly protonated oxalate and dioxygen, have been explicitly considered. The computational results suggest that the enzyme−oxalate complex can adopt two conformations, one with bidentate oxalate and 6-coordinate manganese and the second one with monodentate substrate and coordinatively unsaturated Mn(II). This second species reacts with dioxygen on the quartet potential energy surface, and in a rate-limiting step yields one CO_2 molecule and a reactive intermediate, in which Mn(III) is coordinated by HOO^- and a formyl radical anion. A subsequent fast spin transition, from the quartet to the sextet spin state, allows an electron transfer from the formyl radical anion to Mn(III) and leads to the product−enzyme complexes. It is proposed that the final step of the catalytic cycle involves protonation of these species and release of products. Taken together, the mechanistic proposal presented in this work agrees well with the available experimental data and provides an explanation for the very efficient coupling between the two-electron dioxygen reduction and oxalate oxidation performed by oxalate oxidase.

I. Introduction

Oxalate oxidase, also known as germin, hereafter abbreviated as Oxo, is a protein germination marker usually found in the cereals embryos. Although its role in plant development is still not fully understood, the Oxo catalyzed degradation of oxalate (Scheme 1) releases H_2O_2 which is needed for cross-linking in cell wall and may also promote tissue remodeling.[1] Moreover, some pathogens utilize oxalic acid to reduce pH and in this way stimulate polysaccharolytic enzymes, which digest the plant tissues. For this reason, transgenic crops with elevated Oxo expression are less prone to infection due to their efficiency in oxalic acid decomposition. Finally, Oxo is used as an analytical enzyme in procedures for determination of oxalic acid levels. The reader interested in the broader picture of oxalate metabolism and its enzymology is referred to the currently published review.[2]

Scheme 1: Oxo Catalytic Reaction

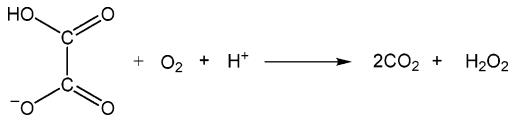

Biochemical studies showed that Oxo is a homohexameric enzyme binding one manganese ion per subunit.[3,4] Since neither flavins nor other transition metals are required for the catalysis, it was proposed that Mn(II) plays an active role in the enzymatic mechanism.[4,5] Barley Oxo shows maximum activity at pH 3.8, which falls between the two pK_a values for oxalic acid, namely 1.2 and 4.1. This, in turn, indirectly indicates that the singly protonated form of oxalate is the reactive species binding to Oxo.[5,6] Further important

* Corresponding author phone: +46 8 55378703; fax: +46 8 55378601; e-mail: borowski@physto.se.
† Stockholm University.
# University of Florida.

10.1021/ct050041r CCC: $30.25
Published on Web 04/29/2005

Scheme 2: Experiment Suggested Mechanisms for the Oxo Catalytic Reaction

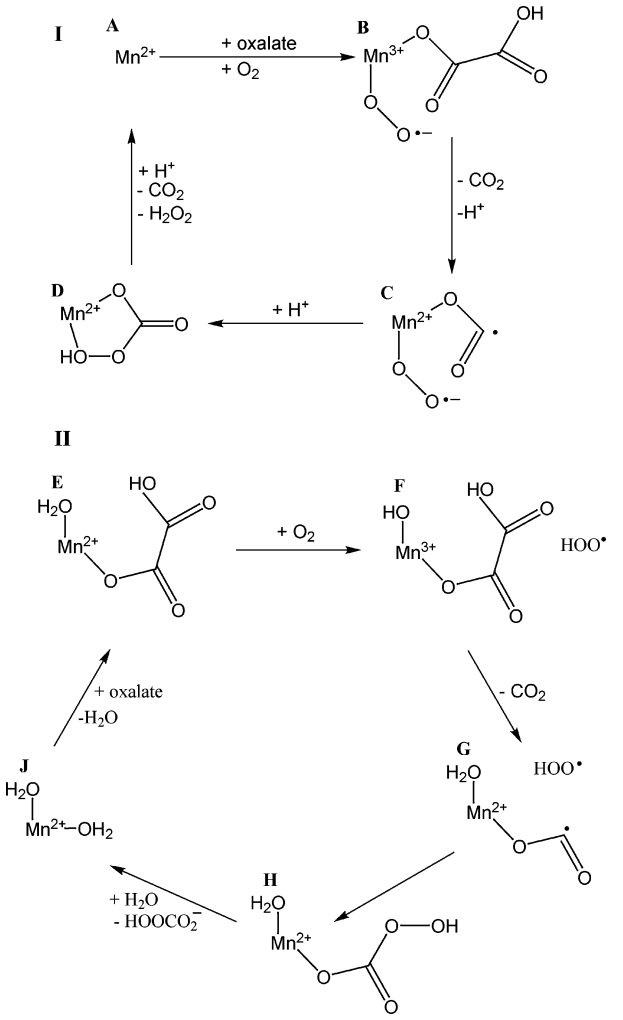

data concerning the reaction mechanism were provided by EPR measurements done both for the native enzyme and under turnover conditions.[6] Notably, it was shown that the native form of Oxo binds high-spin Mn(II) in roughly octahedral environment and that this site is not perturbed in the presence of H_2O_2, which is one of the catalytic reaction products. However, addition of oxalate alters the EPR signal, which indicates that the substrate directly coordinates Mn(II). Like for the native form, the EPR spectrum for this enzyme−substrate complex was found to be consistent with the six-coordinate Mn(II) site. Importantly, the measurements under turnover conditions showed that no free radicals are released into solution, which inevitably implies a tight coupling between dioxygen reduction and oxalate oxidation. In the same study[6] it was found that a minor fraction of the isolated enzyme (ca. 5%) binds high-spin Mn(III) ion in a distorted octahedral environment. Under anaerobic conditions this species reacts with oxalate producing Mn(II) and carboxylate radicals, which demonstrates that the Mn(III) form of the Oxo active site is capable of oxalate oxidation. However, the EPR study under turnover conditions ruled out the possibility that this Mn(III) form of Oxo is catalytically competent. Taken together, the experimental data led to the mechanistic proposals shown in Scheme 2.

In the first step of the mechanism proposed by Bornemann et al. (I in Scheme 2), oxalate binds to Mn(II) in the active site of Oxo and, through lowering the metal red-ox potential, activates it for binding of dioxygen.[4,7] In the reactive ternary Oxo−Mn−oxalate−O_2 complex (**B** in Scheme 2) manganese ion is one-electron oxidized by dioxygen which acquires superoxide character. Subsequent release of the first CO_2 molecule leads to the Oxo−Mn(II)−superoxide−formyl radical complex (**C**), which collapses to the Oxo−Mn(II)−peroxocarbonate complex (**D**). The protonation of **D** leads to its decomposition to H_2O_2 and the second CO_2 molecule. This mechanistic proposal satisfies the requirement of a tight coupling between dioxygen reduction and oxalate oxidation, which guarantees that no radicals escape from the enzyme active site. In addition, assuming that the reactive complex **B** is short-lived, only the Mn(II) species would be detectable, which agrees with the EPR data.[6] The alternative mechanism was proposed by Whittaker and Whittaker, and it is shown in Scheme 2 II.[6] In this case, oxalate is supposed to bind to Mn(II) in a monodentate fashion, and one water molecule remains bound to manganese (**E**). The hydrogen atom transfer from Oxo−Mn(II)−oxalate−OH_2 to externally bound dioxygen gives essentially free hydroperoxide radical and the Oxo−Mn(III)−oxalate−OH complex (**F**). The proton-coupled electron transfer (PCET) within the latter species affords a biradical intermediate **G**, which collapses forming the product complex **H**. The last step is a simple replacement of the peroxocarbonate by a water molecule, which produces the native form of Oxo (**J**).

The 1.6 Å-resolution crystal structure of the native Oxo revealed that Oxo is a homohexamer with the fold characteristic for the cupin superfamily.[8,9] The active site manganese is bound to three histidines (His88, His90, and His137) and one glutamate (Glu95) protein side chains, while the remaining two sites in the coordination octahedron are occupied by water molecules.[8] The structure of the barley Oxo−Mn−oxalate complex is currently not known; however, the putative oxalate decarboxylase (TM1287) from *Thermotoga maritima* was recently cocrystallized with oxalate.[10] Remarkably, in this structure a metal ion has an octahedral coordination with oxalate bound in a bidentate fashion, though the identity of the metal is currently not known. The other ligands are the same as in the barley Oxo (three His and one Glu).

The catalytic rate constant (k_{cat}) of barley Oxo was measured to be 22 s^{-1}, which corresponds to the activation barrier $\Delta G^{\ddagger}$ of 15.6 kcal/mol (at 298 K).[5]

In summary, the experimental data led to the formulation of two hypothetical mechanisms for the Oxo catalytic cycle. Detailed understanding of the chemical steps involved in the reaction is, however, still missing. For example, the point at which the necessary spin-crossing occurs is not known, as is the character of the reactive intermediates formed along the reaction coordinate. In this work hybrid density functional theory (DFT) has been used to study the mechanism of the Oxo catalytic cycle. The results reported here, when combined with known experimental data, lead to a detailed description of the catalytic reaction of Oxo and provide new insight into the Mn/oxalate chemistry.

Scheme 3: Suggested Mechanism for the Oxo Catalytic Reaction

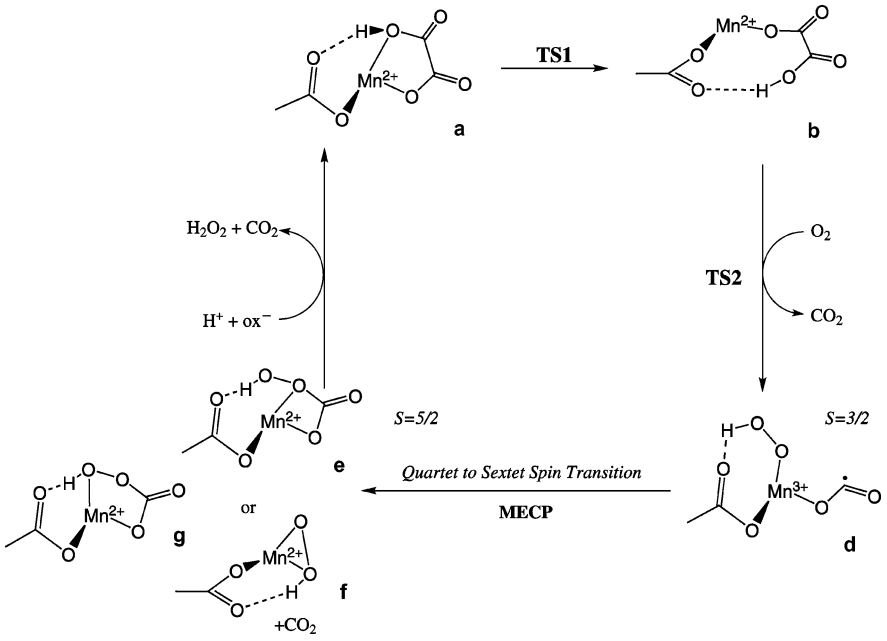

II. Computational Details

The model of the Oxo active site is based on the crystal structure solved for the native protein (PDB code: 1Fl2). Since the amino acids from manganese second coordination shell (Asn, Gln, Phe, Val, and Met) are unlikely to play an active role in catalysis, only the manganese first-shell ligands (His88, His90, His137, and Glu95) are included in the computational model. Histidines are modeled with imidazoles, while glutamate is replaced by acetate. The positions of the hydrogens introduced in place of the omitted parts of histidines are constrained throughout the calculations. For acetate, the position of the methyl carbon is constrained. In this way, the rigidity of the protein matrix is taken into account in an approximate way. Two water molecules coordinating Mn(II) in the native form of the enzyme have been substituted with singly protonated oxalate. The motivation for this charge state of the substrate comes from the biochemical data. Namely, Oxo exhibits maximum activity for pH between the two pK_a values for oxalic acid, which means that the singly protonated oxalate is the dominating form of the substrate under the optimum pH conditions.[5,6]

All calculations have been performed employing hybrid DFT with the B3LYP exchange-correlation functional.[11,12] Two programs, Gaussian03[13] and Jaguar,[14] have been used. Geometry optimizations have been done with a valence double-ζ basis set coupled with an effective core potential describing the innermost electrons on manganese. This particular basis set is labeled lacvp in Jaguar. For the optimized structures the electronic energy has been computed with a bigger basis set of triple-ζ quality with polarization functions on all atoms (labeled lacv3p** in Jaguar). The solvent corrections have been calculated with the self-consistent reaction field method implemented in Jaguar.[15,16] A dielectric constant of 4 with a probe radius of 2.50 Å have been used to model the protein surrounding of the active site.

The structure of the minimum energy crossing point (**MECP**) between noninteracting quartet and sextet states has been located at the B3LYP/lacvp level of theory employing the methodology developed by Harvey et al.[17] Since in this computational procedure it is not possible to use constraints, these calculations have been performed without frozen coordinates, i.e., the activation energy for reaching the **MECP** geometry is computed from the energy of an unconstrained model of intermediate **d** (see Scheme 3).

For the optimized geometry of the quartet−sextet **MECP** the coupling between the two states due to the spin−orbit coupling (SOC) operator has been estimated in the following way. First, the model has been truncated to afford CASSCF calculations. With this respect, the imidazole ligands have been replaced with ammonia molecules and acetate with formate. This model has subsequently been used for spin−orbit coupling calculations, which have been accomplished with the GAMESS program.[18] The wave function of the sextet state has been optimized at the ROHF/6-31G(d) level, and subsequently the quartet wave function has been converged at the CASSCF(5,5) level keeping the core orbitals frozen from the sextet state. The effective one-electron operator approximation has been assumed for the SOC, and the recommended effective nuclear charges have been employed.[19,20] The quartet−sextet transition probability (P) has been estimated from the Landau−Zener formula[21]

$$P = 1 - e^{-2\delta} \tag{1}$$

where

$$\delta = \frac{\pi |H_{ij}|^2}{\hbar \nu |\Delta g_{ij}|} \tag{2}$$

and where H_{ij} is the spin−orbit coupling matrix element between the two electronic states, ν is the velocity with which the system is passing the crossing region, and Δg_{ij} is the difference of the gradients calculated for the two states at

the crossing point. These gradients have been evaluated by numerical differentiation of the energy with respect to a small geometrical (5 degrees) displacement along the approximate spin-transition reaction coordinate, which is the O−C−O angle in the formyl radical anion in species **d**.

Since in several intermediates found in this study the spins on various parts of the complexes are antiferromagnetically coupled, a spin correction to the energy of these species has been calculated using the broken symmetry approach.[22,23] The recommended strong localized limit has been assumed, which means a zero overlap between the magnetic orbitals.[23] This specific computational methodology has successfully been applied to a wide range of redox enzymes with transition metals at their active sites.[24−26]

Finally, a short comment on the energies reported in this work. The reported values are the electronic energies calculated at the B3LYP/lacv3p**//B3LYP/lacvp level of theory plus the solvent effect calculated at the B3LYP/lacvp level. Zero energy corresponds to the isolated reactants, i.e., the Oxo-(singly protonated)oxalate complex and dioxygen. Thus, neither thermal corrections to the energy nor the entropic term are taken into account. However, while the former is usually on the order of a few kcal/mol, the entropy term is significant for the steps where small molecules are either trapped or released. For example, at room temperature the entropy term may contribute up to 10 kcal/mol to the free energy of the reaction in which dioxygen is bound to the model of the metal-containing active site. Therefore, due to this entropic term and to a lesser extent due to the thermal corrections to enthalpy, the true free energy profile will deviate from the one calculated here. However, the main goal of this study is to find the most likely mechanism of Oxo catalytic cycle by testing various a priori plausible mechanisms. For this purpose a semiquantitative description of the free-energy profile along the reaction coordinate seems sufficient because the thermal and entropy corrections are supposedly rather similar for the mechanisms tested in this work. The more quantitative description of the free-energy profile will be based of the QM/MM study which is now in progress.

III. Results and Discussion

Within this work several a priori plausible mechanisms have been tested, but only one involves a reasonable activation barrier, and this mechanism is presented below. The discarded mechanisms involve significantly higher barriers, and they are shortly summarized at the end of the manuscript and in the Supporting Information. The suggested mechanism is shown in Scheme 3, while the elementary steps of which it consists are discussed in detail in the following subsections.

Oxalate Coordination. The EPR data reported for the Oxo−Mn(II)−oxalate complex is indicative of a six-coordinate manganese in the active site, though binding of the substrate markedly changes the spectrum with respect to that for the native enzyme. Therefore, a direct interaction between Mn(II) and oxalate was proposed.[6] Moreover, the crystal structure of TM1287[10] shows a bidentate oxalate, which might suggest a similar binding mode in the Oxo−Mn(II)−oxalate complex. However, such an arrangement

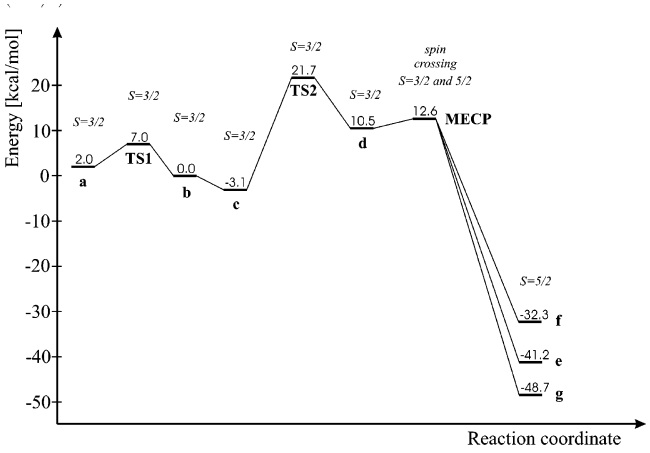

Figure 1. The calculated energy profile along the suggested reaction path for the Oxo catalytic cycle. The reported spin quantum number for **a**, **TS1**, and **b** takes into account the spin of unbound dioxygen (*S*=1) antiferromagnetically coupled with the spin on Mn(II) (*S*=5/*2*).

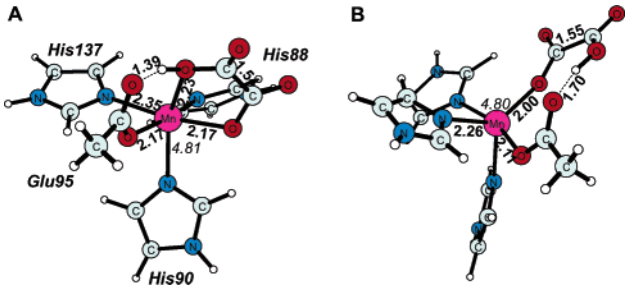

Figure 2. Optimized structures for the two forms of the Oxo−Mn(II)−oxalate complex (*S*=5/2). A. The six-coordinate form **a** and B. the five-coordinate form **b**. Distances in bold, spin populations in italics.

results in a six-coordinate Mn(II) ion, which lacks any vacant site available for dioxygen binding and, therefore, implicates either that dioxygen does not bind to Mn during the reaction or that the coordination number of manganese changes from 6 to 5 before O_2 binding. As shown below, the latter alternative is supported by the calculations.

The Oxo−Mn(II)−oxalate complex is calculated to exist as a nearly unimolar mixture of two species, one with bidentate oxalate (**a** in Scheme 3) and the second, **b**, with a five-coordinate Mn(II) and monodentate substrate. The energy difference between the two species is only 2 kcal/mol (see Figure 1). In the six-coordinate species (**a**), the protonated carboxylic group of the substrate both coordinates Mn(II) and forms a hydrogen bond with Glu95 (see Figure 2A). In the case of the five-coordinate form **b**, the protonated carboxylic group of the substrate is rotated away from manganese so that only the hydrogen bond between this group and Glu95 is preserved.

The transformation of **a** into **b** is favorable by 2 kcal/mol. Since this species is not the one observed experimentally, this indicates a small error in the calculations. However, the energy difference between **a** and **b** is quite small and therefore could change sign if the second shell ligands were taken into account. Indeed, preliminary QM/MM calculations performed for the extended model of the Oxo active site favor

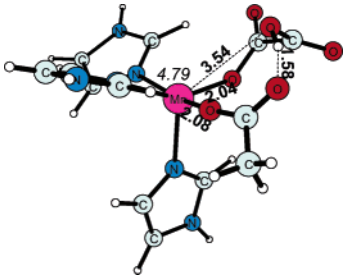

Figure 3. Optimized structure of **TS1** – the transition state which connects the two forms of the Oxo−Mn(II)−oxalate complex (*S*=5/2). Distances in bold, spin populations in italics.

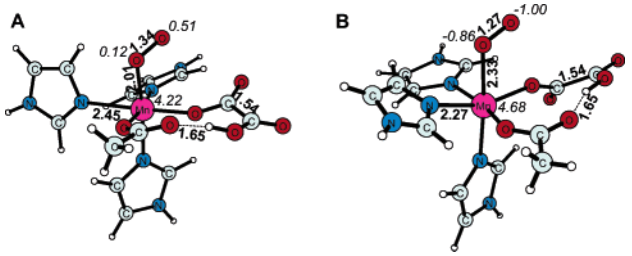

Figure 4. Optimized structures for Oxo−Mn−oxalate−O_2 complexes. A. The sextet species (*S*=5/2) and B. the quartet complex **c** (*S*=3/2). Distances in bold, spin populations in italics.

the six-coordinate species and thus agree well with the EPR data.[6] The transformation of **a** into **b** is a relatively simple geometrical rearrangement and involves a rather low activation barrier of 5 kcal/mol (for the transition state geometry see Figure 3).

Dioxygen Binding. The five-coordinate Oxo−Mn(II) species **b** possesses a vacant position at which dioxygen can bind. Due to the open-shell electronic structure of both high-spin Mn(II) and dioxygen, three possible spin states can be envisaged for the Oxo−Mn−dioxygen complex: octet (S=7/2), sextet (S=5/2), and quartet (S=3/2). In the octet state all of the unpaired electrons of the reactants are ferromagnetically coupled, which leads to no net bonding between dioxygen and manganese. In the optimized octet structure the Mn−dioxygen distance is large (3.3 Å), which together with the spin populations, 4.8 on Mn and 2.0 on dioxygen, clearly indicates that dioxygen does not bind to manganese in the octet spin state.

Flipping one spin in the octet electronic configuration leads to the sextet state, which is best described as a complex between high-spin Mn(III) and a superoxide anion. Indeed, the spin populations (4.2 on Mn and 0.63 on dioxygen) and the O−O bond distance in the dioxygen ligand (1.34 Å, see Figure 4A) support this interpretation. This state is computed to lie quite high in energy, 12.1 kcal/mol above the energy of the separated reactants in their electronic ground state. Even though this energy is not prohibitively high, all attempts to find a feasible reaction mechanism involving this sextet Oxo−Mn−oxalate−O_2 species failed, since in all cases the transition states turned out to have too large barriers (vide infra).

Finally, the antiferromagnetic coupling of spins on manganese and dioxygen leads to the Oxo−Mn−oxalate−O_2 in the quartet state (see Figure 4B). In this case, dioxygen forms

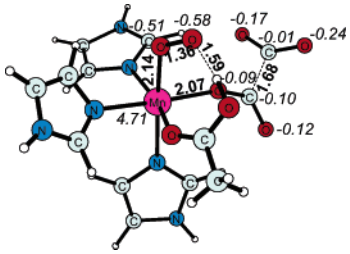

Figure 5. Optimized structure of the transition state (**TS2**) for the initial one-electron oxidation of oxalate (*S*=3/2). Distances in bold, spin populations in italics.

a weak bond to manganese (2.33 Å), while the spin populations indicate that dioxygen preserves its triplet character and Mn remains divalent. The calculated complexation energy is negative, i.e. −3.1 kcal/mol with the broken-symmetry correction, though, too small to compensate for the entropy loss caused by dioxygen trapping (around 8−10 kcal/mol). Therefore, it is concluded that dioxygen does not make any stable complex with the Oxo active site but only short-lived adducts which either react further or decompose back into the reactants. With respect to this instability of the dioxygen-bound species, it is important to notice the difference between the sextet and quartet spin states. Not only is the quartet state far more stable than the sextet counterpart (by 15.2 kcal/mol), but it is also directly accessible on the ground state potential energy surface (PES) of the reactants. In other words, the quartet species directly dissociates to the reactants in their ground state, while for the sextet state a spin transition must first take place before the dissociation.

Reduction of Dioxygen. The second step of the Oxo catalytic reaction is best described as a proton coupled electron transfer (PCET) from oxalate to dioxygen. However, this description is further complicated by the fact that, concomitantly with the proton and the first electron, a second electron, formally from Mn(II), is transferred to the dioxygen ligand. Thus, this step can be viewed as PCET coupled with another electron transfer (ET), since in this reaction dioxygen is reduced to the Mn-bound hydroperoxo anion, oxalate is one-electron oxidized to a formyl radical anion and CO_2, while Mn(II) is oxidized to Mn(III). The optimized structure of the transition state (**TS2**) for this process is presented in Figure 5. Notably, the proton involved in the PCET, originally from oxalate, is bound to Glu95 and positioned appropriately to form a hydrogen bond to the dioxygen ligand. Moreover, two bonds are significantly elongated with respect to the quartet Oxo−Mn−oxalate−O_2 complex (Figure 4B). First, the O−O bond distance in the dioxygen ligand increases from 1.27 to 1.36 Å, and this elongation is accompanied by a decrease of the O_2 spin population from −1.86 to −1.09. Second, the C−C bond of oxalate is elongated from 1.54 to 1.68 Å at the same time as the gross spin population on the oxalate ligand increases from 0.05 to −0.73. The spin on Mn does not change much when going from **c** to **TS2** (from 4.68 to 4.71), which suggests that the second electron 'lags behind'. The normal mode with imaginary frequency, which corresponds to the reaction coordinate, involves the elongation of the C−C bond in

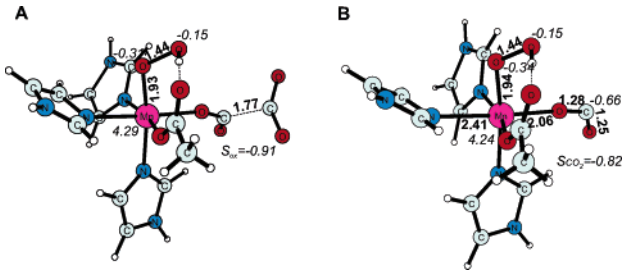

Figure 6. Optimized structures of the products of the initial one-electron oxidation of oxalate. A. The metastable species with oxalate radical anion (S=3/2) and B. the stable complex **d** with formyl radical anion (S=3/2). Distances in bold, spin populations in italics, ox stands for oxalate.

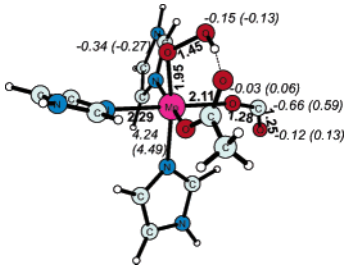

Figure 7. Optimized structure of the quartet−sextet minimum energy crossing point (**MECP**; S=3/2 and 5/2). Distances in bold, spin populations in italics, in parentheses spin populations for the sextet state.

oxalate and the protonated Glu95 approaching the distal O_2 oxygen atom, both movements in phase. Considering the energetics, the calculated activation energy is quite high, i.e., 21.7 kcal/mol, which is 6.1 kcal/mol more than the barrier estimated from the experimentally determined k_{cat} value (15.6 kcal/mol). Since all other investigated mechanisms involve substantially higher barriers, it is believed that the error of 6 kcal/mol is acceptable, and the suggested mechanism is the one used by Oxo.

Once the reacting system traverses **TS2**, the second electron is transferred from Mn(II) to the dioxygen ligand, and the species with a hydroperoxo anion coordinated to Mn(III) is formed. In the optimized complex (Figure 6A), the one-electron oxidized oxalate forms an oxalate radical anion with a carbon−carbon distance of 1.77 Å and a gross spin population of −0.91. However, this species is not stable with respect to the elongation of the C−C bond in the oxalate ligand. More specifically, when this distance is gradually elongated, first the energy remains approximately constant, but at a larger interatomic separation it slowly decreases. Therefore, the computational results indicate that once the **TS2** is passed, the first CO_2 molecule is liberated, while the active site Mn(III) ion binds HOO^- and $CO_2^{\bullet-}$, i.e., intermediate **d** (Figure 6B) is formed. Interestingly, the species **d** is a Jahn−Teller Mn(III) system with a weak J−T axis in the direction of the Mn-formyl radical anion bond. From Figures 4B and 6B it can be noticed that the Mn−His137 distance increases from 2.27 to 2.41 Å when going from **c** to **d**.

Spin-Crossing. In the intermediate **d**, formed in the one-electron oxidation of oxalate, the spins on the Mn(III) ion and the formyl radical anion are antiferromagnetically coupled (see Figure 6B). Such an electronic configuration is responsible for the stability of this species, since the electron transfer to Mn(III) would lead to an excited electronic configuration of manganese center (four d electrons with alpha spins, one with beta). If the electrons had parallel spins, which is the case in the sextet spin state, the electron transfer would be straightforward and would lead to the products in their ground state. For these reasons, the activation barrier connected with the quartet to sextet spin transition has been calculated by finding the minimum energy crossing point (**MECP**) where the two potential energy surfaces cross. The optimized geometry of the **MECP** is shown in Figure 7. Considering the electronic structure, the reported spin populations for the quartet and sextet states show that the spin transition can be viewed as a spin flip of the electron localized mostly on the carbon atom of the formyl radical anion fragment. With respect to the geometrical structure, a comparison of the reported bond lengths with those of intermediate **d** (Figure 6B) shows that the crossing point geometry is very similar to that of the quartet species. The bond lengths in the formyl radical fragment are unchanged, while the O−C−O angle opens slightly from 132.6 to 134.6 degrees.

This very small difference between the **d** and **MECP** geometries has the consequence that the energy gap between them is also very small, i.e., 2.1 kcal/mol (see Figure 1). Thus, provided that the coupling between the two spin states is sufficiently strong, the quartet to sextet spin transition will be very fast. The estimated value of the $< quartet|H_{SO}|\ sextet >$ matrix element is 2.16 cm^{-1}, which is sufficient to produce an effective spin junction in the current system. The quartet and sextet energy surfaces are relatively flat at the **MECP** geometry, $|\Delta g_{ij}| = 12.6$ kcal/mol/rad, which combined with the H_{SO} value and the estimated speed at which the system crosses the **MECP** (1.5×10^9 rad/s; calculated assuming the 500 cm^{-1} frequency and 0.01 rad amplitude for the O−C−O bending mode) gives a crossing probability of 0.58. Taking this value as a preexponential factor leads to the apparent barrier for the spin transition of 2.5 kcal/mol. Notably, even if the crossing probability were 1 order of magnitude smaller, still the apparent barrier would be only 3.9 kcal/mol. Thus, the quartet to sextet spin transition is calculated to be very efficient, which guarantees the quantitative coupling between dioxygen reduction and oxalate oxidation.

Interestingly, the observation that the crossing surfaces are almost parallel (small $|\Delta g_{ij}|$) was also made for the reaction between dioxygen and heme proteins, and this condition was proposed to facilitate the spin transition.[27] Moreover, the fact that MECPs very often lie rather close to the minimum of the higher energy state was also noticed in previous studies.[28,29]

Finally, if oxalate decarboxylase (OxDC), an enzyme closely related to Oxo and catalyzing the breakdown of oxalate to CO_2 and formate, uses a similar mechanism for producing a formyl radical, the manganese second sphere ligands of OxDC must ensure that the protonation of the formyl radical is faster than the quartet to sextet spin transition. We are currently investigating this mechanism,

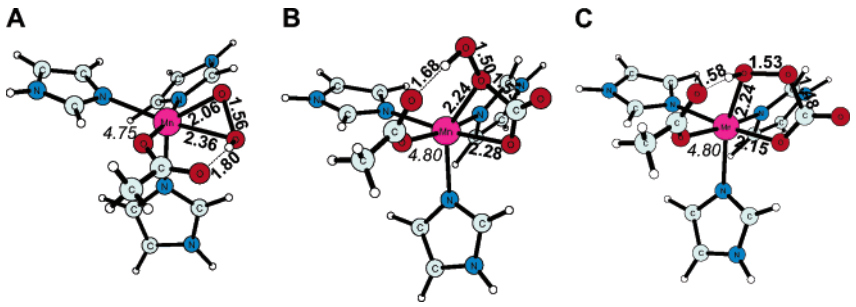

Figure 8. Optimized structures of the product complexes (S=5/2). A. The complex **f** with bidentate hydroperoxide anion, and B. and C. show species **e** and **g** with peroxocarbonate anion. Distances in bold, spin populations in italics.

and the detailed discussion of the means by which OxDC obtains its product specificity will be presented in a forthcoming paper.

Products. The spin transition discussed in the previous section enables a spontaneous electron transfer between the formyl radical anion and Mn(III). Three different products of this ET reaction have been identified. First, the CO_2 molecule formed in this ET reaction can stay in the active site and react (without any barrier) with the hydroperoxo anion. This leads to structure **e** or **g** (Figure 8B and C) with a peroxocarbonate anion chelating Mn(II). Alternatively, the CO_2 molecule can leave the active site, in which case, the hydroperoxo anion forms a second coordination bond with Mn (**f**, see Figure 8A).

The species **g**, which involves a five-member ring formed by peroxocarbonate and manganese, is the most stable form of the product complex. Interestingly, the mode of peroxocarbonate binding to the metal is similar to that observed for an iron synthetic complex.[30]

Protonation of either of these product complexes and subsequent release of H_2O_2 and CO_2 is most probably the final step of the catalytic cycle. The energetics of these steps, however, cannot be reliably calculated with the present models.

Alternative Mechanisms. Several other mechanisms of the catalytic reaction of Oxo have been tested within this study. The scheme presenting them can be found in the Supporting Information, and here only a brief description is given. In the mechanism II shown in Scheme 2 the first step is a hydrogen atom transfer from Oxo−Mn(II)−H_2O to dioxygen. The calculated energy of this reaction is 26.8 kcal/mol, and the barrier is most probably by a few kcal/mol higher. Another investigated mechanism involves the PCET on the sextet PES. This mechanism is similar to that suggested in this work, but in this case the spin transition takes place for the Oxo−Mn−O_2 complex. The calculated barrier for this mechanism is 26.2 kcal/mol. If Glu95 does not mediate the proton transfer, then a direct hydrogen atom transfer from oxalate to Mn-bound dioxygen can occur. The calculated barriers for this mechanism are 28.7 and 29.7 kcal/mol for the quartet and sextet spin states, respectively. The mechanism with an attack of Mn-bound dioxygen on the carboxylate carbon of oxalate parallels the oxidative decarboxylation reaction of α-keto acid dependent dioxygenases.[29,31−33] However, the carboxylic functional group is much less reactive than the carbonyl one. The calculated energies of the tetrahedral intermediate afforded by an attack of dioxygen/superoxide on the oxalate carbon are very high, i.e., 41.8 and 43.4 kcal/mol for the quartet and sextet PES, respectively. Finally, two mechanisms involving dissociation of one histidine ligand from manganese have been considered. In both cases oxalate chelates manganese and the liberated histidine hydrogen bonds to the HOO fragment. In the first mechanism the HOO• radical attacks oxalate, while in the second an electron is transferred from oxalate to Mn(IV). The calculated barriers connected with these mechanisms are 36.1 and 27.2 kcal/mol, respectively. In conclusion, all tested alternative mechanisms involve barriers markedly higher than that calculated for the suggested mechanism (Scheme 3). It is believed that this observation lends additional credence to the mechanistic proposal advocated in this work.

Conclusions

The results of the theoretical investigations reported here together with the published experimental data has allowed us to propose a detailed mechanism of the catalytic cycle of Oxo (see Scheme 3 and Figure 1). In summary, the Oxo−Mn(II)−oxalate complex exists as a mixture of five- and six-coordinate species. The form with coordinatively unsaturated Mn(II) site reacts with dioxygen on the quartet potential energy surface. In this step, the proton from oxalate monoanion is transferred to dioxygen through the first-shell glutamate. The proton-transfer triggers the C−C bond cleavage, and the electron follows the proton. Simultaneously, the second electron, necessary to produce the peroxo species, is provided by manganese. This step, which is also rate-limiting, yields the first CO_2 molecule and the reactive intermediate (**d**) in which the formyl radical anion coordinates the high-spin Mn(III). The quartet to sextet spin transition, which involves a small apparent barrier (ca. 2−4 kcal/mol), allows for the formyl radical → Mn(III) electron transfer. This step leads to the product−active site complex, which upon protonation decays to H_2O_2, CO_2, and the active site is then ready to begin the next catalytic cycle. Notably, the proposed mechanism satisfies the experimentally derived requirement of a tight coupling between oxalate oxidation and dioxygen reduction. Specifically, the radical intermediate **d** is predicted to be very short-lived, which guarantees the observed product specificity and no radical escape. In conclusion, the catalytic role of manganese involves the following: (i) bringing the substrates together, (ii) providing temporarily one electron necessary for dioxygen reduction, and (iii) facilitating the spin transition through an efficient spin−orbit coupling route.

The interplay of these three functions allows Oxo to perform the red-ox chemistry in an efficient and very controlled manner.

Acknowledgment. We are grateful to Sven de Marothy for providing us with his XYZ-Viewer program which was used to produce the molecular graphics presented in this manuscript. T.B. acknowledges the support from the Polish State Committee for Scientific Research (Grant 2 P04A 042 26).

Supporting Information Available: Investigated and discarded mechanism for the catalytic reaction of oxalate oxidase (Scheme S1). This material is available free of charge via the Internet at http://pubs.acs.org.

References

(1) Lane, B.; Dunwell, J.; Ray, J.; Schmitt, M.; Cuming, A. *J. Biol. Chem.* **1993**, *268*, 12239−12242.

(2) Svedruzic, D.; Jonsson, S.; Toyota, C. G.; Reinhardt, L. A.; Ricagno, S.; Lindqvist, Y.; Richards, N. G. J. *Arch. Biochem. Biophys.* **2005**, *433*, 176−192.

(3) Woo, E.-J.; Dunwell, J. M.; Goodenough, P. W.; Pickersgill, R. W. *FEBS Lett.* **1998**, *437*, 87−90.

(4) Requena, L.; Bornemann, S. *Biochem. J.* **1999**, *343 Pt 1*, 185−190.

(5) Kotsira, V.; Clonis, Y. *Arch. Biochem. Biophys.* **1997**, *340*, 239−249.

(6) Whittaker, M. M.; Whittaker, J. W. *J. Biol. Inorg. Chem.* **2002**, *7*, 136−145.

(7) Tanner, A.; Bowater, L.; Fairhurst, S.; Bornemann, S. *J. Biol. Chem.* **2001**, *276*, 43627−43634.

(8) Woo, E.; Dunwell, J.; Goodenough, P.; Marvier, A.; Pickersgill, R. *Nat. Struct. Biol.* **2000**, *7*, 1036−1040.

(9) Dunwell, J. M.; Purvis, A.; Khuri, S. *Phytochemistry* **2004**, *65*, 7−17.

(10) Schwarzenbacher, R. et al. *Proteins* **2004**, *56*, 392−395.

(11) Becke, A. D. J. *Chem. Phys.* **1993**, *98*, 5648−5652.

(12) Lee, C.; Yang, W.; Parr, R. G. *Phys. Rev.* **1988**, *B37*, 785−789.

(13) Frisch, M. J. et al. Gaussian 03, Revision B.03, Gaussian Inc., Pittsburgh, PA, 2003.

(14) Schrödinger, Inc., Portland, Oregon JAGUAR 4.0, 2000.

(15) Tannor, D. J.; Marten, B.; Murphy, R.; Friesner, R. A.; Sitkoff, D.; Nicholls, A.; Ringnalda, M.; Goddard III, W. A.; Honig, B. *J. Am. Chem. Soc.* **1994**, *116*, 11875−11882.

(16) Marten, B.; Kim, K.; Cortis, C.; Friesner, R. A.; Murphy, R.; Ringnalda, M.; Sitkoff, D.; Honig, B. *J. Phys. Chem.* **1996**, *100*, 11775−11788.

(17) Harvey, J. N.; Aschi, M.; Schwarz, H.; Koch, W. *Theor. Chem. Acc.* **1998**, *99*, 95−99.

(18) Schmidt, M. W.; Baldridge, K. K.; Boatz, J. A.; Elbert, S. T.; Gordon, M. S.; Jensen, J. H.; Koseki, S.; Matsunaga, N.; Nguyen, K.; Su, S.; Windus, T. L.; Dupuis, M.; Montgomery, J. A. *J. Comput. Chem.* **1993**, *14*, 1347−1363.

(19) Koseki, S.; Schmidt, M. W.; Gordon, M. S. *J. Phys. Chem.* **1992**, *96*, 10768−10772.

(20) Koseki, S.; Gordon, M. S.; Schmidt, M. W.; Matsunaga, N. *J. Phys. Chem.* **1995**, *99*, 12764−12772.

(21) Nakamura, H. *J. Chem. Phys.* **1987**, *87*, 4031−4041.

(22) Mouesca, J. M.; Chen, J. L.; Noodleman, L.; Bashford, D.; Case, D. A. *J. Am. Chem. Soc.* **1994**, *116*, 11898−11914.

(23) Ciofini, I.; A., D. C. *Coord. Chem. Rev.* **2003**, *238−239*, 187−209.

(24) Siegbahn, P. E. M.; Blomberg, M. R. A. *Chem. Rev.* **2000**, *100*, 421−437.

(25) Blomberg, M. R. A.; Siegbahn, P. E. M. *J. Phys. Chem. B* **2001**, *105*, 9375−9386.

(26) Siegbahn, P. E. M. *Q. Rev. Biophys.* **2003**, *36*, 91−145.

(27) Jensen, K. P.; Ryde, U. *J. Biol. Chem.* **2004**, *279*, 14561−14569.

(28) Lundberg, M.; Siegbahn, P. *Chem. Phys. Lett.* **2005**, *401*, 347−351.

(29) Bassan, A.; Borowski, T.; Siegbahn, P. E. M. *Dalton Trans.* **2004**, *20*, 3153−3162.

(30) Hashimoto, K.; Nagatomo, S.; Fujinami, S.; Furutachi, H.; Ogo, S.; Suzuki, M.; Uehara, A.; Maeda, Y.; Watanabe, Y.; Kitagawa, T. *Angew. Chem.* **2002**, *114*, 1250−1253.

(31) Borowski, T.; Bassan, A.; Siegbahn, P. E. M. *Biochemistry* **2004**, *43*, 12331−12342.

(32) Borowski, T.; Bassan, A.; Siegbahn, P. E. M. *Chem. Eur. J.* **2004**, *10*, 1031−1041.

(33) Borowski, T.; Bassan, A.; Siegbahn, P. E. M. *Inorg. Chem.* **2004**, *43*, 3277−3291.

CT050041R

JCTC Journal of Chemical Theory and Computation

A Polarizable Force Field and Continuum Solvation Methodology for Modeling of Protein−Ligand Interactions

Jon R. Maple,*[,†] Yixiang Cao,[†] Wolfgang Damm,[†] Thomas A. Halgren,[†] George A. Kaminski,[‡] Linda Y. Zhang,[†] and Richard A. Friesner[†,§]

Schrödinger, Inc., 120 West 45th Street, Tower 45, 32nd Floor, New York, New York 10036, and Department of Chemistry, Central Michigan University, Mt. Pleasant, Michigan 48859

Received December 13, 2004

Abstract: A polarizable force field, and associated continuum solvation model, have been developed for the explicit purpose of computing and studying the energetics and structural features of protein binding to the wide range of ligands with potential for medicinal applications. Parameters for the polarizable force field (PFF) are derived from gas-phase ab initio calculations and then utilized for applications in which the protein binding to ligands occurs in aqueous solvents, wherein the charge distributions of proteins and ligands can be dramatically altered. The continuum solvation model is based on a self-consistent reaction field description of solvation, incorporating an analytical gradient, that allows energy minimizations (and, potentially, molecular dynamics simulations) of protein/ligand systems in continuum solvent. This technology includes a nonpolar model describing the cost of cavity formation, and van der Waals interactions, between the continuum solvent and protein/ligand solutes. Tests of the structural accuracy and computational stability of the methodology, and timings for energy minimizations of proteins and protein/ligand systems in the condensed phase, are reported. In addition, the derivation of polarizability, electrostatic, exchange repulsion, and torsion parameters from ab initio data is described, along with the use of experimental solvation energies for determining parameters for the solvation model.

I. Introduction

The explicit incorporation of polarization into molecular mechanics force fields is a long standing objective of force field development efforts. Early work was focused primarily on development of polarizable force field models for liquid water;[1−9] a number of water models have now been produced, many of which display very good properties as compared to experiment. A few publications have addressed small organic molecules other than water[10−13] or small ions;[14−15] in these papers few such molecules has been considered, and parameters have typically been fit to condensed phase experimental data, which is not systematically available for many compounds, including the great majority of pharmaceutically interesting ligands. More recently, a number of efforts have been made to develop a polarizable protein force field[16−18] and to approach the problem of inclusion of polarization in a more systematic fashion.[19−22] However, many of these models are relatively new and untested; it is clear that the problems of achieving accuracy, reliability, and broad coverage, while explicitly incorporating polarization, are substantial and far from solved at the present time.

In a series of previous publications, we have described the development of automated methods for the construction of a polarizable force field for an arbitrary molecule directly

* Corresponding author phone: (858)695-6614; e-mail: maple@schrodinger.com.

† Schrödinger, Inc.

‡ Central Michigan University.

§ Permanent address: Department of Chemistry, Columbia University, New York, NY 10027.

10.1021/ct049855i CCC: $30.25
Published on Web 06/04/2005

from ab initio quantum chemical data.[3,9,16,20−22] The primary goal is to produce a polarizable model that yields accurate results in condensed phase simulations; as we[20] and others[23−25] have discussed previously (this issue is also briefly reviewed below), it appears as though one has to use different polarizability parameters in the gas phase and condensed phase in order to reproduce experimental data reliably. We have developed an approach which has successfully matched experimental heats of vaporization and density for a number of small molecule pure liquid simulations, without explicit fitting to experimental condensed phase data.[20] At the same time, we have shown that our methodology is capable of accurately fitting quantum chemical gas-phase conformational data for dipeptides, thus enabling the creation of a polarizable protein force field.[16]

However, to deploy a polarizable force field for practical problems in drug design, it is necessary to have the ability to represent an arbitrary medicinal compound by a set of polarizable force field parameters. Furthermore, molecular dynamics simulations, employing explicit solvent, require large amounts of computer time and in addition necessitate the use of expensive sampling algorithms, such as replica exchange methods,[26] if free energies of binding are to be determined; for these reasons, this type of approach is currently used very infrequently in modeling projects in the pharmaceutical industry. Instead, a continuum treatment of aqueous solvation, based on for example solution of the Poisson−Boltzmann equation,[27] is utilized, along with approximate sampling algorithms (in many cases, simple minimization). Thus, a continuum solvation model that is complementary to the polarizable force field is required if realistic drug discovery problems, as opposed to a small number of carefully chosen model systems, are to be addressed.

In the present paper, we describe a complete integrated software system and associated parametrization for carrying out polarizable force field calculations in continuum solvent for arbitrary protein−ligand complexes. The key components of the system are as follows:

(1) A package for assigning polarizable force field parameters to an arbitrary medicinal compound. The package includes an atom typing algorithm, default polarizability, and van der Waals parameters for a wide range of atom types, and an extensive set of stretching, bending, and torsional parameters (the former are borrowed from our most recent fixed charge force field development effort, the latter are fit to minimize the deviation with gas-phase quantum chemical data for a ∼600 compound small molecule data set). Atomic point charges, lone pair charges, and permanent dipoles are determined by fitting high level quantum chemical data, using an automated protocol.

(2) A polarizable protein force field that has been extensively fit to quantum chemical data on dipeptides and tested in a variety of simulations. This work is described in more detail in other publications but is summarized here because of its relevance to the computation of protein−ligand interactions, the principal focus of this paper.

(3) A simulation package for carrying out gas-phase polarizable simulations. The polarization equations are solved self-consistently at each geometry. In the present paper we focus on minimization; however, methods for molecular dynamics simulation are in place. These will be discussed elsewhere.

(4) A self-consistent reaction field (SCRF) methodology[28] in which solution of the Poisson−Boltzmann equation is coupled with determination of the polarization response of the protein and ligand, using the package discussed in (3) above. We have extended our previously developed analytical gradient methodology[29,30] to handle the polarizable SCRF model; infrequent evaluation of the PB solver significantly improves computational performance without loss of accuracy. Dielectric radius parameters for a wide range of atom types, suitable for this methodology and the underlying force field, have been developed from a database of 147 small molecules, with an average error in the solvation free energy of 0.35 kcal/mol for neutral molecules and 0.5 kcal/mol for charged species.

With these components in hand, it is possible to carry out optimization of a protein−ligand complex and the ligand in continuum solvent and to calculate the total energy difference (such a difference includes the solvation free energy difference but does not include the conformational entropy difference between the protein−ligand complex and the protein and ligand independently in solution). The simplest application of this type of computation would be to correlate the resulting energy difference directly with binding affinity. However, this capability may also be useful, for example, as a component of MM/PBSA type approaches[31−33] or in continuum solvation based extended linear response calculations.[34] It is an interesting and important question as to whether the use of a more accurate force field and solvation models which incorporate polarization explicitly (and, based on our results to date, reasonably accurately) will improve the performance of approaches of this type. Our present software package enables, for the first time, this question to be addressed with a reasonable amount of effort by the user.

Ultimately, highly accurate binding affinity predictions will be achieved by combining an accurate force field and solvation model with equally accurate phase space sampling. In the context of continuum models, methods for computing absolute free energies via direct phase space integration have been proposed, and successfully employed, for example by Gilson and co-workers.[35] The polarizable model described here could be employed as a component of this methodology, for example to correct the energies of low-lying minima (using a fixed charge force field to do the extensive sampling required to locate the minima and to evaluate entropic terms). It may also be the case that retention of a crucial subset of explicit waters is required to accurately evaluate protein−ligand interactions. The treatment of explicit waters presents no problem in principle to the present approach, and a very simple test case was recently successfully completed.[36] However, robust algorithms for determining the placement of such waters are nontrivial and remain to be rigorously developed and validated.

The present paper is focused on describing the computational methodology associated with the four components enumerated above and providing a demonstration that the

implementation performs properly for a test suite of protein−ligand complexes. The paper is organized as follows. Section II describes the development of the parameters for the medicinal chemistry force field (item (1) above), reviewing our computational methodology and presenting PFF results for hydrogen bond energies and structures of 182 small molecule dimers. Section III discusses the SCRF solvation methodology and presents results for solvation free energies of 147 small molecules which constitute the training set for determining dielectric radii. Section IV presents the full protein−ligand simulation methodology (including a brief overview of the protein polarizable force field), followed by results for a suite of test cases taken from the PDB. In this paper we simply demonstrate that minimizations in gas phase and in solution can be carried out unproblematically and in reasonable CPU time (nontrivial given the possibility of polarization catastrophes and the difficulty of converging solvated large protein minimizations using SCRF methods) and compare the RMSD of the resulting structure with the experimental data; future publications will explore the use of these methods for binding affinity prediction.

II. Development of Polarizable Force Field Parameters for Arbitrary Medicinal Compounds

A. Functional Form of the Polarizable Force Field. We can summarize our conclusions, based on a substantial number of computational experiments,[3,9,16,20−22] with regard to the functional form of the polarizable force field, as follows:

(1) The underlying permanent charge model can be made reasonably accurate via the use of atomic point charges and dipoles. Others have advocated the use of atomic quadrupoles or other more complex charge distributions;[37] our experience is that, while quadrupoles can on occasion make a nontrivial contribution to the electric field, the energy error associated with truncating the electrostatic "basis set" at dipoles is in the vast majority of cases less than 0.5 kcal/mol, which is our overall target accuracy for the force field in the gas phase. On this basis, we judged the additional coding complexity and computational expense of quadrupoles as marginal for the current generation of polarizable models, particularly as the goal is to achieve coverage of medicinal chemistry space, requiring a large scale parametrization effort.

(2) We experimented with the use of both fluctuating charges and polarizable dipoles, individually and in combination. Our conclusions are that fluctuating charges alone are seriously inadequate in describing intermolecular interactions in a significant number of relevant cases; dipoles alone provide reasonable results, and the combination of fluctuating charges and dipoles does not provide a sufficient improvement to dipoles alone (again, in the overall context of the achievable accuracy of current models) to justify the added complexity and difficulties in fitting due to the increased overcompleteness of the model. The use of dipoles only also provides a simpler physical picture of the polarization response. Therefore, we have chosen to employ atomic polarizabilities in the present force field.

(3) It is possible to define new atomic polarizabilities for every atom in each new molecule. At the other extreme, one can simply have a single polarization parameter for each element (i.e. one for oxygen, one for nitrogen, etc.). Our experience has been that the latter approach (at least in our hands) leads to gross inaccuracies in, for example, hydrogen bonding interactions, whereas the former, while technically feasible, is rather expensive both computationally and in terms of human effort. Therefore, we have adopted an intermediate approach in which polarization parameters are defined for various atom types and fit using a suite of model molecules. This approach provides a good compromise between computational efficiency, convenience, and accuracy; results validating our choice of atom types (by demonstrating good ability to reproduce hydrogen bond energies across a wide range of test cases) are presented below.

(4) Long-range dispersion forces are notoriously difficult to compute via ab initio quantum chemistry; on the other hand, liquid-state simulations are very sensitive to these interactions, so arguably they can be obtained by fitting condensed phase experimental data. We hypothesized[20] that one could define a single long-range dispersion parameter (the coefficient of the atomic $1/r^6$ term used to construct the corresponding term in the atom−atom pair potential via the usual combining rules) for each atom and that it would be transferable across a wide range of organic systems. This strategy was highly successful,[20] and a small number of liquids were used to fit parameters for H, C, O, N, and S, while others were then tested using these parameters without adjustment. No doubt greater accuracy could be achieved by allowing the dispersion parameters to vary with atom type; however, the accuracy achieved using the single parameter ansatz appears to be acceptable at present.

(5) For the remainder of the nonpolar atom−atom pair potential, we investigated the use of both the Lennard-Jones $1/r^{12}$ term and the exponential term in the exp-6 pair function. Because we wanted to fit both hydrogen bond energies and bond lengths, while keeping the dispersive term fixed, we decided to employ a combined function in which both types of terms are present; this is discussed in more detail elsewhere. One could in fact use a numerical pair function defined by a look-up table; the key is having sufficient functional flexibility to fit the quantum chemical data adequately. Nonbonded parameters of these types are defined for a list of atom types as presented below.

(6) As is usual in fixed charge force fields, we eliminated 1−2 and 1−3 interactions from the energy calculations; however, 1−4 interactions are included with no scaling.

(7) Stretches and bends were taken from our fixed charge force field (e.g., from the OPLS-AA protein force field[38]). This is a reasonable approximation but will be reexamined in the next generation PFF. Torsions are fit to ab initio calculations on small model molecules; for the present version of the PFF, we used the same training set of ∼600 molecules as has been employed for our fixed charge force field. Future versions of PFF will utilize much larger training sets, so as to eliminate missing torsion parameters for the great majority of medicinal compounds.

Given these choices, the total energy of the PFF force field is defined as

$$E_{PFF} = E_{str} + E_{bend} + E_{tor} + E_{nb} + E_{q/q} + E_{q/u} + E_{u/u} + E_{pol} \quad (1)$$

The stretch, bend, and torsion energy functions in eq 1 are given by

$$E_{str} = \Sigma K_b(b - b_o)^2 \quad (2)$$

$$E_{bend} = \Sigma K_\theta(\theta - \theta_o)^2 \quad (3)$$

$$E_{tor} = {}^1/_2\Sigma\{V_1[1 + \cos(\varphi)] + V_2[1 - \cos(2\varphi)] + V_3[1 + \cos(3\varphi)] + V_4[1 - \cos(4\varphi)]\} \quad (4)$$

where the K_b, K_θ, V_1, V_2, V_3, and V_4 are force constants, b_o and θ_o are reference values, and where b and θ are bond lengths and bend angles. The V_4 term in eq 4 is normally set to a value of 0. Equation 4 gives the deformation energy for twisting about a bond and for out-of-plane deformations (at trigonal centers), so φ represents both dihedral angles and improper torsion angles.

The nonbonded energy function, which includes both dispersion and exchange repulsion terms, is

$$E_{nb} = {}^1/_2\Sigma\{A_{ij}/R_{ij}^{12} - B_{ij}/R_{ij}^{6} + C_{ij}\exp[-R_{ij}/\sigma_{ij}]\} \quad (5)$$

Here R_{ij} is the distance between atoms i and j, and A_{ij}, B_{ij}, C_{ij}, and σ_{ij} are adjustable parameters. The factor of $^1/_2$ is introduced to exclude double counting of interactions.

The interaction energies between all pairs of interacting charges is indicated in eq 6, where q_j is the charge at atomic or virtual (i.e., lone pair) site j and where the factor of $^1/_2$ again excludes double counting.

$$E_{q/q} = {}^1/_2\Sigma q_i q_j/R_{ij} \quad (6)$$

PFF employs permanent dipoles at atomic sites, to model the anisotropy in the charge distribution surrounding each atom. This anisotropy is an inherent result of bonding (in both polar and covalent bonds) and causes the interaction energy of a point charge with an atom to depend on whether the charge (or field due to a distribution of charges) is located parallel or perpendicular to a bond. The permanent dipole (μ_i) on atom i interacts with the total field ($\mathbf{F}^q{}_i$) due to all interacting charges. The interaction energy between the dipole on atom i and the charges is given by $-\mu_i\mathbf{F}^q{}_i$, where both the dipole and field are vector quantities. Consequently, the total interaction energy between all interacting charges and permanent dipoles is determined by summing over all dipoles, as indicated in eq 7.

$$E_{q/u} = -\Sigma\mu_i\mathbf{F}^q{}_i \quad (7)$$

Similarly, permanent dipoles on other atoms create a field ($\mathbf{F}^\mu{}_i$) that also interacts with the dipole on atom i, and the total energy of interaction between all permanent dipoles is given by eq 8. The PFF electrostatic interaction energy is the total energy of interaction between all charges and permanent dipoles and is the sum of eqs 6−8.

$$E_{u/u} = -{}^1/_2\Sigma\mu_i\mathbf{F}^\mu{}_i \quad (8)$$

With PFF all ligand atoms are polarizable, which means that an induced dipole (μ'_i) is created on each atom. As shown by eq 9, the magnitude of the induced dipole (at atom i) is proportional to the polarizability (α_i) of atom i and to the total field exerted at this atom.

$$\mu'_i = \alpha_i(\mathbf{F}^q{}_i + \mathbf{F}^\mu{}_i + \mathbf{F}^{\mu'}{}_i) \quad (9)$$

The last term in eq 9 is the field (at atom i) due to all induced dipoles that interact with the atom. Initially, this field and the induced dipoles are not known, so guess values for the induced dipoles are assumed, and μ'_i and $\mathbf{F}^{\mu'}{}_i$ are then iteratively refined until the value of each induced dipole has converged. For continuum solvent simulations there is an additional field source that is added to eq 9. This is the self-consistent reaction field due to the solvent.

Energy is required to create the induced dipoles, and this energy, which is often called the self-polarization energy,[39] is given in eq 10.

$$E_{self} = {}^1/_2\Sigma\mu'_i(\mathbf{F}^q{}_i + \mathbf{F}^\mu{}_i + \mathbf{F}^{\mu'}{}_i) \quad (10)$$

The net change in interaction energy (that is caused by polarization of each atom) is the sum of the self-polarization energy and the energy of interaction of the induced dipoles with the charges, permanent dipoles, and (all other) induced dipoles, as indicated in eq 11. Due to cancellation of terms, eq 11 reduces to eq 12, which is the PFF polarization energy.

$$E_{pol} = E_{self} - \Sigma\mu'_i(\mathbf{F}^q{}_i + \mathbf{F}^\mu{}_i + {}^1/_2\mathbf{F}^{\mu'}{}_i) \quad (11)$$

$$E_{pol} = -{}^1/_2\Sigma\mu'_i(\mathbf{F}^q{}_i + \mathbf{F}^\mu{}_i) \quad (12)$$

B. **Development of Default PFF Parameters.** The first step in the parametrization of the PFF is the development of polarizability and atomic nonbonded parameters for a set of specified atom types, using a test suite of model molecules. Permanent electrostatic parameters for each model molecule (atomic point charges and dipoles) are obtained by standard electrostatic potential (ESP) fitting methods to high level quantum chemical wave functions. In previous work, we used DFT wave functions to obtain permanent charge distributions.[3,16,20−22] In the course of the more extensive investigation of chemical space carried out for this paper, we have concluded that local second-order Moller−Plesset perturbation theory (LMP2) calculations with large basis sets provide more accurate and reliable results, although the DFT approach is still quite reasonable. An important target for the dimer binding energies was to reproduce results obtained from LMP2 extrapolated to the basis set limit. On the whole using LMP2/cc-pVTZ(-f) derived charge distributions leads to better agreement of the model with the target quantum chemical dimer extrapolated binding energies than does the use of B3LYP/cc-pVTZ(-f) derived charge distributions. As a result of this, it was possible to derive exchange repulsion parameters which gave somewhat better agreement with the extrapolated binding energies when LMP2, rather than DFT, was employed for calculating the permanent charge distributions. Consequently, charge distributions should be derived from LMP2 in order to maintain maximum consistency with

the derived exchange repulsion parameters. Nevertheless, geometry optimizations can be performed at the DFT level, so only single point LMP2/cc-pVTZ(-f) calculations are required, leading to reasonable computational expense as compared with other aspects of the overall modeling protocol. The LMP2 charge distributions are expected to be close to the results one would obtain with fully converged high level quantum chemical calculations. Pseudospectral LMP2 methods in the Jaguar program[40] were used to carry out the LMP2 calculations.

Because of the accuracy of the LMP2 charge distributions, charges and dipoles (both permanent and induced) were allowed to interact without scaling for interactions in which atoms were separated by three (or more) bonds (e.g., 1−4 interactions). As usual for force field calculations, interactions between charges (and dipoles) were not included for atom pairs separated by one or two bonds.

Charges and permanent dipoles were determined from fits of the LMP2/cc-pVTZ(-f) esp, as discussed above, with appropriate constraints and restraints. Eigenvalues calculated by singular value decomposition were consistently very small for the permanent dipoles on buried atoms that were surrounded by other atoms. This is an indication that the permanent dipoles for these atoms are small. These atoms could not be sampled well enough to distinguish the esp due to the charges and dipoles. Consequently, the permanent dipoles on tetrahedrally bonded atoms, such as the carbon and phorphorus atoms in alkyl and phosphate groups, were constrained to a value of 0 (i.e., permanent dipoles were not placed on these atoms). To prevent the occurrence of large (physically unrealistic) charges and dipoles, a penalty function ($0.2p^2$) was also used as a restraint, where p is the charge or dipole parameter value. This penalty function was applied to each charge and (permanent) dipole parameter and was added to the total sum of squared deviations (for the fit of the esp), which was then minimized.

Once the procedure for determining the permanent charge distribution is obtained, the next step is to fit polarizability parameters to reproduce the response of the model molecules to applied electric fields. Dipole probes were used to apply an electric field to the molecule, and these probes consisted of two point charges (0.7815 and −0.7815 e) separated by 0.5774 Å, so that the molecules were exposed to fields which are similar to those that occur in an aqueous solvent. These point charges were used to probe the polarization response of an atom by placing a probe near the atom and then using quantum mechanics to determine the energy of interaction between the molecule and probe, as described below. All atoms, except for those in alkyl groups, were similarly probed.

Dipole probe positioning depended on each atom's bonding and hybridization. Whenever possible, probes were placed in hydrogen bonding positions. For oxygen and sulfur with sp^2 or sp^3 hybridization, the two point charges were oriented along the axis through the atom and lone pair position, and two probes were utilized in these cases (i.e., one probe for each lone pair). Probes for terminal atoms were placed along the bond axis (e.g., along the N−H bonds in formamide) for H, F, Cl, N (e.g., nitriles) and O and S atoms (without sp^2 or sp^3 hybridization, as in methoxide anion, phosphates, and sulfates). For pyramidal atoms, the probes were placed along the pyramidal axis, so that in the case of amine nitrogen, the probe was placed along the axis from the nitrogen to the lone pair. In all of these cases the probes were placed at a distance of 1.8 Å from H, N, O, and F and at a distance of 1.9 Å from P, S, and Cl. For planar atoms, such as sp^2 C and N in amides or C in aromatic rings, the probe was placed along the axis through the atom and perpendicular to the plane (at a distance of 2.0 Å from the plane). For tetrahedral N, P, and S a line was drawn through a bond, and a probe was placed on the other side of the tetrahedral atom (at a distance of 1.8 Å from N and 1.9 Å from P and S). Four of these probes (corresponding to the four bonds) were created for each tetrahedral atom, and then those probes with the closest contacts (to the atoms bonded to the tetrahedral atom) were discarded. Although the polarizability model used here is isotropic, while polarization is inherently anisotropic, the parametrization procedure employed here is optimized to reproduce the polarization response in the direction of greatest importance for intermolecular interactions. For example, oxygens and sulfur are probed in the lone pair direction, arenes are probed perpendicular to the plane of the aromatic ring, and terminal bonds are probed along the bond axis.

When point charges are placed near a molecule, the quantum mechanical interaction energy is given by

$$E = E(\text{molecule} + \text{point charges}) - E(\text{isolated molecule}) - E(\text{point charges}) \quad (13)$$

and

$$E = E_{\text{elec}} + E_{\text{pol}} \quad (14)$$

where E_{elec} and E_{pol} are the electrostatic and polarization components of the interaction energy. Other high intensity field terms (i.e., hyperpolarization) can be neglected at field strengths typical of biomolecular systems, and all other interaction terms (e.g., exchange repulsion and dispersion) are nonexistent in this case. As demonstrated in the Appendix, the electrostatic and polarization components of the interaction energy vary linearly and quadratically, respectively, with the field strength, and this variance in the field strength dependence allows these two energy components to be separately determined. For example, the Appendix demonstrates that for the case of two point charges (q_1 and q_2) the electrostatic and polarization energy components of the interaction energy are given by

$$E_{\text{elec}} = C_1 q_1 + D_1 q_2 \quad (15)$$

$$E_{\text{pol}} = C_2 {q_1}^2 + D_2 {q_2}^2 + C_{11} q_1 q_2 \quad (16)$$

In eq 15 C_1 and D_1 are the molecule's electrostatic potential evaluated at the location of the two charges, while C_2, D_2, and C_{11} are coefficients that are determined from derivatives of the interaction energy with respect to the point charges (evaluated at point charge values of 0). Since these derivatives can be readily evaluated by the method of finite differences, the polarization energy component of the

Table 1. PFF and LMP2/cc-pVTZ(-f) Polarization Energies Are Compared for Formamide Interacting with Dipole Probes for Each Atom

atom	polarizability (Å^3)	polarization energy (kcal/mol)			% difference
		QM	PFF	difference	
H	0.207	−0.636	−0.633	0.003	−0.43
H	0.207	−0.639	−0.640	−0.001	0.18
HC	0.346	−0.940	−0.945	−0.005	0.53
C	0.766	−1.699	−1.698	0.001	−0.04
N	1.291	−1.839	−1.838	0.001	−0.06
O	0.891	−1.883	−1.884	0.000	0.02
O	0.891	−1.825	−1.821	0.004	−0.21

interaction energy can be calculated from quantum mechanics and also from PFF. Thus, the PFF atomic polarizabilities can be parametrized to reproduce polarization energies calculated from quantum mechanics, and this can be done prior to determining the charges and permanent dipoles for the molecule.

The example in Table 1 demonstrates the procedure for deriving atomic polarizabilities for formamide. As previously described, the hydrogens were probed along the N−H and C−HC bonds, and the C and N were probed perpendicular to the plane of the atom, while O was probed along the line between the O and the two lone pairs. Thus, there were two dipole probes for the oxygen and one each for all other atoms. For each system, which consisted of the formamide molecule with one dipole probe, the LMP2/cc-pVTZ(-f) polarization energy was calculated from eq 16, and the resulting polarization energies are given in the third column of Table 1. LMP2/cc-pVTZ(-f) calculations were used for maximum compatibility of the polarizability parameters with the charge and permanent dipoles, which were also determined at this level of theory.

The PFF polarization energy was also computed from eq 16, and the atomic polarizability parameters (in eq 9) were adjusted to reproduce the LMP2 polarization energy. This was done with a sequential and iterative procedure. The polarizability parameter for the first atom, which is a polar hydrogen, was adjusted to reproduce the LMP2 polarization energy (−0.636 kcal/mol) for the system in which this hydrogen was probed. Then, the polarizability parameter for the second atom, which was also a polar hydrogen, was similarly adjusted to fit the −0.639 kcal/mol polarization energy for the system in which this hydrogen was probed. This process was repeated for each system, but only one probe was used during the fitting procedure for the oxygen. This procedure then was repeated several times until convergence was reached. The end result is that 6 atomic polarizability parameters were fitted to 6 LMP2 polarization energies. In the case of the oxygen atom there were two systems in which the oxygen was probed from different directions (corresponding to probing the two lone pairs). The system with the −1.883 kcal/mol LMP2 polarization energy was fitted, but the resulting 6 atomic polarizabilities also reproduced the −1.825 kcal/mol LMP2 polarization energy for the other system in which the oxygen atom was probed. The percentage error in this latter case was −0.21%, which was less than the 1.0% convergence criteria. If the error had exceeded the 1.0% convergence criteria, the target polarization energy would have been adjusted somewhat so that the polarization energy for both systems with the oxygen probe were fitted equally well. Thus, even when there are two probes for a single atom, there will still be only a single target function (i.e., polarization energy) per atom. Therefore, the 6 optimized polarizability parameters (given in column 2) are the nearly exact solution to 6 nonlinear equations for the ab initio polarization energies (given in column 3), as seen by the close agreement (in column 4) of the resulting PFF polarization energies.

Note that the polarization energy for the carbon atom probe (−1.699 kcal/mol) is almost as large as the energy for the nitrogen atom probe (−1.839 kcal/mol), even though the carbon polarizability (0.766 A^3) is much smaller than for the nitrogen (1.291 A^3). The reason for this is that the carbon is in close proximity to two much more polarizable atoms (i.e., oxygen and nitrogen). As a result the dipole probe for the carbon atom also substantially polarizes the oxygen and nitrogen, and the net polarization energy results from the polarization of all atoms. The effect of these overlapping polarizations (i.e., each probe polarizes all atoms and not just the closest atom) is sorted out by the simultaneous solution to the system of N equations (for the polarization energy) with N unknowns (i.e., atomic polarizability parameters).

This procedure was used to optimize polarizability parameters for each atom (except for alkyl carbons and hydrogens) in 153 molecules representing a wide variety of functional groups. Alkyl carbon and hydrogen atoms, which were assigned atomic polarizability parameter values of 1.223 and 0.25 Å^3, were the only atoms that were not probed (and parametrized). A common value for the polarizability of various types of atoms, such as the hydroxyl oxygen in alcohols, was obtained by averaging the polarizability found for all atoms of this type. For cases in which there were large variations within a group, than averages were performed over smaller groups with consistent polarizability values. For example, the polarizabilities for nitrogen in primary (1.36 Å^3), secondary (1.15 Å^3), and tertiary (0.97 Å^3) amides were distinguished, due to large variations. The latter variations were caused by resonance effects, wherein nitrogen alkylation stabilizes resonance structures with delocalization of the lone pair on the nitrogen. The resulting delocalization reduces the lone pair electron density in the vicinity of the nitrogen atom, which in turn reduces the nitrogen polarizability.

After classifying the polarizability parameters, they were placed into parameter files and atom typing algorithms are used to identify which atomic polarizability parameter to assign to each atom in ligands outside the 153 molecule training set.

In computing the polarizabilities, we deliberately do not employ extended basis sets; the smallest exponents in the basis set have values for which the basis function would not strongly overlap a neighboring molecule in the condensed phase. As is discussed in detail elsewhere,[20] the use of extended (diffuse) basis functions in computation of the polarizability in the gas phase is of course correct but leads to serious overpolarization in the condensed phase (as has

been observed by us and others empirically). We hypothesize that the reason for this is that in the condensed phase, diffuse functions have high energy due to the Pauli exclusion principle and Coulomb repulsion; they overlap with occupied orbitals of neighboring molecules, which generate matrix elements leading to higher energies. Simply removing these functions from the basis set is a heuristic approach to correcting the problem but appears to work well in our small molecule liquid-state simulations, which have been described in detail.[20]

Given a complete set of polarizability parameters, we next determine the nonbonded atomic parameters by fitting hydrogen bond energies and geometries of a large set of molecular dimers. Hydrogen bond energies are computed quantum mechanically, using an LMP2 based extrapolation procedure (described in detail elsewhere[41]), which has been benchmarked to yield an accuracy of better than ~0.5 kcal/mol in comparison with high level correlated quantum chemical calculations. Results for a suite of 140 dimers are presented in detail below.

The model compounds used in the dimer calculations are typically small molecules with little conformational flexibility. Nevertheless, geometry optimization of the FF structures is required to compute the hydrogen bond energies. This process therefore has to be performed iteratively in parameter space; for the initial development of the nonbonded parameters, initial guesses for torsions are employed; after torsions are fitted, the dimers are reexamined, and the nonbonded parameters are reoptimized if necessary.

Once a complete set of nonbonded parameters are available, the next step is the development of torsional parameters. As was mentioned above, stretches and bends are taken from our fixed charge parametrization. Torsions are fit to quantum chemical data computed at the LMP2/cc-pVTZ(-f)//B3LYP/6-31G* level. Using the almost identical set of model compounds as have been employed in developing the OPLS_2003 fixed charge force field, 975 new torsional parameters have been fit, which leads to a total of 2281 torsion types and which includes protein specific types and torsion types of nonrotatable bonds. The average RMSD of the PFF and quantum chemical conformational energy differences defining our test suite is 1.02 kcal/mol which is comparable in size to the RMSD when a fixed charge functional form is employed (RMSD=0.77 kcal/mol). Additional torsions will be added as new model compounds are added to the database, something that we expect will be an ongoing process.

The final set of parameters for amides, amines, alcohols, carboxylate anions, and ammonium cations are listed in Tables 2−9. Table 2 lists the symbolic atom types for atoms in molecules with these functional groups, and these are used to define the stretch, bend, torsion, and out-of-plane parameters in Tables 3−6. The Lennard-Jones parameters are listed in Table 7, and the exponential repulsion and polarizability parameters are in Table 8. Equations 1−12 define these parameters. Table 9 lists solvation parameters, which are defined in section III.

The most complex aspect of the parametrization process is the fitting of the nonbonded parameters to agree with the quantum chemical hydrogen bond energies and geometries. Our work on parametrizing small molecules for liquid-state simulations has demonstrated (admittedly for a relatively small set of test cases) that properly fitting accurate quantum chemical data for these quantities in the gas phase leads to good thermodynamic properties in the condensed phase, an average error less than 0.5 kcal/mol for the heat of vaporization and less than 5% for the density, comparable to what is obtained when a fixed charge force field is fit directly to experimental data. However, obtaining agreement with the quantum chemical results and having that agreement be transferable to a significant number of heterodimer complexes (as well as the homodimers employed in our liquid-state parametrization work) is a highly challenging task, and

Table 2. Symbolic Atom Types Used To Define Stretch, Bend, Torsion, and Out-of-Plane Parameters for Alcohols, Amides, Amines, Ammonium Cations, and Carboxylate Anions

C	amide carbon
CA	arene carbon
CO3	carboxylate carbon
CT	alkyl carbon
H	polar hydrogen in amines/amides
HC	alkyl and nonpolar amide hydrogen
HNP	ammonium hydrogen
HO	alcohol hydrogen
N	amide nitrogen
NE	arylamine nitrogen
NP	ammonium nitrogen
NT	aliphatic amine nitrogen
O	amide oxygen
OH	alcohol oxygen
O2Z	carboxylate oxygen

Table 3. Stretch Parameters[a]

K_b	b_o	type
340.000	1.090	HC−CT
268.000	1.529	CT−CT
317.000	1.510	CT−CA
469.000	1.400	CA−CA
367.000	1.080	HA−CA
334.643	1.101	HC−C
570.000	1.229	O−C
490.000	1.335	N−C
434.000	1.010	N−H
317.000	1.522	CT−C
337.000	1.449	N−CT
434.000	1.010	NT−H
434.000	1.010	H−NE
434.000	1.010	NP−HNP
382.000	1.448	NT−CT
481.000	1.340	NE−CA
367.000	1.471	NP−CT
320.000	1.410	OH−CT
553.000	0.945	OH−HO
450.000	1.364	OH−CA
317.000	1.522	CT−CO3
400.000	1.490	CA−CO3
656.000	1.250	O2Z−CO3

[a] Units for K_b and b_o are kcal/mol/Å^2 and Å.

Table 4. Bend Parameters[a]

K_θ	θ_o	type
80.000	120.400	O−C−CT
48.218	123.439	O−C−HC
62.898	111.761	N−C−HC
70.000	116.600	N−C−CT
80.000	122.900	O−C−N
63.000	120.000	CA−CA−CA
35.000	120.000	HA−CA−CA
70.000	120.000	CA−CA−OH
70.000	120.000	CT−CA−CA
70.000	120.100	NE−CA−CA
85.000	120.000	CA−CA−CO3
70.000	117.000	O2Z−CO3−CT
80.000	126.000	O2Z−CO3−O2Z
80.000	120.400	CA−CO3−O2Z
33.000	107.800	HC−CT−HC
37.500	110.700	HC−CT−CT
58.350	112.700	CT−CT−CT
35.000	109.500	HC−CT−C
35.000	109.500	N−CT−HC
35.000	109.500	HC−CT−OH
50.000	109.500	OH−CT−CT
63.187	113.715	OH−CT−CA
35.000	109.500	NT−CT−HC
56.200	109.470	NT−CT−CT
35.000	109.500	NP−CT−HC
35.000	109.500	HC−CT−CO3
23.749	111.033	CT−CT−CO3
80.000	111.200	CT−CT−NP
35.000	119.800	H−N−C
35.000	120.000	H−N−H
50.000	121.900	CT−N−C
38.000	118.400	H−N−CT
50.000	118.000	CT−N−CT
35.000	113.500	H−NE−CA
35.000	109.500	HNP−NP−CT
35.000	109.500	HNP−NP−HNP
62.035	112.251	CT−NP−CT
35.000	109.500	H−NT−CT
43.600	106.400	H−NT−H
51.800	107.200	CT−NT−CT
55.000	108.500	HO−OH−CT
35.000	113.000	HO−OH−CA

[a] Units for K_θ and θ_o are kcal/mol/rad^2 and degrees.

Table 5. Torsion Parameters[a]

V_1	V_2	V_3	type
0.000	0.000	0.300	HC−CT−CT−HC
0.000	0.000	0.300	CT−CT−CT−HC
0.713	0.008	0.574	CT−CT−CT−CT
0.000	0.000	0.934	HC−CT−CT−OH
−0.675	−0.226	0.000	CT−CT−CT−OH
−4.034	0.000	0.000	OH−CT−CT−OH
−1.013	−0.709	0.473	HC−CT−CT−NT
6.439	−3.041	2.285	CT−CT−CT−NP
0.000	7.250	0.000	CA−CA−CA−CA
0.000	7.250	0.000	CA−CA−CA−HA
0.000	7.250	0.000	CT−CA−CA−HA
0.000	7.250	0.000	CA−CA−CA−CT
0.000	7.250	0.000	CA−CA−CA−OH
0.000	7.250	0.000	NE−CA−CA−CA
0.000	7.250	0.000	NE−CA−CA−HA
0.000	0.000	0.000	CA−CA−CT−HC
0.615	1.248	0.680	CA−CA−CT−OH
0.000	0.000	0.000	HC−CT−C−O
0.000	0.000	0.000	HC−CT−C−N
0.000	9.917	0.000	H−N−C−HC
0.000	4.900	0.000	H−N−C−O
0.000	6.089	0.000	CT−N−C−O
2.300	6.089	0.000	CT−C−N−CT
0.000	4.900	0.000	CT−C−N−H
2.834	−0.673	−0.488	CT−N−C−HC
0.000	0.000	−0.139	C−N−CT−HC
0.000	0.000	0.000	H−N−CT−HC
0.000	0.000	0.000	CT−N−CT−HC
0.000	0.000	0.400	H−NT−CT−HC
0.000	0.000	−0.271	CT−NT−CT−HC
−0.190	−0.417	0.418	CT−CT−NT−H
0.000	3.138	0.000	CA−CA−NE−H
0.000	0.000	0.261	HNP−NP−CT−HC
0.000	0.000	0.189	CT−NP−CT−HC
0.895	−0.212	0.454	CT−CT−NP−CT
0.000	0.000	0.347	CT−CT−NP−HNP
0.000	0.000	0.416	HC−CT−OH−HO
1.107	−0.243	0.471	CT−CT−OH−HO
−0.104	0.042	2.066	CA−CT−OH−HO
0.000	1.682	0.000	CA−−CA−OH−HO
0.000	0.000	0.000	HC−CT−CO3−O2Z
2.858	1.055	0.000	CT−CT−CO3−O2Z
0.000	2.444	0.000	CA−CA−CO3−O2Z
0.000	7.250	0.000	CA−CA−CA−CO3

[a] Units are kcal/mol.

one which also tests the adequacy of the nonbonded functional form.

Table 10 presents results for 140 dimers representing a large variety of functional groups. An attempt was made to include functional groups bonded to aliphatic, vinyl, and aromatic groups as well as neutral and charged forms of functionalities that are acidic or basic. In addition, for functional groups that can act as both hydrogen donors and acceptors (e.g., alcohols and amines), dimers with both types of interactions (i.e., hydrogen donating and accepting) were included. In some cases a relatively small number of molecules were used to represent various functionalities, such as those with sulfur, including thioacetone, thiazole, thiols, sulfides, sulfide anions, thioacetate anions, sulfonic acids, sulfamides, sulfoxides, sulfones, and other related functionalities. In other cases (e.g., alcohols, amines, nitro groups, and phosphates) many members of a functional group were included, to get an understanding of how transferable the exchange repulsion parameters were. It can be seen that the average errors in hydrogen bond energies are on the order of 0.6 kcal/mol, with a very small number of outliers displaying individual errors greater than 1 kcal/mol. The ability to adequately reproduce the binding energies of the heterodimers for a significant number of functional group classes is particularly noteworthy.

One particular class of compounds that has given a great deal of trouble in developing fixed charge force field parameters are the amines.[47] Initially, virtually all fixed charge force fields were unable to reproduce the trend in solvation free energy as methyl groups were added to

Table 6. Improper Torsion Parameters (kcal/mol)[a]

V_2	type
21.0	HC−N−C−O
21.0	CT−N−C−O
2.2	CA−HA−CA−CA
2.2	CA−CA−CA−CT
2.2	CA−OH−CA−CA
2.2	CA−NE−CA−CA
21.0	O2Z−CT−CO3−O2Z
21.0	O2Z−CA−CO3−O2Z
2.0	H−C−N−H
2.0	H−C−N−CT
2.0	CT−C−N−CT
2.0	H−CA−NE−H

[a] The third atom in the second column specifies the out-of-plane atom. The V_1 and V_3 terms (see eq 4) are 0.

Table 7. Lennard-Jones Parameters[a]

A	*B*	SMARTS	description
7500.0	740.0	[#6]	all carbon
600.0	20.0	[#1] [#6]	hydrogen bonded to carbon
4000.0	900.0	[#7]	all nitrogen
3500.0	950.0	[#8]	all oxygen

[a] Units for *A* and *B* are Å^{12} kcal/mol and Å^{6} kcal/mol (see eq 5). Parameter assignments are made according to the SMARTS pattern.

ammonia; we attributed this problem to gross deviations of force field amine−water binding energies from accurate quantum chemical data.[42] Subsequently, Jorgensen and coworkers showed that modification of the model (most importantly the charge distributions on primary, secondary, and tertiary amine nitrogens) to achieve better agreement with the quantum chemical hydrogen bonding data results in qualitatively improved hydration free energy trends;[43] however, this required ad hoc adjustment of the charge parameters, which were not derivable from for example ESP-fitting data. It is gratifying to note that in Table 10, the binding energies of the various amines with water accurately reproduce quantum chemical data, using the standard fitting protocols that we apply to all of the compounds in our training set. This demonstrates that the functional form and parametrization protocol we are employing is powerful enough to handle a very challenging case, for which fixed charge force fields failed qualitatively in the past.

To further assess the accuracy of PFF interaction energies, a dimer set consisting of various combinations of water, methanol, dimethyl ether, acetone, formamide, acetamide, *N*-methylformamide, and *N*-methylacetamide was constructed, and both the cis and trans conformers of the latter two molecules were included. The PFF and (high level) ab initio binding energies for this set are compared in Table 11, wherein it can be seen that the rms deviation is 0.6 kcal/mol, which is the same as obtained in Table 10. The binding energy results in Table 10 correspond almost exclusively to binding with water, while Table 11 indicates the same level of accuracy for binding to 7 other molecules, including amides, which are the building blocks for proteins. Binding energy comparisons for 182 distinctive dimer structures are presented in Tables 10 and 11.

Agreement for hydrogen bond lengths in some cases appears somewhat problematic, on the order of 0.1 Å. However, errors of this magnitude typically occur when the hydrogen bond is weak and the potential energy surface relatively flat. In such cases, the exact location of the minimum is not critical for obtaining reasonable predictions of key condensed phase properties, as our liquid-state simulation results indicate. Of course, individual cases may still be cause for concern; this can be ascertained, however, only by deploying the relevant parameters in a realistic condensed phase application.

C. Construction of a Complete PFF Gas-Phase Parametrization for a New Molecule. To assemble a PFF parameter set for a new molecule, the following steps must be executed:

(1) Atom typing software is used to assign atom types to each atom of the molecule.

(2) Quantum chemical calculations of the electrostatic potential at the LMP2/cc-pVTZ(-f) level are used to generate the permanent charge parameters (i.e. atomic point charges and dipoles) specific to the particular molecule in question. An automated least-squares fitting procedure is used to generate charges and permanent dipoles that reproduce the ab initio electrostatic potential. Multiple conformations can be used to simultaneously fit permanent charges and dipoles, when desired. Ordinarily, the fit of data from multiple conformations has not been found to be necessary.

(3) Using the atom types, the program assigns parameters for atomic polarizability, nonbonded atom−atom pair interactions, stretches, bends, and torsions.

III. Self-Consistent Reaction Field Continuum Solvation Methodology Based on Solution of the Poisson−Boltzmann Equation

In a continuum solvation model, aqueous solvent is represented as a continuum of dielectric 80. Solution of the Poisson−Boltzmann (PB) equation[27] provides the electric field in all of space, including the reaction field of the solvent, for a fixed solute charge distribution and dielectric boundary. In previous publications, we have described our PB solver, PBF, which computes not only solvation free energies but also analytical gradients of the solvation free energy, for an arbitrary solute geometry, using finite element methods.[28−30,44,45] A Gaussian surface, constructed based on atomic dielectric radii, is employed to describe the dielectric boundary. The present software package utilizes PBF as an integral component of the solvation model.

As is well-known, in a continuum model the reaction field of the solvent can be exactly represented as a distribution of charge on the dielectric surface (surface charge). Furthermore, the surface charge is readily computed from the solution to the PB equation as proportional to the discontinuous jump in the electrostatic potential across the dielectric boundary in the normal direction. These surface charges can then be used to represent the electric field due to the solvent, which induces additional polarization in the solution, which in turn can be computed via the polarizable force field.

In fact, the problem of determining the solute polarization and reaction field for a given solute configuration using a

Table 8. Exponential Repulsion and Polarizability Parameters[a]

σ	C	α	SMARTS	description
0.3209	10417.0	1.22	[CX4]	CT alkyl carbon
0.25	1500000.0	1.49	[c]	CA arene carbon
0.25	300000.0	0.83	[CX3H](=O)[#7X3H2]	C formamide
0.25	500000.0	0.83	[CX3](=O)[#7X3]	C amide
0.25	10000.0	0.815	[CX3](=[O])[O−]	CO3 carboxylate anions
0.2385	5563.3	0.25	[#1]C	HC alkyl hydrogen
0.2385	2000.0	0.39	[#1][c]	HA arene hydrogen
0.2385	2000.0	0.25	[#1][CX3;H](=O)[#7]	HC amides
0.20	10.0	0.24	[#1][N]∼[*]=O	H amides
0.20	160.0	0.24	[#1][N]	H amines
	0.0	0.22	[#1][OX2]	HO alcohol
0.20	10.0	0.24	[#1][#7X4+	HNP ammonium cations
0.28	150000.0	1.36	[NX3H2][CX3](=O)[#1]	N formamide
0.28	200000.0	1.36	[NX3][CX3H2]=O	N acetamide
0.28	100000.0	1.085	[NX3H][CX3H]=O	N *N*-methylformamide
0.28	160000.0	1.15	[NX3H][CX3]=O	N *N*-methylacetamide
0.28	90000.0	0.97	[NX3H0][CX3]=O	N *N*,*N*-dimethylacetamide
0.28	70000.0	1.33	[NX3]	NT aliphatic amine
0.28	70000.0	1.42	[NX3]−[a]	NE arylamine
0.28	49000.0	0.44	[NX4+]	NP ammonium cations
0.253	320000.0	0.91	O=[CX3][#7X3H2]	O primary amide
0.253	450000.0	0.91	O=[CX3][#7X3H]	O secondary amide
0.253	700000.0	0.91	O=[CX3][#7X3]	O tertiary amide
0.233	700000.0	0.77	[OX2H]	OH alcohol
0.253	520000.0	0.97	[OX1]∼[CX3]∼[OX1]	O2Z carboxylate anions

[a] Parameter assignments are made according to the SMARTS pattern. The symbolic atom types in the last column are included only for the purpose of providing an additional aid to understanding the parameter assignments. Units are Å, kcal/mol, and Å^3 for σ, *C*, and α (see eqs 5 and 9).

polarizable force field is isomorphic to the same problem when the solute is represented by a quantum mechanical Hamiltonian. The latter is a problem we have already addressed, and the solution—a self-consistent reaction field (SCRF) methodology—is described in detail in previous publications.[28,29] Briefly, one first computes the gas-phase charge distribution of the solute, then solves the PB equation using this charge distribution, calculates the surface charge, and then determines the new charges on the solute by solving the solute equations—either quantum mechanical or those of the PFF—in the field of the surface charges. This process is iterated until self-consistency is achieved.

To develop an SCRF methodology for PFF, one simply replaces the quantum chemical Hamiltonian with the PFF Hamiltonian. The principal additional complication in the present case is the presence of dipoles, in addition to point charges, in the PFF functional form, but this is a technical issue that is easily addressed (e.g., by treating each dipole as closely spaced point charges). More challenging is making the methodology efficient for large systems; in the QM case, the SCRF methodology has principally been applied to systems of fewer than 200 atoms, whereas in the present case it must be made to converge for thousands of atoms, with an acceptable level of noise in the gradient. There are similarly performance issues associated with having to solve the PB equation numerous times for a large system, calculate gradients, etc. We have developed a considerable amount of new technology, which will be discussed in more detail elsewhere, to accomplish this task. A key component is that the PB forces are evaluated infrequently, as they vary relatively slowly with geometry, to reduce the computation time. We have also designed the methodology to enable specifying frozen regions of the protein. This is essential for practical applications in which one wishes to focus on the ligand and nearby active site residues, for reasons of both efficiency and reduction of random noise in the total energy.

To have any hope of achieving accurate results for a dielectric continuum methodology, it is necessary to parametrize the dielectric radii as well as a nonpolar (cavity) term representing the energetics associated with immersing the solute in water in the absence of charge on the solute (but including the van der Waals interaction between solute and solvent).[46,47] We use the nonpolar functional form developed by Levy and co-workers[46,47] which has been shown to be significantly more accurate than a simple surface area model for the nonpolar term.

The solvation free energy model we used for the PFF/PBF/NP parametrization can be described by the following equations[46]

$$\Delta G_{\mathrm{solv}} = \Delta G_{\mathrm{elec}} + \Delta G_{\mathrm{NP}} \tag{17}$$

$$\Delta G_{\mathrm{NP}} = \sum_{i=1}^{N} [\gamma_i A_i + \alpha_i S_i] \tag{18}$$

$$S_i = 1/\{1 + B_i \exp[-12.0\,(1.5/B_i - 0.4)]/1.5\} \tag{19}$$

where ΔG_{solv} is the total solvation free energy; ΔG_{elec} is the electrostatic solvation free energy, including the free energy components of both the reaction field of the continuum

Table 9. PFF/PBF/NB Solvation Parameters (See Eqs 18 and 19), Which Are the Reaction Field Radii (R^{RF} in Å), Nonpolar Cavity Radii (R^{C} in Å), Surface Tension Coefficient (γ in kcal/mol/Å^2), and vdW Correction Coefficient (α in kcal/mol)

R^{RF}	R^{C}	γ	α	SMARTS	description
2.050	1.750	0.024713	−1.018973	[CX4]	alkyl C
2.250	1.775	0.016117	−0.885767	[c]	arene C
2.050	1.875	0.012244	−0.466651	[CX3](=O)[NX3;H2]	primary amide
2.050	1.875	0.012244	−0.466651	[CX3](=O)[NX3]	amide
1.900	1.650	0.012244	−0.466651	[CX3](=O)[O−]	carboxylate
1.250	1.250	0.001904	0.513867	[#1][#6]	alkyl H
1.555	1.210	0.016117	0.548275	[#1][c]	aryl H
1.250	1.250	0.001904	0.513867	[#1][CX4][NX3]C=O	in amides
1.250	1.250	0.031394	−0.308647	[#1][CX4][NX3]	in amines
1.250	1.000	0.027081	0.206693	[#1][#7]	amide/amine H
1.250	1.000	0.001904	−0.100305	[#1][#8]	alcohol H
1.000	1.000	0.072353	−0.707296	[#1][#7;+]	ammonium H
2.000	1.625	0.020791	−1.020601	[NX3][CX3]=O	amide N
2.000	1.625	0.020791	−1.020601	[NX3;H2][CX3]=O	primary amide
1.955	1.650	0.010187	−1.674489	[NX3;H2][CX4]	primary amine
1.855	1.650	0.010187	−1.674489	[NX3;H]([CX4])[CX4]	secondary amine
1.830	1.650	0.010187	−1.674489	[NX3]([CX4])([CX4])([CX4])	tertiary amine
1.755	1.650	0.010187	−1.674489	[NX3;R](@[CX4])@[CX4]	NT amine N
2.215	1.650	0.010187	−1.674489	[NX3]c	arylamine N
2.115	1.625	0.010187	−1.909777	[#7X4+]	ammonium N
2.025	1.625	0.010187	−1.255859	[NX4+;H1]([CX4])([CX4])[CX4]	ammonium
2.025	1.625	0.010187	−3.749130	[NX4+;H0]([CX4])([CX4])[CX4]	ammonium
2.025	1.625	0.010187	−1.909777	[NX4+][c]	arylammonium
1.685	1.480	0.010211	−0.466651	[OX1]=[CX3][NX3]	amide O
1.855	1.480	0.010211	−0.466651	[OX1]=C[NX3;H2]	primary amide
1.625	1.560	0.024713	−0.827593	[OX2H]	alcohol O
1.725	1.535	0.024713	−0.827593	[OH][CX4][CX4][OH]	diol O
1.625	1.535	0.024713	−0.827593	[OX2H]c	phenol O
1.600	1.480	0.010211	−0.606651	[OX1]~[#6]~[OX1]	carboxylate O
1.550	1.480	0.010211	−0.606651	[OX1]~[#6](~[OX1])c	arylcarboxylate

solvent and the polarization of the solute molecule. ΔG_{NP} is the nonpolar (NP) solvation free energy; γ_i, A_i, α_i, and S_i are the surface tension coefficient, the solvent accessible surface area, the vdW/correction coefficient, and the switching function for atom i, respectively. B_i is the Born radius of atom i, which is defined by our Surface Generalized Born (SGB)[48] solvent model. The purpose of the switching function is to switch off the van der Waals interaction and hydrogen bond interaction of the solute atom with the solvent as the atom is buried deeper and deeper in the solute molecule.[46,47] The Born radius is used as a measure of how deeply an atom is buried in a molecule. The advantage of using the Born radius, rather than using the distance from the surface, is that the Born radius takes into account the overall geometry/cavity shape of the whole solute molecule.

The training set for the solvation parametrization includes 147 small molecules. The molecules were picked to cover all the typical functional groups and chemical varieties for which the experimental solvation free energies can be found in the literature.

The basic protocol of the parametrization is fitting the molecules class by class, starting with the alkanes. The NP solvation energies and the corresponding parameters, which were originally fitted for the fixed charge SGB solvent model with the same set of molecules, were taken as the initial guess of the NP component of the current PFF/PBF/NP parametrization. Then, the total computed solvation energies were fitted to the experimental data by varying the PBF dielectric radii. Finally, the NP parameters and PBF radii were further adjusted in an iterative fashion. For the sake of the parametrization convenience, the cavity radii for the NP term have been fixed to be the same as the OPLSAA vdW radii. In this way, the electrostatic and the NP components of the solvation energies can be adjusted independently. Moreover, the same switching function used for the SGB model (as described by eq 19) was applied with no modification. Further optimization of the switching function will be considered in our future development. Table 9 lists the final solvation parameters for amides, amines, alcohols, carboxylate anions, and ammonium cations.

Table 12 presents experimental and calculated solvation free energies for 147 small molecule solutes, as computed by the final optimized SCRF model. Table 13 presents the summary of the error analysis of the fitted solvation energies by functional group classes. The average unsigned error of 0.26 kcal/mol for 126 neutral molecules and 0.35 kcal/mol for the whole training set are comparable to that obtained for a fixed charge model for the same set of solutes. Parameters are assigned based on the atom types classified by SMARTS pattern (e.g., see Table 9) based on chemical functional groups, and these parameters can then be used to describe an arbitrary organic compound using the atom type

Table 10. Comparison of 140 Binding Energies (kcal/mol) Calculated by Quantum Mechanics and by PFF[a]

dimer	binding energy (kcal/mol) TZ/QZ[b]	PFF	diff	hydrogen bonds[c]	
		Alcohols			
methanol homodimer	−5.79	−5.66	0.13	OH−HO..OH	
methanol	−4.95	−5.07	−0.12	OH−HO..OW	
phenol	−6.85	−6.17	0.69	OH−HO..OW	
vinyl alcohol	−6.65	−6.21	0.44	OH−HO..OW	
ethanol	−4.90	−4.86	0.04	OH−HO..OW	
tert-butyl alcohol	−4.98	−5.46	−0.48	OH−HO..OW	
cyclohexanol	−4.78	−5.20	−0.42	OH−HO..OW	
benzyl alcohol	−7.09	−5.93	1.16	OH−HO..OW	
ethylene glycol	−5.66	−5.99	−0.34	OH−HO..OW	
p-nitrophenol	−7.98	−7.70	0.29	OH−HO..OW	
m-nitrophenol	−8.02	−7.47	0.55	OH−HO..OW	
methanol	−5.49	−5.31	0.18	OW−HW..OH	
phenol	−4.16	−4.40	−0.24	OW−HW..OH	
vinyl alcohol	−3.98	−3.88	0.10	OW−HW..OH	
ethanol	−5.51	−5.32	0.20	OW−HW..OH	
tert-butyl alcohol	−5.99	−5.66	0.33	OW−HW..OH	
cyclohexanol	−6.10	−5.91	0.18	OW−HW..OH	
benzyl alcohol	−4.77	−5.28	−0.50	OW−HW..OH	
ethylene glycol	−5.77	−5.67	0.11	OW−HW..OH	
p-nitrophenol	−3.21	−3.60	−0.39	OW−HW..OH	
rms =0.43					
		Ethers and Esters			
dimethyl ether	−5.18	−5.46	−0.28	OW−HW..OS	
methylvinyl ether	−4.42	−4.56	−0.14	OW−HW..OS	
tetrahydrofuran	−6.54	−7.48	−0.93	OW−HW..OS	
methylphenyl ether	−3.98	−4.70	−0.72	OW−HW..OS	
methylformate	−2.93	−3.28	−0.35	OW−HW..OS	
rms = 0.57					
		Aldehydes, Ketones, Esters, and Urea			
methylformate	−5.74	−6.65	−0.91	OW−HW..O	
formaldehyde	−5.16	−4.23	0.93	OW−HW..O	
acetone	−5.88	−5.60	0.28	OW−HW..O	
propiolactone	−6.54	−5.54	1.00	OW−HW..O	
acrolein	−5.90	−5.55	0.35	OW−HW..O	
acetophenone	−5.43	−5.55	−0.13	OW−HW..O	
butanal	−5.39	−5.40	−0.01	OW−HW..O	
urea	−9.91	−9.15	0.76	OW−HW..O	N−H..OW
rms = 0.66					
		Carboxylic Acids			
acetic acid	−9.47	−9.50	−0.03	OW−HW..O	OH−HO..OW
trans,trans-oxalic acid	−10.21	−8.61	1.59	OW−HW..O	OH−HO..OW
cis,cis-oxalic acid	−4.01	−5.13	−1.12	OW−HW..O	OW−HW..OH
benzoic acid	−9.55	−9.45	0.10	OW−HW..O	OH−HO..OW
rms = 0.98					
		Oxide Anions			
methoxide anion	−21.17	−21.45	−0.28	OW−HW..OM	
vinyloxide anion	−13.15	−13.46	−0.31	OW−HW..OM	
N-methylhydroxamate anion	−15.62	−15.46	0.16	OW−HW..OM	OW−HW..N
acetate anion	−18.60	−18.71	−0.11	OW−HW..O2Z	OW−HW..O2Z
rms = 0.23					
		Nitro and Nitrite Groups			
nitrobenzene	−3.63	−4.23	−0.60	OW−HW..ON	OW−HW..ON
nitrobenzene	−4.35	−4.63	−0.28	OW−HW..ON	
p-nitrophenol	−3.65	−4.43	−0.77	OW−HW..ON	OW−HW..ON
m-nitrophenol	−3.73	−4.13	−0.40	OW−HW..ON	
m-nitroaniline	−3.69	−4.34	−0.65	OW−HW..ON	OW−HW..ON
nitromethane	−3.28	−3.39	−0.12	OW−HW..ON	OW−HW..ON
methylnitrite	−2.44	−3.03	−0.59	OW−HW..ON	

Table 10 (Continued)

dimer	binding energy (kcal/mol) TZ/QZ[b]	PFF	diff	hydrogen bonds[c]	
		Nitro and Nitrite Groups			
nitroethylene	−3.31	−3.75	−0.44	OW−HW..ON	OW−HW..ON
nitrosomethane	−3.68	−3.21	0.47	OW−HW..ON	
nitroethylene	−5.28	−4.15	1.13	OW−HW..ON	CM−HC..OW
rms = 0.61					
		Aromatic Heterocycles with N and O			
imidazole	−5.94	−6.55	−0.60	NA5−H..OW	
pyrrole	−5.22	−5.59	−0.37	NA5−H..OW	
pyrazole	−7.83	−6.57	1.26	NA5−H..OW	OW−HW..N5A
imidazole cation	−16.75	−16.94	−0.19	N5P−HNP..OW	
pyridine	−6.26	−6.10	0.16	OW−HW..NA	
pyrimidine	−5.60	−5.77	−0.17	OW−HW..NA	
tetrazole anion	−16.09	−16.26	−0.17	OW−HW..N5M	OW−HW..N5M
imidazole	−5.15	−6.04	−0.90	OW−HW..N5B	
oxazole	−4.55	−4.89	−0.34	OW−HW..N5B	
1,2,4-oxadiazole	−5.12	−4.10	1.02	OW−HW..N5B	
isoxazole	−4.16	−3.91	0.25	OW−HW..N5A	
1,2,4-oxadiazole	−3.14	−3.28	−0.14	OW−HW..N5A	
furan	−2.65	−2.71	−0.05	OW−HW..OA	
rms = 0.57					
		Amines			
ammonia	−6.11	−6.10	0.02	OW−HW..N3	
methylamine	−6.62	−7.30	−0.68	OW−HW..NT	
dimethylamine	−6.81	−6.38	0.43	OW−HW..NT	
trimethylamine	−7.31	−6.98	0.33	OW−HW..NT	
tert-butylamine	−7.33	−7.53	−0.20	OW−HW..NT	
aniline	−5.40	−5.21	0.19	OW−HW..NE	
dimethylamine	−2.67	−3.30	−0.63	NT−H..OW	
vinylamine	−3.91	−3.73	0.18	NE−H..OW	
p-nitroaniline	−5.28	−5.08	0.19	NE−H..OW	
m-nitroaniline	−5.68	−5.59	0.09	NE−H..OW	
p-cyanoaniline	−5.20	−4.79	0.41	NE−H..OW	
rms = 0.37					
		Imines			
formamidine	−10.32	−9.75	0.57	OW−HW..NI	
formaldehydeimine	−6.16	−5.61	0.55	OW−HW..NI	
guanidine	−7.00	−10.66	−3.66[d]	OW−HW..NE	NE−H..OW
butadiene Schiff base	−6.43	−7.51	−1.09	OW−HW..NI	
butadiene Schiff base	−3.40	−3.42	−0.02	NI−H..OW	
azomethane	−7.75	−7.55	0.20	OW−HW..NN	
rms = 1.59					
		Imine Cations			
guanidinium cation	−17.18	−16.61	0.57	NG−HNP..OW	
formamidine cation	−16.20	−16.22	−0.02	NG−HNP..OW	
formamidine cation	−18.13	−17.92	0.20	NG−HNP..OW	NG−HNP..OW
formaldehydeimine cation	−19.76	−19.86	−0.10	NIP−HNP..OW	
rms = 0.31					
		Nitriles			
dimethyldiazomethane	−2.82	−3.41	−0.59	OW−HW..NZT	
methyl azide	−4.01	−3.23	0.78	OW−HW..NZT	
acetonitrile	−4.76	−4.77	−0.01	OW−HW..NZ	
rms = 0.56					
		N-Hydroxyl			
methylethylhydroxylamine	−8.37	−8.24	0.13	OH−HO..OW	OW−HW..NT
N-methylhydroxamic acid	−7.29	−7.09	0.20	OH−HO..OW	OW−HW..N
rms = 0.17					

Table 10 (Continued)

dimer	binding energy (kcal/mol) TZ/QZ[b]	PFF	diff	hydrogen bonds[c]	
		Quaternary Ammonium Salts			
methylammonium cation	−18.49	−18.77	−0.28	NP−HNP..OW	
dimethylammonium cation	−17.12	−16.83	0.30	NP−HNP..OW	
rms = 0.29					
		Fluorides			
fluoromethane	−3.51	−3.17	0.34	OW−HW..F	
1,1,1-trifluoromethane	−2.81	−3.01	−0.20	OW−HW..F	OW−HW..F
vinylfluoride	−2.90	−2.88	0.02	OW−HW..F	
rms = 0.23					
		Chlorides			
1-chloropropane	−4.14	−3.67	0.47	OW−HW..Cl	
1,1,1-trichloromethane	−2.72	−3.03	−0.32	OW−HW..Cl	OW−HW..Cl
vinyl chloride	−2.56	−2.73	−0.16	OW−HW..Cl	
rms = 0.34					
		Phosphates and Phosphines			
methyl phosphate	−12.60	−13.17	−0.57	OW−HW..O2Z	OS−HO..OW
phosphineoxide	−6.61	−6.86	−0.24	OW−HW..O2Z	
trimethylphosphineoxide	−9.29	−8.84	0.45	OW−HW..O2Z	
$CH_3-CH_2-PO_2-CH_3$ anion	−17.89	−17.87	0.02	OW−HW..O2Z	OW−HW..O2Z
$CH_3-NH-PO_2$-CH_3 anion	−17.80	−17.43	0.37	OW−HW..O2Z	OW−HW..O2Z
$CH_3-NH-PO_2$-CH_3 anion	−16.57	−17.30	−0.74	OW−HW..O2Z	OW−HW..NX
$CH_3-O-PO_2-CH_3$ anion	−17.89	−17.25	0.63	OW−HW..O2Z	OW−HW..O2Z
phosphoric acid	−12.80	−12.30	0.50	OW−HW..O2Z	OS−HO..OW
dihydrogenphosphate anion	−15.30	−15.98	−0.68	OW−HW..O2Z	OW−HW..OS
dihydrogenphosphate anion	−16.89	−16.58	0.30	OW−HW..O2Z	OW−HW..O2Z
hydrogenphosphate dianion	−23.48	−23.74	−0.26	OW−HW..O2Z	OW−HW..O2Z
methylphosphine	−3.40	−3.21	0.19	OW−HW..PR	
trimethylphosphine sulfide	−7.75	−7.78	−0.02	OW−HW..ST	
rms = 0.45					
		Molecules with Sulfur			
hydrogensulfide homodimer	−1.63	−1.69	−0.06	SH−HS..SH	
hydrogensulfide	−2.84	−2.59	0.25	SH−HS..OW	
thiomethanol	−3.00	−2.55	0.45	SH−HS..OW	
hydrogensulfide	−2.81	−3.22	−0.42	OW−HW..SH	
thiomethanol	−3.79	−4.39	−0.61	OW−HW..SH	
dimethyl sulfide	−5.80	−5.27	0.53	OW−HW..S	
thioacetone	−3.70	−3.56	0.14	OW−HW..S=	
thiophene	−3.46	−3.67	−0.21	OW−HW..SA	
thiazole	−6.99	−6.93	0.06	OW−HW..N5B	
isothiazole	−2.70	−2.86	−0.16	OW−HW..N5A	
methyl sulfide anion	−10.42	−10.53	−0.11	OW−HW..SM	
vinylsulfide anion	−14.48	−14.69	−0.22	OW−HW..SM	OW−HW..CM
thioacetate anion	−14.18	−14.15	0.03	OW−HW..SM2	OW−HW..SM2
$CH_3-NH-SO_2-$phenyl	−8.41	−8.40	0.01	OW−HW..OY	
$CH_3-NH-SO_2-CH_3$	−9.86	−9.11	0.76	OW−HW..OY	
$CH_3-CO-NH-SO_2-$CH3	−10.05	−9.72	0.33	OW−HW..OY	NS−H..OW
methanesulfonic acid	−12.28	−12.80	−0.52	OW−HW..OY	OS−HO..OW
sulfamide	−8.81	−8.71	0.10	OW−HW..OY	NS−H..OW
dimethyl sulfoxide	−9.15	−9.23	−0.08	OW−HW..OZ	
$CH_3-SO(NH)(CH_3)$	−7.52	−7.48	0.05	OW−HW..OY	NST−H..OW
$CH_3-SO_2-N-CH_3$ anion	−17.04	−17.75	−0.71	OW−HW..OY	OW−HW..NM
methylsulfonate anion	−14.87	−15.21	−0.33	OW−HW..OY	OW−HW..OY
sulfate dianion	−18.14	−18.18	−0.04	OW−HW..OY	OW−HW..OY
dimethyl sulfone	−7.40	−7.92	−0.51	OW−HW..OY	
$CH_3-NH-SO_2-CH_3$	−8.59	−9.56	−0.97	OW−HW..OY	NS−H..OW

Table 10 (Continued)

dimer	binding energy (kcal/mol) TZ/QZ[b]	PFF	diff	hydrogen bonds[c]	
		Molecules with Sulfur			
$CH_3-CO-NH-SO_2-CH_3$	−6.75	−7.22	−0.47	OW−HW..OY	OW−HW..O
$CH_3-SO_2-N-CH_3$ anion	−15.34	−15.47	−0.13	OW−HW..OY	OW−HW..OY
rms = 0.40					
overall rms			0.58		

[a] All dimers are heterodimers with water, except for the methanol and hydrogen sulfide homodimers. [b] The TZ/QZ results are binding energies extrapolated to the basis set limit from LMP2/cc-pVTZ(-f) and LMP2/cc-pVQZ(-g) calculations at dimer structures optimized by LMP2/cc-pVTZ(-f). [c] Hydrogen bonds are indicated in the last column, using OW and HW to indicate the oxygen and hydrogen in water and using OPLS2003 symbolic atomtypes for all other atoms. As an example, OH−HO..OW indicates an alcohol oxygen donating a hydrogen to an oxygen in water, while for OW−HW..OH water donates a hydrogen to the alcohol oxygen. [d] The amino groups are puckered in the LMP2/cc-pVTZ(-f) optimized structure of guanidine, while they are planar in the PFF structure. As a result, PFF is no longer able to form a OW−HW..NE hydrogen bond, and PFF gives a different optimized structure. If the improper torsion potential is adjusted to allow amino puckering in guanidine, PFF will not have a problem getting the correct dimer structure and binding energy.

assignment algorithms. We do not yet have data that validates the accuracy of the solvation model in protein and other complex applications.

IV. Modeling of Proteins and Protein−Ligand Complexes

A. Protein Force Field. Construction of a protein PFF represents a special case of the general problem of constructing a PFF for a general organic molecule. Thus, the basic technology is similar to that discussed above in section II, although some rules are required for assembling the force field description of a long polymer from parameters for individual amino acids (see ref 16 for details). Blocked dipeptides are used as model molecules for generating torsional parameters. A large database of rotamer states, which are identical to that employed in developing our fixed charge protein force field, is employed to generate the potential energy surfaces for torsional fitting. The set of dipeptide and alanine tetrapeptide conformers in Tables 14 and 15 were described elsewhere.[16,38] The alanine dipeptide minima were chosen by examination of the complete ϕ/ψ map, and all of the alanine di- and tetrapeptide minima are listed elsewhere.[49] For all other dipeptides a molecular mechanics conformational search was followed by further HF/6-31G** geometry optimizations with Jaguar. The final values of the quantum mechanical conformational energies were determined with single-point LMP2/cc-pVTZ(-f)// HF/6-31G** Jaguar calculations. These calculations were performed without solvent for all electrostatically neutral peptides (in Table 14).

For the charged residues (Table 15), a somewhat different technique was employed. Gas-phase optimizations could not be used to obtain the structures, since a geometry with a favorable gas-phase energy could have a significantly higher relative energy in aqueous solution for the charged species. This is why liquid-phase SCRF HF/6-31G** optimizations were used to find the solvated minimum energy structures. They were followed by gas-phase, single point LMP2/cc-pVTZ(-f) calculations to find the final target energies. Thus, on one hand, the part of the conformational space relevant in aqueous solutions was sampled, and, on the other hand, the final quantum mechanical energies were determined in gas phase and can be compared with the gas-phase PFF results.

In Tables 14 and 15 we summarize the average RMSDs achieved by PFF for relative conformational energies of the various rotamer states, as compared to quantum chemical data generated at the LMP2/cc-pVTZ(-f) level, for the 20 naturally occurring amino acids. The average RMSD of about 0.6 kcal/mol is comparable to that achieved for our small molecule training set discussed in section II above, and it is similar to what is obtained when a fixed charge model is used. Moreover, the average error for the charged residues is ca. 1.5 times smaller than with the fixed charge OPLS-AA/L force field. This suggests that the polarizable force field does better than OPLS-AA in reproducing energetics of systems with strong electrostatic interactions, such as, for example, charged protein residues. To reduce errors beyond this point, further work likely has to be done to improve the valence part of the force field (new stretch and bend parameters, along with cross terms coupling stretches, bends, and torsions, etc.).

B. Minimization Protocol. As an initial deployment of PFF in studying protein−ligand complexes, we have developed a protocol for minimizing such complexes in both the gas phase and in continuum solvent. Minimization of the protein in solution, ligand in solution, and protein−ligand complex in solution allows a crude estimator, which may correlate with the binding free energy to be obtained; as was discussed above, these energy differences may also be useful as a component of a more sophisticated approach. We do not attempt to use the methodology to address the binding free energy problem in the present paper; rather, the objective is to demonstrate that the minimization protocol is robust with regard to parameter assignment and generation for the ligands (which requires, of course, deploying the full protocol for parameter generation described above), does not undergo polarization catastrophes, and produces reasonable RMSDs for the proteins and protein−ligand complexes. We also are able to present an initial calibration of the required CPU time for these computations, although this should not be regarded as highly optimized.

We have carried out a number of initial tests of the protein PFF, for example minimizing protein structures starting from the crystal structure and computing the RMSD of the final result as compared to experiment. In carrying out such minimizations, we begin by minimizing the protein using a

Table 11. Comparison of Binding Energies Calculated by Quantum Mechanics and PFF

dimer[a]	binding energy[b] (kcal/mol) TZ/QZ	PFF	diff	hydrogen bonds	
			Amide/Amide Dimers		
FOR/FOR	−14.23	−14.61	−0.38	N−H..O	N−H..O
ACE/ACE	−13.92	−14.49	−0.57	N−H..O	N−H..O
cNMF/cNMF	−15.55	−15.16	0.39	N−H..O	N−H..O
cNMA/cNMA	−14.97	−13.90	1.07	N−H..O	N−H..O
FOR/FOR	−7.05	−8.26	−1.21	N−H..O	
tNMA/tNMA	−7.95	−8.91	−0.97	N−H..O	
FOR/FOR	−9.62	−8.57	1.05	N−H..O	C−HC..O
FOR/FOR	−5.23	−5.00	0.23	C−HC..O	C−HC..O
FOR/FOR	−3.90	−4.79	−0.89	no H-bond (stacked)	
ACE/ACE	−5.35	−6.13	−0.78	no H-bond (stacked)	
tNMA/tNMA	−5.98	−7.08	−1.10	no H-bond (stacked)	
			Water Dimer		
H2O/H2O	−4.83	−4.81	0.02	OW−HW..OW	
			Amide/Water Dimers		
FOR/H2O	−4.97	−5.09	−0.13	N−H..OW	
ACE/H2O	−4.96	−4.56	0.40	N−H..OW	
tNMF/H2O	−4.98	−5.52	−0.53	N−H..OW	
tNMA/H2O	−5.20	−5.07	0.12	N−H..OW	
H2O/FOR	−5.82	−5.82	0.00	OW−HW..O	
H2O/ACE	−7.50	−7.47	0.03	OW−HW..O	
H2O/tNMF	−7.45	−7.66	−0.21	OW−HW..O	
H2O/tNMA	−7.42	−8.26	−0.85	OW−HW..O	
H2O/ACE	−6.92	−7.54	−0.63	OW−HW..O	CT−HC..OW
H2O/cNMA	−6.95	−6.89	0.07	OW−HW..O	CT−HC..OW
H2O/FOR	−9.32	−8.30	1.02	N−H..OW	OW−HW..O
H2O/ACE	−9.38	−8.84	0.53	N−H..OW	OW−HW..O
cNMA/H2O	−9.48	−8.33	1.14	N−H..OW	OW−HW..O
			Dimers with Methanol		
MEOH/MEOH	−5.79	−5.66	0.13	OH−HO..OH	
H2O/MEOH	−5.50	−5.31	0.19	OW−HW..OH	
MEOH/H2O	−4.95	−5.07	−0.12	OH−HO..OW	
FOR/MEOH	−5.69	−5.92	−0.23	N−H..OH	
ACE/MEOH	−5.64	−5.66	−0.02	N−H..OH	
tNMA/MEOH	−6.11	−6.10	0.01	N−H..OH	
MEOH/tNMA	−7.68	−8.94	−1.27	OH−HO..O	
MEOH/FOR	−9.84	−9.31	0.53	N−H..OH	OH−HO..O
MEOH/ACE	−9.60	−9.70	−0.10	N−H..OH	OH−HO..O
cNMA/MEOH	−9.86	−9.37	0.49	OH−HO..O	N−H..OH
			Dimers with Dimethyl Ether		
H2O/DME	−5.18	−5.46	−0.28	OW−HW..OS	
MEOH/DME	−5.59	−−6.01	−0.42	OH−HO..OS	
FOR/DME	−7.91	−6.99	0.93	N−H..OS	
ACE/DME	−5.86	−6.35	−0.49	N−H..OS	
tNMA/DME	−6.08	−7.01	−0.94	N−H..OS	
cNMA/DME	−7.49	−6.87	0.62	N−H..OS	
			Dimers with Acetone		
H2O/ACETONE	−5.88	−5.60	0.28	OW−HW..O	
MEOH/ACETONE	−6.17	−6.20	−0.03	OH−HO..O	
FOR/ACETONE	−8.29	−8.34	−0.05	N−H..O	
ACE/ACETONE	−5.63	−6.25	−0.62	N−H..O	
tNMA/ACETONE	−5.91	−6.84	−0.93	N−H..O	
cNMA/ACETONE	−8.37	−8.18	0.19	N−H..O	
rms deviation			0.63		

[a] This dimer set was constructed from combinations of water (H2O), methanol (MEOH), dimethyl ether (DME), acetone, formamide (FOR), acetamide (ACE), *trans*- and *cis*-*N*-methylformamide (tNMF and cNMF), and *trans*- and *cis*-*N*-methylacetamide (tNMA and cNMA). [b] The QM binding energies were determined from TZ/QZ binding energy extrapolations, as described in Table 10.

Table 12. Computed PFF/PBF/NP and Experimental Solvation Free Energies (kcal/mol) of 147 Small Molecules

molecule	expt	PFF/PBF/NP	diff	molecule	expt	PFF/PBF/NP	diff
			Alkanes				
methane	1.91	1.78	0.13	2-methylbutane	2.38	2.36	0.02
ethane	1.83	1.90	−0.07	2-methylpentane	2.52	2.55	−0.03
propane	1.96	2.06	−0.10	2,2-dimethylbutane	2.59	2.65	−0.06
butane	2.08	2.18	−0.10	cyclopropane	0.75	0.82	−0.07
isobutane	2.32	2.26	0.06	cyclopentane	1.20	1.11	0.09
pentane	2.33	2.32	0.01	cyclohexane	1.23	1.20	0.03
			Alkenes				
ethylene	1.27	1.26	0.01	*trans*-2-pentene	1.34	1.36	−0.02
1-propene	1.27	1.28	−0.01	cyclopentene	0.56	0.51	0.05
1-butene	1.38	1.48	−0.10	acetylene	−0.01	−0.03	0.02
			Alkynes				
1-propyne	−0.31	−0.16	−0.15	1-buten-3-yne	0.04	−0.09	0.13
1-butyne	−0.16	−0.13	−0.03				
			Arenes				
benzene	−0.87	−0.75	−0.12	1,3-dimethylnaphthalene	−2.47	−2.33	−0.14
toluene	−0.89	−0.48	−0.41	2,7-dimethylnaphthalene	−2.63	−2.30	−0.33
o-xylene	−0.90	−0.50	−0.40	fluorene	−3.44	−3.83	0.39
m-xylene	−0.84	−0.73	−0.11	phenanthrene	−3.95	−4.06	0.11
biphenyl	−2.64	−2.96	0.32	acenaphthalene	−3.15	−3.20	0.05
naphthalene	−2.39	−2.23	−0.16	anthracene	−4.23	−4.06	−0.17
			Alcohols				
methanol	−5.11	−5.61	0.50	cyclopentanol	−5.49	−5.53	0.04
ethanol	−5.01	−5.21	0.20	cyclohexanol	−5.48	−5.47	−0.01
1-propanol	−4.83	−4.41	−0.42	phenol	−6.62	−6.29	−0.33
2-propanol	−4.76	−5.11	0.35	ethandiol	−9.60	−9.96	0.36
1-butanol	−4.72	−4.22	−0.50	2-propene-1-ol	−4.80	−5.12	0.32
			Ethers				
dimethyl ether	−1.90	−1.85	−0.05	phenyl methyl ether	−1.04	−2.06	1.02
diethyl ether	−1.63	−1.50	−0.13	1,3-dioxalane	−4.10	−5.05	0.95
methyl *n*-propyl ether	−1.66	−1.23	−0.43	1,4-dioxane	−5.05	−5.04	−0.01
methyl isopropyl ether	−2.01	−1.98	−0.03	tetrahydropyran	−3.12	−2.16	−0.96
tetrahydrofuran	−3.47	−3.24	−0.23	2-methoxy-1-ethanol	−6.80	−7.57	0.77
2,5-dimethyltetrahydrofuran	−2.92	−2.87	−0.05				
			Ketones, Aldehydes				
acetone	−3.85	−3.16	−0.69	propanal	−3.44	−3.04	−0.40
2-butanone	−3.64	−3.78	0.14	butanal	−3.18	−2.85	−0.33
2-pentanone	−3.53	−3.77	0.24	benzaldehyde	−4.02	−4.22	0.20
acetophenone	−4.58	−4.53	−0.05	p-hydroxybenzaldehyde	−10.48	−10.32	−0.16
ethanal	−3.50	−3.22	−0.28				
			Carboxylic Acid				
acetic acid	−6.70	−6.18	−0.52	butyric acid	−6.36	−6.61	0.25
propionic acid	−6.48	−6.78	0.30				
			Esters				
methyl acetate	−3.32	−2.97	−0.35	methylpropanoate	−2.93	−3.13	0.20
ethyl acetate	−3.10	−2.91	−0.19	ethylpropanoate	−2.80	−3.18	0.38
n-propyl acetate	−2.86	−2.64	−0.22	methylbenzoate	−4.28	−3.96	−0.32
ispropyl acetate	−2.65	−2.58	−0.07	ethylformate	−2.65	−2.68	0.03
			Amines				
methylamine	−4.56	−4.14	−0.42	triethylamine	−3.02	−2.03	−0.99
ethylamine	−4.50	−4.78	0.28	pyrrolidine	−5.48	−5.68	0.20
n-propylamine	−4.39	−4.32	−0.07	piperidine	−5.11	−5.17	0.06
n-butylamine	−4.29	−4.25	−0.04	ammonia	−4.31	−4.51	0.20
dimethylamine	−4.29	−4.49	0.20	aniline	−4.90	−4.61	−0.29
diethylamine	−4.07	−3.81	−0.26	*N*-propylguanidine	−10.92	−11.31	0.39
trimethylamine	−3.24	−4.22	0.98				

Table 12 (Continued)

molecule	expt	PFF/PBF/NP	diff	molecule	expt	PFF/PBF/NP	diff
			Amides				
acetamide	−9.71	−9.63	−0.08	*N*-methyl formamide (NMF)	−10.00	−9.94	−0.06
propionamide	−9.41	−9.73	0.32	*N*,*N*-dimethylacetamide	−8.50	−8.27	−0.23
NMA(trans)	−10.08	−10.30	0.22				
			Nitriles				
acetonitrile	−3.89	−4.31	0.42	butyronitrile	−3.64	−3.13	−0.51
propiononitrile	−3.85	−3.50	−0.35	3-hydroxybenzonitrile	−9.67	−9.07	−0.60
			Nitros				
nitroethane	−3.71	−3.61	−0.10	nitrobenzene	−4.12	−3.99	−0.13
1-nitropropane	−3.34	−3.54	0.20	3-nitrophenol	−9.63	−9.55	−0.08
2-nitropropane	−3.14	−3.12	−0.02				
			N Hetero Aromatic				
pyridine	−4.70	−4.68	−0.02	*N*-methyl-2-pyridone	−10.00	−9.79	−0.21
2-methylpyridine	−4.63	−4.19	−0.44	methylimidazole	−10.25	−10.81	0.56
2-methylpyrazine	−5.52	-5.28	−0.24	methylindole	−5.91	−5.57	−0.34
			Thiols, Sulfides				
methanethiol	−1.24	−1.02	−0.22	dimethyl sulfide	−1.54	−1.23	−0.31
ethanethiol	−1.30	−0.88	−0.42	diethyl sulfide	−1.43	−1.10	−0.33
benzenethiol	−2.55	−2.72	0.17	methyl phenylsulfide	−2.73	−3.02	0.29
			Halogen Compounds				
fluoromethane	−0.22	0.23	−0.45	chloroethane	−0.63	−0.54	−0.09
1,1-difluoroethane	−0.11	0.06	−0.17	1-chloropropane	−0.27	−0.28	0.01
trifluoromethane	0.81	0.55	0.26	chlorobenzene	−1.12	−1.00	−0.12
tetrafluoromethane	3.11	2.54	0.57	tetrachloromethane	0.10	−0.80	0.90
tetrafluoroethene	1.38	2.14	−0.76	hexachloroethane	−1.41	−0.93	−0.48
2,2,2-trifluoroethanol	−4.31	−4.57	0.26	tetrachloroethene	0.05	0.24	−0.19
chloromethane	−0.56	−0.70	0.14				
			Ionic Compounds				
acetate anion	−79.90	−79.49	−0.41	pyrrolidinium cation	−61.60	−62.88	1.28
propionate anion	−79.10	−79.26	0.16	piperidinium cation	−60.00	−59.70	−0.30
benzoate anion	−76.00	−76.50	0.50	trimethylammonium cation	−56.60	−58.64	2.04
ammonium cation	−86.00	−86.18	0.18	triethylammonium cation	−50.20	−49.01	−1.19
methylammonium cation	−71.30	−71.76	0.46	tetramethylammonium cation	−52.30	−53.18	0.88
ethylammonium cation	−68.40	−68.47	0.07	tetraethylammonium cation	−45.30	−44.30	−1.00
isopropylammonium cation	−66.50	−65.69	−0.81	anilinium cation	−66.00	−65.97	−0.03
tert-butylammonium cation	−63.10	−61.88	−1.22	*N*,*N*-dimethylanilinium cation	−52.00	−52.31	0.31
dimethylammonium cation	−63.90	−65.14	1.24	pyridinium cation	−56.10	−57.92	1.82
diethylammonium cation	−58.90	−59.84	0.94	methylimidazolium cation	−64.13	−62.38	−1.75
di-*n*-propylammonium cation	−57.70	−56.96	−0.74				

fixed charge force field in SGB solvent, then switch to PFF using an SCRF description of solvation for the final stage of minimization; this saves significant amounts of CPU time. We also performed minimizations in the gas phase to make sure the methodology is working correctly and to compare optimized structures in the gas phase and in solution. Results for 18 proteins are listed in Table 16, where it can be seen that the average rms structural deviations are 1.85 Å in the gas phase and that these deviations are reduced to an average of 1.10 Å in the continuum solvent.

Finally, we have studied 33 protein−ligand complexes using technology similar to that described above. For most of these cases, we minimize only a small region of the protein around the active site in addition to the ligand. Ligand parameters were produced in accordance with the protocol described in section II. Table 17 presents a list of the 33 systems that have been studied, along with CPU times and RMSDs of the ligand as compared to the crystal structure. The quality of the results from the point of view of structural RMSDs is acceptable. The CPU times are long compared to a fixed charge, gas-phase minimization but are clearly short enough to enable a significant number of complexes and structures to be studied in future work.

V. Conclusion

We have developed a comprehensive polarizable force field methodology which can be used to develop parameters, through a mixture of quantum chemical calculations and atom typing parameter assignment, for an arbitrary small organic molecule. A wide range of functional groups has been addressed, and performance of the methodology in the gas phase has been assessed for a substantial training set, examining both conformational energy differences and the binding energy of pairs of small molecules. The average

Table 13. Summary of the Error Analysis of the PFF/PBF/NP Computed Solvation Free Energies for 147 Small Molecules by Functional Group Classes

functional group	average[a]	rms[a]	molecules[a]
alkanes	0.06	0.07	12
alkenes	0.04	0.05	5
alkynes	0.08	0.10	4
arenes	0.23	0.26	12
alcohols	0.30	0.34	10
ethers	0.42	0.58	11
ketones, aldehydes	0.28	0.33	9
carboxylic acids	0.36	0.38	3
esters	0.22	0.25	8
amines	0.34	0.45	13
amides	0.18	0.21	5
nitrils	0.47	0.48	4
nitro compounds	0.11	0.12	5
N hetero aromatic	0.30	0.35	6
thiols, sulfides	0.29	0.30	6
halogen compounds	0.34	0.43	13
neutral subtotal	0.26	0.35	126
ionic compounds	0.83	1.01	21
grand total	0.34	0.50	147

[a] The first two columns are the average unsigned error (kcal/mol) and the rms error (kcal/mol) relative to the experimental data. The number of molecules in each function group class is listed in the last column.

Table 14. rms Energy Deviations (kcal/mol) from LMP2/cc-pVTZ(-f)//HF/6-31G** for Peptides

peptide	PFF	OPLS-AA/L[a]
tetrapeptide: alanine	0.81	0.56
dipeptides: alanine	0.20	0.27
serine	0.16	0.44/0.34
phenylalanine	0.05	0.15
cysteine	0.31	0.35
asparagine	0.19	0.16
glutamine	0.69	0.96
histidine	0.90	0.85
leucine	0.57	0.34/0.38
isoleucine	1.04	0.38
valine	0.14	0.08/0.16
methionine	0.59	0.59
proline	0.76	1.54
tryptophan	0.63	0.50
threonine	0.61	0.87
tyrosine	0.25	0.39
average[b]	0.55	0.47

[a] Kaminski, G. A.; Friesner, R. A.; Tirado-Rives, J.; Jorgensen, W. L. *J. Phys. Chem. B* **2001**, *105*, 6474. [b] Proline not included.

errors obtained for conformational energy differences are comparable to those obtained for fixed charge force field parametrization. The dimer binding energetics are qualitatively superior, as fixed charge models cannot be rigorously fit to accurate ab initio gas-phase values due to polarization effects in the condensed phase. Similarly, the energy errors observed in the polarization model are relatively small. We have also developed a complementary continuum solvation model, which has been fit to reproduce experimental solvation free energy data for 147 small molecules. Finally, minimization of 18 proteins and 33 protein−ligand complexes in continuum solvent yields reasonable results in terms of RMSDs from experimental data and does not display any major numerical problems (e.g. polarization catastrophes).

Table 15. rms Energy Deviations (kcal/mol) from LMP2/cc-pVTZ(-f)//HF/6-31G** for Charged Dipeptides

peptide	PFF	OPLS-AA/L[a]
aspartic acid	0.41	0.16/1.95
glutamic acid	1.41	1.53
lysine	0.32	0.88
protonated histidine	0.57	0.97
arginine	0.72	1.15
average	0.69	0.94/1.29

[a] Kaminski, G. A.; Friesner, R. A.; Tirado-Rives, J.; Jorgensen, W. L. *J. Phys. Chem. B* **2001**, *105*, 6474.

Table 16. PFF/PBF/NP Minimizations of 18 Proteins[a]

protein	residues	atoms	rmsd (gas)	rmsd (solvent)	cpu times[b]
1aho	64	962	1.30	0.91	87.4
1nps	88	1321	1.17	1.00	154.2
1ew4	106	1659	3.86	1.11	226.2
1dhn	121	1932	2.03	1.30	306.1
1qto	122	1813	3.30	1.97	353.3
1whi	122	1937	1.50	1.00	270.6
1ej8	140	2174	1.54	1.04	318.6
1dvo	152	2482	2.53	1.09	492.5
1bv1	159	2451	1.62	1.02	541.6
1u9a	160	2571	1.98	1.03	520.7
2fcb	173	2686	1.76	1.16	555.8
1bk7	190	2934	1.08	0.94	510.5
1pbv	195	3148	2.40	1.16	677.2
1a8l	226	3622	1.36	0.93	1143.5
1b2p	238	3682	1.23	0.90	1029.5
1qts	247	3913	1.76	1.35	1171.0
1bue	265	4065	1.17	0.83	1339.1
1ako	268	4311	1.64	1.05	1453.6
average			1.85	1.10	

[a] Columns 2 and 3 give the number of residues and atoms, while columns 4 and 5 compare gas phase and continuum solvent rms structural deviations (A) from the experimental structures. The last column specifies the CPU time (minutes) for the optimizations in solvent [b] The convergence criteria for the polarization energy and PB calculation are 0.001 and 0.05 kcal/mol, respectively. Convergence of the final total energy gradient was set to 0.05 kcal/mol/A.

As indicated above, the goal of the present work was the creation of a platform enabling testing of the methodology with regard to improving accuracy in the computation of protein−ligand binding affinities. Several possible approaches in which the methodology could be used were discussed, and computational experiments along these lines on realistic pharmaceutical ligands and targets are now feasible with a limited amount of human effort (as opposed to the formidable problem of generating new ligand parameters for each complex medicinal chemistry compound from scratch). Because there are so many factors that contribute to errors in the various alternative types of calculations, it is difficult to predict how much improvement will be realized in early efforts using existing sampling methods and the current continuum solvation model. Ultimately, however, improvements in all aspects of the calculation will enable

Table 17. PFF/PBF/NP Minimizations of the Protein−Ligand Complex Active Sites with the Ligands[a]

compound name	protein		ligand atoms	rmsd (Å)	cpu times[b] (min.)
	residues	atoms			
1rds	105	1497	63	0.86	207.9
1fkg	107	1664	68	0.56	104.1
1stp	121	1745	31	0.13	142.4
1rob	124	1855	33	0.68	396.2
1lmo	129	1952	57	0.40	500.8
1icn	131	2107	53	0.65	287.0
2ifb	131	2114	49	0.27	283.8
1cbs	137	2200	49	0.19	160.6
4fxn	138	2133	50	0.43	237.9
1rbp	175	2756	51	0.12	315.7
1fen	176	2773	50	0.11	288.3
1aaq	198	3123	91	0.79	353.0
1hpv	198	3125	66	0.48	324.3
1hpx	198	3125	87	0.39	367.8
1hsg	198	3125	92	0.31	287.4
1htf	198	3124	79	0.79	587.5
1odw	198	3118	84	1.01	351.8
1pro	198	3131	80	0.34	271.1
1sbg	198	3131	81	0.42	314.2
2upj	198	3124	81	0.55	554.5
1sre	235	3408	29	0.45	444.5
1hsl	238	3684	20	0.33	631.4
1lah	238	3599	22	0.03	751.2
1lst	238	3581	25	0.21	890.8
1aha	246	3895	15	0.06	353.5
1mrg	246	3899	15	0.06	469.9
1mrk	247	3840	32	0.60	570.5
1di8	283	4618	37	0.14	1345.6
1g5s	283	4618	62	0.33	1359.4
1ulb	289	4496	16	0.07	676.7
1abe	305	4673	20	0.09	1487.5
8abp	305	4678	24	0.10	772.3
9abp	305	4669	24	0.08	956.2

[a] The active site is defined as the residues having any atoms within 5 Å from the ligand atoms. Thirty-three complexes were sorted by the total number of residues in the proteins of the complexes. [b] The convergence criteria for the polarization energy and PB calculation are 0.001 and 0.05 kcal/mol, respectively. Convergence of the final total energy gradient was set to 0.05 kcal/mol/Å.

the polarization model to deliver significant improvements. We believe that the present effort, based on its demonstrated accuracy in test cases and range of coverage, represents a substantial step in this direction.

VI. Appendix

The interaction energy of a molecule with an external field is given by

$$E = E_{\text{elec}} + E_{\text{pol}} + E_{\text{hyp}} \tag{20}$$

where E_{elec}, E_{pol}, and E_{hyp} are the electrostatic, polarization, and hyperpolarization components of the total interaction energy. These energy terms are respectively dependent on the first, second, and higher order powers of the electrostatic potential (ϕ), external field components (F_α, F_β, and F_γ), and the first (F'), second (F''), and higher order derivatives of the field. For example, the electrostatic interaction energy is

$$E_{\text{elec}} = q_{\text{mol}}\phi - [\mu_\alpha F_\alpha + (^1/_2)\theta_{\alpha\beta}F_{\alpha\beta}' + (1/15)\Omega_{\alpha\beta\gamma}F_{\alpha\beta\gamma}'' + ...] \tag{21}$$

In eq 21 implicit summations over the Cartesian coordinate components (α, β, γ) are assumed, and q_{mol} is the net charge of the molecule (e.g., −1 electrons for formate anion). The quantities μ_α, $\theta_{\alpha\beta}$, and $\Omega_{\alpha\beta\gamma}$ are the molecular dipole, quadrupole, and octupole moments components. The polarization energy is given by

$$E_{\text{pol}} = -[(1/2)\alpha_{\alpha\beta}F_\alpha F_\beta + (1/3)A_{\alpha:\beta\gamma}F_\alpha F_{\beta\gamma}' + (1/6)C_{\alpha\beta:\beta\gamma}F_{\alpha\beta}'F_{\beta\gamma}' + ...] \tag{22}$$

where $\alpha_{\alpha\beta}$ is a molecular dipole polarizability tensor component and $A_{\alpha:\beta\gamma}$ and $C_{\alpha\beta:\beta\gamma}$ are molecular quadrupole polarizability tensor components. These energy expressions as well as the higher order hyperpolarization energy terms which depend on the third and higher powers of the field (and field derivatives), have been known for a long time.[50,51]

A. Calculation of ab Initio Electrostatic and Polarization Energies for a Molecule/Point Charge System. When the field source is a point charge, the electrostatic potential, field, and field derivatives are all proportional to the value of the point charge. Consequently, the interaction energy (E) between a molecule and a point charge (q) can be described by the Taylor series expansion

$$E = C_1 q + C_2 q^2 + C_3 q^3 + C_4 q^4 + ... \tag{23}$$

where

$$C_1 = d_1 \quad \text{where } d_1 = (\partial E/\partial q)_{q=0} \tag{24}$$

$$C_2 = d_2/2 \quad \text{where } d_2 = (\partial^2 E/\partial q^2)_{q=0} \tag{25}$$

$$C_3 = d_3/6 \quad \text{where } d_3 = (\partial^3 E/\partial q^3)_{q=0} \tag{26}$$

$$C_4 = d_4/12 \quad \text{where } d_4 = (\partial^4 E/\partial q^4)_{q=0} \tag{27}$$

and where all derivatives are evaluated at $q = 0$ from finite differences. Equation 23 is a special case of eq 20. The physical significance of the four terms in eq 23 is shown below, where the constant C_1 is the electrostatic potential at the position of the point charge.

$$E_{\text{elec}} = C_1 q = \text{ab initio electrostatic energy} \tag{28}$$

$$E_{\text{pol}} = C_2 q^2 = \text{ab initio polarization energy} \tag{29}$$

$$E_{1,\text{hyp}} = C_3 q^3 = \text{ab initio first hyperpolarizability energy} \tag{30}$$

$$E_{2,\text{hyp}} = C_4 q^4 = \text{ab initio second hyperpolarizability energy} \tag{31}$$

In principle, numerical differentiation (by finite differences) can be very accurate (to 8 or more significant figures). However, there is an inherent limit to the precision of ab initio energies. Ideally, the smaller the step size used (for

the finite differences) the more accurate the results, but higher order terms (e.g., the fourth derivative) sometimes require larger step sizes. A step size of 0.10 electrons has been found to be sufficient for energy calculations that are accurate to at least (0.01 kcal/mol), though a step size of 0.05 electrons works just as well. Two evaluations of the ab initio energy are needed for the numerical determination of C_1 and the electrostatic energy (eq 28) for a given location of the point charge. One additional energy evaluation is needed to determine the coefficient in eq 29 for the polarization energy.

Equation 23 has been used to determine the total interaction energy as well as the electrostatic, polarization, and hyperpolarization energy components, for a system consisting of water interacting with Mg^{2+} ion, which was replaced by *a* +2 electron point charge.[52]

B. Calculation of ab Initio Electrostatic and Polarization Energies in Molecule/Dipole Probe Systems. Because dipole probes can be used to impose electric fields that approximate the fields in aqueous solutions, it would be nice to be able to directly calculate electrostatic and polarization interaction energies for systems in which two point charges interact with the molecule. The third-order expansion in eqs 32−35, which can be used to represent a molecule interacting with two point charges, is a special case of eq 20.

$$E(q_1) = C_1q_1 + C_2{q_1}^2 + C_3{q_1}^3 \tag{32}$$

$$E(q_2) = D_1q_2 + D_2{q_2}^2 + D_3{q_2}^3 \tag{33}$$

$$E(q_1,q_2) = C_{11}q_1q_2 + C_{12}q_1{q_2}^2 + C_{21}{q_1}^2q_2 \tag{34}$$

$$E = E(q_1) + E(q_2) + E(q_1,q_2) \tag{35}$$

Here, $E(q_1)$ and $E(q_2)$ describe the dependence of the ab initio interaction energy (E) on the point charges q_1 and q_2, and the coefficients C_1, C_2, and C_3 have already been described (see eqs 28−30). The D_1, D_2, and D_3 coefficients are also determined from eqs 28−30. They are computed at the location of the second point charge (q_2), though. Equation 34 includes three coupling interactions with coefficients calculated as follows:

$$C_{11} = (\partial^2E/\partial q_1\,\partial q_2)_{q=0} - c/r_{12} \tag{36}$$

$$C_{12} = (1/2)(\partial^2E/\partial q_1\,\partial {q_2}^2)_{q=0} \tag{37}$$

$$C_{21} = (1/2)(\partial^2E/\partial {q_1}^2\,\partial q_2)_{q=0} \tag{38}$$

The $(\partial^2E/\partial q_1\ \partial q_2)_{q=0}$ derivative from eq 36 is caused in part by polarization of a molecule by the two point charges q_1 and q_2. However, the interaction energy also includes the Coulombic interaction, which is given by cq_1q_2/r_{12}, between these two point charges, where r_{12} is the distance between them and $c = 332.06$ Å-kcal/(mol-e^2) is a units conversion factor. The second derivative of this Coulombic term is subtracted out in eq 36, so that only the polarization component of the second derivative is left.

The electrostatic, polarization, and first hyperpolarization energies for the molecule/dipole probe system are given by eqs 39−41.

$$E_{elec} = C_1q_1 + D_1q_2 \tag{39}$$

$$E_{pol} = C_2{q_1}^2 + D_2{q_2}^2 + C_{11}q_1q_2 \tag{40}$$

$$E_{1,hyp} = C_3{q_1}^3 + D_3{q_2}^3 + C_{12}q_1{q_2}^2 + C_{21}{q_1}^2q_2 \tag{41}$$

Four evaluations of the ab initio energy are needed for the numerical determination of C_1 and D_1 and, therefore, the electrostatic energy for a given location of the two point charges (q_1 and q_2). Five additional energy evaluations are needed to determine the coefficients in eq 40 for the polarization energy.

References

(1) Rick, S. W.; Stuart, S. J.; Berne, B. J. *J. Chem. Phys*. **1994**, *101* (7), 6141−6156.

(2) Rick, S. W.; Stuart, S. J.; Berne, B. J. *J. Mol. Liq*. **1995**, *65*−*6*, 31−40.

(3) Stern, H. A.; Rittner, F.; Berne, B. J.; Friesner, R. A. *J. Chem. Phys.* **2001**, *115*, 2237−2251.

(4) Bernardo, D. N.; Ding, Y. B.; Kroghjespersen, K.; Levy, R. M. *J. Phys. Chem.* **1994**, *98* (15), 4180−4187.

(5) Dang, L. X. *J. Phys. Chem. B* **1998**, *102* (3), 620−624.

(6) Ren, P. Y.; Ponder, J. W. *J. Phys. Chem. B* **2004**, *108* (35), 13427−13437.

(7) Lamoureux, G.; MacKerell, A. D.; Roux, B. *J. Chem. Phys.* **2003**, *119* (10), 5185−5197.

(8) Jeon, J.; Lefohn, A. E.; Voth, G. A. *J. Chem. Phys.* **2003**, *118* (16), 7504−7518.

(9) Liu, Y.-P.; Kim, K.; Berne, B. J.; Friesner, R. A.; Rick, S. W. *J. Chem. Phys.* **1998**, *108* (12), 4739−4755.

(10) Mannfors, B.; Palmo, K.; Krimm, S. *J. Mol. Struct.* **2000**, *556* (1−3), 1−21.

(11) Caldwell, J. W.; Kollman, P. A. *J. Phys. Chem.* **1995**, *99* (16), 6208−6219.

(12) Rick, S. W.; Berne, B. J. *J. Am. Chem. Soc.* **1996**, *118* (3), 672−679.

(13) Kaminski, G. A.; Jorgensen, W. L. *J. Chem. Soc., Perkin Trans.* **1999**, *2* (11), 2365−2375.

(14) Grossfield, A.; Ren, P. Y.; Ponder, J. W. *J. Am. Chem. Soc.* **2003**, *125* (50), 15671−15682.

(15) Stuart, S. J.; Berne, B. J. *J. Phys. Chem.* **1996**, *100* (29), 11934−11943.

(16) Kaminski, G. A.; Stern, H. A.; Berne, B. J.; Friesner, R. A.; Cao, Y. X.; Murphy, R. B.; Zhou, R.; Halgren, T. A. *J. Comput. Chem*. **2002**, *23* (16), 1515−1531.

(17) Patel, S.; Brooks, C. L. *J. Comput. Chem.* **2004**, *25* (1), 1−15.

(18) Patel, S.; Mackerell, A. D.; Brooks, C. L. *J. Comput. Chem.* **2004**, *25* (12), 1504−1514.

(19) Ren, P. Y.; Ponder, J. W. *J. Comput. Chem*. **2002**, *23* (16), 1497−1506.

(20) Kaminski, G. A.; Stern, H. A.; Berne, B. J.; Friesner, R. A. *J. Phys. Chem. A* **2004**, *108*, 621−627.

(21) Stern, H. A.; Kaminski, G. A.; Banks, J. L.; Zhou, R.; Berne, B. J.; Friesner, R. A. *J. Phys. Chem. B* **1999**, *103* (22), 4730−4737.

(22) Banks, J. L.; Kaminski, G. A.; Zhou, R.; Mainz, D. T.; Berne, B. J.; Friesner, R. A. *J. Chem. Phys.* **1999**, *110* (2), 741−754.

(23) Morita, A.. *J. Comput. Chem*. **2002**, *23* (15), 1466−1471.

(24) Panhuis, M. I. H.; Popelier, P. L. A.; Munn, R. W.; Angyan, J. G. *J. Chem. Phys.* **2001**, *114* (18), 7951−7961.

(25) Giese, T. J.; York, D. M. *J. Chem. Phys.* **2004**, *120* (21), 9903−9906.

(26) Sugita, Y.; Okamoto, Y. *Chem. Phys. Lett.* **1999**, *314* (1−2), 141−151.

(27) Honig, B.; Nicholls, A. *Science* **1995**, *268* (5214), 1144−1149.

(28) Tannor, D.; Marten, B.; Murphy, R.; Ringnalda, M.; Friesner, R.; Nicholls, A.; Goddard III, W. A.; Honig, B. *J. Am. Chem. Soc.* **1994**, *116*, 11875−11882.

(29) Cortis, C.; Langlois, J. M.; Beachy, M.; Friesner, R. *J. Chem. Phys*. **1996**, *105* (123), 5472−5484.

(30) Friedrichs, M.; Zhou, R.; Edinger, S. R.; Friesner, R. A. *J. Phys. Chem. B* **1999**, *103* (16), 3057−3061.

(31) Zoete, V.; Michielin, O.; Karplus, M. *J. Comput.-Aided Mol. Des.* **2003**, *17* (12), 861−880.

(32) Wang, J. M.; Morin, P.; Wang, W.; Kollman, P. A. *J. Am. Chem. Soc.* **2001**, *123* (22), 5221−5230.

(33) Gohlke, H., Case, D. A. *J. Comput. Chem*. **2004**, *25* (2), 238−250.

(34) Zhou, R. H.; Friesner, R. A.; Ghosh, A.; Rizzo, R. C.; Jorgensen, W. L.; Levy, R. M. *J. Phys. Chem. B* **2001**, *105* (42), 10388−10397.

(35) Head, M. S.; Given, J. A.; Gilson, M. K. *J. Phys. Chem. A* **1997**, *101* (8), 1609−1618.

(36) Yu, Z. Y.; Jacobson, M. P.; Josovitz, J.; Rapp, C. S.; Friesner, R. A. *J. Phys. Chem. B* **2004**, *108* (21), 6643−6654.

(37) Stone, A. J.; Alderton, M. *Mol. Phys.* **2002**, *100* (1), 221−233.

(38) Kaminksi, G. A.; Friesner, R. A.; Tirado-Rives, J.; Jorgensen, W. L. *J. Phys. Chem. B* **2001**, *105* (28), 6474−6487.

(39) Ahlström, P.; Wallqvist, A.; Engstrom, S.; Jönsson, B. *Mol. Phys.* **1989**, *68* (3), 563−581.

(40) Murphy, R. B.; Beachy, M.; Ringnalda, M.; Friesner, R. *J. Chem. Phys*. **1995**, *103*, 1481−1490.

(41) Kaminski, G. A.; Maple, J. R.; Murphy, R. B.; Braden, D. A.; Friesner, R. A. *J. Chem. Theory Comput.* **2005** *1* (2), 248−254.

(42) Marten, B.; Kim, K.; Cortis, C.; Friesner, R. A.; Murphy, R. B.; Ringnalda, M. N.; Sitkoff, D.; Honig, B. *J. Phys. Chem.* **1996**, *100* (28), 11775−11788.

(43) Rizzo, R. C.; Jorgensen, W. L. *J. Am. Chem. Soc.* **1999**, *121* (20), 4827−4836.

(44) Cortis, C.; Friesner, R. A. *J. Comput. Chem*. **1997**, *18* (13), 1570−1590.

(45) Cortis, C.; Friesner, R. A. *J. Comput. Chem*. **1997**, *18* (13), 1591−1608.

(46) Gallicchio, E.; Zhang, L. Y.; Levy, R. M. *J. Comput. Chem*. **2002**, *23* (5), 517−529.

(47) Levy, R. M.; Zhang, L. Y.; Gallicchio, E.; Felts, A. K. *J. Am. Chem. Soc.* **2003**, *125* (31), 9523−9530.

(48) Ghosh, A.; Rapp, C. S.; Friesner, R. A. *J. Phys. Chem. B* **1998**, *102* (52), 10983−10990.

(49) Beachy, M. D.; Chasman, D.; Murphy, R. B.; Halgren, T. A.; Friesner, R. A. *J. Am. Chem. Soc.* **1997**, *119*, 5908−5920.

(50) Buckingham, A. D. *Adv. Chem. Phys*. **1967,** 112, 107−142.

(51) McLean, A. D.; Yoshimine, M. *J. Chem. Phys*. **1967**, 47, 1927−1935.

(52) Maple, J. R.; Ewig, C. S. *J. Chem. Phys*. **2001** 115 (11), 4981−4988.

CT049855I

JCTC Journal of Chemical Theory and Computation

Structural Determinants of Transmembrane β-Barrels

Themis Lazaridis*

Department of Chemistry, City College of New York/CUNY, 138th Street & Convent Avenue, New York, New York 10031

Received March 6, 2005

Abstract: The recognition of β-barrel membrane proteins based on their sequence is more challenging than the recognition of α-helical membrane proteins. This goal could benefit from a better understanding of the physical determinants of transmembrane β-barrel structure. To that end, we first extend the IMM1 implicit membrane model in a way that allows the modeling of membrane proteins with an internal aqueous pore. The new model (IMM1-pore) gives stable molecular dynamics trajectories for three β-barrel membrane proteins of different sizes and negative water-to-membrane transfer energies of reasonable magnitude. It also discriminates the correct fold for a pair of 10-stranded and 12-stranded transmembrane β-barrels. We then consider a pair of β-barrel proteins: OmpA, which is a membrane β-barrel with hydrophobic residues on the exterior and polar residues in the interior, and retinol binding protein, which is a water soluble protein with polar residues on the exterior and hydrophobic residues in the interior. By threading the sequence of one onto the structure of the other we make two pairs of structures for each sequence, one native and the other a decoy, and evaluate their energy. The energy function discriminates the correct structure. By decomposing the energy into residue contributions we examine which features of each sequence make it fold into one or the other structure. It is found that for the OmpA sequence the largest contribution to stability comes from interactions between polar residues in the interior of the barrel. The major factor that prevents the retinol binding protein sequence from adopting a transmembrane fold is the presence of polar/charged residues at the edges of the putative transmembrane β-strands as well as the less favorable interior polar residue interactions. These results could help design simplified scoring functions for fold recognition and structure prediction of transmembrane β-barrels.

Introduction

The known membrane protein structures belong to two categories: all α-helical and transmembrane β-barrels (TMBB). TMBBs occur in the outer membrane of Gram negative bacteria and presumably also of mitochondria and chloroplasts. They have from 8 to 22 β-strands (always an even number). Their N and C termini are on the periplasmic side and the loops on that side are short while those on the extracellular side can be very long.[1] These proteins perform a wide range of functions, such as allowing passive diffusion of ions and hydrophilic molecules, specific import of nutrients, energy dependent export of toxins, and cell adhesion.

Discriminating TMBBs from soluble β-proteins based on sequence is more challenging than discriminating helical membrane proteins because TMBBs lack the 20-residue hydrophobic stretches that characterize the latter. Early work utilized the alternate hydrophobicity of TM β strands;[2,3] however, this approach gives a lot of false positives. Over the past few years a number of bioinformatic approaches have been developed for the prediction and discrimination of TMBBs based on either neural networks[4−6,7] or Hidden Markov models.[8−11] The accuracy of these methods is typically around 80%. Wimley[12] developed an empirical score based on the relative abundance of amino acid types

* Corresponding author phone: (212)650-8364; fax: (212)650-6107; e-mail: tlazaridis@ccny.cuny.edu.

10.1021/ct050055x CCC: $30.25
Published on Web 05/27/2005

in TMBBs. Liu et al. attempted to discriminate TMBBs from soluble β sheet proteins based on their amino acid composition.[13] Other methods utilize a wider variety of properties,[14] including the presence of a signal peptide.[15]

While the above methods can be successful in recognizing a sequence as a TMBB or predicting the number of strands and the topology, they do not produce an atomic-level three-dimensional model. The methods available for doing so are homology modeling and fold recognition. Application of homology modeling requires significant sequence identity between the sequence under investigation and a protein of known structure, which is not often the case in TMBBs. Fold recognition appears more promising for TMBBs because these proteins have a limited number of folds.

The first goal of the present work was to develop an atomic-level energy function that can discriminate the native state of TMBBs. We do this by modification of IMM1, an implicit membrane effective energy function. IMM1 represents the membrane as a slab of nonpolar solvent. By embedding a cylinder of aqueous solvent into this slab we created a function that can be applied to TMBBs. The second goal was to use this energy function to obtain insights into the determinants of TMBB structure, i.e., investigate the features that make a certain sequence fold into a TMBB as opposed to a soluble β-protein. We do this by considering a pair of β-barrels of the same number of strands, one that is a TMBB (OmpA) and another that is a soluble β-barrel (retinol binding protein). We thread each sequence on the structure of the other sequence, evaluate the energy, and examine which residues contribute most to the energy difference between the correct and the incorrect structure.

Methods

IMM1-Pore. The origin of the energy function developed here is EEF1,[16] an effective energy function for soluble proteins

$$W_{\mathrm{EEF1}} = E + \Delta G^{\mathrm{slv}} \tag{1}$$

where E is the intramolecular energy of the protein, given by a modified form of the CHARMM polar hydrogen force field, and ΔG^{slv} is the solvation free energy, given by

$$\Delta G^{\mathrm{slv}} = \sum_i \Delta G_i^{\mathrm{slv}} = \sum_i \Delta G_i^{\mathrm{ref}} - \sum_i \sum_{j \neq i} g_i(r_{ij}) V_j \tag{2}$$

where $\Delta G_i^{\mathrm{slv}}$ is the solvation free energy of atom i, r_{ij} is the distance between i and j, g_i is the solvation free energy density of i (a Gaussian function of r_{ij}), V_j is the volume of atom j, and $\Delta G_i^{\mathrm{ref}}$ is the solvation free energy of an isolated atom. In addition, EEF1 employs a distance-dependent dielectric constant ($\epsilon = r$ in Å) and a neutralized form of the ionic side chains. A more recent version with updated parameters for the charged and polar side chains is referred to as EEF1.1.[17]

IMM1 is a generalization of EEF1 appropriate for modeling proteins in lipid bilayers.[17] In IMM1 $\Delta G_i^{\mathrm{ref}}$ is a linear combination of values for water and for cyclohexane (which models the nonpolar core of the membrane)

$$\Delta G_i^{\mathrm{ref}}(z') = f(z')\Delta G_i^{\mathrm{ref,wat}} + (1 - f(z'))\Delta G_i^{\mathrm{ref,chex}} \tag{3}$$

where $z' = |z|/(T/2)$ and T is the thickness of the nonpolar core of the membrane. The function $f(z')$ describes the transition from one phase to the other:

$$f(z') = \frac{z'^n}{1 + z'^n} \tag{4}$$

The exponent n controls the steepness of the transition. A value of 10 gives a region of 6 Å over which the environment goes from 90% nonpolar to 90% polar. The midpoint of the transition (f=0.5) corresponds to the hydrocarbon-polar headgroup interface (roughly the level of the ester carbonyls in phospholipids). The strengthening of electrostatic interactions in the membrane is effected by a modified dielectric screening function

$$\epsilon = r^{f_{ij}} \tag{5}$$

where r is the distance in Å (but ϵ is dimensionless), and f_{ij} depends on the position of the interacting atoms with respect to the membrane. Far from the membrane, f_{ij} is equal to 1, and we recover the linear distance-dependent dielectric model. For f_{ij} we employed the empirical model

$$f_{ij} = a + (1 - a)\sqrt{f(z_i)\ f(z_j)} \tag{6}$$

with a being an adjustable parameter. The value $a = 0.85$ was found to give membrane insertion or adsorption energies of the expected order of magnitude.[17]

To make IMM1 applicable to membrane proteins with aqueous channels we replace f in eq 3 and eq 6 by F

$$\Delta G_i^{\mathrm{ref}}(z', r') = F(z', r')\Delta G_i^{\mathrm{ref,wat}} + (1 - F(z', r'))\Delta G_i^{\mathrm{ref,chex}} \tag{7}$$

where

$$F(z', r') = f(z') + h(r') - f(z')h(r') \tag{8}$$

$$h(r') = 1 - \frac{r'^n}{1 + r'^n}, \quad r' = r/R, \quad r = \sqrt{x^2 + y^2} \tag{9}$$

where R is the radius of the aqueous pore. The definition of F ensures that $F = 0$ when f and h are zero and $F = 1$ when f, or h, or both of them are equal to 1. Figure 1 shows the contour of the line $F = 0.5$ on the xz plane. The same value of n is used for both f and h, but that could be changed. The code was implemented in the program CHARMM, version c32a1.

To test this energy function (IMM1-pore) we performed molecular dynamics (MD) simulations on the following proteins: OmpA (pdb code 1BXW[18]), the translocator domain of NalP (pdb code 1UYN[19]), and FhuA (pdb code 1BY3[20]). The extra Met residue at the N terminus of OmpA was omitted. The missing loop of NalP was built in an arbitrary conformation. The parameter R in eq 9 was set equal to the radius of the barrel at the level of Cα atoms. In one case it was varied to identify the value that gives the lowest

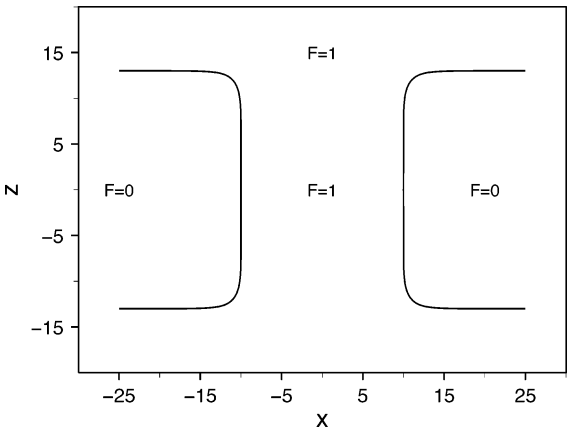

Figure 1. The boundary between nonpolar and aqueous regions in IMM1-pore (where *F* of eq 7 is equal to 0.5).

energy. All simulations proceeded with (a) generation of hydrogen coordinates using HBUILD, (b) a 300-step ABNR energy minimization, and (c) 1 ns MD simulation at 300 K using SHAKE, the Verlet algorithm, and 2 fs time step. In all cases the width of the membrane (*T*) was set to 26 Å.

Generation of the Decoys. To investigate the features that distinguish TMBBs from soluble β-barrels we first identified the closest possible water soluble analogue of OmpA, which seems to be retinol binding protein (RBP, pdb code 1AQB[21]). This protein has 8 β-strands and an additional helix at the C terminus (Figure 3). The structure is less regular than OmpA (the strands are shorter and more bent). The α helix was omitted in this study, i.e., only residues 1−141 were simulated. No disulfide bridges were built, to avoid having different numbers of bonds in the native structure and the decoy.

The decoys were generated using the program MODELLER 7v7.[22] The first hydrophobic residue of each β strand of RBP was aligned with the same from OmpA. The placement of the TM strands on RBP was adjusted slightly to maximize the hydrophobicity of the lipid-exposed residues. The final alignment is OMPA/RBP: 8/20, 38/39, 50/53, 78/67, 92/82, 120/103, 136/116, and 161/131. The maximal possible number of residues was aligned, and all insertions and deletions were placed in the middle of the loops. The MODELLER alignment files are given as Supporting Information.

Results

MD Simulations and Membrane Insertion Energies of TMBBs. Two criteria are used for testing the IMM1-pore energy function. First, MD simulations of TMBBs should give stable structures with small root-mean-square deviations (RMSDs) from the experimental structure. Second, the energy of insertion of a TMBB structure into the membrane (W in the membrane − W of the same conformation in water) should be negative.

The smallest TMBBs are 8-stranded. The best studied of these is OmpA.[18] The insertion energy of OmpA calculated by the standard IMM1 is positive, due to the unfavorable change in solvation free energy of the polar and charged residues in the interior of the barrel, which IMM1 treats as nonpolar. As a result, upon MD with the standard IMM1 the protein moves out of the membrane. Using IMM1-pore, the protein remains stably in the membrane. The energy in the membrane depends on the value of *R* and is lowest for $R = 11$ Å, which is close to radius of the cylinder formed by the Cβ atoms of the lipid-exposed residues. Using this value, the membrane insertion energy of the minimized

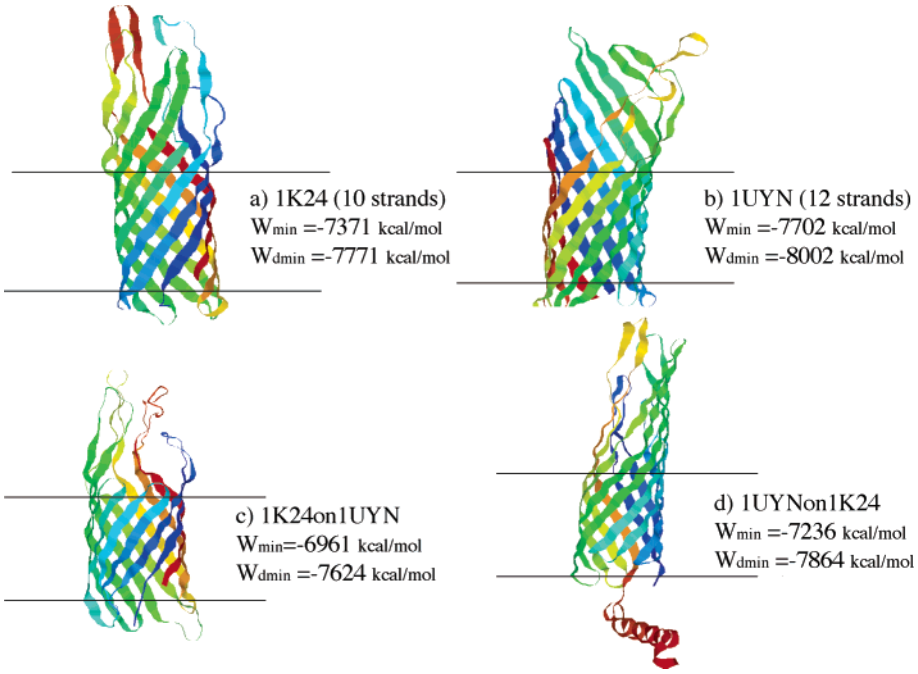

Figure 2. Native states and decoys for the fold recognition test: (a) native 1K24 (10 strands), (b) native 1UYN (12 strands), (c) the sequence of 1K24 threaded onto the structure of 1UYN, and (d) the sequence of 1UYN threaded onto the structure of 1K24. The structures shown are after 50 ps dynamics and minimization. Wmin are energies after minimization and Wdmin are energies after dynamics and minimization.

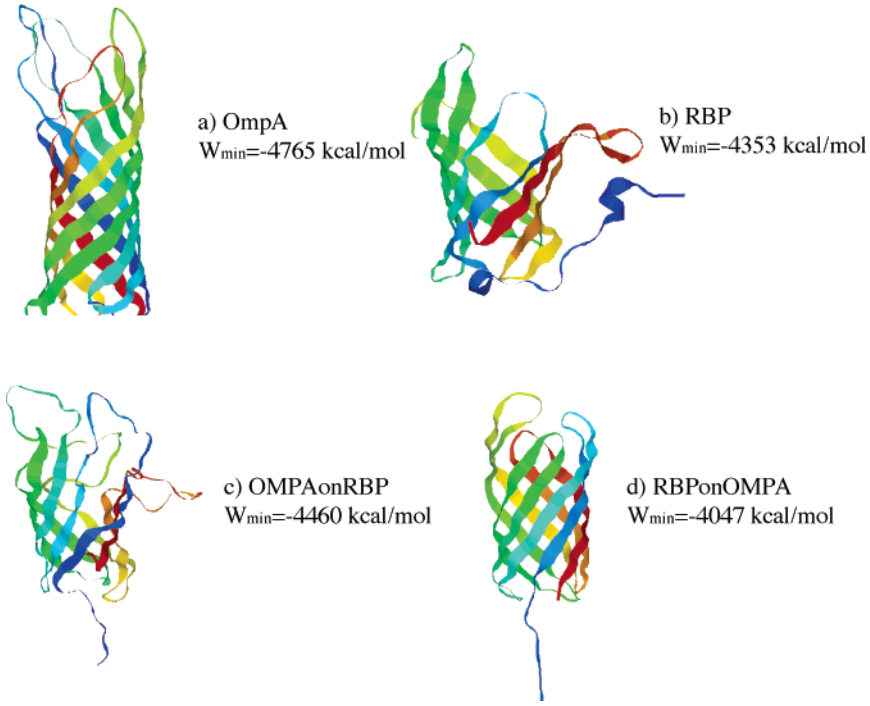

Figure 3. Native states and decoys: (a) native OmpA, (b) native RBP, (c) the sequence of OmpA threaded onto the structure of RBP, and (d) the sequence of RBP threaded onto the structure of OmpA. Wmin are energies after minimization.

OmpA structure is −14 kcal/mol. A 1 ns MD simulation with the same value of R gave a backbone RMSD of 2.9 Å (0.63 Å for the TM region only). These are comparable to previous explicit solvent results. Simulations of OmpA in an explicit lipid bilayer gave a Cα RMSD of about 2 Å for all residues and 0.75 Å for the TM region.[23] Somewhat larger deviations (3.8 Å loops, 1.5 Å TM region) were found in a more recent simulation of spontaneous DPC micelle formation around OmpA.[24] A simulation of OmpX, another 8-stranded TMBB, in water gave about 2 Å RMSD for all Cα atoms and about 1 Å for the TM region.[25] The 1 ns simulation of OmpA with IMM1-pore took 12.2 CPU h on a 3GHz Xeon processor. This is about 20 times faster than the explicit solvent simulations of OmpX.[25]

The translocator domain of the bacterial autotransporter NalP is a TMBB with 12 β-strands. It has been crystallized with an α-helix inside the lumen of the barrel.[19] The helix was omitted from this study. A 1 ns MD simulation of this TMBB gave a backbone RMSD of 1.9 Å for the TM region. The RMSD including the mobile loops was 4.2 Å (3.4 Å excluding the missing loop that was built in an arbitrary conformation). The membrane insertion energy for the minimized structure after dynamics was −15 kcal/mol.

A much larger TMBB is the FhuA receptor (pdb code 1BY3), which has 695 residues, 22 strands, and an N-terminal domain inside the β-barrel. A 1 ns MD simulation of this system with $R = 25$ Å gave overall backbone RMSD 3.9 Å. The backbone RMSD of the N-terminal domain alone was 3.4 Å and that of the TM β-barrel region 2.1 Å. For the final minimized structure, the optimal R is 28 Å and for that value of R the membrane insertion energy is −4 kcal/mol.

In summary, IMM1-pore shows the desired behavior: stable MD simulations, modest RMSDs, and favorable membrane insertion energies for TMBBs of different sizes.

Discrimination of TMBB Folds. Another important test of an effective energy function is whether it can discriminate the correct fold of a protein. For this test to be meaningful, one has to be able to create good-quality decoys. In the case of TMBBs, the sequence and the template must be of similar length, the lipid-exposed sides of all β-strands must be hydrophobic, and the extramembranous portions must be plausible. One pair where these conditions are met is the 10-stranded OpcA adhesin (pdb code 1K24) and the 12-stranded NalP (pdb code 1UYN, without the internal helix).

To convert OpcA into a 12-stranded TMBB we looked for two additional plausible TM β-strands, i.e., 10-residue stretches with good one-sided hydrophobicity. The best were found in the long loop between strands 3 and 4. The lipid-exposed residues on these two additional TM strands were N, I, L, T, E and K, V, L, T, and V. The Lys and Glu fall on the edge of the membrane, which is commonly observed. The two threonines are unfavorable in the hydrophobic core of a membrane but not excessively so. To convert NalP into a 10-stranded TMBB we removed the last two TM strands and built them into an extramembranous α-helix (when left unfolded, the effective energy was somewhat higher). Three-dimensional models for the decoys were built using MODELLER. The decoys and the native structures were energy-minimized and then subjected to a short (50-ps) MD simulation. R was 11 Å for the 10-stranded structures and 12 Å for the 12-stranded structures.

Figure 2 shows the native and decoy structures after MD and minimization together with their energies after minimization or after MD+minimization. They all remained folded in the membrane. Both the minimized and MD+minimized energies clearly discriminate the correct fold.

OmpA vs Retinol Binding Protein. Understanding of the sequence features that dictate the formation of a TMBB could

be enhanced by comparison of sequences that form TMBBs and sequences of similar length that form soluble β-barrels. TMBBs have nonpolar residues on the exterior and a mixture of polar and nonpolar residues in the interior. The opposite is true for water-soluble β-barrels. For OmpA the closest water soluble analogue seems to be retinol binding protein (RBP). It forms an eight-stranded β-barrel and has an additional helix attached on the exterior of the barrel.[21] In this work the helix was omitted. The first hydrophobic residue on each β-strand of RBP was approximately aligned with the first hydrophobic residue on each strand of OmpA. The alignment was provided to the program MODELLER to create two decoys: one for the sequence of OmpA adopting the structure of RBP (OMPAonRBP) and the other for the sequence of RBP adopting the structure of OmpA (RBPonOMPA). The energetics of the decoys was then compared to the energetics of the native structure for each sequence. The membrane-embedded forms (OmpA and RBPonOMPA) were simulated with IMM1-pore and the water soluble forms (RBP and OMPAonRBP) with EEF1.1 (which is equivalent to IMM1-pore far from the membrane). Native RBP gave a backbone RMSD of 2.65 Å upon 1 ns MD simulation with EEF1.1.

Figure 3 shows the decoys and the native structures. The loops in OMPAonRBP are clearly longer than those of a typical globular protein. In contrast, the loops of RBPonOMPA are a bit too tight. The minimized energies are shown in Figure 3. The native structures clearly have much lower energy than the decoys. The energy difference between natives and decoys may be exaggerated because the decoys are generated by an imperfect modeling procedure and may be unrefined compared to actual, crystallographic protein structures, especially in the loop regions. To examine the impact of this we made a model for OmpA based on the structure of another 8-stranded TMBB, NspA (pdb code 1P4T). The energy of the model (−4613 kcal/mol) was higher than that of native OmpA but still much lower than the energy of the soluble decoy (−4460 kcal/mol).

Unconstrained MD simulations of the decoys gave large RMSDs from the initial structure. RBPonOMPA moved completely out of the membrane in 0.5 ns and gave a backbone RMSD of 10.5 Å. OMPAonRBP gave a backbone RMSD of 6.1 Å. The final energies after dynamics were still higher than the energy of the native structure subjected to the same simulation protocol.

Having confirmed that the IMM1-pore energy function discriminates the correct structure for the OmpA and the RBP sequences, we proceed to analyze the contributions to the observed energy difference. The energy function, like its predecessors EEF1 and IMM1, is pairwise additive. Therefore, one can decompose the total energy into contributions from atoms, residues, or groups of residues. Here we consider residue contributions, including both side chain and backbone atoms. The contribution of a residue to the effective energy is equal to the sum of three terms: the intraresidue energy (SELF), one-half of the interaction energy of the residue with all other residues (INTE), and the solvation free energy of all atoms in the residue.[26] The sum of the residue contributions defined this way is equal to the total effective energy of the system. In practice, it is more convenient to include desolvation effects in the pairwise interactions. In that case, the third term is the *reference* solvation free energies of all the atoms in the residue (GREF). The latter make a contribution when membrane proteins are considered because the reference solvation free energies are not constant (see eq 7). This term accounts for the change in background environment. The residues are split into three categories: exterior (E, facing the lipid), interior (I, facing the aqueous pore), and loops (L). The contribution of each category is also reported. For this analysis the minimized structures were used because the decoys are unstable upon MD simulations.

Table 1. Contributions of Selected Residues to the Difference in Effective Energy Going from Native to Decoy for the OmpA Sequence (kcal/mol)[a]

		SELF	INTE	GREF	total	type
THR	152	−7.5	−6.4	0.0	−14.0	
ASN	145	2.6	0.2	−9.8	−7.0	E
LYS	12	−0.3	−0.1	−0.4	−0.8	I
ASP	56	−0.8	3.5	−0.1	2.7	I
LEU	83	0.3	4.0	2.7	7.0	E
GLN	78	2.0	6.4	−0.7	7.7	I
GLN	142	0.5	9.2	0.0	9.6	I
TYR	55	5.1	7.1	−1.5	10.7	E
total		81.2	251.5	−27.8	305	
E		45.4	48.4	11.4	105	
I		38.2	122.3	−25.7	135	
L		−2.4	80.8	−13.5	65	

[a] E and I denote barrel residues facing the lipid and the interior, respectively. All others are loop (L) residues. These values are based on the energy-minimized structures. A complete version of this table is given as Supporting Information.

Table 2. Contributions of Selected Residues to the Difference in Effective Energy Going from Native to Decoy for the RBP Sequence (kcal/mol)[a]

		SELF	INTE	GREF	total	type
ASN	66	−1.8	−10.0	0.0	−11.8	I
ASP	131	0.5	2.2	4.5	7.2	E
PHE	20	−4.1	9.0	2.8	7.7	E
TRP	24	0.4	6.5	1.0	7.9	E
LYS	30	−2.5	4.4	6.2	8.1	E
ASP	39	1.0	−3.1	12.7	10.7	E
ASP	126	−1.8	−3.0	17.3	12.5	E
ARG	139	−2.6	7.5	22.2	27.1	E
total		−14.3	186.3	133.5	306	
E		−11	87.3	75.3	152	
I		3.5	−11.2	38.6	31	
L		−6.8	110.3	19.6	123	

[a] E and I denote barrel residues facing the lipid and the interior, respectively. All others are loop (L) residues. These values are based on the energy-minimized structures. A complete version of this table is given as Supporting Information.

Tables 1 and 2 show the contributions of selected residues to the ΔW for the two sequences (the results for all residues are given as Supporting Information). The contributions are sorted from negative (favoring the decoy) to positive (favoring the native structure). For the OmpA sequence the largest contributions come from the I residues, then the E residues, and finally the loop residues. The I contribution comes primarily from interactions and secondly from self-

energy. The L contribution also comes primarily from interactions. Interactions and self-energy make equal contributions for E residues, with a smaller contribution coming from the change in environment (GREF). Overall, interactions make the largest contribution to ΔW, followed by self-energy, while the change in environment favors the water soluble decoy (polar residues are much "happier" in water).

For the 1AQB sequence the largest contributions to discrimination come from the E residues, followed by the L residues, with only a small contribution from the I residues. The E contribution comes from interactions and change in environment. The L contribution comes primarily from interactions. The I contribution comes primarily from change in environment.

For a more in-depth analysis we can look at individual residue contributions. For the OmpA sequence, Tyr55 makes the largest positive contribution, primarily because it hydrogen bonds to Gln75 in the native (N) structure and makes no such interactions in the decoy. The value of this contribution is probably exaggerated by the use of a single, energy-minimized conformation. A number of I residues make positive contributions because they lose favorable interactions from N to decoy. For example, Gln142 interacts with Gln78, Lys12, and Asp56 inside the pore in the N state but lacks such interactions in the decoy. Several E residues make positive contributions too, which come from a mixture of SELF, INTE, and GREF terms. For example, Leu83 loses some backbone interactions because the RBP β-sheet is less regular at the edges. It also loses some GREF energy because it goes from a position exposed to lipid to a position that is partly exposed to water (there is a cavity in the interior of the barrel in RBP which is presumably filled with water). The largest negative contributions are from loop residues that happen to form better interactions in the decoy. For example, Thr152 has a chance to make a hydrogen bond with Asn145 in the decoy but not in the N structure. Asn145's contribution is also negative because of change in environment; it goes from the edge of the membrane to an aqueous environment.

For the RBP sequence, the largest positive contribution comes from Arg139, primarily due to change in environment. In the decoy Arg139 is close to the edge of the membrane, whereas in the N structure it is exposed to water. Large positive contributions are made by other charged E residues that are on the edge of the membrane (e.g. Asp126, Asp39, Asp131, and Lys30). Some nonpolar E residues, such as Trp24 and Phe20, also make positive contributions because of favorable interactions in the soluble N state. Many of the large negative contributions are from I residues that happen to make good interactions in the TMBB decoy structure.

Discussion

A simple extension of the IMM1 implicit membrane model led to an energy function that can be used to study membrane proteins with an aqueous pore. MD simulations of a range of TMBBs with this function gave stable trajectories and favorable membrane insertion energies. In principle the function could be used with non-β-barrel MPs, such as ion channels. However, the simple cylindrical shape of the pore makes it best for cylindrical molecules. Other pore shapes could be accommodated by changing the definition of the function $h(r')$ in eq 9. For example, the pore cross section could be made elliptical, or it could be made to vary along the z axis.

One limitation is that the aqueous pore is static. Therefore, the energy function cannot be used to study, for example, concerted protein insertion and aqueous pore formation. This problem could conceivably be addressed by making the pore shape and size a dynamic variable in the MD simulation, in much the same way as the piston in constant pressure simulations[27] or the titration variables in constant-pH simulations.[28]

One important application of IMM1-pore stems from its ability to discriminate the native state of TMBBs. Because it is based on physics, it can be used to obtain insights into the features that drive or do not drive protein sequences into TMBB conformations. A first attempt to do so was made here by comparing OmpA with RBP. The major conclusions from this comparison are the following:

(1) The interior residues make a significant contribution to TMBB stability by engaging in favorable interactions with other interior residues. This effect may be largest for small barrels, where the interior residues are in contact with residues across the pore.

(2) Polar and charged residues at the edges of the exterior face of the β-strands destabilize the putative TMBB fold. For the positively charged residues this effect will depend on the nature of the lipids (zwitterionic or anionic).

The results have implications for bioinformatic approaches to TMBB structure prediction. Neural networks and Hidden Markov Models recognize amino acid composition and perhaps certain sequence patterns. Wimley's analysis of amino acid abundance at exterior and interior positions is essentially a one-body term. None of these approaches includes the effect of specific interactions between residues. It appears that inclusion of a pairwise score (as, for example, in soluble protein structure prediction[29,30]) should improve the discrimination.

Acknowledgment. This work was supported by the National Science Foundation (MCB-0316667). Some computational resources were provided by an RCMI grant from NIH (5G12RR003060).

Supporting Information Available: MODELLER alignment files and the complete versions of Tables 1 and 2. This material is available free of charge via the Internet at http://pubs.acs.org.

References

(1) Schulz, G. E. *Curr. Opin. Struct. Biol.* **2000**, *10*, 443.

(2) Vogel, H.; Jahnig, F. *J. Mol. Biol.* **1986**, *190*, 191.

(3) Schirmer, T.; Cowan, S. W. *Protein Sci.* **1993**, *2*, 1361.

(4) Jacoboni, I.; Martelli, P. L.; Fariselli, P.; De Pinto, V.; Casadio, R. *Protein Sci.* **2001**, *10*, 779.

(5) Gromiha, M. M.; Ahmad, S.; Suwa, M. *J. Comput. Chem.* **2004**, *25*, 762.

(6) Diederichs, K.; Freigang, J.; Umhau, S.; Zeth, K.; Breed, J. *Protein Sci.* **1998**, *7*, 2413.

(7) Natt, N. K.; Kaur, H.; Raghava, G. P. S. *Proteins: Struct., Funct., Bioinformatics* **2004**, *56*, 11.

(8) Martelli, P. L.; Fariselli, P.; Krogh, A.; Casadio, R. *Bioinformatics* **2003**, *18*, S46.

(9) Bagos, P. G.; Liakopoulos, T. D.; Spyropoulos, I. C.; Hamodrakas, S. J. *Bmc Bioinformatics* **2004**, *5*, 29.

(10) Bigelow, H. R.; Petrey, D. S.; Liu, J.; Przybylski, D.; Rost, B. *Nucleic Acids Res.* **2004**, *32*, 2566.

(11) Liu, Q.; Zhu, Y. S.; Wang, B. H.; Li, Y. X. *Comput. Biol. Chem.* **2003**, *27*, 69.

(12) Wimley, W. C. *Protein Sci.* **2002**, *11*, 301.

(13) Liu, Q.; Zhu, Y.; Wang, B.; Li, Y. *Comput. Biol. Chem.* **2003**, *27*, 355.

(14) Berven, F. S.; Flikka, K.; Jensen, H. B.; Eidhammer, I. *Nucleic Acids Res.* **2004**, *32*, W394.

(15) Zhai, Y.; Saier, M. H., Jr. *Protein Sci.* **2002**, *11*, 2196.

(16) Lazaridis, T.; Karplus, M. *Proteins* **1999**, *35*, 133.

(17) Lazaridis, T. *Proteins* **2003**, *52*, 176.

(18) Pautsch, A.; Schulz, G. E. *Nature Struct. Biol.* **1998**, *5*, 1013.

(19) Oomen, C. J.; Van Ulsen, P.; Van Gelder, P.; Feijen, M.; Tommassen, J.; Gros, P. *Embo J.* **2004**, *23*, 1257.

(20) Locher, K. P.; Rees, B.; Koebnik, R.; Mitschler, A.; Moulinier, L.; Rosenbusch, J. P.; Moras, D. *Cell* **1998**, *95*, 771.

(21) Zanotti, G.; Panzalorto, M.; Marcato, A.; Malpeli, G.; Folli, C.; Berni, R. *Acta Crystallogr. D Biol. Crystallogr.* **1998**, *54 (Pt 5)*, 1049.

(22) Marti-Renom, M. A.; Stuart, A. C.; Fiser, A.; Sanchez, R.; Melo, F.; Sali, A. *Annu. Rev. Biophys. Biomol. Struct.* **2000**, *29*, 291.

(23) Bond, P. J.; Sansom, M. S. P. *J. Mol. Biol.* **2003**, *329*, 1035.

(24) Bond, P. J.; Cuthbertson, J. M.; Deol, S. S.; Sansom, M. S. P. *J. Am. Chem. Soc.* **2004**, *126*, 15948.

(25) Bockmann, R. A.; Caflisch, A. *Biophys J.* **2005**, *88*, 3191.

(26) Lazaridis, T.; Karplus, M. Microscopic basis of macromolecular thermodynamics. In *Thermodynamics in biology*; DiCera, E., Ed.; Oxford University Press: Oxford, 2001; p 3.

(27) Feller, S. E.; Zhang, Y. H.; Pastor, R. W.; Brooks, B. R. *J. Chem. Phys.* **1995**, *103*, 4613.

(28) Lee, M. S.; Salsbury, F. R., Jr.; Brooks, C. L., III. *Proteins* **2004**, *56*, 738.

(29) Sippl, M. J. *Curr. Opin. Struct. Biol.* **1995**, *5*, 229.

(30) Simons, K. T.; Kooperberg, C.; Huang, E.; Baker, D. *J. Mol. Biol.* **1997**, *268*, 209.

CT050055X

JCTC Journal of Chemical Theory and Computation

Free Energy Landscape of Protein−Protein Encounter Resulting from Brownian Dynamics Simulations of Barnase:Barstar

Alexander Spaar and Volkhard Helms*

Center for Bioinformatics, Saarland University, Im Stadtwald, D-66041 Saarbrücken, Germany

Received February 24, 2005

Abstract: Over the past years Brownian dynamics (BD) simulations have been proven to be a suitable tool for the analysis of protein−protein association. The computed rates and relative trends for protein mutants and different ionic strength are generally in good agreement with experimental results, e.g. see ref 1. By design, BD simulations correspond to an intensive sampling over energetically favorable states, rather than to a systematic sampling over all possible states which is feasible only at rather low resolution. On the example of barnase and barstar, a well characterized model system of electrostatically steered diffusional encounter, we report here the computation of the 6-dimensional free energy landscape for the encounter process of two proteins by a novel, careful analysis of the trajectories from BD simulations. The aim of these studies was the clarification of the encounter state. Along the trajectories, the individual positions and orientations of one protein (relative to the other) are recorded and stored in so-called *occupancy maps*. Since the number of simulated trajectories is sufficiently high, these occupancy maps can be interpreted as a probability distribution which allows the calculation of the entropy landscape by the use of a locally defined entropy function. Additionally, the configuration dependent electrostatic and desolvation energies are recorded in separate maps. The free energy landscape of protein−protein encounter is finally obtained by summing the energy and entropy contributions. In the free energy profile along the reaction path, which is defined as the path along the minima in the free energy landscape, a minimum shows up suggesting this to be used as the definition of the *encounter state*. This minimum describes a state of reduced diffusion velocity where the electrostatic attraction is compensated by the repulsion due to the unfavorable desolvation of the charged residues and the entropy loss due to the increasing restriction of the motional freedom. In the simulations the orientational degrees of freedom at the encounter state are found to be less restricted than the translational degrees of freedom. Therefore, the orientational alignment of the two binding partners seems to take place beyond this free energy minimum. The free energy profiles along the reaction pathway are compared for different ionic strength and temperature. This novel analysis technique facilitates mechanistic interpretation of protein−protein encounter pathways which should be useful for interpretation of experimental results as well.

Introduction

The association of two proteins is commonly described by a simple picture where initially the free proteins diffuse randomly in solution until they enter into the electrostatic field of the other, the so-called steering region. In this region they move by directional diffusion toward the so-called *encounter complex*. Once the encounter complex is formed, it can either dissociate or evolve into the final complex. The process of association to finally form a bound complex can

* Corresponding author phone: +49 681 302 64165; e-mail: volkhard.helms@bioinformatik.uni-saarland.de.

10.1021/ct050036n CCC: $30.25
Published on Web 05/18/2005

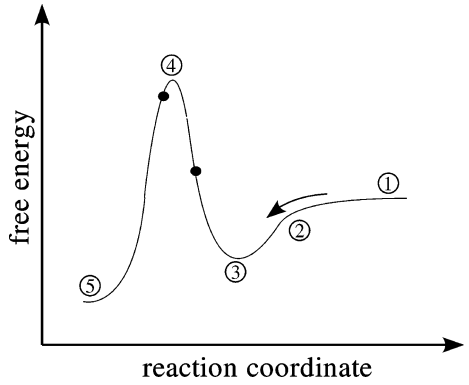

Figure 1. Sketch of the free energy profile along the reaction pathway: (1) denotes the region of free diffusion, (2) the steering region, (3) a minimum of free energy, here used as a definition of the encounter complex, (4) the transition state, and (5) the bound state. The region up to the first black circle, including the steering region and the formation of the encounter complex, can be well modeled by BD simulations. The second circle indicates the point-of-no-return, i.e., where the proteins are committed to form a bound complex.

thus be divided into two steps, where the first one is the formation of the encounter complex, the end-point of the diffusional encounter, while in the second step the proteins subsequently rearrange to form the final bound complex.[2] Figure 1 shows a sketch of the free energy profile along the path of minimal free energy, also called reaction pathway, for an electrostatically steered association: (1) denotes the region of free diffusion, (2) the steering region, (3) a minimum of free energy, here used as definition of the encounter complex, (4) the transition state, and (5) the bound state. Since the first process including the formation of the encounter complex is diffusion limited, it can be modeled by Brownian Dynamics (BD) simulations. The computed association rates from these simulations are in excellent agreement with experimental results once a definition of the so-called *diffusional encounter complex* (which is different from our definition) is used.[1] This diffusional encounter complex is supposed to be located just behind the transition state (4). In the transition state there is a 50:50 chance of binding or association; a position closer than the transition state reflects a 100% probability of binding.

Typical BD simulations of protein−protein encounter employ a series of simplifications: the proteins are modeled as rigid bodies and short-range interactions such as van der Waals forces and the formation of hydrogen bonds and salt bridges are not modeled. However, both aspects become important when the proteins approach the bound conformation, i.e., in the region beyond the diffusion limited regime. To model this second step in the process of association, the transition from the encounter to the bound state, likely more detailed simulation methods have to be applied. In Figure 1 the region up to the first black circle, including the steering region and the formation of the encounter complex, can be well modeled by BD simulations. The second circle indicates the point-of-no-return, i.e., where the proteins are committed to form a bound complex.

While the above-described two-step model of protein−protein association certainly holds true, the detailed steps in diffusional protein−protein encounter are still subject of discussion. In particular the definition of the encounter complex, the intermediate step before the formation of the bound complex, is not completely clear. In a recent article[3] Gabdoulline and Wade have summarized several structural approaches, e.g. the formation of two or three contacts with a certain maximum distance (set by comparison with experimental results),[4] the rotational restriction and the surface area buried in the protein−protein interface,[5] or a maximum deviation of two orientational angles from the bound structure.[6] On the other hand, Camacho and co-workers[7] suggested defining the encounter state as a local minimum in the free energy landscape, an approach which has been taken up in this work. Since protein−protein encounter can be understood as diffusional motion on a funnel-shaped potential energy surface, the knowledge of the free energy landscape should provide a full picture about the encounter process. In their work, the free energy landscape, which was defined as the sum of the electrostatic and desolvation energy, was determined by a systematic sampling of the 6-dimensional conformation space. A disadvantage of this systematic sampling is the immense computational effort if it is performed even at medium resolution. For example, a resolution of 10° for the five angular coordinates and 5 Å for the radial coordinate in a range of 50 Å results in a computation of $36^3 * 18^2 * 10 \sim 10^8$ values. An attractive alternative are simulation methods that give a preferential sampling of the energy landscape, i.e., along the energy valleys.

Here, we present results from BD simulations for the example of barnase and barstar with the aim of clarifying the definition of the encounter state. The ribonuclease barnase and its inhibitor barstar provide a well characterized model system of electrically steered diffusional encounter.[1,5−10] In our studies we examined the electrostatic and desolvation energy along the protein trajectories and additionally recorded the occupancy of the configuration space. This additional information provides insight into the restrictions of the positional and orientational degrees of freedom during the encounter process. These occupancy maps are interpreted as probability distributions in order to derive the entropy landscape by applying a locally defined entropy function. This entropy function takes into account the occupancies of all those configurations, which are reachable from the particular position and orientation within one Brownian dynamics time step.

Estimations of the loss of translational and rotational entropy during the complex formation of barnase and barstar using geometric constraints gave values around 15 kcal/mol,[5] while the application of the gas-phase expressions of the translational and rotational entropy results in 28 kcal/mol.[11] In contrast, Frisch and co-workers showed in an experimental study that the activation entropy at the transition state is close to zero.[12] In this case the entropy corresponds to the loss of translational, rotational, and internal degrees of freedom as well as the entropy of the surrounding solvent, i.e., neither of these processes is very pronounced, or their contributions cancel each other. These examples show that the issue of

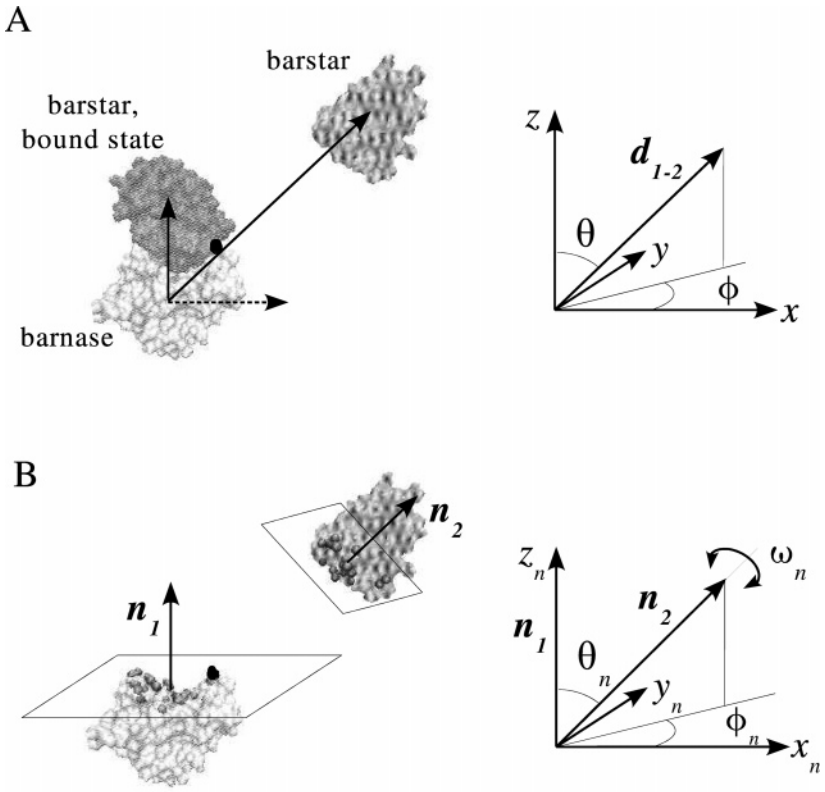

Figure 2. Definition of the reference coordinate system: (A) the positional coordinates and (B) the orientational coordinates. Barnase (protein 1) is displayed in light gray, barstar (protein 2) in dark gray. The black points indicate the position of SER38:OG used for the definition of the *x*-axis. The definition of the coordinates and the angles is given in the text. Figures 2 and 8 were generated using the VMD program.[28]

deriving the entropy for protein−protein association is controversial.

As a final point of our analysis, the free energy landscape is computed by summing the electrostatic and desolvation energies as well as the translational and rotational entropy losses. The free energy profile along the reaction path, which is defined as the path along the minima of the free energy landscape, contains detailed information about the encounter process. The characteristic minimum in the free energy profile is located at the intersection of a favorably decreasing electrostatic interaction energy with an unfavorable desolvation energy and, most notably, with the unfavorable restriction of translational and rotational degrees of freedom. This minimum should be amenable to time-resolved spectroscopic investigation, possibly only in the future.

Methods

Structures. We used the coordinates of barnase and barstar (see Figure 2) as they were prepared by Gabdoulline and Wade and included in the SDA software package.[10]

In their work, the coordinates of the barnase-barstar complex, determined to 2.0 Å resolution by Buckle and coworkers,[8] were taken from the protein data bank (PDB code 1brs). For barnase chain A was used and for barstar chain D. The two other pairs of chains in the crystal structure were used to model the missing side chain atoms in the A and D chains. Crystallographic water molecules were removed. Polar hydrogen atoms were added, and their positions were optimized by energy minimization with the CHARMM program[13] using the QUANTA molecular graphics package.[14] Side-chain conformations were kept the same as in the barnase−barstar complex.

Computation of Forces. In the BD simulations of this work the computation of forces and torques which act on the proteins are performed as it is described in ref 15. First we give a brief overview of the steps involved: For each protein electrostatic potential grids are computed, taking into account the inhomogeneous dielectric medium and the surrounding ionic solvent. A set of effective charges is computed for each protein which represent the external electrostatic potential of the molecule. These sets of effective charges are used to calculate the intermolecular electrostatic interactions during the BD simulation. A further contribution is computed for the interaction of the charges of the proteins with precomputed desolvation grids representing the penalty due to charge desolvation by the low dielectric of the protein interior. Short-range forces are treated in a rather coarse manner by prohibiting overlap of the exclusion volumes of the proteins. The results of our work, the analysis of the encounter pathways and the encounter free energy profiles, are complementary to recent studies of association rates of barnase and barstar, in particular to the work of R. R. Gabdoulline and R. C. Wade. To allow a comparison to their results, we used the same parameters for the computation of forces as in ref 1.

Now the individual steps are described in detail. For the modeling of the long-range electrostatic interaction of the proteins, solutions of the full Poisson−Boltzmann equation

Table 1: Shown Are the Solvent Dielectric ϵ_{solv}, Viscosity η, and Diffusion Coefficients for Barnase and Barstar for the Temperatures Used in the Simulations[a]

T [K]	ϵ_{solv}	η [Pa s]	D [Å^2/ps]	$D_{R,bn}$ [rad^2/ps]	$D_{R,bs}$ [rad^2/ps]
200	122.4	4.01×10^{-2}	4.40×10^{-4}	5.87×10^{-7}	6.60×10^{-7}
220	111.9	1.39×10^{-2}	1.39×10^{-3}	1.86×10^{-6}	2.09×10^{-6}
240	102.2	5.78×10^{-3}	3.67×10^{-3}	4.89×10^{-6}	5.50×10^{-6}
260	93.3	2.74×10^{-3}	8.37×10^{-3}	1.12×10^{-5}	1.26×10^{-5}
280	85.2	1.45×10^{-3}	1.71×10^{-2}	2.28×10^{-5}	2.56×10^{-5}
300	77.7	8.33×10^{-4}	3.18×10^{-2}	4.24×10^{-5}	4.77×10^{-5}
320	70.9	5.13×10^{-4}	5.51×10^{-2}	7.34×10^{-5}	8.26×10^{-5}
340	64.7	3.35×10^{-4}	8.97×10^{-2}	1.20×10^{-4}	1.35×10^{-4}
360	59.0	2.29×10^{-4}	1.39×10^{-1}	1.85×10^{-4}	2.08×10^{-4}
380	53.8	1.63×10^{-4}	2.06×10^{-1}	2.75×10^{-4}	3.09×10^{-4}
400	49.0	1.20×10^{-4}	2.94×10^{-1}	3.93×10^{-4}	4.42×10^{-4}

[a] D is the relative translational diffusion coefficient, and $D_{R,bn}$ and $D_{R,bs}$ are the rotational diffusion coefficients for barnase and barstar, respectively.

were computed for each protein using the UHBD program.[16] Partial atomic charges and atomic radii were assigned from the OPLS parameter set.[17] The protonation states of titratable residues were assigned according to their standard protonation states at the experimental pH of 8.0.[9] Grids with dimensions of 150 × 150 × 150 nodes and a 1.0-Å spacing centered on each of the proteins were used. The ionic strength of the solvent was varied in 10 logarithmic steps from 0 to 1600 mM at a constant temperature of 300 K. To model infinite ionic strength one simulation was performed where all the interaction forces except for the exclusion forces were switched off. For the study of the temperature dependence, the ionic strength was set to 50 mM, while the temperature was varied in steps of 20 K in the range between 200 and 400 K. Phase transitions of water at $T = 273$ and 373 K were not considered (see Discussion). In all calculations the dielectric constant for the protein interior was set to 4.0. The external solvent dielectric was calculated by a polynomial fit of the dielectric constant of water for the temperatures as given in ref 18, at 300 K being 77.7. [Besides the polynomial approach $\epsilon(T) = b_0 + b_1T_c + b_2T_c^2 + b_3T_c^3$, $T_c = T - 273.15$ K, an exponential fitting equation $\epsilon(T) = exp(b_0 + b_1T_c)$ is suggested in ref 18. The relative deviation of the fitted to the given values, however, was much smaller for the polynomial approach. Again, phase transitions were omitted.] The values for the solvent dielectric which were used in the simulations are listed in Table 1.

The effective charge method (ECM)[19] was used to derive charges that represent the external electrostatic potential of the molecule in a uniform dielectric medium. The effective charges were fitted to reproduce the electrostatic potential in a 3 Å thick layer starting at the accessible surface defined by a probe of radius 4 Å and extending outward from the protein. To compute forces and torques acting on protein 2(1), the array of effective charges for protein 2(1) is placed on the electrostatic potential grid of protein 1(2).

Short-range repulsive forces are treated by an exclusion volume prohibiting van der Waals overlap of the proteins. The exclusion volume is precalculated on a grid with 0.5 Å grid spacing. If a move during the BD simulation would result in van der Waals overlap, the BD step is repeated with different random numbers until no overlap occurs. The surface-exposed atoms of the smaller protein are listed, and steric overlap is defined to occur when one of the surface-exposed atoms is projected on a grid point which represents the interior of the larger protein.[20]

Charge desolvation penalties are computed in an approximate fashion which treats the solvation of each charge independently.[15] The charge desolvation penalty of one protein is taken as the sum of desolvation penalties of each charge of that protein. The desolvation penalty of each charge is the sum of desolvation penalties due to the low dielectric cavity of each atom of the other protein. The desolvation energy of protein 1, due to the presence of protein 2, is approximated as

$$\Delta G_{ds} = \alpha \frac{\epsilon_s - \epsilon_p}{\epsilon_s(2\epsilon_s + \epsilon_p)} \sum_{ij} (1 + \kappa r_{ij})^2 \, e^{-2\kappa r_{ij}} \frac{q_i^2 a_j^3}{r_{ij}^4} \quad (1)$$

where κ is the Debye−Hückel parameter, ϵ_s and ϵ_p are the dielectric constants of the solvent and the protein, respectively, q_i is the effective charge on the ith atom of protein 1, a_j is the radius of the jth atom of protein 2, and r_{ij} is the distance between the two atoms. The summation is carried out over all possible pairs of effective charges on protein 1 and atoms on protein 2. The scaling factor α for the weighting between electrostatic interaction and desolvation terms was set to 1.67. The validity of this choice may be assessed from the electrostatic interaction free energy calculations shown in Figures 1 and 2 of ref 1.

The atom−atom contacts of the *reaction patches* are assigned in a fully automated way independent of which residue each atom is in ref 10. Possible contacts are those pairs between hydrogen-bond donor and acceptor atoms having a separation distance of less than 5.0 Å in the X-ray structure of the complex.

Brownian Dynamics Simulation. For the BD simulations we used the software package SDA (Simulation of Diffusional Association of proteins)[4,10] which was modified to allow for a detailed analysis of the trajectories. As in other BD simulations of protein−protein encounter like UHBD[16] or MacroDox,[21] SDA makes simplifications which become important only at small protein−protein separations: the proteins are modeled as rigid bodies and short-range interactions as van der Waals forces and the formations of hydrogen bonds and salt bridges are not modeled.

For each set of parameters, 10 000 trajectories were simulated. The trajectories start with the two proteins at a center-to-center distance b with randomly chosen orientations and finish when the proteins reach a center-to-center distance $c > b$. In all simulations b was chosen as 100 Å and c as 500 Å. This corresponds to 7.4 and 36.8 Debye lengths at 300 K and 50 mM. The diffusion equation is solved by the Ermak−McCammon algorithm.[22] The translational Brownian motion of two interacting proteins is simulated as the displacement $\Delta\mathbf{r}$ of the relative separation vector $\mathbf{r}$ during a time step Δt according to the relation

$$\Delta\mathbf{r} = \frac{D\Delta t}{k_B T}\mathbf{F} + \mathbf{R}, \text{ with } \langle\mathbf{R}\rangle = 0 \text{ and } \langle\mathbf{R}^2\rangle = 6D\Delta t \quad (2)$$

where **F** is the systematic interparticle force, k_B is the Boltzmann constant, T is the temperature, and **R** is the stochastic displacement arising from collisions of the proteins with solvent molecules. Two analogous formulas are used to generate the rotational motions of the two proteins in terms of rotation angle $\mathbf{w}_j = (w_{1j}, w_{2j}, w_{3j})$, torque $\mathbf{T}_{ij}$ acting on protein i due to protein j, and rotational diffusion constant D_{iR} of each protein i ($i, j = 1, 2, i \neq j$):

$$\Delta\mathbf{w}_i = \frac{D_{iR}\Delta t}{k_B T}\mathbf{T}_{ij} + \mathbf{W}_i \text{ with } \langle\mathbf{W}_i\rangle = 0 \text{ and } \langle\mathbf{W}_i^2\rangle = 6D_{iR}\Delta t \quad (3)$$

The diffusional properties of the molecules are assumed to be isotropic. In ref 1 a relative translational diffusion constant of 0.030 Å^2/ps was used, based on the individual diffusion constants of 0.015 Å^2/ps assigned to both barnase and barstar in aqueous solution at 298 K, and rotational diffusion constants of 4.0×10^{-5} and 4.5×10^{-5} radian^2/ps for barnase and barstar, respectively. Based on these values, we calculated the diffusion coefficients for temperatures in the range from 200 to 400 K according to the Einstein−Stokes relationship $D \propto T/\eta(T)$. Here the temperature dependence of the solvent viscosity is approximately given by the Arrhenius behavior $\eta(T) = Ae^{E_a/RT}$, and E_a is the activation energy for the solvent molecules in their respective cages (water: $A = 1.05 \times 10^{-6}$ Pa s, $E_a = 4.02$ kcal/mol[23]). Table 1 lists the viscosity and the diffusion coefficients for the temperatures used in the simulations.

For $T = 300$ K, the time step was set to 1.0 ps for center-to-center distances up to 75 Å. For larger distances it increased linearly with the intermolecular separation up to about 200 ps at 500 Å. This corresponds to an average random displacement of 0.4 Å at small and medium separations and 6.0 Å at the largest separation of 500 Å. For the simulations at higher or lower temperature the time step was adjusted to keep the average random displacement constant, according to $\Delta r = \sqrt{6D\Delta t}$.

To reduce the computational cost of the simulations, no hydrodynamic interactions were considered. It was shown that the effect on the protein−protein association rates is rather small.[24] Also in previous BD studies with simplified cytochrome *c* molecules it was found that hydrodynamics has only a small influence.[25] Hydrophobic forces are not included, since they are assumed to become important only at small contact distances.

The simulation software SDA also allows for the computation of association rates. This was covered in detail in previous work by others.[1,10,26] In this study, we concentrate on the analysis of the trajectories, largely omitting the computed association rates.

For the simulation at 300 K and 50 mM the computation time for 10 000 trajectories including the trajectory analysis and entropy calculation amounts to about 160 h on one pentium IV processor (2.8 GHz). With an average length of a single trajectory of about 70 000 steps, the average simulated time of one trajectory is 1.5 μs. For the simulations with different ionic strength and temperature these values are similar.

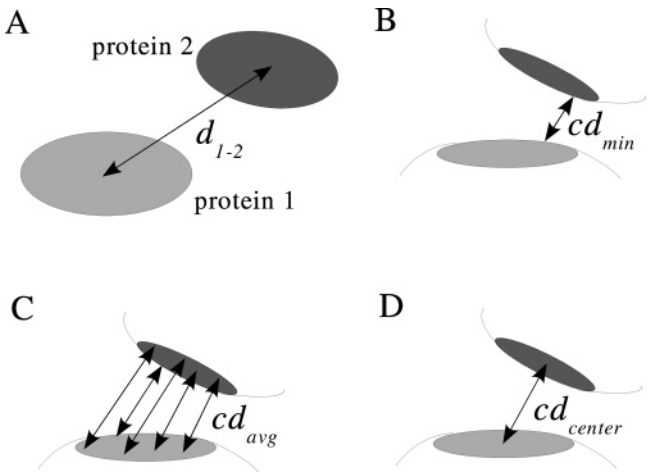

Figure 3. Four possible definitions of the distance axis used here: the center-to-center distance (A), the minimum contact distance (B), the average contact distance (C), and the distance between the geometric centers of the contact surfaces (D).

Trajectory Analysis. After each time step of the simulated trajectories the positional and orientational coordinates of protein 2 (relative to protein 1) are computed with respect to a reference coordinate system of the 6-dimensional configuration space. During the simulations these coordinates are assigned to the nodes of a 6-dimensional grid on which the occupancy, energy, and entropy maps are computed. Note that the maps for the positional and orientational coordinates were computed separately since the handling of a 6-dimensional grid even at moderate resolution is computationally not feasible.

For the positional coordinates a spherical coordinate frame was chosen. If the center-to-center distance d_{1-2} is defined as the reaction coordinate, the origin of the coordinate frame is the center of protein 1. In the case of using a contact distance as reaction coordinate (see below), the origin is the geometric center of the interaction patch of protein 1. The *z*-axis is defined as the vector from the center of protein 1 to the center of protein 2 in the bound state of the crystal structure, see Figure 2A. Without loss of generality, the *x*-axis is defined (orthogonal to the *z*-axis) by the vector from the center of the reaction patch of protein 1 to the first atom in the list of reaction atoms. In the case of barnase this was SER38:OG (shown as black sphere in Figure 2). Therefore, the negative *x*-axis points approximately into the direction from the patch center towards the guanine binding loop. The *y*-axis is defined orthogonal to the *x*- and *z*-axes. The angle between the *z*-axis and the center-to-center vector for a given trajectory position is denoted as the polar angle θ. The azimuthal angle ϕ is the angle in the *xy*-plane from the *x*-axis. For the visualization of the computed occupancy maps (Figure 4A, see below), the coordinates θ and ϕ are replaced by 'semi-Cartesian' coordinates ϕ_x and ϕ_y, which are the *x*- and *y*-contributions of the normalized center-to-center vector.

The orientational coordinates are defined similarly to the positional coordinates (see Figure 2B) by exchanging the center-to-center vectors with the normal vectors of the reaction patches of the proteins (denoted as $\mathbf{n_1}$ and $\mathbf{n_2}$). Here, the normal vector of protein 1 is defined to point outward

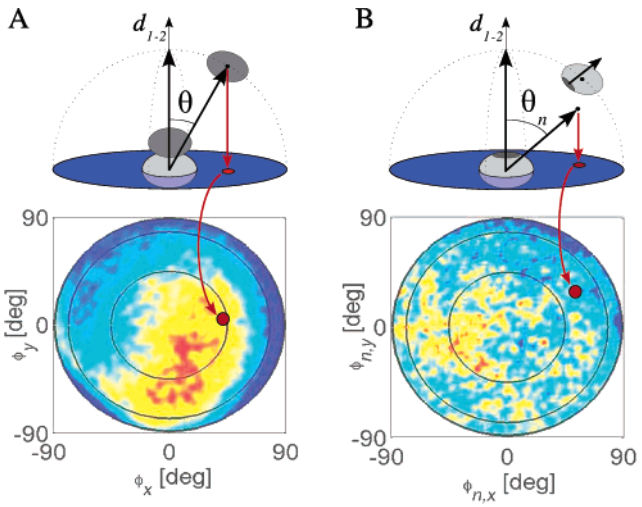

Figure 4. The computation of the occupancy maps, displayed by the projection of the position (A) and orientation (B) of protein 2 (relative to protein 1) onto a plane, which is perpendicular to the center-to-center vector of the proteins in the bound state, and to the normal vector of the reaction patch of protein 1, respectively (see text). The colors in the occupancy maps change from blue (low) to red (high).

of the protein, while the normal vector of protein 2 is defined to point inward, so that in the bound state the two vectors are approximately parallel. The z_n-axis is given by the normal vector of protein 1, and the x_n-axis is defined analogously using the first reaction atom of protein 1. Index n refers to the normal vectors of the reaction patches. The y_n-axis is defined orthogonal to the x_n- and z_n-axis. Again, θ_n is the angle between the vectors and ϕ_n the azimuthal angle. The third orientational coordinate, the angle ω_n, is given by the rotation of protein 2 around the normal vector of the reaction patch, $\omega_n = 0$ denoting the orientation of protein 2 in the bound state. Analogous to the positional coordinates, the orientational coordinates θ_n and ϕ_n are replaced by $\phi_{n,x}$ and $\phi_{n,y}$ for the visualization of the computed occupancy maps (Figure 4B, see below).

When aiming at a global description of the encounter of the two proteins, the center-to-center distance d_{1-2} (Figure 3A) is certainly the ideal definition for the *reaction coordinate* (the third positional coordinate). This definition, however, is independent of the orientation of the proteins with respect to their reaction patches and is therefore problematic for analyzing the encounter of the interaction patches. At closer distances it is therefore preferable to define a so-called 'contact distance'. Gabdoulline and Wade[10] used the definition of the minimum contact distance cd_{min} (Figure 3B), i.e., the minimal distance between all contact pairs. Alternatively, the average value of all contact pair distances, cd_{avg} (Figure 3C), gives a balanced description of the orientation of both interfaces. A further possible definition is the distance between the geometric centers of the protein interfaces, cd_{center} (Figure 3D).

As already mentioned, the occupancy, energy, and entropy maps are computed on a grid while treating the positional and orientational coordinates separately. One set of 3-dimensional matrices is computed for the translational coordinates, a second set for the rotational coordinates $\phi_{n,x}$ and $\phi_{n,y}$ plus the distance coordinate, and a third matrix for ω_n and the distance coordinate.

Computing the occupancy maps with respect to the positional coordinates can be understood as projecting the position of protein 2 onto a plane which is perpendicular to the center-to-center vector d_{1-2} of the proteins in the bound state, see Figure 4A. The origin of these occupancy maps is given by the position of protein 2 in the bound state. After each time step, the occupancy value of the grid element associated with the position of protein 2 is increased by 1. Note that for positions of protein 2 above the denoted plane (for $\theta \leq \pi$) and below (for $\theta > \pi$) two distinct sets of matrices are needed which represent the upper and lower half spheres.

The occupancy maps with respect to the orientational coordinates $\phi_{n,x}$ and $\phi_{n,y}$ are computed similarly. The normal vector of protein 2 is projected onto a plane which is perpendicular to the normal vector of protein 1, see Figure 4B. Here, the origin is the tip of the normal vector of the reaction patch of protein 1. Again, two distinct sets of matrices are needed which represent the upper and lower half spheres.

Figure 5 displays the resulting occupancy maps of the simulation at 50 mM and 300 K. A detailed description is given in the Results section. The electrostatic and desolvation energies as well as the translational and rotational entropy losses (see below) are recorded in further sets of matrices (not shown). In the matrices assigned to the electrostatic and desolvation energies the minimum values for the given position/orientation are stored, thus allowing to finally identify the minimum free energy paths.

The spacing of the grid representing the conformation space should be chosen large enough to ensure a good statistics, but at the same time fine enough to reveal the details of the encounter process, especially in combination with the choice of Δr and Δw in the entropy definition, see below. Along the angles ϕ_x and ϕ_y as well as $\phi_{n,x}$ and $\phi_{n,y}$ we used a discretization with 2×101 nodes (for the upper and lower half spheres), i.e., an average step size of 1.8°. For ω_n we used a step size of 4°, i.e., 90 nodes. Along the distance axis a spacing of 2 Å was used over a distance of 80 Å. The initial value was set by the corresponding distance of the proteins in the bound state. Finally, the occupancy maps were normalized with respect to the size of the volume elements of the grids.

Calculation of the Entropy Landscape. By interpreting the computed occupancy maps as probability distributions, the contribution of the translational and rotational entropy to the free energy landscape is computed by the restriction of the degrees of motional freedom. The total entropy loss of protein−protein encounter is calculated as the sum of the translational and rotational entropy[27]

$$\Delta S = \Delta S_{trans} + \Delta S_{rot} \tag{4}$$

The splitting of the entropy into the translational and rotational parts is valid if the positions and the orientations of the proteins are decoupled. This certainly holds true if the proteins are far apart. Therefore, eq 4 can be assumed to be approximately valid in the region of free diffusion until

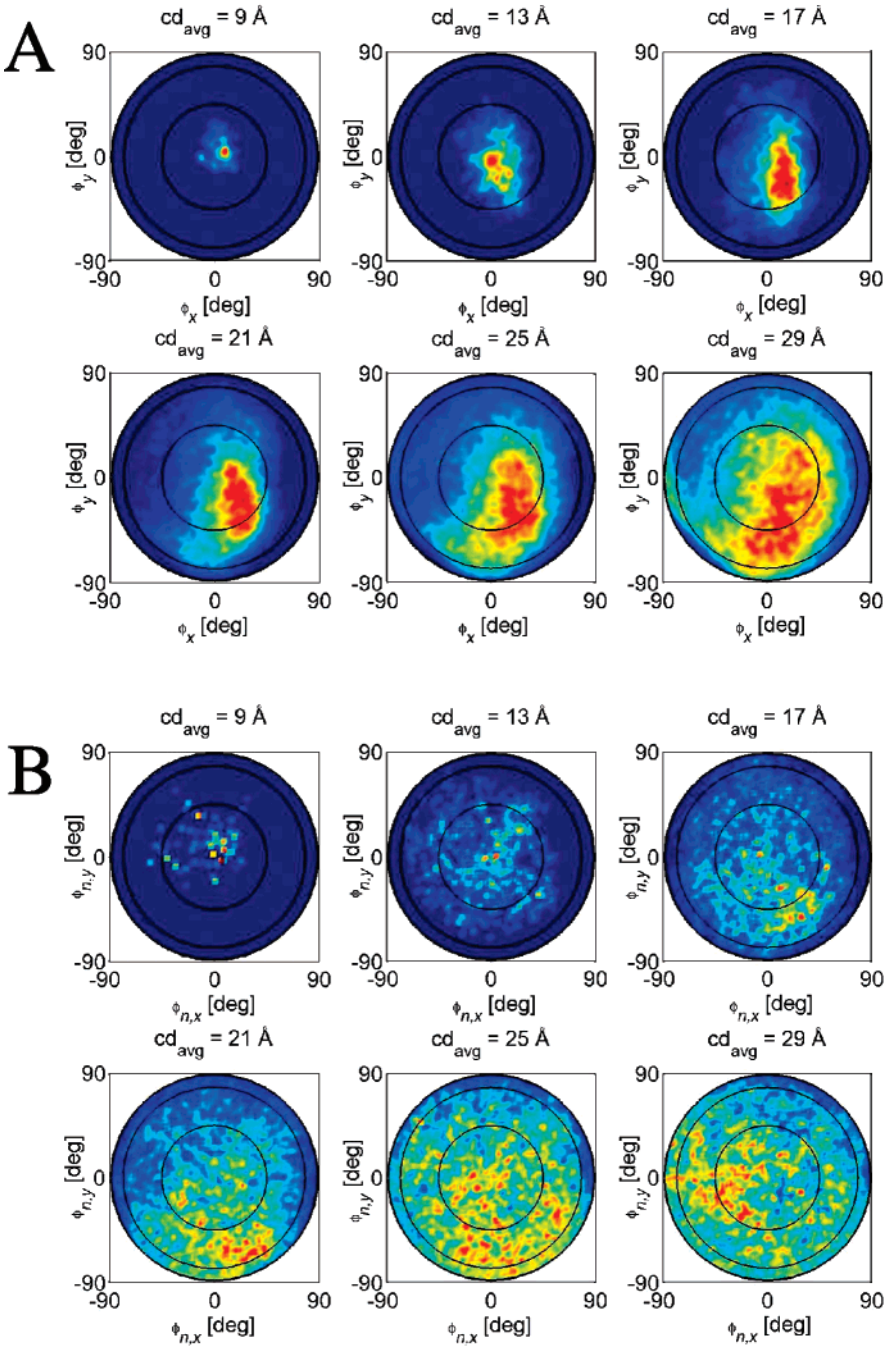

Figure 5. The computed occupancy maps after 10 000 trajectories as a function of the average contact distance cd_{avg}: (A) for the positional coordinates ϕ_x and ϕ_y and (B) for the orientational coordinates $\phi_{n,x}$ and $\phi_{n,y}$. Red means high occupancy and blue low occupancy.

the proteins form the encounter complex (see below). The splitting into the translational and rotational parts allows the separate computation of the entropy maps with respect to the positional and orientational coordinates. The computed values are stored in a further set of matrices, representing the entropy landscape. These matrices have the same grid sizes as the occupancy and energy matrices (see above). The entropy loss is computed separately for all grid nodes of the spatial and angular space which together represent the entropy landscape.

Since the proteins are simulated as rigid bodies we do not account for the internal entropy loss of the proteins concerning vibrational modes and side chain conformations. However, it can be assumed that this entropy contribution only becomes important for protein−protein separations of a few Å, i.e., in a regime, where the protein motions are not diffusion-limited anymore. Also, the entropy of the solvent is not considered here. Again, this contribution can be assumed to be limited to small protein−protein distances.

If the process of protein encounter is considered as a step-by-step process on a molecular level, it is clear that a protein at a certain position and with a certain orientation cannot explore the full configuration space within a Brownian dynamics time step. Therefore, we are interested in calculating the position and orientation dependent (local) entropy loss, rather than the total (global) entropy loss during the

association process. For the computation of the local entropy loss it seems reasonable to take into account the occupancies of all those configurations (positions and orientations), which are reachable from the particular position and orientation within one Brownian dynamics time step, i.e., which are within its *accessible volume* of the configuration space. The size of the accessible spatial and angular volumes V and $\mathscr{Y}$ should be in the range of the mean positional and orientational displacements during a Brownian dynamics time step. Since the protein motions are isotropic on average, we chose V as a sphere around the position of the protein and $\mathscr{Y}$ as a sphere around its orientation. The corresponding radii are $\Delta\rho$ and $\Delta\omega$, respectively.

In general, the entropy of a system with N states is given by

$$S = -k_B \sum_{n=1}^{N} P_n \ln P_n \tag{5}$$

where the P_n are the probabilities for each state n. In the case where all states are equally probable, i.e., $P_n = 1/N$ for all n, this is the famous formula $S = k_B \ln N$. To compute the local entropy loss at the given position and orientation from the occupancy of the positions and orientations (the states) within the accessible volumes V and $\mathscr{Y}$, we applied the basic formula, eq 5, by interpreting the occupancy landscape as a probability distribution. This configuration dependent entropy value is then compared to the entropy with a constant, isotropic probability distribution, which is the reference state if the proteins are far apart. Note that the entropy loss is computed separately for all grid nodes of the positional and orientational configuration space, which finally represent the entropy landscape. The translational entropy loss relative to the reference state at a given position is calculated in the following way: If the occupancy of a given state n in the volume V is F_n and the total occupancy of all states within V is F_{tot}, then the probability for state n is $P_n = F_n/F_{tot}$. According to eq 5 the entropy is

$$S_{tr} = -k_B \sum_{n=1}^{N} P_n \ln P_n = k_B \left(\ln F_{tot} - \frac{1}{F_{tot}} \sum_{n=1}^{N} F_n \ln F_n \right) \tag{6}$$

where N is the number of states within V, i.e., the number of grid points in this volume. Relative to the isotropic reference state with $P_n = 1/N$, the translational entropy loss during the process of protein−protein encounter is

$$\Delta S_{tr} = S_{tr} - k_B \ln N \tag{7}$$

The rotational entropy loss is computed analogously. It should be noted that the numerical value of the entropy as calculated by the above procedure is sensitive to the resolution of the occupancy maps (i.e. the number of states within the volumes V and $\mathscr{Y}$). We tested grid sizes between 21 and 201 nodes. The computed entropy curves (not shown) are quite similar, and only the smallest resolution results in too large values due to the decreasing statistics.

According to the formulas for the Brownian motion of two interacting proteins, eqs 2 and 3, the average translational and rotational displacement of barnase and barstar during a time step of $\Delta t = 1.0$ ps is $\Delta r = \sqrt{6D\Delta t} \simeq 0.4$ Å and $\Delta w_i = \sqrt{6D_{iR}\Delta t} \simeq 1.3°$ at a temperature of 300 K. These are, however, minimum values for $\Delta\rho$ and $\Delta\omega$ (the radii of V and $\mathscr{Y}$), since the displacements can be larger in a combined translational and rotational motion. Additionally, the average translational displacement is much larger when measured with respect to the contact distance, instead of the center-to-center distance. Some further, more technical aspects have to be taken into account for the choice of $\Delta\rho$ and $\Delta\omega$: On one hand, they should not be smaller than the resolution of the occupancy maps to ensure that the number of states within the volume of the configuration space $V\mathscr{Y}$ is not too small. On the other hand, $\Delta\rho$ and $\Delta\omega$ should be in the range of the average displacement in a BD time step to keep the idea of the local entropy definition.

Free Energy Landscape. In the sections above we described the computation of the energy and entropy landscapes. The contributions of electrostatic and desolvation energies as well as the translational and rotational entropy loss are stored in matrices, which represent the 6-dimensional configuration space. These matrices have the same grid sizes as the occupancy maps, and they are computed separately for the positional and orientational coordinates. In the energy matrices the minimum values for the given position/orientation are stored, finally allowing to identify the minimum free energy path. The translational and rotational entropy maps are calculated by interpreting the occupancy maps as probability distributions, i.e., by the restriction of the degrees of motional freedom.

With the energy and entropy contributions as functions of the translational and rotational coordinates, the free energy landscape of the encounter process is given by the sum of the electrostatic energy, the desolvation energy, and the translational/rotational entropy:

$$\Delta G = \Delta E_{el} + \Delta G_{ds} - T\Delta S_{tr},\ \Delta S_{tr} = \Delta S_{trans} + \Delta S_{rot} \tag{8}$$

Note that the free energy is calculated for each grid node of the spatial and angular space, representing the free energy landscape of the protein−protein encounter.

The reaction path is defined as the path along the minima of the free energy landscape. In Figure 6 the electrostatic interaction energy (A), the (negative) translational and rotational entropy loss (B), the desolvation energy (C), and the free energy (D) of protein−protein encounter along the reaction path is displayed for $\Delta\rho$ and $\Delta\omega$ varying from 2 to 5 Å and 2 to 5°, respectively. $\Delta\rho$ and $\Delta\omega$ denote the sizes of accessible volumes, i.e., the regions which are reachable from a certain position and orientation within one Brownian dynamics time step (see above). The entropic contribution is only weakly dependent on the volumes V and $\mathscr{Y}$ (Figure 6B). In all further simulations we used $\Delta\rho = 3$ Å and $\Delta\omega = 3°$. These values were kept constant also for varying temperature, since the time step in these simulations was adjusted to the average displacement at $T = 300$ K.

Results

The trajectories from BD simulations of protein−protein encounter were analyzed for the model system barnase−

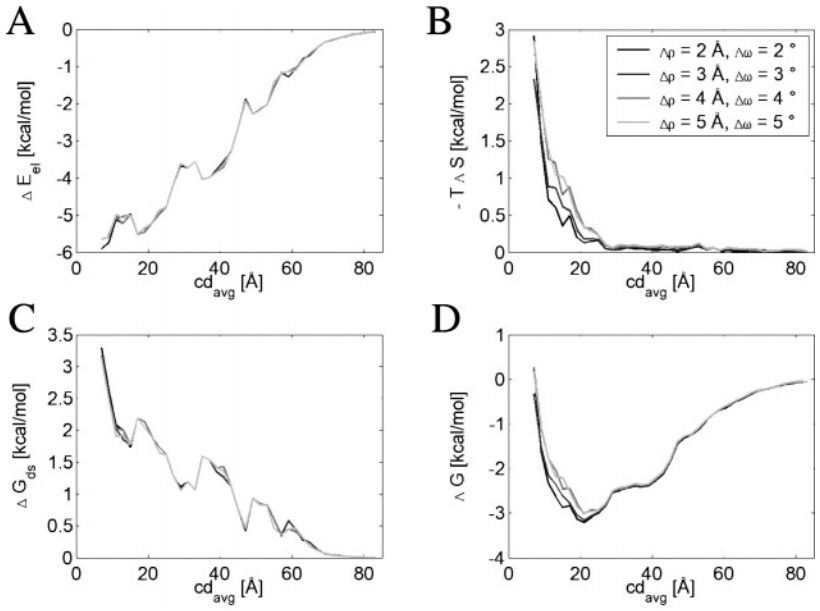

Figure 6. Contributions to the encounter free energy for varying volumes V and $\mathscr{V}$ in the entropy definition, i.e., for varying $\Delta\rho$ and $\Delta\omega$, as a function of the average contact distance: (A) the electrostatic energy, (B) the desolvation energy, and (C) the translational and rotational entropy. In (D) the free energy is displayed, the characteristic minimum at 21 Å denotes the position of the encounter complex.

barstar in order to clarify the nature of the encounter state. As explained in the previous chapter, the occupancy of the conformation space for the protein−protein encounter of barnase and barstar was computed on grids representing the 6-dimensional configuration space: one set of 3-dimensional matrices for the translational coordinates, one set for the rotational coordinates $\phi_{n,x}$ and $\phi_{n,y}$ plus the distance coordinate, and another matrix for ω_n and the distance coordinate. In Figure 5 the occupancy is displayed as a function of the average contact distance cd_{avg}, ranging from 9 to 29 Å with a step size of 2 Å (here only every second image is shown). While the average contact distance between the reaction patches of barnase and barstar in the crystal structure of the bound state is 4.0 Å, the closest configuration found in any trajectory is at 7 Å. It is to be expected that the particle density at such close distances is underestimated due to the neglect of adhesive interactions such as hydrophobic forces. The results shown in Figures 5−8 refer to the trajectory analysis of barnase and barstar at 300 K and 50 mM. In Figure 9 the dependence on ionic strength and temperature is investigated.

Figure 5A displays the occupancy as a function of the positional coordinates ϕ_x and ϕ_y (i.e. of θ and ϕ) for increasing cd_{avg}. Every disk shows the occupancy on the upper half (for $\theta < \pi$) of a shell with a thickness of 2 Å, projected on the plane perpendicular to the center-to-center vector of the proteins in the bound state (see Figure 4A). The black circles denote $\theta = 30°$, 60°, and 90°. For small cd_{avg} up to 17 Å, the occupied positions are quite close to the position of the proteins in the bound state, while the occupancy cloud is spread wider for increasing distance. At larger distances this cloud also becomes more anisotropic with respect to the angle ϕ, and the maximum of the occupancy cloud moves downward. For even larger contact distances ($cd_{avg} > 35$ Å) the maximum of the occupancy cloud is found in the leftmost part of the maps as indicated already in the lower right map ($cd_{avg} = 29$ Å). This means that the encounter is steered along a certain pathway towards the guanine binding loop of barnase. This nonisotropic encounter of the proteins can be understood from the charge distributions of barnase and barstar. The occupancy maps for the lower half spheres are not shown, since they are not significantly populated for distances shorter than $cd_{avg} \sim 40$ Å.

In Figure 5B the occupancy is shown as a function of the orientational coordinates $\phi_{n,x}$ and $\phi_{n,y}$ (i.e. of θ_n and ϕ_n), again for the upper half sphere ($\theta_n < \pi$). These maps are constructed similarly to the maps described above for the translational coordinates (see Figure 4B). For small cd_{avg} the orientation of the proteins is close to that in the bound state. With increasing contact distance the occupancy cloud is getting larger but also anisotropic with respect to the interface normal of protein 1. Again, the center of the occupancy cloud is displayed downward. Together with the interpretation of Figure 5A (an encounter of protein 2 from the left side is favorable) this means that already at a contact distance of 25 Å the binding interfaces of the proteins are preoriented and pointing roughly toward the binding interface of the other protein. The occupancy as a function of the third orientational coordinate ω_n (not shown here) has a funnel-like shape as well, converging toward $\omega_n = 0°$ for small contact distances, i.e., toward the configuration of the proteins in the bound state.

From these occupancy maps the entropy landscape was computed by the use of the above-defined local entropy function. Together with the electrostatic and desolvation energy, the free energy landscape is calculated as the sum of all terms. As mentioned above, the reaction pathway of the protein−protein encounter is given as the path along the minima in the free energy landscape. Figure 6 displays the

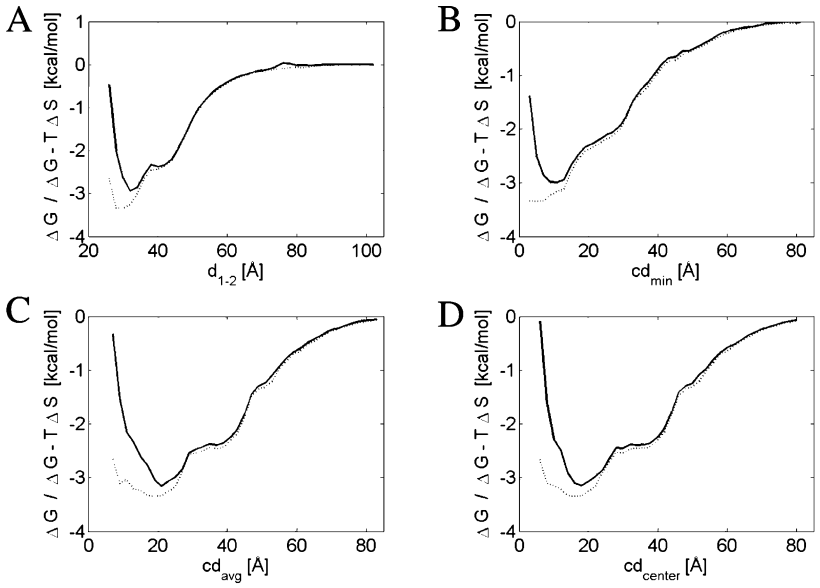

Figure 7. The profile of the encounter free energy as a function of the 4 different definitions of the distance axis (see Figure 3): (A) the center-to-center distance d_{1-2}, (B) the minimum contact distance cd_{min}, (C) the average contact distance cd_{avg}, and (D) the distance between the geometric centers of the reaction patches cd_{center}.

energy profiles along the reaction path as functions of the average contact distance for varying volumes V and $\mathscr{J}$ in the entropy calculation, $\Delta\rho$ and $\Delta\omega$ ranging from 2 to 5 Å and 2 to 5°, respectively. The electrostatic interaction energy (A) strongly decreases as the proteins get closer down to −6 kcal/mol, while the desolvation energy (C) is moderately increasing up to 3 kcal/mol. The (negative) entropic contribution (B) is negligible for $cd_{avg} > 25$ Å but increases rapidly as the proteins approach each other. At a distance of 8 Å the entropy loss amounts to ∼2.5 kcal/mol. The encounter free energy (D) decreases up to a distance of about 20 Å due to the favorable electrostatic interaction and increases again for smaller distances because of the desolvation energy and the entropy loss. The characteristic minimum between appears as a useful definition for the position of the encounter complex. In the following, we refer to 'minimum' when talking about the one-dimensional free energy profiles for protein−protein encounter. The term 'encounter complex' is used to discuss the conformations corresponding to these minima.

Having reached the encounter state, the proteins may spend some time in this free energy minimum in order to rearrange their interfaces including the orientation of the side chains. Moving the proteins closer than the encounter complex involves on one hand the (for barnase and barstar) unfavorable desolvation of the proteins and finally the loss of approximately all degrees of freedom of one of the proteins but on the other hand also the favorable formation of hydrophobic contacts, hydrogen bonds, and salt bridges. The entropy loss at the position of the minimum in Figure 6D is still very small (∼0.2 kcal/mol). This means that almost all the entropy is lost during the binding process from the encounter to the bound complex. The variation of the volumes V and $\mathscr{J}$ for the computation of the entropy leads to an increase of the entropy loss for increasing $\Delta\rho$ and $\Delta\omega$. This increase is only moderate leading to a slight shift of ΔG for $cd_{avg} \leq 20$ Å. For the subsequent simulations we chose $\Delta\rho = 3$ Å and $\Delta\omega = 3°$. These values are in the range of the BD time steps and of the resolution of the occupancy maps.

In Figure 7 (solid lines) the profile of the encounter free energy along the reaction pathway is shown for different definitions of the distance axis (see Figure 3): (A) the center-to-center distance d_{1-2}, (B) the minimum contact distance cd_{min}, (C) the average contact distance cd_{avg}, and (D) the distance between the centers of the reaction patches cd_{center}. All four graphs show the characteristic minimum in the profile denoting the position of the encounter state. The free energy values of the minimum conformations are quite close to each other ranging from −2.9 to −3.2 kcal/mol. The differences arise from the varying discretizations of the configuration space. The dotted lines show the sum of the electrostatic and desolvation energies, i.e., the free energy without the entropy loss. In all graphs the sum of the electrostatic and desolvation energies at the position of the minimum is lower than the free energy, while the position of the minimum is shifted toward smaller distances. These differences emphasize the importance of the entropy contribution for the definition of the encounter state.

To illustrate the effect of the four different definitions of the distance axis, representative pdb-structures of the encounter complex were constructed from the positions and orientations of the corresponding minimum free energy conformations. In Figure 8 they are shown for comparison: barnase is displayed as a gray van der Waals surface, barstar is schematically shown as a tube with the atoms of the reaction patch as spheres. For the bound structure (in black) only the reaction atoms are displayed. The encounter complex conformation of barstar is colored in blue for the minimum position in the free energy profile with the distance axis d_{1-2} (Figure 7A), in red for cd_{min} (Figure 7B), in green for cd_{avg} (Figure 7C), and in purple for cd_{center} (Figure 7D). The positions of the encounter complex for the different definitions of the distance axis and the corresponding RMSDs to

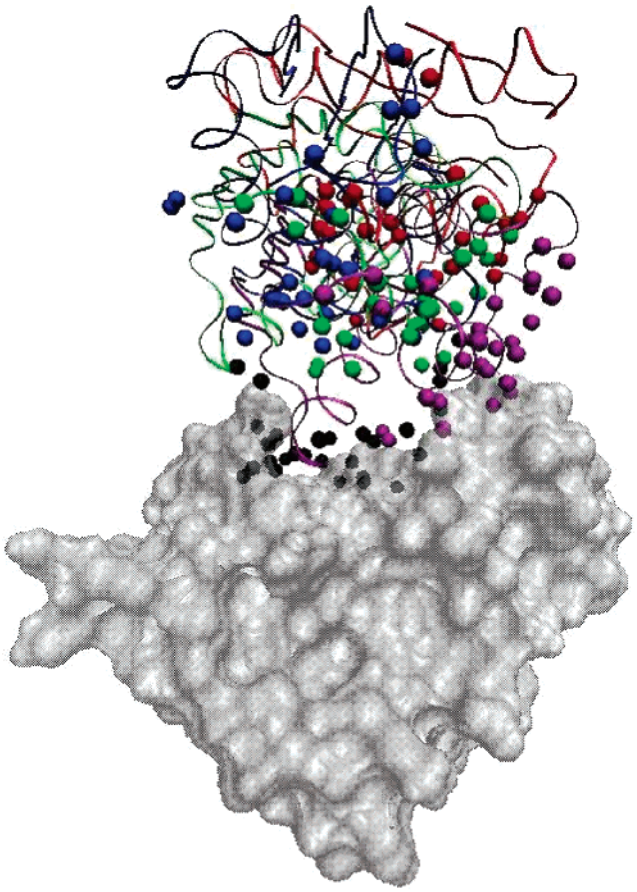

Figure 8. Comparison of representative conformations of the encounter complex structures, as defined by the minima in the encounter free energy profiles in Figure 7. Barnase is displayed as a gray van der Waals-surface, barstar is schematically shown as a tube with the reaction atoms as spheres. For the bound structure (in black) only the reaction atoms are displayed. The encounter complex conformation of barstar is colored in blue for the minimum position in the free energy profile with the distance axis d_{1-2} (Figure 7A), in red for cd_{min} (Figure 7B), in green for cd_{avg} (Figure 7C), and in purple for cd_{center} (Figure 7D).

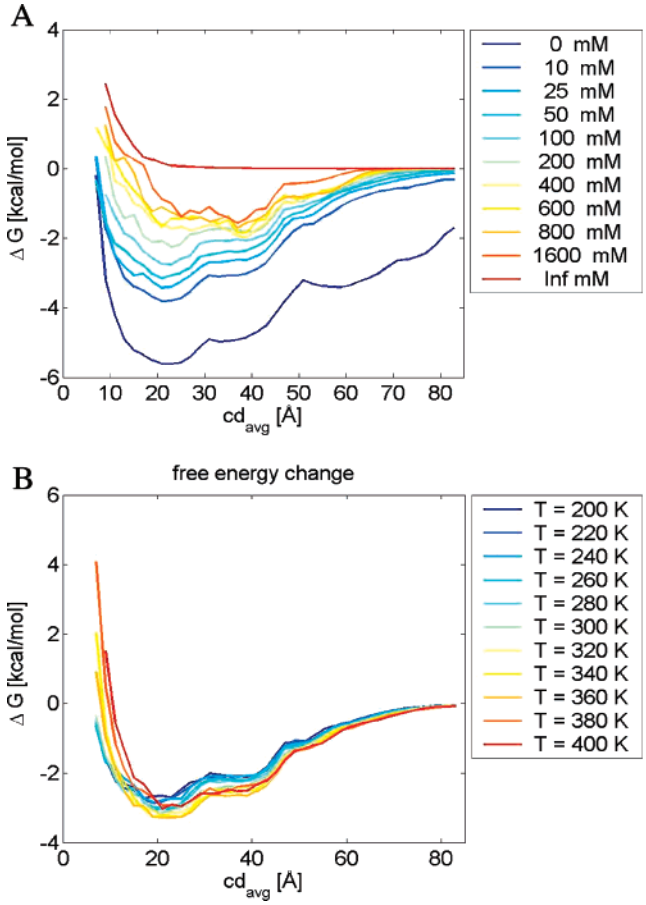

Figure 9. The encounter free energy profiles (A) for varying ionic strength at a constant temperature of 300 K and (B) for varying temperature at a constant ionic strength of 50 mM.

the bound configuration are as follows: $d_{1-2} = 32$ Å (RMSD = 16.4 Å), $cd_{min} = 11$ Å (RMSD = 18.6 Å), $cd_{avg} = 21$ Å (RMSD = 18.2 Å), and $cd_{center} = 18$ Å (RMSD = 18.7 Å). The pairwise distance between the protein centers in the 4 encounter complex configurations is 7.1 ± 5.2 Å. The pairwise RMSD, however, has a large spread: 14.4 ± 7.2 Å. This indicates that the translational degrees of freedom are much more restricted in the encounter complex than the rotational degrees of freedom. The occupancy maps in Figure 5 show the same behavior. The occupancy as a function of the positional coordinates at $cd_{avg} = 21$ Å is confined to a rather small area (lower left image of Figure 5A), while the occupancy cloud for the orientational coordinates at the same distance is still quite large (lower left image of Figure 5B).

Satisfied by these results we added two series of simulations in order to investigate the dependence of the free energy profile, in particular the position of the minimum, on the ionic strength and on the temperature of the solvent. For the analysis of the ionic strength dependence, the temperature was set to 300 K, while the ionic strength was varied in logarithmic steps from 0 mM up to 1600 mM. One simulation was performed where the electrostatic and desolvation forces were switched off in order to model infinite ionic strength. The results of this study are shown in Figure 9A. The depth of the free energy minimum decreases continuously with increasing ionic strength due to increasing shielding of the electrostatic interactions. The entropy contribution (not shown separately) is almost independent of the ionic strength. The distance of the minimum is approximately 22 Å for low and moderate ionic strength, ranging from 0 mM up to 200 mM. [These values are computed by a parabolic fit of the free energy profile around the minimum position.] At even higher values this minimum disappears involving a rapid jump of the encounter complex position to ≥ 38 Å. At infinite ionic strength the free energy profile has no minimum since the entropy loss is the only contribution. Further sets of simulations were performed with the same values for temperature and ionic strength but using the linear instead of the full Poisson−Boltzmann equations (PBE) for the computation of the electrostatic grids. Although the depth of the energy minimum is more shallow in the simulations where the full PBE were used, the shapes of the free energy profiles (not shown) for varying ionic strength are quite similar to the profiles displayed in Figure 9A. For example, the minimum free energy value at 50 mM and 300 K is −3.2 kcal/mol when the full PBE were used and −4.4 for the linear PBE. This effect is most relevant for values of

the ionic strength ≤ 200 mM, but also the curves at larger values are slightly shifted.

In the simulations where the full PBE were used, the solvent dielectric ϵ_s was varied according to its temperature dependency, while in the other simulations (where the linear PBE were used) it was set to the value of 78. As mentioned above, in all simulations the phase transitions of water at 273 and 373 K and an eventual unfolding of the proteins were omitted. The energy and entropy profiles (not shown) for the latter set of simulations (using the linear PBE at constant ϵ_s) reflect the expected behavior: For increasing temperature the electrostatic and desolvation energies decrease slightly. This is accompanied by a small increase of the entropy. Both effects can be understood by the increasing mobility of the proteins at increasing temperature. The overall shape of the free energy profiles is quite similar, while the depth of the potential well decreases moderately with increasing temperature.

The effect of the varying solvent dielectric in the former set of simulations (using the full PBE at temperature dependent ϵ_s) is somehow surprising. It can be explained by the better ordering of the water molecules at low temperature and by the decreasing shielding of water at increasing temperature. Therefore, the electrostatic and desolvation energies increase for increasing temperature. Again, the entropy slightly increases for increasing temperature. The effects of increasing electrostatics, desolvation, and entropy almost cancel each other. Thus, the free energy profiles (Figure 9B) seem to be somehow independent of the temperature. For increasing temperature the distance of the minimum systematically increases from 19.7 Å up to 23.6 Å.

Discussion

By analyzing Brownian dynamics trajectories of barnase and barstar we gained additional insight into the mechanism of protein−protein encounter, information that is complementary to the computation of their association rates. From the detailed evaluation of the trajectories we can learn about the encounter pathways as well as the degree of preorientation of the proteins with respect to their reaction patches. Furthermore, by the definition of a local entropy function, we are able to compute the free energy landscape as the sum of the electrostatic and desolvation energies plus the contribution from the translational and rotational entropy. In the free energy profile along the reaction pathway, defined as the path along the minima of the free energy function, a minimum at small protein−protein separations shows up. Having reached this minimum position after the initial free diffusion, the proteins may spend some time there in order to rearrange their interfaces for the formation of the bound complex. This characteristic minimum is therefore a suitable definition for the encounter complex, the intermediate state before the final complexation of the proteins. The positions of the encounter complex, computed for 4 different definitions of the distance axis, are close to each other, while the orientational degrees of freedom at the encounter state are not much restricted. This behavior is reflected in the occupancy maps in Figure 5. It underlines that the encounter state as defined by the minimum of free energy is not a single conformation like the bound state but rather a cloud of conformations with almost the same, minimal free energy.

It is often assumed that protein−protein complexes with strong electrostatic steering show a significant degree of preorientation of both binding partners. Our analysis suggests that this preorientation mostly affects the translational degrees of freedom, while the rotational preorientation takes place during the desolvation phase (between (3) and (4) in Figure 1). In another simulation at 50 mM and 300 K with an exchange of barnase and barstar (the motion of barnase is computed relative to barstar) we found that for barstar the translational degrees of freedom are more restricted than for barnase. Because of the stochastic nature of BD trajectories we did not consider it meaningful to distinguish between 'successful' and 'nonsuccessful' trajectories. At any point of the occupancy maps, an individual trajectory may proceed into any arbitrary direction. On the other hand, the behavior of ensembles of trajectories is determined by the free energy funnel computed from the occupancy maps. It should be feasible to compute time scales for transitions between any two points by a Kramers-like approach. Such analysis will be presented in a subsequent manuscript.

One may certainly ask whether BD simulations are a suitable tool for defining the location of the encounter complex considering that the encounter complex is denoted as end-point of the diffusional encounter. As mentioned in the Introduction, typical BD simulations of protein−protein encounter make simplifications which become important when the proteins approach the bound conformation, at protein−protein separations shorter than ∼10 Å. In our studies we found the position of the free energy minimum at an average contact distance of about 20 Å. For the system studied here, the region of the encounter complex is therefore in the regime where the BD simulation would still be valid.

The distance of the minimum position ($cd_{avg} \simeq 21$ Å) corresponds to a minimum contact distance of about 11 Å (see Figure 7B). This distance is larger than the value of 7.5 Å which was suggested by Gabdoulline and Wade by comparing the computed association rates with experimental data for the 3-contacts criterion[3] and is significantly larger than the 6 Å which was used for the criterion of 2 independent contacts between hydrogen-bond donors and acceptors.[1] These authors denoted this position as the *diffusional encounter complex*, the end point of diffusional encounter at which the proteins are committed to form a bound complex. It can be assumed to be located just after the transition state (see Figure 1). Since this position is closer to the bound complex than the encounter complex as defined in this work by the minimum of free energy, the association rate at the position of the diffusional encounter complex is significantly reduced compared to the rate at the free energy minimum. We computed the association rates in the simulation at 300 K and 50 mM ionic strength as 3.44×10^8 M^{-1} s^{-1} for 2 independent donor−acceptor contacts shorter than 6.0 Å (i.e. for the diffusional encounter complex) and as 4.07×10^9 M^{-1} s^{-1} for 1 donor−acceptor contact shorter than 10 Å (i.e. for the encounter complex). For comparison, the experimental value is 2.86×10^8 M^{-1} s^{-1}.[9] The computed

values are expected to overestimate the measured rates by about 30% due to the neglect of the hydrodynamic interactions.[1] The position of the diffusional encounter complex defined by Gabdoulline and Wade therefore yields computed rates that are comparable to experimental values. On the other hand, the state of minimal free energy characterized in this work should be useful for interfacing BD simulations for protein−protein encounter with atomistic MD simulations to study the details of the final steps during the binding process. The free energy minimum should characterize a short-lifetime intermediate state that may eventually become accessible to experimental observations. As a note of caution one should add that many interacting protein−protein pairs do not show electrostatic complementarity.[1] It remains to be seen whether these systems also show a small free energy minimum before the onset of freezing rotational and translational degrees of freedom.

A more detailed analysis of the reaction pathway and the occupancy maps in Figure 5 shows that barstar is indeed steered toward the guanine binding loop of barnase in consistency with the results of Gabdoulline and Wade[10] and Camacho et al.[7] Along the encounter process the proteins are guided by a free energy well: At large distances, barstar moves toward Lys66 (in Figure 5A from the left) and then turns to the center of the barnase reaction patch, and, at $cd_{avg} \sim$ 25 Å, barstar is steered toward the guanine binding loop of barnase converging to its bound conformation. This encounter behavior partly reproduces the result of the Boltzmann factor calculation of Gabdoulline and Wade (Figure 5(a) in ref 1). The middle and back part of their probability distribution is similar to the described pathway. The front part, however, was found to be energetically unfavorable.

The free energy profiles were evaluated for varying ionic strength and temperature. The variation of the ionic strength has a large impact on the profiles, both for the depth and for the position of the minimum. The dominating effect is the increasing shielding of the electrostatic interactions due to the increasing ionic strength of the solvent which results in a destabilization of the encounter state for values of the ionic strength ≥ 400 mM. The variation of the temperature of the solvent, in contrast, has only a small effect on the free energy profiles: For increasing temperature the electrostatic and desolvation energies as well as the entropy increase in a manner that their effects on the free energy profile almost cancel out each other. The distance of the minimum increases continuously by about 4 Å for increasing temperature. From these studies we can conclude that for low and moderate ionic strength the position of the encounter complex is slightly dependent on the temperature but almost constant for varying ionic strength. At high ionic strength, however, the encounter complex is destabilized involving a jump of the position of minimum free energy. The depth of the minimum varies about 4 kcal/mol between 10 and 1600 mM ionic strength and about 0.6 kcal/mol in the temperature range from 200 to 400 K. The stability of the encounter complex is therefore mostly affected by varying ionic strength compared to variations in temperature. For protein systems with weaker electrostatic interactions we can therefore expect that the free energy well at the encounter complex is flatter. The contribution of the translational and rotational entropy is expected to depend strongly on the steepness of the encounter funnel.

Studies of this kind may provide a basis for theoretical predictions of FRET signals for protein−protein interaction. Also, they may shed light on the interesting question why protein surfaces have been formed by evolution into what we find today. In the future we want to apply our simulation method to more complex systems such as the encounter of cytochrome *c* and cytochrome *c* oxidase.[26] The focus will be more on the analysis of the association and dissociation pathways (ongoing work) and also on time-dependent aspects of association such as the lifetime of the observed free energy minimum.

Acknowledgment. We gratefully acknowledge the financial support from the Deutsche Forschungsgemeinschaft via the Center for Bioinformatics in Saarbrücken. We thank Rebecca C. Wade for the provision of their SDA program and valuable comments on the manuscript. A. Spaar thanks Dagmar Flöck for helpful advice in the beginning of this project.

References

(1) Gabdoulline, R. R.; Wade, R. C. *J. Mol. Biol.* **2001**, *306*, 1139−1155.

(2) Schreiber, G. *Curr. Opin. Struct. Biol.* **2002**, *12*, 41−47.

(3) Gabdoulline, R. R.; Wade, R. C. *J. Mol. Recognit.* **1999**, *12*, 226−234.

(4) Gabdoulline, R. R.; Wade, R. C. *Methods* **1998**, *14*, 329−341.

(5) Janin, J. *Proteins* **1997**, *28*, 153−161.

(6) Vijayakumar, M.; Schreiber, K. Y. W. G.; Fersht, A. R.; Zhou, A. S. H. Z. *J. Mol. Biol.* **1998**, *278*, 1015−1024.

(7) Camacho, C. J.; Weng, Z.; Vajda, S.; DeLisi, C. *Biophys. J.* **1999**, *76*, 1166−1178.

(8) Buckle, A. M.; Schreiber, G.; Fersht, A. R. *Biochemistry* **1994**, *33*, 8878−8889.

(9) Schreiber, G.; Fersht, A. R. *J. Mol. Biol.* **1995**, *248*, 478−486.

(10) Gabdoulline, R. R.; Wade, R. C. *Biophys. J.* **1997**, *72*, 1917−1929.

(11) Tidor, B.; Karplus, M. *J. Mol. Biol.* **1994**, *238*, 405−414.

(12) Frisch, C.; Fersht, A.; Schreiber, G. *J. Mol. Biol.* **2001**, *308*, 69−77.

(13) Brooks, B. R.; Bruccoleri, R. E.; Olafson, B. D.; States, D. J.; Swaminathan, S.; Karplus, M. *J. Comput. Chem.* **1983**, *4*, 187−217.

(14) QUANTA, *Molecular modelling software package;* Molecular Simulations, Inc.: San Diego, CA, 1992.

(15) Elcock, A. H.; Gabdoulline, R. R.; Wade, R. C.; McCammon, J. A. *J. Mol. Biol.* **1999**, *291*, 149−162.

(16) Davis, M. E.; Madura, J. D.; Luty, B. A.; McCammon, J. A. *Comput. Phys. Comm.* **1991**, *62*, 187−197.

(17) Jorgensen, W. L.; Tirado-Rives, J. *J. Am. Chem. Soc.* **1988**, *110*, 1657−1666.

(18) Archer, D. G.; Wang, P. *J. Phys. Chem. Ref. Data* **1990**, *19*, 371.

(19) Gabdoulline, R. R.; Wade, R. C. *J. Phys. Chem.* **1996**, *100*, 3868−3878.

(20) Northrup, S. H.; Boles, J. O.; Reynolds, J. C. L. *J. Phys. Chem.* **1987**, *91*, 5991−5998.

(21) Northrup, S. H. *MacroDox v.2.0.2: Software for the Prediction of Macromolecular Interaction;* Tennessee Technological University: Cookeville, TN, 1995.

(22) Ermak, D. L.; McCammon, J. A. *J. Chem. Phys.* **1978**, *69*, 1352−1360.

(23) Jones, R. A. L. *Soft Condensed Matter;* Oxford University Press: Oxford, 2002.

(24) Antosiewicz, J.; Briggs, J. M.; McCammon, J. A. *Eur. Biophys. J.* **1996**, *24*, 137−141.

(25) Gorba, C.; Geyer, T.; Helms, V. *J. Chem. Phys.* **2004**, *121*, 457−464.

(26) Flöck, D.; Helms, V. *Biophys. J.* **2004**, *87*, 65−74.

(27) Ben-Tal, N.; Honig, B.; Bagdassarian, C. K.; Ben-Shaul, A. *Biophys. J.* **2000**, *79*, 1180−1187.

(28) Humphrey, W.; Dalke, A.; Schulten, K. *J. Mol. Graph.* **1996**, *14*, 33−38.

CT050036N

JCTC Journal of Chemical Theory and Computation

A Molecular Dynamics Simulation of the Binding Modes of D-Glutamate and D-Glutamine to Glutamate Racemase

Eduard Puig,[†] Mireia Garcia-Viloca,[‡] Àngels González-Lafont,[†,‡] Inés López,[‡] Xavier Daura,[‡,§] and José M. Lluch*[,†,‡]

Departament de Química and Institut de Biotecnologia i de Biomedicina, Universitat Autònoma de Barcelona, 08193 Bellaterra, Barcelona, Spain, and Institució Catalana de Recerca i Estudis Avançats (ICREA), 08010 Barcelona, Spain

Received November 19, 2004

Abstract: Classical molecular dynamics simulations of the D-Gln/*Aquifex pyrophilus* MurI and D-Glu/*Aquifex* pyrophilus MurI complexes have been carried out. Since the active site of the enzyme contains many charged and polar residues, several binding modes are possible. Thus, three very different stable conformations of the substrate analogue D-Gln have been found, and at least three binding modes are possible for the substrate D-Glu. These qualitative results give an explanation for the apparent disagreement between the D-Gln bound MurI X-ray crystal structure and the expected position and orientation of the substrate D-Glu in order to make it possible the assumed Cα deprotonation (by Cys70)/reprotonation (by Cys178) racemization mechanism.

Introduction

D-Amino acids are essential components of peptidoglycans (alternatively, mureins), which are the rigidifying components of the bacterial cell walls and protect the organism from osmotic lysis.[1] In particular, D-glutamate is a required biosynthetic building block added by the enzyme MurD ligase to the peptidoglycan intermediate uridine 5′-diphosphate-*N*-acetylmuramyl-L-alanine.[2,3] The enzyme glutamate racemase (MurI, EC 5.1.1.3) catalyzes the interconversion of glutamate enantiomers in a cofactor-independent fashion and provides bacteria with a source of D-glutamate.[1,4] Mutagenesis knockout experiments in *Streptococcus pneumoniae* (one of the most frequent causes of bacterial respiratory infection and meningitis) have shown that glutamate racemase is essential for the viability of this bacteria.[5] Thus, inhibition of glutamate racemase is a very attractive target for the design of new antibacterial agents,[6,7] specially taking into account the alarming increase in antimicrobial resistance.[8,9]

* Corresponding author phone: 34 93 581 2138; fax: 34 93 581 2920; e-mail: lluch@klingon.uab.es.

[†] Departament de Química, Universitat Autònoma de Barcelona.

[‡] Institut de Biotecnologia i de Biomedicina, Universitat Autònoma de Barcelona.

[§] Institució Catalana de Recerca i Estudis Avançats (ICREA).

Glutamate racemase, as all known amino acid racemases, seems to operate via an initial deprotonation of the amino acid's α-proton, followed by a reprotonation on the opposite face of the resulting planar anionic intermediate.[10,11] Mutagenesis studies support the idea that two cysteines are the catalytic acid/base residues. These two cysteine residues and surrounding residues are strictly conserved among all MurI and other cofactor-independent racemases, including aspartate racemase.[12] In the *Lactobacillus fermenti* glutamate racemase enzyme only two cysteine residues (Cys73 and Cys184) are present, and mutation of either of them to alanine eliminates the racemase activity.[13] Similar results were obtained with Cys-to-Thr/Ala mutants of the *Escherichia coli* enzyme.[14,15] In addition, Tanner et al. have used an irreversible inhibitor, aziridino-glutamate,[16] to show that at least one of the cysteines is in the proper vicinity to the α-carbon of the bound glutamate. Further studies by Glavas and Tanner[4,17,18] have determined that Cys73 is responsible for the deprotonation of the Cα atom of D-glutamate, whereas Cys184 is responsible for the reprotonation of the Cα atom of L-glutamate.

Recently, the X-ray crystallographic structure of glutamate racemase from *Aquifex pyrophilus* has been solved by Hwang et al.[19] at 2.3 Å resolution for both apo-MurI and MurI complexed with a substrate analogue, D-glutamine. The

10.1021/ct049881g CCC: $30.25
Published on Web 05/24/2005

corresponding coordinates have been deposited in the Protein Data Bank (PDB) with the accession codes 1b73 and 1b74, respectively. To our knowledge, apart from the case of the diaminopimelate epimerase,[20−22] no other structures of a cofactor-independent amino acid racemase are nowadays available. In this crystal, MurI exists as a tightly associated dimer, and the two monomers are related by a crystallographic 2-fold symmetry axis. Each monomer consists of two compact domains with α/β structure. A large groove is formed between the two domains. The dominant feature of the dimerization is an insertion of a loop and a α-helical region of one monomer into the large groove between the two domains in the other monomer. This way a deep pocket comprising residues from both monomers is formed in the region of the large groove.

In *Aquifex pyrophilus* the two catalytic cysteines are Cys70 and Cys178. The binding site of the inhibitor D-Gln has been observed to be in the deep pocket formed by the two monomers. A root-mean-square deviation (rmsd) of just 0.72 Å between apo- and D-Gln bound MurI structures indicates that the binding of D-Gln to MurI does not induce any important conformational changes. Surprisingly, while the Cδ atom of D-Gln has been found by Hwang et al.[19] to be sandwiched by the two thiol groups of Cys70 (5.1 Å) and Cys178 (3.0 Å), the Cα atom is more than 5.3−7.6 Å away from the two catalytic cysteines. Thus, in the active site D-Gln appears to be flipped 180° from the expected binding of the substrate D-Glu, in such a way that the Cδ and Cγ atoms of D-Gln occupy the positions of the Cα and Cβ atoms of D-Glu, respectively. Despite these results, Hwang et al.[19] have proposed, from mutagenesis studies, a Cα atom deprotonation (by Cys70)/reprotonation (by Cys178) mechanism for the racemization of D-Glu by MurI, in agreement with the mechanism suggested by Glavas and Tanner.[17,18] On the other hand, we have to point out[23] that the 1b74 structure deposited in the PDB is not the real crystal structure obtained by Hwang et al.[19] for the D-Gln Mur I complex but a theoretical model (described in ref 19). In this model the D-Gln coordinates were twisted 180° in order to be compatible with the Tanner's mechanism. This fact can be easily verified by analysis of the interatomic distances in the 1b74 structure, specially the Cα−Cys70 and Cα−Cys178 distances. To our knowledge this is still the situation at the moment of writing this paper.

Since the crystal structure actually determined by Hwang et al.[19] does not appear to be consistent with the assumed catalytic mechanism, several scenarios can be envisaged: (a) the binding mode of D-Glu is different from that of D-Gln; (b) the crystallographic model for the binding of D-Gln to Aquifex pyrophilus MurI does not correspond to the predominant binding mode in solution; and (c) racemization of the substrate D-Glu by MurI does not take place through the Cα atom deprotonation/reprotonation mechanism being the two cysteines the acid/base residues. Since experimental determination of the substrate D-Glu bound MurI crystal structure has not been done, a theoretical analysis of scenarios (a) and (b) can shed light on this question. To this aim, we present here classical molecular dynamics simulations of the D-Gln/Aquifex pyrophilus MurI and D-Glu/Aquifex pyrophilus MurI complexes. Our structural results will provide an adequate starting point for later reactivity studies.

Methods

Models of the Enzyme−Ligand Complex. In the present study, a total of 6 models have been used to computationally determine the possible orientations of the inhibitor D-Gln and the substrate D-Glu in the active site of MurI. The D-Gln-X-ray model is based on the Cartesian coordinates actually determined by X-ray crystallography, which were kindly given to us by Hwang, Cho, and co-workers. The D-Gln-modeled model is based on the Cartesian coordinates contained in the Protein Data Bank at the moment of writing this paper (code 1b74). These two sets of coordinates only differ in the ligand coordinates. The 1b73 file (containing the coordinates of the ligand-free enzyme) has been used to start the docking simulation explained below, and the results of this simulation have provided the initial structure for the D-Gln-docked model. In the case of the three models used to represent the D-Glu/*Aquifex pyrophilus* MurI complex, the starting Cartesian coordinates are the same sets of coordinates cited above but replacing the D-Gln ligand by a D-Glu molecule or using a D-Glu molecule as the ligand in the docking simulation.

In all 6 models the coordinates of the hydrogen atoms of the ligand, the protein, and the crystallographic waters were determined using the HBUILD facility in the program CHARMM (Chemistry at HARvard Macromolecular Mechanics).[24] According to the mutagenesis studies by Glavas and Tanner[17] and Hwang et al.,[19] the strictly conserved residues Asp7 (Asp10 in *L. fermenti*), His180 (His186), and Glu147 (Glu152) have an important catalytic role in either stabilizing the carbanionic intermediate by hydrogen bonding interactions or assisting the cysteine bases in the deprotonation of glutamate. In addition, Glavas and Tanner[17] have also suggested that Glu147 (Glu152) play a role in glutamate binding.

Since the aim of this paper is to discern if the actual crystal structure determined by Hwang et al.[19] is compatible with Tanner's mechanism, we have assumed that Asp7, Glu147, and His180 are protonated in the active site of MurI at neutral pH. On the other hand, we have deprotonated the catalytic Cys70 residue to be consistent with its proposed role as the base that abstracts the α-proton in the D to L direction of the racemase reaction. Thus, the active site protonation state assumed to be coherent with the proposed mechanism shows a deprotonated Cys70 close to a protonated Asp7. The measured kinetic isotope effects suggest that Asp7 could assist Cys70 either by hydrogen bonding to the thiolate or by deprotonating the thiol.[17] To check which of these two situations is more favorable, or in other words, which of the two residues would be preferentially protonated, two energy minimizations have been done. The first one corresponding to the state with Asp7 protonated and Cys70 deprotonated and the second one with Asp7 deprotonated and Cys70 protonated. The minimizations have been carried out on a 24 Å sphere around the substrate's Cα atom with a gradient tolerance of 0.001 kcal/molÅ, applying a nonbonded cutoff of 13 Å, and a switch function from 12 to 13 Å. The

solvation interactions have been modeled with one of the most accurate analytic Generalized Born approaches, the GB-MV2[25] method (the parameters used for this method are listed in the Supporting Information, Table 1) implemented in CHARMM c31.[24] It has to be noted that the GB-MV2 model is one of the most accurate analytic GB formalisms designed to mimic the standard molecular volume based Poisson−Boltzmann solvation energies.[24] We have found that the model with Cys70 deprotonated/Asp7 protonated is 2.5 kcal/mol more stable than the Cys70 protonated/Asp7 deprotonated model in terms of Gibbs free energy, thus confirming that the reactive model assumed in the present work is plausible. The protonation states for all other ionizable residues were set according to standard pK_a values and a pH of 7. Histidine residues were modeled as neutral or protonated, with the proton on Nϵ or/and Nδ, on the basis of possible hydrogen bond interactions in the X-ray crystallographic structure. The ligand was modeled in its amino acid zwitterionic form, that is, with the amino group protonated and the carboxylic group deprotonated.

In all 6 models, to mimic the aqueous environment, we used the stochastic boundary molecular dynamics (SBMD)[26,27] simulation technique by adding a 24 Å sphere of preequilibrated waters centered on the Cα atom of the substrate. Crystallographic water molecules beyond 24 Å of the origin of this sphere were removed. Water molecules with their oxygen atom at a distance of 2.5 Å or less from any non-hydrogen protein, ligand, or crystallographic water atom were also deleted. This procedure was repeated three times with randomly rotated water spheres. Then, a molecular dynamics simulation (5 ps) was carried out to relax energetically bad contacts, and the 3-fold cycle of superposition, rotation, and deletion was repeated to fill in additional cavities generated from the equilibration calculations. The final 6 models have slightly different total number of atoms comprised between 10 600 and 10 677. This resulting configurations are called "initial" in this paper.

In all the simulations, the protein and ligand atoms were modeled with the CHARMM22[28] force field, and the TIP3P[29] model was used for water. We note that in CHARMM22 only the protonated form of cysteine is an standard residue, and thus, we have used molecular mechanics parameters for a deprotonated cysteine residue extracted from the CHARMM22 standard parameters of ethylthiolate (see Supporting Information, Figure 1 and Tables 2−4).

Molecular Dynamics Simulations. The SBMD technique is an efficient approach to carry out molecular dynamics simulations of a region of the enzymatic system called the reaction zone. It reduces the total number of atoms that must be included in the simulation of the solvated system and, hence, minimizes the computational costs. The rest of the system or reservoir zone is held fixed during the simulations and provides a static field that supplies important electrostatic interactions of protein atoms near the reaction zone-reservoir zone boundary. In the present study, the reaction zone contains the active site residues and all protein and solvent atoms within a sphere of 24 Å centered on the C_α atom of the substrate. The reaction zone is further divided into the molecular dynamics region (containing the ligand, the enzymatic residues, and the water molecules within 20 Å of the center of the sphere), which is treated with Newtonian molecular dynamics, and the buffer region (from 20 to 24 Å), which represents a simplified heat bath and is treated by Langevin dynamics. For each ligand-MurI model, protein atoms were assigned to one or another region according to a reference structure at the beginning of the simulation and they retained their labels throughout the simulation, whereas water molecules were allowed to diffuse between the molecular dynamics region and the buffer region. The Langevin dynamics regime imposes a friction coefficient and a random force on the heavy atoms in the buffer region. These atoms are further restrained by imposing a harmonic restoring force to keep them close to their average positions and to help to maintain the structural integrity of the enzyme. The harmonic force constants were taken as 1.22 kcal mol^{-1} Å^{-2} for the main-chain O atoms, 1.30 kcal mol^{-1} Å^{-2} for all other main-chain atoms, and 0.73 kcal mol^{-1} Å^{-2} for side-chain atoms and atoms of water molecules. The friction constants were 200 ps^{-1} for the protein atoms and 62 ps^{-1} for the water atoms in the buffer region. A deformable boundary potential was imposed on water molecules at the buffer/reservoir interface to represent the effect of bulk solvent outside this boundary.

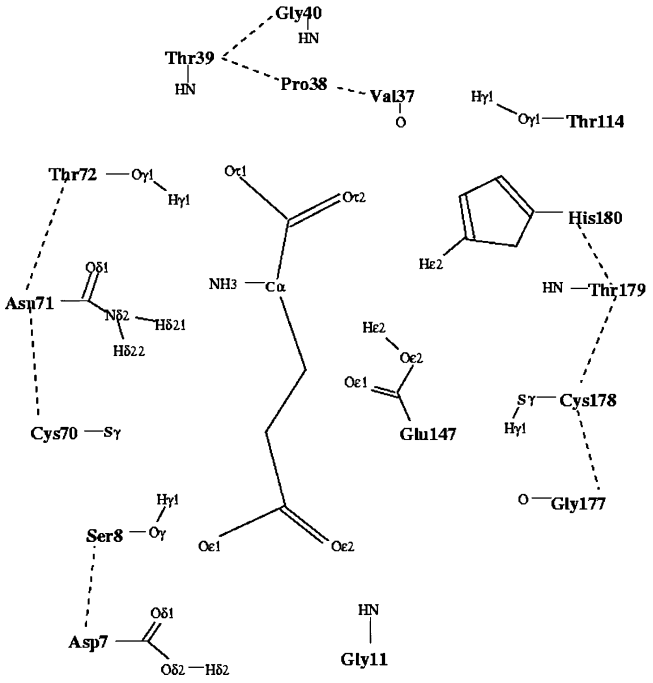

Figure 1. Schematic representation of the active site of MurI from *Aquifex pyrophilus* with a substrate molecule (glutamate) bounded. The labels on the atoms of the substrate and the enzymatic residues are the ones used in the tables.

To test the possible existence of larger-scale effects of the protein on the active site, we have repeated a SBMD simulation with a sphere of 30 Å to define the reaction zone. The results corresponding to the D-Glu-modeled system (see Supporting Information, Figure 2 and Table 5) show that, although some particular MurI−substrate interactions change, most of them are maintained. The essential trends of the relative orientation of the substrate are not modified when the reaction zone is enlarged from 24 to 30 Å.

We used an integration time step of 1 fs during the heating and equilibration simulations described below along with a nonbonded cutoff of 13 Å based on the center-of-mass separation between interacting groups. A switch function was added in the region from 12 to 13 Å to feather the interaction energy to zero. The nonbonded pair list was updated every 35 steps, which is suitable in a rather rigid system as an enzyme's active site. All bond lengths involving hydrogen atoms were constrained by the SHAKE algorithm,[30] and the relative dielectric permittivity was set to 1. Initially, we carried out 30 ps of SBMD simulations to heat the system up to 300 K and then 100 ps more to equilibrate it at this temperature. From the final structure we ran simulations for at least 1 ns, saving the generated structures at every 200 steps. These data were used for later structural analysis.

Docking Method. As mentioned above, the dimer was built from the monomer coordinates contained in PDB-entry 1b73. All crystallographic water molecules were removed. Initial models for D-Gln and D-Glu were generated from standard geometries. The AutoDock Tools[31] were used to add polar hydrogen atoms and to assign Kollman united-atom partial charges,[32,33] atomic solvation parameters,[32,33] and fragmental volumes.[32,33] The grid maps were calculated using AutoGrid 3.0,[33] with $61 \times 61 \times 61$ points and a grid-point spacing of 0.375 Å. The maps were centered at the midpoint between the sulfur atoms of Cys70 and Cys178 (active site).

Ten docking runs were performed for each ligand using the Lamarckian Genetic Algorithm implemented in AutoDock 3.0,[33] which combines a genetic algorithm and an adaptative local-search algorithm. All torsional bonds of the ligand were allowed to rotate during the docking process. The step size was 0.2 Å for translations and 5° for orientations and torsions. These step sizes determine the relative size of mutation in the local search. The Cauchy distribution parameters α and β, determining the size of the mutation in the genetic algorithm, were set to 0 and 1, respectively.

The parameters for the genetic algorithm were set as follows: an initial population of 50 random individuals, a maximum of 1.5×10^6 energy evaluations, a maximum of 27 000 generations, an elitism value of 1 (number of top individuals that automatically survive into the next generation), a mutation rate of 0.02 (probability that a gene undergoes a random change), and a crossover rate of 0.80 (probability that two individuals undergo crossover). Proportional selection was used, where the average of the worst energy was calculated over a window encompassing the previous 10 generations. The pseudo-Solis and Wets local-search algorithm were chosen, with the following parameter settings: a maximum of 300 iterations per local search, a probability of 0.06 of performing local search on an individual in the population, a maximum of 4 consecutive successes or failures before doubling or halving, respectively, the local-search step size (ρ), and a lower bound on ρ (termination criterion for the local search) of 0.01.

Results and Discussion

Binding of D-Gln in the Active Site of MurI. Three models have been built to represent the D-Gln/*Aquifex pyrophilus* MurI complex, which only differ in the orientation of the ligand in the active site. The crystal structure files used to build these models contain the Cartesian coordinates for the enzyme atoms of the monomer contained in the crystallographic asymmetric unit (253 enzymatic residues) with one or no D-Gln molecule bound and 104 to 107 crystallographic waters. However, in the crystal, MurI exists as a tightly associated dimer, and the active site of each monomer in the dimer contains residues from the other monomer (for example, Glu147). On the basis of this crystallographic result Hwang et al.[19] proposed that dimerization is important for the racemase function and stability of *Aquifex pyrophilus* MurI. Thus, we have assumed that the dimer is the active form of MurI. A complete multimer, which corresponds to the known biologically significant oligomerization state of the molecule, has been generated by applying the operations of symmetry of the space group P6522, and from this structure we have trimmed a dimer.

The first model, the so-called D-Gln-X-ray model, is based on the ligand and enzyme Cartesian coordinates obtained by X-ray crystallography, whereas in the D-Gln-modeled model we have taken as relative orientation of the ligand in the active site the one modeled by Hwang et al.[19] on the basis of the proposed catalytic mechanism. In addition, a third model called D-Gln-docked has been built from the coordinates obtained after docking a D-Gln residue in the active site of MurI by using a docking computational method. Starting from the different orientations of the ligand, classical molecular dynamics simulations have been carried out to investigate the binding interactions between D-Gln and the enzymatic residues in the active site of MurI, which are schematically represented in Figure 1.

We start by analyzing the results obtained with the D-Gln-X-ray model. Figure 2 compares the initial configuration with the position of the ligand in the active site of MurI obtained after 1.2 ns of SBMD (following 130 ps of heating and equilibration). Figure 2a, together with the initial distances shown in the last column of Table 1, indicate that Asn71 is the only enzymatic residue that forms an important interaction with D-Gln at the initial structure. Weaker interactions may be deduced from the distances between the main-chain ammonium group nitrogen of the ligand and both the main-chain oxygen of Gly177 and the side-chain Oδ1 atom of Asn71. As mentioned by Hwang et al.,[19] the observation of very few interactions between D-Gln and MurI in the crystallized structure is in agreement with its low inhibitory activity (KI = 50 mM). The comparison between the initial distances and the average distances calculated over 6000 saved configurations, and listed in the seventh column of Table 1, suggests that no new interactions are formed during the simulation. In the structures of the equilibrated system the hydrogen bond between the Oϵ1 atom of D-Gln and Asn71 is weaker than in the initial configuration. The relatively low occupancy, short average lifetime, and large number of times that this hydrogen bond is reformed agree with the longer interaction distance. On the contrary, the interactions between the main-chain amino group of the ligand and the enzyme are shorter in the structures generated during the SBMD simulations. Interestingly, these results

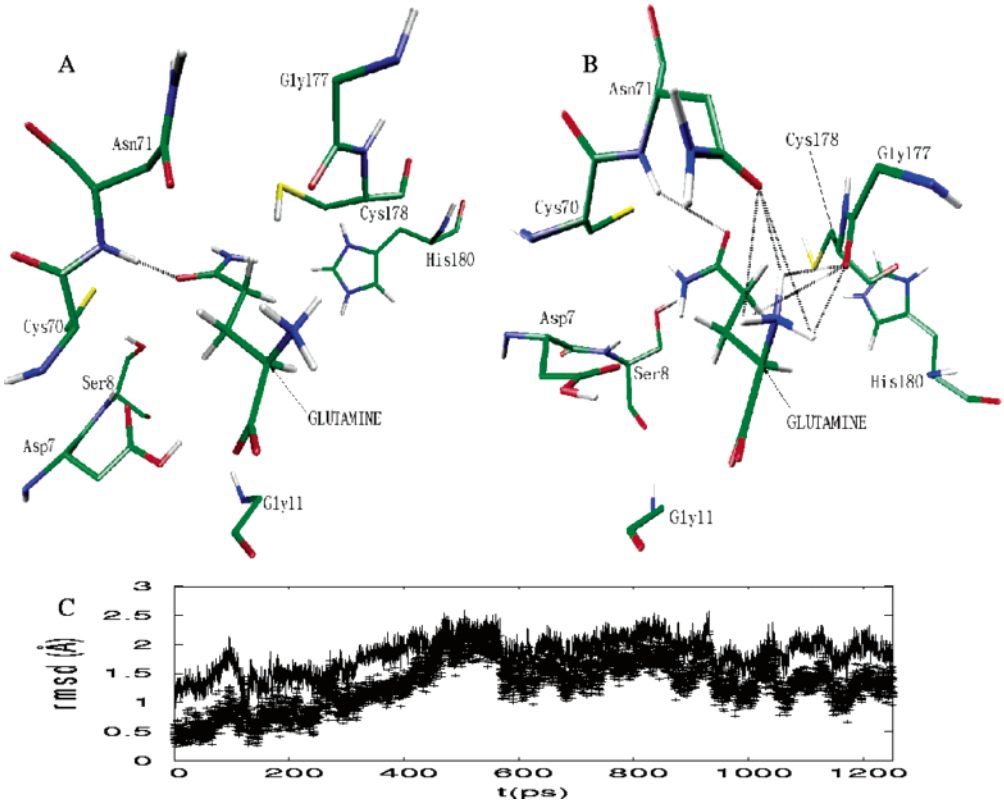

Figure 2. **(**a**)** Partial view of the active site of the D-Gln-X-ray model at the initial configuration. The shortest interactions between the ligand and the enzyme are marked with a dotted line. **(**b**)** Same as **(**a**)** at the final configuration of the 1.2 ns simulation. **(**c**)** Root-mean-square deviation (rmsd) of the ligand in the D-Gln-X-ray model as a function of the time along the sampling trajectory. The reference structure is the initial configuration (solid line) or the last configuration generated during the equilibration stage (crosses). In both cases, each frame has been reoriented in order to minimize the rmsd of the backbone atoms of the enzyme + ligand system with respect to the reference structure.

indicate that the D-Gln ligand remains in the flipped orientation found by Hwang et al.[19] despite being weakly bound in the active site of MurI.

To compare two different structures we have used the following strategy: First, we have reoriented the second structure in order to minimize the root-mean-square deviation (rmsd) of the backbone atoms of the enzyme + ligand system with respect to the corresponding atoms of the first structure; then, we have calculated the rmsd of just all the atoms of the ligand of the reoriented second structure with respect to the corresponding atoms of the first structure. So, Figure 2c shows the calculated rmsd of the ligand in the D-Gln-X-ray model along the 1.2 ns simulation using two different reference structures. The rmsd of the ligand with respect to both, the initial structure and the last structure generated during the equilibration stage, is small at the beginning of the trajectory and increases during the first 500 ps to reach a more stable behavior. The trends are almost parallel between the two calculated rmsds, which indicates that there is a very small difference between the two reference structures. Overall, the average rmsds of the ligand calculated over the trajectory are relatively small, with values of 1.83 and 1.31 Å with respect to the initial structure and the last configuration generated during the equilibration stage, respectively. These results are in agreement with the small deviation of the D-Gln orientation from the flipped configuration mentioned above. Thus, our simulation indicates that the relative orientation of D-Gln deduced from the X-ray experiment is stable, although weakly bound (see also the ligand-environment interaction energy section below), in the active site of MurI. Importantly, our results also indicate that this orientation is not suitable for the reaction. That is, the calculated average distances between the α-carbon of D-Gln and the sulfur atoms of the catalytic cysteines are larger than 7.0 Å.

Next, we analyze the results obtained with the D-Gln-modeled model. Figure 3 clearly indicates that the change from the initial to the final structures obtained with this model is larger than the one obtained with the D-Gln-X-ray model. At the initial configuration, the only short interaction between the ligand and the enzyme is the hydrogen bond between the Oτ2 atom of D-Gln and the protonated carboxylic group of Glu147 (see last column of Table 1). In addition, the protonated Cys178 forms a weak interaction with the other main-chain carboxylate oxygen of the ligand, and, like in the case of D-Gln in the flipped orientation (see above), there is a weak interaction between the NH3-group of D-Gln and the side chain of Asn71. These three interactions are maintained during the simulation of the equilibrated system (see the seventh column of Table 1), although the hydrogen bond distance between the ligand and Glu147 elongates, suggesting that this interaction is weakened. This is concomitant with the appearance of three new hydrogen bonds between D-Gln and the enzymatic residues. Specifically, the main-chain amino group of Thr179 interacts with the Oϵ1 atom of D-Gln, and the two main-chain carboxylate oxygens

Table 1. Important Hydrogen Bond Interactions between D-Glutamine and Enzymatic Residues for the Simulations of the Different Models Defined in the Text[a]

ligand atom	residue-atom	occu	time	events	dist	fluct	init
			D-Gln-X-ray				
Oϵ1	Asn71-HN	0.58	0.7	1106	2.41	0.45	1.65
NH3	Gly177-O	0.95	8.1	146	2.80	0.21	3.45
NH3	Asn71-Oδ1	0.88	2.6	420	2.86	0.25	4.18
			D-Gln-Modeled				
Oϵ1	Thr179-HN	0.84	4.4	240	2.17	0.61	6.18
O$_t$1	His180-Hϵ2	0.26	2.1	151	3.06	0.76	8.98
O$_t$1	Cys178-Hγ1	0.21	0.5	514	3.58	1.17	3.25
O$_t$2	His180-Hϵ2	0.89	3.3	333	1.93	0.40	6.95
O$_t$2	Glu147-Hϵ2	0.52	2.1	298	2.83	1.25	1.67
NH3	Asn71-Oδ1	0.75	1.9	503	3.06	0.51	3.67
			D-Gln-Docked				
Oϵ1	Asn71-HN	0.56	2.1	260	2.95	1.14	1.95
Oϵ1	Asn71-Hδ22	0.52	1.9	278	3.33	1.80	1.66
Oϵ1	Glu147-Hϵ2	0.26	1.5	176	3.16	0.86	4.90
O$_t$2	Tyr39-HN	0.96	5.4	178	1.96	0.21	2.02
O$_t$2	Gly40-HN	0.70	0.9	750	2.27	0.27	2.21
O$_t$2	Thr72-Hγ1	0.92	3.4	271	1.91	0.29	4.53
NH3	Val37-O	0.96	6.3	153	2.80	0.14	2.73

[a] For a given interaction, columns 4−9 show the following: hydrogen bond occupancy, average lifetime (in ps), number of times that the hydrogen bond is reformed (events), average interaction distance (in Å), root-mean-square (rms) fluctuations of the interaction distance (in Å), and hydrogen bond distance at the initial configuration (in Å). The criterion used to define the formation of a hydrogen bond is a distance smaller than 2.4 Å between the hydrogen and the acceptor atom. In the case of interactions between the amino group (NH3) of the ligand and the enzymatic residues, a hydrogen bond is considered to exist when any of the amino group hydrogens accomplishes the criterion explained above. In general, the interaction distance and its rms fluctuations refer to the distance between the hydrogen and the acceptor atom in the hydrogen bond, with the exception of the interactions involving the amino group (NH3) of the ligand, for which the distance between the donor and the acceptor atoms is given. Figure 1 indicates the meaning of the atom labels used in the table.

of the ligand become bound to His180. The short distances of these three hydrogen bonds agree well with the calculated occupancy, the average lifetime, and the number of events.

Figure 3c shows the rmsd of the ligand in the D-Gln-modeled model along the trajectory with respect to the initial structure and the last structure from the equilibration period. Similarly to the results obtained for the D-Gln-X-ray model, the rmsds at the beginning of the trajectory are small, and the parallelism of the two curves in Figure 3c suggests that the two reference states are quite similar. The D-Gln ligand slightly deviates from the modeled orientation during the first 500−600 ps, but at this point there is a jump in both rmsds, suggesting the occurrence of a significant conformational change. The comparison between parts a and b of Figure 3 highlights the movement of the main-chain atoms of D-Gln toward the contiguous residues Thr179-His180 to form interactions that were not present in the initial state. Consequently, the ligand moves far away from the Asp7-Ser8 residues and slightly from Glu147. The analysis of the evolution of the distance between these residues and D-Gln has given us a possible explanation for the sudden change of the rmsd value after 600 ps. Figure 3d summarizes these findings. At the beginning of the trajectory, the interaction found between the ligand and Glu147 in the initial configuration is maintained. However, His 180 gradually approaches to the Oτ2 atom of D-Gln and around the 500−600 ps region the interactions of the ligand with these two residues become competitive. After 700 ps and for ca. 400 ps, His 180 displaces Glu147, but the interaction with the latter is recovered after this period and stays in competition with the His180 interaction. Thus, there has probably been a change in the conformation of the ligand that allows these two interactions to occur simultaneously. In summary, the D-Gln molecule significantly moves from the position modeled by Hwang et al.[19] This is reflected by the higher values obtained with this model for the average rmsd of the ligand (2.79 and 1.62 Å, taking as reference the initial structure and the last structure of the equilibration period, respectively) in comparison with the D-Gln-X-ray model. In addition, as a consequence of the deviation of the ligand from the modeled position, which was suitable for reaction, its distance to the catalytic cysteines increases. The calculated average distance between the α-carbon and the sulfur atom of Cys70, which is proposed to abstract the α-proton, is 7.18 Å, 2.92 Å away from the modeled position, which suggests that the ensemble of equilibrated structures obtained for glutamine from the D-Gln-modeled model is not reactive.

The initial structure for the third model, the D-Gln-docked model, has been obtained from the analysis of the docked configurations obtained with 10 runs of the Lamarckian Genetic Algorithm implemented in AutoDock 3.0.[33] The configurations generated for the ligand were clustered using an rmsd tolerance of 0.5 Å. Then the clusters whose configurations were not suitable for catalysis were eliminated. Finally, the configuration with the lowest binding free energy in the most populated surviving cluster was selected as the initial structure for the D-Gln-docked model SBMD simulation (shown in Figure 4a). The distances given in the last column of Table 1 indicate that in this initial structure the shortest hydrogen bonds are formed between residue Asn71 and the Oϵ1 atom of D-Gln. The ligand is also bound by its carboxylate end to residues Tyr39 and Gly40, and there is a somewhat longer hydrogen bond between the NH3 group and Val37. In comparison to the relative orientation of D-Gln in the two previous models, the D-Gln-docked model resembles more the D-Gln-modeled system. However, docking has translated the ligand inside the active site in such a way that it interacts with residues not present in the close environment of the two previous models. During the simulation after the equilibration period, the hydrogen bond with Asn71 elongates (mainly due to a rotation of the ligand which can then connect through Oϵ1 with Glu147). At the carboxylate end, a new hydrogen bond is formed between the Oτ2 atom and residue Thr72 which presents the shortest distance and a high occupancy. Interestingly, the average value (5.18 Å) of the distance between the α-proton of D-Gln and the Sγ atom of Cys70 is quite shorter than the corresponding distance in the D-Gln-X-ray and D-Gln-modeled systems (8.03 and 7.20 Å, respectively). In addition, the Cα of D-Gln is closer to the two sulfur atoms of the

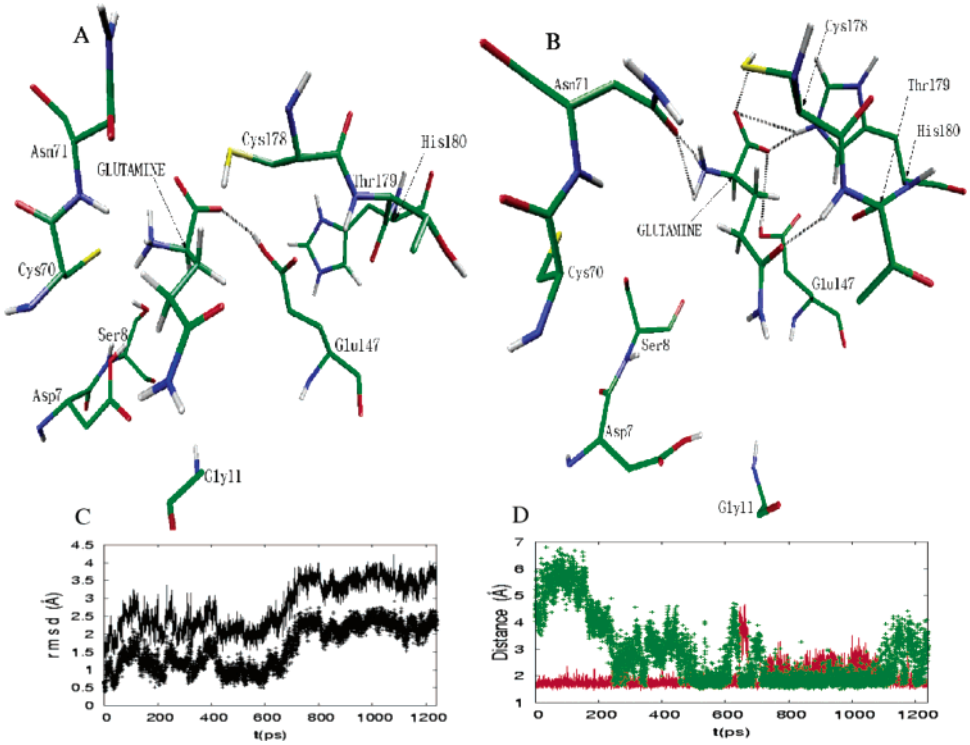

Figure 3. (a)−(c) Same as Figure 2(a)−(c) for the D-Gln-modeled model. (d) Interaction distances between the Hϵ2 atom of Glu147 (solid line, red) or the Hϵ2 atom of His180 (crosses, green) with the Oτ2 atom of glutamine along the sampling trajectory of the D-Gln-modeled model.

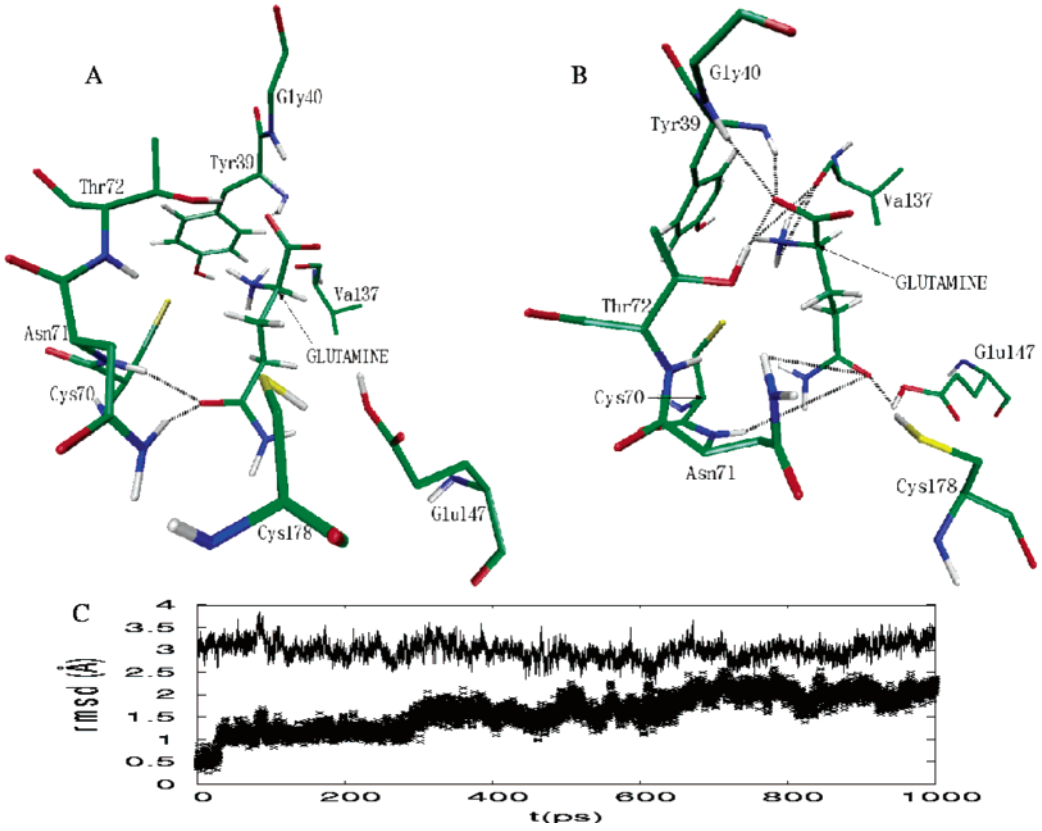

Figure 4. (a)−(c) Same as Figure 2(a)−(c) for the D-Gln-docked model.

catalytic cysteines (4.43 and 5.80 Å from Cys70 and Cys178, respectively) than in the D-Gln-modeled model, and both distances are shorter than the values observed by Hwang et al.[19] from their crystallographic studies on MurI (5.3 and 7.6 Å, respectively). These results indicate that the D-Gln inhibitor may also be found in a conformation similar to the one that would be reactive (in the case of D-Glu substrate) in the mechanism proposed by Glavas and Tanner.[17]

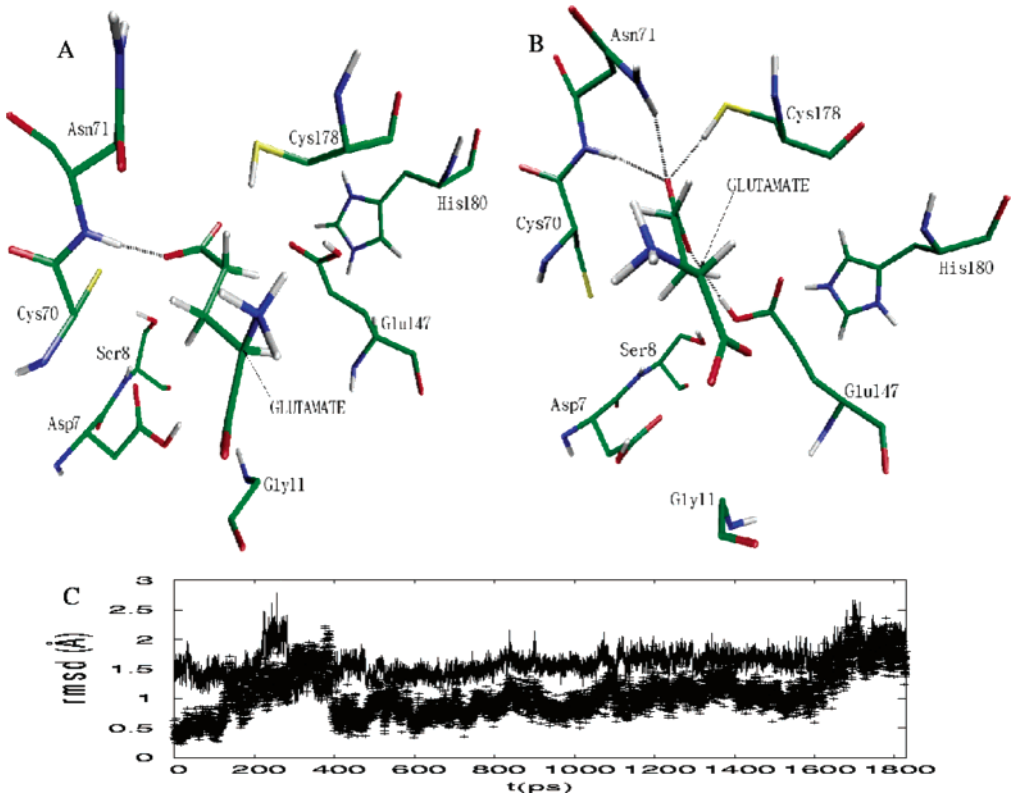

Figure 5. (a)−(c) Same as Figure 2(a)−(c) for the D-Glu-X-ray model.

The average rmsd of the ligand in the D-Gln-docked model with respect to the initial structure and calculated over the trajectory is rather big: 2.98 Å. This value shows that the D-Gln ligand has significantly moved from its initial location in the docked structure. The two rmsds calculated along the simulation steps and plotted in Figure 4c are clearly different. The rmsd value with respect to the initial docked structure is large but oscillates somewhat along the sampling stage, whereas the calculated rmsd with respect to the last structure of the equilibration stage experiments a significant increase along the simulation. These results indicate that the D-Gln ligand does not reach a stable position within the 1.0 ns time range, consequently with the lack of tight bindings to surrounding residues.

Binding of D-Glu in the Active Site of MurI. The different models of the D-Glu/*Aquifex pyrophilus* MurI complex are based on the same enzyme Cartesian coordinates used to build the D-Gln/*Aquifex pyrophilus* MurI models. However, for the D-Glu ligand we have taken the coordinates of the inhibitor D-Gln obtained from X-ray crystallography and the ones modeled by Hwang et al.,[19] and, in both cases, we have replaced the side chain group −NH2 of this molecule by a carboxylic oxygen to represent the carboxylate side-chain group of D-Glu. The resulting models are called D-Glu-X-ray and D-Glu-modeled, respectively, in this paper. We have followed the procedure indicated in the Methods section to prepare the initial structure for the simulation. In addition, a third model of the D-Glu/*Aquifex pyrophilus* MurI complex has been built using the coordinates obtained after docking a D-Glu molecule in the active site of MurI. This third model is called D-Glu-docked in this paper.

In Figure 5 the initial and the final configuration of the 1.8 ns SBMD simulation for the D-Glu-X-ray model can be compared. Like in the initial structure of the D-Gln-X-ray complex, only one significant ligand−enzyme interaction could be detected in the D-Glu-X-ray model (see Figure 5a and the last column in Table 2) corresponding to a short H-bond between Asn71 and the main-chain Oϵ1 atom of D-Glu. In addition, the D-Glu initial structure presents some other weaker substrate−enzyme interactions with Cys178, Glu147, and Gly177. From the average distance values included in the seventh column of Table 2 and the final configuration plotted in Figure 5b, it can be inferred that the D-Glu substrate modifies its location inside the MurI active center. After equilibration, the substrate tightens its interactions with the side chains of Asn71, Cys178, and Glu147 in addition to preserving, although somewhat longer, the initial Oϵ1-Asn71-NH hydrogen bond. Asn71 interacts now with the Oϵ1 atom of D-Glu also via its Hδ22, and the hydrogen bond with Cys178 has become shorter. However, the shortest hydrogen bond, with the highest occupancy, longest average lifetime, and smallest number of events (indicating that this hydrogen bond has not been broken and reformed often along the simulation), corresponds to the interaction between the main-chain Oϵ2 atom of D-Glu and Glu147. At this point, it is worth recalling that Glu147 (Glu152 in *L. fermenti*) has been proposed by Glavas and Tanner[17] to play an important role in substrate binding since the E152Q mutant showed only a modest decrease in the value of k_{cat}, whereas the value of K_M for D-Glu increased by 13-fold.

Table 2. Important Hydrogen Bond Interactions between D-Glutamate and Enzymatic Residues for the Simulations of the Different Models Defined in the Text[a]

ligand atom	residue-atom	occu	time	events	dist	fluct	init
			D-Glu-X-ray				
Oϵ1	Asn71-HN	0.96	5.8	304	1.98	0.21	1.65
Oϵ1	Asn71-Hδ22	0.93	3.1	553	2.01	0.25	5.30
Oϵ1	Cys178-Hγ1	0.37	0.4	1580	2.75	0.69	3.41
Oϵ2	Glu147-Hϵ2	0.98	24.8	72	1.80	0.25	3.83
NH3	Gly177-O	0.38	0.8	835	3.12	0.34	3.45
			D-Glu-Modeled				
Oϵ2	Asp7-Hδ2	1.00	412.5	3	1.68	0.11	5.68
Oϵ2	Gly11-HN	0.35	0.8	565	2.66	0.51	6.61
O$_\tau$1	Thr72-Hγ1	0.89	3.1	356	1.98	0.31	3.68
O$_\tau$2	Glu147-Hϵ2	0.92	11.3	101	1.84	0.40	1.62
O$_\tau$2	Cys178-Hγ1	0.48	0.7	882	2.67	0.75	2.94
O$_\tau$2	Thr72-Hγ1	0.38	0.8	619	2.53	0.43	5.57
NH3	Ser8-Oγ	0.84	1.6	647	2.95	0.20	6.36
NH3	Asp7-Oδ1	0.78	2.4	401	3.03	0.45	6.02
			D-Glu-Docked				
Oϵ1	Tyr39-HN	0.65	2.4	267	2.36	0.67	3.67
Oϵ1	Gly40-HN	0.77	9.3	82	2.32	0.76	2.22
Oϵ2	Thr72-Hγ1	0.63	39.2	16	3.10	1.87	3.21
Oϵ2	Thr114-Hγ1	0.78	65.3	12	2.63	1.68	4.04
O$_\tau$1	Asn71-Hδ22	0.48	1.5	323	2.48	0.57	5.52
O$_\tau$1	Thr72-HN	0.52	4.8	109	2.58	0.76	3.93
O$_\tau$1	Thr72-Hγ1	0.35	6.5	54	3.63	1.40	5.51
O$_\tau$2	Asn71-Hδ22	0.46	1.2	384	2.74	0.77	7.63

[a] See Table 1 for details of the content of each column.

All the changes in the D-Glu arrangement inside the MurI active site in the D-Glu-X-ray model indicate that the substrate modifies its hydrogen bond network relative to the initial structure. Despite this, the calculated average rmsd (1.61 Å) of D-Glu with respect to the initial structure is small; in fact, even smaller than the corresponding value for D-Gln (1.83 Å). The average rmsd for D-Glu with respect to the last structure of the equilibration stage is 1.06 Å (compared to 1.31 Å for D-Gln). Figure 5c shows the evolution of the rmsd of the substrate ligand with respect to the two different reference structures as a function of the simulation time. It can be seen that no significant structural instability appears. To understand these low average rmsds we have superimposed the initial and the final structure of the simulation. The comparison of the two structures indicates that the formation of new interactions is mainly due to movements of the enzyme residues side chains. This more stable behavior of the D-Glu ligand along the simulation explains the smaller value obtained for the average rmsd. The same trends are followed by the rmsd of the ligand referred to the last structure of the equilibration stage. In any case, our results about the relocation of the substrate ligand inside the active site do not significantly change the flipped orientation found by Hwang et al.[19] for D-Gln, and used by us to build the D-Glu-X-ray model. This is confirmed by the long average distances of 7.10 and 6.62 Å between the α-carbon of D-Glu and the Sγ atom of Cys70 and Cys178, respectively. Thus, our results show that the D-Glu substrate can be bound inside the active site of MurI in a stable conformation which, however, is not adequate to initiate the first chemical step proposed in Tanner's mechanism.[17]

The second model built to study D-Glu binding in MurI has been called D-Glu-modeled. In Figure 6 the initial and final structures corresponding to the 1.2 ns SBMD simulation carried out on this D-Glu-modeled system have been plotted. Like in the D-Gln-modeled case, the only existing interaction at the initial state between the ligand and the enzyme corresponds to a short hydrogen bond between the Oι2 atom of D-Glu and the protonated carboxylic group of Glu147 (see the last column of Table 2). In addition, the ligand forms two other weaker interactions with the enzyme: a long hydrogen bond between the same Oι2 atom of D-Glu and the protonated Cys178 and another long hydrogen bond between the other main-chain carboxylate oxygen of the ligand and Thr72. The average distances presented in Table 2 show that these three interactions are maintained along the simulation of the equilibrated system although with some changes: the hydrogen bond between the substrate and Glu147 slightly elongates, whereas the hydrogen bond with Thr72 clearly shortens. In addition, five new interactions are formed between the substrate and the enzyme once the system has been equilibrated. From Figure 6b and the average distances given in Table 2, it can be observed that the D-Glu substrate is hydrogen-bonded to the enzyme by the positively charged ammonium group (which is stabilized by Ser8 and Asp7) and by the two negatively charged carboxylate groups (the main-chain carboxylate interacts with Glu147, Cys178, and also Thr72, whereas the side-chain carboxylate interacts with Asp7 and Gly11). The shortest hydrogen bond in the ensemble of equilibrated structures of the D-Glu-modeled system corresponds to the interaction between Hδ2 of Asp7 and Oϵ2 of D-Glu. This hydrogen bond has an occupancy of 1.00, a very long average lifetime, very small fluctuations, and in only 3 events along the simulation it is broken and reformed. All this three observations are clear proofs of its high stability. As indicated above, the mutagenesis studies carried out by Glavas and Tanner[17] have supported the important role in catalysis of Asp7 (Asp10 in *L. fermenti*).

In agreement with the large differences between the initial and average distance values for the interactions listed in Table 2, Figure 6c indicates that the D-Glu ligand in the D-Glu-modeled system has clearly changed its relative orientation in the active site with respect to the initial coordinates of the D-Glu-modeled model. The average rmsd of the ligand with respect to the initial structure is 2.81 Å, clearly larger than the corresponding values obtained in the D-Glu-X-ray model and in the D-Gln-X-ray one. In addition, the differences observed between the calculated rmsds of the ligand, one with respect to the initial structure and the other with respect to the last structure of the equilibration stage, reflect that in this case the two reference states are not alike. The average rmsd with respect to the last structure of the equilibration stage takes a value of only 1.09 Å, corroborating the tight binding of the D-Glu ligand in this model. Interestingly, the calculated average distance between the α-carbon and the residue proposed to abstract the α-proton in the first chemical step of Tanner's mechanism[17] (Cys70) is 4.62 Å, a smaller value than the one calculated for the

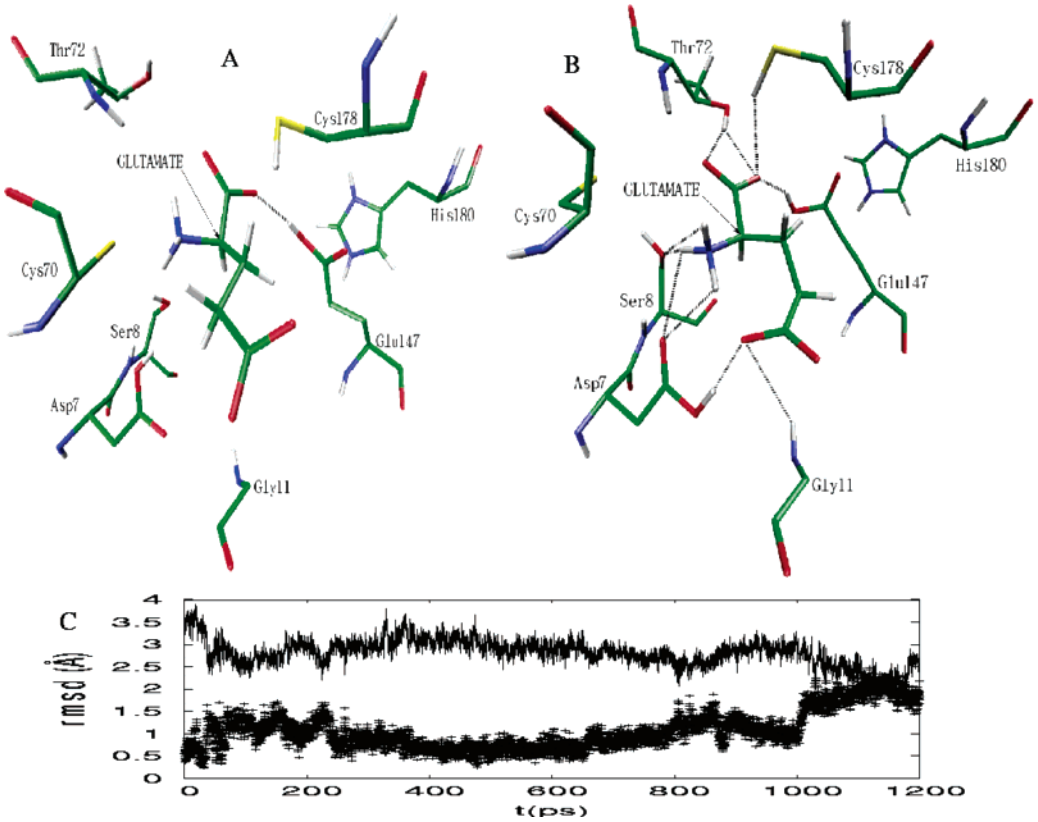

Figure 6. (a)−(c) Same as Figure 2(a)−(c) for the D-Glu-modeled model.

D-Glu-X-ray model. This result suggests that the equilibrated structure for the D-Glu substrate in the D-Glu-modeled system may be a good starting point for the study of the reactivity of MurI.

The initial structure for the third model of binding of D-Glu in the active site of MurI (D-Glu-docked) has been obtained following the flexible docking protocol detailed in the Methods section. In accordance with the three selection criteria used for the D-Gln ligand, one docked structure (plotted in Figure 7a) was selected to initiate the SBMD simulation. In this structure the D-Glu ligand adopts a relative orientation to the enzyme rather similar to the one in the D-Glu-X-ray model, that is, flipped 180° with respect to the substrate location in the D-Glu-modeled system. However, the center of mass of D-Glu is translated with respect to its position in the previous two models. As a consequence, the Cα-Sγ distance is 4.17 Å for Cys70. This distance is clearly shorter than in the initial structure of the D-Glu-X-ray model and even shorter than in the D-Glu-modeled system initial structure. In addition, in Table 2 (last column) it can be observed that in this initial configuration the ligand forms a hydrogen bond with Gly40 and two other rather longer hydrogen bonds with Thr72 and Tyr39. These are maintained along the simulation in addition to some other hydrogen bonds which are newly formed. All these interactions retain the substrate in a rather stable conformation bound by the two negatively charged carboxylate ends to residues Gly40, Tyr39, Thr114, and Thr72 at one side and to residues Asn71 and Thr72 at the other side (see Figure 7b). In any case, the rather long average distances of these hydrogen bonds, their large fluctuations, along with the low occupancies indicate that D-Glu is not tightly bound in the D-Glu-docked model. Interestingly, two of the new residues which enter the scene (Tyr39, and Thr114) are strictly conserved, and they have been proposed as candidates for the residues of glutamate racemase that are thought to stabilize the anionic intermediate by hydrogen bonding to the carboxylate group.

The rmsds (in Figure 7c) of the ligand in the D-Glu-docked model with respect to both, the initial structure and the last structure generated during the equilibration stage, increase during the first 500 ps to reach a more or less stable behavior. The trends are almost parallel between the two calculated rmsds, which indicates that there is not much difference between the two reference states. Overall, the average rmsds of the ligand calculated over the trajectory are rather high, with values of 3.45 and 2.32 Å obtained with respect to the initial structure and with respect to the last structure after the equilibration stage, respectively. These results are in agreement with the weak binding of the substrate observed in this model and with the changes in its conformation, mainly due to a rotation movement of the ligand around itself that takes place along the simulation steps. However despite being weakly bound, the distance between the Cα of the ligand and the Sγ of Cys70 (4.02 Å) indicates that the ensemble of the equilibrated structures is suitable for reaction.

Finally, we have lengthened the SBMD simulation time for the D-Glu-X-ray (up to 2528 ps) and D-Glu-modeled (up to 2236 ps) models to test the convergence of the results. As shown in the Supporting Information (see Figures 3−21 and Tables 6−16), no significant changes in the main MurI-substrate interactions appear at longer simulation times.

Ligand-Environment Interaction Energy. We have also calculated the electrostatic component of the interaction energy (ΔE_{SE}) between the ligand and the enzyme-aqueous

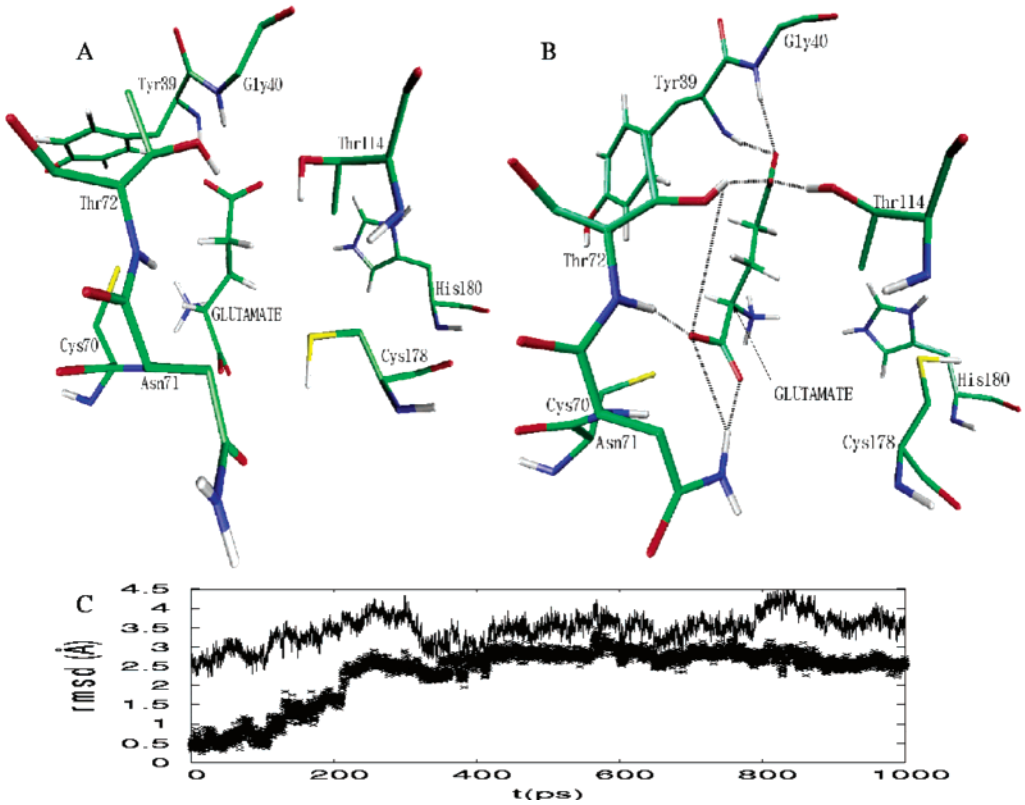

Figure 7. (a)−(c) Same as Figure 2(a)−(c) for the D-Glu-docked model.

Table 3. Electrostatic Component of the Ligand-Environment Interaction Energy and Its Decomposition in Different Terms[a]

model	ΔE_{SE}	ΔE_{perm}	ΔE_{pol}	ΔE_{stab}	ΔE_{dist}
D-Gln-X-ray	−106.69	−96.35	−10.34	−20.29	9.95
D-Gln-modeled	−114.92	−101.59	−13.33	−26.06	12.73
D-Glu-X-ray	−216.11	−202.65	−13.46	−26.39	12.93
D-Glu-modeled	−130.49	−124.75	−5.74	−11.22	5.48

[a]See text. All the energies are given in kcal/mol.

environment. First, the whole system is divided in a quantum mechanical (QM) subsystem (the ligand) and a molecular mechanical (MM) subsystem (the enzyme + aqueous environment). Then that electrostatic component is defined[34,35] as the difference between the energy of the ligand inside the enzyme + aqueous environment and that in the gas phase. ΔE_{SE} can be decomposed into the interaction energy between the unpolarized ligand and the environment (the permanent interaction energy, ΔE_{perm}) and the polarization energy of the ligand due to the environment (ΔE_{pol}). In turn, ΔE_{pol} may be further decomposed into a polarization stabilization term (ΔE_{stab}) and a ligand electronic distortion term (ΔE_{dist}).

For several models, and starting from the corresponding previously equilibrated systems, the energies have been obtained after averaging 10 ps of a SBMD simulation at 300 K on a QM/MM potential energy surface. The QM subsystem corresponding to the ligand (D-glutamine or D-glutamate) was represented by the AM1 semiempirical molecular orbital method.[36] The results are shown in Table 3. It can be seen that D-glutamate is clearly tighter bound to the enzyme than D-glutamine, specially in the D-Glu-X-ray model. In all cases the main contribution comes from the permanent interaction energy, although the polarization energy is also favorable and significant.

Conclusions

The active site of glutamate racemase from *Aquifex pyrophilus* contains many charged and polar residues. As a consequence, many ligand (D-glutamine or D-glutamate)−enzyme interactions can exist, making several binding modes possible. When the ligand is D-glutamine, our molecular dynamics simulations reveal three very different stable conformations of the inhibitor. One of them corresponds to the X-ray structure determined by Hwang et al.,[19] in which the α-carbon of D-glutamine is quite far from the two catalytic cysteines, confirming the experimental results. In the second conformation, derived from the structure modeled by Hwang et al.,[19] the α-carbon is not close to the two cysteines either. Only in a third conformation D-glutamine would be ready to initiate the reactive mechanism proposed by Glavas and Tanner[17] if it could behave as a substrate. In turn, at least three binding modes are possible for the substrate D-glutamate. In two of them D-glutamate is tightly bound (clearly more than D-glutamine) in the active site. One of these conformations comes from the X-ray structure determined for D-glutamine, whereas the other is related to the structure modeled for D-glutamine. In this second conformation the α-carbon is close to the two thiol groups of Cys70 and Cys178, making possible the deprotonation/reprotonation mechanism proposed by Glavas and Tanner[17] for the racemization of D-glutamate.

The existence of multiple modes of binding of the inhibitor D-glutamine and the substrate D-glutamate into the active site

of glutamate racemase might explain the apparent and surprising disagreement between the position and orientation of the inhibitor, inferred from X-ray crystallography data, and the expected position and orientation of the substrate, derived from the reaction mechanism proposed by Glavas and Tanner.[17] At this point, it has to be noted that accurate and expensive free energy calculations would be needed in order to determine the relative binding free energies of the different binding modes. However, the less costly molecular dynamics simulations of equilibrated complexes carried out in this paper are enough to provide an important structural information which shows the multiplicity of binding modes.

The initial coordinates for the theoretical study of the kinetics and mechanism of an enzymatic reaction are usually taken from a crystal structure of the enzyme complexed with a suitable inhibitor. However, in the present case, the unexpected features of the X-ray structure determined for D-glutamine prevents its use as an appropriate starting point for any reactivity study. Then, although we are rather interested in the kinetics of the deprotonation/reprotonation steps of D-glutamate, we have been forced to undertake the molecular dynamics simulation presented here. We think that our structural results provide reasonable starting points for the study of the reaction mechanism of glutamate racemase, which is already in progress in our laboratory. In any case, we think that, as already stated by Möbitz and Bruice,[37] the observation that D-glutamate can be accommodated in the active site of glutamate racemase according to several competitive binding modes, not all of them adequate for the racemization reaction, can have clear consequences on the kinetics of interconversion of glutamate enantiomers. As a matter of fact, the k_{cat} values of the glutamate racemization (0.25 s^{-1} for the Aquifex pyrophilus variant[38]) lies on the low range of k_{cat} values of enzymatic reactions. The biological reasons for favoring the presence of nonproductive enzyme−substrate complexes are at this stage unclear.

Acknowledgment. We are grateful for financial support from the Spanish "Ministerio de Ciencia y Tecnología" and the "Fondo Europeo de Desarrollo Regional" through Project No. BQU2002-0031 and the use of computational facilities of the CESCA.

Supporting Information Available: Parameters for the GB-MV2 method, molecular mechanics parameters for a deprotonated cysteine, SBMD simulation results with a sphere of 30 Å to define the reaction zone for the D-Glu-modeled system, and SBMD simulation results at longer times for the D-Glu-X-ray and D-Glu-modeled models. This material is available free of charge via the Internet at http://pubs.acs.org.

References

(1) Van Heijenoort, J. In *Escherichia coli and Salmonella*; Neidhart, F. C., Curtis, R., III, Ingraham, J. L., Lin, E. C. C., Low, K. B., Magasanik, B., Resnikoff, W. S., Riley, M., Schaechter, M., Umbarger, H. E., Eds.; American Society for Microbiology: Wahington, DC, 1996; p 1025.

(2) Ashiuchi, M.; Yoshimura, T.; Kitamura, T.; Kawata, Y.; Nagai, J.; Gorlatov, S.; Esaki, N.; Soda, K. *J. Biochemistry* **1995**, *117*, 495.

(3) Ashiuchi, M.; Kuwana, E.; Yamamoto, T.; Komatsu, K.; Misono, H. *J. Biol. Chem.* **2002**, *277*, 39070.

(4) Glavas, S.; Tanner, M. E. *Biochemistry* **1999**, *38*, 4106.

(5) de Dios, A.; Prieto, L.; Martín, J. A.; Rubio, A.; Ezquerra, J.; Tebbe, M.; López de Uralde, B.; Martín, J.; Sánchez, A.; LeTourneau, D., L.; McGee, J. E.; Boylan, C.; Parr, T., R., Jr.; Smith, M. C. *J. Med. Chem.* **2002**, *45*, 4559.

(6) Chu, D. T. W.; Plattner, J. J.; Katz, L. *J. Med. Chem.* **1996**, *39*, 3853.

(7) Gale, E. F.; Cundliffe, E.; Reynolds, P. E.; Richmond, M. H.; Waring, M. J. *The Molecular Basis of Antibiotic Action*, 2nd ed.; Wiley and Sons: London, 1981.

(8) Davis, J. *Science* **1994**, *264*, 375.

(9) Travis, J. *Science* **1994**, *264*, 360.

(10) Tanner, M. E.; Kenyon, G. L. In *Comprehensive Biological Catalysis*; Sinnott, M., Ed.; Academic Press: San Diego, 1998; p 7.

(11) Gerlt, J. A.; Kenyon, G. L.; Kozarich, J. W.; Neidhart, D. J.; Petsko, G. A.; Powers, B. M. *Curr. Opin. Struct. Biol.* **1992**, *2*, 736.

(12) Yamauchi, T.; Choi, S.-Y.; Okada, H.; Yohda, M.; Kumagai, H.; Esaki, N.; Soda, K. *J. Biol. Chem.* **1992**, *267*, 18361.

(13) Tanner, M. E.; Gallo, K. A.; Knowles, J. R. *Biochemistry* **1993**, *32*, 3998.

(14) Ho, H.-T.; Falk, P. J.; Ervin, K. M.; Krishnan, B. S.; Discotto, L. F.; Dougherty, T. J.; Pucci, M. J. *Biochemistry* **1995**, *34*, 2464.

(15) Doublet, P.; Van Heijenoort, J.; Mengin-Lecreulx, D. *Microb. Drug. Resist.* **1996**, *2*, 43.

(16) Tanner, M. E.; Miao, S. *Tetrahedron Lett.* **1994**, *35*, 4073.

(17) Glavas, S.; Tanner, M. E. *Biochemistry* **2001**, *40*, 6199.

(18) Tanner, M. E. *Acc. Chem. Res.* **2002**, *35*, 237.

(19) Hwang, K. Y.; Cho, C.-S.; Kim, S. S.; Sung, H.-C.; Yu, Y. G.; Cho, Y. *Nat. Struct. Biol.* **1999**, *6*, 422.

(20) Wiseman, J. S.; Nichols, J. S. *J. Biol. Chem.* **1984**, *259*, 8907.

(21) Higgins, W.; Tardif, C.; Richaud, C.; Krivanek, M. A.; Cardin, A. *Eur. J. Biochem.* **1989**, *186*, 137.

(22) Cirilli, M.; Zheng, R.; Scapin, G.; Blanchard, J. S. *Biochemistry* **1998**, *37*, 16452.

(23) Cho, Y., personal communication.

(24) Brooks, B. R.; Bruccoleri, R. E.; Olafson, B. D.; States, D. J.; Swaminathan, S.; Karplus, M. *J. Comput. Chem.* **1983**, *4*, 187.

(25) Lee, S. M.; Feig, M.; Salsbury, R., Freedie, J. R.; Brooks, C. L., III *J. Comput. Chem.* **2003**, *24*, 1348.

(26) Brooks, C. L., III; Karplus, M. *J. Chem. Phys.* **1983**, *79*, 6312.

(27) Brooks, C. L., III; Karplus, M. *J. Mol. Biol.* **1989**, *208*, 159.

(28) Mackerell, J., A. D.; Bashford, D.; Bellot, M.; Dunbrack, J., R. L.; Evanseck, J. D.; Field, M. J.; Fischer, S.; Gao, J.; Guo, H.; Ha, S.; Joseph-McCarthy, D.; Kuchnir, L.; Kuczera, K.; Lau, F. T. K.; Mattos, C.; Michnick, S.; Ngo, T.; Nguyen, D. T.; Prodhom, B.; Reiher, I., W. E:; Roux, B.; Schlenckrich, M.; Smith, J. C.; Stote, R.; Straub, J.; Watanabe, M.; Wiorkiewicz-Kuczera, J.; Yin, D.; Karplus, M. *J. Phys. Chem. B* **1998**, *102*, 3586.

(29) Jorgensen, W. L.; Chandrasekhar, J.; Madura, J. D.; Impey, R. W.; Klein, M. L. *J. Chem. Phys.* **1983**, *79*, 926.

(30) Rychaert, J. P.; Cicotti, G.; Berendsen, H. J. C. *J. Comput. Phys.* **1977**, *23*, 327.

(31) http://www.scripts.edu/pub/olson-web/dock/autodock/.

(32) Morris, G. M.; Goodsell, D. S.; Huey, R.; Olson, A. J. *J. Comput.-Aided Mol. Des.* **1996**, *10*, 293.

(33) Morris, G. M.; Goodsell, D. S.; Halliday, R. S.; Huey, R.; Hart, W. E.; Belew, R. K.; Olson, A. J. *J. Comput. Chem.* **1998**, *19*, 1639.

(34) Gao, J.; Xia, X. *Science* **1992**, *258*, 613.

(35) Garcia-Viloca, M.; Truhlar G., D.; Gao, J. *J. Mol. Biol.* **2003**, *327*, 549.

(36) Dewar, M. J. S.; Zoebisch, E. G.; Healy, E. F.; Stewart, J. J. P. *J. Am. Chem. Soc.* **1985**, *107*, 3902.

(37) Möbitz, H.; Bruice, T. C. *Biochemistry* **2004**, *43*, 9685.

(38) Bae, H.-S.; Hong, S.-P.; Lee, S.-G.; Kwak, M.-S.; Esaki, N.; Sung, M.-H. *J. Mol. Catal. B* **2002**, *17*, 223.

CT049881G

JCTC Journal of Chemical Theory and Computation

A QM/MM Exploration of the Potential Energy Surface of Pyruvate to Lactate Transformation Catalyzed by LDH. Improving the Accuracy of Semiempirical Descriptions

Silvia Ferrer,[#] J. Javier Ruiz-Pernía,[#] Iñaki Tuñón,*[,#] Vicente Moliner,*[,§] Mireia Garcia-Viloca,[‡] Angels González-Lafont,[‡,†] and José M. Lluch[‡,†]

Departament de Química Física/IcMol, Universitat de València, València, Spain, Departament de Ciències Experimentals, Universitat Jaume I, Castelló, Spain, Institut de Biotecnologia i de Biomedicina, Universitat Autònoma de Barcelona, Spain, and Departament de Química, Universitat Autònoma de Barcelona, Barcelona, Spain

Received February 2, 2005

Abstract: We present a QM/MM study of the potential energy surface of the pyruvate to lactate transformation catalyzed by L-lactate dehydrogenase. The transformation involves a hydride and a proton transfer which are followed by means of the corresponding antisymmetric combination of the distances from the hydrogen atom to the donor and the acceptor atoms. To discriminate among the possible reaction mechanisms we have considered different improvements of the AM1/MM description: reoptimization of the van der Waals parameters and inclusion of corrections to the QM energy associated with both transfer coordinates. The QM subsystem has been also enlarged to include charge-transfer effects from the substrate to some specific residues. In our best treatment, the transformation is described as a concerted process through a single transition structure in which the hydride transfer is more advanced than the proton transfer. From the methodological point of view, the correction schemes tested here improve the quality of the semiempirical potential energy surface although they also present deficiencies attributed to consideration of the proton and hydride transfer corrections as separable ones.

1. Introduction

L-Lactate dehydrogenase (LDH) is a highly stereospecific metabolic enzyme which catalyzes the interconversion of pyruvate and L-lactate using the NADH/NAD^+ pair as redox cofactor. Formally, the reaction in the pyruvate → L-lactate direction is achieved by reducing the carbonyl group with a hydride anion transferred from NADH and a proton transfer from a protonated His195 residue:[1]

$$CH_3COCOO^- + NADH + H^+ \rightleftharpoons CH_3CH(OH)COO^- + NAD^+$$

Much information on the mechanism has come from kinetic and site-directed mutagenesis experiments.[2] These studies characterize the enzyme (structure and details about the active site and mechanism) setting up that, while in the wild-type enzyme the rate-limiting step of both, the pyruvate reduction or the lactate oxidation process is a unimolecular rearrangement of the enzyme−NADH−pyruvate complex, and the rate of catalysis in the mutants is limited by the chemical reaction. In this regard, it is still unknown whether the reaction mechanism involves sequential proton and hydride ion transfers or if both transfers take place in a concerted way (see Scheme 1). The difference in the timing of the hydride transfer and the proton transfer is a matter of interest in mechanistic enzymology. Computational studies from different groups[3−7] suggested that the sequential mechanism is more likely, but the proposals differ in the order in which the proton and hydride ions are transferred. Thus, Ranganathan and Gready[6,7] found a mechanism in which the hydride transfer preceded proton transfer in a stepwise

* Corresponding authors e-mail: tunon@uv.es (I.T.) and moliner@exp.uji.es (V.M.).
† Departament de Química, Universitat Autònoma de Barcelona.
‡ Institut de Biotecnologia i de Biomedicina.
§ Universitat Jaume I.
# Universitat de Valencia.

10.1021/ct050016l CCC: $30.25
Published on Web 05/10/2005

Scheme 1

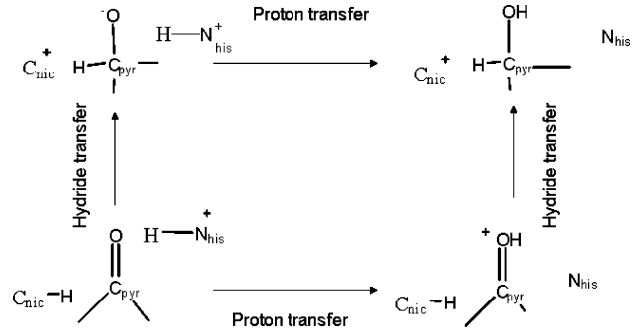

manner, in accordance with a previous study by Warshel et al. using an empirical valence bond study,[8] but contrasting with the usual chemical and enzymatic arguments for hydride transfer processes and with other theoretical studies[3,4,8] that predicted a concerted but asynchronous reaction in which the proton transfer was in a very advanced stage of the reaction. Finally, a more flexible quantum mechanical/molecular mechanical (QM/MM) treatment[5] allowed tracing the two distinct reaction pathways across the energy hypersurface. Nevertheless, as it was pointed out in this study,[5] the results at this point did not allow for making a definitive statement as to which mechanism was preferred. Without considering the fact that accurate determination of transition state properties would require statistical averaging over many configurations, each one individually being a transition state structure,[5,9] the previous study presented a limitation since a semiempirical Hamiltonian was employed to describe the quantum region. This, together with the fact that both pathways presented similar energy barriers, prevented to answer the question of which mechanism was preferred. To get more reliable energetics thus allowing to answer this question, a higher level of theory should be used in the QM/MM calculations.

Because of the reasons mentioned above, this enzymatic reaction provides an excellent example to illustrate the need of improving the accuracy of the QM/MM methods where the QM region is described by means of semiempirical Hamiltonians. One of the final goals of a theoretical study is usually to obtain the free energy profile of the desired enzymatic reaction. This free energy profile can be compared to experimental data and is also a powerful tool to get a deeper insight into the different contributions to catalysis. Obviously, the quality of these calculations is determined by the accuracy of the potential energy surface employed to describe the process. In the current example the selection of a theoretical level can be decisive to favor one or another reaction path. The conclusions reached by a theoretical study will be relevant only if we can be confident on the quality of our theoretical method to describe with similar accuracy different possible reaction mechanisms. This purpose is obviously limited by the computational cost. High level quantum potential energy and gradient calculations for medium-sized systems interacting with a large classical environment are still prohibitive taking into account that optimizations in highly dimensional energy surfaces require hundreds or even thousands of steps. In this paper we test different correction schemes in order to improve semiempirical descriptions at a low additional computational cost. These schemes are applied to discern between the two possible reaction mechanisms appearing on the semiempirical potential energy surface. We also address the other questions affecting the accuracy of the QM/MM calculations such as the optimization of the van der Waals parameters for the interaction between the QM and the MM subsystems and the size of the QM region. Considering all these aspects, and bearing in mind the limitations of the computational approach, the most favored reaction mechanism for the pyruvate to lactate transformation catalyzed by LDH in our treatment is a concerted but asynchronous mechanism where the hydride transfer is more advanced that the proton transfer at the transition state structure. Mechanistic details are dependent on the computational level chosen to describe the reaction.

2. Theory

In the present work, we have modeled the potential energy surface (PES) by a combined quantum-mechanical and molecular-mechanical (QM/MM) approach[10,11] that includes the generalized hybrid orbital (GHO)[12] method to treat the boundary between the quantum-mechanical (QM) and the molecular-mechanical (MM) fragments of the system. We used the semiempirical Austin model 1 (AM1)[13] to describe the QM subsystem. A semiempirical description can be quite inaccurate in some cases, and its use requires the previous calibration of the Hamiltonian. Obviously, it would be ideal to use a higher level ab initio molecular orbital or density functional theory (DFT) method to represent the reactive part of the system. However, these calculations are still too time-consuming to be practical at the present time for enzymatic systems considering that PES exploration, location, and characterization of stationary structures and molecular dynamics simulations (if needed) may require thousands of energy and gradient evaluations. An alternative dramatic reduction of the MM region size would not be realistic as the effect of long-range interactions as well as the flexibility of the system would be lost. There are several alternatives to improve the semiempirical description at a moderate or negligible computational cost. In principle one can develop specific reaction parameters (SRP)[14] designed to reproduce higher level results or to include correction energy terms to the original PES. We have here employed two of this last kind of methods.

As explained before we are interested in a chemical process which is composed of two elementary chemical steps: a hydride transfer and a proton transfer. These hydrogen transfers are here described using as reaction coordinates the antisymmetric combination of the distances from the hydrogen atom to the donor (r_{DH}) and the acceptor (r_{AH}) atoms:

$$R = r_{DH} - r_{AH}$$

We will use the symbols R_1 for the hydride transfer and R_2 for the proton transfer (see below for details). We will consider in this work two independent corrections to the semiempirical electronic energy associated with each one of these two coordinates.

The two correction methods used in this work are carried out by introducing two energy terms, which are functions that depend exclusively on R_1 and R_2 reaction coordinates, respectively.

The first correction method is the Simple Valence Bond (SVB)[15,16] In this method, the total potential energy of the system is given by the following equation

$$E_{tot} = E_{qm} + E_{mm} + E_{qm/mm} + E_{SVB,R1} + E_{SVB,R2} \quad (1)$$

where E_{qm} is the energy of the QM subsystem, E_{mm} is the energy of the MM subsystem, $E_{qm/mm}$ is the interaction energy between the QM and the MM regions, which include both electrostatic and van der Waals terms, and the E_{SVB} terms represent the SVB correction to the semiempirical E_{qm} energy in a particular reaction coordinate R_i. The following function has been proposed for this correction term

$$E_{SVB,Ri}(r_{DH}, r_{DA}, r_{AH}) = \frac{1}{2}[M_1(r_{DH}) + M_2(r_{AH})] - \frac{1}{2}([M_1(r_{DH}) - M_2(r_{AH})]^2 + 4[V_{12}(r_{DA})]^2)^{1/2} + \Delta D_{DH} \quad (2)$$

where r_{DA} is the distance between the donor and the acceptor atoms, the function V_{12} is given by

$$V_{12}(r_{DA}) = D_{DA}\exp[-\alpha_{12}(r_{DA} - r^0_{DA})] \quad (3)$$

and

$$M_i(r_{XH}) = \Delta D_{XH}(\exp[-2\alpha_{XH}(r_{XH} - r^0_{XH})] - 2\exp[-\alpha_{XH}(r_{XH} - r^0_{XH})]) \quad (4)$$

where XH represents the different pairs of atoms: donor-hydrogen (DH) or acceptor-hydrogen (AH) in the Morse potentials M_1 and M_2, respectively, and r^0_{XH} is the equilibrium distance of the corresponding bond. We set the two values ΔD_{XH} equal to the difference in dissociation energy between a high level theory calculation (in this work we use second-order Moller Plesset (MP2) level of calculation with a 6-31+G(d) basis set) and the lower level (the AM1 semiempirical method); α_{XH} is calculated as

$$\alpha_{XH} = \left(\frac{k_{XH}}{2D^0_{XH}}\right)^{1/2} = \upsilon_{XH}\left(\frac{2\pi^2\mu}{D^0_{XH}}\right)^{1/2} \quad (5)$$

where D^0_{XH} is the bond energy, μ is the reduced mass of atoms X and H, and k is the force constant. The parameters D_{DA} and α_{12} in eq 3 are adjusted to obtain the desired barrier height, which is the barrier height calculated at the higher level in gas phase.

The second correction method is the interpolated corrections (IC) scheme based on the use of cubic splines under tension.[17] The total potential energy is given by the following equation:

$$E_{tot} = E_{qm} + E_{mm} + E_{qm/mm} + \Delta E_{IC}(R_1) + \Delta E_{IC}(R_2) \quad (6)$$

This correction term is obtained as the difference between the qm energy provided by the high level method (HL) and the low level (LL) one for a particular configuration of the system obtained along the chosen reaction coordinate (R_i).

$$\Delta E(R_i) = E^{HL}_{QM}(R_i) - E^{LL}_{QM}(R_i) \quad (7)$$

Several structures are selected to calculate the energy difference between the high level and the low level methods at different values of the R_i coordinates. Then, following the work of Truhlar et al.,[18,19] a spline under tension is used to interpolate this correction term at any value of R_i. In this way we obtain a continuous function in R_i, with continuous first and second derivatives, which are necessary to perform molecular dynamics simulations. To preserve the general applicability of the method the spline fit is carried out in terms of a mapping coordinate z, defined as

$$z_i = \frac{2}{\pi}\arctan\left(\frac{R_i - R_{i0}}{L}\right) \quad (8)$$

The new variable allows us to map the energy correction term onto the finite interval $[-1,+1]$. The constants R_{i0} and L are chosen for centering and scaling the mapping function in the range of interest.[19] Then the final interpolated correction is obtained as

$$\Delta E_{IC}(R_i) = \text{spline}\{\Delta E[z_i(R_i)]\} \quad (9)$$

3. Calculations and Computational Details

3.1. Model of the Enzyme−Substrate−Coenzyme Complex. The X-ray structure of lactate dehydrogenase from *Bacillus stearothermophilus* comes from the PDB code 1LDN which is an octamer, although in this work only the tetramer is used (Figure 1). X-ray studies have proposed that the tetramer is the functional form of lactate dehydrogenase from *Bacillus stearothermophilus.*[20] In each monomer the crystal structure contains a total of 316 amino acid residues, the cofactor NADH, and the inhibitor oxamate (OXM), which is replaced by pyruvate in our study.

The coordinates of the hydrogen atoms of the protein and coenzyme were determined using the HBUILD facility of the CHARMM package.[21] All the ionizable groups were set to their normal ionization state at pH 7 with the exception of His195, which was modeled in its protonated form. Other histidine residues of the protein were modeled as neutral with the proton at Nδ.

Then, the system was partitioned into a quantum mechanical region consisting of 52 atoms and a molecular mechanical region containing the rest of the system. The QM subsystem includes 9 atoms of the pyruvate, 13 atoms of the His195 residue (including the C_α as a boundary atom), and 30 atoms of the NADH, which include the dihydronicotinamide and ribose rings, and the C5′ ribose atom as a boundary atom. The QM subsystem is described using the AM1 Hamiltonian and the boundary atoms are represented by the GHO method. A picture of the active site showing the partition into QM and MM subsystems is presented in Figure 2. First, the total energy of the system was minimized for 20 steps with the Adopted Basis Newton−Raphson (ABNR)[21] method by moving only the QM part of the system. Then, the system was solvated with a 24 Å radius sphere of TIP3P[22] water molecules centered on the pyruvate center of mass (see Figure 1). Water molecules that were within 2.5 Å of any non-hydrogen atom were removed. The

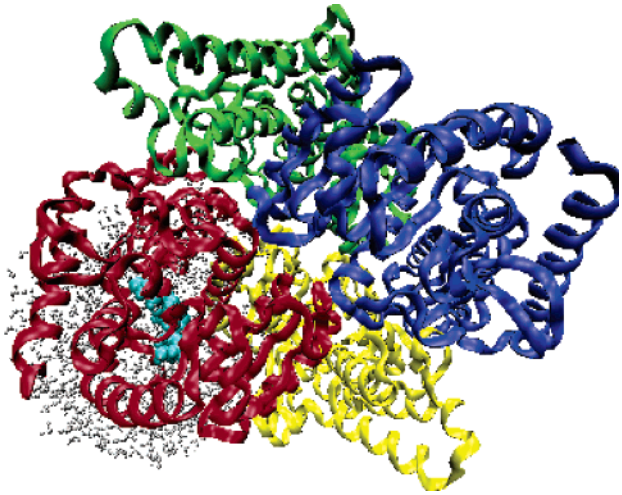

Figure 1. Tetramer of LDH with one of the active sites (NADH, pyruvate, and His-195) in blue balls. A sphere of water molecules with a radius of 24 Å water molecules has been centered on the center of mass of pyruvate.

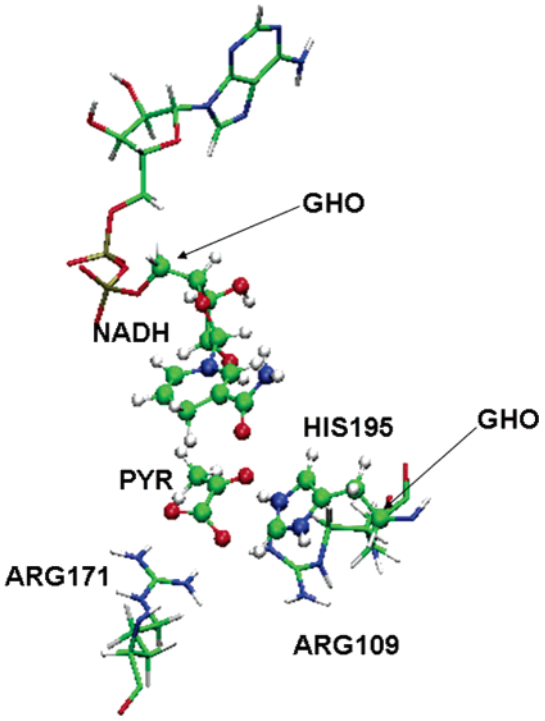

Figure 2. Snapshot of the LDH active center with the substrate (pyruvate) and the cofactor (NADH): The QM region is represented using balls and sticks. The position of the GHO atoms used to define the boundary with the MM region is also indicated.

resulting system was resolvated four more times using different relative orientations between the protein and the water sphere to ensure a good solvation of the system. Then, water positions were optimized for 20 steps followed by the optimization of the geometry of the part of the system included in a sphere of 24 Å. Finally, a molecular dynamics simulation of the waters (5 ps) was carried out to relax energetically unfavorable contacts, and the 3-fold cycle of superposition, deletion, and rotation was then repeated to fill in additional cavities generated during the dynamics simulation. The final model has 22 139 atoms, 19 862 of them are atoms from the protein or the ligands, and the rest, 2277, are atoms from the water molecules.

3.2. Reaction Coordinates. As explained before two reaction paths have been proposed in previous studies[5] (see Scheme 1). The first one is a mechanism where the hydride transfer precedes the proton transfer. This mechanism has been described as stepwise, where the initial step is the hydride transfer from a carbon atom of dihydronicotinamide, C_{nic} (donor atom), to the carbonyl carbon atom of pyruvate, C_{pyr} (acceptor atom), and in a second step a proton is transferred, from the N atom of His195, N_{his} (donor atom), to the carbonyl oxygen atom of pyruvate, O_{pyr} (the acceptor atom). The second proposed mechanism is a concerted but asynchronous mechanism where the proton and the hydride transfer take place through a single transition state (TS), being as how the proton transfer is now more advanced than the hydride transfer. For clarity purposes we will denote these two mechanisms as the hydride plus proton transfers pathway (the HP Pathway) and the proton plus hydride transfer pathway (the PH Pathway), respectively. Both mechanisms can be described on a single PES obtained as a function of two reaction coordinates (see Scheme 1). The reaction coordinate R_1 for the hydride transfer is defined in this work as the difference in the distances of the bonds between the transferring hydride-ion and the donor (C_{nic}) and the acceptor (C_{pyr}) atoms (eq 10). For the proton transfer a reaction coordinate R_2 is defined as the difference in the distance of the bonds between the transferring proton and the donor (N_{his}) and the acceptor (O_{pyr}) atoms (eq 11)

$$R_1 = r_{C_{nic}H_1} - r_{C_{pyr}H_1} \tag{10}$$

$$R_2 = r_{N_{his}H_2} - r_{O_{pyr}H_2} \tag{11}$$

The exploration of the PES was then carried out using the R_1 and R_2 coordinates defined before. These coordinates seem a reasonable choice to define a reduced PES, as they change smoothly along the surface. However, it must be taken into account that reduced surfaces give approximate descriptions of chemical processes. The CHARMM program was employed to carry out this exploration by means of the use of the RESDISTANCE keyword to define the reaction coordinates (R_i).

3.3. Exploration of the Potential Energy Surfaces. In this work, we have calculated two-dimensional (2D) potential energy surfaces (PES) at four different levels of theory: the uncorrected AM1/MM, the AM1-SVB/MM, the AM1-IC/MM, and the 2D-MP2sp/MM (bidimensional single-point calculations at the MP2 level). Gradient and energy calculations have been performed for the first three methods, whereas the 2D-MP2sp/MM is the result of single-point energy calculations on the AM1/MM optimized structures.

During all the optimizations, those atoms 24 Å away from the active site, 14 996 atoms, were kept frozen in order to reduce the computational cost, while 7143 atoms were allowed to move. In all the cases, the total energy of the system was minimized with the ABNR[21] method until the norm of the gradient with R_1 and R_2 directions projected out was less than 0.001 kcal mol^{-1}·$Å^{-1}$.

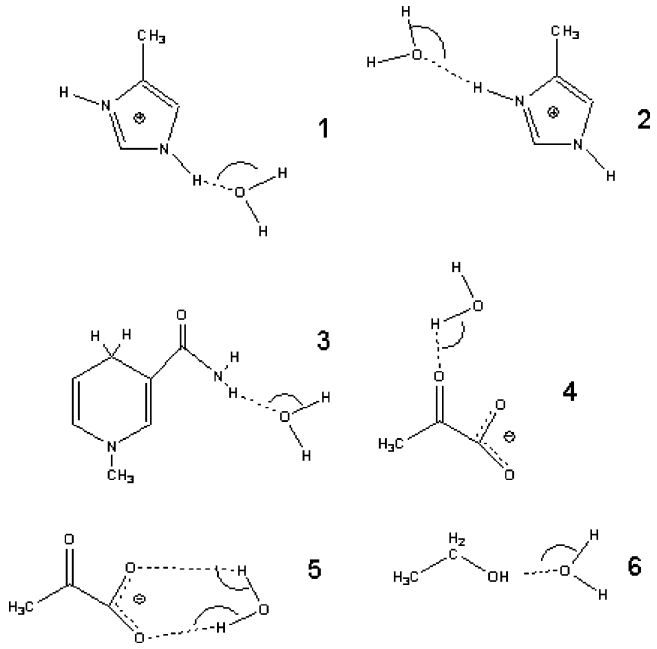

Figure 3. Bimolecular complexes of histidine fragment, nicotinamine ring model, pyruvate, and ethanol with water molecules.

3.4. QM/MM van der Waals Parameters. Prior to the PES exploration we have recalibrated the QM/MM potential by adjusting the van der Waals parameters of the QM atoms, employed to evaluate the interaction with the MM region. With this purpose we have obtained the interaction energy between some molecules that mimic the QM molecules and TIP3P water molecules by the procedure described by Freindorf and Gao.[23] We have considered complexes of water with models of the histidine and nicotinamide rings, with pyruvate and with ethanol to optimize the van der Waals parameters of the nitrogen atoms, hydroxyl oxygens, polar hydrogens bonded to nitrogen or oxygen, and also the carbon and oxygen atoms of pyruvate. Figure 3 shows the bimolecular complexes used to calculate the intermolecular interaction energy. The calculations were carried out describing all the complexes using quantum mechanics, at the HF/6-31G(d) level of theory and also using a hybrid QM/MM scheme where water molecules were described using TIP3P and the rest of the complex at the AM1 level. In all cases we have frozen the internal degrees of freedom of the QM fragments at gas-phase optimized values at the corresponding QM level, while the water intramolecular parameters have been fixed to the experimental geometry. To reproduce the HF/6-31G(d) results we have only modified the Lennard-Jones parameters, ϵ_{ab} and σ_{ab}, of selected QM atoms in the QM/MM interaction Hamiltonian $H_{qm/mm}$. As starting values for the Lennard-Jones parameters we used those provided by Gao and co-workers.[24] Table 1 provides the total interaction energies of the complexes at the HF level and also using QM/MM calculations with the van der Waals parameters obtained from the CHARMM force field, from Gao and co-workers, or after our optimization procedure. As it can be seen, in Table 1 we improved the energetic description of the complexes established with the histidine fragment and ethanol changing the parameters associated with nitrogen, oxygen, H(N), and H(O) atoms. However, we were not able to reproduce the full QM interaction with the carbon and oxygen atoms of pyruvate following this scheme. The reason for this behavior could be related to the noninclusion of charge transfer effects in our QM/MM Hamiltonian between pyruvate and water molecules. The magnitude of the charge transfer term is probably too big to be accounted by fitting the van der Waals parameters. The importance of the charge-transfer effect in pyruvate will be further addressed below. The original CHARMM parameters, those of ref 24, and the optimized ones are listed in Table 2. Geometries and absolute energies at the HF/6-31G(d) level of the complexes are given as Supporting Information.

Table 1. Total Interaction Energies (in kcal/mol) for the Complexes Appearing in Figure 3[a]

complex no.	ΔE(HF)	ΔE(1)	ΔE(2)	ΔE(3)
1	−16.02	−12.92	−13.9	−15.82
2	−16.18	−13.03	−14.03	−15.98
3	−5.24	−5.03	−5.07	−5.62
4	−10.81	−14.74	−14.84	−14.84
5	−13.02	−17.63	−17.68	−17.68
6	−5.47	−3.17	−3.80	−3. 89

[a] Each column shows the results obtained at the HF/6-31G(d) level of theory and at the AM1/MM level using the van der Waals parameters of the CHARMM force field (1), those provided in ref 24 (2), and the optimized parameters (3) given in Table 2.

3.5. Evaluation of Corrections to the Potential Energy. To improve the performance of the AM1 model through the use of the SVB or IC schemes, we carried out gas-phase ab initio calculations for smaller model reactions (Figure 4): In the selected model, 42 atoms constitute the three species that are involved in the two chemical processes: the hydride and the proton transfer. In a previous study[3−5] of the same reaction, where we used a smaller model for the enzyme−substrate system (LDH monomer), the stationary points were localized on a AM1/MM potential energy surface. Here, we have used the stationary points of the HP Pathway to cut the Cartesian coordinates for the 42 atoms of the gas-phase model (Figure 4). The Cartesian coordinates for additional

Table 2. van der Waals Parameters for the Quantum Atoms[e]

	this work		Gao et al.[a]		CHARMM	
atom	σ	ϵ	σ	ϵ	σ	ϵ
N(H)/N(H2)[b]	1.00	−0.14	1.57	−0.15	1.85	−0.20
H(N)[b]	0.35	−0.08	0.45	−0.10	0.2245	−0.046
H(O)[b]	0.28	−0.10	0.45	−0.10	0.2245	−0.046
O(H)[b]	1.08	−0.08	1.65	−0.20	1.70	−0.12
C(═O)[b]	1.65	−0.20	1.65	−0.20	1.70	−0.12
C(H)[b]	1.96	−0.08	1.96	−0.08	1.99	−0.07
O(═C)[b]	1.65	−0.20	1.65	−0.20	1.70	−0.12
O[c]	1.65	−0.20	1.65	−0.20	1.70	−0.12
H[d]	1.12	−0.01	1.12	−0.01	1.32	−0.022

[a] Reference 24. [b] A(B) stands for atoms A bound to atom or group B. [c] Oxygen of a carboxylate group. [d] On C. [e] The parameters are given according to the criteria of the CHARMM force field in Å and kcal/mol.

structures between have been obtained from AM1/MM optimizations at different values of the R_1 and R_2 coordinates on the LDH monomer model. Then, we have carried out single-point calculations on the 42 atoms gas-phase model at the AM1 level and by including electron correlation at the second-order Moller−Plesset perturbation theory with a polarized split valence basis set (MP2/6-31G(d,p)). The GAUSSIAN98[25] and CHARMM[21] programs were used for these calculations. Table 3 gives the gas-phase relative energies calculated at the AM1 and MP2 levels. From comparison between semiempirical and MP2 values a non-negligible error can be expected when obtaining the PES of the enzymatic process using the AM1 Hamiltonian. In particular, the use of these Hamiltonian results in a single-point recalculated reaction energy about 26 kcal/mol higher for the hydride transfer and a single-point recalculated reaction energy about 18 kcal/mol lower for the proton transfer. It also produces an important error in the hydride transfer barrier (the difference in the single-point recalculated barriers is 16.9 kcal/mol). Thus, consideration of correction schemes seems to be necessary to improve the accuracy of our computational model. The parameters determined for the SVB correction terms (see eqs 1−5) using these values are shown in Table 4.

For the IC method, we used the same gas-phase results on the 42 atoms model (Figure 4) to determine the two correction terms as a function of R_1 and R_2, respectively. For a given value of R_1 or R_2 the correction term is the difference between the single-point potential energy obtained using high level (MP2) and low level (AM1) methods. Two independent cubic splines are used to fit the correction energies as a function of the reaction coordinates (R_i).

It must be pointed out that according to the procedure described the structures selected to parametrize both correction schemes are obtained from the same region of the PES (if we divide the PES presented in Scheme 1 with a diagonal traced from reactants to products, the selected structures have been taken exclusively from the upper half part), and thus the correction procedures are expected to work more properly in this region. This important limitation will be discussed in more detail later on.

4. Results

4.1. Potential Energy Surfaces. Figure 5 shows the PES obtained using R_1 and R_2 coordinates at the AM1/MM level without corrections. The PES shows two distinct mechanistic pathways with very similar features to those found in a previous work on the LDH monomer using link atoms instead of GHO.[5] The hydride plus proton transfer pathway (HP Pathway) is a stepwise mechanism involving first the hydride transfer from the dihydronicotinamide ring of the NADH to a carbon atom of pyruvate followed by a proton transfer from the protonated His195 to the carbonyl O atom of pyruvate. On the other hand, the proton plus hydride transfer pathway (PH Pathway) is a concerted mechanism in which the proton transfer is considerably more advanced than the hydride transfer in the transition state (TS3). Table 5 gives the most relevant bond distances and the relative energies of the stationary points located on the AM1/MM PES. From the values of the distances given in Table 5 it is evident that TS1 corresponds to the hydride transfer where the proton transfer has been only slightly advanced. TS2 is the transition state structure associated with the proton transfer once the hydride has been already transferred. TS3 is the transition state structure associated with a concerted but very asynchronous proton and hydride transfers, where the proton transfer is considerably more advanced than the hydride transfer. The energy barriers for the HP Pathway are about 52 kcal/mol from reactants (pyruvate) to the intermediate and 14 kcal/mol from the intermediate to products (lactate), while the energy barrier in the PH Pathway is about 41 kcal/mol. Thus, on the AM1/MM PES the PH Pathway is the favored mechanism but taking into account the expected errors of the AM1 description, these results are still inconclusive about the preferred mechanism for the pyruvate to lactate transformation.

Figure 6 shows the PES calculated with the inclusion of the two SVB correction terms. As it can be seen it is possible to define again the two same mechanisms with similar features. Thus, the HP Pathway is a stepwise mechanism presenting an intermediate after the hydride transfer, and the PH Pathway is a concerted but asynchronous process. The differences with respect to the uncorrected AM1/MM PES appear in the relative energies of the stationary structures. In the HP Pathway the energy barriers are of about 29 kcal/mol from reactants (pyruvate) to intermediate (TS1) and about 11 kcal/mol from intermediate to products (TS2)—see Table 6. In the PH Pathway the energy barrier is again about 41 kcal/mol. We can stress at least two important conclusions at this point. First, the energy barriers now found seem to be more reasonable for an enzymatic process as they are considerably lower than in the uncorrected exploration. Second, while the PH Pathway presents a lower energy barrier on the uncorrected AM1/MM PES, now the prevalence of the HP Pathway is quite clear, because it presents noticeably lower energy barriers. The preference for this mechanism was clearly established by means of PES explorations carried out using a symmetric combination of the R_1 and R_2 coordinates. Starting from both, the reactants or the products, and using this new distinguished reaction coordinate, the chemical transformation always took place

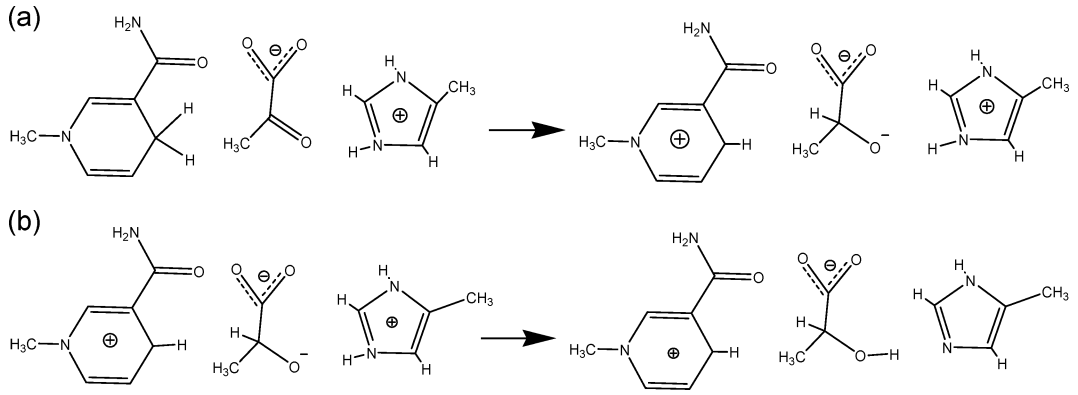

Figure 4. Molecular models used to calibrate the performance of the AM1 method versus MP2/6-31G(d,p) calculations: (a) model used for the hydride transfer reaction: from reactants (NADH and pyruvate) to intermediate (NAD^+ and $PyrH^-$) and (b) model used for the proton-transfer reaction: intermediate ($PyrH^-$ plus protonated His195) to products (lactate and His195).

Table 3. Single-Point (SP) Recalculated Gas-Phase Reaction Energies and Barrier Heights (kcal/mol) for the Hydride-Transfer Reaction and the Proton-Transfer Reaction in the Molecular Model Presented in Figure 4[a]

	SP recalculated barrier	SP recalculated reaction energy
	Hydride Transfer	
AM1	76.27	93.11
MP2/6-31G(d,p)	59.38	66.96
	Proton Transfer	
AM1	−5.07	−61.57
MP2/6-31G(d,p)	−7.07	−43.14

[a] Recall that the geometries are taken from AM1/MM calculations.

Table 4. Parameters of the SVB Functions for the Hydride (a) and Proton Transfer Steps (b)[a]

(a)

ΔD_{DH}	α_{DH}	ΔD_{AH}	α_{AH}	D_{DA}	α_{DA}
0.01	1.36	26.15	6.43	1.5	0.50

(b)

ΔD_{NH}	α_{NH}	ΔD_{OH}	α_{OH}	D_{NO}	α_{NO}
21.27	1.49	1.46	1.09	7.1	1.00

[a] ΔDs are given in kcal/mol and α in $Å^{-1}$.

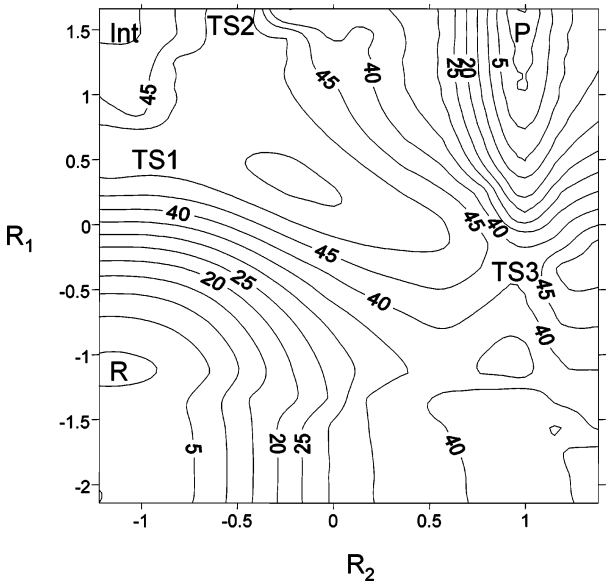

Figure 5. Potential energy surface at the AM1/MM level. R_1 and R_2 are the coordinates (in Å) associated with the hydride and proton transfers (see eqs 10 and 11). The position of reactants (R), intermediate (Int), products (P), and transition state structures (TS1, TS2, and TS3) is qualitatively shown. Isoenergetical lines are depicted each 5 kcal/mol.

Table 5. Relevant Distances (Å) and Relative Energies (kcal/mol) of the Stationary Structures Appearing on the AM1/MM PES

	$r_{C_{nic}H_1}$	$r_{C_{pyr}H_1}$	$r_{N_{his}H_2}$	$r_{O_{pyr}H_2}$	energy
reactants	1.15	2.29	1.00	2.22	0
TS1	1.70	1.24	1.01	2.03	52
intermediate	2.80	1.15	1.00	2.22	38
TS2	2.79	1.14	1.06	1.68	52
products	2.79	1.13	1.98	0.99	−5
TS3	1.30	1.44	1.96	0.99	41

through the HP Pathway. The energy profiles obtained using the R_1+R_2 coordinate are provided as Supporting Information.

Figure 7 shows the PES calculated with the inclusion of ICs through the use of two independent cubic splines associated with the R_1 and R_2 coordinates. The obtained PES is very similar to the previous one. In fact, by inspection of the PES it is possible to define again the two same reaction mechanisms. Thus, the HP Pathway is a stepwise mechanism and the PH Pathway is a concerted one. The energy barrier for the hydride transfer in the HP Pathway is of about 34 kcal/mol —see Table 7—while for the subsequent proton transfer is of about 11 kcal/mol (from the intermediate). In the PH Pathway the energy barrier is about 52 kcal/mol. Therefore, also within this correction methodology the preferred mechanism is the HP Pathway. Differences with respect to the previous methodology are found in the geometry of the stationary structures. Thus, reactants are now found at larger distances from pyruvate atoms to the hydride and the proton. However, these changes are not very relevant in energy as the reactants are found in a very flat valley, and then its exact position can change noticeably depending on the particularities of the energy function employed. Geometrical changes are also found in the structure of TS3 with respect to the SVB surface. On this new PES the TS3

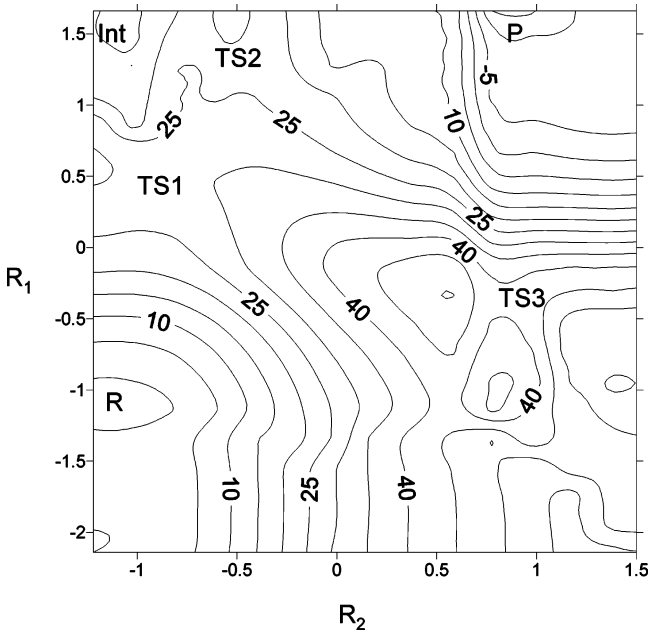

Figure 6. Potential energy surface at the AM1-SVB/MM level. R_1 and R_2 are the coordinates (in Å) associated with the hydride and proton transfers, respectively (see eqs 10 and 11). The position of reactants (R), intermediate (Int), products (P), and transition state structures (TS1, TS2, and TS3) is qualitatively shown. Isoenergetical lines are depicted each 5 kcal/mol.

Table 6. Relevant Distances (Å) and Relative Energies (kcal/mol) of the Stationary Structures Appearing on the PES Obtained at the AM1/MM Level with the Inclusion of SVB Correction Terms

	$r_{C_{nic}H_1}$	$r_{C_{pyr}H_1}$	$r_{N_{his}H_2}$	$r_{O_{pyr}H_2}$	energy
reactants	1.14	2.29	1.01	2.03	0
TS1	1.62	1.16	1.00	2.02	29
intermediate	2.79	1.13	1.01	2.03	14
TS2	2.79	1.13	1.06	1.67	25
products	2.79	1.13	1.96	0.98	−15
TS3	1.21	1.55	1.77	0.99	41

structure appears at slightly less advanced values of the hydride and proton-transfer coordinates.

At this point it is important to stress the fact that the two correction schemes display very similar behavior because they have been parametrized to reproduce the same high level quantum method energies using structures taken from the same region of the uncorrected PES. As described above, the reference structures used to obtain the correction energies were selected from the HP Pathway of an uncorrected PES. Thus, it would be reasonable to question the ability of the two methods to give accurate predictions of the PES in the region corresponding to the PH Pathway. For this reason we decided to obtain a new corrected PES based on bidimensional energy single-point calculations at the MP2/6-31G(d,p) level using the gas-phase model in Figure 4 and taking the geometries from the AM1/MM-2D PES (Figure 5). This new PES was obtained using the following energy function

$$E = E_{AM1} + E_{AM1/MM} + E_{MM} + (E'_{MP2} - E'_{AM1}) \quad (12)$$

where E' are the result of single-point energy calculations

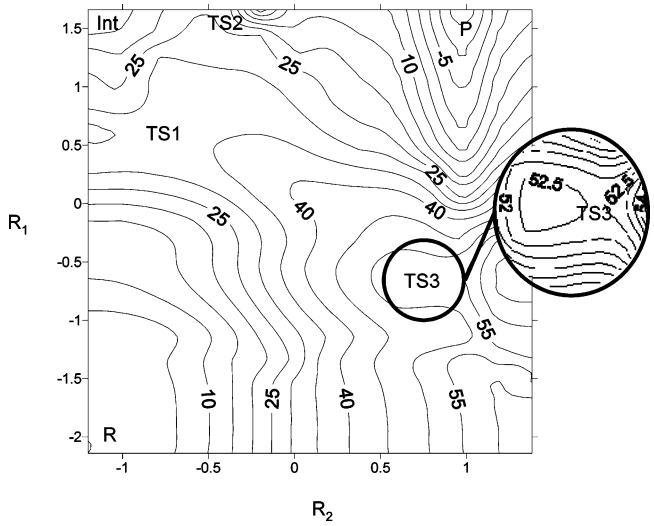

Figure 7. Potential energy surface at the AM1-IC/MM level. R_1 and R_2 are the coordinates (in Å) associated with the hydride and proton transfers (see text). The position of reactants (R), intermediate (Int), products (P), and transition state structures (TS1, TS2, and TS3) is qualitatively shown. Isoenergetical lines are depicted each 5 kcal/mol (0.5 kcal/mol in amplified zone).

Table 7. Relevant Distances (Å) and Relative Energies (kcal/mol) of the Stationary Structures Appearing on the PES Obtained at the AM1/MM Level with the Inclusion of Interpolated Corrections

	$r_{C_{nic}H_1}$	$r_{C_{pyr}H_1}$	$r_{N_{his}H_2}$	$r_{O_{pyr}H_2}$	energy
reactants	1.13	3.27	1.00	2.22	0
TS1	1.86	1.20	1.03	1.85	34
intermediate	2.80	1.15	1.00	2.22	13
TS2	2.79	1.13	1.11	1.53	24
products	2.79	1.13	1.98	0.99	−19
TS3	1.20	1.75	1.98	1.00	52

in gas phase obtained for the reduced QM model corresponding to the molecules presented in Figure 4. This new PES is presented in Figure 8, and the coordinates and relative energies of the stationary structures are gathered in Table 8. There are significant differences with the previous PESs. The most evident is that the intermediate appearing after the hydride transfer to the pyruvate has disappeared and a new intermediate (Int2) is found after the proton transfer. Thus, on the new PES the HP Pathway is a concerted mechanism taking place through a single transition state structure (TS4). This new transition state structure roughly corresponds to TS1 found on the previous PESs although it is now located at more advanced values of the proton-transfer coordinate. The PH Pathway is now described as a stepwise mechanism with two transition states (TS5 and TS6). The first corresponds to a very advanced proton transfer and the second to an early hydride transfer to the protonated intermediate (Int2). The energy of this structure is of about 37 kcal/mol above the reactants. At the reactant structure the carbon atom of pyruvate is found at a larger distance from the hydride (as in the PES with interpolated corrections). The products are now found at much larger values of the proton-transfer coordinate than in any of the discussed PES. This is due to the larger distance between histidine to the transferred proton. From the kinetic point of view, the concerted HP Pathway

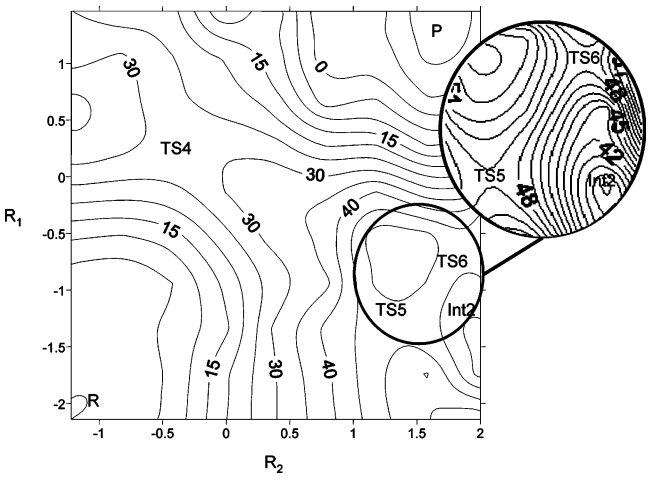

Figure 8. Potential energy surface obtained with bidimensional single-point MP2/6-31G(d,p) energy corrections. R_1 and R_2 are the coordinates (in Å) associated with the hydride and proton transfers (see text). The position of reactants (R), products (P), intermediate (Int2), and transition state structures (TS4, TS5, and TS4) is qualitatively shown. Isoenergetical lines are depicted each 5 kcal/mol (1 kcal/mol in amplified zone).

Table 8. Relevant Distances (Å) and Relative Energies (kcal/mol) of the Stationary Structures Appearing on the PES Obtained with Bidimensional MP2/6-31G(d,p) Single-Point Energy Corrections

	$r_{C_{nic}H_1}$	$r_{C_{pyr}H_1}$	$r_{N_{his}H_2}$	$r_{O_{pyr}H_2}$	energy
reactants	1.13	3.27	1.01	2.22	0
TS4	1.53	1.28	1.10	1.53	29
TS5	1.14	2.49	2.39	1.01	49
Int2	1.15	2.50	2.98	1.01	37
TS6	1.20	1.75	2.77	1.00	48
products	2.59	1.13	2.56	0.98	−13

seems to be the preferred mechanism on the PES (29 versus 48 kcal/mol).

It is interesting to comment on the performance of both correction methods when compared to the PES obtained with single-point corrections. Both the SVB and the IC schemes assume that differences between the high and low computational levels (MP2 and AM1 in this case) in the R_1 and R_2 coordinates are mutually independent. This is, the errors associated with the semiempirical description are expected to be approximately the same when the proton is transferred to the substrate (with charge −1 au) or to the intermediate (with a charge of −2 au). This is obviously not the case. However, despite the inherent deficiency both correction methods considerably improve the energetic description of both mechanisms when compared to the uncorrected AM1/MM PES. As compared to the PES obtained with bidimensional MP2 corrections, the AM1 surface has an average error in barrier heights of 15 kcal/mol and an average error in the four key geometrical variables at the two transition states of 0.32 Å. The SVB correction reduces these average errors to 4 kcal/mol and 0.31 Å, and the IC correction reduces them to 4 kcal/mol and 0.25 Å, respectively. It seems that separable correction schemes do a good job correcting the energies but not as well for correcting geometries of dynamical bottlenecks. This feature was already reported for the IC methodology,[18] and it seems that the SVB one presents a similar behavior. Anyway, the most important question is that both schemes are successfully predicting the HP Pathway as the preferred one, while on the uncorrected PES the PH Pathway displayed a lower energy barrier. The SVB method gives energy barriers in better agreement with the PES with bidimensional corrections for the HP Pathway, while the IC method agrees better with the bidimensional corrected PES in the PH Pathway.

Table 9. Interaction Energies (E_{int}, in kcal/mol) and Mulliken Charge on the Pyruvate (Q, in au) for the Complexes Formed between Pyruvate and Arg171 and Pyruvate and Arg109[a]

	Arg171/Pyr		Arg109/Pyr	
	E_{int}	Q	E_{int}	Q
HF/6-31G(d)	−111.21	−0.868	−68.76	−0.966
AM1	−98.37	−0.920	−62.80	−0.991
AM1/MM	−77.76	−1.000	−40.18	−1.000

[a] Geometries are taken from the reactant structure of the AM1/MM PES.

4.2. The Size of the QM Subsystem. The interaction between the substrate (pyruvate) and some residues in the MM part obviously play an essential role defining the possible reaction mechanisms. It has been proposed that the role of the Arg109 is to enhance the polarization of the pyruvate carbonyl group in the ground state and to stabilize the transition state in the HP Pathway, whereas the role of Arg171 is to assist in the binding of the substrate.[1,2] As previously described, when we tried to optimize the van der Waals parameters of the QM/MM interaction between pyruvate and water molecules we found a systematic deviation with respect to the QM values. This difference could be due to charge transfer effects, a term not included in standard QM/MM calculations. Obviously, this possible source of error requires some further studies in our system because the charge transfer could be even larger in the case of pyruvate surrounded by positively charged arginine residues. To address this issue we have compared the interaction energy between pyruvate and both arginines in the enzyme active site by means of gas-phase single-point energy calculations at the HF/6-31G(d) level, with those obtained at the AM1 and AM1/MM levels. These interaction energies are given in Table 9. As it can be seen, the AM1/MM calculations show important deviations from the HF values. The main contribution to this error is not the use of the AM1 Hamiltonian as the results are much improved when all the system is described by means of this semiempirical method. The magnitude of the error is directly correlated with the charge transfer (estimated from the Mulliken charges), and thus we attribute this error to the lack of charge-transfer effects in the QM/MM treatment.

Obviously, if the error is kept more or less constant all along the PES, then one could ignore this contribution. The charge of the substrate is the same in reactants (pyruvate) and products (lactate). However, it must be taken into account that after the hydride transfer the charge of the substrate increases from −1 to −2, and then the charge-transfer effect on the energy could be different in that region of the PES. For this reason we decided to explore again the AM1/MM

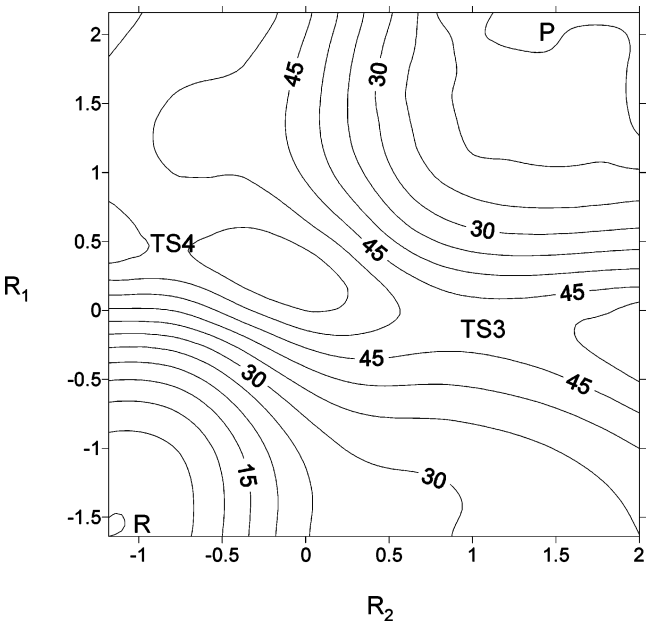

Figure 9. Potential energy surface obtained at the AM1/MM level with a QM region including Arg109 and Arg171. R_1 and R_2 are the coordinates (in Å) associated with the hydride and proton transfers (see text). The position of reactants (R), products (P), and transition state structures (TS3 and TS4) is qualitatively shown. Isoenergetical lines are depicted each 5 kcal/mol.

Table 10. Relevant Distances (Å) and Relative Energies (kcal/mol) of the Stationary Structures Appearing on the AM1/MM PES Obtained When the QM Region Includes Arg109 and Arg171

	$r_{C_{nic}H_1}$	$r_{C_{pyr}H_1}$	$r_{N_{his}H_2}$	$r_{O_{pyr}H_2}$	energy
reactants	1.13	2.77	1.01	2.17	0
TS4	1.78	1.22	1.03	1.81	54
TS3	1.36	1.39	2.01	0.99	47
products	3.08	1.12	2.40	0.98	13

2D uncorrected PES using the same reaction coordinates but increasing now the size of the QM region to include both Arg109 and Arg171 (resulting in a total of 78 QM atoms). This requires the introduction of two new GHOs placed at Cγ of each arginine. The new PES obtained for the larger QM subsystem is shown in Figure 9. As previously, we found two different mechanisms for the transformation of pyruvate into lactate: the HP Pathway and the PH Pathway in which the proton transfer precedes the hydride transfer. On this PES we only located two transition state structures (TS4 in the HP Pathway and TS3 in the PH Pathway), so both mechanisms are now described as concerted ones. The geometries and energies of the stationary structures are given in Table 10. The energy barrier in the HP Pathway (TS4) is about 54 kcal/mol and in the PH Pathway (TS3) is of about 47 kcal/mol. This description can be compared with the uncorrected AM1/MM PES with the smaller (52 atoms) QM subsystem. In that case the HP Pathway presented an energy barrier of about 52 kcal/mol associated with the first step (the hydride transfer), while the PH Pathway had a unique transition state structure with an associated energy barrier of about 41 kcal/mol (see Table 5). The reaction energy also changes noticeably, being of about −5 kcal/mol with the smaller QM subsystem and about 13 kcal/mol with the larger one. Then, the main effect of the inclusion of the arginines into the QM subsystem is to destabilize the intermediate which appeared after the hydride transfer, increasing the energy of that region of the PES. As a consequence the reaction path associated with the HP Pathway is now considerably more concerted than in our previous PES. All these changes can be rationalized considering that when Arg109 and Arg171 are described classically, electrostatic interactions with the intermediate obtained after the hydride transfer and with the protonated His195 are overestimated. This results in too large a stabilization of the intermediate, with a charge of −2, and also in too large an interaction with the protonated His195, with a positive charge. When these arginines are described quantum mechanically and the charge can be more delocalized, this overestimation of electrostatic interactions disappears, and thus the intermediate is no longer a minimum on the PES. This interpretation is confirmed by analysis of the charge distribution on the QM subsystem when it contains 52 or 78 atoms. For the intermediate, the absolute charge on the substrate is about 0.1 electrons smaller when the QM region includes both arginines. The magnitude of this charge transfer is confirmed by analysis of Mulliken and NPA charges[26,27] (a representation of the atomic charges for the stationary structures obtained at different levels is given as Supporting Information).

Because of the magnitude of the changes taking place when the size of the QM region was increased we decided to obtain a new PES for the large QM region including corrections to the AM1 description. According to the conclusions reached in the previous section we decided to include corrections by means of bidimensional single-point energy calculations at the MP2/6-31G(d,p) level, following the same procedure as before (see eq 12). The corrected PES is presented in Figure 10. The most relevant distances and the energies of the stationary structures corresponding to this PES are presented in Table 11. In this case we have an important difference with respect to the previously presented PESs: only one reaction mechanism is found. The unique transition state structure corresponds to a concerted hydride and proton transfers where the hydride transfer is considerably more advanced than the proton transfer, i.e., we have a concerted HP Pathway. The energy barrier is about 30 kcal/mol, and the reaction energy is close to zero (−0.7 kcal/mol).

5. Conclusions

We have here presented a QM/MM study of the PES corresponding to the pyruvate to lactate transformation catalyzed by LDH. This transformation takes place by means of a hydride and a proton transfer to the substrate. The order in which the hydride and the proton are transferred defines two different mechanistic routes for the process: a hydride transfer followed by a proton transfer (the so-called HP Pathway) and a proton transfer followed by a hydride transfer (the PH Pathway). Previous theoretical studies differ in the preferred mechanism as well as in their concerted or stepwise nature. For this reason we decided to improve the standard AM1/MM description of the reaction. In particular we have

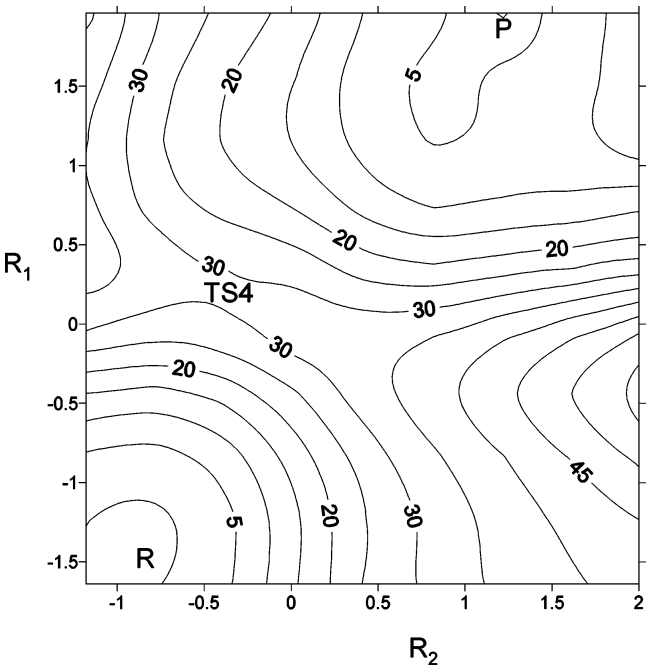

Figure 10. Potential energy surface obtained at the AM1/MM level with a QM region including Arg109 and Arg171 and bidimensional single-point MP2/6-31G(d,p) corrections. R_1 and R_2 are the coordinates (in Å) associated with the hydride and proton transfers (see eq 10). The position of reactants (R), products (P), and transition state structure (TS4) is qualitatively shown. Isoenergetical lines are depicted each 5 kcal/mol.

Table 11. Relevant Distances (Å) and Relative Energies (kcal/mol) of the Stationary Structures Appearing on the PES with Bidimensional MP2/6-31G(d,p) Single-Point Energy Corrections Obtained when the QM Region Includes Arg109 and Arg171

	$r_{C_{nic}H_1}$	$r_{C_{pyr}H_1}$	$r_{N_{his}H_2}$	$r_{O_{pyr}H_2}$	energy
reactants	1.13	2.77	1.01	2.17	0
TS4	1.62	1.26	1.12	1.50	30
products	3.06	1.12	2.20	0.95	−1

considered the effect of the van der Waals parameters used in the QM subsystem, the correction of the QM energy by two different schemes (SVB and IC), and the size of the QM subsystem to take into account charge-transfer effects.

While the change in the van der Waals parameters is quite modest, the inclusion of correction terms evaluated at the MP2 level into the AM1 energy has important consequences on the studied PES. The PH Pathway presents a lower energy barrier on the uncorrected AM1/MM PES, but when both correction schemes are considered the HP Pathway presents noticeably lower energy barriers. However, both correction schemes display some deficiencies associated with the fact that the correction energies associated with the proton and the hydride transfer coordinates are taken as independent. The most important consequence is that both methods describe the HP Pathway as a stepwise mechanism, while it appears as a concerted one when corrections with single-point calculations on the whole PES at the MP2 level are carried out. This feature of the PES is stressed when the QM subsystem is enlarged to include also Arg109 and Arg171. A classical description of these two residues results in an overstabilization of the structure appearing after the hydride transfer to the substrate. Note that the terms stepwise and concerted refer here just to the presence or absence, respectively, of an intermediate on the PES. Indeed, only a dynamical study could show the actual relevance of the intermediate for the reaction mechanism.

Thus, in our best treatment, the pyruvate to lactate transformation catalyzed by LDH is described as a concerted hydride and proton transfer mechanism with a single transition structure where the hydride transfer is considerably more advanced than the proton transfer. However, the mechanistic details depend on the particular computational level chosen to describe the process. The energy barrier found is of about 30 kcal/mol, a value that seems to be overestimated when compared to the experimental estimations of the activation free energy barrier (with an upper limit of about 15 kcal/mol[28]). Entropic contributions, tunneling, higher QM level, and a better QM/MM description are expected to contribute to diminish the gap with the experimental estimations. The protonation state of some residues close to the active site, here assumed to be found in their standard protonation states at pH 7, could also be a source of discrepancy with experiments. Studies are underway to evaluate all these contributions. In any case, and as a methodological conclusion of the present work, dynamical treatments of this system should be carried out on a PES including high level corrections to the QM energy for the proton and the hydride transfers, and, importantly, these corrections should not be included independently in order to have an accurate description.

Acknowledgment. Authors thank Prof. D. G. Truhlar for reading and commenting the manuscript. We thank the DGI for projects DGI BQU2003-04168-C03 and BQU-2002-00301, BANCAIXA for project P1A99-03, and Generalitat Valenciana for project GV01-324, GV04B-21, GV04B-131, and GRUPOS04/28. S.F. and J.J.R.-P. acknowledge a doctoral fellowship of the Ministerio de Ciencia y Tecnología. S.F. also acknowledges the Ministerio for financial support during her visit to the UAB and the warm hospitality of all the people of the Departament de Química of the Universitat Autònoma de Barcelona.

Supporting Information Available: Geometries (in Å) and absolute energies at the HF/6-31G(d,p) level (in au) of the complexes shown in Figure 3, energy profiles (kcal/mol) obtained using the $R_1 + R_2 = R_4$ coordinate, and atomic charges (in au) obtained for stationary structures of the HP pathway. This material is available free of charge via the Internet at http://pubs.acs.org.

References

(1) Clarke, A. R.; Atkinson, T.; Holbrook, J. J. *Trends Biochem. Sci.* **1989**, *14*, 145−148.

(2) Burger, J. W. I.; Ray, W. J. J. *Biochemistry* **1984**, *23*, 3620−3626.

(3) Moliner, V.; Turner, A. J.; Williams, I. H. *Chem. Commun.* **1997**, 1271−1272.

(4) Moliner, V.; Williams, I. H. *Chem. Commun.* **2000**, 1843−1844.

(5) Turner, A. J.; Moliner, V.; Williams, I. H. *Phys. Chem. Chem. Phys.* **1999**, *1*, 1323−1331.

(6) Ranganathan, S.; Gready, J. E. *J. Phys. Chem. B* **1997**, *101*, 5614−5618.

(7) Ranganathan, S.; Gready, J. E. *J. Chem. Soc, Faraday Trans.* **1994**, *90*, 2047−1456.

(8) Yadav, A.; Jackson, R. M.; Holbrook, J. J.; Warshel, A. *J. Am. Chem. Soc.* **1991**, *113*, 4800−4805.

(9) Truhlar, D. G.; Gao, J. L.; Garcia-Viloca, M.; Alhambra, C.; Corchado, J.; Sanchez, M. L.; Poulsen, T. D. *Int. J. Quantum Chem.* **2004**, *100*, 1136−1152.

(10) Field, M. J.; Bash, P. A.; Karplus, M. *J. Comput. Chem.* **1990**, *11*, 700−733.

(11) Gao, J.; Thompson, M. A. *Combined quantum mechanical and molecualr mechanical methods*; Washington, DC, 1988.

(12) Gao, J.; Amara, P.; Alhambra, C.; Field, M. J. *J. Phys. Chem. A* **1998**, *102*(24), 4714−4721.

(13) Dewar, M. J. S.; Zoebisch, E. G.; Healy, E. F.; Stewart, J. J. P. *J. Am. Chem. Soc.* **1985**, *107*, 3902−3909.

(14) Gonzalez-Lafont, A.; Truong, T. N.; Truhlar, D. G. *J. Phys. Chem.* **1991**, *95*, 4618−4627.

(15) Devi-kesavan, L. S.; Garcia-Viloca, M.; Gao, J. *J. Theor. Chem. Acc.* **2003**, *109*, 133−139.

(16) Poulsen, T. D.; Garcia-Viloca, M.; Gao, J.; Truhlar, D. G. *J. Phys. Chem. B* **2003**, *107*, 9567−9578.

(17) Ruiz-Pernia, J. J.; Silla, E.; Tuñón, I.; Martí, S.; Moliner, V. *J. Phys. Chem. B* **2004**, *108*, 8427−8433.

(18) Chuang, Y.; Corchado, J. C.; Truhlar, D. *J. Phys. Chem. A* **1999**, *103*, 1140−1149.

(19) Corchado, J. C.; Coitiño, E. L.; Chuang, Y.; Fast, P. L.; Truhlar, D. *J. Phys. Chem. A* **1998**, *102*, 2424−2438.

(20) Wigley, D. B.; Gamblin, S. J.; Turkenburg, J. P.; Dodson, E. J.; Piontek, K.; Muirhead, H.; Holbrook, J. J. *J. Mol. Biol.* **1992**, *223*, 317−335.

(21) Brooks, B. R.; Bruccoleri, R. E.; Olafson, B. D.; States, D. J.; Swaminathan, S.; Karplus, M. J. *J. Comput. Chem.* **1983**, *4*, 187−217.

(22) Jorgensen, W. L.; Chandrasekhar, J.; Madura, J.; Impey, R. W.; Klein, M. L. *J. Chem. Phys.* **1983**, *79*, 926−935.

(23) Freindorf, M.; Gao, J. *J. Comput. Chem.* **1996**, *17*, 386-395.

(24) Gao, J.; Xia, X. *Science* **1992**, *258*, 631−635.

(25) Frisch, M. J.; Trucks, G. W.; Schlegel, H. B.; Gill, P. M. W.; Johnson, B. G.; Robb, M. A.; Cheeseman, J. R.; Keith, T.; Peterson, G. A.; Montgomery, J. A.; Raghavachari, K.; Al-Laham, M. A.; Zakrzewski, V. G.; Ortiz, J. V.; Foresman, J. B.; Cioslowski, J.; Stefanov, B. B.; Nanayakkara, A.; Challacombe, M.; Peng, C. Y.; Ayala, P. Y.; Chen, W.; Wong, M. W.; Andres, J. L.; Replogle, E. S.; Gomperts, R.; Martin, R. L.; Fox, D. J.; Binkley, J. S.; Defrees, D. J.; Baker, J.; Stewart, J. P.; Head-Gordon, M.; Gonzalez, C.; Pople, J. A. Pittsburgh, PA, 1995.

(26) Reed, A. E.; Curtis, L. A.; Weinhold, F. *Chem. Rev.* **1988**, *88*, 899−926.

(27) Foster, J. P.; Weinhold, F. *J. Am. Chem. Soc.* **1980**, *102*, 7211−7218.

(28) Clarke, A. R.; Wigley, D. B.; Chia, W. N.; Barstow, D.; Atkinson, T.; Holbrook, J. J. *Nature* **1986**, *324*, 699−702.

CT050016L

JCTC Journal of Chemical Theory and Computation

Structural Optimization of Silver Clusters up to 80 Atoms with Gupta and Sutton-Chen Potentials

Xueguang Shao,* Xiaomeng Liu, and Wensheng Cai

Department of Chemistry, University of Science and Technology of China, Hefei, Anhui 230026, P.R. China

Received December 6, 2004

Abstract: The structure of silver clusters containing up to 80 atoms is optimized by using a random tunneling algorithm (RTA). The Gupta-type many-body potential and the Sutton-Chen (SC) many-body potential are used to account for the interactions among the atoms in the cluster, respectively. It is found that many of the structural configurations optimized with the two potentials are different, especially at a small size, and the structures with the Gupta potential are highly strained and apt to be the disordered motifs, whereas the structures with the SC potential are less-strained and the ordered morphologies are more favorable. Due to the difference of long-range interaction and pair contribution between two potentials, the assignment of outermost-shell atoms in decahedron and the missing atoms on the surface of the icosahedral motifs are also different for the two potentials. Furthermore, a new global minimum of the 68-atom silver cluster with the decahedral motif is found for both two potential models.

1. Introduction

Clusters provide a bridge between a few atoms or molecules and the bulk materials and show unique aspects of chemical and physical properties.[1] Therefore, studies on microclusters have increased rapidly in both experimental[2] and theoretical[3−5] investigations. In recent years, metal clusters gradually become a hotspot in cluster studies,[6] and silver clusters are particularly interesting.[7−17] First, silver clusters and small particles have practical importance in photography[7] and catalysis,[8] including their potential use in new electronic materials.[9] Second, adsorbates on silver surfaces seem to have a cluster counterpart observed by the enhanced Raman effect.[10] Also, silver clusters play an important role in metal alloy clusters.[11,16]

The geometry structure is a key property of a cluster in understanding the transition from the microscopic structure to the macroscopic structure of material. The most stable structure often possesses the lowest potential energy. Until now, large numbers of theoretical simulations have been done on the subject of silver clusters. For metal clusters, because of the *d* electrons and shell effect,[6] interaction between two atoms depends on not only distance but also local surroundings. Therefore, simple pairwise potential, such as Lennard-Jones (LJ) potential, is not suitable for metal clusters. It is widely recognized that empirical many-body potentials provide with good accuracy on the structural and thermodynamic properties of most transition metals. Wales et al.[18] also proved that many-body potential models play a crucial role in metal clusters.

Lots of empirical many-body potentials have been introduced for the global optimization of metal clusters, such as the Gupta potential,[19] the Sutton-Chen (SC) potential,[20,21] the Erkoc potential,[22] and so on. They had been widely used in the optimization of Ag, Au, Zn, Cd, Ni, and Cu[13−17,23−27] clusters. However, up to now, no single potential function model can totally reflect the structural motifs of silver clusters obtained by experiment. Therefore, the comparison of different potentials is necessary and important.

In this work, two commonly used potentials, the Gupta potential model and the SC potential model, were adopted in the global optimization of silver clusters to seek for further understanding of the potentials and the parameters in metal cluster simulation. The putative global minima of silver clusters up to 80 atoms are found by using an effective random tunneling algorithm (RTA)[28] with the two potential

* Corresponding author phone: +86-551-3606160; fax: +86-551-3601592; e-mail: xshao@ustc.edu.cn.

10.1021/ct049865j CCC: $30.25
Published on Web 06/07/2005

models. By comparison of the results, it is found that the assignments of outer-shell atoms are different in the decahedral and icosahedral structures for the two potentials. Furthermore, the growth patterns at smaller size are also found to be different. Moreover, a new global minimum with decahedral motif of 68-atom silver clusters is found for both two potentials.

2. Method

2.1. Potential Models. The Gupta potential[19] is based on the second moment approximation of the electron density of states in the tight-binding (TB) theory and is depicted in the following form

$$V = \frac{U_n}{2}\sum_{i=1}^{n} V_i \tag{1}$$

where n is the number of atoms in the cluster, and

$$V_i = \left[A\sum_{j\neq i}\exp\left[-p\left(\frac{r_{ij}}{r_0}-1\right)\right] - \left(\sum_{j\neq i}\exp\left[-2q\left(\frac{r_{ij}}{r_0}-1\right)\right]\right)^{1/2}\right] \tag{2}$$

r_{ij} is the distance between atoms i and j and r_0 is the equilibrium nearest-neighbor distance in the bulk metal. The parameters p and q represent the repulsive interaction range and the attractive interaction range, respectively. The parameter A is fitted to experimental values of the cohesive energy. U_n is a function of the atom number n. In eq 2, the first term gives a pairwise repulsion energy of the Born−Mayer type, and the second term represents the n-body attractive contribution.

The Sutton-Chen (SC) potential[20] is described by eq 3

$$E = \epsilon\sum_i\left[\frac{1}{2}\sum_{j\neq i}\left(\frac{\alpha}{r_{ij}}\right)^n - c\sqrt{\rho_i}\right] \tag{3}$$

where

$$\rho_i = \sum_{j\neq i}\left(\frac{\alpha}{r_{ij}}\right)^m \tag{4}$$

r_{ij} is the distance between atoms i and j. The constant α is the bulk lattice constant, c is a dimensionless parameter, ϵ is a parameter with dimensions of energy, and the exponents n and m are integers. They are also the key parameters determining the repulsive and the attractive interaction range. All of the above parameters are obtained by fitting to the 0 K properties of metals. Similarly, the potential energy is also given as a sum of a pairwise repulsion term and a many-body density dependent cohesion term.

The values of the parameters in the above equations used in the work are listed in Table 1.[14,25] In the following calculations, the reduced units with $r_0 = 1$, $U_n = 1$, $\epsilon = 1$, and $\alpha = 1$ are adopted.

2.2. Global Optimization Method. A global optimization algorithm called random tunneling algorithm (RTA)[28] is used to deal with the problem of searching the lowest minima of silver clusters. The RTA is derived from the terminal repeller unconstrained subenergy tunneling (TRUST) algorithm. TRUST is a deterministic global optimization approach that has been successfully used in exploratory seismology.[29,30] Based on the subenergy tunneling technique of TRUST, the stochastic algorithm RTA was developed for the purpose of solving multi- or high-dimensional global optimization problems. RTA has two optimization phases, a global phase and a local phase. The global phase is also termed the tunneling phase, in which the global sampled points are generated by a random tunneling technique. In the local phase, the gradient method limited memory BFGS (LBFGS)[31] is applied to these points, yielding various local optima. The procedure of RTA can be summarized in two steps, i.e., first, a population of configurations is generated covering the whole solution space and then the random tunneling and local minimization are executed circularly until the global minimum is found or the circulatory count reaches a preset value. The efficiency of RTA has been investigated with a set of standard multidimensional test functions.[28] By comparison of the RTA with some well-known global optimization methods, it was shown that the algorithm is efficient for searching the multidimensional problem. The algorithm was also applied to the structural optimization of LJ clusters and successfully located the lowest known minima containing up to 100 atoms.[28] Furthermore, all the known minima of LJ clusters with the size lower than 330 were successfully located by the parallelization of the RTA with the improved seeding technique.[32] A more detailed description of the algorithm can be found in refs 28 and 32.

Table 1. Parameters Used in the Gupta and Sutton-Chen Potential Models for Silver Clusters

Gupta potential			Sutton-Chen potential		
A	*p*	*q*	*c*	*n*	*m*
0.09944	10.12	3.37	144.41	12	6

3. Results and Discussion

3.1. The Optimization Results of Silver Clusters up to 80 Atoms. The optimized results, including the potential energies and the structural configurations of the global minima of the silver clusters up to 80 atoms, are summarized in Table 2. It can be seen that the structural motifs obtained with the two potential models are different at many cluster sizes. This implies that the potential model plays an important role in the structural configuration.

The structural motifs of silver clusters for each size containing up to 80 atoms optimized with the Gupta potential are shown in Figure 1. In the magic number sequence, such as the size $n = 13$, 19, 38, 55, and 75, the same structures are found by using the two potentials and also the same from $n = 6$ to 13. Except for the eight-atom dodecahedron, the structures between 6 and 13 lead to a growth sequence to a complete 13-atom icosahedron. From the size $n = 15$ to 47, most of the optimized structural motifs with the two potentials are different. It shows the different growth patterns of the silver clusters with the two potentials. This will be discussed in detail in the next section. From the size $n = 55$ to 75, silver clusters complete the transform from icosahedron

Table 2. Global Minima for Silver Clusters Optimized by the Gupta Potential and the Sutton-Chen Potential[a]

Gupta potential						Sutton-Chen potential					
N	energy	SD	N	energy	SD	N	energy	SD	N	energy	SD
3	−2.175900		42	−43.029888	dis	3	−1704.6905		42	−39301.6696	M
4	−3.211187		43	−44.110792	d4	4	−2601.8447		43	−40341.8543	M
5	−4.197445		44	−45.199405	dis	5	−3461.3452		44	−41310.9157	M
6	−5.236519		45	−46.249608	dis	6	−4378.8875		45	−42345.0912	d4
7	−6.238864		46	−47.359604	dis	7	−5271.2947		46	−43436.2827	M
8	−7.212287		47	−48.410801	dis	8	−6129.7564		47	−44405.1884	M
9	−8.230424		48	−49.549968	d4	9	−7048.7552		48	−45470.1069	d4
10	−9.249730		49	−50.614913	M	10	−7972.0971		49	−46521.2131	M
11	−10.258679		50	−51.701995	c	11	−8889.9627		50	−47518.6719	c
12	−11.305364		51	−52.725760	M	12	−9871.2458		51	−48522.4267	M
13	−12.472315	M	52	−53.867489	M	13	−10968.5082	M	52	−49616.1377	M
14	−13.406669	aM	53	−54.995380	M	14	−11798.8479	aM	53	−50706.4665	M
15	−14.455938	da	54	−56.142189	M	15	−12742.9841	aM	54	−51796.0777	M
16	−15.481217	dis	55	−57.255433	M	16	−13672.6475	aM	55	−52884.6808	M
17	−16.520324	dis	56	−58.205738	aM	17	−14606.3231	aM	56	−53756.6516	aM
18	−17.544132	dis	57	−59.256129	d5	18	−15535.3810	aM	57	−54700.1733	aM
19	−18.621146	aM	58	−60.361585	aM	19	−16595.0561	aM	58	−55753.8515	aM
20	−19.627271	aM	59	−61.395937	d5	20	−17510.9209	aM	59	−56751.4572	c
21	−20.678291	dis	60	−62.499086	aM	21	−18433.0300	aM	60	−57763.6760	aM
22	−21.757355	dis	61	−63.614111	aM	22	−19422.7209	dis	61	−58809.0448	aM
23	−22.809005	dis	62	−64.675376	d5	23	−20383.3977	dis	62	−59765.2180	aM
24	−23.835809	dis	63	−65.787033	d5	24	−21315.4208	h	63	−60822.3826	d5
25	−24.865922	dis	64	−66.946249	d5	25	−22339.6319	d3	64	−61925.6244	d5
26	−25.942226	dis	65	−67.985547	d5*	26	−23337.2211	h	65	−62903.7387	d5
27	−27.014674	dis	66	−69.074581	d5	27	−24284.3891	h	66	−63959.3105	d5
28	−28.082239	dis	67	−70.201134	d5	28	−25276.9501	M	67	−65011.2767	d5
29	−29.128461	dis	68	−71.273853	d5	29	−26263.2779	d4	68	−65983.2888	d5
30	−30.204287	dis	69	−72.334831	d5*	30	−27253.8536	d3	69	−67020.4042	d5
31	−31.260336	dis	70	−73.465005	d5	31	−28274.4371	d4	70	−68114.9462	d5
32	−32.331501	dis	71	−74.620916	d5	32	−29265.3320	M	71	−69216.6518	d5
33	−33.387556	d4*	72	−75.659788	d5*	33	−30274.9603	d4	72	−70171.4663	d5
34	−34.444690	dis	73	−76.752234	d5	34	−31231.7697	c	73	−71225.8547	d5
35	−35.536870	dis	74	−77.880111	d5	35	−32280.3945	d4	74	−72318.7243	d5
36	−36.587712	dis	75	−79.037373	d5	36	−33253.9352	M	75	−73421.0521	d5
37	−37.685406	d4	76	−80.075806	d5*	37	−34302.6067	c	76	−74375.6975	d5
38	−38.820496	f	77	−81.170022	d5	38	−35419.9804	f	77	−75430.9852	d5
39	−39.858635	f	78	−82.209914	d5*	39	−36364.8587	f	78	−76385.4318	d5
40	−40.896664	f	79	−83.337830	c	40	−37324.3708	M	79	−77456.0255	c
41	−41.960532	d4	80	−84.365961	d5	41	−38316.5698	c	80	−78414.6271	c

[a] The structural distribution (SD) are as follows: decahedral with *n* atoms along the decahedral axis (dn); icosahedral with a Mackay (M) or an anti-Mackay (aM) overlayer; disordered morphologies (dis); closed-packed fcc (f), hcp (h), a mixture of stacking sequences and twin planes (c); clusters with disclination axis (da). Different atom assignments are marked with * in the Gupta decahedral.

to decahedron, leading from the complete 55-atom Mackay icosahedron to the 75-atom Marks decahedron. This provides a validation of the structural transformation reported before.[17,18,25]

The comparison of the finite difference of the energy ΔE and the second finite difference of the energy $\Delta_2 E$ with the two potentials are plotted in Figure 3(a),(b). The ΔE and $\Delta_2 E$ have the form as follows

$$\Delta E(n) = E(n) - E_J(n) \tag{5}$$

where

$$E_J(n) = a + bn^{1/3} + cn^{2/3} + dn$$

$$\Delta_2 \mathrm{E}(n) = E(n+1) + E(n\text{-}1) - 2E(n) \tag{6}$$

$E_J(n)$ is a four-parameter fit of the energy of global minimum. $\Delta_2 E$ measures the stability of an *n*-atom cluster structure with respect to its neighboring cluster size. It can be seen that the Gupta and the SC results have similar shape. Valleys in ΔE and peaks in $\Delta_2 E$ are both in well accord with the magic numbers observed in mass spectra.[33] This also explains the stability of the magic number clusters. In a few different inflection points in the figure, different structural motifs or different atom assignment are found for the two potentials correspondingly.

At the 68-atom cluster size, a close-packed structure motif (Figure 2a) had been reported.[25] In this work, a new global minimum is found with a decahedral motif (Figure 2b) for both potentials. The energy of $(Ag)_{68}$ in this work with the SC potential is -65983.2888ϵ, which is lower than the energy -65980.5983ϵ in ref 25. Furthermore, the global minimum at 68-atom cluster size is also found to be the decahedral motif for the Gupta potential. Although the new

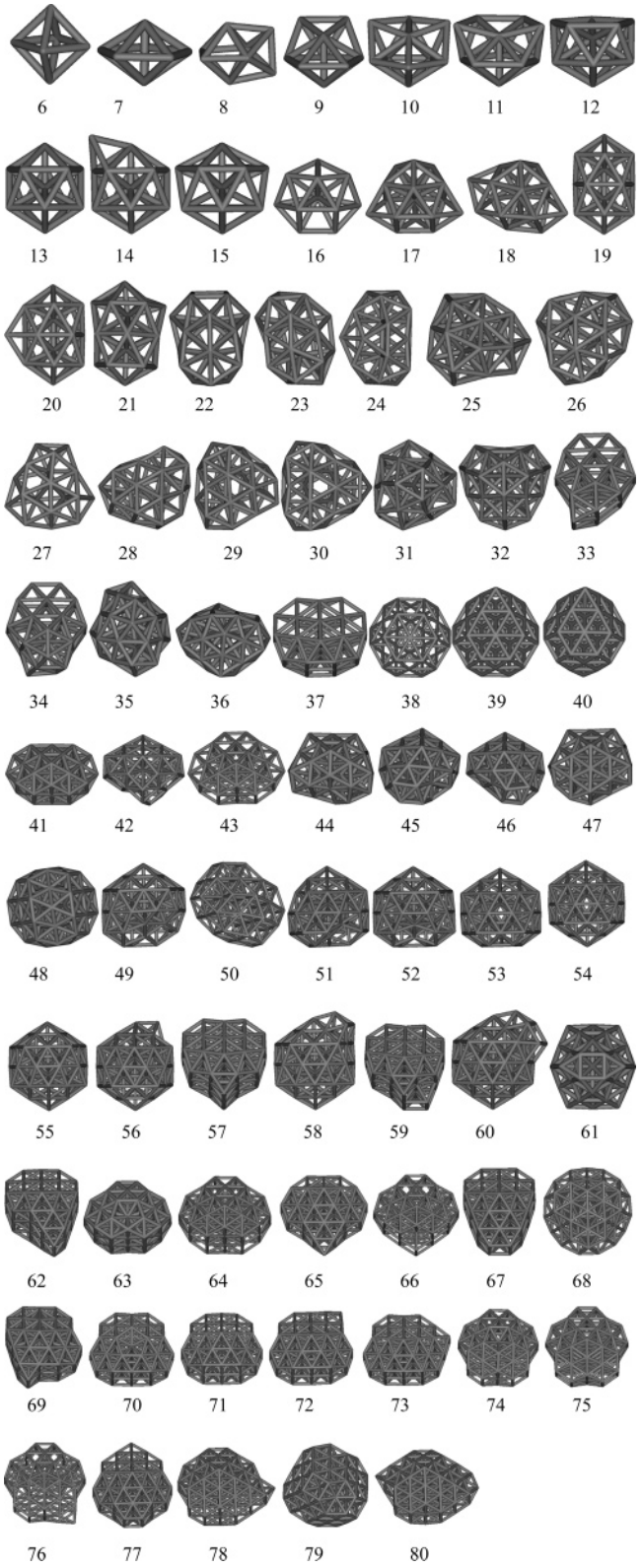

Figure 1. Structures of the global energy minima for silver clusters with the Gupta potential.

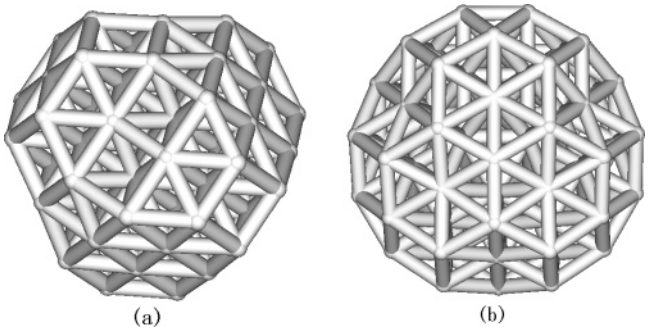

Figure 2. The global energy minima of a 68-atom silver cluster. (a) Closed-packed structure from ref 25. (b) Decahedral structure with the Sutton-Chen and the Gupta potential.

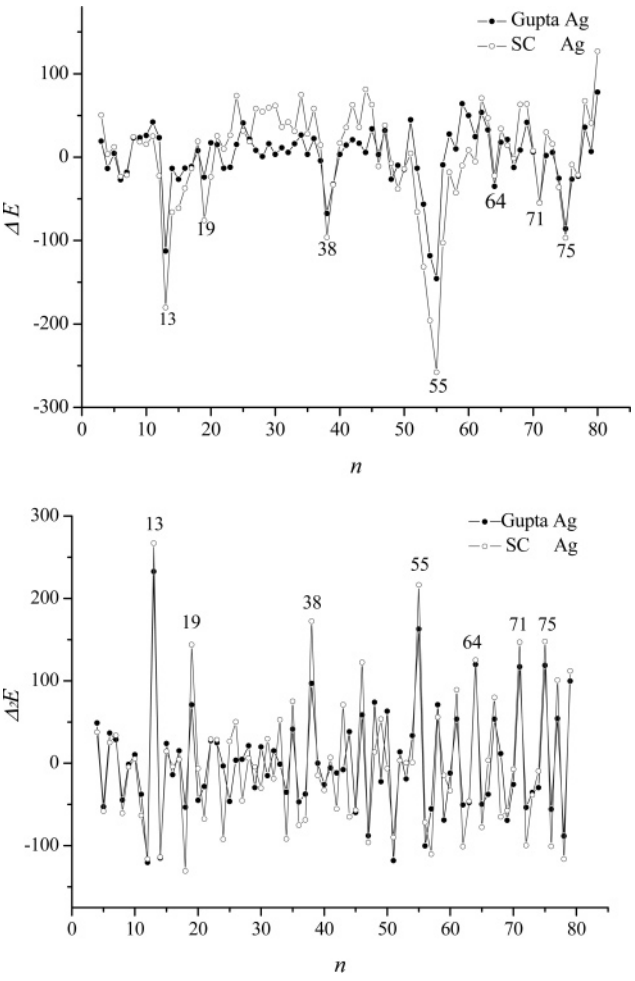

Figure 3. Stability analysis of Ag clusters: (a) the comparison of ΔE for two potentials and (b) the comparison of $\Delta_2 E$ for two potentials. $E_J(n) = 1.5859 - 1.54692n^{1/3} + 1.03058n^{2/3} - 1.23123n$ for the Gupta potential, where the coefficients are obtained by the best fit to the energies of the global minima; $E_J(n) = 940.63759 - 994.91694n^{1/3} + 1126.623n^{2/3} - 1201.40809n$ for the Sutton-Chen potential, the same way to get the coefficients.

global minimum is not so stable in comparison with the magic number clusters, it can be seen from Figure 3 that the new SC-68 cluster is actually in a relative stable position, especially compared with its isomer found before.

3.2. Growth Patterns at Smaller Size of Silver Clusters. From Table 2, it can be seen that a big difference between the results of the two potentials exist in the range $n = 15$ to 47. In this range, the silver cluster structures with the two potentials are different except the size $n = 19$, 20, 22, 38, and 39. Most of the Gupta results are disordered morphologies, but the SC results are mostly ordered structures. The

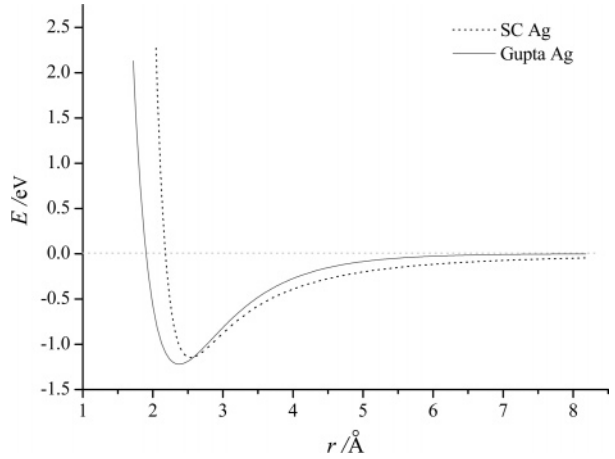

Figure 4. Plots of the Gupta potential and the Sutton-Chen potential for the diatomic interaction of silver clusters.

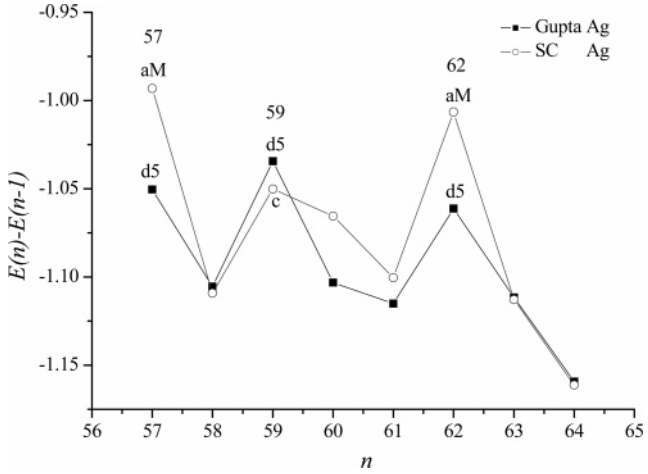

Figure 5. $E(n) - E(n-1)$ versus the number of the atom n from 57 to 64 for the Gupta potential and the Sutton-Chen potential.

15-atom cluster displays a unique motif with a disclination axis and the central atom connects with the other 14 atoms. As shown in Figure 1, from $n = 16$ to 18, the global minima of the Gupta potential are based on distorted decahedra, however, that of the SC potential grow with an anti-Mackay icosahedral pattern. The structures with the Gupta potential from $n = 21$ to 30 are based on the distorted face-sharing icosahedra and disordered in various ways. From the size $n = 42$ to 47, the Gupta clusters grow with a distorted incomplete Mackay icosahedral pattern except for the d4 decahedral motif of the 43-atom cluster.

The motifs of 19-, 20-, 22-, 38-, and 39-atom clusters in the range 15−47 (as shown in Figure 1) are the only five same structures optimized by the two potentials, corresponding to a 19-atom double icosahedron, a 38-atom truncated octahedron, and their derivants, respectively. The Gupta 41-atom global minimum is a decahedron with 4 atoms along the decahedral axis; however, the structure with the SC potential of the 41-atom silver cluster displays the close-packed configuration. Interestingly, this close-packed structure is also obtained by the Gupta potential with a little higher energy than the Gupta 41-atom global minimum.

Clearly, the structural configurations show the different growth patterns with the two potential models at smaller size. To explain the differences, the interactions of a dimer expressed by the two potentials are plotted in Figure 4. It can be seen that the bottom of the Gupta potential is broad, whereas it is narrow and sharp for the SC potential. The Gupta potential model can be more tolerant of strain than the SC potential model. The structures with the Gupta potential are highly strained, near spherical, and not based on regular packing, while those with the SC potential are less-strained, and the ordered morphologies are more favorable. Therefore, these differences bring to the different growth patterns. At smaller size, most of the structures obtained by the Gupta potential model display the disordered motifs because this configuration is highly strained, whereas the ordered motifs are more preferable for the SC potential model because it is less strained. Lots of theoretical[14,34,35] and experimental[36] works have been investigated to explain the growth patterns at smaller size. The studies suggest that the global minima show disordered structures at a smaller size, but they will disappear at a larger size. Most of the disordered structures are more spherical and have a larger number of nearest-neighbor contacts, and this makes them become more stable than the ordered morphologies. But it does not exist at larger size because of the energetic penalty for the strain scales with the volumes.[25,34]

3.3. Structural Motifs in the Transition from Icosahedron to Decahedron. As shown in Figure 1, there is transition from icosahedra to decahedra between the size $n = 55$ to 75. The SC results lead to a decahedral growth sequence from the 63-atom cluster and for the Gupta results from the size 62. Interestingly, the SC results complete the transform from 62 to 63; however, the Gupta structures alternate between the two conformations from 57 to 61. The structural stability in the transition is plotted as $E(n) - E(n-1)$ versus the number of the atoms n in Figure 5. Peaks in two curves correspond to the different structures optimized by the two potentials, which are both unstable. In the transition, two conformations have fierce competition, and their energy differences are extremely small. Therefore, different structural motifs of the global minimum are found. It can be found that the crossover between icosahedron and decahedron is a gradual process. Silver clusters in the transition may have the concurrent motifs until one motif becomes the preferential conformation.

3.4. Assignment of the Outermost-Shell Atoms in Decahedron or Icosahedron. At several sizes, the global minima of silver clusters with both two potentials are similar, such as the 33-, 65-, 69-, 72-, 76-, and 78-atom decahedra and the 51-, 52-, 53-, and 54-atom icosahedra. However their assignments of the outermost-shell atoms are different. The projection-drawings of 65-, 72-, 76-, 78-atom decahedral structures with the two potentials are shown in Figure 6. From the figure it can be found that the motifs optimized by the Gupta potential have a common property, i.e., the atom marked with a black ball is apt to be located in the furthest shell of the decahedral morphologies. Contrarily, the SC results display a distribution of another pattern, where the atom first fills in the vacancy of a relative inner shell of the decahedral motif. From Figure 4, it can be found that

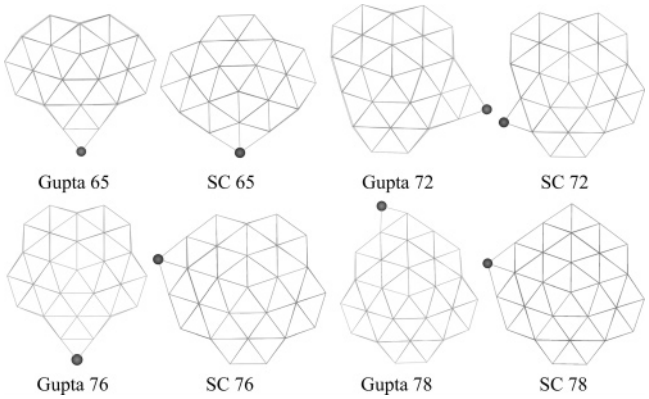

Figure 6. The projection drawings of different atom assignments on the decahedral surface of the 65-, 72-, 76-, and 78-atom Ag clusters.

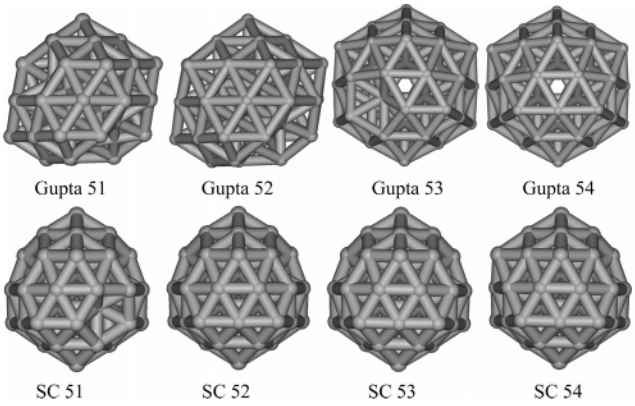

Figure 7. The structural motifs with different missing atoms on the icosahedral surface of 51-, 52-, 53-, and 54-atom Ag clusters.

the long-range interaction (far from the equilibrium position) of the SC potential model is stronger than that of the Gupta potential model. The energy of the Gupta potential model quickly approaches to zero and its long-range interaction is weak. Therefore, the strain energy play a more important role in the configuration of the Gupta potential than that of the SC potential.[34] The single atom (marked with a black ball in Figure 6) will easily grow to the furthest shell for the Gupta potential because in this configuration the four nearest atoms are in a plane so that there is almost no tensile force. On the contrary, under the SC potential, the single atom will be located not in the furthest shell but in the relative inner shell because the strain energy has not so much effect on its configuration. This should be the reason that causes the difference of the outermost-shell atom assignment in Figure 6.

Similarly, in the growth toward the 55-atom complete Mackay icosahedron, the structures obtained by the two potentials also display different patterns. The 51-, 52-, 53-, and 54-atom icosahedral structures described by the two potential models are shown in Figure 7. It can be seen that the missing atoms on the surface of the icosahedral motifs of the SC results are symmetrically distributed but that of the Gupta results are not. Interestingly, the structures of the Gupta results show the central atom vacancy (there is no atom at the center of icosahedron) at the sizes 53 and 54. In LJ clusters, there shows the central vacancy in icosahedron in the range $561 \leq n \leq 923$.[37] Also, the central vacancy has existed in different metal clusters.[15] The study finds that at large sizes, the icosahedron of silver cluster with central vacancy will become the dominant morphology. The global minimum of the 54-atom aluminum cluster also shows a hollow icosahedron.[38] The contraction of the inner shells for the icosahedral structure leads to a strong pressure on the central core. When the central atom energy is higher than that of the atom on edges and faces of the outermost shell, the central atom will escape from the central site to the surface sites of the outer layer. This reason causes the competition between hollow and centered icosahedral structures. Due to the difference of the pair contribution to the two potential models, which leads to the different compression to the center, there displays hollow and centered icosahedral motifs of 53- and 54-atom clusters for the Gupta potential and the SC potential, respectively.

4. Conclusion

Two empirical potentials frequently applied in the description of metal clusters are used to find the structural motifs of silver clusters with the atom numbers up to 80. By comparison of the results optimized with the Gupta and the SC potential, respectively, it was found that the potential model has a great influence on the global minima of silver clusters. The structures of the global minima for the two potentials have different growth patterns in the range 15−47. The structures with the Gupta potential are highly strained and apt to be the disordered motifs, whereas the structures with the SC potential are less-strained and the ordered morphologies are more favorable. Through the comparison of the structures in the transition from icosahedron to decahedron with the two potentials, it can be found that the crossover between icosahedron and decahedron is a gradual process. Different structures in this transition have fierce competition that there may have the concurrent motifs. Due to the reason that two potentials have different long-range interactions and have a different pair contribution, atom assignments on the surface of decahedra and icosahedra are different. At the 68-atom silver cluster, a new lowest energy minimum of decahedral motif is found by using the two potentials.

Acknowledgment. This study is supported by the outstanding youth fund (No. 20325517) from National Natural Scientific Foundation of China (NNSFC) and the Teaching and Research Award Program for Outstanding Young Teachers (TRAPOYT) in higher education institutions of the Ministry of Education (MOE), P. R. China.

References

(1) Wales, D. J.; Scheraga, H. A. *Science* **1999**, *285*, 1368−1372.

(2) Chesnovsky, O.; Taylor, K. J.; Conceicao, J.; Smalley, R. E. *Phys. Rev. Lett.* **1990**, *64*, 1785−1788.

(3) Shao, X. G.; Cheng, L. J.; Cai, W. S. *J. Comput. Chem.* **2004**, *25*, 1693−1698.

(4) Xiang, Y. H.; Jiang, H. Y.; Cai, W. S.; Shao, X. G. *J. Phys. Chem. A* **2004**, *108*, 3586−3592.

(5) Hartke, B. *Struct. Bond.* **2004**, *110*, 33−53.

(6) Alonso, J. A. *Chem. Rev.* **2000**, *100*, 637−677.

(7) Eachus, R. S.; Marchetti, A. P.; Muenter, A. A. *Annu. Rev. Phys. Chem.* **1999**, *50*, 117−144.

(8) Koretsky, G. M.; Knickelbein, M. B. *J. Chem. Phys.* **1997**, *107*, 10555−10566.

(9) Kim, S. H.; Medeiros-Ribeiro, G.; Ohlberg, D. A. A.; Stanley Williams, R.; Heath, J. R. *J. Phys. Chem. B* **1999**, *103*, 10341−10347.

(10) Chan, W. T.; Fournier, R. *Chem. Phys. Lett.* **1999**, *315*, 257−265.

(11) Lee, I.; Han, S. W.; Kim, K. *Chem. Commun.* **2001**, *18*, 1782−1783.

(12) Fournier, R. *J. Chem. Phys.* **2001**, *115*, 2165−2177.

(13) Erkoc, S.; Yilmaz, T. *Physica E* **1999**, *5*, 1−6.

(14) Michaelian, K.; Rendon, N.; Garzon, I. L. *Phys. Rev. B* **1999**, *60*, 2000−2010.

(15) Mottet, C.; Treglia, G.; Legrand, B. *Surf. Sci. Lett.* **1997**, *383*, L719−L727.

(16) Johnston, R. L. *Dalton Trans.* **2003**, 4193−4207.

(17) Baletto, F.; Mottet, C.; Ferrando, R. *Phys. Rev. B* **2001**, *63*, 155408(10).

(18) Uppenbrink, J.; Wales, D. J. *J. Chem. Phys.* **1992**, *96*, 8520−8534.

(19) Gupta, R. P. *Phys. Rev. B* **1981**, *23*, 6265−6270.

(20) Sutton, A. P.; Chen, J. *Philos. Mag. Lett.* **1990**, *61*, 139−146.

(21) Rafiitabar, H.; Sutton, A. P. *Philos. Mag. Lett.* **1991**, *63*, 217−224.

(22) Erkoc, S. *Phys. Status Solidi B* **1992**, *171*, 317−324.

(23) Darby, S.; Mortimer-Jones, T. V.; Johnston, R. L.; Roberts, C. *J. Chem. Phys.* **2002**, *116*, 1536−1550.

(24) Baletto, F.; Ferrando, R.; Fortunelli, A.; Montalenti, F.; Mottet, C. *J. Chem. Phys.* **2002**, *116*, 3856−3863.

(25) Doye, J. P. K.; Wales, D. J. *New J. Chem.* **1998**, *22*, 733−744.

(26) Cagin, T.; Dereli, G.; Uludogan, M.; Tomak, M. *Phys. Rev. B* **1999**, *59*, 3468−3473.

(27) Cleri, F.; Rosato, V. *Phys. Rev. B* **1993**, *48*, 22−33.

(28) Jiang, H. Y.; Cai, W. S.; Shao, X. G. *Phys. Chem. Chem. Phys.* **2002**, *4*, 4782−4788.

(29) Barhen, J.; Protopopescu, V.; Reister, D. *Science* **1997**, *276*, 1094−1097.

(30) Cetin, B. C.; Barhen, J.; Burdick, J. W. *J. Optimiz. Theory App.* **1993**, *77*, 97−126.

(31) Liu, D. C.; Nocedal, *J. Math. Progm.* **1989**, *45*, 503−528.

(32) Shao, X. G.; Jiang, H. Y.; Cai, W. S. *J. Chem. Inf. Comput. Sci.* **2004**, *44*, 193−199.

(33) Clemenger, K. *Phys. Rev. B* **1985**, *32*, 1359−1362.

(34) Doye, J. P. K.; Wales, D. J.; Berry, R. S. *J. Chem. Phys.* **1995**, *103*, 4234−4249.

(35) Wetzel, T. L.; DePristo, A. E. *J. Chem. Phys.* **1996**, *105*, 572−580.

(36) Alameddin, G.; Hunter, J.; Cameron, D.; Kappes, M. *Chem. Phys. Lett.* **1992**, *192*, 122−128.

(37) Shao, X. G.; Xiang, Y. H.; Cai, W. S. *Chem. Phys*. **2004**, *305*, 69−75.

(38) Lioyd, L. D.; Johnston, R. L.; Roberts, C.; Mortimer-Jones, T. V. *Chem. Phys. Chem.* **2002**, *3*, 408−415.

CT049865J